

# **The design and synthesis of supramolecular hosts for biological anion recognition**

Hiral A. Kotak



University College London  
Department of Chemistry

*Thesis for the degree of Doctor of Philosophy*

November 2024

## **Declaration**

I, Hiral A. Kotak, confirm that the work presented in my thesis is my own. Where information has been derived from other sources, I confirm that this has been indicated in the thesis.

## Abstract

Anions are essential in everyday life, especially within biological systems. Their significance spans from simple anions used for pH regulation to larger anionic structures like phospholipids and deoxyribonucleic acid (DNA). Consequently, the binding of anions has the potential to aid in the treatment of channelopathies – diseases associated with dysfunctional ion channels. However, designing anion-binding molecules can be challenging, although recent advancements with metal-organic complexes have shown promise.

Chapter 2 details the design and synthesis of the tripodal iron(II) complex **52**, which incorporates urea groups for anion binding. The anion-binding properties of this metal-organic complex were evaluated against various anions, demonstrating that complex **52** effectively binds several simple anions, including chloride and benzoate. This prompted an investigation into its indicator displacement properties; complex **52** quenched the fluorescence of multiple fluorophores, some of which could be displaced by introducing simple anions. Furthermore, complex **52** displayed potential anion transport capabilities, particularly in chloride/nitrate antiport and  $M^+$ /chloride symport.

Chapter 3 delves deeper into tripodal anion-binding motifs, detailing efforts to synthesise enantiopure tripodal metal-organic complexes for the binding of chiral anions. The synthesis of chiral tripodal amines succeeded through the reductive amination of phenylalanine-derived aldehydes. However, the creation of metal-organic complexes presented difficulties, with spectroscopic analysis indicating that only a small quantity of chiral Zn(II) complexes might have formed. Ultimately, the crude product was neither chemically nor enantiomerically pure. Hence, a chiral cleft for chiral guest recognition was not synthesised.

Chapter 4 investigates supramolecular self-associating amphiphiles (SSAs) that exhibit antibacterial properties, using computational chemistry to focus on their interactions with various lipid headgroups. SSAs **75** and **78** displayed a preference for binding to bacterial-type lipid headgroups over mammalian-type lipid headgroups, highlighting the importance of forming SSA-lipid complexes in the mode of action of SSAs against bacteria.

## Impact statement

The research presented in this thesis explores various applications of host-guest binding, both in synthetic and computational contexts. Host-guest binding is a fundamental concept across several disciplines, with the binding of anions being particularly significant in biological and environmental chemistry.

In Chapter 2, a novel metal-organic anionophore (**52**) was synthesised using subcomponent self-assembly, a method that can be easily tailored to achieve a desired solubility by altering the metal salt. The successful synthesis of **52** has established a foundation for the potential development of water-soluble metal-organic anionophores. It was demonstrated that **52** can bind to several anions, including chloride and benzoate. It was then revealed that **52** could bind anionic fluorophores and subsequently be displaced by adding another anion. Although a completely suitable fluorophore was not found, this research provides the foundation for **52** (or similar molecules) to be used in molecular sensing applications. Molecular sensors and probes allow for the detection of analytes and their quantification, too, as fluorescence intensity can be measured. This can be useful for *in vivo* detection of biological analytes or in detecting anions in wastewater. **52** may have also demonstrated anion transport properties, which may help develop new anion-binding molecules for the treatment of channelopathies – diseases characterised by malfunctioning ion channels.

Chapter 4 focused on the binding of hosts, specifically supramolecular self-associating amphiphiles (SSAs), to various lipid headgroups *via* computational chemistry to support experimental work that demonstrated their potential use as antibacterial agents. It was found that SSAs preferentially bound to bacterial-type lipid headgroups, suggesting they possess selective toxicity against bacteria. This work lays a foundation upon which further studies can be done into using SSAs as antibiotics. Ultimately, the development of a new antibacterial agent is crucial in the ongoing battle against antimicrobial resistance.



# UCL Research Paper Declaration Form 1

referencing the doctoral candidate's own published work(s)

## 1. For a research manuscript that has already been published

### a) What is the title of the manuscript?

Metal-organic ion transport systems

### b) Please include a link to or doi for the work

<https://doi.org/10.1016/j.ccr.2022.214705>

### c) Where was the work published?

Coordination Chemistry Reviews

### d) Who published the work? (e.g. OUP)

Elsevier B.V

### e) When was the work published?

July 2022

### f) List the manuscript's authors in the order they appear on the publication

Kylie Yang<sup>‡</sup>, Hiral A. Kotak<sup>‡</sup>, Cally J. E. Haynes\*

### g) Was the work peer reviewed?

Yes.

### h) Have you retained the copyright?

No, but this paper was published under a [Creative Commons license \(CC BY 4.0\)](#).

### i) Was an earlier form of the manuscript uploaded to a preprint server? (e.g. medRxiv). If 'Yes', please give a link or doi)

No, but this paper was published under a [Creative Commons license \(CC BY 4.0\)](#).

## 2. For multi-authored work, please give a statement of contribution covering all authors

**KY:** Conceptualisation, writing – original draft, writing – review & editing; **HAK:** Conceptualisation, writing – original draft, writing – review & editing; **CJEH:** Conceptualisation, writing – original draft, writing – review & editing.

**3. In which chapter(s) of your thesis can this material be found?**

Chapter 2

**4. e-Signatures confirming that the information above is accurate** (this form should be co-signed by the supervisor/ senior author unless this is not appropriate, e.g. if the paper was a single-author work)

*Candidate*

Hiral A. Kotak

*Date:*

08/11/2024

*Supervisor/ Senior Author (where appropriate)*

Cally J. E. Haynes

*Date*

08/11/2024

## UCL Research Paper Declaration Form 2

referencing the doctoral candidate's own published work(s)

### 1. For a research manuscript that has already been published

#### a) What is the title of the manuscript?

Establishing the selective phospholipid membrane coordination, permeation and lysis properties for a series of 'druggable' supramolecular self-associating antimicrobial amphiphiles

#### b) Please include a link to or doi for the work

<https://doi.org/10.1039/D2SC02630A>

#### c) Where was the work published?

Chemical Science

#### d) Who published the work? (e.g. OUP)

Royal Society of Chemistry

#### e) When was the work published?

August 2022

#### f) List the manuscript's authors in the order they appear on the publication

Jessica E. Boles, Charlotte Bennett<sup>‡</sup>, Jennifer Baker<sup>‡</sup>, Kira L. F. Hilton, Hiral A. Kotak, Ewan R. Clark, Yifan Long, Lisa J. White, Hin Yuk Lai, Charlotte K. Hind, J. Mark Sutton, Michelle D. Garrett, Anne Cheasty, Jose L. Ortega-Roldan, Mark Charles,\* Cally J. E. Haynes \* and Jennifer R. Hiscock\*

#### g) Was the work peer reviewed?

Yes.

#### h) Have you retained the copyright?

No, but this paper was published under a [Creative Commons license \(CC BY 3.0\)](#).

#### i) Was an earlier form of the manuscript uploaded to a preprint server? (e.g. medRxiv). If 'Yes', please give a link or doi)

No, but this paper was published under a [Creative Commons license \(CC BY 3.0\)](#).

**2. For multi-authored work, please give a statement of contribution covering all authors**

**JEB:** investigation; validation; writing – original draft, review & editing. **CB** and **JB:** investigation; validation; writing – review & editing. **KLFH:** investigation; validation; writing – original draft, review & editing. **HAK:** investigation; validation; writing – original draft, review & editing. **ERC:** validation; writing – original draft, review & editing. **YL:** investigation; validation. **LJW:** investigation; writing – review & editing. **HYL:** investigation; validation. **CKH:** investigation; validation; writing – review & editing. **JMS:** validation; writing – review & editing. **MDG:** validation; writing – review & editing. **AC:** supervision; validation; writing – review & editing. **JLOR:** supervision; validation; writing – review & editing. **MC:** validation; writing – review & editing. **CJEH:** investigation; validation; writing – review & editing. **JRH:** conceptualization; funding acquisition; project administration; supervision; writing – original draft, review & editing.

**3. In which chapter(s) of your thesis can this material be found?**

Chapter 4

**4. e-Signatures confirming that the information above is accurate** (this form should be co-signed by the supervisor/ senior author unless this is not appropriate, e.g. if the paper was a single-author work)

*Candidate*

Hiral A. Kotak

*Date:*

08/11/2024

*Supervisor/ Senior Author (where appropriate)*

Mark Charles, Jennifer R. Hiscock, Cally J. E. Haynes

*Date*

08/11/2024

## Publications

Works included in this thesis:

- Kylie Yang<sup>‡</sup>, Hiral A. Kotak<sup>‡</sup> and Cally J. E. Haynes. “Metal-organic ion transport systems.” *Coordination Chemistry Reviews*, 2022, **470**, 214705. This material is referenced in Chapter 2.
- Jessica E. Boles, Charlotte Bennett<sup>‡</sup>, Jennifer Baker<sup>‡</sup>, Kira L. F. Hilton, Hiral A. Kotak, Ewan R. Clark, Yifan Long, Lisa J. White, Hin Y. Lai, Charlotte K. Hind, J. Mark Sutton, Michelle D. Garrett, Anne Cheasty, Jose L. Ortega-Roldan, Mark Charles, Cally J. E. Haynes and Jennifer R. Hiscock. “Establishing the selective phospholipid membrane coordination, permeation and lysis properties for a series of ‘druggable’ supramolecular self-associating antimicrobial amphiphiles.” *Chem. Sci.*, 2022, **13**, 9761–9773. Original material from this paper is included in Chapter 4.

Additional publications produced during this PhD project but not included in this thesis:

- Hiral A. Kotak, Nicholas G. White, Cally J. E. Haynes. “(Self) assembled news: recent highlights from the supramolecular chemistry literature (Quarter 2, 2023).” *Supramolecular chemistry*, 2023, **34(2)**, 61–63.
- Kylie Yang, Lana C. Lee, Hiral A. Kotak, Evelyn R. Morton, Soo Mei Chee, Duy P. M. Nguyen, Alvaro Keskküla, Cally J. E. Haynes. “High-throughput and Automated Anion Transport Assays.” *ChemRxiv*, 2024. This content is a preprint and has not been peer-reviewed.

<sup>‡</sup> denotes equal contribution.

## Contributions

Some computational calculations for SSA **78** included in Chapter 4 were contributed by Yifan Long, a master’s student in the Haynes group in 2021.

## Acknowledgements

This PhD has definitely been a team effort, and I'd like to acknowledge everyone involved.

First and foremost, I'd like to thank my supervisor, Dr Cally Haynes, for her help and guidance, whether chemistry-related or otherwise. Thank you for your support and belief, especially when I struggled to find it myself.

These four years would not have been the same without Ana, Evie and Kylie. Ana, thanks for indulging my ridiculous and hypothetical scenarios, all the dancing and being as excited about spin class as I am. Evie, thanks for being such a fun fumehood buddy and putting up with my repetitive music. Kylie, I am so grateful for everything you've done for me. Thank you for your help in the lab, especially the fluorescence studies, and for showing me the kindness I needed. Thank you to our wonderful master's students who kept the lab fun with their shenanigans and laughter. A special thanks to Alvaro for being such a wonderful friend. Thank you for your compassion and all the Beyoncé you played in the lab.

Thanks to (the past and present members of) the Howorka group for their help and advice, falcon tubes and lunchtime hilarity. Thanks to the Anderson group for answering my silly synthesis questions and letting me 'borrow' the potassium permanganate solution and blast shield.

I want to express gratitude to the academics and university staff involved. Thank you to Prof. Jen Hiscock for collaborating on the SSAs project and Dr Ewan Clark for being patient with me and teaching me about computational chemistry. I'd like to thank Dr Kersti Karu for her help with MS and Dr Abil Aliev for his help with NMR. A big thanks to Ethan Powell for obtaining the CD spectra, Dr Andy Surman for the polarimeter help and Prof. Bob Schroeder for allowing me to use the microwave. Thanks to Tony in stores for his help and for the boxes!

Finally, I'd like to thank my friends and family for keeping me afloat. Racquel, thank you so much for your kindness, the motivating text messages, and our lovely walks. Shiv and Leo, thank you for being great WFH companions. Mum and Dad, thank you for your love and unwavering support; તમારો ઘણો આભાર.

# Table of Contents

<i>List of abbreviations</i> .....	14
<i>List of figures</i> .....	17
<i>List of schemes</i> .....	22
<i>List of tables</i> .....	23
<i>List of equations</i> .....	24
<b>1 Introduction</b> .....	<b>26</b>
<b>1.1 Anion binding</b> .....	<b>26</b>
1.1.1 Challenges .....	27
1.1.2 Dual hydrogen bonding motifs .....	28
1.1.3 Strategies to improve anion binding .....	32
<b>1.2 Anion transport</b> .....	<b>39</b>
1.2.1 Ion transport in cell membranes.....	39
1.2.2 Common ways to test anion transport.....	40
<b>1.3 Metal-organic complexes</b> .....	<b>45</b>
4.3.1 Coordination-driven self-assembly of metal-organic complexes.....	45
1.3.2 Subcomponent self-assembly.....	46
<b>1.4 Thesis overview</b> .....	<b>51</b>
<b>2 Functionalised ligands for anionic binding clefts</b> .....	<b>52</b>
<b>2.1 Metal-organic complexes as anionophores</b> .....	<b>52</b>
<b>2.2 Metal-organic complexes and indicator displacement assays</b> .....	<b>56</b>
2.2.1 Fluorescence mechanisms.....	56
2.2.2 Metal-organic complexes for IDAs.....	58
<b>2.3 Research aims</b> .....	<b>63</b>
<b>2.4 Ligand synthesis</b> .....	<b>63</b>
2.4.1 Sonogashira route .....	63
2.4.2 CuAAC route.....	66
<b>2.5 Self-assembled complexes in acetonitrile</b> .....	<b>73</b>
2.5.1 Synthesis of squaramide-containing self-assembled complexes.....	74
2.5.2 Synthesis of urea-containing self-assembled complexes .....	76
<b>2.6 Guest binding studies</b> .....	<b>77</b>
2.6.1 Guest screening.....	77
2.6.2 NMR titrations.....	80
<b>2.7 Indicator displacement assay</b> .....	<b>84</b>
<b>2.8 Anion transport studies</b> .....	<b>91</b>
<b>2.9 Conclusions and future work</b> .....	<b>96</b>
<b>3 Chiral amines for enantiopure complexes</b> .....	<b>97</b>
<b>3.1 Chiral clefts</b> .....	<b>97</b>

3.2	Metal-organic complexes and chirality.....	99
3.3	Research aims .....	102
3.4	Chiral amine synthesis .....	103
3.4.1	Aziridine route .....	103
3.4.2	Amino-aldehyde route .....	107
3.5	Self-assembled complexes .....	109
3.6	Conclusions .....	117
4	<i>Interactions between SSAs and lipid headgroups.....</i>	<i>118</i>
4.1	Introduction to SSAs .....	118
4.2	SSAs against bacteria .....	119
4.3	Lipid bilayers .....	122
4.4	Research aims .....	123
4.5	Methodology.....	124
4.5.1	m-lipids .....	124
4.5.2	Computational method.....	125
4.5.3	Computational workflow .....	127
4.6	Results and discussion .....	129
4.6.1	SSA 78 .....	129
4.6.2	SSA 75 .....	134
4.6.3	Comparing both SSAs .....	137
4.7	Conclusions and future outlooks .....	138
5	<i>Thesis recap and broader outlooks.....</i>	<i>139</i>
5.1	Metal-organic complexes for anion binding.....	139
5.1.1	Recap .....	139
5.1.2	Current work in this field.....	140
5.2	SSAs .....	141
5.2.1	Recap .....	141
5.2.2	Current work on SSAs .....	141
5.3	Broader outlook .....	142
6	<i>Experimental.....</i>	<i>144</i>
6.1	General synthetic remarks.....	144
6.2	Synthetic procedures .....	145
6.2.1	Synthetic procedures for Chapter 2.....	145
6.2.1	Synthetic procedures for Chapter 3.....	156
6.3	Guest binding screens.....	162
6.4	<sup>1</sup> H NMR titrations .....	163
6.5	Vesicle studies.....	164
6.5.1	General remarks.....	164
6.5.2	Vesicle preparation.....	164
6.5.3	Chloride/nitrate antiport experiments .....	164



6.5.4	Lucigenin assay .....	165
6.5.5	Cationophore-coupled assay .....	165
6.5.6	Sodium/chloride symport experiments .....	165
<b>6.6</b>	<b>Fluorescence studies .....</b>	<b>166</b>
6.6.1	Fluorimeter measurements.....	166
6.6.2	Plate reader measurements.....	166
<b>6.7</b>	<b>Computational calculations .....</b>	<b>167</b>
<b>7</b>	<b>References .....</b>	<b>168</b>
<b>Appendix</b> .....		<b>178</b>
<b>A1 Chapter 2 data</b> .....		<b>178</b>
A1.1	<sup>1</sup> H NMR .....	178
A1.2	<sup>13</sup> C NMR .....	201
A1.3	IR 215 .....	
A1.4	MS.....	224
A1.5	Guest screening data.....	239
A1.6	Titration data .....	256
A1.7	Fluorescence data .....	262
A1.8	Vesicles studies data .....	264
<b>A2 Chapter 3 data</b> .....		<b>269</b>
A2.1	<sup>1</sup> H NMR .....	269
A2.2	<sup>13</sup> C NMR .....	289
A2.3	IR 295 .....	
A2.4	MS.....	301
<b>A3 Chapter 4 data</b> .....		<b>309</b>
A3.1	Cartesian coordinates calculated using ab initio methods .....	310
A3.2	Cartesian coordinates calculated using DFT methods.....	339

## List of abbreviations

- 3D – three-dimensional
- 7ACC-1 – 7-diethylaminocoumarin-3-carboxylic acid
- ATP – adenosine triphosphate
- Boc – *tert*-butoxycarbonyl
- BzO – benzoate
- cAMP – cyclic adenosine monophosphate
- CD – circular dichroism
- CFTR – cystic fibrosis transmembrane regulator
- CL – cardiolipin
- CuAAC – copper(I)-catalysed azide-alkyne cycloaddition
- DFT – density functional theory
- DIPEA – N,N-diisopropylethylamine
- DMF – dimethylformamide
- DMPC – 1,2-dimyristoyl-*sn*-glycero-3-phosphocholine
- DMSO – dimethylsulfoxide
- DNA – deoxyribonucleic acid
- DOPC – 1,2-dioleoyl-*sn*-glycero-3-phosphocholine
- DPA – dipicolylamine
- DPPC – 1,2-dipalmitoylphosphatidylcholine
- dppp – bis(diphenylphosphino)propane
- *E. coli* – *Escherichia coli*
- ESI – electrospray ionisation
- EY – Eosin Y
- EYPC – egg yolk phosphatidylcholine
- *fac* – facial
- FRET – Förster resonance energy transfer
- GABA -  $\gamma$ -aminobutyric acid
- Glu – gluconate
- GSH – glutathione
- h – hours

- HF – Hartree-Fock
- HINA – 3-hydroxyisonicotinaldehyde
- HPTS – 8-hydroxypyrene-1,3,6-trisulfonic acid (aka pyranine)
- ICT – intramolecular charge transfer
- IDA – indicator displacement assay
- IEDDA – inverse electron demand Diels Alder
- ISE – ion-selective electrode
- $K_a$  – association constant
- LUV – large unilamellar vesicles
- *mer* – meridional
- MLV – multilamellar vesicles
- MOC – metal-organic cage
- MOF – metal-organic framework
- *MRSA* – *methicillin-resistant Staphylococcus aureus*
- MVV – multivesicular vesicles
- NMR – nuclear magnetic resonance
- OTf – triflate
- PC – phosphatidylcholine
- PE – phosphatidylethanolamine
- PG – phosphatidylglycerol
- POPC – 1-palmitoyl-2-oleoyl-sn-glycero-3-phosphocholine
- PS – phosphatidylserine
- RNA – ribonucleic acid
- RT – room temperature
- SCC – supramolecular coordination complexes
- SEM – scanning electron microscopy
- SMA – styrene maleic anhydride
- SMD – solvent model density
- SSA – supramolecular self-associating amphiphiles
- SUV – small unilamellar vesicles
- TBA – tetrabutylammonium
- TFA – trifluoroacetic acid

- THF – tetrahydrofuran
- TLC – thin layer chromatography
- TMS – trimethylsilyl
- TREN – tris(2-aminoethyl)amine
- Ts – tosyl
- UV – ultraviolet
- XRD – x-ray diffraction

## List of figures

Figures 1.3, 1.21, 1.23, 1.24, 1.25, 1.26, 1.28, 2.26, and 3.5 were created with BioRender.

- 1.1 Metanil yellow, an anionic dye
- 1.2 Hofmeister series of anions
- 1.3 Examples of different anion geometries. Dark green = chlorine; black = carbon; blue = nitrogen; red = oxygen; yellow = boron; orange = phosphorus; light green = fluorine.
- 1.4 Diarylurea host containing nitro groups in the meta position for guest binding.
- 1.5 (Thio)urea anion receptors synthesised by Wilcox and co-workers.
- 1.6 Naphthalimide-containing thioureas synthesised by Pfeffer and co-workers.
- 1.7 Urea **7a** and squaramide **7b** synthesised by Fabrizzi *et al.*
- 1.8 Squaramides as ‘molecular valves’ to regulate chloride binding.
- 1.9 General structures of deltamides (left) and croconamides (right).
- 1.10 Spherand **9** and podand **10** synthesised by Cram and co-workers.
- 1.11 a) Isophthalamide **11** and b) dipicolineamide **12** synthesised by Crabtree *et al.*; c) boron-functionalised isophthalamide **13** synthesised by Smith and co-workers.
- 1.12 Predominant conformations of isophthalamides.
- 1.13 Hydroxylated isophthalamide **14** synthesised by Gale and colleagues.
- 1.14 Nitro-containing isophthalamides **15** and **16** synthesised by Gale and colleagues.
- 1.15 Dipicolineamide **17** synthesised by Gokel *et al.*
- 1.16 Tripodal clefts **18**, **19**, and **20** generated by Reinhoudt *et al.*
- 1.17 Tripodal amide receptors **21** and **22** used in fluoride recognition.
- 1.18 Proposed binding of ATP to tripodal cleft **23**.
- 1.19 Tris-ureas **24** and **25** synthesised by Custelcean *et al.*
- 1.20 Proposed binding of sulfate ions to (thio)urea groups on tripodal cleft **26**.
- 1.21 Series of tris-ureas and tris-thioureas screened for anion transport.
- 1.22 Transmembrane transport of ions through either uniport, symport or antiport mechanisms.
- 1.23 Structures of a) POPC, b) DPPC, c) DOPC.
- 1.24 Cartoon representation of chloride-selective ISE. Purple = synthetic anionophore.
- 1.25 Cartoon representation of HPTS assay. F = HPTS.

- 1.26 Cartoon representation of lucigenin assay. Purple membrane = incorporation of synthetic anionophore into vesicles; F = lucigenin, quenched upon adding chloride.
- 1.27 Example of subcomponent self-assembly with Fe(II) salt to form  $M_4L_6$  cage.
- 1.28 Fe(II) pentafoil knots synthesised by Leigh and co-workers. Purple = Fe(II).
- 1.29 Anion exchange to induce phase transfer between ethyl acetate and water. Purple sphere = cage.
- 1.30 Self-assembly of water-soluble Zn(II) and Cd(II) complexes from tritopic subcomponents.
- 2.1 Metal-induced preorganised anion receptor synthesised **28** by Caltagirone and colleagues.
- 2.2 Anionophores Pd(dppp)<sub>2</sub>Cl<sub>2</sub> (**29**) and Pd(dppp)<sub>2</sub>(OTf)<sub>2</sub> (**30**) synthesised by Tecilla and co-workers.
- 2.3 Platinum anionophores **31**, **32**, **33** and **34** synthesised by Gale and co-workers.
- 2.4 Iridium anionophores **35** and **36** containing imidazole groups for anion binding.
- 2.5 Gold complexes reduced by glutathione to reveal anion binding site. GSH = glutathione.
- 2.6 a) Cartoon representation of indicator displacement assays; b) cartoon representation of the expected fluorescence increase upon addition of guest. Purple = host; dark green = bound dye; orange = guest; light green = unbound dye.
- 2.7 Jablonski diagram of ICT mechanism. Black arrows = energy transfer.
- 2.8 a) Cartoon representation of overlap in donor emission and acceptor excitation wavelength for ideal FRET pair. Blue = donor, red = acceptor, grey = donor-acceptor overlap; b) Jablonski diagram for Förster resonance energy transfer. NRD = non-radiative decay.
- 2.9 Tripodal Cu(II) cleft **37** composed of guanidinium motifs for anion binding synthesised by Anslyn and co-workers.
- 2.10 Structure of colorimetric phosphate sensor **38** designed by Kim and co-workers containing DPA units chelating to Zn<sup>2+</sup>.
- 2.11 Zinc receptors containing covalently-bound coumarin molecules for intramolecular IDAs. Green = coumarin molecule.
- 2.12 Mass spectrum of self-assembled complex **51**.
- 2.13 a) Aromatic and aliphatic NH proton on **52** shown in blue and red, respectively.; b) Stacked <sup>1</sup>H NMR spectrum of successful phase 1 guest binding screenings in MeCN-d<sub>3</sub> with the position of NH protons indicated (600 MHz). All are anions of TBA salts. Receptor concentration = 2 mM; guest concentration = 20 mM.
- 2.14 <sup>1</sup>H NMR spectrum of titration of **52** with TBA chloride (0-6.48 eq) in MeCN-d<sub>3</sub> (500 MHz). \* = aliphatic proton on **52**; \* = aromatic proton on **52**.

- 2.15 Changes in chemical shift of aliphatic NH proton (\*) on **52** upon addition of various TBA salts in MeCN-d<sub>3</sub>.
- 2.16 Changes in chemical shift of aromatic NH proton (\*) on **52** upon addition of various TBA salts in MeCN-d<sub>3</sub>.
- 2.17 Residuals of titration of **52** with TBACl fitted to a 1:1 binding model.
- 2.18 Absorbance spectrum of **52** in 1:1 MeCN/H<sub>2</sub>O.
- 2.19 Structures of dyes surveyed for indicator displacement; a) fluorescein; b) calcein; c) HPTS; d) HINA; e) 7ACC-1.
- 2.20 Overlap of the absorbance spectrum of **52** (red) (5 μM in 1:1 MeCN/TRIS buffer pH 9.0) and fluorophore emission spectrum of a) fluorescein, b) calcein, c) HPTS, d) HINA and e) 7ACC-1 (black). The fluorophore solutions were 20 μM in 1:1 MeCN/TRIS buffer pH 7.4 or 9.0.
- 2.21 Initial emission spectra of fluorophores, followed by addition of **52** (20 μM) and either chloride or benzoate. Fluorophores shown: a) fluorescein, b) calcein, c) HPTS, d) HINA and e) 7ACC-1. The fluorophore solutions were 20 μM in 1:1 MeCN/TRIS buffer pH 7.4 or 9.0.
- 2.22 Fluorescence intensity of mixture of **52** and HINA upon the addition of increasing anion equivalents. Orange = chloride; green = bromide; purple = iodide; yellow = benzoate. All anions are TBA salts.
- 2.23 Formation of HINA-hydrate in aqueous solvent.
- 2.24 Changes in fluorescence intensity of mixture of **52** and 7ACC-1 upon the addition of increasing anion equivalents. Orange = chloride; green = iodide; purple = benzoate. All anions are TBA salts.
- 2.25 Chloride efflux promoted by control (black) and **52** at 1 mol% (red) and 10 mol% (blue). Control = acetonitrile only.
- 2.26 Fluorescence intensity of lucigenin assay plotted as a function of time. Control = vesicles without transporter.
- 2.27 Cartoon representation of cationophore-coupled assay with valinomycin (green). Transporter = purple.
- 2.28 Chloride efflux promoted by **52** only (black), valinomycin only (red) and **52** + valinomycin (blue).
- 2.29 Comparison of % chloride efflux promoted by **52** with NaCl (black) or KCl (red).
- 2.30 Example of proposed modified ligand.

- 3.1 Racemisation of Tröger's base (**53**) in acidic media.
- 3.2 a) Pyridine diamide analogue of Tröger's base; b) binding of dicarboxylic acid in the cleft of **54**.
- 3.3 a) Kagan's ether **55**; b) Kagan's ether analogue **56** synthesised by Harmata *et al.*; c) crystal structure of **56** binding trinitrobenzene.
- 3.4 Bisureas **57** and **58** synthesised by Steed *et al.*
- 3.5 Lambda and delta stereoisomers, and fac and mer geometric isomers of octahedral complexes.
- 3.6 Amines studied by Nitschke and colleagues when quantifying factors impacting stereochemical control around the metal centre.
- 3.7 <sup>1</sup>H NMR spectrum of crude product from attempted subcomponent self-assembly with **66**.
- 3.8 a) paramagnetic <sup>1</sup>H NMR spectrum of attempted subcomponent self-assembly with **66**, picolinaldehyde and Fe(ClO<sub>4</sub>)<sub>2</sub>; b) zoomed-in paramagnetic <sup>1</sup>H NMR spectrum.
- 3.9 UV-vis spectrum of supposed zinc(II) complexes **69** and **70**, along with achiral zinc(II) complex composed from TREN + picolinaldehyde.
- 3.10 a) CD spectrum of achiral zinc(II) complex, **69** and **70**; b) zoomed-in CD spectrum (-10-10 mdeg); c) zoomed-in CD spectrum (190-220 nm).
- 3.11 Tris(3-aminopropyl)amine (TRPN).
- 4.1 a) general structure of an SSA molecule where X = O/S; Y = a hydrophilic group; and A = a counteranion; b) possible hydrogen bonding bonds.
- 4.2 a) SSA **71** monomer; b) SSA **72** monomer; c) heterogenous dimer of SSA **71** and **72**.
- 4.3 SSA **73**.
- 4.4 a) SSA **74**; b) SSA **74** with *E. coli* (yellow) and MRSA (red), T = 30 min; c) SSA **74** with *E. coli* (yellow) and MRSA (red), T = 5 hours. Figure adapted from Hiscock *et al.*
- 4.5 SSA **75**.
- 4.6 a) SSA **70**; b) SSA **71**.
- 4.7 a) SSA **69**; b) SSA **72**.
- 4.8 SSA **78**-m-PC conformations with their corresponding binding energies. Blue = values from ab initio calculations. Green = values from DFT calculations. Dashed line = hydrogen bond.
- 4.9 a) SSA **78**-m-PE conformations with their corresponding binding energies. Blue = values from ab initio calculations. Green = values from DFT calculations. Dashed line = hydrogen bond; b) Graphic illustrating hydrogen bonding in conformation **D**.



- 4.10 SSA **78**-m-PG conformations with their corresponding binding energies. Blue = values from ab initio calculations. Red = values from DFT calculations. Dashed line = hydrogen bond.
- 4.11 Correlation data between binding energies calculated *via* ab initio and DFT methods for SSA **78**.
- 4.12 SSA **75**-m-PC conformations with their corresponding binding energies. Dashed line = hydrogen bond.
- 4.13 SSA **75**-m-PE conformations with their corresponding binding energies. Dashed line = hydrogen bond.
- 4.14 SSA **75**-m-PG conformations with their corresponding binding energies. Dashed line = hydrogen bond.
- 5.1 Ni(II) complexes synthesised by Yang and co-workers.

## List of schemes

- 2.1 Proposed synthesis of the tripodal cleft with anion-binding motifs using subcomponent self-assembly. Green circle = anion-binding group.
- 2.2 Proposed synthesis of anion-binder-containing pyridine aldehyde *via* Sonogashira cross-coupling. Green = anion-binding group – i.e. squaramide, thiourea, urea.
- 2.3 Two-step synthesis of squaramide **43**.
- 2.4 Mechanism of amine addition to squarate ester *via* zinc triflate chelation.
- 2.5 Proposed mechanism of CuAAC reaction.
- 2.6 Proposed synthesis of anion-binder-containing pyridine aldehyde *via* CuAAC. Green = anion-binding group – i.e. squaramide, thiourea, urea.
- 2.7 Synthesis of 3-azidopropylamine **45**.
- 2.8 Synthesis of alkyne-containing pyridine aldehyde **44**.
- 2.9 Synthesis of squaramide-containing pyridine aldehyde **48** *via* CuAAC.
- 2.10 Synthesis of urea-containing pyridine aldehyde **50** *via* CuAAC.
- 2.11 Proposed synthesis of metal-organic complexes using anion-binder-containing pyridine aldehyde ligands *via* subcomponent self-assembly. Green = anion-binding group.
- 2.12 Subcomponent self-assembly with TREN, **48** and zinc triflate to form zinc complex **51**.
- 2.13 Subcomponent self-assembly with TREN, **50** and iron(II) perchlorate to form iron complex **52**.
- 3.1 Example scheme showing chiral induction through chiral subcomponent substitution.
- 3.2 Proposed synthesis of enantiopure metal complex with chiral amine *via* subcomponent self-assembly.
- 3.3 General routes to synthesising chiral tripodal amines *via* a) aziridines or b) amino aldehydes.
- 3.4 Proposed synthesis of tripodal chiral amine using tosyl protecting group.
- 3.5 Formation of aziridine **63** from (*S*)-valinol.
- 3.6 Proposed synthesis of chiral tripodal amine using Boc protecting group.
- 3.7 Synthesis of Boc-protected chiral tripodal amine **65**.
- 3.8 Deprotection of amine **65** to form amine **66**.
- 3.9 Synthesis of Boc-protected chiral tripodal amine **67** and subsequent formation of chiral tripodal amine **68**.
- 3.10 Subcomponent self-assemblies attempted with  $\text{Zn}(\text{ClO}_4)_2$  with chiral amines **66** and **68** to form complexes **69** and **70**, respectively.

## List of tables

- 2.1 Reaction conditions for attempted Sonogashira cross-coupling reactions.
- 2.2 Outcomes of self-assemblies conducted.
- 2.3 Outcomes of guests screened in acetonitrile or acetonitrile/water mixtures. TBA = tetrabutylammonium.
- 2.4 Reasons for not using BindFit models for all anions in  $^1\text{H}$  NMR titrations. 1:1 refers to 1:1 host/guest model; 1:2 refers to 1:2 host/guest model; 2:1 refers to 2:1 host/guest model.
- 2.5 Properties of dyes surveyed for indicator displacement.
- 3.1 Conditions used to synthesise **64** from **63**.
- 3.2 Attempted conditions used to deprotect **63**.
- 3.3 Outcomes of self-assemblies with different metal salts.
- 4.1 Structures of phospholipids vs structure of m-lipids; blue = fatty acid group where R = alkyl chain.
- 4.2 SSA **72**-PG conformation binding energy values in water, gas phase, and hexane.
- 4.3 Different types of hydrogen bond strengths and their properties.
- 4.4 Lowest binding energy conformations with values for SSA **78** with m-lipids.
- 4.5 Lowest binding energy conformations with values for SSA **75** with m-lipids.
- 4.6 Lowest binding energy conformations for SSA **75** and **78**.
- 6.1 Layout of 96-well plate for plate reader measurements. Concentration of TBA salt solution added given in each well (mM). Blue = chloride; orange = bromide; green = iodide; yellow = benzoate.

## List of equations

- 1.1 Stern-Volmer equation used to calculate quenching of fluorescence by lucigenin.  $F_0$  = fluorescence intensity without quencher;  $F$  = fluorescence intensity with quencher;  $K_{SV}$  = Stern-Volmer constant;  $[Q]$  = quencher concentration.
- 4.1 Calculation of SSA-lipid binding energy.



# 1 Introduction

In 1987, Donald J. Cram, Jean-Marie Lehn and Charles Pedersen were awarded the Nobel Prize for Chemistry for their ground-breaking work on generating multidentate ligands for cation binding.<sup>1</sup> Lehn, in his Nobel lecture, described supramolecular chemistry as “chemistry beyond the molecule”<sup>2</sup> and highlighted its potential for further exploration in the broader field of host-guest chemistry. This type of chemistry involves binding a guest within a receptor molecule, typically through non-covalent interactions such as hydrogen bonds, electrostatic interactions and hydrophobic interactions. Host-guest chemistry is widely observed, with the interactions of enzymes with active sites serving as a classic example.<sup>3</sup> There has been a growing interest in recreating such interactions synthetically, leading to significant advancements in the field of host-guest chemistry since the publication of the first artificial host-guest complex by Pederson.<sup>4</sup> This progress has led to the design of numerous synthetic hosts capable of binding a wide range of guests.

This thesis examined the binding of anions to various hosts. In particular, a key aim of the synthetic work undertaken was to create preorganised hosts for anionic guests. As such, sections 1.1 and 1.2 introduce the fields of anion recognition and anion transport. Section 1.3 explores the application of metal-ligand coordination chemistry in constructing stable hosts with well-defined coordination geometries for anion binding.

## 1.1 Anion binding

Anions play a significant role in our daily lives. Deoxyribonucleic acid (DNA), which carries our genetic information, is polyanionic. Smaller anions, such as chloride and bicarbonate, help maintain body pH,<sup>5</sup> while phosphate, also a by-product of adenosine triphosphate (ATP) breakdown, regulates metabolic processes.<sup>6</sup> Additionally, ATP plays a vital role in biology, whether in the duplication or transcription of DNA or energy transfer within cells.<sup>7</sup> Anions like nitrate can be found in rivers and lakes due to eutrophication,<sup>8</sup> and metanil yellow (Figure 1.1) is an anionic compound previously used as a food colouring.<sup>9</sup> The binding of anions using synthetic anion binders has applications in wastewater treatment, molecular sensing and the treatment of channelopathies – a set of illnesses derived from dysfunctional ion channels in the body – such as Bartter syndrome, cystic fibrosis and neuromyotonia.<sup>10</sup>

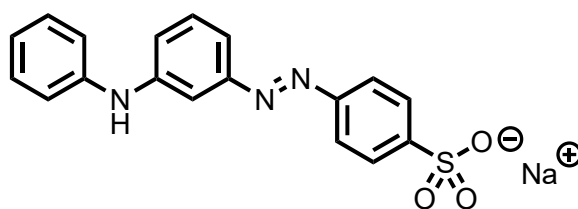


Figure 1.1: Metanil yellow, an anionic dye.

### 1.1.1 Challenges

Although the field of anion binding is extensive, several issues must be overcome when designing systems to bind negatively charged ions. Firstly, anions are typically significantly larger than their isoelectronic cation counterparts. This means they have a lower charge density, i.e. a low charge-to-radius ratio, making them harder to bind than cations.<sup>11</sup> Additionally, solvent choice requires careful consideration as anions are often solvated. In the context of anion recognition, the Hofmeister series (Figure 1.2) helps in predicting anion desolvation energies.<sup>12</sup> Anions to the left of chloride are known as kosmotropic, meaning they are well-hydrated and have high desolvation penalties – these anions preferentially bind in non-polar solvents.

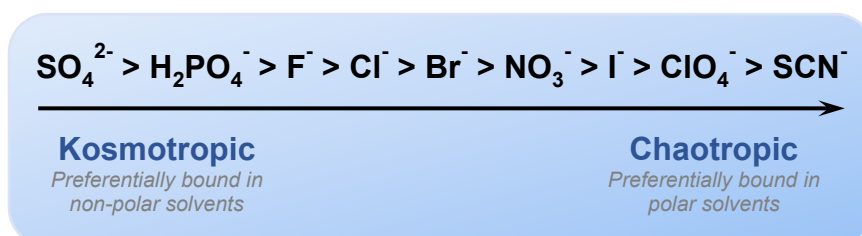


Figure 1.2: Hofmeister series of anions.<sup>12</sup>

Chaotropic anions are weakly hydrated and preferentially bind to synthetic receptors in polar solvents. Chloride is neither.<sup>12</sup> Anions are also sensitive to pH, as they can protonate at lower pH levels, leading to lower binding. Finally, anions exhibit different geometries. Shape complementarity between the host and guest is essential for strong binding, and this is not always possible when binding a range of anions.<sup>13</sup> A range of anions with varying geometries is given in Figure 1.3.

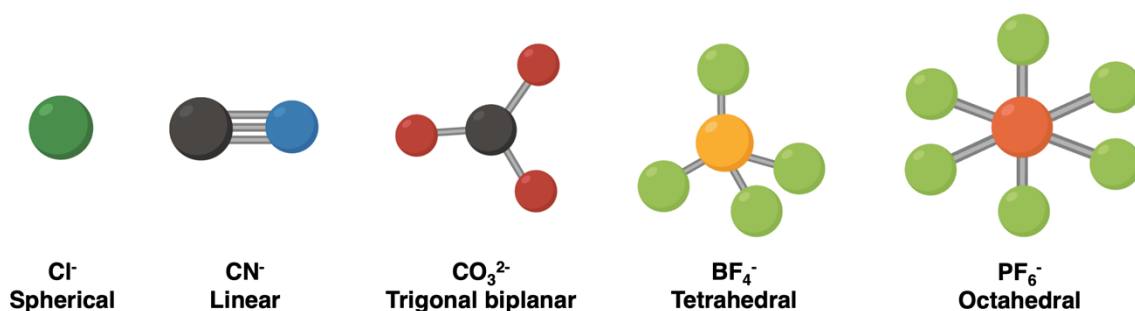


Figure 1.3: Examples of different anion geometries. Dark green = chlorine; black = carbon; blue = nitrogen; red = oxygen; yellow = boron; orange = phosphorus; light green = fluorine.

### 1.1.2 Dual hydrogen bonding motifs

Quiococho *et al.* reported the first discovery of hydrogen bonds for anion binding in 1985 when they solved the structure of the sulfate-binding protein in *Salmonella typhimurium*.<sup>14</sup> They found the charged oxygen atoms of the sulfate anion are stabilised by hydrogen bonds from amino acid residues within the binding cavity. This study also highlighted an essential property of hydrogen bonds – directionality. This was subsequently confirmed by X-ray diffraction (XRD) studies<sup>15</sup> and computational calculations,<sup>16</sup> which suggested that hydrogen bonds tend to form in approximately the directions of oxygen  $sp^2$  lone pairs. Therefore, the donor-acceptor interaction angle is often fixed in place, which is crucial for hydrogen bond stabilisation.

Dual hydrogen bond donors possess a significant advantage over single hydrogen bond donors due to the additive effect of two donors binding and chelating to one anion. The literature has thoroughly reviewed these compounds; hence, this section will introduce dual hydrogen bonding motifs with a few examples.

Ureas and thioureas have been extensively used for anion binding, with Panunto *et al.* being one of the first.<sup>17</sup> A library of diarylureas was generated and tested in various solvents like acetone, dimethylsulfoxide (DMSO), ethanol and tetrahydrofuran (THF). It was found that adding electron-withdrawing group substituents at the meta position (Figure 1.4), in particular two nitro groups, allowed for stronger host-guest interactions due to increased N-H bond acidity.



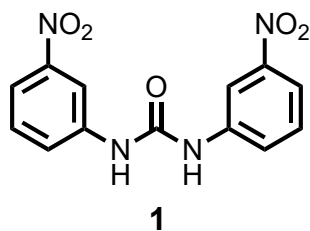


Figure 1.4: Diarylurea host containing nitro groups in the meta position for guest binding.<sup>17</sup>

Based on this finding, Wilcox and co-workers synthesised a urea and thiourea receptor (Figure 1.5), which bound various tetrabutylammonium oxoanions in chloroform.<sup>18</sup> Strong binding of urea **2** with all anions was observed, with an association constant ( $K_a$ ) of  $3 \times 10^4 \text{ M}^{-1}$  for acetate. In an attempt to add another N-H group, Pfeffer and co-workers synthesised naphthalimide-containing thioureas **4**, **5**, and **6** (Figure 1.6), and binding was tested to a range of anions in DMSO – acetate, dihydrogen phosphate, fluoride, bromide and iodide.<sup>19</sup> Bromide and iodide did not bind to any receptor. <sup>1</sup>H nuclear magnetic resonance (NMR) analysis of the solution of **6** with fluoride showed the presence of a new peak at 16 ppm, assigned to the formation of the bifluoride ( $[\text{FHF}]^-$ ) anion. Additionally, the solution changed colour, suggesting that the naphthalimide proton was deprotonated. This, once again, highlights the pH sensitivity of anion binding. Dihydrogen phosphate seemingly bound the naphthalimide proton, as well as both thiourea protons, but not very strongly.

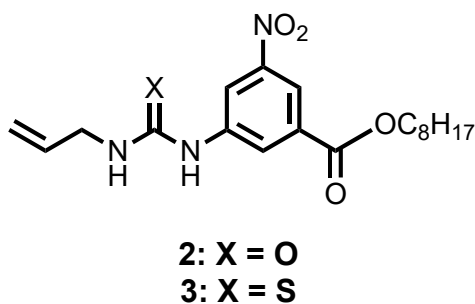


Figure 1.5: (Thio)urea anion receptors synthesised by Wilcox and co-workers.<sup>18</sup>

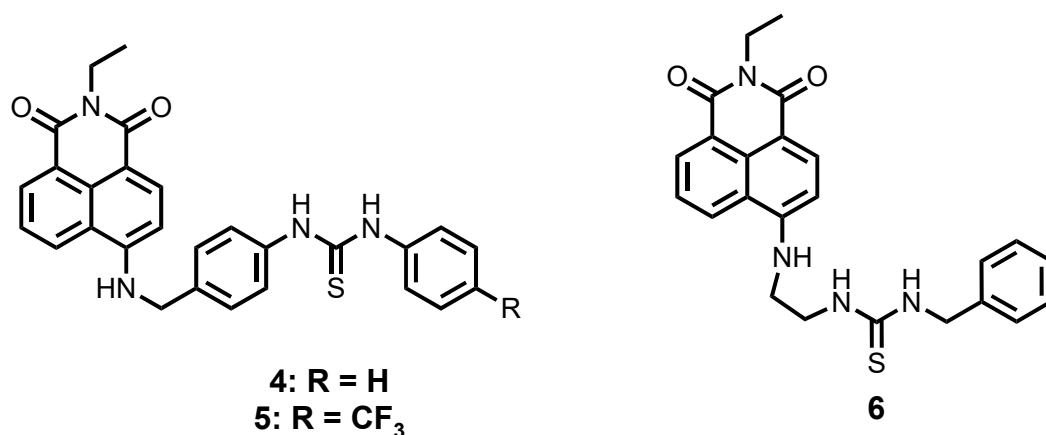


Figure 1.6: Naphthalimide-containing thioureas synthesised by Pfeffer and co-workers.<sup>19</sup>

Following the first reports of squaramide-based anion receptors in 1998,<sup>20</sup> Fabbrizzi *et al.* have studied the binding capabilities of squaramides compared to other dual hydrogen bond donors in acetonitrile.<sup>21,22</sup> Analysis of the binding of squaramide **7b** (Figure 1.7) showed that this host-guest complex is 1-2 orders more stable than its urea counterpart (**7a**), likely due to two additional hydrogen bonds donated from the phenyl rings adjacent to the N-H protons ( $\alpha$  and  $\beta$  protons, Figure 1.7).<sup>21</sup> Similarly, Muthyala *et al.* have explored using squaramides as ‘molecular valves’ to bind chloride by altering the groups adjacent to the N-H groups (Figure 1.8). They found chloride bound to **8** in polar solvents and was subsequently released in polar solvents due to conformational changes (‘Open’ conformation, Figure 1.8), further confirmed by computational calculations.<sup>23</sup>

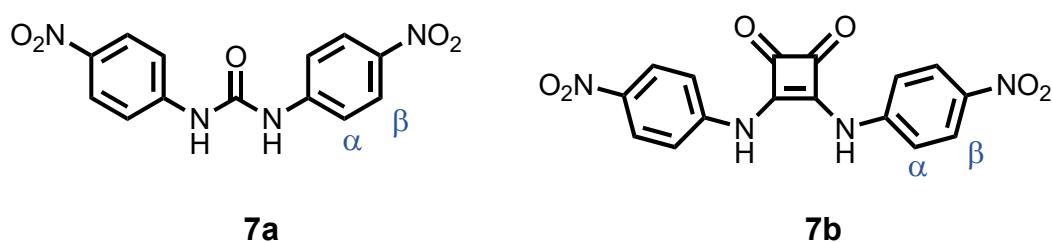


Figure 1.7: Urea **7a** and squaramide **7b** synthesised by Fabbrizzi *et al.*<sup>21</sup>

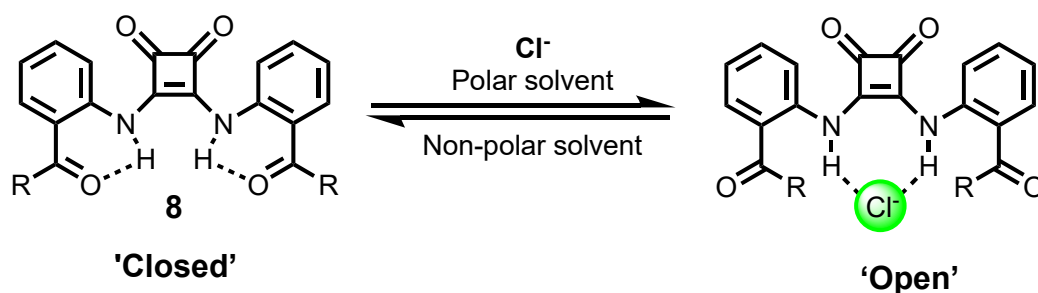


Figure 1.8: Squaramides as 'molecular valves' to regulate chloride binding.<sup>23</sup>

Since then, other dual hydrogen bonding motifs, such as croconamides and deltamides (Figure 1.9), have been discovered. Jolliffe and colleagues explored the binding of novel dialkyl and diaryl deltamides and croconamides in acetonitrile and DMSO with various anions whilst comparing the binding of analogous ureas and squaramides.<sup>24</sup> The dialkylcroconamides exhibited higher anion affinities than the diarylcroconamides, seemingly deprotonated at neutral pH, reducing their ability to bind anions. The deltamides exhibited the same anion preferences as ureas and squaramides, in which the diaryl analogues exhibited higher anion binding. Diaryldeltamides containing electron-withdrawing groups exhibited even higher anion-binding affinities.

Interestingly, the deltamides displayed a higher affinity for the dihydrogen phosphate anion than the carboxylate and oxoanions – tosylate, acetate and benzoate. The authors attributed this to the difference in N-H positioning, with the dihydrogen phosphate anion being a perfect geometric match for the deltamide cavity. This further highlights the importance of shape complementarity in anion binding.

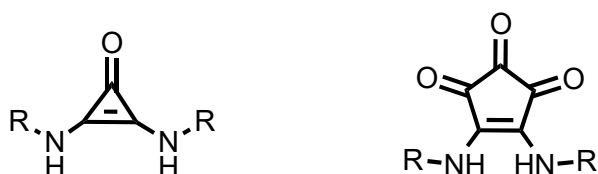


Figure 1.9: General structures of deltamides (left) and croconamides (right).

### 1.1.3 Strategies to improve anion binding

#### 1.1.3.1 Preorganisation

The preorganisation of supramolecular structures is key for guest binding. Spherands provide a classic example of the advantages of preorganisation.<sup>25</sup> For instance, spherand **9** (Figure 1.10) is preorganised for binding, with the central oxygen atoms buried in a hydrocarbon shell, allowing them to remain unsolvated and readily bind guests, such as sodium and lithium. The free energy for organising **9** into a single conformation whilst desolvating it was done during synthesis, thereby keeping entropy low. In contrast, podand **10** (Figure 1.10) lacks a central cavity for binding and can adopt several possible conformations, with only two conformations available to bind cations octahedrally. **10** is, therefore, not preorganised – instead, it is randomised to maximise the entropy of its conformers and the attractions between the solvent and itself. Desolvation and organisation of **10** during complexation would incur an energetic penalty.<sup>25,26</sup>

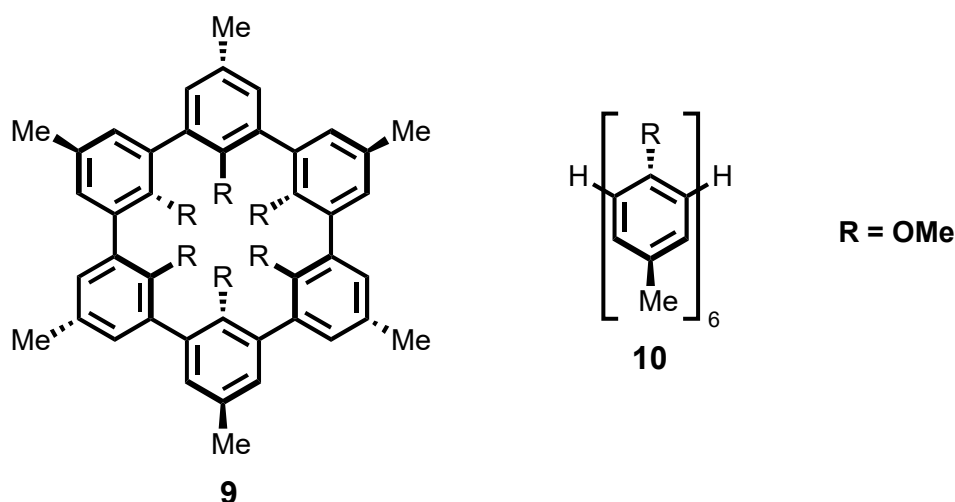


Figure 1.10: Spherand **9** and podand **10** synthesised by Cram and co-workers.<sup>26</sup>

Preorganisation of hosts for anion binding is seemingly less common – however, isophthalamides and dipicolineamides are some key examples, with Crabtree *et al.* publishing some of the first (Figure 1.11a and 1.11b).<sup>27</sup> Investigation of the free receptor conformations of **11** and **12** showed that the syn-anti conformation (Figure 1.12) of **11** is the lowest in energy. In contrast, the syn-syn conformation (Figure 1.12) – where both NH groups point in and towards each other – is the lowest for **12**. **12** is, therefore, preorganised for binding, meaning it

is able to bind anions more strongly. Smith and co-workers further elaborated on this work by attaching boronate groups to the phenyl ring (**13**, Figure 1.11c).<sup>28</sup> This increased the association constant of acetate binding by up to 3 kcal/mol compared to **11**, likely due to the intramolecular coordination, which pre-organises the structure, induces a larger host dipole moment and strengthens the host/guest ion-dipole interaction.

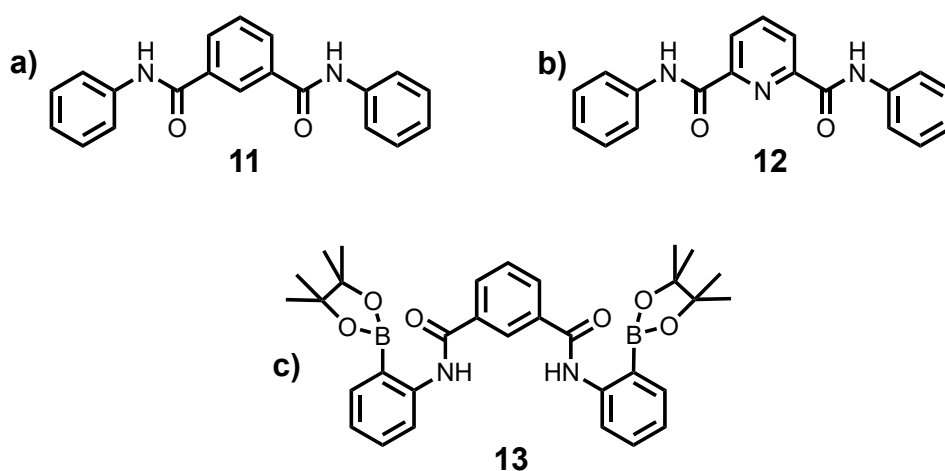


Figure 1.11: a) Isophthalamide **11** and b) dipicolineamide **12** synthesised by Crabtree *et al.*; c) boron-functionalised isophthalamide **13** synthesised by Smith and co-workers.<sup>26,28</sup>

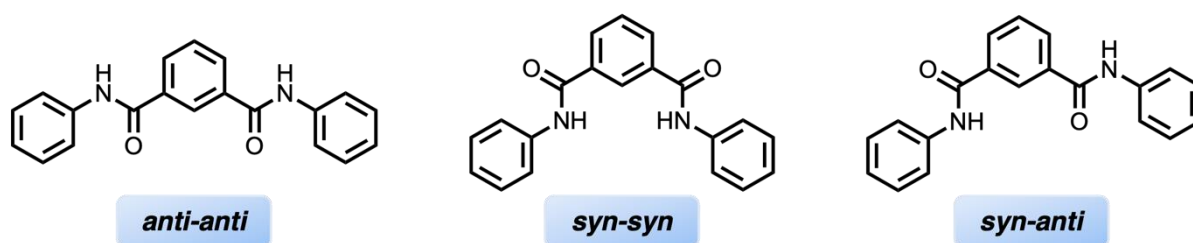


Figure 1.12: Predominant conformations of isophthalamides.

Hydroxylated analogues of isophthalamides have been also synthesised by Gale and colleagues.<sup>29</sup> Much like the boron-functionalised analogues (Figure 1.11), the presence of the hydroxyl group fixes the structure into a syn-syn conformation due to the intramolecular hydrogen bonding (Figure 1.13). This was confirmed *via* <sup>1</sup>H NMR, where the OH protons showed a downfield shift. Replacing the hydroxyl group with a methoxy group fixed the structure into an anti-anti conformation, supported by a downfield shift in the NH proton of this methoxylated isophthalamide. The same proton on **14** did not exhibit a downfield shift,

indicating it is not involved in hydrogen bonding and further confirming the syn-syn conformation.

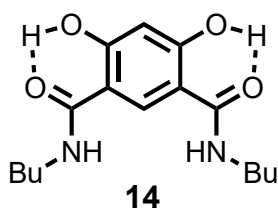


Figure 1.13: Hydroxylated isophthalamide **14** synthesised by Gale and colleagues.<sup>29</sup>

Gale and colleagues achieved increased NH acidity by attaching nitro groups to the phenyl rings (Figure 1.14).<sup>30</sup> This increases the ability of the NH proton to bind anions and likely fixes the structure in a syn-syn conformation. It was found that both compounds were able to bind fluoride, with a supposed 2:1 fluoride:host binding model at higher fluoride concentrations.

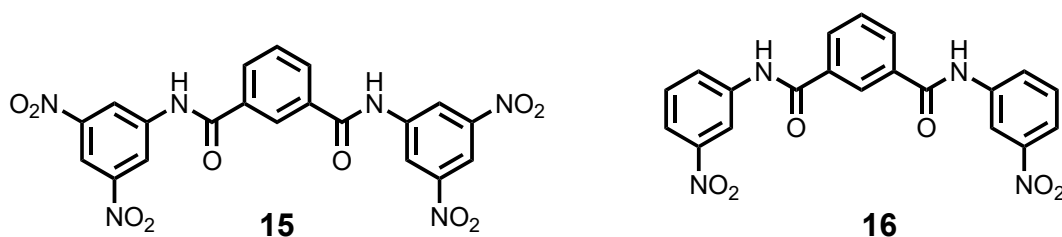


Figure 1.14: Nitro-containing isophthalamides **15** and **16** synthesised by Gale and colleagues.<sup>30</sup>

Caltagirone and colleagues generated a small library of isophthalamides and dipicolineamides, many of which contained electron-withdrawing groups.<sup>31</sup> Through <sup>1</sup>H NMR titrations, it was determined that compounds containing electron-withdrawing groups exhibited stronger chloride binding. These titrations also revealed a downfield shift in the aromatic proton located among the amide groups, suggesting its involvement in bonding, likely due to the formation of the syn-syn conformer.

The preorganisation of isophthalamides and dipicolineamides for anion binding has potential applications in anion transport. For example, Gokel *et al.* synthesised dipicolineamide **17** (Figure 1.15),<sup>32</sup> which can transport chloride *via* carrier and channel mechanisms. Yang and co-workers synthesised isophthalamides containing amino residues, which demonstrated

chloride/bicarbonate antiport activity.<sup>33</sup> Compounds containing less bulky amino acid substituents showed higher ion transport, likely due to easier formation of the syn-syn conformer.

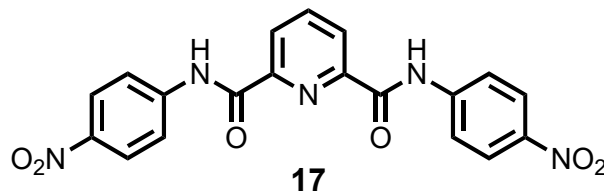


Figure 1.15: Dipicolineamide **17** synthesised by Gokel *et al.*<sup>32</sup>

### 1.1.3.2 Tripodal clefts

The literature extensively uses tripodal clefts, primarily synthesised using tripodal ligands. The alignment of each ligand ‘arm’ allows for the formation of a C<sub>3v</sub> symmetric cavity, which helps provide a pre-organised binding cavity that can encapsulate and bind anions. Reinhoudt *et al.* generated the first tripodal clefts in 1993 (Figure 1.16) in an attempt to mimic biological binding clefts.<sup>34</sup> <sup>1</sup>H NMR titrations were carried out with tetrabutylammonium (TBA) hydrogen phosphate, TBA sulfate and TBA chloride. A clear binding order was established for all tripodal hosts: phosphate > chloride > sulfate, with **20** showing the highest affinity to the hydrogen phosphate anion. This is likely due to the increased electrophilicity of NH protons of the sulfonamide groups, as well as the formation of a preorganised cleft due to the  $\pi$ - $\pi$  stacking interactions of the naphthyl rings. **18a** and **19a** were able to bind the anions more strongly compared to **18b** and **19b**, perhaps due to the inductively electron-withdrawing effect of the chlorine.

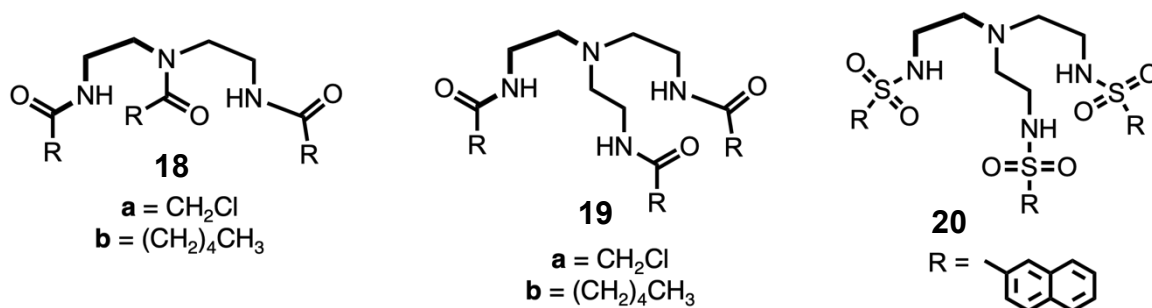


Figure 1.16: Tripodal clefts **18**, **19**, and **20** generated by Reinhoudt *et al.*<sup>34</sup>

Bowman-James and co-workers synthesised a simple benzyl-functionalised tripodal cleft by reacting tris(2-aminoethyl)amine (TREN) with benzaldehyde, followed by imine reduction *via* the addition of sodium borohydride to form a tripodal amine capable of binding phosphate, sulfate and bromide ions.<sup>35</sup> Ghosh and co-workers synthesised fluorophenyl amide-functionalised tripodal clefts **21** and **22** (Figure 1.17) that exhibited selective binding towards fluoride.<sup>36</sup>

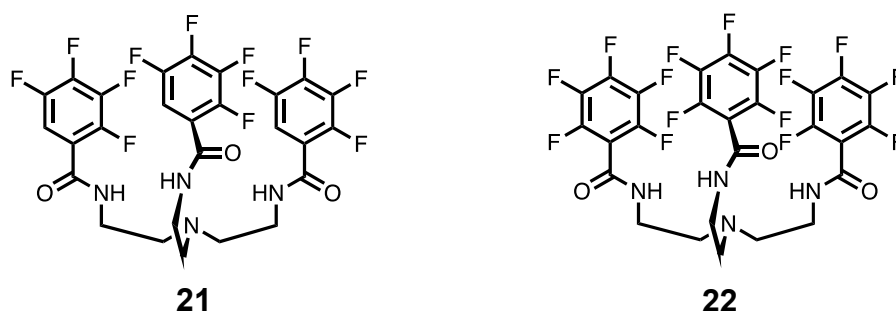


Figure 1.17: Tripodal amide receptors **21** and **22** used in fluoride recognition.<sup>36</sup>

Tripodal clefts can also be used to bind larger anionic compounds. Ghosh *et al.* utilised non-covalent interactions to create cleft **23** to sense ATP selectively (Figure 1.18).<sup>37</sup> The three pyridinium groups create a cationic pocket suitable for binding anionic species, such as pyrophosphate groups, and the hydrogen bonding interactions between the phosphate and amides further strengthen the binding.  $\pi$ - $\pi$  stacking interactions between adenosine and naphthalene rings further enhance the binding of ATP to the cleft.

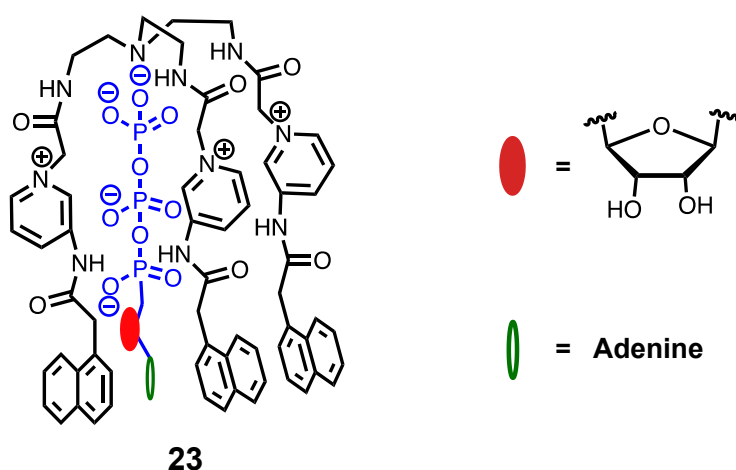


Figure 1.18: Proposed binding of ATP to tripodal cleft **23**.<sup>37</sup>



Tripodal clefts can also be a part of larger supramolecular structures. For example, Custelcean *et al.* designed an Ag(I)-based metal-organic framework composed of tripodal tris-urea linkers (**24**, Figure 1.19) capable of encapsulating sulfate using twelve hydrogen bonds.<sup>38</sup> The self-assembly of a tripodal tris-urea was investigated with several Ag(I) salts, including Ag<sub>2</sub>SO<sub>4</sub>, AgNO<sub>3</sub> and AgOAc. However, it was found that sulfate bound the strongest, which created a metal-organic framework containing a cavity to bind sulfate. Custelcean *et al.* also synthesised a pre-organised metal-organic complex containing a well-defined cavity able to bind sulfate ions.<sup>39</sup> The crystallisation tris-urea ligand **25** (Figure 1.19) was attempted with various MSO<sub>4</sub> salts (M = Zn, Co, Cd, Mg) to form MSO<sub>4</sub>L<sub>2</sub>(H<sub>2</sub>O)<sub>6</sub> complexes. The central sulfate ion was bound to the ligand *via* 12 hydrogen bonds from the urea motifs, and the SO<sub>4</sub><sup>2-</sup>L<sub>2</sub> complex was incorporated into a hydrogen bonding capsule *via* 12 additional hydrogen bonds from the surrounding water molecules.

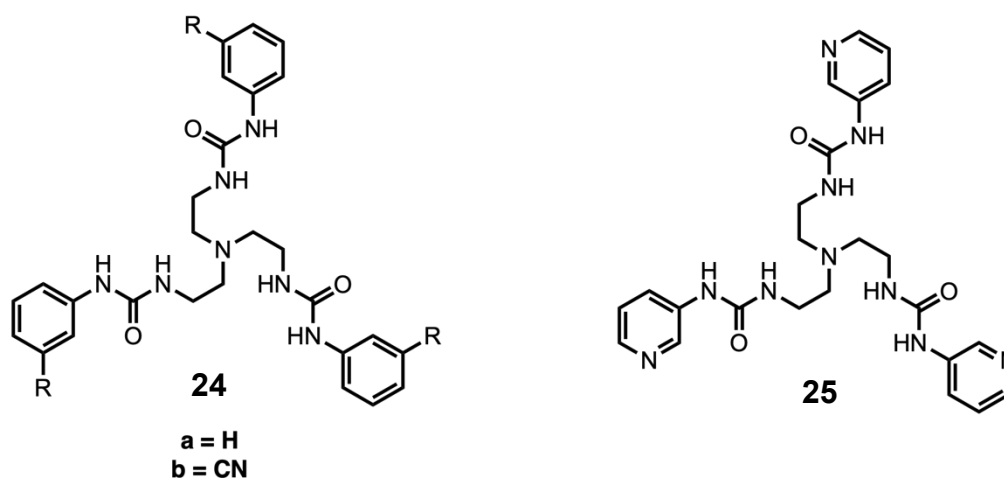


Figure 1.19: Tris-ureas **24** and **25** synthesised by Custelcean *et al.*<sup>38,39</sup>

Additionally, dual hydrogen bond donor motifs have been used in tripodal clefts to capture anions. Hossain and colleagues generated a tripodal hexafunctional urea/thiourea receptor **20**,<sup>40</sup> containing two binding clefts for sulfate binding (Figure 1.19) – the outer cleft containing a thiourea group and the inner cleft containing a urea group. <sup>1</sup>H NMR titrations were carried out with various anionic guests; however, TBA sulfate demonstrated the strongest binding. This also revealed a two-step sulfate binding process – due to the increased acidity of the thiourea group, sulfate first bound the outer cleft.

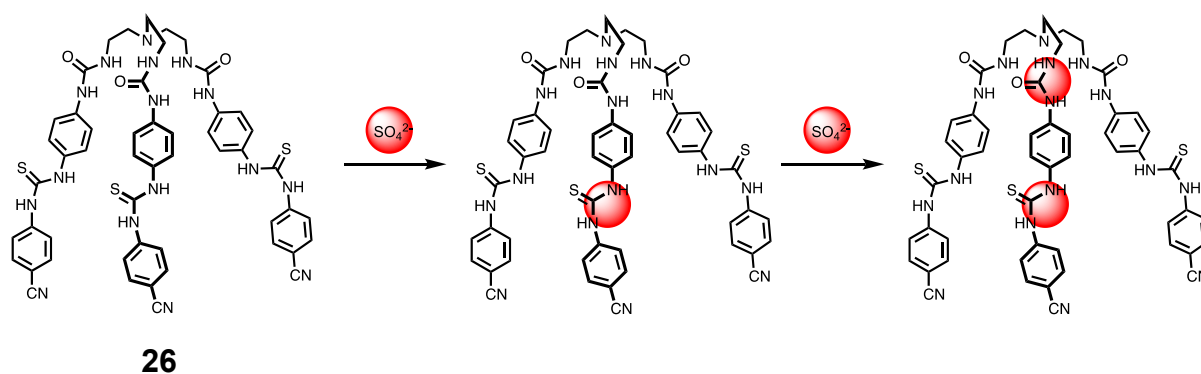


Figure 1.20: Proposed binding of sulfate ions to (thio)urea groups on tripodal cleft **26**.<sup>40</sup>

Tripodal clefts have shown applications in anion transport. For example, Smith and co-workers demonstrated that a simple tris-urea could bind and transport HCl.<sup>41</sup> Similarly, Gale and colleagues were able to transport chloride and bicarbonate using a tripodal tris-thiourea.<sup>42</sup> It was observed that the thiourea exhibited better transport activity than its urea counterpart, likely due to its increased acidity, allowing it to bind anions more effectively. Subsequently, a series of functionalised tris-ureas and tris-thioureas (Figure 1.21) were tested for anion transport.<sup>43</sup> The fluorinated substrates exhibited higher levels of anion transport, possibly due to the increased lipophilicity induced by the fluorine atoms.

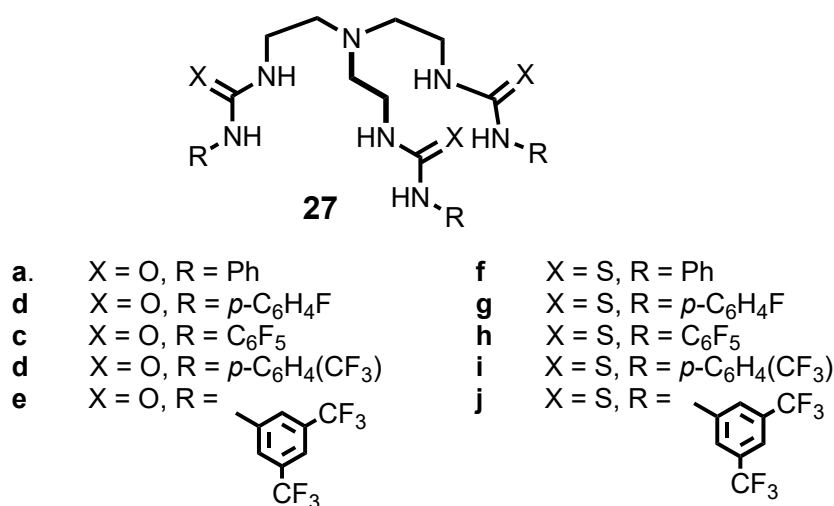


Figure 1.21: Series of tris-ureas and tris-thioureas screened for anion transport.<sup>43</sup>

## 1.2 Anion transport

### 1.2.1 Ion transport in cell membranes

The transport of molecules across cell membranes is integral to various biological processes. Due to the membrane's amphiphilic nature, transport is highly dependent on the size and polarity of molecules. Small, neutral molecules – gases like oxygen and carbon dioxide – can pass through cell membranes *via* passive diffusion, as can polar yet uncharged molecules like water and ethanol. Ions and other less permeable molecules are transported *via* membrane transport proteins, otherwise known as transporters. These compensate for the high energy penalty of a hydrophilic ion's movement through a hydrophobic medium.<sup>44</sup>

Two types of ion transporters exist – channels and carriers. Ion channels are large proteins that form hydrophilic pores across membranes, which allow for the passage of several million ions when open; ion carriers, or ionophores, are lipid-soluble molecules that bind a select few ions and carry themselves through the membrane. Both work through one of three mechanisms (Figure 1.22). Uniport involves the transport of one species; symport consists of the transport of two oppositely charged ions in the same direction, and antiport is the transport of two similarly charged ions in opposite directions. Both are affected by stimuli – i.e. voltage, stress or ligand binding.<sup>45</sup>

Although several necessary biological anions exist, the most important is arguably chloride, the primary extracellular anion transported across membranes through various processes. Several types of chloride channels exist within the body. The cystic fibrosis transmembrane regulator (CFTR) is a transmembrane chloride/bicarbonate antiporter belonging to the family of cyclic adenosine monophosphate (cAMP) activated channels.<sup>46</sup> The binding of ATP regulates this family of channels, and defects in this channel can lead to cystic fibrosis. Another example is ligand-gated chloride channels, which are essential in modulating inhibitory signals within the central nervous system.<sup>47</sup> The two most common channels require  $\gamma$ -aminobutyric acid (GABA) and glycine binding to facilitate chloride transport. There are also carriers present within the body that utilise chloride. Cation-chloride cotransporters work by cation-chloride symport – either sodium/chloride, potassium/chloride or sodium and potassium with two chloride ions – and all have important roles in kidney function and regulation.<sup>48</sup> Chloride/bicarbonate antiporters work to transport and remove carbon dioxide from tissues to

the lungs in the form of bicarbonate to the lungs.<sup>33</sup> Defects to these channels and carriers would be detrimental to human health, thus requiring synthetic equivalents.

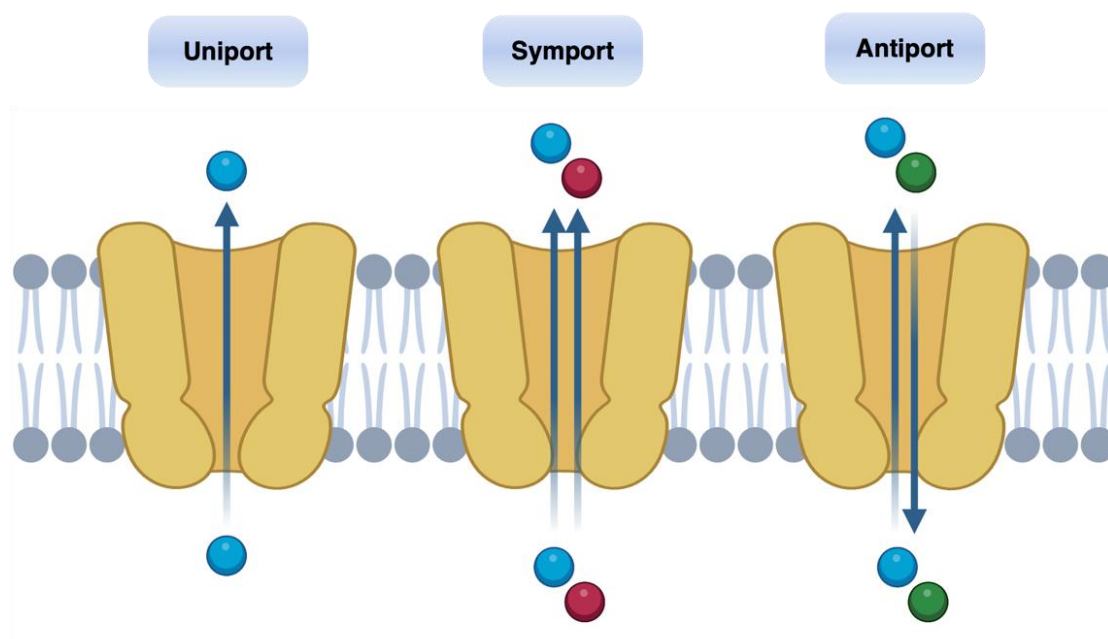


*Figure 1.22: Transmembrane transport of ions through either uniport, symport or antiport mechanisms.*

### 1.2.2 Common ways to test anion transport

The efficiency of a synthetic anion transporter can be measured *via* its ability to move a target ion through an artificial lipid bilayer. The rate of this transport process can be measured *via* assays based on various techniques, including NMR, fluorescence and ion-selective electrodes.<sup>49,50</sup> Synthetic membranes are a good model for biological membranes, and it is possible to synthesise liposomes – i.e., small spherical vesicles – as cell membrane mimics to test the transport of synthetic anionophores. Liposome composition and type highly depend on its function and purpose. There are four categories of liposomes – 1) small unilamellar vesicles (SUVs); 2) large unilamellar vesicles (LUVs); 3) multilamellar vesicles (MLVs); 4) multivesicular vesicles (MVVs).<sup>51</sup> Unilamellar vesicles are composed of a mono-phospholipid bilayer, whereas multilamellar vesicles are comprised of several phospholipid layers. MVVs are composed of several unilamellar vesicles within a larger liposome. Typically, the encapsulation efficiency of a liposome increases with size but is reduced in liposomes with several phospholipid bilayers.<sup>52</sup> Thus, LUVs are well-suited for testing synthetic anionophores.

Various phospholipids can be used to synthesise liposomes; however, phospholipids that incorporate choline into the headgroup—i.e. phosphatidylcholine (PC)—are often used since they primarily comprise cell membranes.<sup>51</sup> 1-Palmitoyl-2-oleoyl-sn-glycero-3-phosphocholine (POPC, Figure 1.23a) is naturally present in eukaryotic cell membranes and is a good choice for liposome formation.<sup>53</sup> Vesicles can be made from egg yolk phosphatidylcholine (EYPC) – composed of a mixture of fatty acyl PCs, of which POPC comprises 33% – or soybean PC, which consists of 16% POPC.<sup>54,55</sup> 1,2-Dipalmitoylphosphatidylcholine (DPPC, Figure 1.23b) vesicles and 1,2-dioleoyl-sn-glycero-3-phosphocholine (DOPC, Figure 1.23c) have been used to test membrane functionality in different phases since DPPC exists as a solid-like gel at room temperature (RT), whereas DOPC exists in a liquid-like state.<sup>56,57</sup> Cholesterol can also be added to vesicles, rigidifying them and allowing for the impact of membrane stiffness on anion transport to be tested.<sup>58</sup>

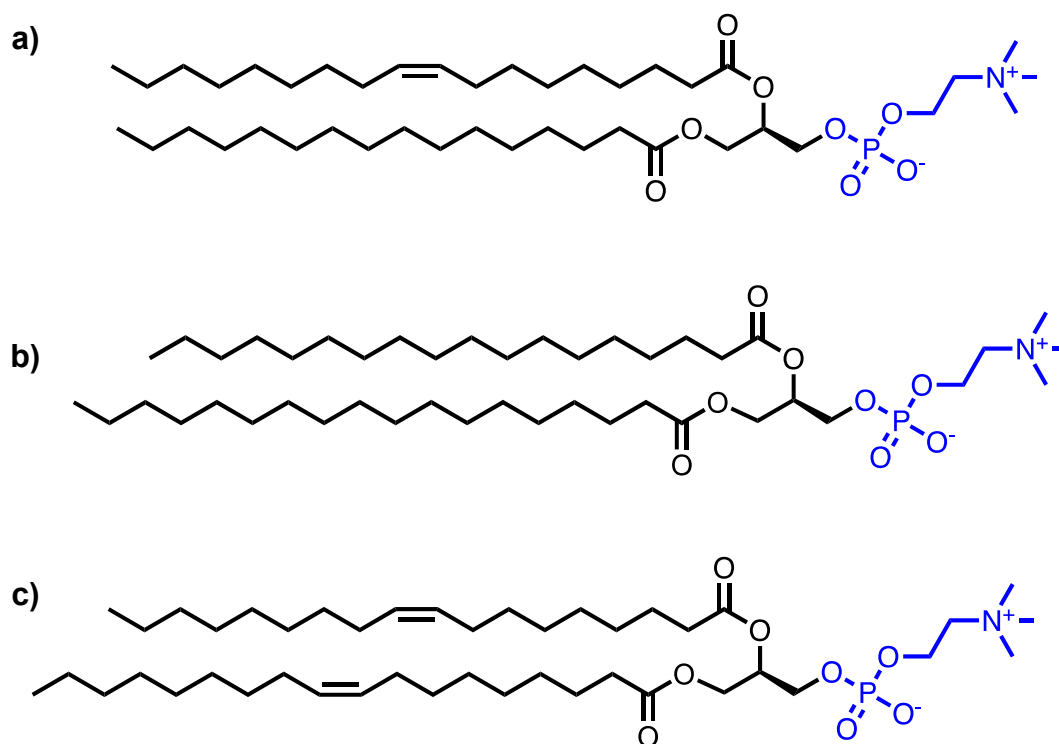


Figure 1.23: Structures of a) POPC, b) DPPC, c) DOPC.

The salt composition can also be varied according to application. When testing for direct chloride transport, vesicles are classically prepared in sodium chloride buffer and subsequently suspended in sodium nitrate buffer, allowing chloride/nitrate antiport to be tested following the addition of a transporter. Conversely, if testing for chloride/cation symport, vesicles prepared

in sodium chloride buffer would be suspended in a salt solution of a hydrophilic anion unable to pass through the phospholipid bilayer<sup>59–61</sup> – e.g. sulfate or gluconate.

#### 1.2.2.1 The ion-selective electrode (ISE)

This technique is based on electrodes that selectively detect the ion of interest in solution – e.g. chloride, potassium. When the ion of interest is encapsulated within the vesicle, it is effectively invisible to the electrode, which is only in contact with the external buffer. When transport occurs, the internal ions leak out of the vesicle and are subsequently detected.<sup>61,62</sup>

Due to its versatility, the ion-selective electrode assay is one of the most widely used methods in the literature. It is compatible with DMSO – the solvent for delivering highly insoluble and lipophilic ionophores. As section 1.2.2 mentions, the internal and external salts can also be altered to investigate cation and anion dependency and electrogenic vs. electroneutral effects. A wide range of dual-host assays also enable coupled transport processes to be studied.<sup>63,64</sup> The chloride-selective electrode is commonly used to investigate chloride/nitrate antiport (Figure 1.24).

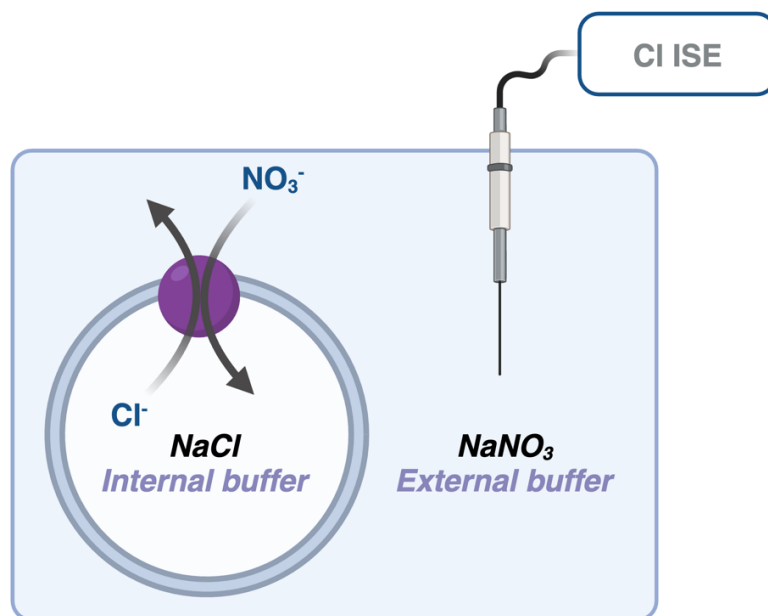


Figure 1.24: Cartoon representation of chloride-selective ISE. Purple = synthetic anionophore.

### 1.2.2.2 Fluorescent indicators

Fluorescent indicators can also be used to monitor ion transport. They are particularly useful when trying to detect the movement of different types of ions, such as hydroxide. Indicators include pyranine (HPTS), a pH-sensitive dye, and lucigenin, a dye whose fluorescence is typically quenched in the presence of halides.<sup>50</sup> Safranin O is a biological stain sometimes used as an indicator of anion transport as it is sensitive to changes in membrane potential.<sup>50,65,66</sup> All of these dyes are charged and, therefore, can be encapsulated within the vesicle with minimal leakage over the time course of the experiment. Consequently, they can be used to report changes in the internal solution. However, using HPTS does not allow for the direct measurement of halide transport. Instead, it measures changes in pH, which is an indirect consequence of anion transport (Figure 1.25).<sup>67,68</sup>

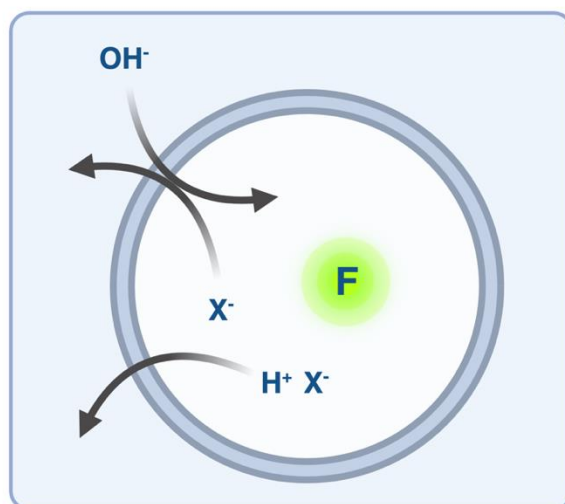
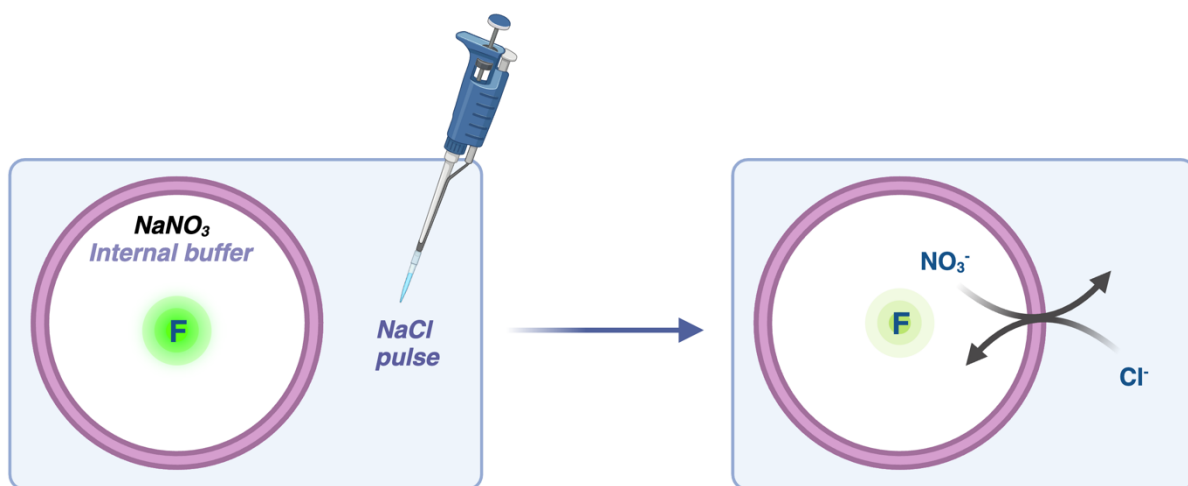


Figure 1.25: Cartoon representation of HPTS assay. *F* = HPTS.

Therefore, the lucigenin assay is commonly used to investigate direct chloride transport. It is also useful for testing compounds with poor deliverability through the aqueous phase. In this assay, the transporter is pre-incorporated into the vesicle as the addition of DMSO quenches lucigenin. A pulse of sodium chloride is added to the external buffer to begin the assay, and anion transport causes a subsequent influx of chloride, quenching the fluorescence (Figure 1.26) based on the Stern-Volmer equation (Equation 1.1). Here, there is a proportional relationship between the inverse of the fluorescence intensity and chloride concentration.<sup>69</sup>

$$\frac{F_0}{F} = 1 + K_{SV}[Q]$$

*Equation 1.1: Stern-Volmer equation used to calculate quenching of fluorescence by lucigenin.  $F_0$  = fluorescence intensity without quencher;  $F$  = fluorescence intensity with quencher;  $K_{SV}$  = Stern-Volmer constant;  $[Q]$  = quencher concentration.*



*Figure 1.26: Cartoon representation of lucigenin assay. Purple membrane = incorporation of synthetic anionophore into vesicles;  $F$  = lucigenin, quenched upon adding chloride.*

Ultimately, these assays are used to compare the activity of different synthetic transporters, and the  $EC_{50}$  is a widely used indicator of transport efficiency. The  $EC_{50}$  is determined *via* dose-dependent experiments, where different concentrations of the transporter are assayed, and the theoretical concentration that achieves 50% ion influx or efflux at the end of the assay (usually 5 minutes) is known as the  $EC_{50}$ . Therefore, the lower the  $EC_{50}$ , the more potent the transporter.<sup>70</sup> Alternatively, the specific transport rate can be determined, typically from the Stern-Volmer equation, which is the transport rate – calculated *via* data fitting – divided by the transporter: lipid ratio. This allows for a more accurate comparison between transporters over a large range of activities.<sup>69,71</sup>



## 1.3 Metal-organic complexes

The mystery of transition metal complexes – or ‘double salts’ – was first solved in 1913 by Nobel prize-winning chemist Alfred Werner, who proposed assigning coordination numbers and oxidation states to metals.<sup>72</sup> Since then, metal-organic architectures have significantly increased in popularity, with different metals and ligands being utilised and several different geometries forming, too.<sup>73</sup>

Several types of metal-organic architectures are available, the most common of which are metal-organic frameworks (MOFs), metal-organic cages (MOCs), and discrete coordination complexes, i.e., metal-organic complexes.<sup>74</sup> MOFs are extended, potentially three-dimensional metal-organic compounds where metal ions are bridged by coordinating organic ligands. They have regularly sized cavities surrounded by the structure's ‘framework’. MOCs are similar to MOFs because they have clearly defined cavities but are discrete, unlike large three-dimensional (3D) structures. Although larger metal-organic architectures have found applications in biomedicine, wastewater treatment and catalysis, there is often a high cost associated with their synthesis, alongside low chemical stability. Metal-organic complexes can often be more accessible, have higher solubility in various solvents and have several applications.<sup>75,76</sup> Cisplatin, a well-known platinum coordination complex, is an anti-cancer drug, alongside other platinum, palladium and ruthenium complexes;<sup>77,78</sup> chromium, gold, and copper coordination complexes have applications as antibacterial agents<sup>79</sup> and complexes of various metals have environmental applications in green chemistry.<sup>80</sup>

### 4.3.1 Coordination-driven self-assembly of metal-organic complexes

The self-assembly of metal-organic complexes is extremely useful and often takes inspiration from nature. The self-assembly of proteins is one of many such examples. Linear sequences of amino acids self-assemble to form secondary structures, like  $\alpha$ -helices or  $\beta$ -pleated sheets, which comprise polypeptide backbones. These further assemble into 3D structures, often called domains, which further assemble into larger structures. Haemoglobin is a prime example of a quaternary structure within the body, and its active unit comprises four domains.<sup>81</sup>

Based on this, Philp and Stoddart discussed the four main lessons synthetic chemists can exploit from observing self-assembly in biological systems.<sup>82</sup>

- Self-assembly processes are economical because of their high convergence.
- Stable and structurally diverse assemblies can be rapidly, accurately, and efficiently synthesised from relatively simple sub-units.
- Using identical subunits within an assembly enables the extensive range of interactions to be kept to a minimum, economising on the information required to describe a structure.
- Molecular recognition using many weak and non-covalent bonding interactions leads to a dynamic, reversible, and ‘intelligent’ synthetic pathway. This pathway is self-checking and self-correcting and affords a product representing a thermodynamic minimum.

Coordination-driven self-assembly involves the self-assembly of subcomponents, utilising various non-covalent interactions, like hydrogen bonding and  $\pi$ - $\pi$  stacking; multiple structures, like helicates<sup>83</sup> and cyclic peptides,<sup>82</sup> have been made through this technique. This is a ‘bottom-up’ approach to synthesis, where the precursors, or starting materials, decide the final structure of the desired product, as opposed to ‘top-down’ synthesis, where the starting materials require external stimuli to form the final structure.<sup>84</sup>

Metal-organic complexes can be synthesised using coordination-driven self-assembly, often known as supramolecular coordination complexes (SCCs). Utilising metal-ligand bonding is advantageous for self-assembly due to the directionality and well-defined geometries that transition metals possess.<sup>82,85</sup> Additionally, the self-assembly of metal-organic complexes is typically entropically favourable due to the preorganisation of subcomponents in desired conformations.<sup>82,86</sup> The chelate effect around metal centres provides additional stability and driving force for self-assemblies.<sup>87</sup> SCCs are now widely used, with some having applications in drug delivery,<sup>88</sup> optical sensing<sup>89</sup> and energy storage.<sup>90</sup>

### 1.3.2 Subcomponent self-assembly

Subcomponent self-assembly is a type of coordination-driven self-assembly that facilitates the one-pot synthesis of metal-organic complexes. This technique was pioneered by Busch<sup>91</sup> and has since been further developed by Hannon<sup>92</sup> and Nitschke.<sup>93,94</sup> Over time, significant advancements have been made, enabling the synthesis of water-soluble metal-organic cages,<sup>93,95,96</sup> as opposed to the initial capability of synthesising only small metal-organic

complexes in organic solvents.<sup>92</sup> While the initial focus was on synthesising silver(I) and copper(I) complexes, this has expanded to encompass various transition metals.<sup>95,96</sup>

This technique involves the formation of covalent bonds between subcomponents and dative covalent bonds from the subcomponents to the metal ion.<sup>93</sup> The subcomponent is often formed of pyridylimines.<sup>93,95–98</sup> These structures provide a chelating linkage that can be used to solubilise and stabilise metal ions, especially in aqueous conditions where imine linkages can be cleaved.<sup>99</sup> Pyridylimine formation can be done *via* the condensation of a) an amine and a pyridine aldehyde or b) an amine functionalised with pyridine groups and an aldehyde. Both subcomponents are added to the solution, along with a metal salt, to form a metal-organic complex (Figure 1.27). The work in this thesis used the former option. The metal ion acts as a ‘template’ to organise the final structure, driven by the chelate effect. Additionally, this provides stability to the metal ion *via* dative covalent bonds from the chelating imine linkage.<sup>100</sup>

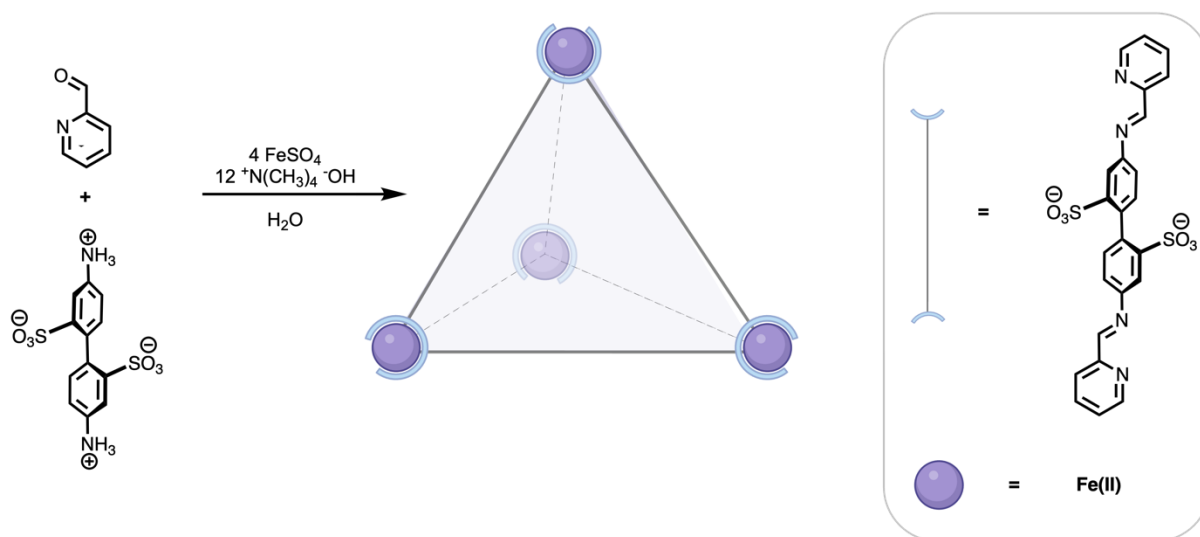


Figure 1.27: Example of subcomponent self-assembly with Fe(II) salt to form M<sub>4</sub>L<sub>6</sub> cage.<sup>95</sup>

This self-assembly technique has several benefits. First, it significantly increases molecular complexity in one step, often from commercially available starting materials. Several large architectures have been synthesised using subcomponent self-assembly with relatively minimal synthetic effort. For example, Leigh and co-workers synthesised an octahedrally-coordinated rotaxane in one step.<sup>101</sup> The diiminopyridine motif was utilised for chelation around the metal centre. Several self-assemblies with different metals were tested, with the Co(II) rotaxane being synthesised with 99% yield. Leigh and co-workers have also devised the one-pot synthesis of



Similarly, anion exchange was used for phase transfer and chemical separation. Three iron(II) cages were synthesised using iron(II) sulfate for aqueous solubility. Following the addition of the anion  $\text{B}(\text{C}_6\text{F}_5)_4^-$ , all three cages became soluble in ethyl acetate and could undergo phase transfer, which was reversible after adding TBA sulfate (Figure 1.29). When adding  $\text{B}(\text{C}_6\text{F}_5)_4^-$  to a mixture of two cages, one cage would become soluble in an organic solvent. In contrast, the other would remain water soluble, thus allowing for the chemical separation of a mixture of two cages.

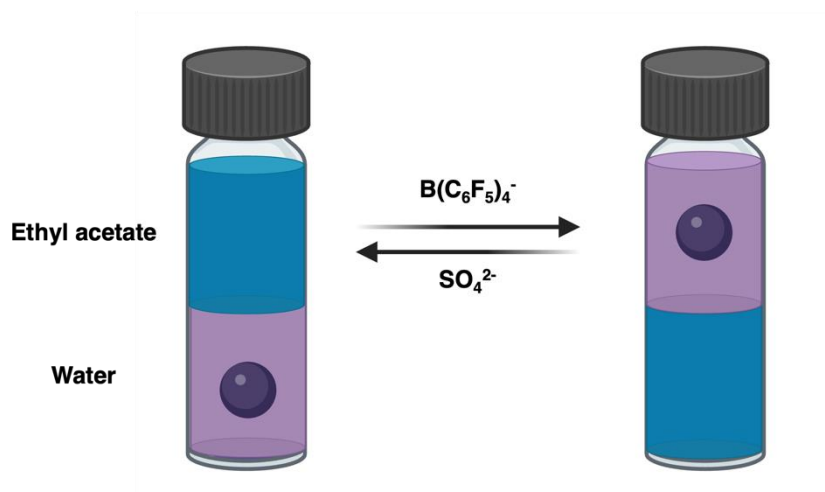


Figure 1.29: Anion exchange to induce phase transfer between ethyl acetate and water.

Purple sphere = cage.<sup>107</sup>

The Nitschke group has synthesised several so-called ‘waterproof’ metal-organic architectures; however, one paper published in 2019 is particularly fascinating due to the use of ditopic and tritopic ligands for water stability (Figure 1.30).<sup>96</sup> These ligands are advantageous for metal-organic complexes as they allow labile metal ions to be incorporated into the architecture *via* chelation. Once again, subcomponent self-assembly was used to synthesise various metal-organic capsules with different metal ions [ $\text{M} = \text{Ni}(\text{II})$ ,  $\text{Co}(\text{II})$ ,  $\text{Zn}(\text{II})$ ,  $\text{Cd}(\text{II})$ ] to determine which were stable in water, as well as acetonitrile. The nickel and cobalt capsules containing monotopic amines were stable in acetonitrile and water, unlike the zinc and cadmium capsules. Following this, they used tritopic amine ligands for subcomponent self-assembly, allowing the zinc and cadmium capsules to be stable in water and acetonitrile. Typically, imines are not stable towards hydrolysis, and  $\text{Zn}(\text{II})$  and  $\text{Cd}(\text{II})$  ions are more labile than  $\text{Ni}(\text{II})$  and  $\text{Co}(\text{II})$ ; however, the chelate effect from the tripodal amine ensures the metal-organic complex is water stable.<sup>87</sup>

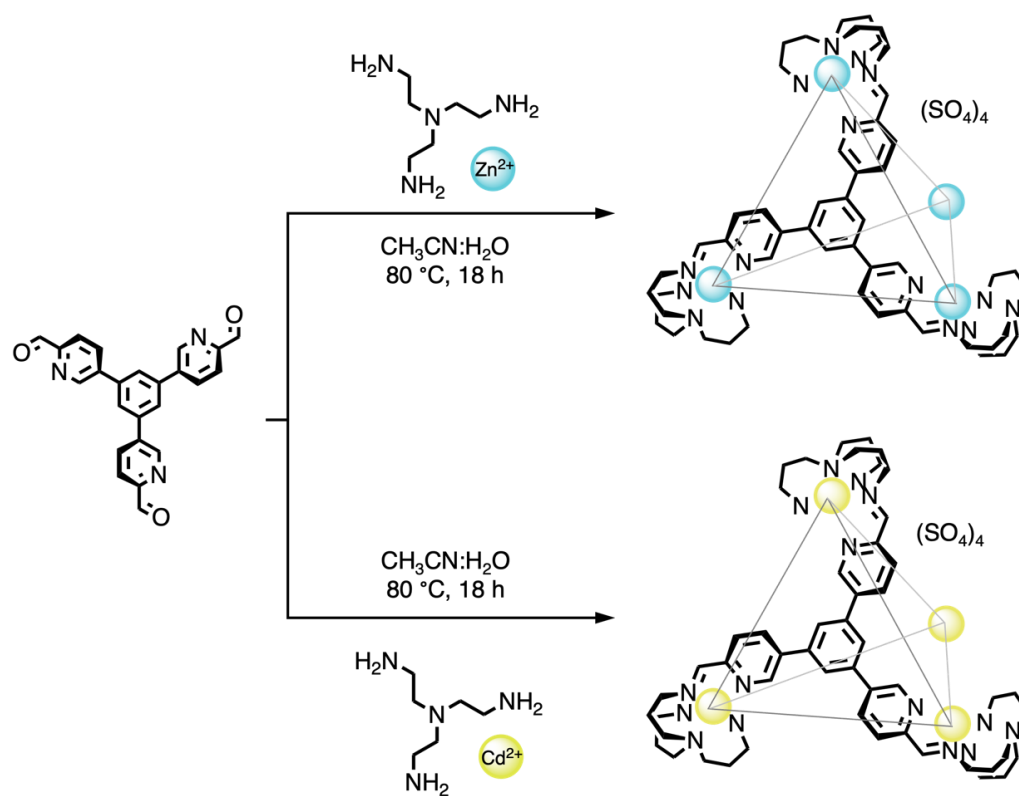


Figure 1.30: Self-assembly of water-soluble Zn(II) and Cd(II) complexes from tritopic subcomponents.<sup>96</sup>

## 1.4 Thesis overview

Considering their vast applications in biomedicine, environmental chemistry, and catalysis, anion-binding molecules are in high demand. Synthesising new anion-binding architectures requires new approaches. This thesis discusses the design, synthesis and fine-tuning of novel anion binders.

This thesis comprises three research chapters. Chapters 2 and 3 outline the synthetic work conducted, while chapter 4 delves into computational work. Chapter 2 investigates the use of subcomponent self-assembly to create metal-organic complexes for anion binding, with potential applications in anion transport and molecular sensing. Chapter 3 builds upon these studies by utilising chiral amines in subcomponent self-assembly, aiming to create clefts capable of chiral guest recognition. Chapter 4 explores a class of molecules called supramolecular self-assembling amphiphiles (SSAs), which have demonstrated antibacterial activity. This chapter uses computational chemistry to investigate the binding mechanism of SSAs to bacterial and mammalian lipids.

## 2. Functionalised ligands for anionic binding clefts

While several motifs and strategies have been employed to bind anions, the recent shift towards synthesising more efficient anion-binding molecules through metal-organic chemistry, as detailed in Chapter 1, presents an innovative and intriguing avenue for exploration in anion transport and molecular sensing applications.

### 2.1 Metal-organic complexes as anionophores

The synthesis of metal-organic complexes for use as anion receptors is not particularly common. Still, there are some reports in the literature indicating the formation of anion receptors composed of octahedral, tetrahedral and square planar metal ions. For instance, Beer *et al.* reported the synthesis and characterisation of an octahedrally-coordinated ruthenium(II) complex using functionalised bipyridine ligands.<sup>108</sup> They tested the binding of three TBA salts – chloride, nitrate and acetate – and observed solvent-dependent binding preferences. In less polar systems, chloride bound preferentially, then nitrate, then acetate. Conversely, nitrate bound the strongest, chloride, and acetate in more polar systems. This is in agreement with the Hofmeister series (see Chapter 1). Caltagirone and colleagues discuss the metal-induced preorganisation anion receptor **28** (Figure 2.1).<sup>109</sup> Indole-functionalised bipyridine ligands were reacted with  $\text{PtCl}_2(\text{DMSO})_2$ , forming a square planar complex around the platinum(II) centre and a pre-organised indole cleft capable of binding anions. They found an increased selectivity for dihydrogen phosphate and even optical sensing applications for fluoride.

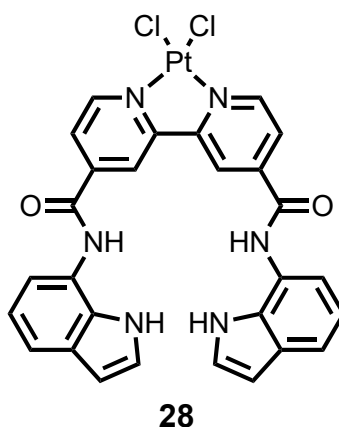


Figure 2.1: Metal-induced preorganised anion receptor **28** synthesised by Caltagirone and colleagues.



Utilising metal-organic complexes as anionophores, or anion carriers, is also a relatively recent concept. As discussed in Chapter 1, anionophores are compounds that directly bind anions to facilitate their transport across a lipid membrane. Metal-organic complexes offer two distinct advantages as anion carriers. Firstly, using different metals allows for diverse coordination structures, providing multiple ion-binding sites. Secondly, the lipophilicity of metal-organic structures can readily be adjusted *via* ligand exchange.<sup>110</sup> This is crucial for effective transport across a lipid membrane, where a delicate balance of lipophilicity and hydrophilicity is required.

Tecilla and colleagues were among the first to report metal-organic anionophores (Figure 2.2).<sup>111</sup> Both palladium complexes exhibited square planar geometry and differed only by one ligand – either triflate (OTf) or chloride. Using the pH-sensitive HPTS, the OH<sup>-</sup>/X<sup>-</sup> symport properties of **29** and **30** were examined. Both compounds showed similar transport activity, indicating that anion binding occurred through displacement of the triflate and chloride anions. Additionally, the anion transport properties of two control molecules, PdCl<sub>2</sub> and 1,3-bis(diphenylphosphino)propane (dppp), underscored the advantages of utilising metal-organic complexes as anion carriers.

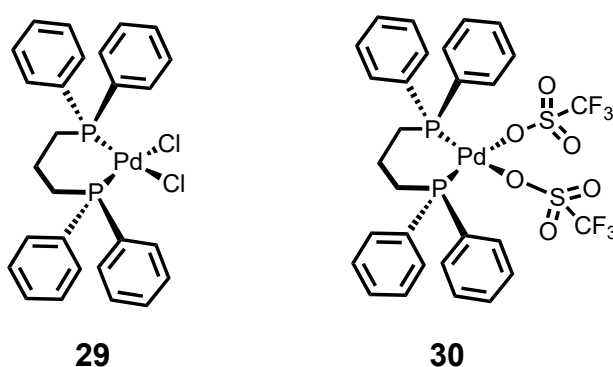


Figure 2.2: Anionophores Pd(dppp)<sub>2</sub>Cl<sub>2</sub> (**29**) and Pd(dppp)<sub>2</sub>(OTf)<sub>2</sub> (**30**)  
synthesised by Tecilla and co-workers.<sup>111</sup>

Gale and co-workers again studied the use of labile ligands in metal-organic complexes to aid anion transport; they synthesised platinum complexes containing labile triflate ligands (Figure 2.3).<sup>112</sup> These ligands were displaced by water to form the hydroxido complex, which is highly lipophilic and allows the partition of the metal-organic complex into the lipid bilayer. An increase in intravesicular pH, monitored *via* the HPTS assay, confirmed the formation of the

hydroxido complex and the subsequent release of hydroxide ions. Anion transport did not occur when more strongly coordinating ligands, like nitrate (**34**), replaced the triflate ligands.

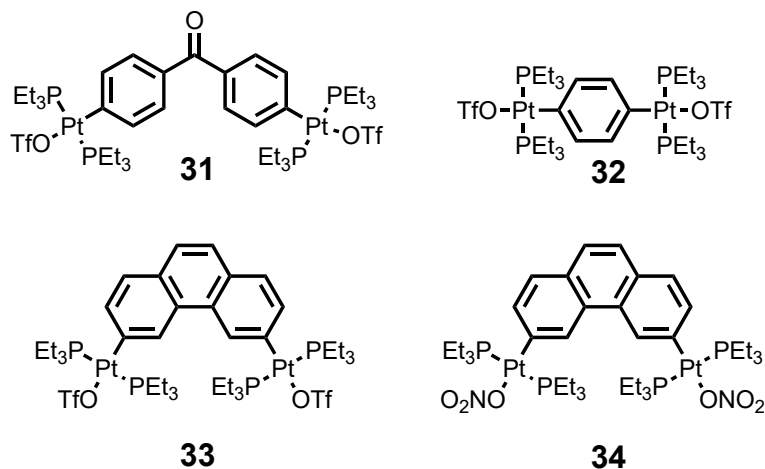


Figure 2.3: Platinum anionophores **31**, **32**, **33** and **34** synthesised by Gale and co-workers.<sup>112</sup>

Further investigating lipophilicity, Gale and co-workers assessed the anion transport capabilities of PtL<sub>4</sub> complexes with varying alkyl chain lengths.<sup>113</sup> This ranged from methyl groups to substantial decyl chains. The transport properties of all compounds regarding their Cl<sup>-</sup>/NO<sub>3</sub><sup>-</sup> antiport activity were examined using the chloride-selective electrode. The research revealed that compounds with longer alkyl chains (> 3 carbons) were excessively lipophilic to dissolve effectively in the aqueous buffer.

Preorganisation due to chelation around metal centres often plays a crucial role in some metal-organic transporters. Wright and co-workers published one such example in 2020.<sup>114</sup> Phosphazane ligands were coordinated to different metals, specifically Rh(I), Mo(0) and Au(I) and their antiport transport activity was tested *via* the HPTS assay. The rhenium and molybdenum complexes exhibited better transport activity as the active conformation was fixed in place *via* chelation around the metal centre. Additionally, the conformation with the best transport activity contained electron-withdrawing CF<sub>3</sub> groups close to the NH groups to make the NH proton more acidic and a better anion binder.

The comparison between **35** and **36**, synthesised by Mao and colleagues (Figure 2.4), again highlights the significance of fixed active conformations.<sup>115</sup> Both iridium(III) compounds were evaluated for Cl<sup>-</sup>/NO<sub>3</sub><sup>-</sup> and Cl<sup>-</sup>/HCO<sub>3</sub><sup>-</sup> antiport using chloride-selective electrode studies. **35**,

which contains two imidazole groups, transported approximately 90% of chloride anions in 200 seconds, while **36** only transported around 20%. This suggests that having more than one anion-binding motif enhances ion transport. Cell studies on **35** and **36** were conducted due to their significant chloride transport activity. Both compounds exhibited cytotoxicity against various cell lines and  $\text{Cl}^-/\text{HCO}_3^-$  antiport led to an elevation in lysosomal pH and subsequent lysosome dysfunction.

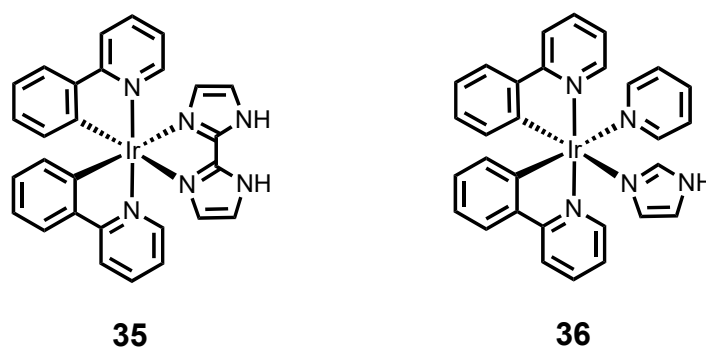


*Figure 2.4: Iridium anionophores **35** and **36** containing imidazole groups for anion binding.<sup>115</sup>*

The redox-active nature of metals can also be beneficial for switchable anion transport. Gale and colleagues designed a set of anion transporters (Figure 2.5) that coordinated a gold complex, rendering it inactive.<sup>116</sup> To reveal the anion-binding site, glutathione (GSH) could reduce the gold complex, a biologically relevant reductant.  $\text{Cl}^-/\text{NO}_3^-$  antiport activity of all compounds was tested using the chloride selective electrode. All transporters exhibited good chloride transport activity, with the most potent transporters containing strongly electron-withdrawing groups to polarise the NH for better hydrogen bonding.

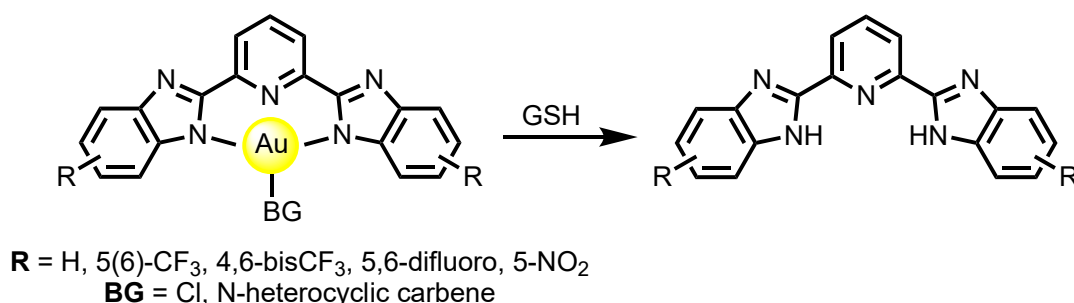


*Figure 2.5: Gold complexes reduced by glutathione to reveal anion binding site. GSH = glutathione.<sup>116</sup>*

## 2.2 Metal-organic complexes and indicator displacement assays

Molecular sensors allow for the rapid detection of analytes by visualising the probe-analyte interaction, typically optically or *via* fluorescence.<sup>117</sup> The first-ever molecular sensor was synthesised in 1867.<sup>118</sup> It comprised a flavone that fluoresced when chelated to aluminium(III). Since then, various molecular sensors have been synthesised, particularly those to sense anions, which have found applications in fields such as medical diagnostics and environmental chemistry.

The indicator displacement assay (IDA) is a common approach to sensing anions.<sup>119</sup> In this assay, a host molecule binds a dye, which is subsequently displaced by adding another, often anionic, guest (Figure 2.6a). The photophysical properties of the bound and unbound dye should be different, allowing for quick signal detection (Figure 2.6b).<sup>120,121</sup>

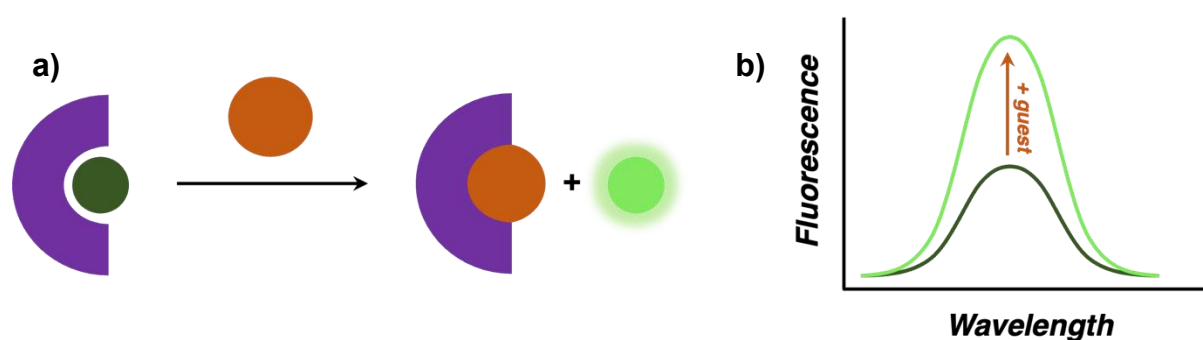


Figure 2.6: a) Cartoon representation of indicator displacement assays; b) cartoon representation of the expected fluorescence increase upon addition of guest. Purple = host; dark green = bound dye; orange = guest; light green = unbound dye.

### 2.2.1 Fluorescence mechanisms

There are several mechanisms *via* which fluorescent sensors can function. However, for IDAs, the most common mechanisms are intramolecular charge transfer (ICT) and Förster resonance energy transfer (FRET).

ICT systems (Figure 2.7) can also be known as ‘push-pull’  $\pi$  systems since they comprise an electron-donating moiety conjugated to an electron-accepting moiety. Electron density moves from the donating moiety to the accepting moiety following photoexcitation, polarising the fluorophore in the excited state and creating a more significant dipole moment. ICT results in

a bathochromic shift in emission – i.e. a redshift. The more significant the dipole moment, the higher the wavelength shift, thus resulting in a higher bathochromic shift.<sup>122,123</sup> ICT can be modulated to achieve an on-off fluorescence sensing response – a helpful quality for IDAs. For example, coordinating a metal ion or proton with the donor lone pair quenches its fluorescence.<sup>124</sup>

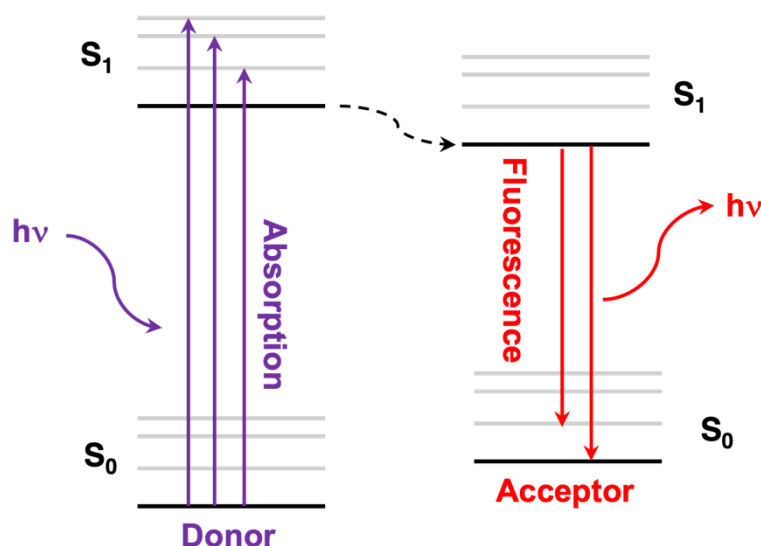


Figure 2.7: Jablonski diagram of ICT mechanism. Black arrows = energy transfer.

FRET systems consist of two components: a donor fluorophore and an acceptor dye with an absorbance peak overlapping with the emission of the donor (Figure 2.8a). The acceptor can either be a non-emissive dye (e.g. a quencher) or a fluorophore, and this will give rise to intensity-based or ratiometric probes, respectively. Ratiometric fluorescence is a method that detects response changes based on the fluorescence intensity ratio at two or more different emission wavelengths.<sup>125</sup> In this process, the emission of the donor fluorophore is quenched *via* the non-radiative energy transfer from an excited donor to a nearby acceptor *via* long-range dipole-dipole interactions. Figure 2.8b depicts the Jablonski diagram of a FRET process. FRET efficiency highly depends on the distance between the donor and acceptor, with energy transfer efficiency proportional to  $1/d^6$ , where  $d$  = distance. FRET-based systems are, therefore, susceptible to small changes in conformation.<sup>122</sup> An example of an IDA that utilises FRET was developed by Naktani and co-workers, in which the fluorescence of xanthone-based fluorophores was quenched upon binding to ribonucleic acid (RNA) due to the short host-guest distance.<sup>126</sup> Subsequent displacement of the fluorophore *via* ligand addition resulted in an increased fluorescence response caused by the greater donor-acceptor distance and reduced FRET.

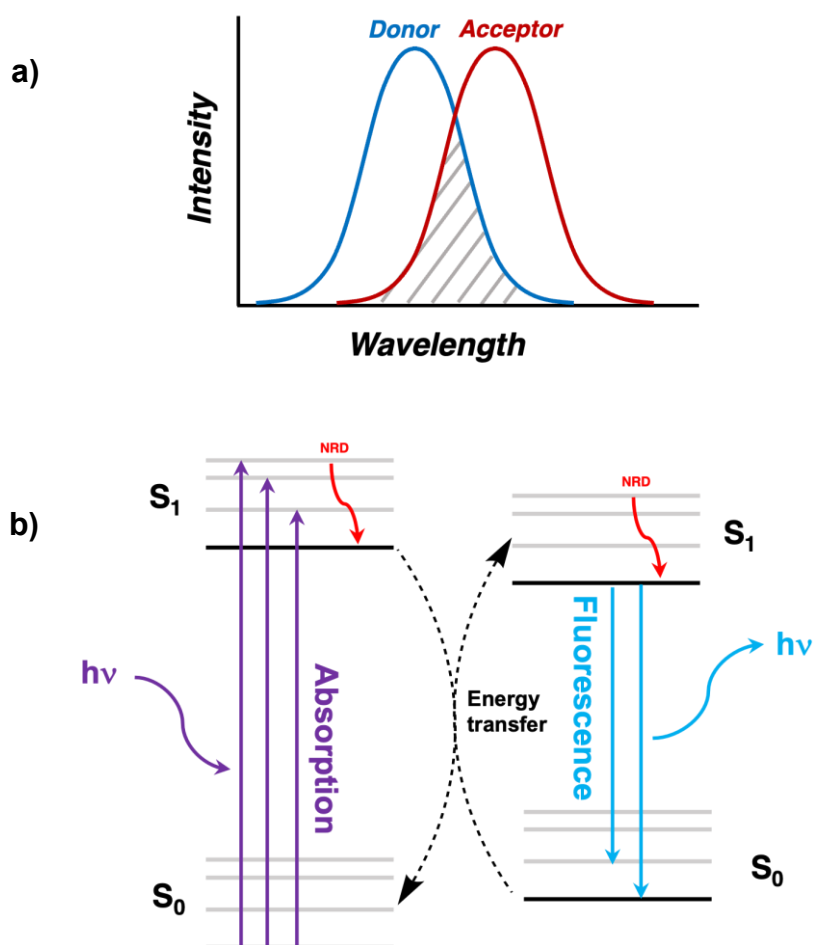


Figure 2.8: a) Cartoon representation of overlap in donor emission and acceptor excitation wavelength for ideal FRET pair. Blue = donor, red = acceptor, grey = donor-acceptor overlap; b) Jablonski diagram for Förster resonance energy transfer. NRD = non-radiative decay.

### 2.2.2 Metal-organic complexes for IDAs

Numerous instances showcase the use of metals in indicator displacement assays despite this being a relatively recent concept. One of the initial documented metal IDAs was only brought to light in the early 2000s.<sup>127</sup> This method of IDAs offers several benefits. As discussed in Chapter 1.1, metals can exhibit a variety of coordination structures, potentially allowing for ligand binding to the metal in conjunction with the receptor. Moreover, metal IDAs have been observed in highly polar solvents, such as water, a feat not frequently achievable with IDAs.<sup>128</sup>

### 2.2.2.1 Copper

Copper(II) is one of the most commonly used metals for IDA, likely due to its high stability in aqueous media.<sup>129</sup> Additionally, it is a biologically relevant ion and thus has low biological toxicity. Some initial examples of copper IDAs highlight the importance of guest size on fluorophore displacement.

Fabrizzi *et al.* synthesised a copper(II) cage composed of TREN units joined by ditolyl spacer units.<sup>130</sup> The large number of amine groups allows for the binding of a range of dicarboxylate molecules. This is useful as carboxylic acid functional groups are present in various biological molecules, particularly amino acids and proteins. Carboxyrhodamine, a fluorophore with two carboxylate groups, was the fluorophore of choice, and its fluorescence was almost entirely quenched by the copper(II) cage. Several aliphatic dicarboxylate guests were tested to turn the fluorescence response back on. Glutarate (n=3) and adipate (n=4) seemed to displace rhodamine entirely, as seen from the increase in fluorescence; however, the addition of succinate (n=2) and pimelate (n=5) showed almost no increase in fluorescence.

In a study conducted by Anslyn and colleagues, a tripodal Cu(II) complex with guanidinium units was designed to bind oxyanions on inorganic phosphate and phosphate-containing molecules (Figure 2.9).<sup>131</sup> Various phosphate-containing guests were utilised to displace 5-carboxyfluorescein, thereby activating the fluorescence response. Initially, the binding of three guests to **37** was examined: inorganic phosphate, 4-nitrophenylphosphate and bis(4-nitrophenyl)phosphate. The results showed that inorganic phosphate exhibited the strongest binding, followed by 4-nitrophenylphosphate, while the phosphodiester showed no evidence of binding. This was attributed to the higher charge of inorganic phosphate compared to the phosphate ester, as well as the strongly electron-withdrawing groups on the phosphate ester, which further reduced charge density. Additionally, the size of the phenyl rings of the phosphate ester may have been too large to fit into the host cavity. The study further confirmed the steric influence on guest binding and subsequent fluorophore displacement by examining phosphorylated amino acids, where phosphorylated serine bound much stronger than phosphorylated threonine.

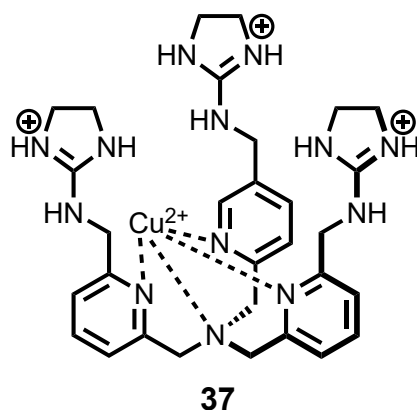


Figure 2.9: Tripodal Cu(II) cleft **37** composed of guanidinium motifs for anion binding synthesised by Anslyn and co-workers.<sup>131</sup>

#### 2.2.2.2 Zinc

Like copper, zinc is not highly toxic in biological contexts, making it another ideal candidate for metal IDAs. The literature reports several examples of zinc IDAs, with many systems being able to discriminate between guests. These systems often comprise dipicolylamine (DPA) ligands that chelate zinc(II) ions.

Detecting anions like phosphate in water or other polar media is difficult due to competing anion solvation effects. However, Kim and co-workers developed a colorimetric phosphate sensor that operates in aqueous solutions at neutral pH (Figure 2.10).<sup>132</sup> An aqueous solution of **38** appeared colourless but turned purple upon adding pyrocatechol violet, a pH-sensitive dye. The displacement of the dye was tested using several anionic species; however, hydrogen phosphate was the only successful anion. This change was seen spectrophotometrically and visually, with the hydrogen phosphate solution turning yellow.

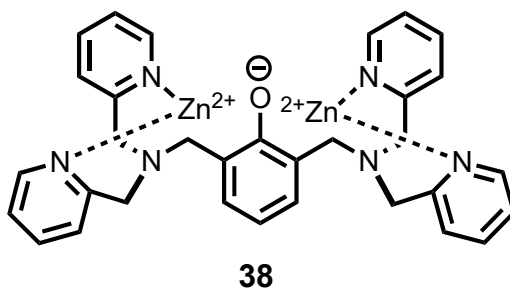


Figure 2.10: Structure of colorimetric phosphate sensor **38** designed by Kim and co-workers containing DPA units chelating to  $\text{Zn}^{2+}$ .<sup>132</sup>



Jolliffe *et al.* have developed similar colorimetric pyrophosphate sensors. They have synthesised a library of cyclic peptide hosts with DPA units, and their indicator displacement properties have been evaluated with many fluorophores, such as fluorescein, eosin Y (EY), and coumarin.<sup>133,134</sup> These hosts display selectivity for pyrophosphate, both spectrophotometrically and visually. The Jolliffe group has also developed a novel type of molecular sensor in which the fluorophore is covalently bound to the receptor.<sup>135</sup> This is known as an intramolecular IDA. One particular study evaluated the difference between intramolecular and intermolecular IDAs. Figure 2.11 shows three complexes used in this study, all containing a covalently bound coumarin molecule. Analogues of **39** and **40** were also synthesised but without the fluorophore. It was found that compound **39** exhibited higher selectivity for pyrophosphate. The lower pyrophosphate selectivity of **40** is likely due to the strong binding of coumarin to both DPA units due to its positioning, making it harder to displace by pyrophosphate.

#### 2.2.2.3 Other metals

The use of alternative metals for metal IDAs is relatively rare, with rhodium,<sup>136,137</sup> titanium,<sup>138</sup> and zirconium<sup>139</sup> being some examples. A recent development involved the utilisation of an octanuclear  $M_8L_{12}$  cobalt cage with a 16+ charge for indicator displacement.<sup>140,141</sup> The binding of four anionic fluorophores – HPTS, fluorescein, 6-carboxyfluorescein and EY – was examined, revealing that six fluorophores could bind to the  $M_8L_{12}$  cage. This suggests that one fluorophore binds to each face of the cage. Subsequent testing of fluorophore displacement indicated that anions with low desolvation energies, such as  $F^-$ , exhibited stronger binding compared to  $Cl^-$  and  $Br^-$ . Notably, this represents the first instance of a metal-organic cage being used for metal IDAs.

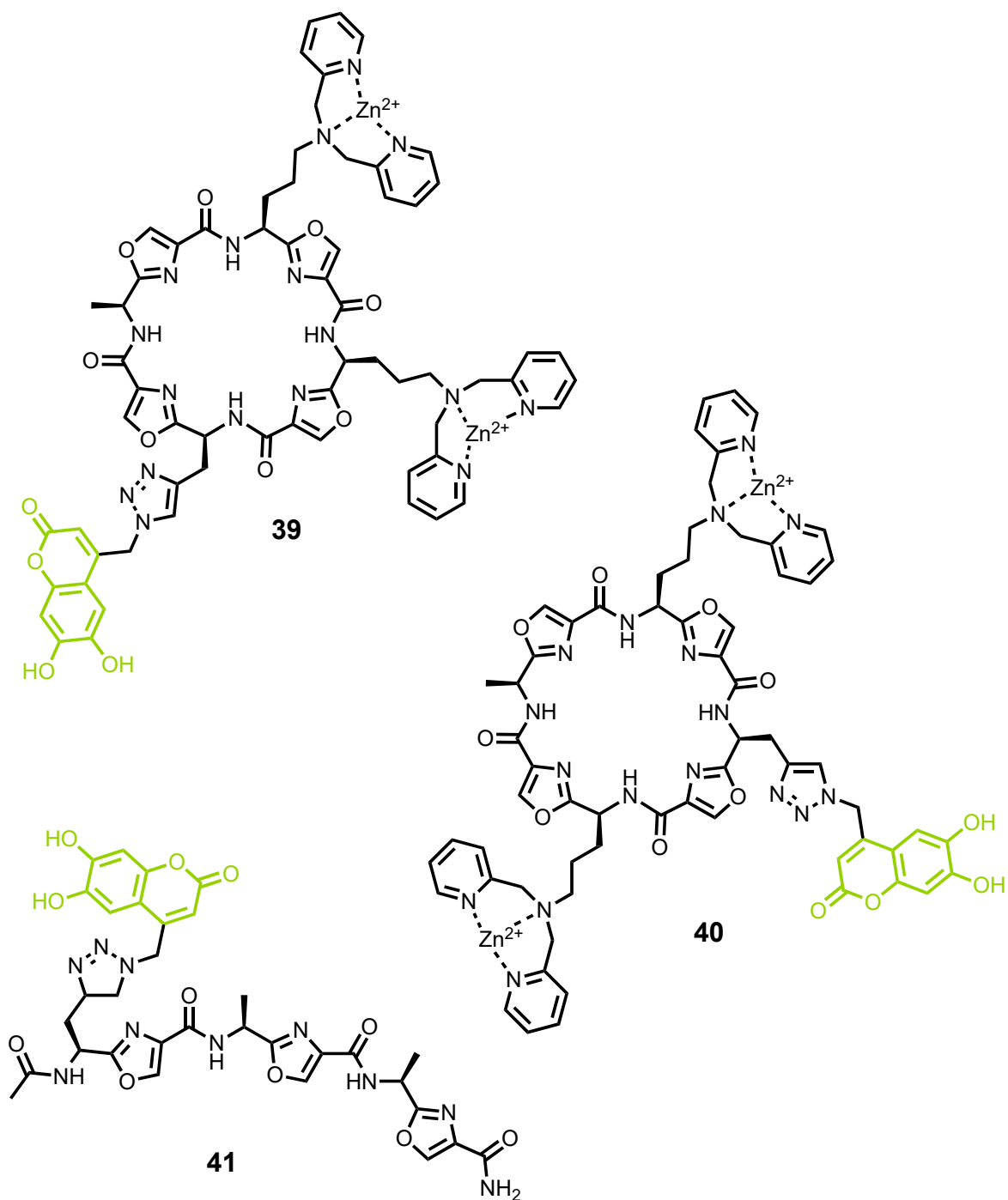
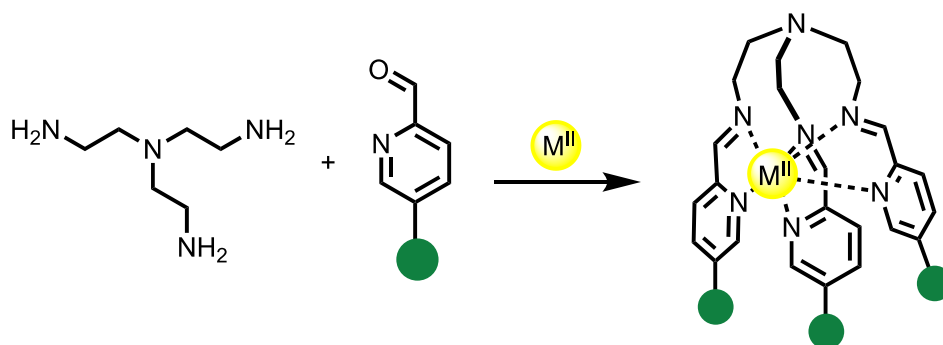


Figure 2.11: Zinc receptors containing covalently-bound coumarin molecules for intramolecular IDAs. Green = coumarin molecule.<sup>135</sup>

## 2.3 Research aims

Chapter 1.3 discusses subcomponent self-assembly as a simple, one-step method for synthesising metal-organic complexes. The objective of this project was to utilise this technique to create a novel metal-organic complex that can function as an anionophore and molecular sensor. More specifically, this project aimed to synthesise novel pyridine aldehyde ligands containing anion-binding motifs to produce a pre-organised metal-organic tripodal cleft (Scheme 2.1). As discussed in section 1.3.2, the incorporation of tripodal amines for subcomponent self-assembly allows for potential water solubility, with tripodal cleft having precedence in the literature. The anion-binding motifs included were based on the dual hydrogen bond donors explored in section 1.1.2 – namely, ureas, thioureas and squaramides – to further enhance the anion-binding capabilities of the tripodal cleft.

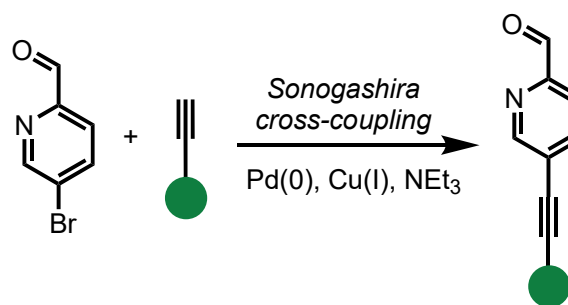


*Scheme 2.1: Proposed synthesis of the tripodal cleft with anion-binding motifs using subcomponent self-assembly. Green circle = anion-binding group.*

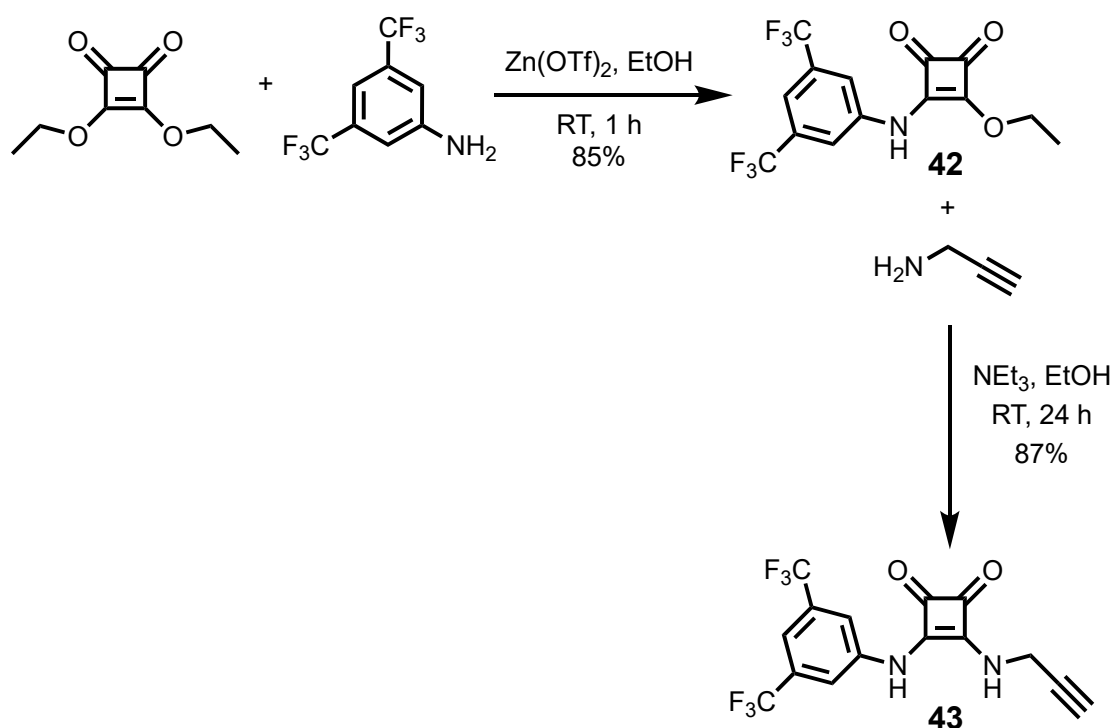
## 2.4 Ligand synthesis

### 2.4.1 Sonogashira route

At first, due to its facile nature, the Sonogashira cross-coupling method was employed to attach the pyridine aldehyde to the anion-binding group. The plan was to make an anion binder with an alkyne handle and subsequent Sonogashira cross-coupling with 5-bromopicolinaldehyde (Scheme 2.2).



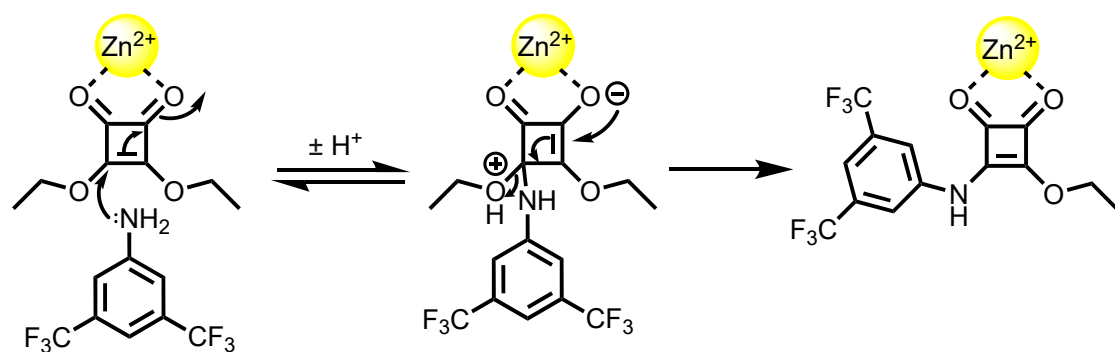
*Scheme 2.2: Proposed synthesis of anion-binder-containing pyridine aldehyde via Sonogashira cross-coupling. Green = anion-binding group – i.e. squaramide, thiourea, urea.*



*Scheme 2.3: Two-step synthesis of squaramide 43.*

Squaramide **37** was synthesised *via* a two-step reaction (Scheme 2.3). It contained an alkyne handle on one side and an aromatic ring with trifluoromethyl groups attached to aid anion binding – electron-withdrawing groups make the conjugated NH proton more acidic and thus more likely to hydrogen bond. The first step involved adding 3,5-bis(trifluoromethyl)phenyl aniline to a squarate ester in ethanol for 1 hour at RT.<sup>142</sup> Zinc triflate was added to the reaction

mixture, as zinc chelation to the carbonyl group ensures regioselective amine addition (Scheme 2.4).<sup>142</sup> The crude product was triturated in water to yield the desired yellow solid **42**. Subsequently, **42** was reacted with propargylamine in ethanol overnight at RT. Finally, it was triturated in 2% aqueous acetic acid to yield the desired product **43** as a yellow solid.<sup>143</sup>



*Scheme 2.4: Mechanism of amine addition to squarate ester via zinc triflate chelation.*<sup>142</sup>

The Sonogashira cross-coupling was first attempted with squaramide **43**. The reaction was conducted using an encapsulated palladium catalyst, Pd EnCat TPP30; this catalyst prevents the palladium from contaminating the product and is also an economical option as the palladium species can be reused. The Sonogashira cross-coupling with 5-bromopicolinaldehyde was done using previously established conditions – adding triethylamine as the base, using acetonitrile as the solvent and stirring the reaction for 1.5 hours at 100 °C in the microwave reactor (Table 2.1, attempt 1). These conditions seemed too harsh for the squaramide reagent as it decomposed. The reaction was repeated using previously successful and milder conditions<sup>144</sup> (Table 2.1, attempt 2) but did not occur. Subsequently, these challenges prompted the search for an alternative conjugation method due to the issues encountered with this cross-coupling reaction. This led us to consider the copper(I)-catalysed azide-alkyne click reaction.

Table 2.1: Reaction conditions for attempted Sonogashira cross-coupling reactions.

Attempt	Substrate	Reaction conditions	Outcome
1	43	Pd EnCat TPP30, NEt <sub>3</sub> , MeCN, 100 °C, 1.5 h, microwave reactor	43 decomposed, therefore reaction did not occur.
2	43	Pd(PPh <sub>3</sub> ) <sub>4</sub> , CuI, NEt <sub>3</sub> , PhMe, RT, 24 h	Reaction did not occur.

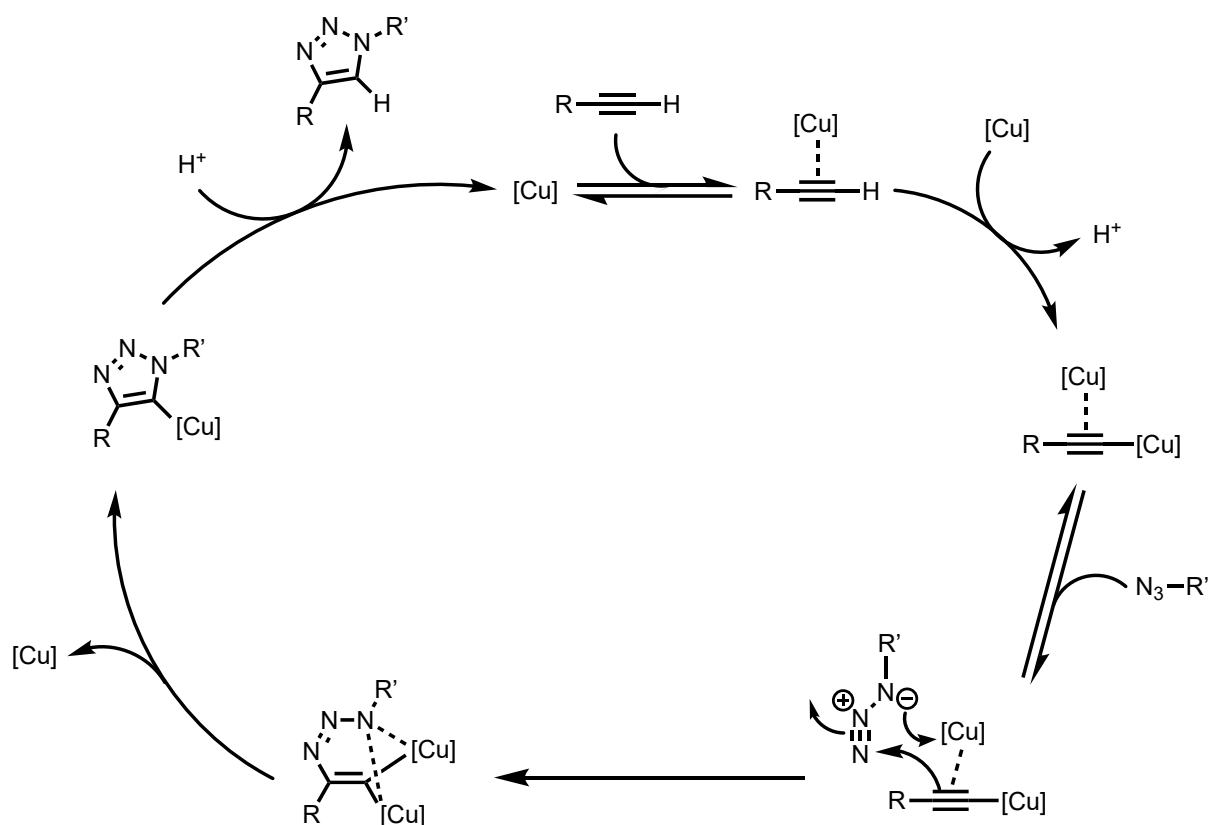
#### 2.4.2 CuAAC route

The copper(I)-catalysed azide-alkyne click reaction (CuAAC) is the most widely used type of click reaction. When Kolb, Finn and Sharpless first defined click chemistry, they emphasised the reaction's 'green' nature, as if to emulate nature.<sup>145</sup> A click reaction must:

1. Be modular.
2. Be broad in scope.
3. Be high-yielding.
4. Generate inoffensive by-products that can be removed *via* non-chromatographic methods.
5. Be stereospecific.
6. Have simple reaction conditions.
7. Have readily available starting materials and reagents.
8. Use benign solvents or solvents that are easily removed.
9. Require little to no purification.

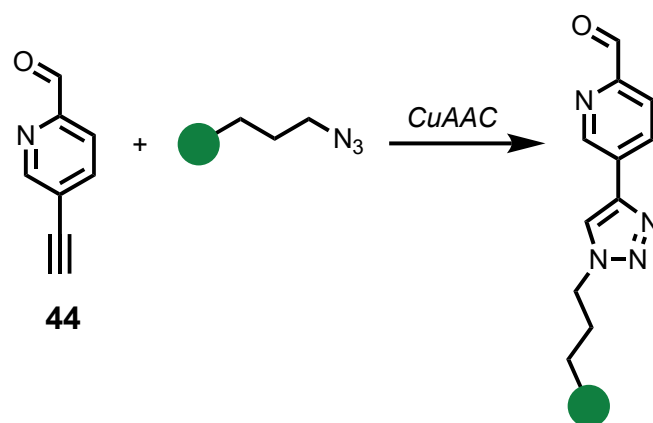
Strictly speaking, the CuAAC does not meet the criteria to be explicitly called a click reaction. For example, the catalyst can be added in one of two ways. On the one hand, the copper(I) species can be generated in situ by reducing copper(II) sulfate with sodium ascorbate. This reaction is typically done in aqueous conditions at room temperature while eliminating the addition of a base. However, the copper(I) catalyst can often be directly added to the reaction mixture using copper(I) halides; here, inert reaction conditions are required due to the sensitive nature of these reagents. This violates criteria number 6. Additionally, reagent solubility can be an issue, requiring more toxic solvents like THF and dimethylformamide (DMF), which

violates criteria number 8. Nevertheless, even though the CuAAC does not strictly follow the rules of click chemistry, this method is often effective for conjugating two molecular fragments. The mechanism of this reaction is still unclear, but a version predicted by DFT studies is given in Scheme 2.5.<sup>146</sup>



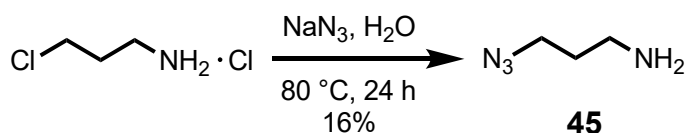
*Scheme 2.5: Proposed mechanism of CuAAC reaction.<sup>146</sup>*

A proposed reaction scheme for synthesising these functionalised pyridine aldehyde ligands is given in Scheme 2.6.



*Scheme 2.6: Proposed synthesis of anion-binder-containing pyridine aldehyde via CuAAC. Green = anion-binding group – i.e. squaramide, thiourea, urea.*

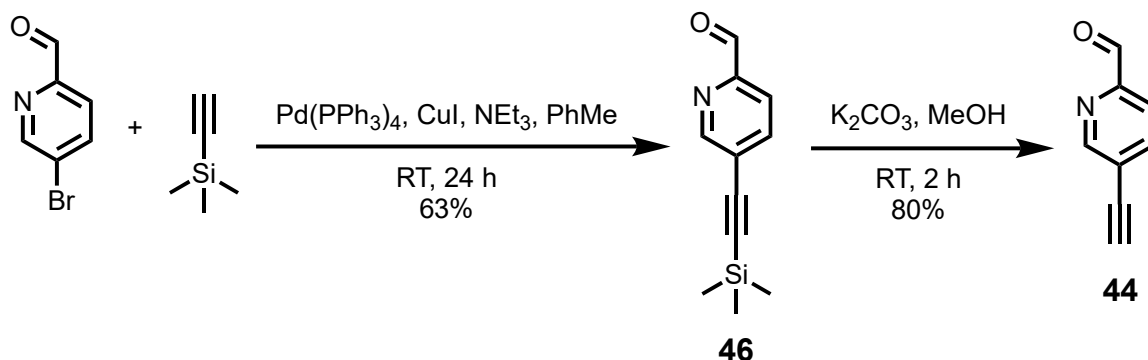
The same azide reagent **45** was used to synthesise all ligands. Sodium azide was added to a solution of 3-chloropropylamine hydrochloride in water, and the reaction mixture was stirred at 80 °C overnight (Scheme 2.7).<sup>147</sup> The reaction mixture was basified by adding 15% aqueous potassium hydroxide, and the product was extracted by washing the aqueous phase with diethyl ether. Its synthesis proved more challenging than anticipated as this compound is quite volatile,<sup>148</sup> which made it difficult to isolate the product from diethyl ether. The synthesis of **45** must indeed be challenging, as later steps carried out with the commercially purchased version proved to be unsuccessful.



*Scheme 2.7: Synthesis of 3-azidopropylamine **45**.*

As shown in Scheme 2.9, the same pyridine aldehyde-containing alkyne reagent **44** was used in all reactions. A two-step literature process was used to synthesise this,<sup>144</sup> with the first step involving a Sonogashira cross-coupling with 5-bromopicolinaldehyde and trimethylsilylacetylene to form **46**. The trimethylsilyl (TMS) group was subsequently deprotected using potassium carbonate in methanol. The full reaction conditions are given in Scheme 2.8. Overall, the synthesis of this reagent was facile and high-yielding.

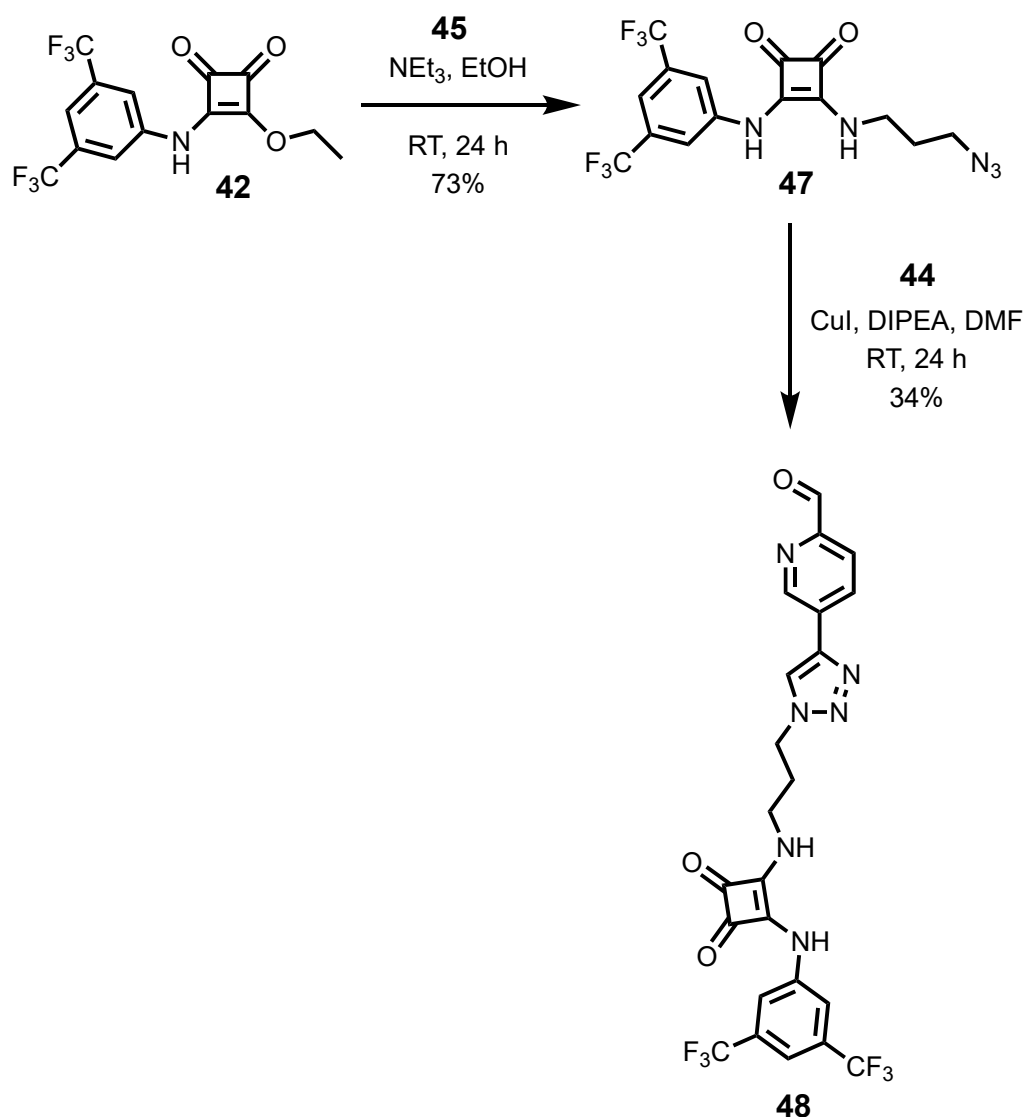




*Scheme 2.8: Synthesis of alkyne-containing pyridine aldehyde **44**.*

#### 2.4.2.1 Synthesis of a squaramide-containing ligand

Initially, the synthesis of the azide-containing squaramide **47** was attempted. The squarate ester containing the bis(trifluoromethyl)aniline (**42**) had already been synthesised for the Sonogashira cross-coupling and so was used for this reaction. Attaching the azide moiety to this reagent was simple and high-yielding – **42** and **45** were dissolved in ethanol and stirred overnight.<sup>143</sup> The crude mixture was triturated with 2% aqueous acetic acid to afford the desired product **47** as a yellow solid (Scheme 2.9, step 1). The click reaction was first attempted using copper(I) iodide, diisopropylethylamine (DIPEA) and THF. The reaction did not occur due to the squaramide's poor solubility in THF. The reaction was then attempted in DMF, which dissolved the squaramide. As mentioned, though, more complex squaramides have been shown to have poor solubilities in most solvents. Hence, the purification of this compound became increasingly more difficult as the purity of the compound increased. Nevertheless, 25 mg of **47** was synthesised and taken to the self-assembly stage.



*Scheme 2.9: Synthesis of squaramide-containing pyridine aldehyde **48** via CuAAC.*

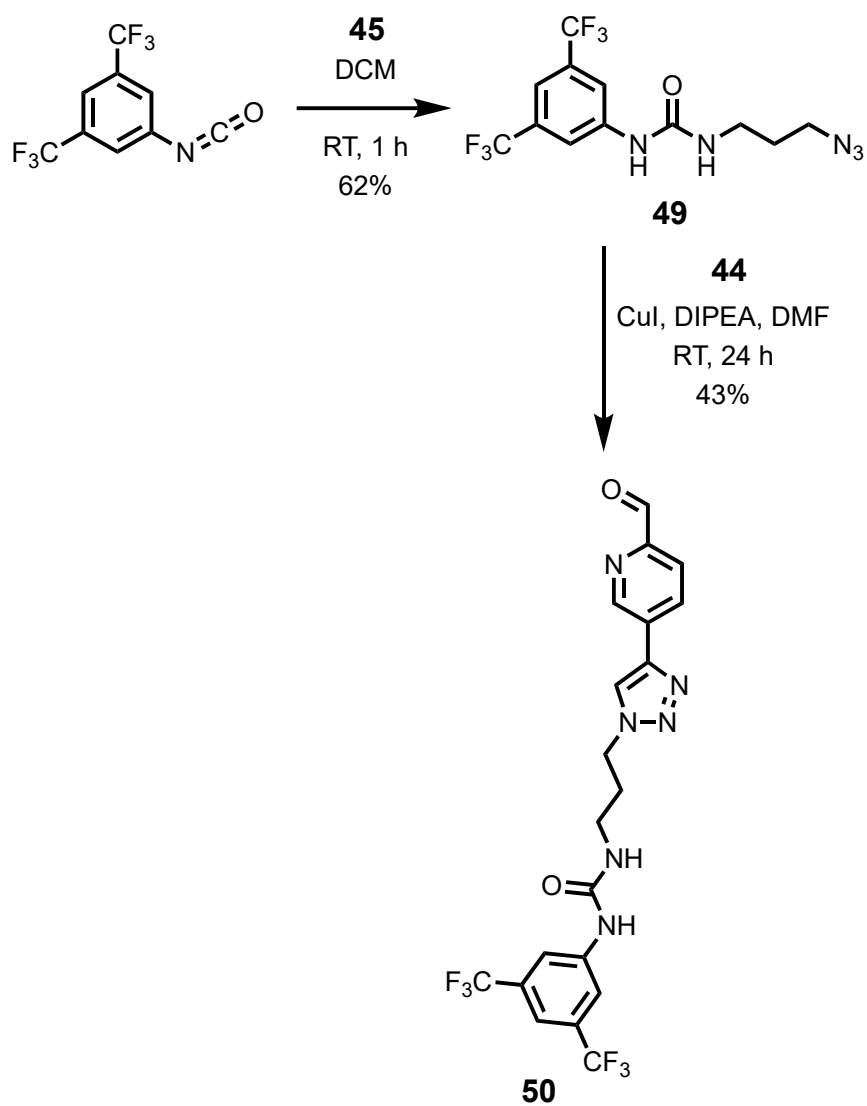
#### 2.4.2.2 Synthesis of a thiourea-containing ligand

Subsequently, the synthesis of the azide-containing thiourea was attempted. To a solution of 3,5-bis(trifluoromethyl)phenyl isothiocyanate in acetonitrile, 3-azidopropylamine was added, and the reaction mixture was stirred for 2 hours at RT. The reaction mixture was triturated in water but with little success. The crude mixture was subsequently extracted with DCM, and the reaction contents were monitored *via* thin layer chromatography (TLC). Several spots were present, so purification *via* column chromatography was attempted, but none corresponded to

the desired product. Likely, the reaction did not occur. The reaction was repeated with an increased stirring time, and the purification steps were repeated. One of the column fractions looked promising but was impure. Column chromatography was attempted again, but it was unsuccessful.

#### *2.4.2.3 Synthesis of a urea-containing ligand*

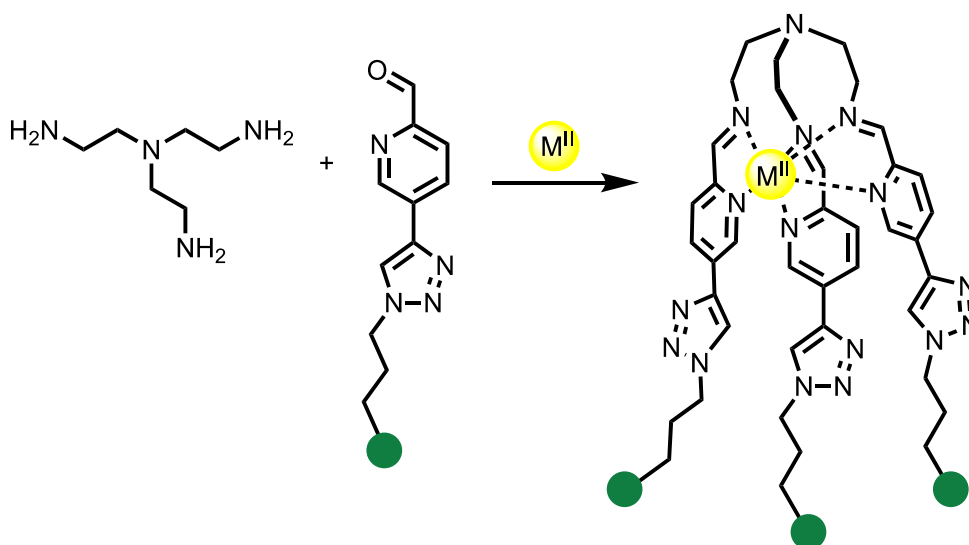
Finally, the synthesis of the azide-containing urea **49** was attempted. The commercially available starting material, 3,5-bis(trifluoromethyl)phenyl isocyanate, was dissolved in DCM, after which 3-azidopropylamine **45** was added. The reaction mixture was stirred at RT for 30 minutes. The desired product precipitated upon adding hexane; overall, this reaction was simple and high-yielding (Scheme 2.10). The click reaction was attempted with **44** using the same conditions as the synthesis of **48** (shown in Scheme 2.9), and the desired product **50** was afforded as a white solid post-purification. The reaction was repeated several times to ensure adequate quantities were available for self-assemblies.



*Scheme 2.10: Synthesis of urea-containing pyridine aldehyde **50** via CuAAC.*

## 2.5 Self-assembled complexes in acetonitrile

Several attempts were made to synthesise a self-assembled complex containing an anion-binding group (Scheme 2.11). This was first tried in acetonitrile with organic-soluble metal salts, as the anion-binding ligands were only soluble in polar organic solvents, like acetone and acetonitrile. The combinations of attempts are presented in Table 2.2. It should be noted that the reaction conditions for entries 1 and 2 are identical; however, different batches of **48** were utilised for each reaction. For entry 1, a slightly more impure version of **48** is likely to have been used, with the impurities enabling **48** to be soluble in acetonitrile.



*Scheme 2.11: Proposed synthesis of metal-organic complexes using anion-binder-containing pyridine aldehyde ligands via subcomponent self-assembly. Green = anion-binding group.*

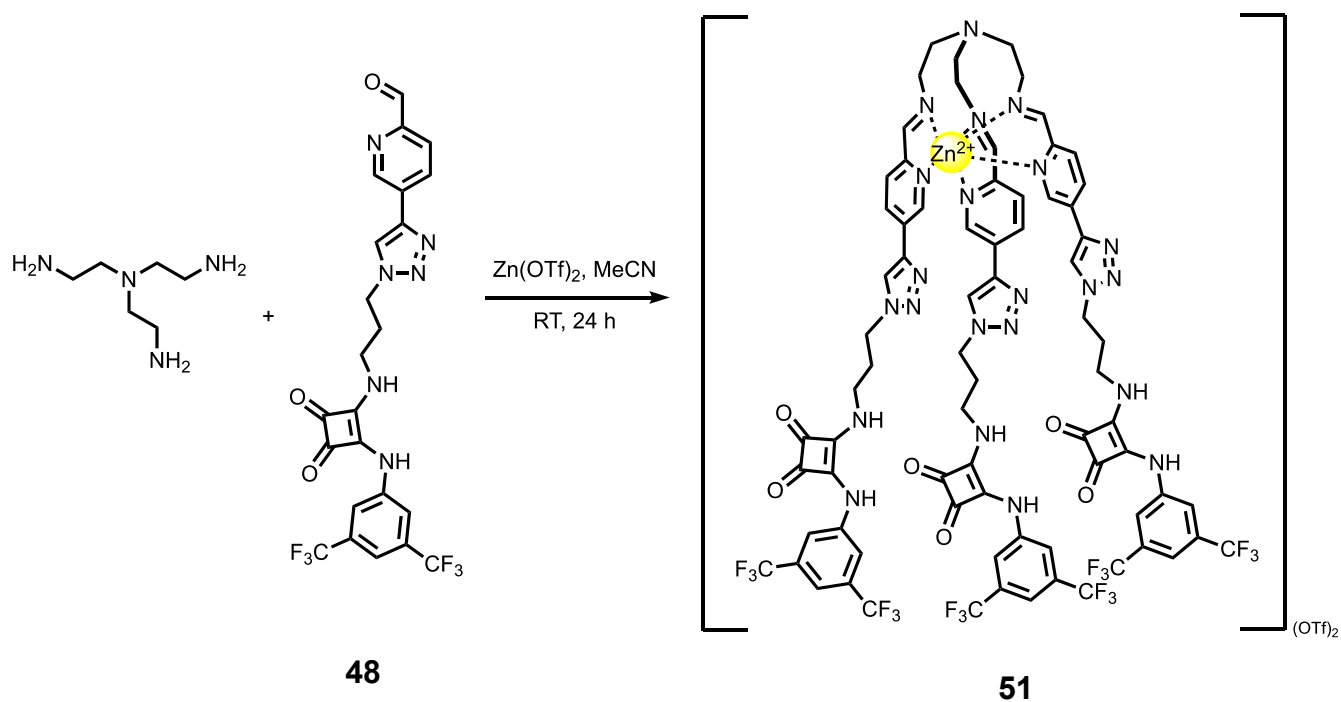
*Table 2.2: Outcomes of self-assemblies conducted.*

	Reaction conditions	Outcome
1	TREN, <b>48</b> , Zn(OTf) <sub>2</sub> , MeCN, RT, 24 h	Successful
2	TREN, <b>48</b> , Zn(OTf) <sub>2</sub> , MeCN, RT, 24 h	Unsuccessful – <b>48</b> insoluble in MeCN
3	TREN, <b>48</b> , Fe(OTf) <sub>2</sub> , MeCN, RT, 24 h	Unsuccessful – <b>48</b> insoluble in MeCN
4	TREN, <b>50</b> , Zn(OTf) <sub>2</sub> , MeCN, RT, 24 h	Unsuccessful – reaction did not proceed

<b>5</b>	TREN, <b>50</b> , Fe(OTf) <sub>2</sub> , MeCN, RT, 24 h	Unsuccessful – reaction proceeded, but unfeasible purification
<b>6</b>	TREN, <b>50</b> , Fe(OTf) <sub>2</sub> , MeCN, RT, 24 h	Unsuccessful – reaction proceeded, but unfeasible purification
<b>7</b>	TREN, <b>50</b> , Fe(ClO <sub>4</sub> ) <sub>2</sub> , MeCN, 50 °C, 24 h	Successful

### 2.5.1 Synthesis of squaramide-containing self-assembled complexes

At first, using zinc triflate, self-assemblies were attempted with squaramide **48** and TREN (Scheme 2.12). A solution of **48**, TREN and zinc triflate was stirred overnight at RT. Immediately, the reaction mixture turned yellow, indicating the formation of a metal-organic complex containing zinc. The reaction mixture was concentrated *in vacuo* until a minimum amount of acetonitrile remained, and diethyl ether was added in portions until a fine yellow solid precipitated. This mixture was centrifuged, and the pellet was washed with water and dried. Although potentially successful, this reaction was very low-yielding and performed on a small scale; hence, there was just enough sample to analyse *via* mass spectrometry (Figure 2.12) – this revealed the presence of the +2 and +1 ions. The presence of the +1 ion is unusual initially; however, this confirms the acidity of the NH proton adjacent to the aromatic ring containing strongly electron-withdrawing groups. Due to the solubility issues encountered with starting material **48**, further investigation into self-assemblies using this substrate was not pursued.



Scheme 2.12: Subcomponent self-assembly with TREN, **48** and zinc triflate to form zinc complex **51**.

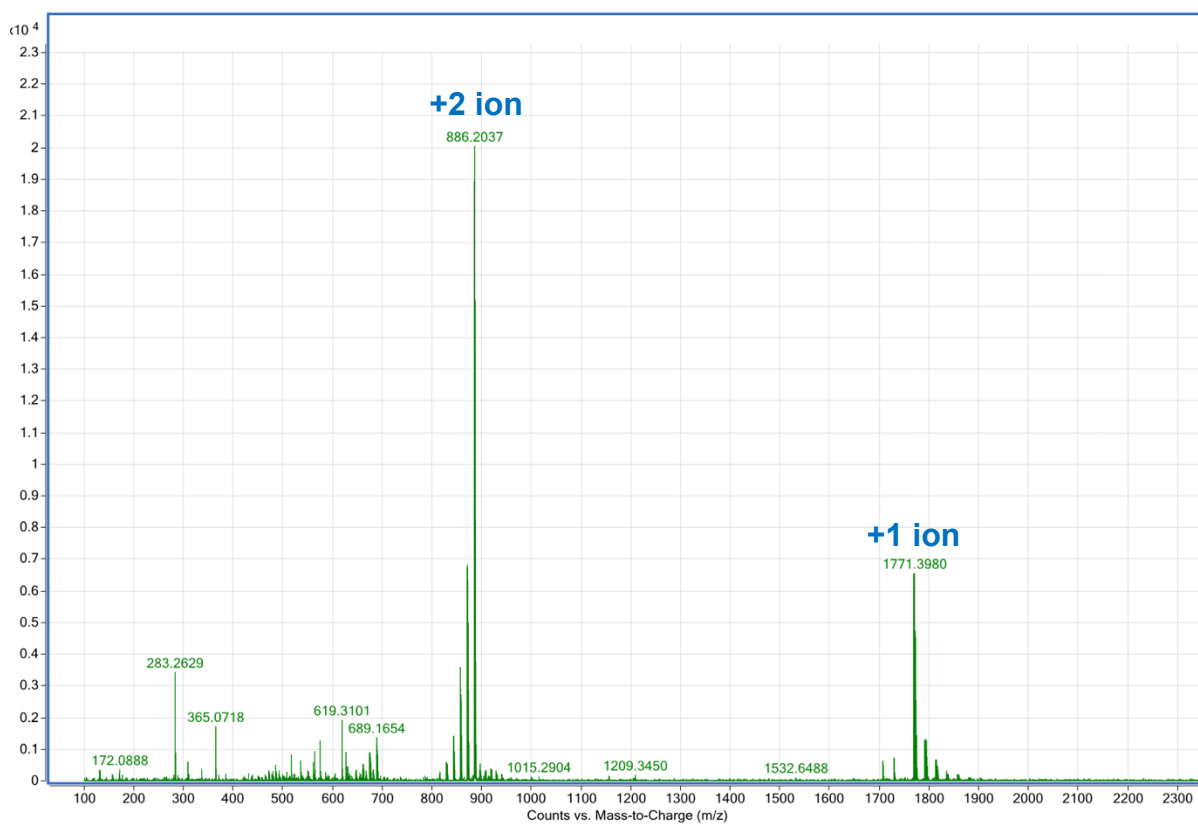


Figure 2.12: Mass spectrum of self-assembled complex **51**.

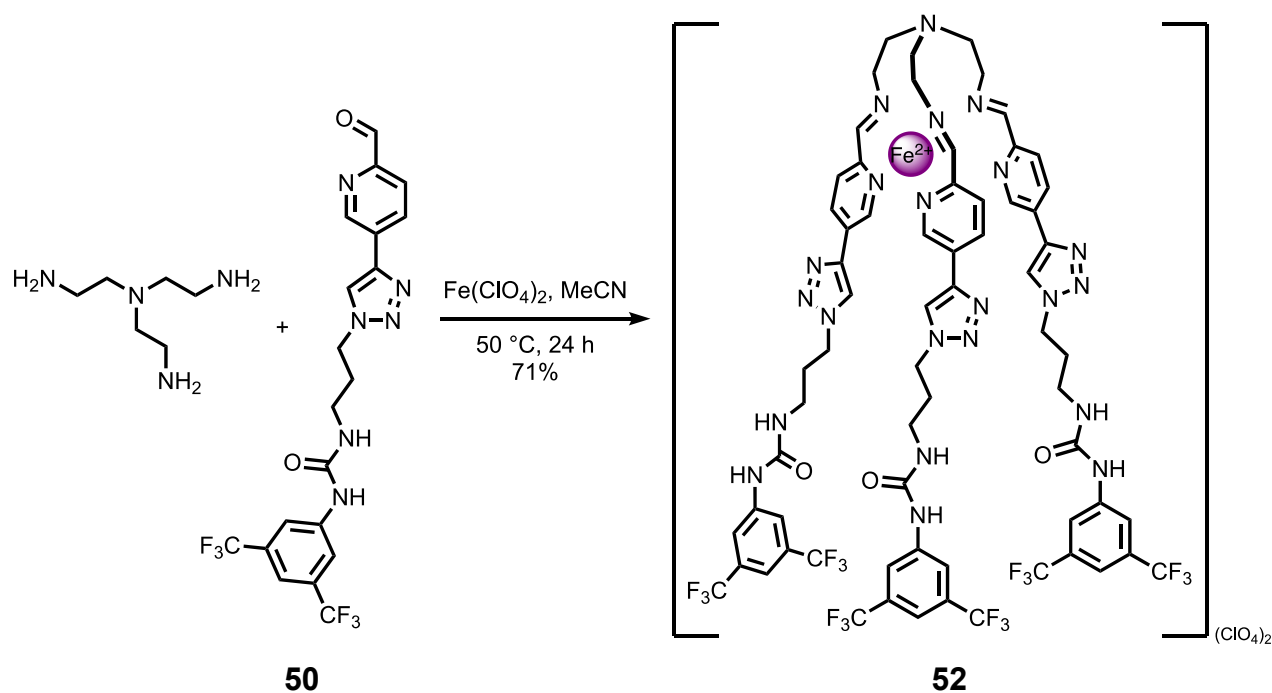
Subcomponent self-assembly with **48** and TREN was also attempted using iron triflate. It was noted that **48** did not immediately dissolve in acetonitrile, but the reaction mixture was left to stir overnight at RT under inert conditions to prevent oxidation of the metal. The reaction mixture had turned brown, likely indicating the oxidation of  $\text{Fe}^{2+}$  to  $\text{Fe}^{3+}$  and iron(III) hydroxide production.<sup>149</sup> The reaction was repeated under inert conditions with the same outcome, implying that the self-assembly is very slow, perhaps due to the poor solubility of **48** in acetonitrile.

## 2.5.2 Synthesis of urea-containing self-assembled complexes

Although there was little success with the triflate salts and squaramide **48**, subcomponent self-assembly was attempted with **50** with both triflate salts. These were performed at RT and left to stir overnight. Both looked promising as the reaction mixtures instantly changed colours (zinc-containing to yellow and iron-containing to purple). Initial analysis of both reaction mixtures indicated the absence of the aldehyde peak, suggesting that **50** had been consumed to form a self-assembled complex. Diethyl ether was added to both reaction mixtures until a fine solid precipitated, which was subsequently centrifuged and the obtained pellet was washed with water. The fine solid was analysed *via*  $^1\text{H}$  NMR spectroscopy, which revealed the samples were impure. Purification *via* size exclusion chromatography, further recrystallisation and trituration were subsequently attempted, but it was unsuccessful.

Efforts were directed to another counterion – perchlorate – also known to have good solubility in non-aqueous solvents.<sup>150</sup> A degassed solution of urea **50** and TREN in acetonitrile was stirred at 35 °C for 20 minutes to ensure reactant solubility; iron perchlorate was subsequently added, and the reaction mixture was stirred overnight at 50 °C under an inert atmosphere to ensure the iron perchlorate did not oxidise (Scheme 2.13). Diethyl ether was added to the reaction mixture until a fine purple solid precipitated, which was centrifuged. The pellet was then washed with water to remove excess TREN. This reaction was successful – the desired iron complex **52** was synthesised in good yield as a fine purple solid.



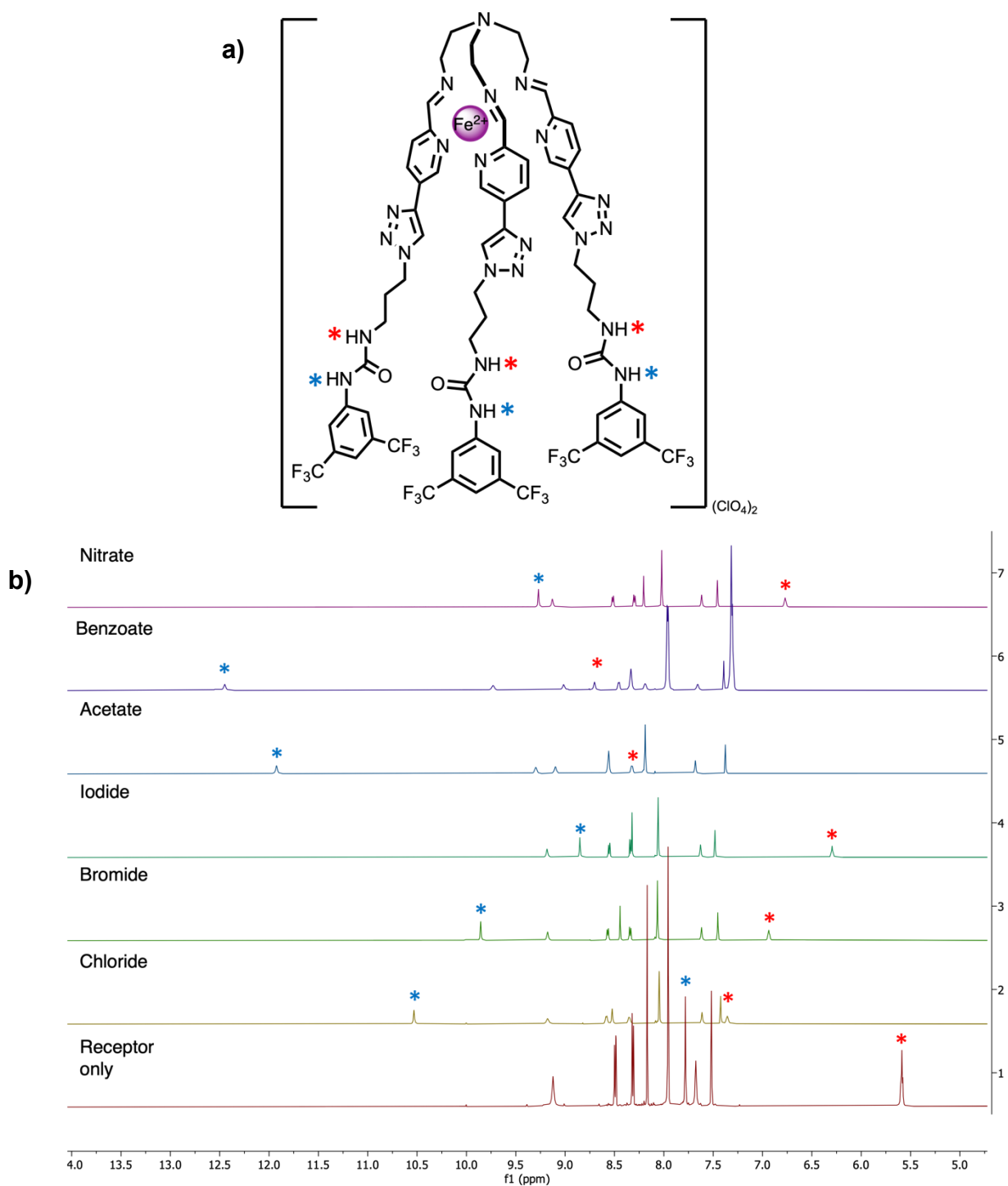


*Scheme 2.13: Subcomponent self-assembly with TREN, **50** and iron(II) perchlorate to form iron complex **52**.*

## 2.6 Guest binding studies

### 2.6.1 Guest screening

At first, simple anions as TBA salts were screened for binding against complex **52** (Table 2.3, phase 1). This was done by adding a significant excess of the guest (10 equivalents) to a 2 mM solution of complex **52** in  $\text{MeCN-d}_3$ . Binding would be indicated by changes in the  $^1\text{H}$  NMR shifts of the NH protons shown in Figure 2.13a. From this, NMR titrations could be carried out to determine the association constant and binding model. All guests, apart from three, screened in phase 1 showed binding. Successful anions are shown in Figure 2.13b, from which it can be inferred that the benzoate, acetate and chloride anions show the most significant response to **52**. Successful anions were taken further for NMR titrations, as described in section 5.2. It should be noted that all singly charged anions in phase 1 were successful, unlike the multi-charged anions – pyrophosphate and citrate. Upon adding the more highly charged guest to a solution of **52** in MeCN, the solution immediately changed from purple to yellow, potentially implying the decomposition of complex **52**, which is supported by  $^1\text{H}$  NMR (see section A1.5).



More complex guests were then screened (Table 2.3, phase 2). Various sugars able to hydrogen bond and previously shown to bind metal-organic complexes in MeCN-d<sub>3</sub> were screened.<sup>151</sup> At first, these were screened in MeCN-d<sub>3</sub>/D<sub>2</sub>O. Due to the rapid exchange of hydrogen and deuterium, the NH protons on the urea ligand could not be seen. Although the NH proton peaks were not visible due to H/D exchange, it was determined that the sugars did not bind **52**, as the other peaks did not shift either. L-arabinose, a sugar completely soluble in the solvent mixture, was again screened for binding with **52**, but in MeCN-d<sub>3</sub>/H<sub>2</sub>O – this confirmed the sugars did not bind the metal-organic complex.

*Table 2.3: Outcomes of guests screened in acetonitrile or acetonitrile/water mixtures. TBA = tetrabutylammonium.*

Phase	Guest screened	Solvent(s)	Outcome
1	TBA chloride	MeCN-d <sub>3</sub>	Binding observed
1	TBA bromide	MeCN-d <sub>3</sub>	Binding observed
1	TBA iodide	MeCN-d <sub>3</sub>	Binding observed
1	TBA acetate	MeCN-d <sub>3</sub>	Binding observed
1	TBA benzoate	MeCN-d <sub>3</sub>	Binding observed
1	TBA hydrogen phosphate	MeCN-d <sub>3</sub>	<b>52</b> decomposed – solution turned from purple to yellow
1	TBA nitrate	MeCN-d <sub>3</sub>	Binding observed
1	TBA citrate	MeCN-d <sub>3</sub>	<b>52</b> decomposed – solution turned from purple to yellow
1	TBA pyrophosphate	MeCN-d <sub>3</sub>	<b>52</b> decomposed – solution turned from purple to yellow
2	L-Arabinose	1:1 MeCN-d <sub>3</sub> /H <sub>2</sub> O 1:1 MeCN-d <sub>3</sub> /D <sub>2</sub> O	Binding not observed
2	D-Fructose	1:1 MeCN-d <sub>3</sub> /D <sub>2</sub> O	Binding not observed
2	α-D-Glucose	1:1 MeCN-d <sub>3</sub> /D <sub>2</sub> O	Binding not observed
2	L-Glucose	1:1 MeCN-d <sub>3</sub> /D <sub>2</sub> O	Binding not observed
2	Methyl-β-D-glucopyranoside	1:1 MeCN-d <sub>3</sub> /D <sub>2</sub> O	Binding not observed
2	Sodium glucuronate	1:1 MeCN-d <sub>3</sub> /D <sub>2</sub> O	Binding not observed

### 2.6.2 NMR titrations

Based on the preliminary guest screening experiments, <sup>1</sup>H NMR titrations were performed with different anions — chloride, bromide, iodide, acetate, benzoate, and nitrate — to attempt to determine the association constants and binding model. A 2 mM solution of **52** was titrated against up to 7 equivalents of the guest in MeCN-d<sub>3</sub>, and a <sup>1</sup>H NMR spectrum was obtained after each addition of anion. Figure 2.14 shows the stack plot from the <sup>1</sup>H NMR titration with TBA chloride.

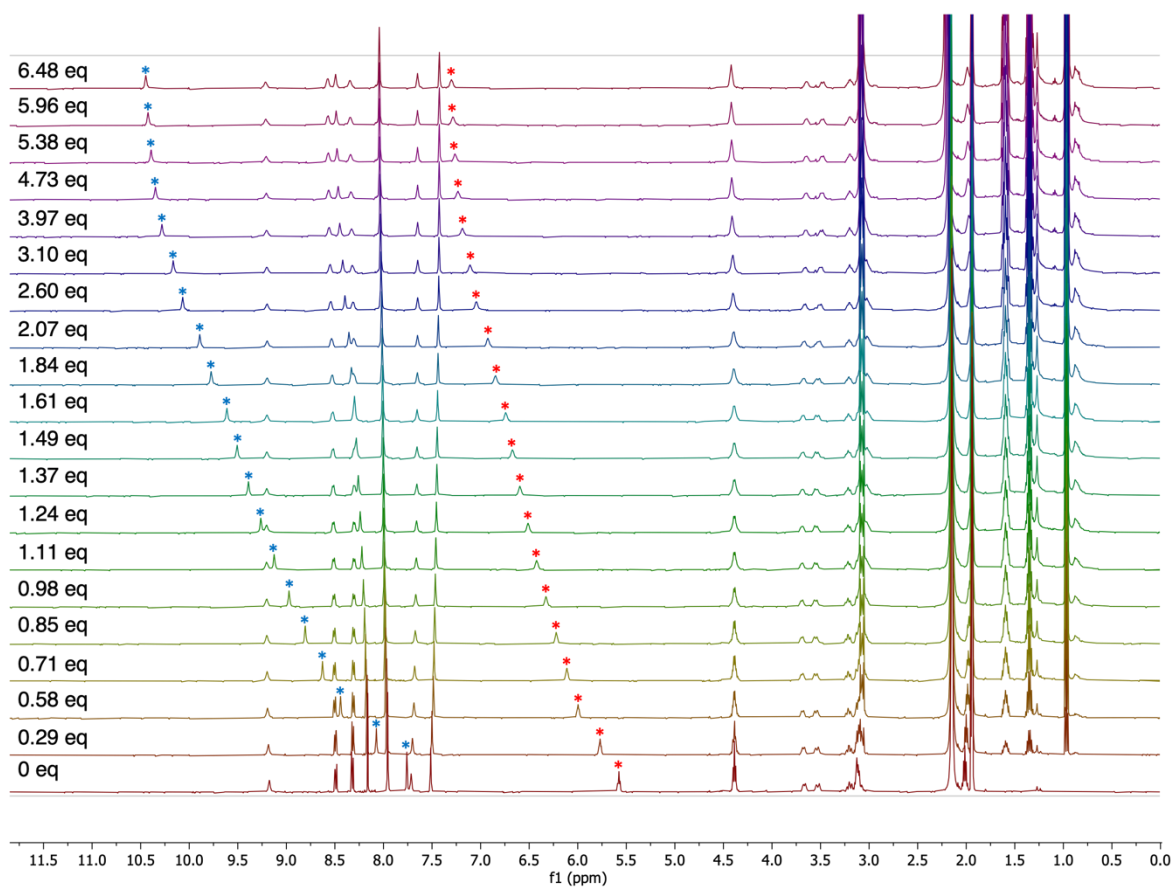


Figure 2.14: <sup>1</sup>H NMR spectrum of titration of **52** with TBA chloride (0-6.48 eq) in MeCN-d<sub>3</sub> (500 MHz). \* = aliphatic proton on **52**; \* = aromatic proton on **52**.

The changes in chemical shift values of the aliphatic NH (\*) and aromatic NH (\*) protons upon adding anion are shown in Figures 2.15 and 2.16, respectively. Both graphs show the same binding preference. The benzoate anion shows the most significant change in chemical shift,

which could indicate strong binding to **52**, followed by the acetate and chloride anions. It should be noted that the addition of increasing equivalents of TBA nitrate caused the formation of a purple precipitate.

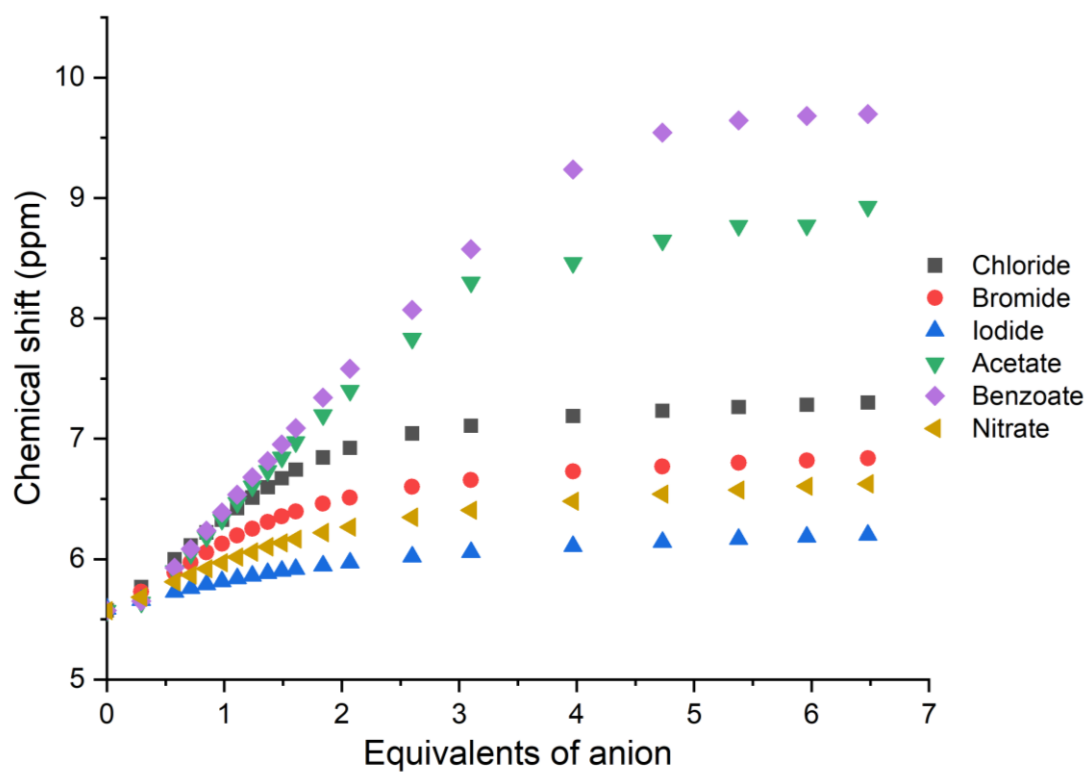


Figure 2.15: Changes in chemical shift of aliphatic NH proton (\*) on **52** upon addition of various TBA salts in MeCN- $d_3$ .

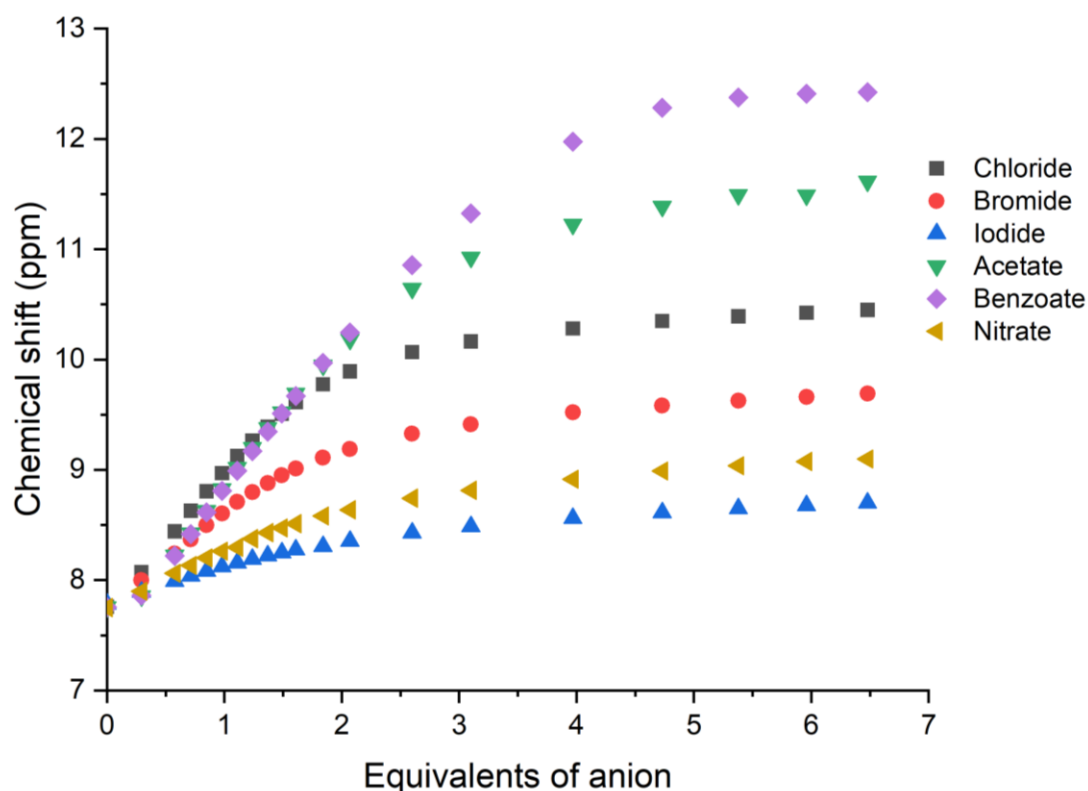


Figure 2.16: Changes in chemical shift of aromatic NH proton (\*) on **52** upon addition of various TBA salts in MeCN- $d_3$ .

The data was subsequently inputted into BindFit to attempt to calculate each anion's association constant and binding model. This online calculator inputs the host and guest concentrations and the chemical shift values for the relevant proton(s) into a binding equation implemented by Python. Along with the desired data, BindFit provides a graph of the residuals for each data point. The residual values on a model predictor can be interpreted as the difference between the predicted and actual values. Assuming the model fits the data well, the residuals approximate random errors and should not display systematic patterns. BindFit could not accurately determine the binding model or association constant values for all titrations for any anion tested. The reasons for each binding model and anion have been outlined in Table 2.4. The residuals displayed were not random for most of the anions and models. They often displayed a sinusoidal curve, and the residuals for the 1:1 binding model for chloride (Figure 2.17) are an excellent example. Due to the tripodal and doubly cationic nature of **52**, the binding model could potentially be 1:3 – one host molecule binding three guest molecules – which is not possible to model on BindFit. There may also be a complex mix of binding modes that are

not well represented by the models on BindFit. Previously, Job plots were used to determine binding stoichiometry. Here, the total concentration of the interacting species is kept constant, but each component's mole fraction is systematically varied. The difference in chemical shift is then plotted as a function of the mole fraction. However, recently, this method has been discredited. Firstly, it assumes linear binding and does not consider more complex systems – i.e., cooperative binding or aggregation. Additionally, the graphs formed can be subjected to visual bias – it is not entirely quantitative.<sup>152</sup> Due to this, we decided not to use Job plots.

*Table 2.4: Reasons for not using BindFit models for all anions in <sup>1</sup>H NMR titrations. 1:1 refers to 1:1 host/guest model; 1:2 refers to 1:2 host/guest model; 2:1 refers to 2:1 host/guest model.*

<b>Anion</b>	<b>Reason(s) for not using BindFit model</b>
Chloride	1:1 – Residuals not random 1:2 – Residuals not random 2:1 – Negative association constants
Bromide	1:1 – Residuals not random 1:2 – Residuals not random 2:1 – Residuals not random
Iodide	1:1 – Residuals not random 1:2 – Residuals not random 2:1 – Residuals not random
Acetate	1:1 – Residuals not random 1:2 – Negative association constant 2:1 – Negative association constant
Benzoate	1:1 – Residuals not random 1:2 – Residuals not random 2:1 – Negative association constants
Nitrate	1:1 – Residuals not random 1:2 – Residuals not random 2:1 – Residuals not random

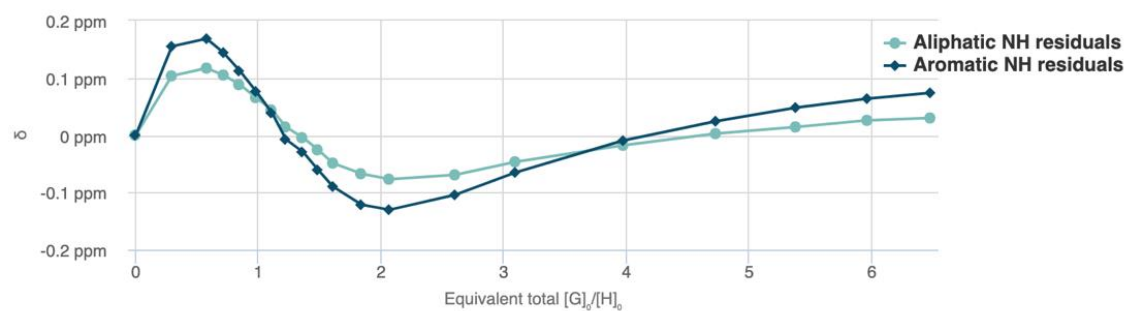


Figure 2.17: Residuals of titration of **52** with TBACl fitted to a 1:1 binding model.

Overall, though, these titrations and the binding screening experiment (Figure 2.13b) could infer (based on the magnitude of the change in chemical shift) a binding order: benzoate > acetate > chloride > bromide > nitrate > iodide. The carboxylates (benzoate and acetate) bind strongest to **52**. Both anions have resonance forms, allowing both oxygen atoms to bind to the urea groups, thus creating a more substantial binding effect. The small and highly charge dense chloride anions within the halide series bind more strongly than bromide and iodide. The poor charge density of nitrate could be contributing to its apparent weak binding to **52**. However, it should be noted that a purple precipitate started forming upon adding TBA nitrate to the host solution. This is likely to be the nitrate salt of the metal-organic complex, where the perchlorate counterion has been exchanged. Hence, another reason for the apparent weak **52**-nitrate binding could be the nitrate anion immediately being removed from the solution to form the insoluble nitrate complex.

## 2.7 Indicator displacement assay

The indicator displacement properties of complex **52** were evaluated based on the established use of metal-organic complexes in IDAs (see section 2.2). We hypothesised that **52** could be utilised in FRET-based indicator displacement assays because it displays a broad absorbance at around 575 nm (Figure 2.18), and its chromophore is near the urea binding cleft. As a result, we hypothesised that it would be feasible to a) observe the binding of an anionic dye due to a decreased fluorescence intensity from the FRET quenching effect and b) subsequently displace the dye by introducing other anionic guests, resulting in increased fluorescence intensity.



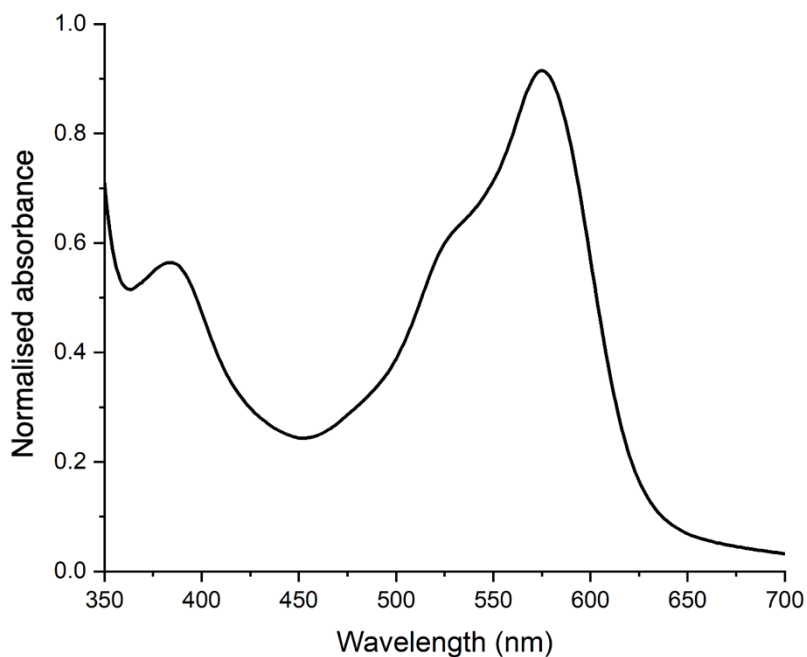


Figure 2.18: Absorbance spectrum of **52** in 1:1 MeCN/H<sub>2</sub>O.

In order to confirm the suitability of compound **52** as both a FRET acceptor and host for various commercially available dyes, we ensured that the emission spectrum of each fluorophore overlapped with the absorbance spectrum of **52**. Following this, the following criteria would have to be met for a successful indicator displacement assay:

1. Quenching of indicator fluorescence by **52**.
2. Regaining of fluorescence intensity after the addition of a more strongly binding anion.
3. Binding of fluorophore to **52** seen *via* <sup>1</sup>H NMR spectroscopy.
4. Fluorescence response discriminates between anions. We hypothesise that the binding strength may influence the discrimination between anions, as weakly bound dyes may be better at distinguishing weaker binding analytes.

Table 2.5: Properties of dyes surveyed for indicator displacement.<sup>153–157</sup>

Fluorophore	$\lambda_{\text{ex}}$ (nm)	$\lambda_{\text{em}}$ (nm)	Colour	pH dependent emission?
Fluorescein	498	517	Green	Yes – fluorescent above pH

Calcein	494	514	Green	Yes – fluorescent above pH 6.5
Pyranine (HPTS)	452	512	Green	Yes – fluorescent above pH 5.5
3-Hydroxyisonicotinaldehyde (HINA)	385	525	Green/ yellow	Yes – fluorescent above pH 7.1
7-aminocarboxycoumarin (7ACC1)	409	473	Blue	Yes – fluorescent above pH 7.0

Various blue, green, and yellow dyes were tested (Table 2.5; Figure 2.19). Several factors were considered when choosing the fluorophores. Fluorophores of different sizes were selected to determine whether fluorophore size contributed to binding. Additionally, different types of anionic dyes were chosen — i.e. phenolates, sulfonates, and carboxylates — to see if there was a binding preference. Dyes were also selected according to their emission spectra and overlap with the absorbance spectra of **52** (Figure 2.20). All fluorophores showed good-to-moderate overlap between their absorbance and emission spectra.

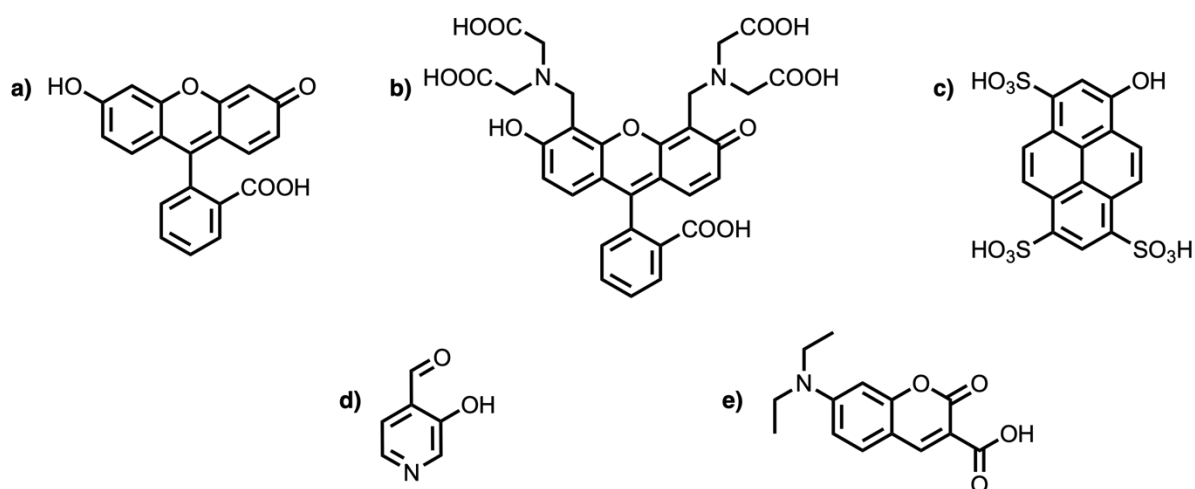


Figure 2.19: Structures of dyes surveyed for indicator displacement; a) fluorescein; b) calcein; c) HPTS; d) HINA; e) 7ACC-1.

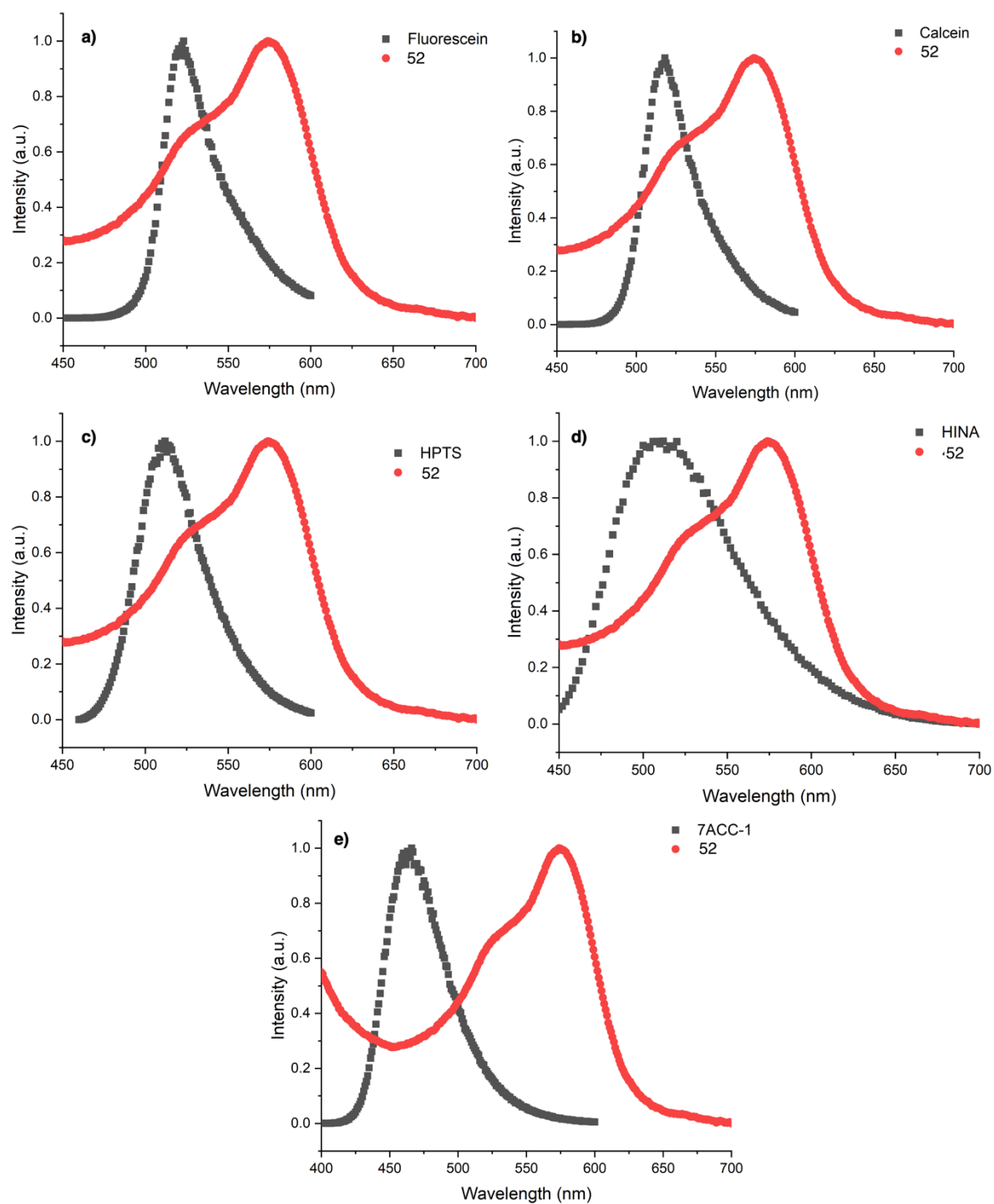


Figure 2.20: Overlap of the absorbance spectrum of **52** (red) ( $5\ \mu\text{M}$  in 1:1 MeCN/TRIS buffer pH 9.0) and fluorophore emission spectrum of a) fluorescein, b) calcein, c) HPTS, d) HINA and e) 7ACC-1 (black). The fluorophore solutions were  $20\ \mu\text{M}$  in 1:1 MeCN/TRIS buffer pH 7.4 or 9.0.

Based on this, we then examined the quenching abilities of **52** by adding aliquots of a 20  $\mu$ M solution to a solution of the fluorophores and monitoring the fluorescence intensity (see section 5.6.2 for further details). Figure 2.21 shows that all fluorophores showed reduced fluorescence intensity upon adding **52**, suggesting that **52** quenches their fluorescence and may even bind to **52**. To further study this, a pulse of sodium chloride or TBA benzoate was added to the solution of the fluorophore and **52**. Adding a competitive guest, such as chloride or benzoate, should only increase the fluorescence of dyes bound to **52**. Interestingly, only the fluorescence of 3-hydroxyisonicotinaldehyde (HINA) and 7-aminocarboxycoumarin (7ACC-1) was restored after spiking the host-dye solution with concentrated chloride or benzoate solutions – this can be seen in Figure 2.21. This suggests that the cleft of **52** is small, allowing only small dyes to bind.

Having seemingly identified a suitable response to chloride for HINA, we then aimed to investigate whether other ions could be detected by adding increasing equivalents of different anions, specifically TBA salts of chloride, bromide, iodide and benzoate, and subsequently measuring the fluorescence intensity. Figure 2.22 shows the fluorescence intensity of HINA after adding increasing equivalents of TBA chloride, bromide, iodide and benzoate. Chloride increases the fluorescence intensity the most, followed by bromide and benzoate. Primarily, iodide did not affect the fluorescence intensity, which aligns with the results from the NMR titration, where iodide did not bind strongly to **52** (Figures 2.15 and 2.16). An NMR titration was subsequently conducted to determine the association constant and binding model of HINA binding to **52**. Surprisingly, there was no downfield shift of any peaks, implying HINA did not bind to **52**. Further  $^1\text{H}$  NMR analysis of HINA in solution revealed that the hydrate was present (Figure 2.23) due to the binding studies being conducted in aqueous solvent mixtures – this is in line with literature references to HINA hydrolysing over time.<sup>156</sup> We concluded that the potential presence of competing equilibria could complicate the results, limiting the practical utility of the assay. Additionally, a large amount of anion is needed to elicit a response, making this system unsuitable for use as a real sensor.

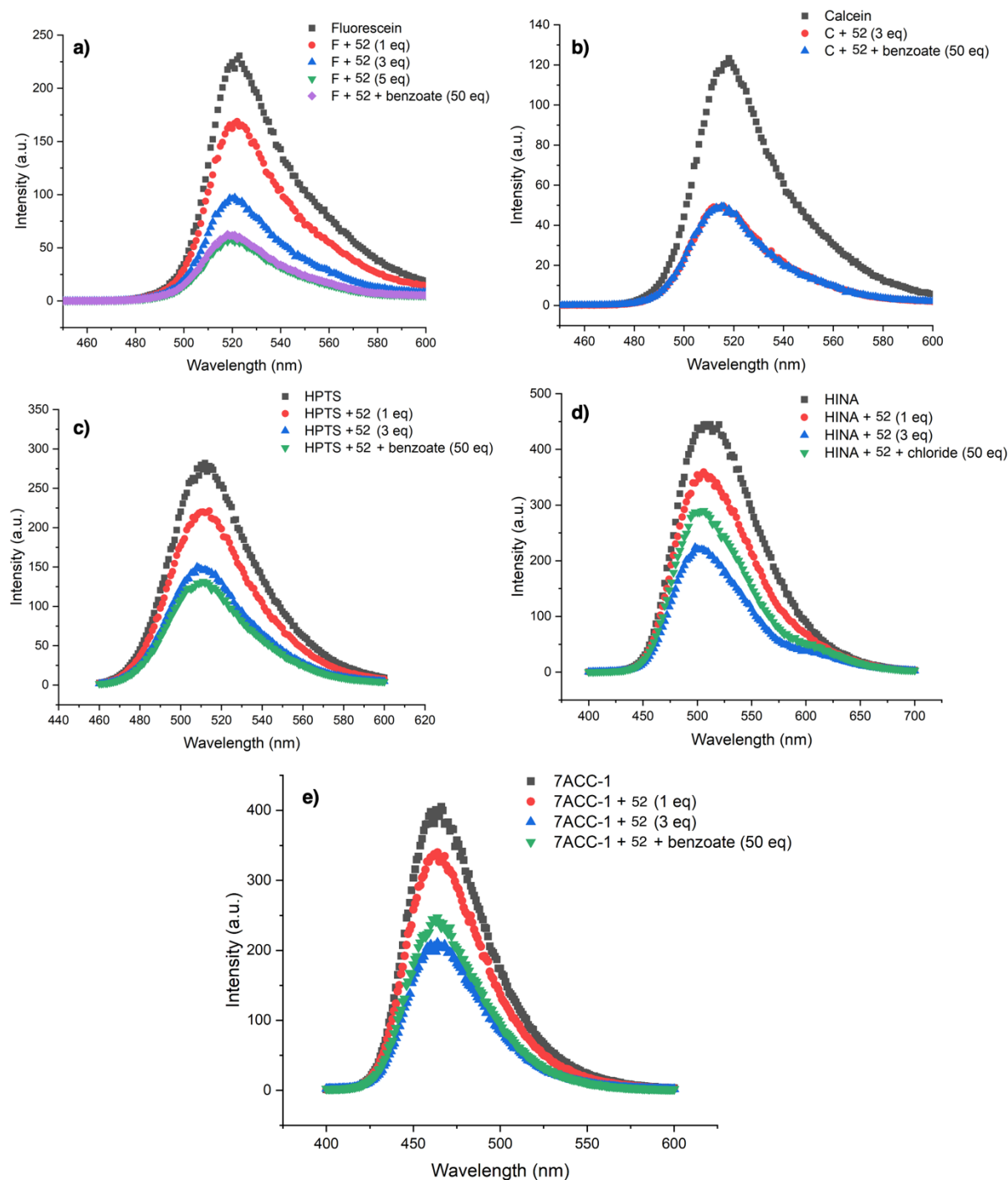


Figure 2.21: Initial emission spectra of fluorophores, followed by addition of 52 (20  $\mu\text{M}$ ) and either chloride or benzoate. Fluorophores shown: a) fluorescein, b) calcein, c) HPTS, d) HINA and e) 7ACC-1. The fluorophore solutions were 20  $\mu\text{M}$  in 1:1 MeCN/TRIS buffer pH 7.4 or 9.0.

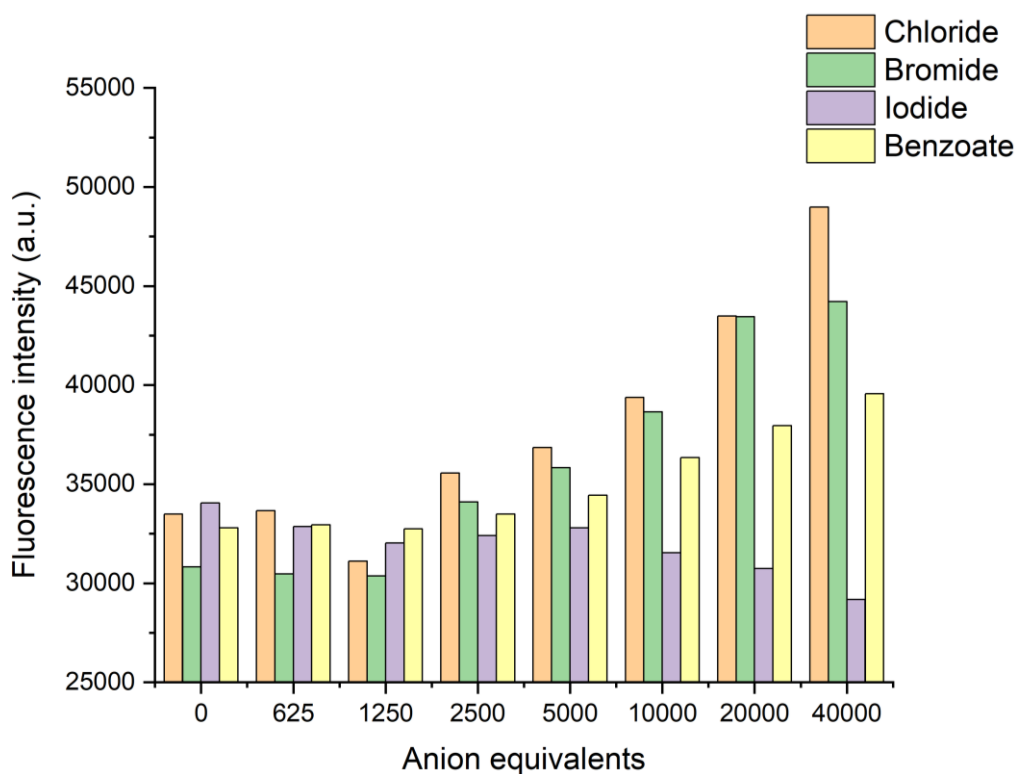


Figure 2.22: Fluorescence intensity of mixture of **52** and HINA upon the addition of increasing anion equivalents. Orange = chloride; green = bromide; purple = iodide; yellow = benzoate. All anions are TBA salts.

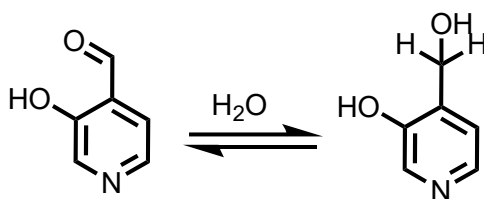
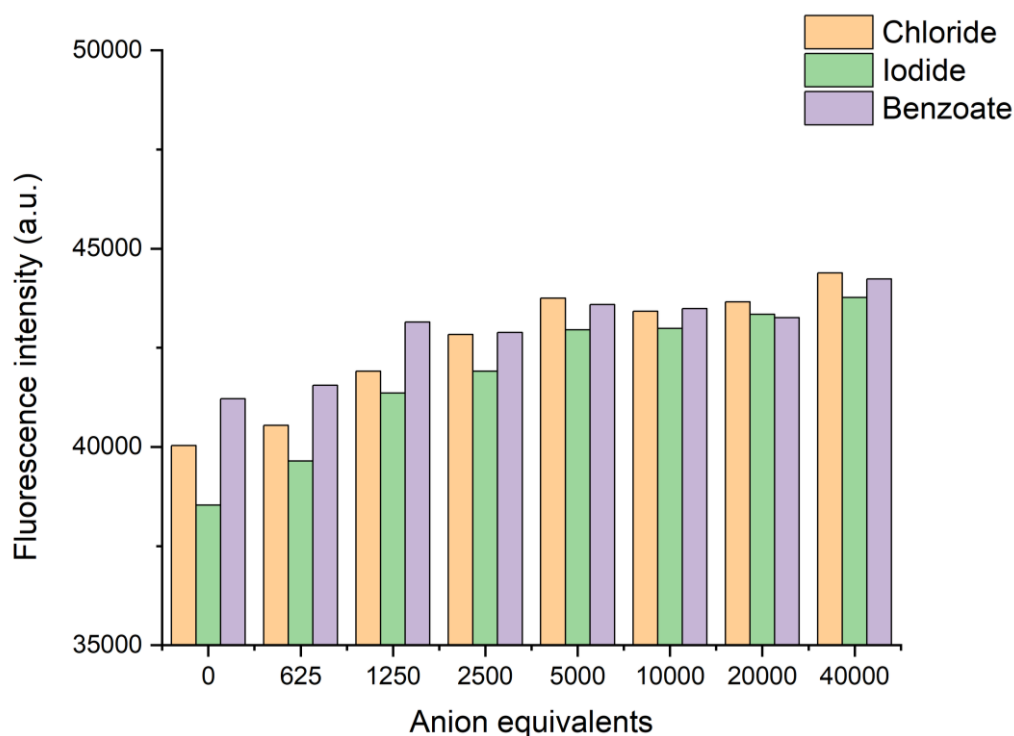


Figure 2.23: Formation of HINA-hydrate in aqueous solvent.

The fluorescence intensity of the mixture of **52** and 7ACC-1 also slightly increased upon the addition of TBA benzoate, leading us to investigate its displacement from **52** using other anions. Additionally, 7ACC-1 is a coumarin-based dye that is stable towards hydrolysis. Host-fluorophore binding was observed through  $^1\text{H}$  NMR, indicating a 0.1 ppm downfield shift in NH proton peaks, suggesting weak fluorophore binding to **52**. Subsequently, increasing equivalents of TBA salts (chloride, iodide, benzoate) were introduced to the host-dye solutions,

and fluorescence intensity was measured (Figure 2.24). This figure shows no significant discrimination between ions, alongside the, once again, large amounts of anion required to elicit a response. This suggests that 7ACC-1 is not an optimal candidate for indicator displacement assays with **52** and is not suitable as real sensor.



*Figure 2.24: Changes in fluorescence intensity of mixture of **52** and 7ACC-1 upon the addition of increasing anion equivalents. Orange = chloride; green = iodide; purple = benzoate. All anions are TBA salts.*

## 2.8 Anion transport studies

The anion transport capabilities of **52** were evaluated, and **52** was tested for  $\text{Cl}^-/\text{NO}_3^-$  antiport activity using the chloride ion-selective electrode assay. Unilamellar POPC vesicles containing NaCl were suspended in  $\text{NaNO}_3$ , and the sample, either containing a solution of acetonitrile as a control or varying concentrations of **52**, was added at 30 seconds. The vesicles were lysed at 330 seconds using 10% Triton X-100, a detergent, to allow for 100% chloride efflux. The results of these vesicle studies are given in Figure 2.24. The 1 mol% solution of **52** exhibited minimal activity compared to the control solution. When the acetonitrile solution of the transporter was added to the vesicles, it resulted in the formation of a purple precipitate. Although adding the 10 mol% solution of **52** turned the vesicle solution purple, a purple

precipitate began to form again. Surprisingly, moderately high chloride transport activity was observed, with approximately 60% efflux after 5 minutes (Figure 2.25). As seen in the binding experiments with  $\text{TBANO}_3$  (Chapter 2.6), the nitrate complex of **52** is highly insoluble, and it is probable that the same insoluble complex forms here due to the high concentration of nitrate ions in the  $\text{NaNO}_3$  external buffer. As a result, it was decided that alternative methods for testing anion transport without the need to expose the transporter to nitrate anions were required.

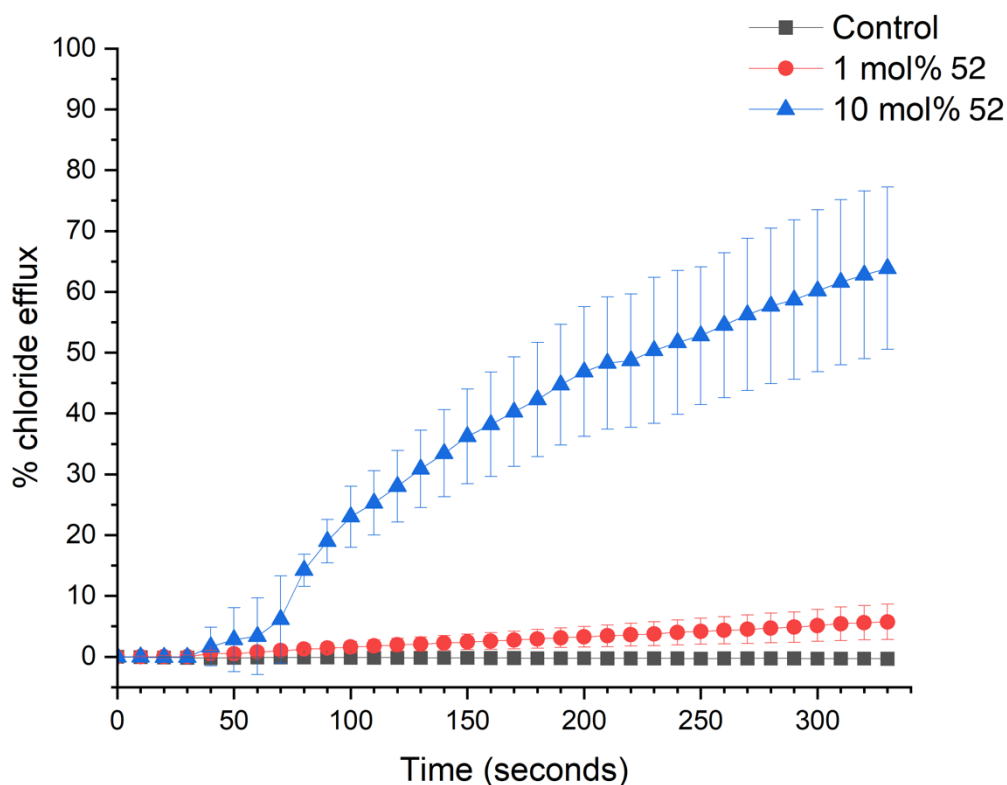
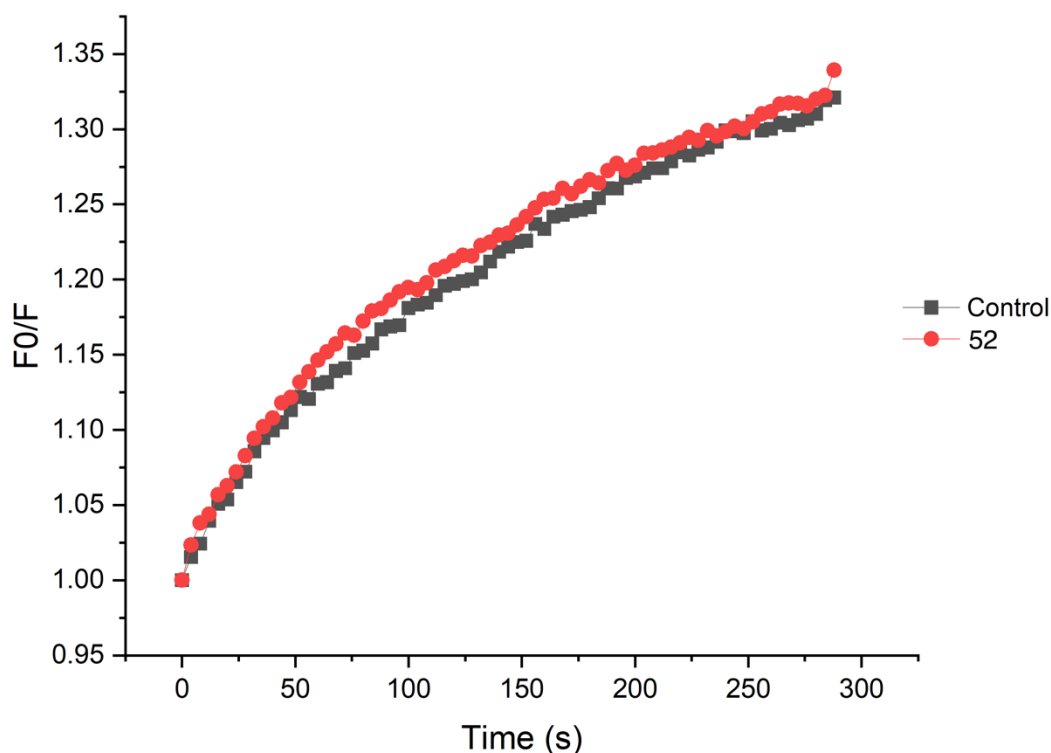


Figure 2.25: Chloride efflux promoted by control (black) and **52** at 1 mol% (red) and 10 mol% (blue). Control = acetonitrile only.

$\text{Cl}^-/\text{NO}_3^-$  antiport was further investigated *via* a fluorescence assay using lucigenin and membrane pre-incorporation. We hoped pre-incorporating **52** into the vesicle membrane would prevent it from precipitating when exposed to the nitrate-containing buffer. Complex **52** was pre-incorporated into unilamellar POPC vesicles that contained lucigenin and  $\text{NaNO}_3$  buffer. The vesicles were suspended in  $\text{NaNO}_3$  buffer and were spiked with  $\text{NaCl}$  solution at 30 seconds. The fluorescence of the vesicles was subsequently monitored over 5 minutes, after which the vesicles were lysed with Triton X-100. Only a low concentration of **52** (1 mol%) could be tested as it was not possible to extrude the vesicles containing higher concentrations of **52** (10 mol%), probably due to the formation of insoluble materials. The results from these



studies are shown in Figure 2.26, where the fluorescence intensity ( $F_0/F$ ) is plotted as a function of time (Equation 1.1). The control and **52** both show similar fluorescence intensities, implying that **52** exhibits poor chloride transport at this loading. However, this was not unexpected, as the 1 mol% solution did not exhibit significant chloride transport when testing chloride/nitrate antiport activity (Figure 2.24).



*Figure 2.26: Fluorescence intensity of lucigenin assay plotted as a function of time. Control = vesicles without transporter.*

We carried out further studies into the transport mechanism of **52** using a cationophore-coupled assay. Specifically, valinomycin, a  $K^+$  uniporter, was used with potassium gluconate (KGlu) as the external buffer. Gluconate is a large, hydrophilic ion unable to pass through the lipid bilayer, thus preventing chloride efflux and effectively ‘switching off’ transport. The addition of valinomycin switches on transport again as  $K^+/Cl^-$  symport occurs. This process is depicted in Figure 2.27.

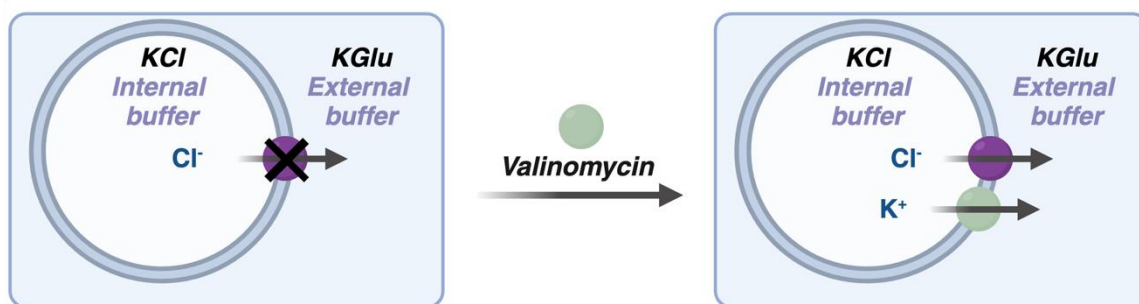


Figure 2.27: Cartoon representation of cationophore-coupled assay with valinomycin (green). Transporter = purple.

Unilamellar POPC vesicles containing KCl were suspended in KGlu, with samples being added at 30 seconds – specifically, either **52**, valinomycin or **52** & valinomycin. Chloride efflux was measured using a chloride ISE. The vesicles were lysed at 330 seconds using 10% Triton X-100 to allow for 100% chloride efflux. The results of these experiments are depicted in Figure 2.28. Surprisingly, **52** demonstrated approximately 30% chloride efflux on its own, indicating its potential capability for  $M^+/Cl^-$  symport. However, the addition of valinomycin to **52** enhanced chloride efflux to around 50%. To assess cation selectivity, studies with just **52** were repeated with sodium salts. **52** was added at 30 seconds, and the vesicles were lysed at 330 seconds using Triton X-100. Figure 2.29 compares the percentage of chloride efflux with sodium and potassium salts. Notably, **52** appears to show no cation selectivity, with **52** exhibiting around 30% efflux for both cations. Typically, symporters can facilitate potassium transport more efficiently than sodium due to the higher hydration energy of sodium. Therefore, these findings suggest that **52** may be inducing vesicle lysis and subsequent anion leakage. Assays designed to investigate vesicle lysis involve encapsulating a fluorescent dye within vesicles that is self-quenching at high concentrations.<sup>158</sup> When membrane disruption occurs through the addition of a transporter, a significant increase in fluorescence should be observed as the dye disperses. However, in this case, if **52** does lyse the vesicles, accurately monitoring the fluorescence response would be challenging as compound **52** quenches the fluorescence of dyes used to test for membrane lysis, including calcein.

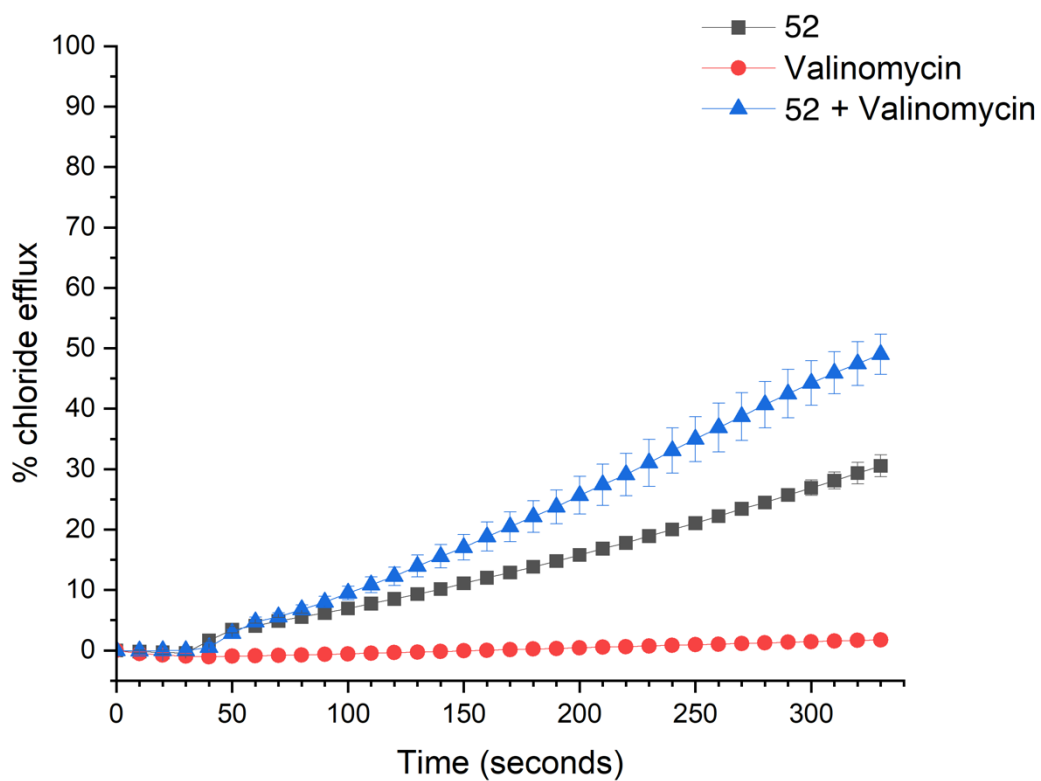


Figure 2.28: Chloride efflux promoted by **52** only (black), valinomycin only (red) and **52** + valinomycin (blue).

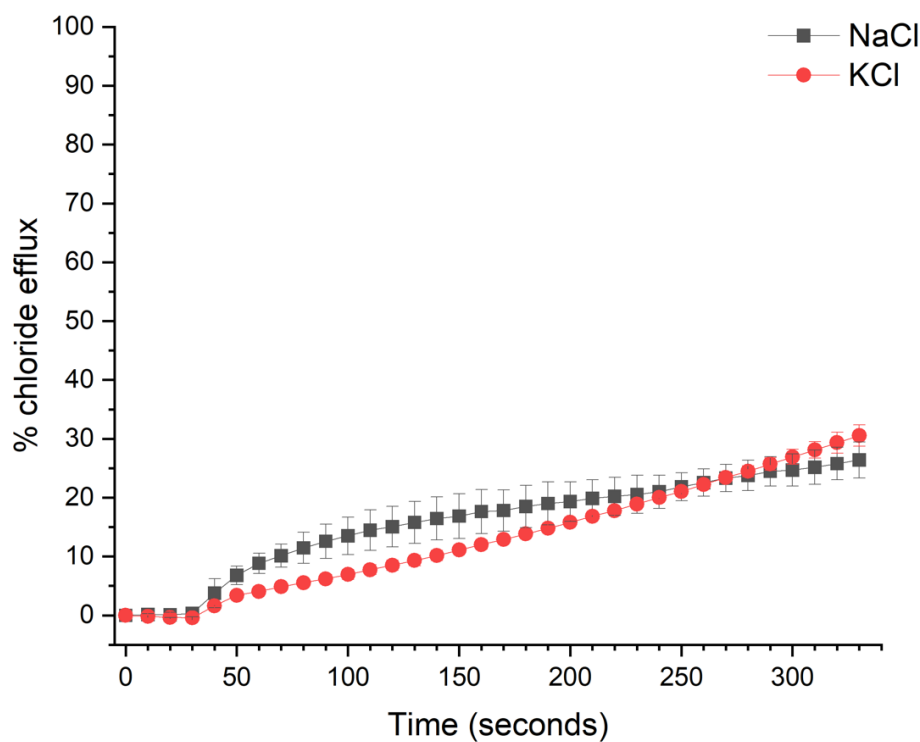


Figure 2.29: Comparison of % chloride efflux promoted by **52** with NaCl (black) or KCl (red).

## 2.9 Conclusions and future work

In conclusion, this chapter explored the design and synthesis of novel anion-binding ligands for subcomponent self-assembly. Two novel metal-organic complexes, **51** and **52**, were synthesised, with the synthesis of **52** scaled up to investigate its potential applications. Complex **52** was shown to bind various anions, with benzoate and acetate displaying the most significant response, as evidenced by  $^1\text{H}$  NMR. Indicator displacement assays conducted with a variety of dyes revealed that **52** effectively quenched the fluorescence of several dyes. The anion-binding cleft within **52** is capable of accommodating small dyes, such as 7ACC-1, which can be displaced upon introducing anions like chloride. Furthermore, complex **52** appeared to exhibit anion transport properties, specifically chloride/nitrate antiport and  $\text{M}^+$ /chloride symport; however, it is possible that it may be inducing vesicle lysis rather than facilitating transport.

Future research could concentrate on enhancing the indicator displacement properties of this molecule. To facilitate the binding of larger dyes, cleft size could be increased. One potential strategy to achieve this could involve the incorporation of longer alkyl chains (Figure 2.30). On the other hand, when considering anion transport properties, it may be prudent to alter the metal used for subcomponent self-assembly to enhance the performance of fluorescent assays – e.g., zinc(II) complexes are typically yellow and, therefore, unlikely to quench the fluorescence of green dyes. This would streamline the process of finding fluorophores that are quenched *via* binding to the host instead of quenching *via* other mechanisms, like FRET.

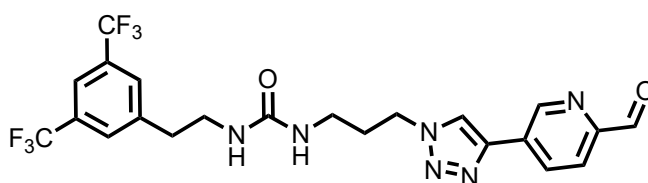


Figure 2.30: Example of proposed modified ligand.

Ultimately, it would be interesting to explore the water solubility of such complexes using sulfate counter ions. As mentioned in Section 1.3.2, the solubility of metal-organic complexes synthesised using subcomponent self-assembly can be altered by changing the counterion of the metal salt.<sup>96</sup> Changing the perchlorate ion, or other organic-soluble ions, to a sulfate ion would bring about water solubility – a useful property for applications in indicator displacement assays and anion transport.

### 3 Chiral amines for enantiopure complexes

#### 3.1 Chiral clefts

As discussed in Chapter 1, clefts are multidentate cavities that can contain and bind a variety of guests. Clefts can often comprise chiral molecules, which may affect their binding and subsequent applications. They have similar structures with very rigid backbones.

In 1887, Carl Julius Ludwig Tröger published the first example of a chiral cleft containing a bicyclic aliphatic unit and two aromatic groups on either side.<sup>159</sup> This molecule is well-known as Tröger's base (**53**), which includes a hydrophobic cavity capable of binding guests. Additionally, Tröger's base is C<sub>2</sub>-symmetric and is thus chiral.<sup>160</sup> Interestingly, Vladimir Prelog subsequently reported the racemisation of Tröger's base in acidic media, with its mechanism shown in Figure 3.1.<sup>161</sup> Although there was no spectroscopic evidence for iminium intermediate, this claim is indirectly supported by the stability of ethyl-bridged analogues of Tröger's base in acidic media. This molecule was primarily used to evaluate chiral chromatographic techniques; however, its analogues have been used for guest binding.<sup>160,161</sup> The binding of chiral guests using chiral clefts has not been investigated.

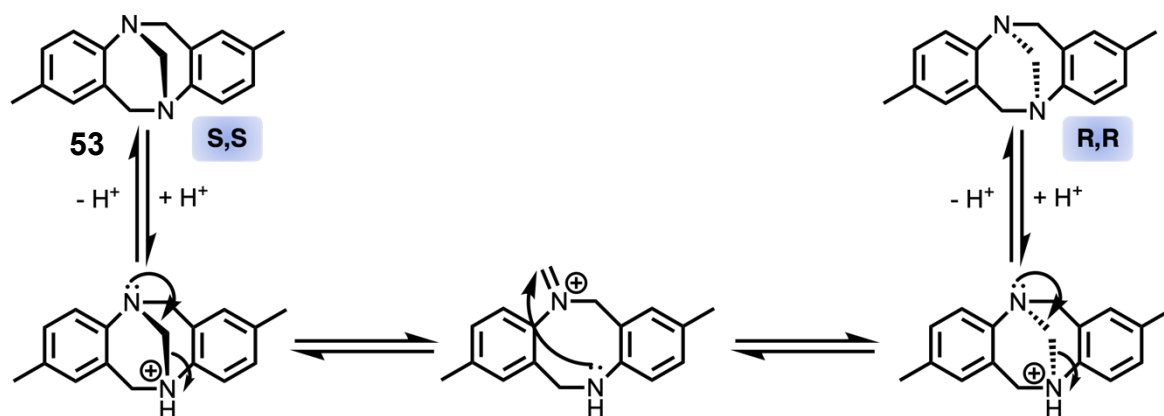


Figure 3.1: Racemisation of Tröger's base (**53**) in acidic media.<sup>161</sup>

For example, Goswami and co-workers synthesised a pyridine diamide analogue of Tröger's base (**54**, Figure 3.2a).<sup>162</sup> They tested its binding abilities to various dicarboxylic acids with *n* ranging from 3 to 10 (Figure 3.2b) via <sup>1</sup>H NMR titrations. Suberic acid (*n*=6) had an association

constant ( $K_a$ ) value one order of magnitude ( $K_a \approx 10^4$ ) higher than that of glutaric acid ( $K_a \approx 10^3$ ), likely due to the high shape complementary between the host and guest.

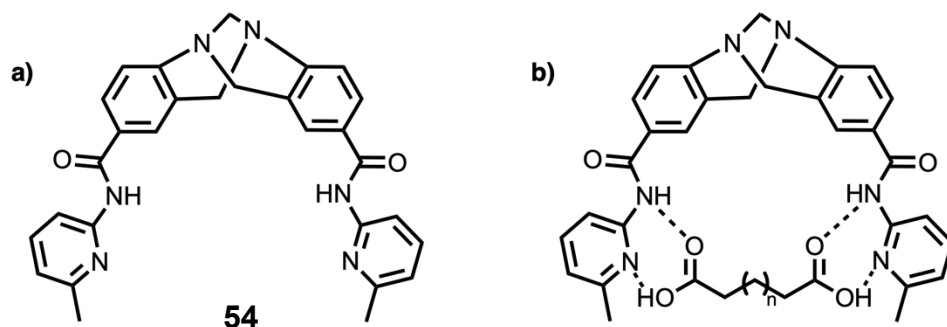


Figure 3.2: a) Pyridine diamide analogue of Tröger's base; b) binding of dicarboxylic acid in the cleft of **54**.<sup>162</sup>

Kagan and co-workers designed a similar scaffold, now known as Kagan's ethers (Figure 3.3.a).<sup>163</sup> Due to the bridged, perpendicular arrangement of the aromatic rings, these are suitable scaffolds for clefts to bind aromatic molecules. Kagan's ether analogues have been used to synthesise chiral 'molecular tweezers', which contain two distinct binding clefts and can bind aromatic molecules. Harmata *et al.* synthesised a Kagan's ether analogue containing dibenzofuran groups on either end (Figure 3.3b). Figure 3.3c indicates that this compound can bind trinitrobenzene within the cleft, and  $\pi$ - $\pi$  stacking interactions strengthen this interaction.<sup>164,165</sup>

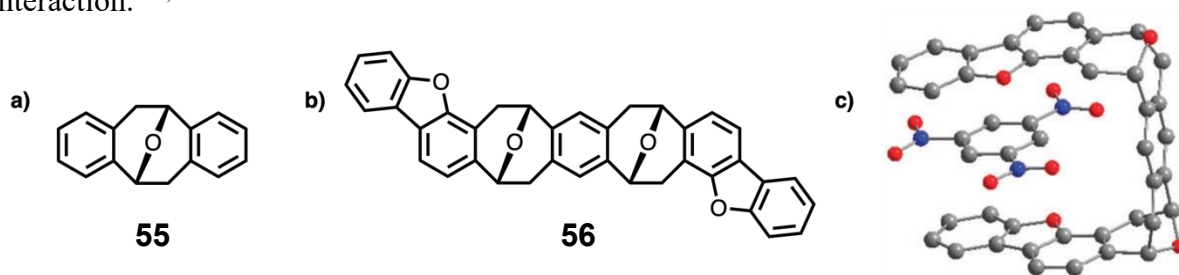


Figure 3.3: a) Kagan's ether **55**; b) Kagan's ether analogue **56** synthesised by Harmata *et al.*; c) crystal structure of **56** binding trinitrobenzene.<sup>163–165</sup>

Some chiral clefts utilise hydrogen bonding to strengthen host-guest interactions further. For example, Steed *et al.* synthesised a chiral cleft composed of a bisurea moiety containing two chiral centres (**57**, Figure 3.4).<sup>166</sup> Its rigid and planar nature, combined with the presence of hydrogen bonding motifs, allows for the formation of a well-defined cavity. They also synthesised **58** (Figure 3.4); however, the carbon spacer between the urea moiety and pyridine

ring introduces flexibility, thus hindering the formation of a well-defined cavity. The host-guest properties of **58** were tested in the solid state *via* crystallisation using different solvents; it was found that small solvents like acetone, ethanol and cyclopentanone were able to bind **58**. Further expanding, Orentas and co-workers synthesised a full supramolecular chiral ‘molecular tweezer’ solely based on hydrogen bonding. This contained urea motifs and Tröger base-like architectures to ensure a rigid V-shape.<sup>167</sup>

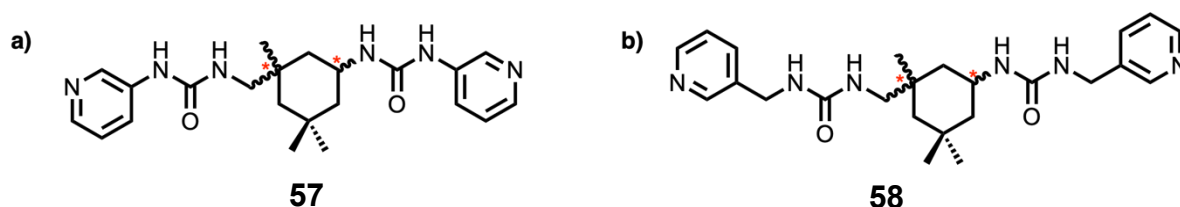


Figure 3.4: Bisureas **57** and **58** synthesised by Steed *et al.*<sup>166</sup>

Chiral clefts have also been inspired by naturally occurring chiral molecules, like amino acids. Xing and colleagues synthesised several molecular tweezers based on a tryptophan-tryptophan dipeptide sequence.<sup>168</sup> Their library of molecular tweezers included amino acids like glycine, alanine, phenylalanine, serine, and tryptophan to observe the effect of side chains on guest binding. All were tested for binding to a series of aromatic guests functionalised with various groups, like long alkyl chains, halides, cyano and nitro groups. Density functional theory (DFT) calculations found that the more electron-deficient guests bound the strongest, and NMR and MS further confirmed these results.

### 3.2 Metal-organic complexes and chirality

Chiral metal-organic complexes can be defined as metal-organic complexes formed of chiral ligands. For example, although not used for guest binding, Gao *et al.* synthesised palladium and iridium complexes comprising Tröger’s base-like ligands.<sup>169</sup> Additionally, Shanmugaraju and co-workers generated a small library of ruthenium-based metallocycles composed of amino-1,8-naphthalimide Tröger’s bases.<sup>170</sup> The binding site within the metallocycle was large enough to bind heparin – an anti-coagulant drug – inducing a change in the fluorescence response. The detection of heparin is of use as excess drug in the bloodstream can lead to heart attacks, strokes and pulmonary embolisms.<sup>171</sup>

Alternatively, chiral metal-organic complexes can also refer to so-called ‘chiral-at-metal’ complexes. This is, in fact, a misnomer, as this term refers to the different isomers that can form around the metal centre. Expressly, octahedrally-coordinated metal-organic complexes with bidentate ligands can adopt either lambda ( $\Lambda$ ) or delta ( $\Delta$ ) stereoisomers.  $\Lambda$  denotes the left-handed helicity of a metal-organic complex, meaning it rotates anticlockwise, whereas  $\Delta$  denotes the right-handed helicity, meaning it rotates clockwise. When achiral ligands are often used to synthesise metal-organic complexes, the product is a 1:1 mixture of the two possible enantiomers. Additionally, octahedral complexes with bidentate ligands exhibit geometric isomerism – facial (*fac*) or meridional (*mer*) isomers (Figure 3.5)

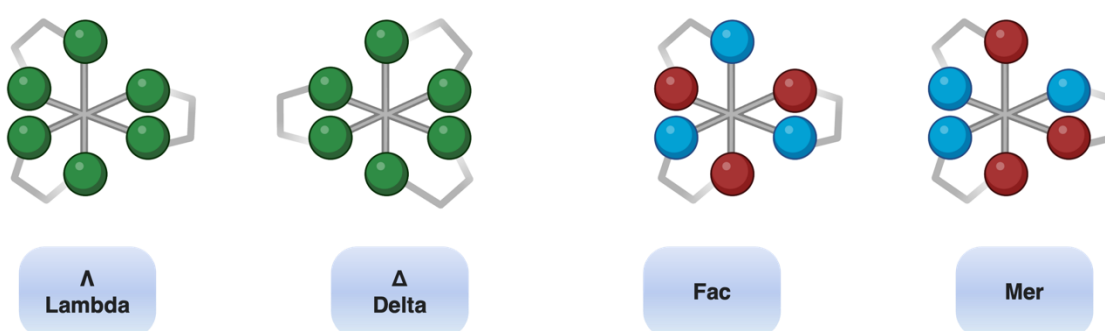


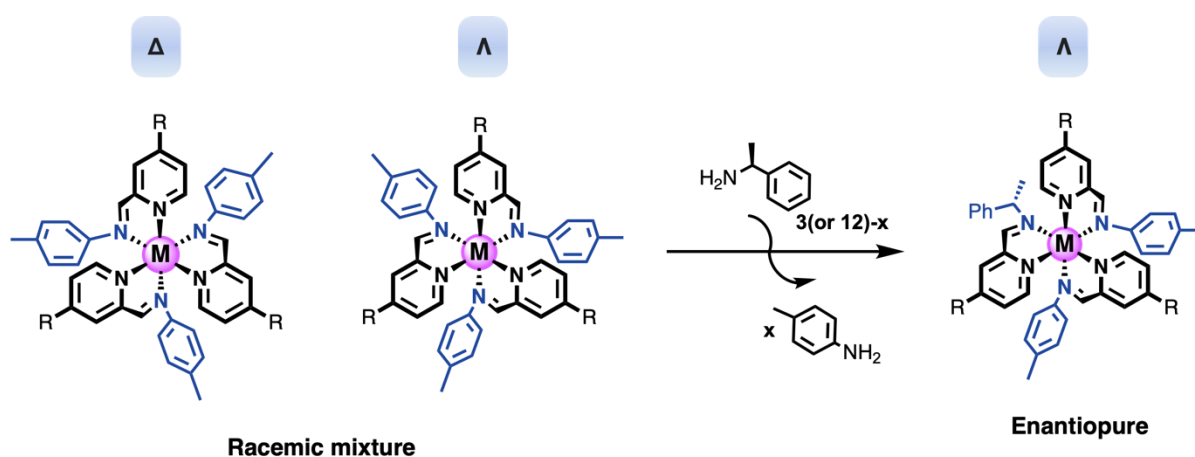
Figure 3.5: Lambda and delta stereoisomers, and *fac* and *mer* geometric isomers of octahedral complexes.

Scott *et al.* reported the synthesis of optically pure iron(II) complexes.<sup>172</sup> Initially, benzylamine and 2-acetylpyridine were added to a solution of iron(II) perchlorate in acetonitrile to form an octahedral iron(II) complex. This formed a mixture of racemic products. However, substituting benzylamine of (*R*)-methylbenzylamine gave an enantiopure *fac*- $\Delta$  iron(II) complex. Scheme 3.1 depicts this idea.

Nitschke and colleagues developed a statistical method to measure the influence of different factors on stereochemical communication in metal-organic complexes formed *via* subcomponent self-assembly.<sup>173</sup> These factors include the choice of metal, the chirality and size of the ligands, and temperature. The model assessed the energy cost of disrupting stereochemical communication, taking into account penalties for incorporating an ‘incorrect’ amine enantiomer, for example. Initially, self-assemblies with four different amines (Figure



3.6) were analysed. It was observed that **60** significantly influenced the configuration at the metal centre, followed by **61** – possibly due to the steric bulk and pi-stacking effects of **60**. Subsequently, self-assemblies were carried out with iron(II), cobalt(II) and zinc(II), and it was found that the iron(II) self-assemblies exhibited the most stereochemical control. The authors suggest that this is due to the reduced metal-ligand bond strength as the metal changes from iron to cobalt to zinc, resulting in a decrease in the steric gearing needed for effective stereochemical control. The structure of the ligands also had a notable impact on stereochemical control. Tritopic ligands – those capable of coordinating at three different sites – imposed a rigid structure on the self-assembled complex, leading to strong stereochemical control.



*Scheme 3.1: Example scheme showing chiral induction through chiral subcomponent substitution.<sup>172,173</sup>*

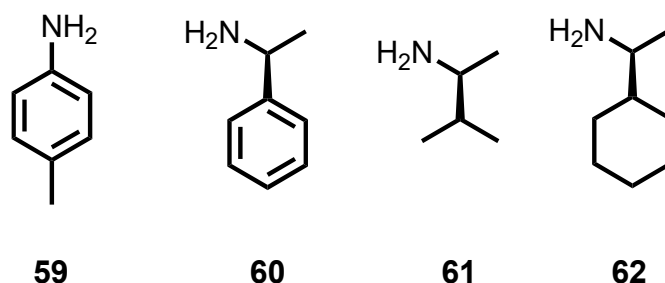
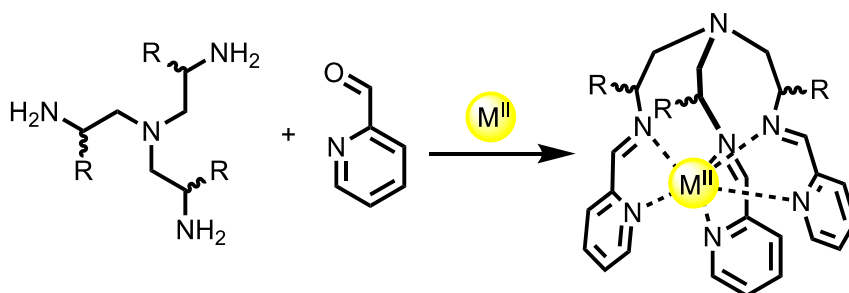


*Figure 3.6: Amines studied by Nitschke and colleagues when quantifying factors impacting stereochemical control around the metal centre.<sup>173</sup>*

Additionally, Nitschke and co-workers found switching between  $\Lambda$  and  $\Delta$  stereoisomers through solvent changes was possible.<sup>174</sup> They synthesised zinc(II) and cobalt(II) cages from tetrakis(pentafluorophenyl) porphyrin in acetonitrile, which primarily gave the all- $\Lambda$  stereoisomer. The reaction was also conducted in nitromethane, which preferentially formed the  $\Delta$  isomer. The authors hypothesise that the favouring of the  $\Lambda$  isomer in acetonitrile is likely due to its hydrogen bonding abilities, which restrict the conformational freedom of metal vertices by accepting hydrogen bonds from the amide group. Nitschke and co-workers also reported guest-induced isomer interconversion of a  $\text{Fe}^{\text{II}}\text{L}_4$  cage.<sup>175</sup> This allowed for enantioselective separation and selective guest extraction, which has potential applications in molecular sensing and catalysis. Additionally, a recent paper published shows the applicability of another  $\text{Fe}^{\text{II}}\text{L}_4$  cage in chiral recognition for steroid molecules.<sup>176</sup>

### 3.3 Research aims

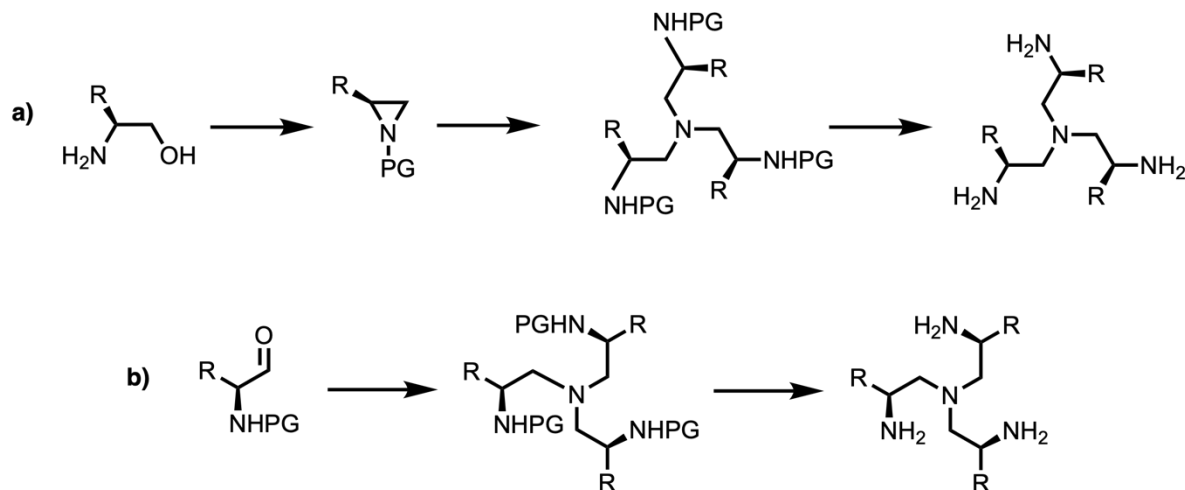
Scott and Nitschke have demonstrated the synthesis of enantiopure metal-organic complexes. The work in this project aimed to build upon their work by synthesising two isomers of a chiral amine to produce enantiopure metal-organic complexes, ideally with opposite chirality, *via* subcomponent self-assembly. This is valuable for investigating the binding of chiral guests – potentially chiral anions – and assessing the potential for chiral discrimination. As shown in Scheme 3.2, a tripodal amine will be used for self-assembly, allowing for rigid cleft synthesis and higher stereochemical control around the metal centre. Additionally, as shown by Nitschke *et al.*, the use of tripodal amines in subcomponent self-assembly allows for the incorporation of more labile metal, like zinc, into the synthesis of water-soluble architectures.



*Scheme 3.2: Proposed synthesis of enantiopure metal complex with chiral amine via subcomponent self-assembly.*

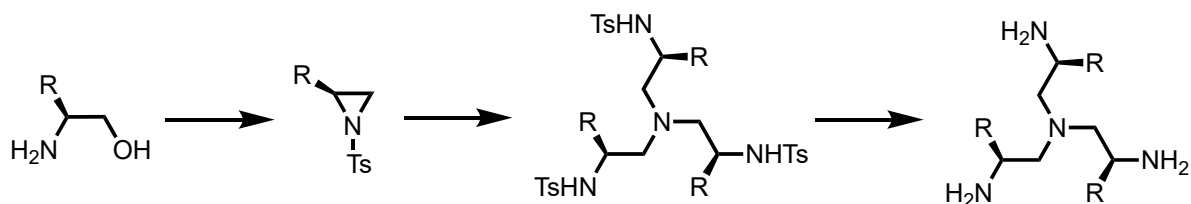
### 3.4 Chiral amine synthesis

Chiral tripodal amines have previously been synthesised in the literature, often using amino-acid-derived starting materials. There are two main ways to synthesise chiral tripodal amines. The first involves the synthesis and subsequent nucleophilic attack of aziridines.<sup>177–179</sup> A general scheme is shown in Scheme 3.3a. The second method consists of the reductive amination of amino-aldehydes (Scheme 3.3b).<sup>180–185</sup>



*Scheme 3.3: General routes to synthesising chiral tripodal amines via a) aziridines or b) amino aldehydes.*

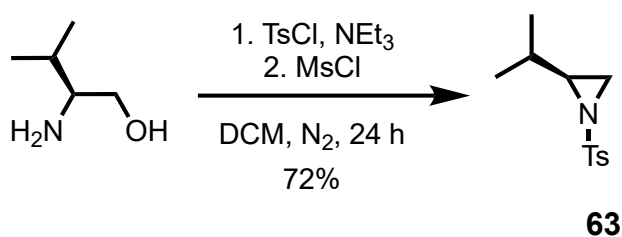
#### 3.4.1 Aziridine route



*Scheme 3.4: Proposed synthesis of tripodal chiral amine using tosyl protecting group.*

Moberg *et al.* proposed a route to synthesising chiral tripodal ligands from an amino acid-derived starting material (Scheme 3.4).<sup>178</sup> This route used the uncommon tosyl protecting group to protect the nitrogen atoms, which was deprotected in the final step of the synthesis. Our initial efforts focussed on reproducing and adapting this synthesis.

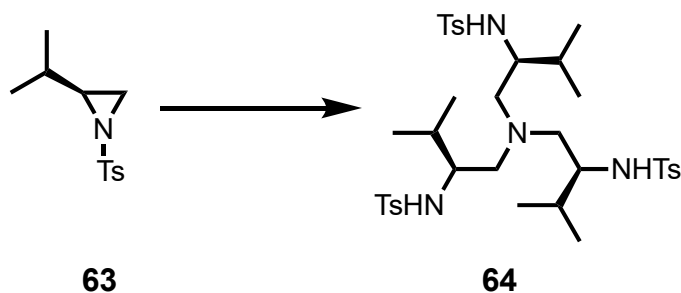
The first step was performed using (*S*)-valinol to form (*S*)-2-isopropyl-1-tosylaziridine (**63**), as reported by Moberg *et al.* (Scheme 3.5).



Scheme 3.5: Formation of aziridine **63** from (*S*)-valinol.

The reagents were added at -25 °C and stirred at RT overnight. Purification *via* column chromatography afforded the desired aziridine as a fluffy white solid; however, the yield was meagre at 0.31 %. The reaction was attempted again by adding 4 Å molecular sieves to increase the yield and maintain anhydrous conditions. This proved successful, and the target aziridine was obtained with a 72% yield.

Table 3.1: Conditions used to synthesise **64** from **63**.



<b>Attempt 1</b>	NH <sub>3</sub> , MeOH, reflux, 50 °C, 4 days
<b>Attempt 2</b>	1. NH <sub>3</sub> , MeOH, 50 °C, 3 days 2. MeCN, reflux, 90 °C, 10 days, N <sub>2</sub> 3. MeOH, 100 °C, 30 min, microwave

The second step of the chiral amine synthesis was subsequently attempted (Table 3.1, attempt 1). In the literature, this step was conducted in the microwave – aziridine **63** was dissolved in a solution of ammonia in methanol and stirred for 75 minutes at 160 °C.<sup>177</sup> However, given that this temperature is significantly above the boiling point for ammonia, performing this reaction

in a sealed tube was judged to have a high risk of explosion. Thus, alternative synthesis methods were sourced. The first attempt at this reaction was done with the same reagents but using less harsh conditions as an alternative to conducting the reaction in the microwave. A solution of ammonia in methanol was added to a flask containing the starting material dissolved in methanol, and the reaction mixture was left to stir for four days under the reflux apparatus. On the second day, the reaction mixture was taken off the stirrer plate and sonicated, as the starting material had not entirely dissolved. After four days, it seemed that all the ammonia and methanol had evaporated, meaning the reaction did not occur, and this was confirmed *via*  $^1\text{H}$  NMR spectroscopy.

The second attempt consisted of three main steps (Table 3.1, attempt 2). The first step involved the same reactants as attempt 1; however, the reaction was conducted in a sealed tube to ensure the ammonia did not evaporate. After four days, a  $^1\text{H}$  NMR spectrum of the reaction mixture likely revealed that a mixture of the mono-, di-, and tri-substituted compounds had potentially formed. Subsequently, more aziridine (**63**) was added, and the reaction mixture was refluxed in acetonitrile for ten days at 90 °C —this step was adapted from a paper by Tan and co-workers.<sup>186</sup> during refluxing, it was found that the solid was not entirely in solution—instead, it had surrounded the edges of the flask. The crude product was then dissolved in methanol and additional aziridine starting material and heated in the microwave at 100 °C for 30 minutes. Upon cooling, a solid product precipitated from the reaction mixture. The contents of the microwave vial were filtered and washed with cold methanol to form the desired tosylated tripodal amine (**64**), which was confirmed with  $^1\text{H}$  NMR.

The removal of a tosyl group was needed to synthesise the final chiral tripodal amine ligand. Some common amine detosylation strategies are employed in the literature – either in acidic or neutral reflux conditions or using electrochemistry.<sup>187</sup> The deprotection strategies attempted in this project are detailed in Table 3.2.

Table 3.2: Attempted conditions used to deprotect **64**.



<b>Attempt 1</b>	HBr, PhOH, 200 °C, reflux
<b>Attempt 2</b>	MeCN, TBAPF <sub>6</sub> , RT, 5 hours Undivided electrochemical cell
<b>Attempt 3</b>	MeCN, NaPF <sub>6</sub> , RT, 2 hours IKA electrasyn 2.0

At first, a literature procedure by Moberg et al. was followed using strongly acidic conditions (Table 3.2, attempt 1).<sup>178</sup> Once finished, the pH of the reaction was increased to allow for product isolation *via* extraction. Following solvent removal, the crude product was analysed *via* <sup>1</sup>H NMR, which showed peaks in the aromatic region corresponding to the tosyl groups—this implies that the deprotection had not worked.

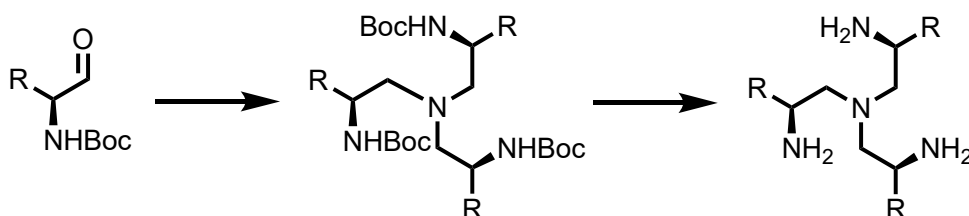
Another deprotection strategy was adapted from a paper by Quintard and co-workers (Table 2, attempt 2), in which they electrochemically deprotected N-benzenesulfonyl groups in acetonitrile, using tetrabutylammonium hydrogensulfate (Bu<sub>4</sub>NHSO<sub>4</sub>) as an electrolyte.<sup>188</sup> The electrochemical deprotection was performed on a 5 μmol scale with tetrabutylammonium hexafluorophosphate (TBAPF<sub>6</sub>). The reaction mixture was subsequently analysed *via* TLC. When visualised under an ultraviolet (UV) light lamp, no spot indicated that an aromatic moiety was absent. Conversely, a purple spot was present when stained with ninhydrin, indicating a free amine. After a basic workup of the reaction mixture, the crude product was analysed *via* MS. This showed the presence of the TBA cation ([M+H]<sup>+</sup> = 242) but not the desired amine ([M+H]<sup>+</sup> = 272). This is likely due to the hydrophobicity of the TBA cation, making it difficult to remove during the workup, as well as the hydrophilicity of the tripodal amine, making product extraction from the aqueous phase difficult.

Electrochemical deprotection was attempted again using the IKA electrasyn 2.0 (Table 2, attempt 3). This instrument is convenient for setting up an undivided electrochemical cell without elaborate setups or conditions and can also determine the required reaction voltage. This time, NaPF<sub>6</sub> was the electrolyte of choice for easier product isolation. Compound **64** was dissolved in acetonitrile, and NaPF<sub>6</sub> was added to the solution. The reaction voltage was determined to be 4 V, so the reaction mixture was stirred at RT for the determined reaction time (5 minutes). The reaction mixture was analysed *via* TLC, which showed the presence of starting material. The reaction was re-started, and reaction progress was continually monitored *via* TLC for 4 days. Unfortunately, no product formation was seen.

Due to ongoing difficulties in removing the tosyl protecting group, we explored alternative synthetic strategies utilising more labile protecting groups.

### 3.4.2 Amino-aldehyde route

Scheme 3.6 shows a proposed route for synthesising chiral tripodal amines from Boc-protected amino acid derivatives. This procedure was adapted from Verkade and co-workers' use of amino acid-derived aldehydes.<sup>184</sup> The authors used a phenylalanine-derived aldehyde (R = Bn); thus, in the hopes of a smooth synthesis, the same aldehyde was used in this project.

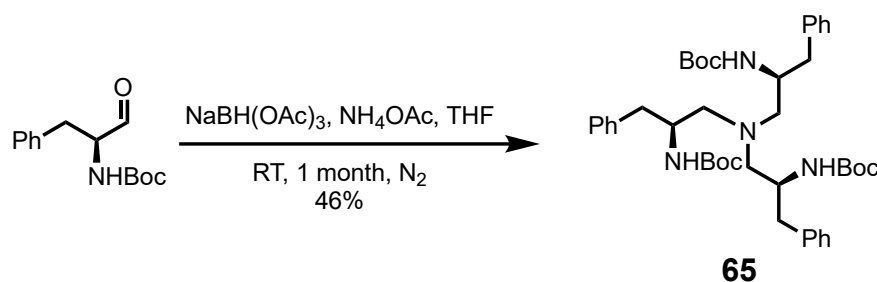


*Scheme 3.6: Proposed synthesis of chiral tripodal amine using Boc protecting group.<sup>184</sup>*

The commercially available N-Boc-L-phenylalaninal was first dissolved in THF, after which sodium triacetoxyborohydride and ammonium acetate were added. The reaction mixture was then stirred at RT overnight. Reaction progress was subsequently monitored *via* TLC, which showed that the aldehyde had not reacted. The reaction mixture was left to stir for two more days – analysis *via* TLC showed the presence of another spot. The reaction mixture was

quenched with 10% acetic acid in methanol. Following a basic workup, an attempt was made at purification *via* column chromatography, but the product was not isolated.

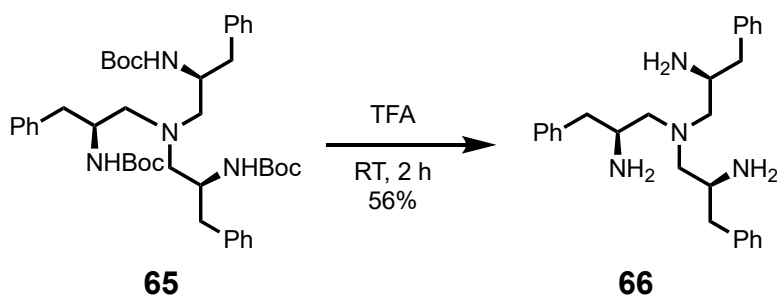
The reaction was attempted again with extra precautions. Dry THF was used, and the reaction was placed in an inert atmosphere. After stirring for three days, the reaction mixture was analysed *via* TLC, revealing the same outcome as the previous attempt. The reaction was taken off the hotplate and left for three weeks. Analysis of the reaction mixture *via* TLC showed the presence of four spots – this indicated the mono, di, and tri-substitutions may have occurred, but the starting material was still present. The crude product was nevertheless purified *via* column chromatography to afford the desired amine. Following this, the reaction was scaled up and left to stir for a month at RT (Scheme 3.7) while being monitored *via* TLC. **65** was afforded as a white solid with 46% yield.



*Scheme 3.7: Synthesis of Boc-protected chiral tripodal amine 65.*

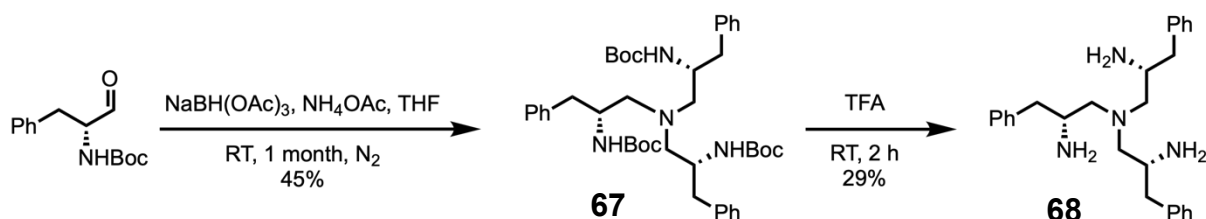
The Boc group was subsequently deprotected under acidic conditions. Amine **65** was dissolved in trifluoroacetic acid (TFA) and stirred at RT for 2 hours (Scheme 3.8). Following a basic workup, the amine was purified using an Isolute SCX-2 column. This column, used to isolate basic compounds, contains silica gel functionalised with propylsulfonic acid, which allows neutral and acidic compounds to pass through. Basic compounds can be isolated after the addition of ammonia. The column gave the product (**66**) as an orange solid with a 56% yield.





*Scheme 3.8: Deprotection of amine **65** to form amine **66**.*

Additionally, the D-isomers of both tripodal amines were synthesised (Scheme 3.9) to allow us to observe the effect of ligand chirality on self-assembled product formation. N-Boc-D-phenylalaninal was stirred at RT under inert conditions for 1 month and quenched with 10% acetic acid in methanol. Following a basic workup, product **67** was isolated *via* column chromatography as a white solid. Amine **67** was subsequently stirred in TFA for 2 hours at RT and worked up under basic conditions. Purification *via* an Isolute SCX-2 column afforded amine **68** as an orange solid with 29% yield.



*Scheme 3.9: Synthesis of Boc-protected chiral tripodal amine **67** and subsequent formation of chiral tripodal amine **67**.*

### 3.5 Self-assembled complexes

Following the successful synthesis of amine **66**, a self-assembly was attempted with picolinaldehyde and iron perchlorate. This salt was found to have the best success in other self-assemblies attempted (ref. chapter 2) and was therefore used here.

A degassed solution of **66** and picolinaldehyde in acetonitrile was stirred at 35 °C for 20 minutes to ensure all reactants had dissolved. After that, iron perchlorate was added, and the reaction mixture was stirred at 50 °C overnight under an inert atmosphere. Initially, just by visual inspection, the reaction looked promising, as the colour had changed from orange to

purple, indicating the potential presence of an iron(II) complex. The reaction mixture was analysed *via*  $^1\text{H}$  NMR spectroscopy, which revealed an imine peak at approximately 9 ppm. Diethyl ether was added to the reaction mixture until a fine purple solid precipitated. Analysis of the solid *via*  $^1\text{H}$  NMR spectroscopy (Figure 3.7) revealed a confusing mixture of products. A second attempt at self-assembly was made under the same conditions. Upon adding the iron perchlorate, the reaction mixture turned brown, indicating inert conditions may not have been maintained during this reaction attempt and, therefore, the potential oxidation of the iron salt.

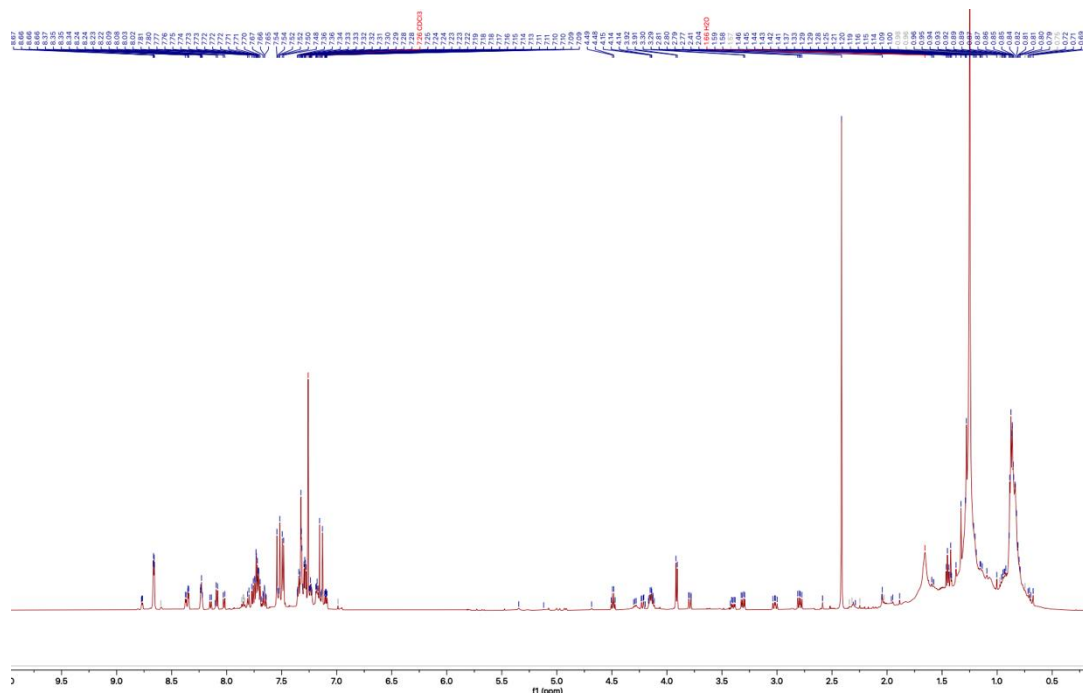


Figure 3.7:  $^1\text{H}$  NMR spectrum of crude product from attempted subcomponent self-assembly with **66**.

Changing our approach, we decided to synthesise the imine first and subsequently add the metal salt. Imine synthesis proved challenging, requiring anhydrous conditions and long reaction times. A solution of **66** and picolinaldehyde in ethanol was stirred at 60 °C, with reaction progress monitored *via* TLC. After four days of stirring, several new spots were observed, and the crude product was purified *via* column chromatography. The tripodal imine was likely isolated; however, the product may have degraded on the column due to the fragile nature of imines, so three sets of peaks were visible for one spot. These were likely to be the mono, di and tri-substituted imine.

Nevertheless, this looked promising enough, and iron perchlorate was added to a solution of the isolated product in acetonitrile.  $^1\text{H}$  NMR analysis of the reaction mixture showed broad peaks spanning from -1 to 16 ppm, which could indicate the iron(II) had transitioned from diamagnetic (low spin) to paramagnetic (high spin). This is further supported by paramagnetic  $^1\text{H}$  NMR (Figure 3.8) and the reaction mixture turning orange instead of purple. A recent paper by McConnell *et al.* shows that it is possible to form high-spin iron(II) metal-organic complexes using bulky ligands.<sup>189</sup> The steric bulk around the metal coordination site lengthens the metal-ligand bond, stabilising the high-spin iron(II) state. The same effect may influence the formation of the complexes with **66** due to several aromatic rings in close proximity to one another. The data suggested that a single, discrete complex was not formed cleanly, leading to self-assemblies with other metals being sought.

Small-scale self-assemblies were conducted with commercially available zinc(II) and cobalt(II) salts with different counterions (Table 3.3). A solution of **66**, picolinaldehyde and the metal salt was stirred at 60 °C for 24 h; additionally, the cobalt(II) self-assemblies were conducted under inert conditions. The self-assemblies conducted with cobalt(II) did not occur, which was confirmed by paramagnetic  $^1\text{H}$  NMR. The self-assemblies with zinc(II) looked promising *via*  $^1\text{H}$  NMR due to the presence of a potential imine peak at around 9 ppm. Since all zinc self-assemblies looked similar *via*  $^1\text{H}$  NMR, subsequent reactions were conducted with just  $\text{Zn}(\text{ClO}_4)_2$ .

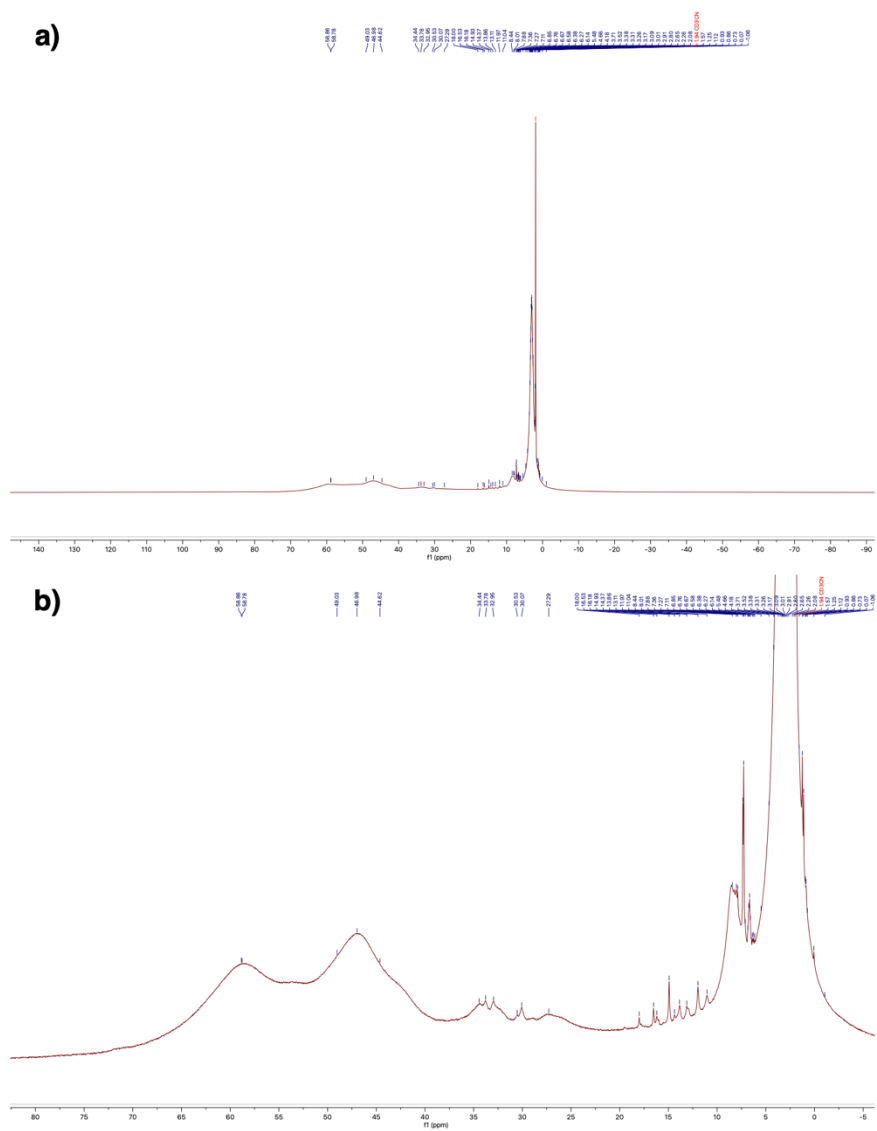


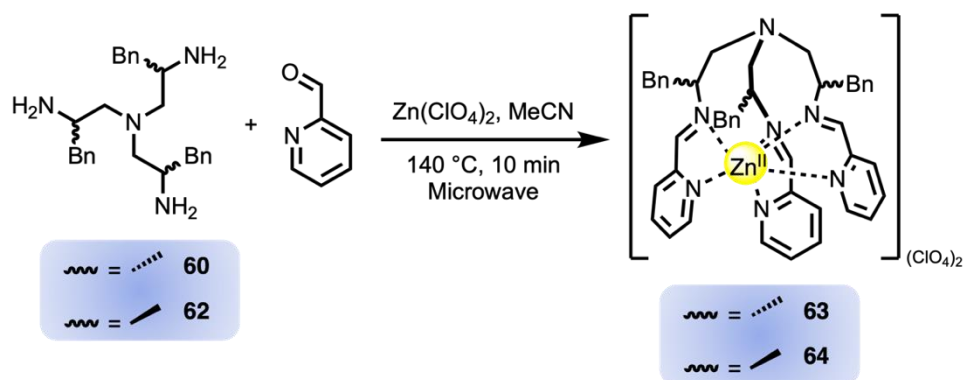
Figure 3.8: a) paramagnetic  $^1\text{H}$  NMR spectrum of attempted subcomponent self-assembly with **66**, picolinaldehyde and  $\text{Fe}(\text{ClO}_4)_2$ ; b) zoomed-in paramagnetic  $^1\text{H}$  NMR spectrum.

Table 3.3: Outcomes of self-assemblies with different metal salts.

	Metal salt used	Reaction conditions	Outcome
1	Co(ClO <sub>4</sub> ) <sub>2</sub>	MeCN, 60 °C, 24 h, N <sub>2</sub>	Reaction did not occur.
2	Co(BF <sub>4</sub> ) <sub>2</sub>	MeCN, 60 °C, 24 h, N <sub>2</sub>	Reaction did not occur.
3	Zn(ClO <sub>4</sub> ) <sub>2</sub>	MeCN, 60 °C, 24 h	Reaction looked partially successful – presence of imine peak on <sup>1</sup> H NMR.
4	Zn(BF <sub>4</sub> ) <sub>2</sub>	MeCN, 60 °C, 24 h	Reaction looked partially successful – presence of imine peak on <sup>1</sup> H NMR.
5	Zn(NTf <sub>2</sub> ) <sub>2</sub>	MeCN, 60 °C, 24 h	Reaction looked partially successful – presence of imine peak on <sup>1</sup> H NMR.

More forcing conditions were used in order to force the reaction to completion since there was still an aldehyde peak at around 10 ppm. The starting materials were dissolved in acetonitrile and stirred in the microwave for 10 mins at 100°C. Diethyl ether was added to the reaction mixture until a yellow solid precipitated. The mixture was centrifuged, and the pellet was left to air dry. Analysis *via* <sup>1</sup>H NMR revealed the presence of an aldehyde peak. The solid was dissolved in acetonitrile, precipitated with ethyl acetate, and centrifuged. The pellet was dried, and <sup>1</sup>H NMR analysis showed the absence of the aldehyde peak. Although the peaks were unresolved and the NMR sample seemed quite dilute due to a low yield of (crude) product, the peak at approximately 8.2 ppm looked promising as an imine peak. Furthermore, the presence of additional, albeit unresolved, peaks in the aromatic region, specifically around 7 and 8 ppm – likely corresponding to the phenyl ring and pyridine protons, respectively – prompted us to think that the self-assembly may have occurred.

The reaction was repeated at 140 °C with the same workup procedure; the reaction did not go to completion here either, with similar observations on the <sup>1</sup>H NMR spectrum (see Figure A2.19). However, as mentioned, since this looked promising, we investigated its potential chiral properties using circular dichroism (CD). The self-assembly with Zn(ClO<sub>4</sub>)<sub>2</sub> was also repeated with **68** (Scheme 3.10) to compare the influence of ligand chirality on metal centre chirality. Similar observations on the <sup>1</sup>H NMR spectrum were made (see Figure A2.20).



*Scheme 3.10: Subcomponent self-assemblies attempted with  $\text{Zn}(\text{ClO}_4)_2$  with chiral amines **66** and **68** to form complexes **69** and **70**, respectively.*

UV-vis (UV-visible) measurements (Figure 3.8) were conducted prior to the CD measurements (Figure 3.10). For comparison, an achiral  $\text{Zn}(\text{II})$  complex synthesised from TREN and picolinaldehyde was also tested. **69** and **70** clearly show two distinct bands for each complex. The CD measurements potentially show that it is possible to influence metal chirality through the use of chiral ligands, as the CD spectrum of **70** mainly showed bands with positive values. The CD spectra of the achiral complex and **69** showed little to no variation, implying the presence of a racemic mixture. The low intensity of the bands in the CD spectrum of **70** also suggests that a) there may be a racemic mixture of two enantiomers, b) the metal-organic complex formed is not well-defined or c) the metal-organic complex is not present in significant quantities. The products appear to exhibit some opposing chirality at around 200 nm (Figure 3.10b), but it remains uncertain whether this is due to unreacted **66** or **68** or potential products **69** and **70** being formed. Further investigation of potential products **69** and **70** through mass spectrometry indicated that both products were impure and the major product was not the desired product, as the  $2+$  ion could not be found. The overall evidence leads us to conclude that a discrete, enantiopure complex was not successfully formed.

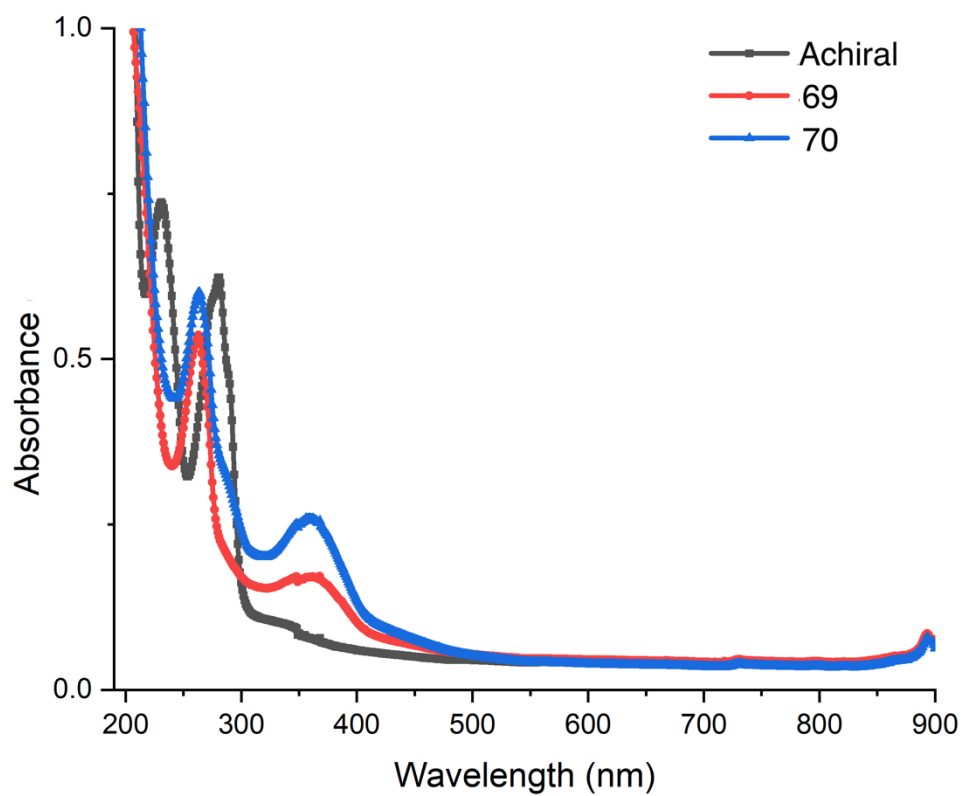


Figure 3.9: UV-vis spectrum of supposed zinc(II) complexes **69** and **70**, along with achiral zinc(II) complex composed from TREN + picolinaldehyde.

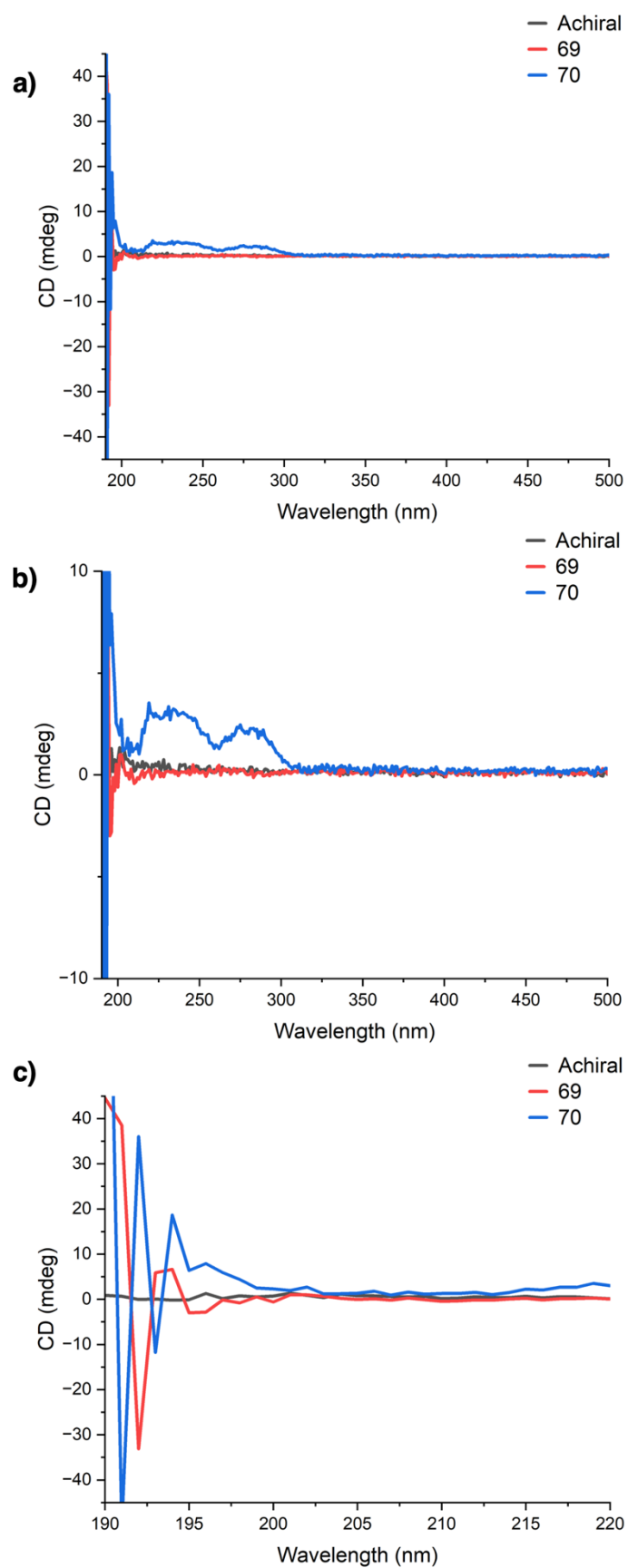


Figure 3.10: a) CD spectrum of achiral zinc(II) complex, **69** and **70**; b) zoomed-in CD spectrum (-10-10 mdeg); c) zoomed-in CD spectrum (190-220 nm).



### 3.6 Conclusions

In conclusion, chiral Boc-protected tripodal amines **65** and **67** were synthesised *via* reductive amination and subsequently deprotected to yield **66** and **68**. Efforts to synthesise chiral tripodal amines using the Ts-protected aziridines, such as **63**, to form tripodal amines, like **64**, encountered difficulties, particularly with removing the Ts group. The Boc-protected amine route proved to be more favourable. Subcomponent self-assembly was attempted with **66** and **68** with a variety of metals. The Fe(II) complexes potentially partially transitioned from diamagnetic to paramagnetic, and the self-assemblies with Co(II) were unsuccessful. The Zn(II) self-assemblies showed promise due to an imine peak in the  $^1\text{H}$  NMR spectrum. However, various sets of forcing conditions tested to ensure reaction completion ultimately did not yield complete conversion to a discrete product that could be isolated.

Future work should focus on incorporating alternative side chains instead of the benzyl groups on **66** and **68**. These groups may be too bulky, hindering subcomponent self-assembly due to the spatial arrangement of the three benzyl groups around the metal ion, in addition to the pyridine rings, which was likely unfavourable. Alternative amines could include the valine-derived chiral tripodal amines akin to **64**.<sup>178</sup> Additionally, it may be interesting to conduct self-assemblies with alanine-derived amines to compare the effect of steric bulk from the sidechains around the metal centre. Furthermore, using an amine with a longer alkyl chain may mitigate steric crowding around the metal centre. For example, Nitschke *et al.* have previously used tris(3-aminopropyl)amine (TRPN) (Figure 3.11) for subcomponent self-assembly.<sup>96</sup> Functionalising this amine in order to make it chiral may ease the steric bulk around the metal centre.

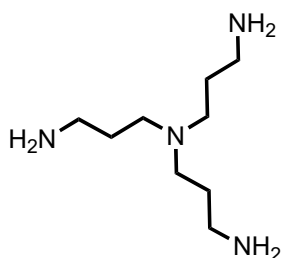


Figure 3.11: Tris(3-aminopropyl)amine (TRPN).

If successful, it may be possible to synthesise metal-organic complexes with sulfate salts for aqueous solubility, which may allow for the synthesis of chiral clefts capable of binding biologically relevant guests – often which are chiral.

## 4 Interactions between SSAs and lipid headgroups

### 4.1 Introduction to SSAs

Supramolecular self-associating amphiphiles (SSAs), a novel class of molecules, were first unveiled by the Hiscock group in 2016. These molecules have the same general structure, as depicted in Figure 4.1a.<sup>190,191</sup>

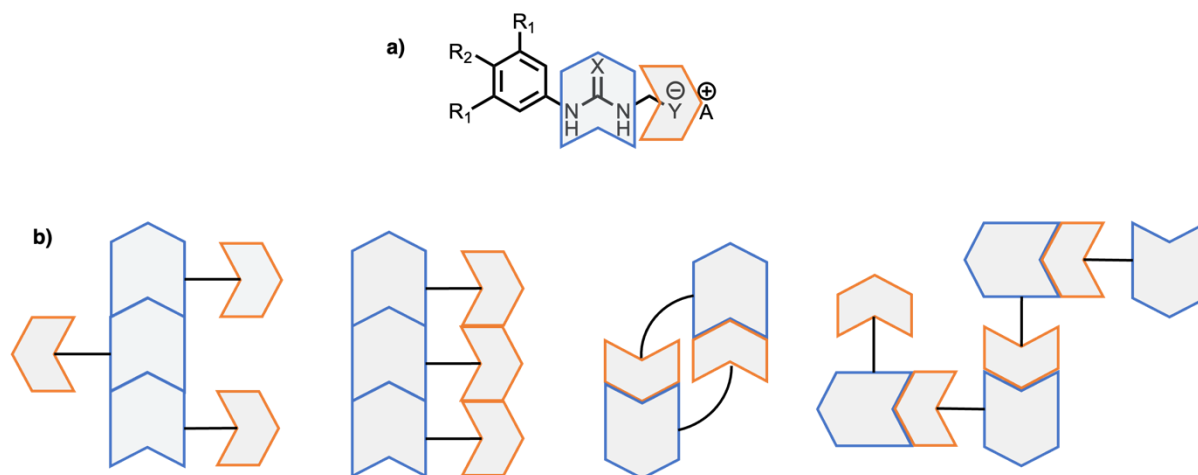


Figure 4.1: a) general structure of an SSA molecule where  $X = O/S$ ;  $Y = a$  hydrophilic group; and  $A = a$  counteranion; b) possible hydrogen bonding bonds.

There are a variety of hydrogen bond donors (the (thio)urea NHs) and acceptors (the carbonyl O/S and hydrophilic group). Due to this, they can form so-called “frustrated” polymeric systems characterised by their several hydrogen bonding modes (figure 4.1b).<sup>191</sup> This was confirmed *via* single-crystal X-ray spectroscopy on SSA **71** (figure 4.2a), in which Hiscock *et al.* saw the anionic monomer forming a urea-sulfonate dimer.

Additionally, studies on another single crystal isolated from a mixture of SSAs **71** and **72** (Figure 4.2b) in deuterated DMSO revealed the presence of a mix of dimerised species. The hydrated dimer of **71** was the minor product, with 15% occupancy, and the hydrated dimer of **71** and **72** was the major product, with 85% occupancy.<sup>192</sup> Further analysis of this mixture *via* powder X-ray diffraction confirmed the major product was indeed the heterogenous dimer of **71** and **72** (Figure 4.2c). It was hypothesised that the dimerisation occurs to stabilise the

complex, which contains an electron-rich anthracene and an electron-poor anthraquinone ring.<sup>191</sup> The nature of the aggregates is highly dependent on the environment in which they are present. Hiscock *et al.* found that SSAs formed spherical aggregates in H<sub>2</sub>O or 19:1 H<sub>2</sub>O: EtOH solutions, likely due to their amphiphilic nature. These spherical aggregates formed hydrogel fibres upon adding a salt solution, which was confirmed *via* scanning electron microscopy (SEM).<sup>192</sup>

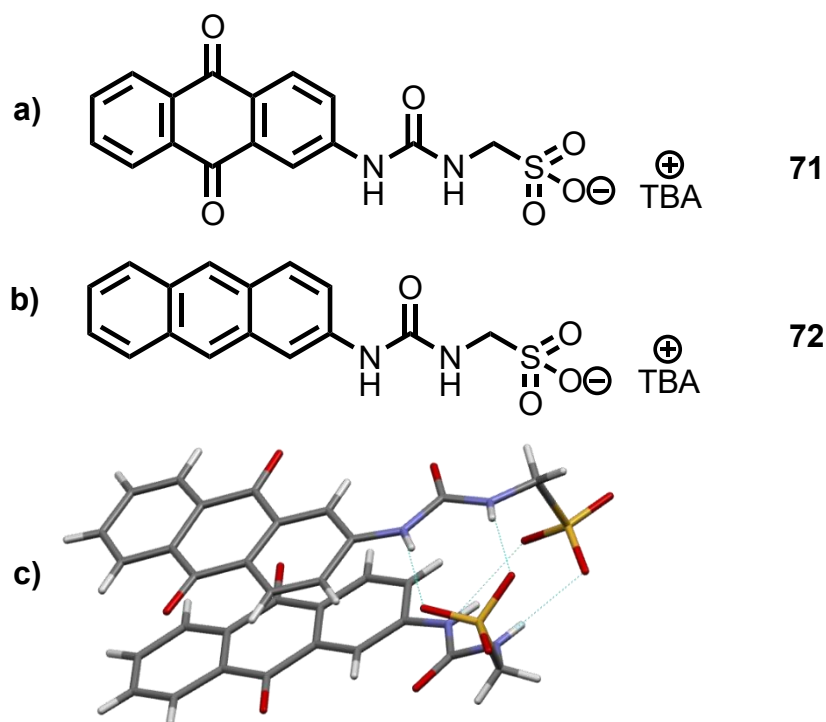


Figure 4.2: a) SSA 71 monomer; b) SSA 72 monomer; c) heterogenous dimer of SSA 71 and 72.

## 4.2 SSAs against bacteria

Since their discovery, SSAs have been found to possess a myriad of beneficial properties, including electrochemical,<sup>193</sup> anti-cancer,<sup>194</sup> and ion-transport abilities.<sup>195</sup> In particular, the antibacterial properties of SSAs have been studied in detail due to the rise of antimicrobial resistance and the need for alternative antimicrobial agents.

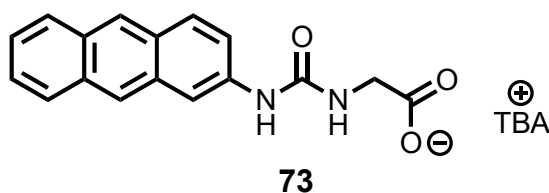


Figure 4.3: SSA **73**.

One of the first studies of SSAs as antibacterial agents was explored in 2019, in which Hiscock *et al.* found activity against Gram-positive methicillin-resistant *Staphylococcus aureus* (MRSA).<sup>196</sup> Spherical aggregates of SSAs **71** (figure 4.2a), **72** (figure 4.2b), and **73** (figure 4.3) in 19:1 H<sub>2</sub>O : EtOH solutions were shown to illicit an antagonistic effect on bacterial growth, with the most effective aggregate being a 1:1 mixture of SSAs **71** and **72**. This study provided insight into the structure-activity relationship of SSAs as antimicrobial agents – i.e. the importance of the sulfonate group over the carboxylate group – whilst confirming the formation of the heterogenous dimer of SSAs **71** and **72** (figure 4.2c).

The mode of antibacterial action was further explored in a paper by Hiscock *et al.* in 2020.<sup>192</sup> In this, it was found that SSAs present as self-associated aggregates on the surface of bacterial cells. This study involved incubating fluorescent SSA **74** (figure 4.4a) with Gram-negative *Escherichia coli* (*E. coli*) and Gram-positive MRSA and monitoring the bacteria over 5 hours using fluorescence imaging (figure 4b-c). At T = 0 min, the authors found that SSA **74** aggregated at the surface of the bacterial cell. However, after 30 minutes had elapsed, these aggregates could not be observed; instead, the SSA had coated the exterior of the bacterial cells (figure 4.4b). After 5 hours, the SSAs had internalised entirely within the cell membranes (figure 4.4c). Based on this, a preliminary mechanism of action has been hypothesised. Firstly, the SSAs dimerise and adhere to the surface of the bacterial cell, after which they are internalised and subsequently exhibit antibacterial action.<sup>192</sup>

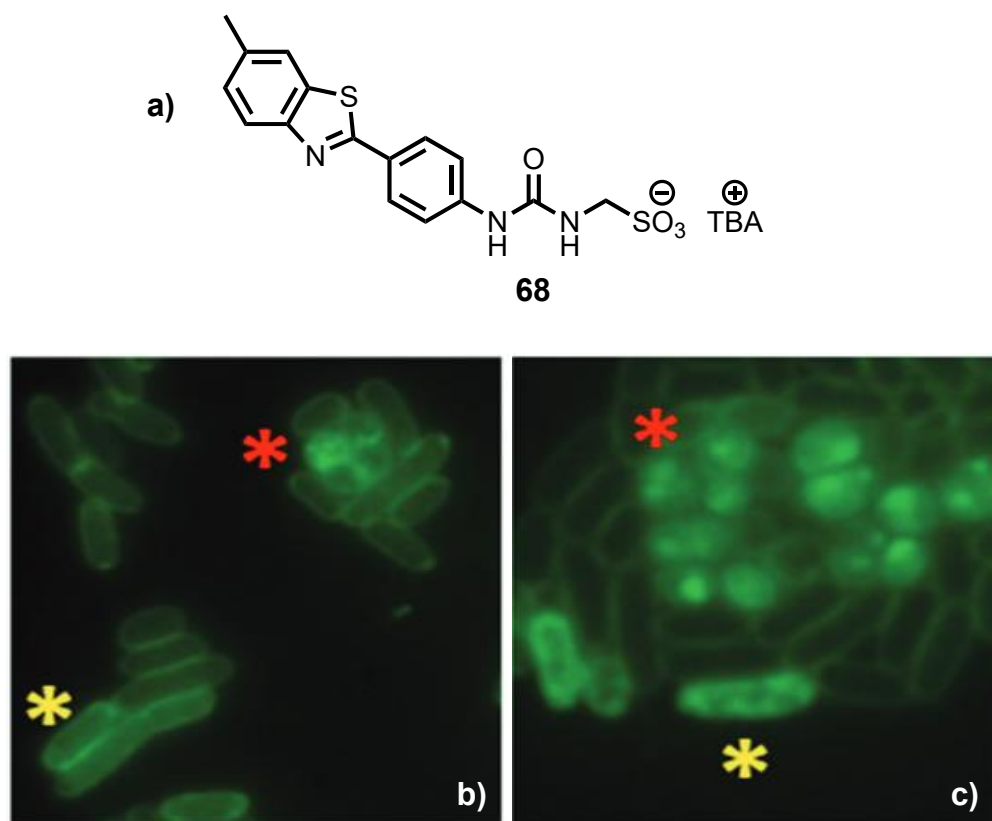


Figure 4.4: a) SSA 74; b) SSA 74 with *E. coli* (yellow) and MRSA (red),  $T = 30$  min; c) SSA 74 with *E. coli* (yellow) and MRSA (red),  $T = 5$  hours.

Figure adapted from Hiscock *et al.*<sup>192</sup>

SSAs have also been shown to enhance the antimicrobial activity of existing drugs on the market. Hiscock *et al.* used SSA 75 (figure 4.5) with five antimicrobial agents against Gram-negative *E. coli* and found that the activity of three of these antimicrobial agents was enhanced.<sup>197</sup> It was revealed that the order in which the reagents were supplied was crucial to the activity. For octenidine, a membrane-disrupting antiseptic agent, there was an 11% increase in antibacterial action when the SSA was added after incubation of the SSA with octenidine. For ampicillin, an antibiotic that disrupts cell wall synthesis, it was found that approximately a 7% enhancement was seen after prior incubation of the bacteria with a) SSA 75 and b) ampicillin. The starkest enhancement of 35% was seen with the previous incubation of *E. coli* with SSA 69 and the subsequent addition of cisplatin, a DNA-chelating agent.<sup>197</sup>

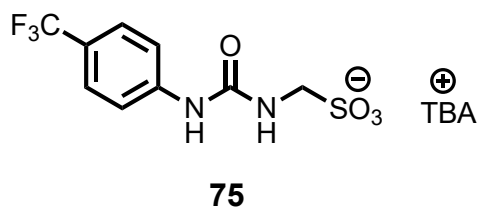


Figure 4.5: SSA 75.

Since then, a library of SSAs with varying structures has been synthesised to investigate the structure-activity relationship of SSAs against MRSA and *E. coli*. This vast library has sizeable structural diversity, including, but not limited to, dianionic SSAs and adamantane-appended SSAs.<sup>198–200</sup>

### 4.3 Lipid bilayers

Living cells comprise different types of lipids, and their structure is related mainly to their function. Lipid bilayers, composed primarily of phospholipids, are responsible for the cell membrane's structure and allow for the passage of molecules. All phospholipids have the same general structure. A phosphate group characterises them in the headgroup, and an alcohol residue – often derived from glycerol – connects the hydrophilic headgroup to the hydrophobic tail.<sup>201</sup>

The three main phospholipid head groups that comprise mammalian cells are PC, phosphatidylethanolamine (PE), and phosphatidylserine (PS), and their compositions are 45–55%, 15–25%, and 10–15%, respectively.<sup>202</sup> Due to its relative simplicity and ease of propagation, *E. coli* is the most studied bacterial species. These cells mainly comprise phosphatidylethanolamine (PE), phosphatidylglycerol (PG), and cardiolipin (CL), with approximate compositions of 75%, 20%, and 5%, respectively.

The interactions of SSAs with different lipid bilayers have previously been researched using phospholipid nanodiscs.<sup>203</sup> These synthetic mimics have been shown to emulate the properties of phospholipid bilayers – i.e. thickness – and are composed of a single disc-shaped planar phospholipid bilayer ‘belted’ with membrane scaffold proteins or synthetic polymers. In this case, either *E. coli* and 1,2-dimyristoyl-*sn*-glycero-3-phosphocholine (DMPC) vesicles were ‘belted’ with a styrene-maleic acid (SMA; 2:1 ratio respectively) copolymer. SSAs **75**, **76** and

**77** (Figures 4.5 and 4.6) were added to the nanodiscs, and the interaction was monitored *via*  $^1\text{H}$  NMR; signal suppression upon nanodisc association implies strong binding. The proton signals of all SSAs were suppressed upon binding to the *E. coli* nanodisc; however, SSA **77** showed the highest affinity for the bacterial nanodisc and the lowest affinity for the mammalian nanodisc.<sup>203</sup> The combination of a para-substituted benzothiazole and a sulfonate group may have contributed to the high bacterial lipid affinity. However, further work is required to study structure-function relationships in more depth.

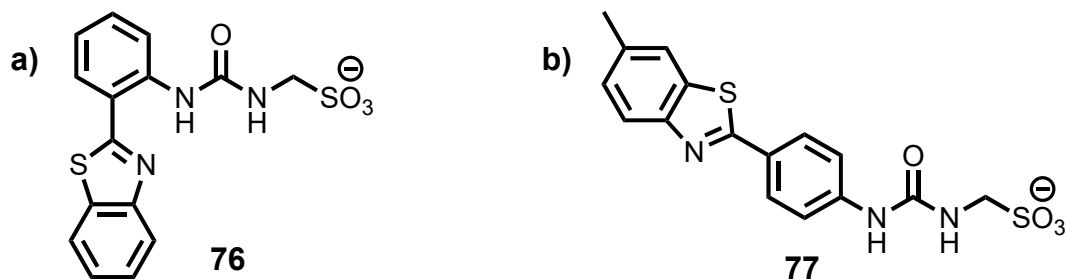


Figure 4.6: a) SSA **76**; b) SSA **77**.

#### 4.4 Research aims

Previous studies have shown that the SSA mode of antibacterial action requires binding to lipid headgroups. Stronger binding to lipids that comprise bacterial cell membranes could derive the selectivity of SSAs for bacterial membranes. Hence, this project explored the binding interactions between SSAs **75** and **78** (figure 4.7) and the major lipid headgroups comprising mammalian and bacterial cell membranes *via* computational chemistry. Although the Hiscock group has determined that SSAs can act as antibacterial agents through antimicrobial screenings, this project aimed to support previous experimental data by providing further insight into how SSAs bind to mammalian and bacterial lipid membranes. This, in conjunction with the experimental data, could help fine-tune the structure of SSAs, allowing them to adhere more firmly to bacterial cell membranes – ultimately creating optimal antibacterial agents.

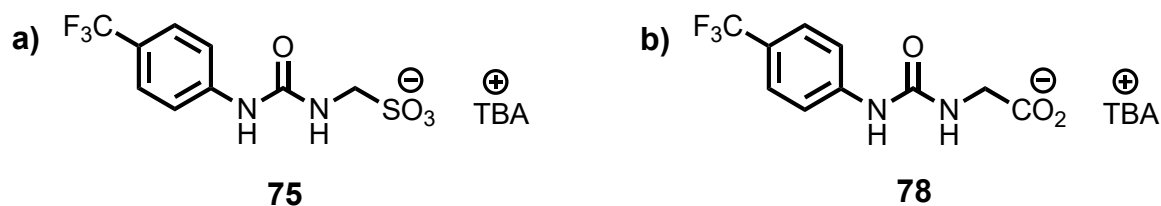


Figure 4.7: a) SSA 75; b) SSA 78.

## 4.5 Methodology

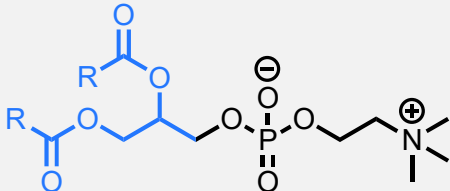
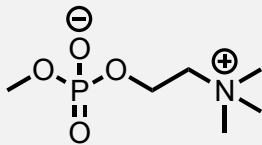
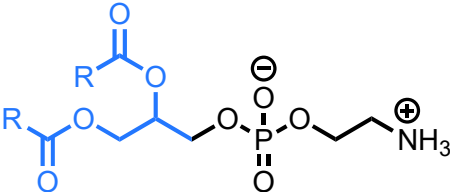
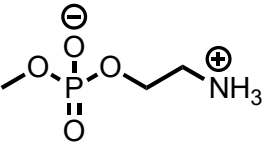
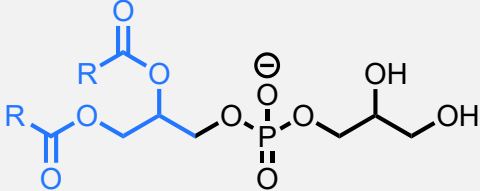
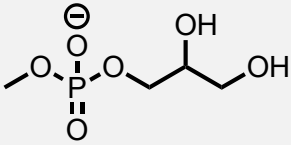
SSAs **75** and **78** were chosen for several reasons. First, these molecules were candidates undergoing antibacterial testing within the Hiscock group. Second, both are relatively structurally simple and thus were simple to model computationally whilst containing key structural features standard to a wide range of the SSA library. Finally, choosing these two compounds made it possible to compare the effect of the sulfonate group versus the carboxylate group on overall antibacterial activity. For computational simplicity, the tetrabutylammonium (TBA) cation was not included in the calculations.

### 4.5.1 m-lipids

The phospholipid head groups studied in this project were PC, PE, and PG, the most prevalent lipids in mammalian and *E. coli* cells. Real phospholipids are long-chain molecules with high conformational flexibility, which is difficult to model computationally. Additionally, SSAs have been found to interact with the phospholipid headgroup preferentially. These two factors led us to model so-called model lipids, or m-lipids (Table 4.1), which comprised only the lipid headgroup. For computational simplicity, the flexible fatty acid chains were replaced by a methyl group



Table 4.1: Structures of phospholipids vs structure of m-lipids; blue = fatty acid group where R = alkyl chain.

	Structure of phospholipid	Structure of m-lipid
PC		
PE		
PG		

#### 4.5.2 Computational method

Two types of calculations were initially used in this project — *ab initio* and DFT calculations —based on the Schrödinger equation. *Ab initio* calculations provide a wavefunction for a molecule and are solely derived from theoretical principles, meaning there are no empirical or semi-empirical parameters. Conversely, DFT calculations directly derive the electron distribution from the Schrödinger equation. Some DFT methods also include parametrisation.<sup>204</sup>

This project utilised the Hartree-Fock (HF) method for the *ab initio* calculations. HF calculations are one of the simplest types of *ab initio* calculations, where the wavefunction is derived with electron-electron repulsion not explicitly being considered, only its average effect.<sup>205</sup> *Ab initio* calculations are often known for underestimating hydrogen bonding interactions compared to other methods.<sup>206,207</sup> However, the HF method was chosen for this project as it is fast and inexpensive. It could also estimate any hydrogen bonds present and the geometry of the different SSA-phospholipid conformations.

DFT calculations are much more suitable for estimating hydrogen bonding interactions.<sup>204,207</sup> In a study by Dessent *et al.*, the M062X functional was used to estimate hydrogen bonding interactions between tautomers of modified amino acids. They found that M062X could accurately predict energies for the tautomers in a relatively short amount of time, and this method even had predictions similar to those when more complex computational methods were used.<sup>208</sup>

Both methods are suitable for calculations with small, novel molecules due to their reduced, or even lack of, parametrisation and fast calculation times.<sup>209</sup>

A basis set comprises a set of functions that turn the partial differential equations of the method – i.e., HF or M062X – into algebraic equations that a computer can use to represent the wavefunction. The 3-21G basis set was used for the HF calculations (HF/3-21G), and the 6-31G basis set was used for the M062X calculations (M062X/6-31G). The difference between those two basis sets is their size – the former has three Gaussian orbitals comprising each core atomic basis function, whereas the latter has six. This makes the 6-31G basis set larger, thus providing a more accurate estimate of hydrogen bonding interactions.<sup>209,210</sup>

All computational calculations were run with a solvation model based on density (SMD model). More specifically, this is a universal continuum solvation model in which the solvent is not represented as discrete solvent molecules; instead, it is a dielectric medium with surface tensions at the solute-solvent interface.<sup>211</sup> It can be used for any known solvent or liquid media. The solvent chosen for this project was water to replicate biological studies and cell environments. Our choice to use a solvent model with water was confirmed by running *ab initio* calculations on an SSA **78**-PG conformation in the gas phase and a hexane solvent model (Table 4.2). It can be seen that the values for the gas phase and hexane calculations are significantly bigger than the value for the same conformation in water. This order of magnitude is unlikely for a hydrogen bonding interaction.<sup>212</sup>

Table 4.2: SSA 78-PG conformation binding energy values in water, gas phase, and hexane.

	Binding energy (kJ/mol)
Water	-161
Gas phase	-305819
Hexane	-305761

### 4.5.3 Computational workflow

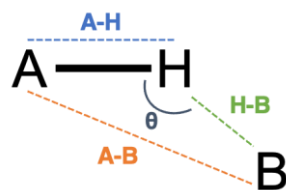
A computational workflow was developed to determine the binding energy between the SSAs and m-lipids. Firstly, input files were created for the SSA-lipid pair. This was done by aligning the molecules in the desired geometry on Gaussview and saving the structures as an xyz file. This file contained information about the atomic coordinates, multiplicity and charge of the structures, and other information necessary for the calculation – i.e., the solvation model. Input files were also created individually for the m-lipids and SSAs. The calculation was subsequently run on the UCL NTC cluster using Gaussian v09, and a text file containing information about the calculation was returned. The binding energy of the complex was hence calculated using Equation 4.1. If the binding energy of a conformation was positive, it was excluded from the final studies as this indicated the process was thermodynamically unfavourable.

$$\text{SSA-lipid binding energy} = \text{SSA-lipid energy} - (\text{SSA energy} + \text{lipid energy})$$

Equation 4.1: Calculation of SSA-lipid binding energy.

Additionally, the length of the hydrogen bonds between the SSA-lipid complex could be determined using Avogadro. These bonds were also visualised using Mercury. We utilised the definitions reported by Jeffrey, as shown in Table 4.3.<sup>213</sup>

Table 4.3: Different types of hydrogen bond strengths and their properties.<sup>213</sup>



	Strong	Moderate	Weak
<b>A-H—B interaction</b>	Mostly covalent	Mostly electrostatic	Electrostatic
<b>Bond lengths</b>	$A-H \approx H-B$	$A-H < H-B$	$A-H \ll H-B$
<b>H—B (Å)</b>	~1.2 - 1.5	~1.5 - 2.2	~2.2 - 3.2
<b>A—B (Å)</b>	2.2 - 2.5	2.5 - 3.2	3.2 - 4.0
<b>Bond angles (<math>\theta</math>) (°)</b>	175 - 180	130 - 180	90 - 150

## 4.6 Results and discussion

### 4.6.1 SSA 78

Initially, the binding energy of SSA **78** with three m-lipids was investigated. Input files were created for each SSA **78**-m-lipid conformation, and ab initio and DFT calculations were run, allowing for each conformation's binding energy to be calculated using Equation 4.1. The lowest binding energy conformations, hence the most stable arrangements, were sought.

We found two potential low-energy binding modes between SSA **78** and m-PC (Figure 4.8). Each structure contained two hydrogen bonds between the urea NH groups and either one or two oxygen atoms from the phosphate moiety. Based on the calculated energies, conformation **B** was judged to be the most stable binding arrangement.

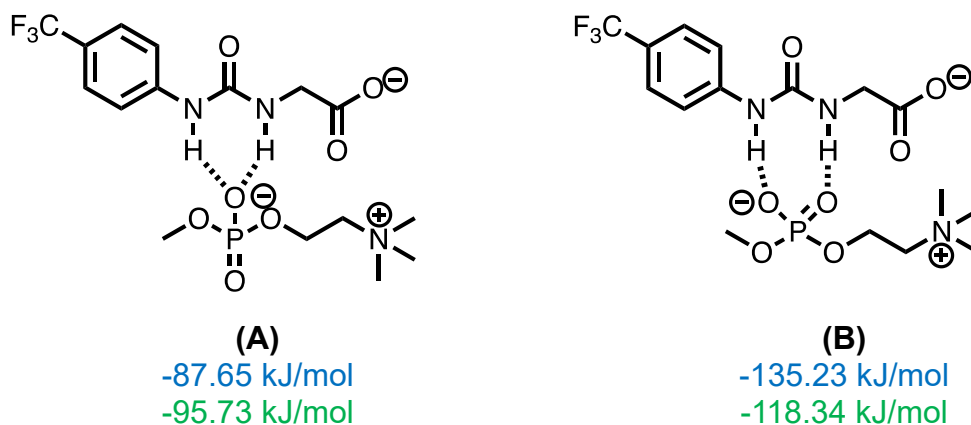


Figure 4.8: SSA **78**-m-PC conformations with their corresponding binding energies. Blue = values from ab initio calculations. Green = values from DFT calculations. Dashed line = hydrogen bond.

Three low-energy binding modes were found between SSA **78** and m-PE (Figure 4.9). Compared to the m-PC conformations, additional hydrogen bonds were present. In addition to hydrogen bonds from one or two of the phosphate oxygen atoms to the urea NH groups, there were bonds from the carboxylate group to the ammonium group on m-PE. Conformations **C** and **D** also contained an intramolecular hydrogen bond. The ab initio calculations showed conformation **D** as the most stable binding arrangement, whereas the DFT calculations suggested that conformation **C** was preferred.

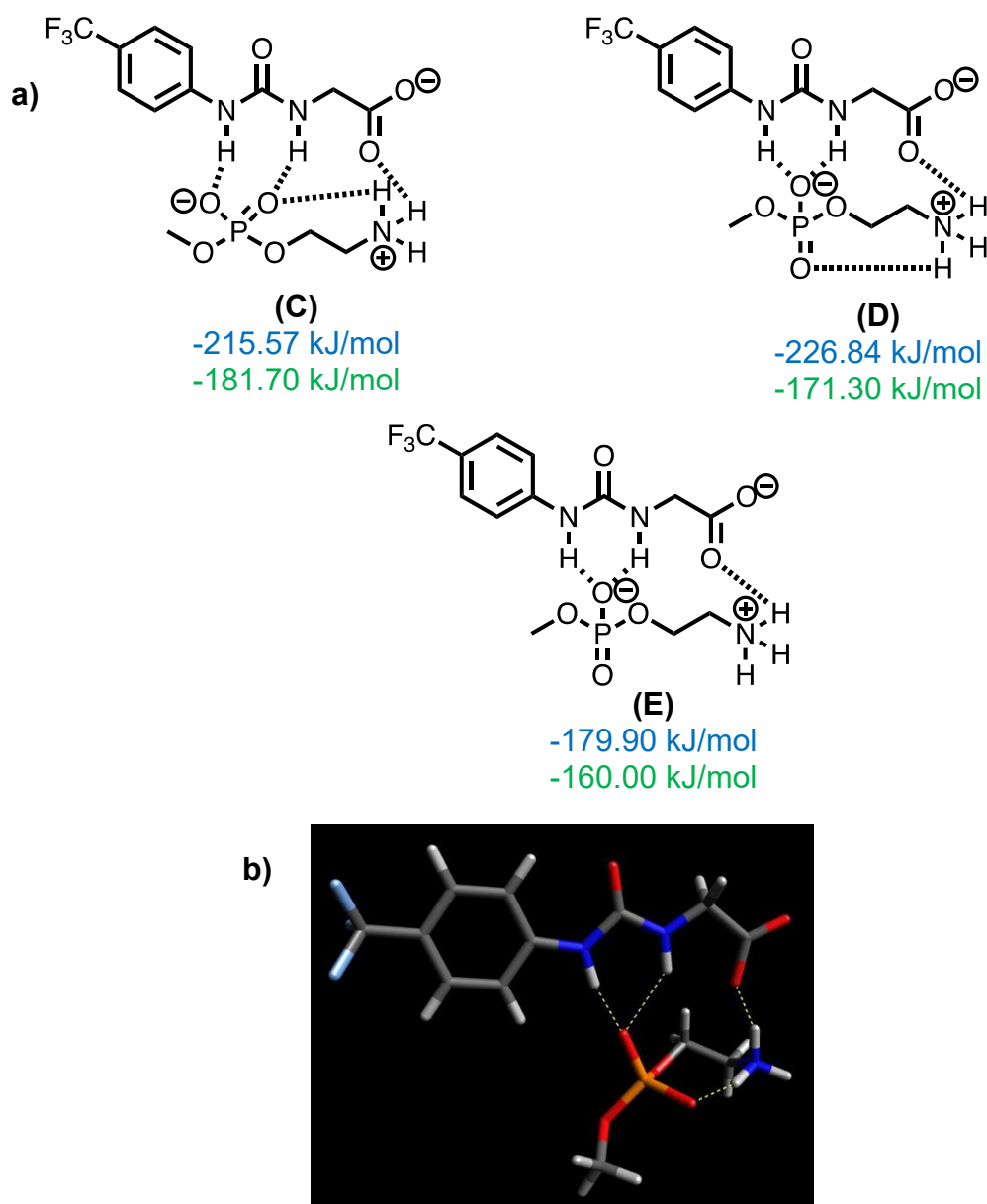
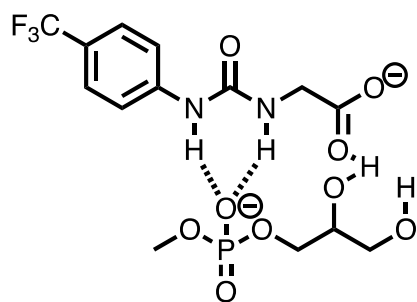
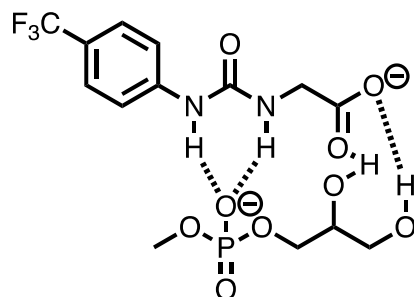


Figure 4.9: a) SSA **78**-m-PE conformations with their corresponding binding energies. Blue = values from *ab initio* calculations. Green = values from DFT calculations. Dashed line = hydrogen bond; b) Graphic illustrating hydrogen bonding in conformation **D**.

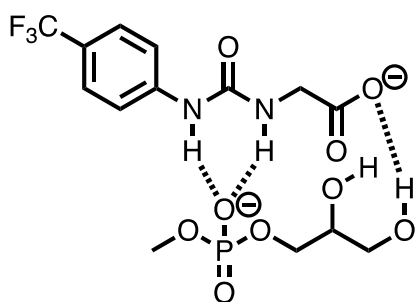
Ten low-energy binding modes were found between SSA **78** and m-PG. Like the m-PE conformations, several hydrogen bonding modes were found. The presence of the two hydroxyl groups on m-PG contributed to this. Once again, two conformations, **J** and **K**, contained intramolecular hydrogen bonds. Conformation **I** showed the most stable binding arrangement for both sets of calculations.



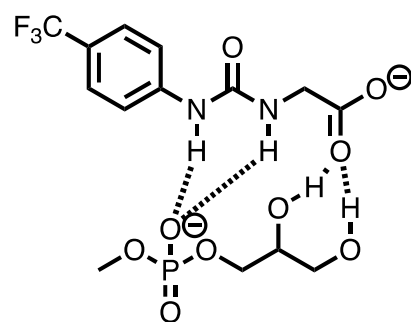
**(F)**  
-153.59 kJ/mol  
-134.89 kJ/mol



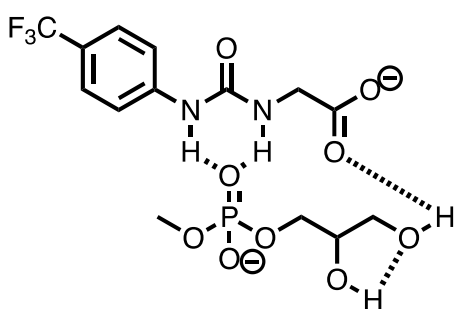
**(G)**  
-159.98 kJ/mol  
-126.44 kJ/mol



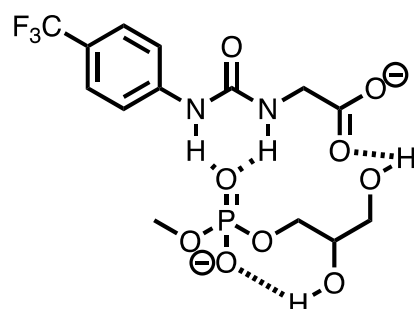
**(H)**  
-132.73 kJ/mol  
-117.39 kJ/mol



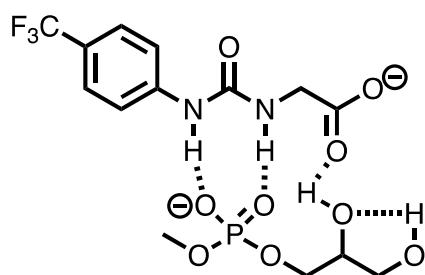
**(I)**  
-182.71 kJ/mol  
-143.54 kJ/mol



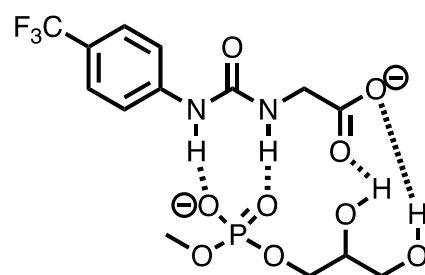
**(J)**  
-147.88 kJ/mol  
-122.51 kJ/mol



**(K)**  
-155.93 kJ/mol  
-123.97 kJ/mol



**(L)**  
-131.83 kJ/mol  
-116.48 kJ/mol



**(M)**  
-131.83 kJ/mol  
-128.52 kJ/mol

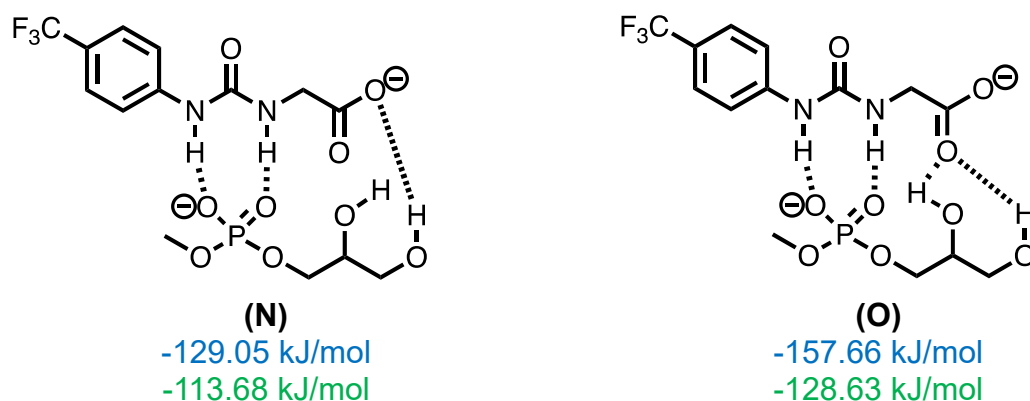


Figure 4.10: SSA 78-m-PG conformations with their corresponding binding energies. Blue = values from *ab initio* calculations. Red = values from DFT calculations. Dashed line = hydrogen bond.

Figures 4.8, 4.9 and 4.10 show the different conformations exhibited by SSA 78 and the three m-lipids. The lowest binding energy conformations were extracted from this dataset to compare the binding energies of the m-lipids (Table 4.4).

Table 4.4: Lowest binding energy conformations with values for SSA 78 with m-lipids.

	Ab initio results	DFT results
<b>m-PC</b>	<b>(B)</b> -135.24 kJ/mol	<b>(B)</b> 118.34 kJ/mol
<b>m-PE</b>	<b>(D)</b> -226.84 kJ/mol	<b>(C)</b> -181.70 kJ/mol
<b>m-PG</b>	<b>(I)</b> -182.71 kJ/mol	<b>(I)</b> -143.54 kJ/mol

Table 4.4 shows that the lowest binding energy conformations – hence the most favourable – contain several hydrogen bonds between SSA 78 and m-lipid that stabilise the structures. An m-lipid binding preference is observed for both sets of calculations – PE > PG > PC. The preference for the bacterial lipids PE and PG implies that SSA 78 may preferentially interact with the bacterial cell membranes.



#### 4.6.1.1 Correlation between calculations

Once both sets of calculations were completed, the correlation between both methods could be determined. As shown in Figure 4.11, the correlation between both methods is reasonable, showing a linear relationship and an  $R^2$  value of 0.90. This suggests a high similarity between both sets of results. From this, it was determined that only ab initio calculations would be used for binding energy calculations for SSA **75** to facilitate a more rapid screening process.

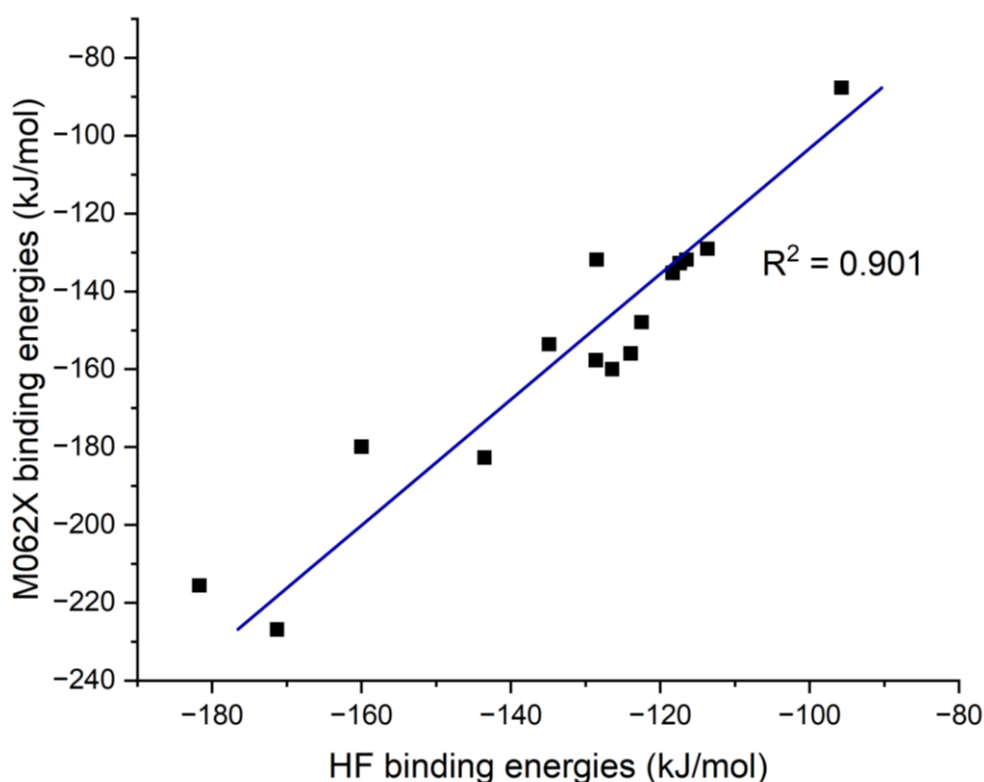


Figure 4.11: Correlation data between binding energies calculated via ab initio and DFT methods for SSA **78**.

#### 4.6.2 SSA 75

Next, the binding energy of SSA 5 was investigated using only ab initio calculations. Like with SSA 75, input files were created for each SSA 75-m-lipid conformation with the hope of calculating the binding energy of each conformation using Equation 4.1. The lowest binding energy, hence the most stable, conformations for each m-lipid were sought.

Two potential low-energy binding modes between SSA 75 and m-PC were found (Figure 4.12). Hydrogen bond formation was only seen between the urea NH and one or two oxygen atoms from the phosphate moiety for both structures. This can be justified, as the cationic portion of m-PC does not allow for hydrogen bond formation. The most stable binding arrangement was deemed to be conformation Q.

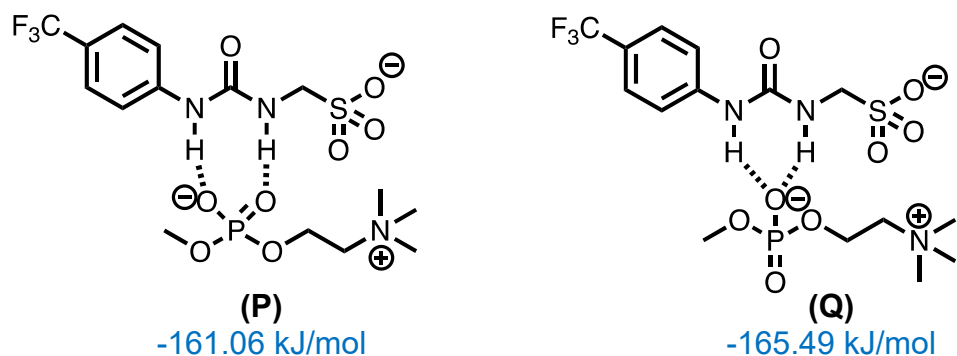


Figure 4.12: SSA 75-m-PC conformations with their corresponding binding energies. Dashed line = hydrogen bond.

Four low-energy binding modes were found between SSA 75 and m-PE (Figure 4.13). The ammonium moiety and the sulfonate group allow more hydrogen bonds to form between conformations, in addition to the hydrogen bonds forming between the urea NH and phosphate moiety. Once again, intramolecular hydrogen bonds can be seen with m-PE conformations in conformations S and T. Conformation T gave the most stable binding arrangement.

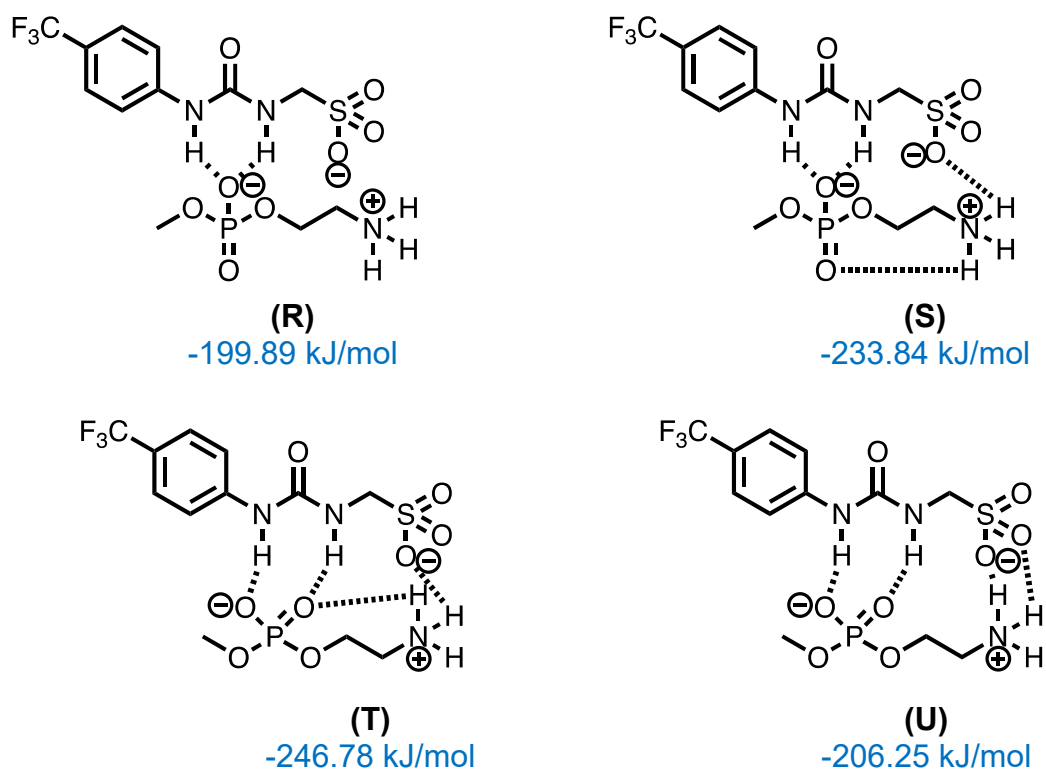
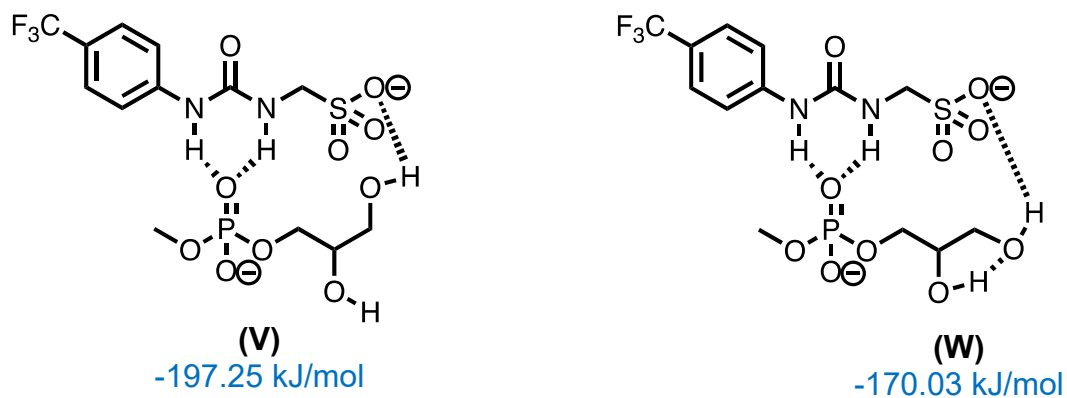


Figure 4.13: SSA **75**-m-PE conformations with their corresponding binding energies. Dashed line = hydrogen bond.

Eight low-energy binding modes were found between SSA **75** and m-PG. Each structure had two hydrogen bonds from the oxygen(s) from the phosphate moiety to the urea NH and at least one hydrogen bond from the hydroxyl groups to the sulfonate groups. Conformation **Y** was deemed to have the most stable binding arrangement.



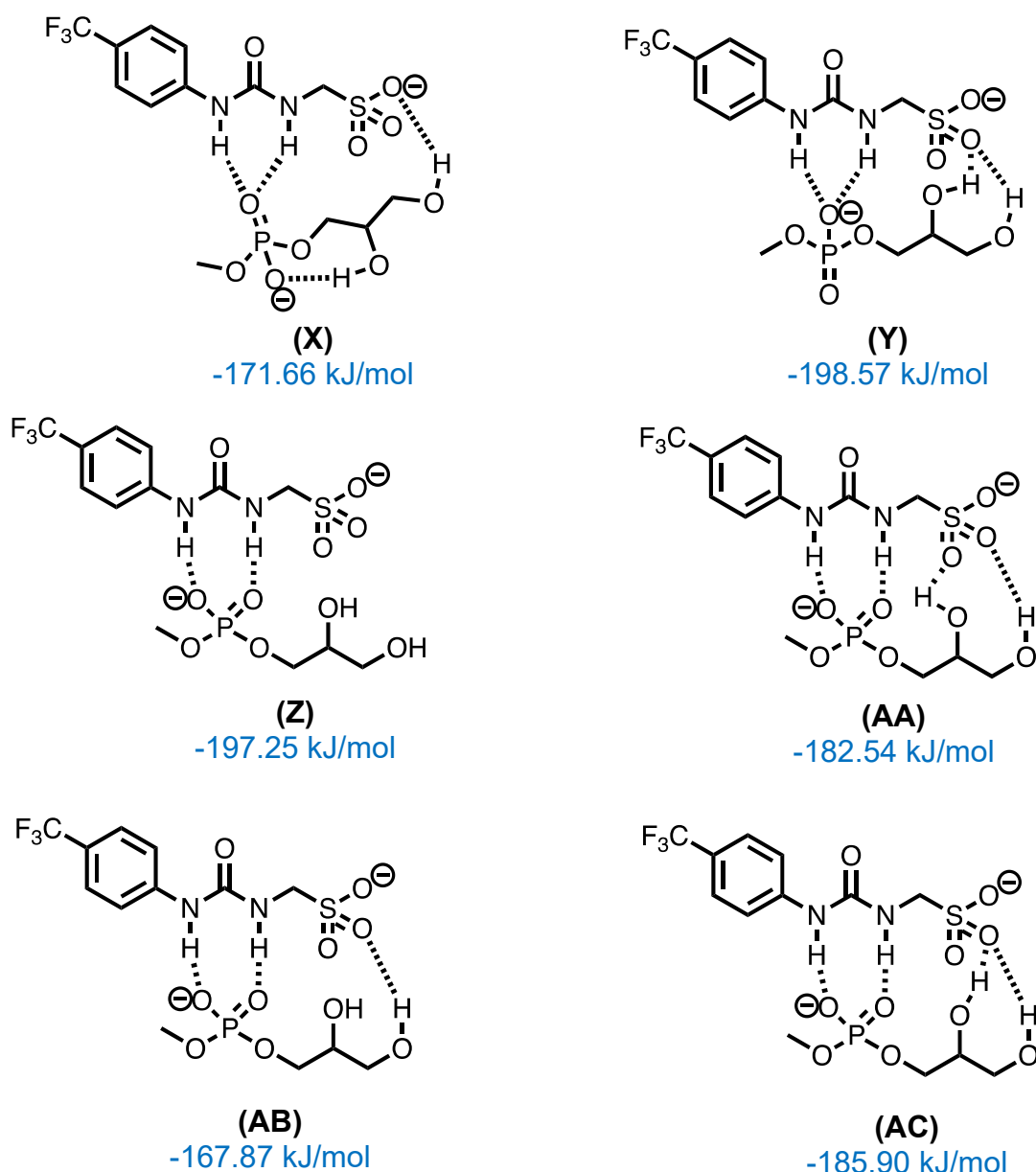


Figure 4.14: SSA **75**-m-PG conformations with their corresponding binding energies. Dashed line = hydrogen bond.

Figures 4.12, 4.13 and 4.14 show the different conformations of SSA **75** and the three m-lipids and their binding energies. The lowest binding energy conformations were extracted from this dataset to compare the binding energies of the m-lipids (Table 4.5). Once again, the data from Table 4 shows that the more hydrogen bonds present between the SSA-lipid pair, the more favourable its formation is. The same m-lipid preference can be seen for SSA **75** – PE > PG > PC, indicating that this SSA may also preferentially bind to bacterial cell membranes.

*Table 4.5: Lowest binding energy conformations with values for SSA 75 with m-lipids.*

<b>m-PC</b>	<b>(Q)</b> -165.49 kJ/mol
<b>m-PE</b>	<b>(T)</b> -246.78 kJ/mol
<b>m-PG</b>	<b>(Y)</b> -198.57 kJ/mol

#### 4.6.3 Comparing both SSAs

Comparing the lowest binding energies from the ab initio calculations for both SSAs shows that it is more favourable for all m-lipids to bind to SSA 75 (Table 4.6). This suggests that having a sulfonate group on the SSA is preferable for lipid binding compared to a carboxylate group. This is likely due to the presence of an additional hydrogen bond acceptor.

*Table 4.6: Lowest binding energy conformations for SSA 75 and 78.*

	<b>SSA 75</b>	<b>SSA 78</b>
<b>m-PC</b>	-165.49 kJ/mol	-135.24 kJ/mol
<b>m-PE</b>	-246.78 kJ/mol	-226.84 kJ/mol
<b>m-PG</b>	-198.57 kJ/mol	-182.71 kJ/mol

Both SSAs follow the same m-lipid pattern. The ammonium group on m-PE allows for more hydrogen bonds to form between the SSA-m-lipid pair, and it is a comparatively better hydrogen bond donor than the other functionalities in the lipid headgroups. Overall, this suggests that binding to bacterial phospholipids is preferred over binding to mammalian phospholipids and implies their use as selective antibacterial agents. Hiscock and co-workers' further findings support these results. A synthetic vesicle lysis assay was conducted, and vesicles with different lipid compositions containing calcein were prepared.<sup>214</sup> Calcein is a fluorescent dye that self-quenches at high concentrations. The addition of the SSAs should lyse

the vesicles, decreasing the internal calcein concentration and increasing the fluorescence emission, which is proportional to vesicle lysis. It was found that SSAs **75** and **78**, amongst others, preferred bacterial lipids. In particular, selective lysis was shown for 100% PG vesicles – a synthetic equivalent to MRSA – and *E. coli* vesicles. In general, it was found that SSAs containing sulfonate groups (over carboxylate groups) performed better in the vesicle lysis assay, supporting the computational results found.<sup>214</sup>

## 4.7 Conclusions and future outlooks

In conclusion, this computational project, although brief, has helped increase the understanding of how SSAs bind to lipid headgroups, thereby giving additional insight into how these molecules can act as selective antibacterial agents. It has been found that bacterial lipids, PE and PG, can form more hydrogen bonds with both SSAs, hence increasing the stability of the SSA-lipid complex and making their formation more favourable. SSAs containing sulfonate groups can form more hydrogen bonds with all lipid types, especially with PE, than carboxylate-containing SSAs. This finding is further supported by experimental work conducted by Hiscock and co-workers.<sup>214</sup>

More complex models and techniques are required to gain a more in-depth insight into the binding of SSAs to lipid bilayers. One way to improve future calculations is to examine the whole lipid bilayer instead of individual lipids. Félix and co-workers used molecular dynamics (MD) simulations to study the interactions of tris-thiourea tripodal anion transporters with a type of PC membrane model.<sup>215</sup> The authors were able to shed light on specific events occurring within the process of transmembrane chloride transport, which would not have been possible with more straightforward computational calculations.

Ultimately, a diverse and ever-expanding library of SSAs is yet to be studied computationally, and this project has provided a foundation for this to be a possibility.

## 5 Thesis recap and broader outlooks

Anion binding has applications in many fields, and generating new supramolecular hosts to bind such guests is crucial for furthering these fields. This thesis has explored, in different capacities, the design and synthesis of supramolecular hosts that bind biologically relevant anions. The main guests explored were chloride, bromide, iodide, acetate, benzoate, nitrate and phospholipids.

### 5.1 Metal-organic complexes for anion binding

#### 5.1.1 Recap

Chapter 2 looked at the synthesis of tripodal metal-organic hosts via subcomponent self-assembly. One metal-organic host, **52**, was scaled up to investigate its potential applications in anion binding and transport. Using  $^1\text{H}$  NMR titrations, it was found that **52** bound several anions: chloride, bromide, iodide, acetate, benzoate, and nitrate. Acetate and benzoate bound the strongest. This led to the testing of applications in indicator displacement assays, where small anionic dyes were able to bind **52** and be subsequently displaced via the addition of strongly binding anions, like benzoate and chloride. Additionally, the anion transport applications of **52** were tested. Using the ion-selective electrode and lucigenin assays, **52** showed potential chloride/nitrate antiport and  $\text{M}^+$ /chloride symport activity. In light of these promising results, further work is needed to fine-tune metal-organic hosts, like **52**, for success in ‘real-world’ applications – some specific suggestions to aid this have been noted in section 2.9.

Regarding the indicator displacement assay, a huge anion concentration was required to displace the anionic fluorophore; this suggests that **52** was not a very sensitive probe. With potential modifications, this type of cleft could be suitable for use in IDAs or even fluorescent sensing arrays, as **52** was responsive towards more than one type of anion. Vesicle lysis assays must be conducted for applications in anion transport to confirm a transport mechanism. However, success is more likely with differently coloured complexes that do not quench the dyes involved in vesicle lysis (i.e., calcein).

Chapter 3, furthering the work in Chapter 2, explored the potential for chiral cleft synthesis using subcomponent self-assembly in the hopes of binding biologically relevant chiral anions.

After several attempts, two chiral tripodal amines, **66** and **68**, were synthesised via reductive amination of an amino aldehyde and put forward for subcomponent self-assembly with various metals. Potential success with zinc salts was seen for both amines; however, a discrete product could not be isolated, which was confirmed via NMR and CD analysis. The difficulty in synthesising a chiral tripodal cleft was likely due to the steric bulk of the tripodal amine around the metal centre; thus, for future work, there may be more success with using a less bulky amino acid-derived amine, like alanine or even valine.

### 5.1.2 Current work in this field

In the field of metal-organic chemistry for anion binding, the focus seems to be on larger architectures, like metal-organic cages (MOCs) and metal-organic frameworks (MOFs). As mentioned in Chapter 1.3, their synthesis often involves a high cost. However, with the growing need to bind and encapsulate guests of different shapes and sizes, MOCs and MOFs seem more suited. For example, Xie *et al.* utilised three Zr-MOFs to bind ATP-related physiological phosphates.<sup>216</sup> The varying size of the MOF cavities allowed for a distinction between each type of phosphate. Additionally, each guest exhibited a different fluorescent response when bound to the MOFs, allowing for the formation of a fluorescent sensor array.

Nevertheless, new metal-organic complexes are still being synthesised for this use. For example, Yang and co-workers synthesised Ni(II) complexes formed from N,N'-ethylenebis(salicylimine) ligands (Figure 5.1), which were preorganised for anion binding.<sup>217</sup> They were able to bind a variety of anions – chloride, bromide, fluoride, hydrogen phosphate and acetate in deuterated DMSO. However, the anion-binding behaviour of the nickel(II) complexes depended on the pK<sub>a</sub> of the anion. The more basic anions – hydrogen phosphate and acetate – bound more strongly than chloride, which often competed with solvent molecules, as seen using single-crystal X-ray crystallography. Fluoride, the most basic, deprotonated the (thio)urea moiety. The authors also mention anion size as an important factor in binding, with chloride binding the strongest, followed by bromide.



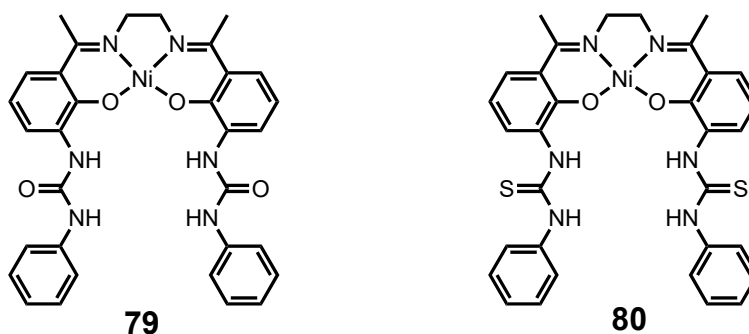


Figure 5.1: Ni(II) complexes synthesised by Yang and co-workers.<sup>217</sup>

As mentioned in Chapter 1.1, the binding of anions often requires a delicate balance between pKa, size and shape. With coordination complexes, getting the size and shape of guests correct is often more difficult, hence the apparent shift towards larger metal-organic architectures.

## 5.2 SSAs

### 5.2.1 Recap

Chapter 4 investigated the binding of SSAs to three modified lipid headgroups using Hartree-Fock and DFT methods. SSAs **75** and **78** showed preferential binding to bacterial lipid headgroups compared to mammalian ones *via* hydrogen bonding. Additionally, SSA **75** – containing a sulfonate group – showed stronger binding to all lipid headgroups compared to SSA **78**, which included a carboxylate group. These computational studies were confirmed through calcein vesicle lysis assays conducted by the Hiscock group, where SSAs **75** and **78** preferentially lysed bacterial lipids.

### 5.2.2 Current work on SSAs

As mentioned, the Hiscock group has developed a library of SSAs – all of which are being tested for antimicrobial activity. In a paper from 2023, Pohl and co-workers tested the effectiveness of several SSAs against biofilms made from *P. aeruginosa* and *C. albicans*.<sup>218</sup> The former is a Gram-negative bacteria, and the latter is a pathogenic yeast.<sup>219</sup> Using optical density measurements, it was found that SSAs **75** and **78**, amongst others, exhibited antimicrobial activity. SSA **75** and other sulfonate-containing SSAs inhibited monomicrobial growth but not polymicrobial, which is typically more resistant to antimicrobial agents. Carboxylate-containing SSAs, like SSA **78**, proved to be more effective with polymicrobial

inhibition; this may be due to the increased basicity of the anionic functionality, increasing the strength of hydrogen bond donating/accepting ability. Interestingly, replacing the trifluoromethyl group with a benzothiazole moiety increased the efficacy towards *C. albicans* monomicrobial films, likely due to the pi-pi stacking interactions between SSAs through the film. Additionally, increasing the lipophilicity of the SSA – i.e. increasing chain length between the (thio)urea moiety and hydrophilic group – increased activity against both microbes. Since then, Hiscock *et al.* have shown enhanced antimicrobial activity against pathogenic biofilms via 1:1 co-formulations of various SSAs, with the composition depending on the target pathogen.<sup>220</sup>

More recently, amino acid-appended SSAs were explored for their activity against MRSA and an ovarian cancer cell line.<sup>221</sup> This group of SSAs built on existing structure-activity relationships – much like those investigated in this thesis – while incorporating hydrophobic amino acid residues to increase the stability of SSA transmembrane structure within the hydrophobic portions of the phospholipid bilayer through shielding of the hydrophilic groups on the SSA anion. It was found that the incorporation of these residues enhanced biological activity against disease-causing cells. Notably, SSAs have been shown to act as ion transport agents.<sup>195</sup> This paper shows that SSAs can form ion channels or pores, suggesting that this mechanism of action is how cell death (on cancer cell lines) may occur.

### 5.3 Broader outlook

The binding of anions is growing to be immensely important in the field of medicinal chemistry. At present, the binding of biologically relevant anions has limited applications in medicinal contexts due to the specific requirements of biological tools – namely, a need to balance deliverability, solubility and lipophilicity of the host. However, some promising research is underway, with the research on SSAs being a good starting point. Additionally, Elmes and co-workers recently published a paper on squaramide-based anionophores that display antimicrobial activity *via* chloride transport and subsequent membrane disruption.<sup>222</sup> Recent research has also focused on targeting disorders linked with the dysfunction of the Golgi apparatus, a vital organelle responsible for maintaining cellular homeostasis and physiological function, as it houses chloride transport proteins. Gale and co-workers have synthesised a squaramide-based fluorescent anionophore that can accumulate in cells and exert cytotoxic

effects.<sup>223</sup> Similarly, Chen and colleagues have developed a urea-based anionophore that targets the Golgi apparatus and induces apoptosis in cancer cells.<sup>224</sup>

As we enhance our understanding of the structures of hosts suitable for anion binding in medicinal chemistry, we can anticipate more hosts being taken forward for clinical applications. The field of anion binding in biological and medicinal chemistry presents significant potential, and the research presented in this thesis may lay the groundwork for future molecular tools to address challenges in medicine and drug discovery.

## 6 Experimental

### 6.1 General synthetic remarks

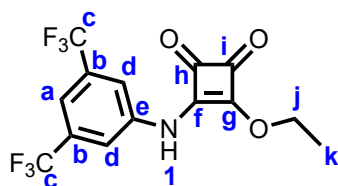
All chemicals and solvents were purchased from commercial suppliers and used without further purification. All reactions requiring anhydrous conditions were performed under nitrogen and using anhydrous solvents. Organic phases were dried using magnesium sulfate or sodium sulfate and filtered. Ether refers to diethyl ether. EtOAc refers to ethyl acetate. Thin layer chromatography (TLC) was performed using Sigma Aldrich TLC plates with F254 fluorescent indicator and were visualised under UV light. Normal phase flash column chromatography was carried out using silica gel with pore size 60 Å (43-60 mm) using the solvent ratios shown. MS was performed on the Waters Acquity UPLC SQD mass spectrometer, equipped with a C8 column using a gradient of 5-95% acetonitrile over 5 mins, with HPLC grade water (0.1% v/v formic acid) and acetonitrile (0.1% v/v formic acid) as the mobile phases. **51** was analysed on the Agilent 6530 Q-ToF LC-MS/MS system. The separation was achieved using mobile phase A (water with 0.1% formic acid) and B (acetonitrile, with 0.1% formic acid) using a gradient elution at the flow rate 0.3 mL/min. The column effluent was continuously electrosprayed into capillary electrospray ionisation (ESI) source of the Agilent 6510 QTOF mass spectrometer. ESI mass spectra were acquired in positive ESI mode at the  $m/z$  range 1,000–3,200 in profile mode. The raw data was converted to zero charge mass spectra using maximum entropy deconvolution algorithm within the MassHunter software version B.07.00. IR was performed using the Bruker Alpha II FTIR spectrometer and the samples were used neat unless stated otherwise. Melting point was determined using the Fischer Scientific electrothermal IA900 melting point apparatus. Optical rotation measurements were performed on the Bellingham + Stanley ADP430 series polarimeter or the Anton Paar MCP100. CD measurements were conducted on the Chirascan V100 circular dichroism spectrometer. Both  $^1\text{H}$  and  $^{13}\text{C}$  NMR were performed using the Bruker Neo Avance 400, 500, 600 and 700 MHz instruments at 25 °C. Chemical shift values ( $\delta$ ) are reported in parts per million and are reported relative to the resonance of the residual solvent peak. The following abbreviations are used to describe signal multiplicity for  $^1\text{H}$  and  $^{13}\text{C}$  NMR spectra – b: broad, s: singlet, d: doublet, t: triplet, q: quartet, p: pentet (or quintet), dd: doublet of doublets, ddd: doublet of doublet of doublets, dt: doublet of triplets, td: triplet of doublets, dddd: doublet of doublet of doublet of doublets, m: multiplet.  $^1\text{H}$  NMR solvent peaks –  $\text{CDCl}_3$ : 7.26 ppm (multiplicity = 1);  $\text{CD}_3\text{CN}$ : 1.94 ppm (multiplicity

= 5); (CD<sub>3</sub>)<sub>2</sub>CO: 2.05 (multiplicity = 5); (CD<sub>3</sub>)<sub>2</sub>SO: 2.50 (multiplicity = 5). <sup>13</sup>C NMR solvent peaks – CDCl<sub>3</sub>: 77.3 ppm (multiplicity = 3); CD<sub>3</sub>CN: 118.7 ppm (multiplicity = 1), 1.39 ppm (multiplicity = 7); (CD<sub>3</sub>)<sub>2</sub>CO: 206.17 (multiplicity = 1), 29.84 (multiplicity = 7); (CD<sub>3</sub>)<sub>2</sub>SO: 39.52 (multiplicity = 7). POPC was supplied by Avanti. Chloride concentrations during transport experiments were determined using a Cole-Parmer chloride ISE electrode. Lucigenin assay was conducted on the Horiba Fluorolog-3 Fluorimeter. Other fluorescence measurements were conducted on the Cary Eclipse Fluorescence Spectrometer and the Tecan spark multimode microplate reader. UV-Vis measurements were conducted on the Varian Cary 100 Bio UV-Visible Spectrophotometer.

## 6.2 Synthetic procedures

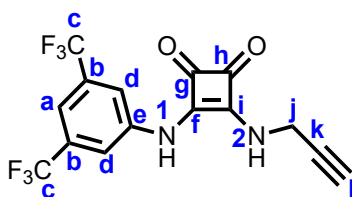
### 6.2.1 Synthetic procedures for Chapter 2

#### *3-((3,5-Bis(trifluoromethyl)phenyl)amino)-4-ethoxycyclobut-3-ene-1,2-dione (42)*



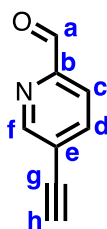
To a stirred solution of 3,4-diethoxycyclobut-3-ene-1,2-dione (0.880 mL, 6.00 mmol) and zinc triflate (0.181 g, 0.500 mmol) in EtOH (15.0 mL) was added 3,5-bis(trifluoromethyl)aniline (0.779 mmol, 5.00 mmol). The reaction mixture was left to stir at RT for 1 h. The reaction mixture was added dropwise into DI water (100 mL) and filtered to afford the desired product as a yellow powder (1.51 g, 85%). <sup>1</sup>H NMR  $\delta$ (500 MHz, (CD<sub>3</sub>)<sub>2</sub>SO) = 11.20 (s, 1H, N<sup>1</sup>H), 8.03 (s, 2H, C<sup>d</sup>H), 7.77 (s, 1H, C<sup>a</sup>H), 4.80 (q, J = 7.1 Hz, 2H, C<sup>j</sup>H), 1.42 (t, J = 7.1 Hz, 3H, C<sup>k</sup>H) ppm. <sup>13</sup>C NMR  $\delta$ (500 MHz, (CD<sub>3</sub>)<sub>2</sub>SO) = 187.45 (C<sup>f</sup>), 184.52 (C<sup>g</sup>), 179.27 (C<sup>h</sup>), 169.19 (C<sup>i</sup>), 140.17 (C<sup>e</sup>), 131.14 (q, J = 33.0 Hz, C<sup>b</sup>), 123.09 (q, J = 272.8 Hz, C<sup>c</sup>), 119.43 (C<sup>d</sup>), 116.31 (C<sup>a</sup>), 70.14 (C<sup>j</sup>), 15.36 (C<sup>k</sup>) ppm. IR  $\nu_{\max}$  = 3252 (NH), 3099 (CH), 3004 (CH), 1716 (C=O), 1632 (C=C), 1599 (C=C) cm<sup>-1</sup>. m.p. = 186.1-189.3 °C. LRMS (ESI-): m/z = 352.3 ([M-H]<sup>-</sup>). Characterisation is in line with published data.<sup>142</sup>

3-((3,5-bis(trifluoromethyl)phenyl)amino)-4-(prop-2-yn-1-ylamino)cyclobut-3-ene-1,2-dione  
(43)



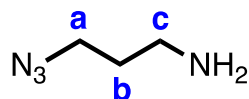
To a stirring solution of 3-((3,5-bis(trifluoromethyl)phenyl)amino)-4-ethoxycyclobut-3-ene-1,2-dione (0.352 g, 1.00 mmol) in EtOH (30.0 mL) and triethylamine (0.556 mL, 4.00 mmol) was added propargylamine (0.0769 mL, 1.20 mmol). The reaction mixture was left to stir overnight at RT. The reaction mixture was added dropwise to 1% acetic acid (aq., 200 mL) to form a filtered and dried suspension to afford the desired product as a yellow solid (0.306 g, 85%).  $^1\text{H}$  NMR  $\delta$  (600 MHz,  $\text{CD}_3\text{SO}_2$ ) = 10.20 (s, 1H,  $\text{N}^1\text{H}$ ), 8.00 (s, 2H,  $\text{C}^d\text{H}$ ), 7.66 (s, 1H,  $\text{C}^a\text{H}$ ), 4.45 (s, 2H,  $\text{C}^j\text{H}$ ), 3.44 (t,  $J = 2.5$  Hz, 1H,  $\text{C}^a\text{H}$ ) ppm.  $^{13}\text{C}$  NMR  $\delta$  (600 MHz,  $\text{CD}_3\text{SO}_2$ ) = 184.89 ( $\text{C}^g$ ), 180.96 ( $\text{C}^h$ ), 169.18 ( $\text{C}^f$ ), 162.99 ( $\text{C}^i$ ), 140.98 ( $\text{C}^e$ ), 131.33 (q,  $J = 33.1$  Hz,  $\text{C}^b$ ), 123.21 (q,  $J = 272.2$  Hz,  $\text{C}^c$ ), 118.31 ( $\text{C}^d$ ), 115.01 ( $\text{C}^a$ ), 80.06 ( $\text{C}^k$ ), 75.77 ( $\text{C}^l$ ), 33.34 ( $\text{C}^j$ ) ppm. IR  $\nu_{\text{max}}$  = 3319 ( $\text{C}\equiv\text{H}$ ), 3193 (NH), 3091 (CH), 1795 ( $\text{C}=\text{O}$ ), 1588 ( $\text{C}=\text{C}$ ), 1570 ( $\text{C}=\text{C}$ )  $\text{cm}^{-1}$ . m.p. = 240.9-243.5  $^\circ\text{C}$ . LRMS (ESI+): 363.2 ( $[\text{M}+\text{H}]^+$ ), 404.3 ( $[\text{M}+\text{MeCN}+\text{H}]^+$ ). LRMS (ESI-):  $m/z$  = 361.2 ( $[\text{M}-\text{H}]^-$ ), 723.3 ( $[\text{2M}-\text{H}]^-$ ). Accurate mass ( $\text{C}_{15}\text{H}_8\text{F}_6\text{N}_2\text{O}_2$   $[\text{M}+\text{H}]^+$ ) =  $m/z$  = 363.0563 (calculated); 363.0562 (found).  $R_f$  = 0.30 (50% EtOAc in hexanes).

*5-Ethynylpicolinaldehyde (44)*



To a solution of 5-((trimethylsilyl)ethynyl)picolinaldehyde (1.44 g, 7.08 mmol) in MeOH (75.0 mL) was added potassium carbonate (0.0800 g, 0.580 mmol). The reaction mixture was stirred at RT for 3 h. The solvent was removed under reduced pressure, and the residue was suspended in DI water (30.0 mL), after which the suspension was sonicated and filtered. The solid was washed with DI water (3 x 20.0 mL) and left to dry on a vacuum, which afforded the desired product as a brown amorphous solid (0.746 g, 80%).  $^1\text{H}$  NMR  $\delta$  (500 MHz,  $\text{CDCl}_3$ ) = 10.07 (s, 1H,  $\text{C}^{\text{a}}\text{H}$ ), 8.85 (t,  $J$  = 1.5 Hz, 1H,  $\text{C}^{\text{f}}\text{H}$ ), 7.95-7.91 (m, 2H,  $\text{C}^{\text{c}}\text{H}$ ,  $\text{C}^{\text{d}}\text{H}$ ), 3.43 (s, 1H,  $\text{C}^{\text{h}}\text{H}$ ) ppm.  $^{13}\text{C}$  NMR  $\delta$  (500 MHz,  $\text{CDCl}_3$ ) = 192.66 ( $\text{C}^{\text{a}}$ ), 153.17 ( $\text{C}^{\text{f}}$ ), 151.57 ( $\text{C}^{\text{b}}$ ), 140.26 ( $\text{C}^{\text{d}}$ ), 123.76 ( $\text{C}^{\text{e}}$ ), 121.00 ( $\text{C}^{\text{c}}$ ), 84.22 ( $\text{C}^{\text{h}}$ ), 79.85 ( $\text{C}^{\text{g}}$ ). IR  $\nu_{\text{max}}$  = 3213 ( $\text{C}\equiv\text{H}$ ), 2105 ( $\text{C}\equiv\text{C}$ ), 1701 ( $\text{C}=\text{N}$ ), 1688 ( $\text{C}=\text{O}$ ), 1579 ( $\text{C}=\text{C}$ )  $\text{cm}^{-1}$ . m.p. = 113.4-116.3  $^{\circ}\text{C}$ . LRMS (ESI $^{+}$ ):  $m/z$  = 164.2 ( $[\text{M}+\text{MeOH}+\text{H}]^{+}$ ). Characterisation was in line with published data.<sup>144</sup>

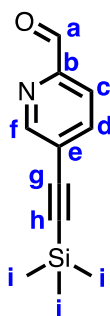
*3-Azidopropan-1-amine (45)*



To 3-chloropropylamine hydrochloride (1.54 g, 11.8 mmol) in water (20.0 mL) was added sodium azide (2.26g, 34.8 mmol). The reaction mixture was heated to 80 °C and stirred overnight behind a blast shield. The reaction mixture was left to cool to RT before handling, and the flask was subsequently cooled in an ice bath. 15% KOH (aq., 4.00 mL) was added, and the product was washed with diethyl ether (3 x 20.0 mL), water (20.0 mL), and brine (20.0 mL). The combined organic phases were dried with Na<sub>2</sub>SO<sub>4</sub>. Around 80% of the solvent was removed under reduced pressure as the product was volatile. However, the product was obtained as a clear solution in Et<sub>2</sub>O (0.196 g, 16%). <sup>1</sup>H NMR  $\delta$  (500 MHz, CDCl<sub>3</sub>) = 3.06 (t, J = 6.7 Hz, 2H, C<sup>a</sup>H or C<sup>c</sup>H), 2.49 (t, J = 6.7 Hz, 2H, C<sup>a</sup>H or C<sup>c</sup>H), 1.40 (p, J = 6.7 Hz, 2H, C<sup>b</sup>H) ppm. Other characterising data could not be obtained as the product is very volatile and had to be used immediately. Characterisation is in line with published data.<sup>147</sup>

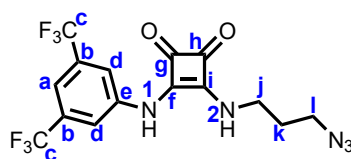


5-((Trimethylsilyl)ethynyl) (46)



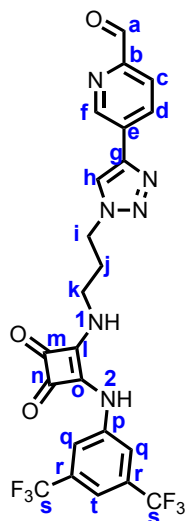
TMS-acetylene (6.81 mL, 49.2 mmol) was added to a degassed solution of 5-bromo-2-pyridinecarboxaldehyde (3.14 g, 16.9 mmol) in toluene (75.0 mL) and triethylamine (25.0 mL), and N<sub>2</sub> was bubbled into the solution for 5 mins. Pd(PPh<sub>3</sub>)<sub>4</sub> (0.462 g, 0.400 mmol) and CuI (0.463 g, 2.43 mmol) were added, and the solution was degassed again and subsequently stirred at RT overnight under an inert atmosphere. The solvent was removed under vacuum, and the solid residue was dissolved in DCM (30.0 mL). The solution was washed with sat. NH<sub>4</sub>Cl (30.0 mL) and subsequently brine (30.0 mL). The combined organic phases were dried with Na<sub>2</sub>SO<sub>4</sub>, and the solvent was removed *in vacuo*. The crude product was purified *via* column chromatography (20% EtOAc in hexanes), and the solvent was removed under vacuum to afford the desired product as a brown solid (2.15 g, 63%). <sup>1</sup>H NMR δ (500 MHz, CDCl<sub>3</sub>) = 10.05 (s, 1H, C<sup>a</sup>H), 8.80 (t, J = 1.4 Hz, 1H, C<sup>f</sup>H), 7.89 (d, J = 1.4 Hz, 2H, C<sup>e</sup>H, C<sup>d</sup>H), 0.28 (s, 9H, C<sup>i</sup>H) ppm. <sup>13</sup>C NMR δ (500 MHz, CDCl<sub>3</sub>) = 192.69 (C<sup>a</sup>), 152.96 (C<sup>f</sup>), 151.11 (C<sup>b</sup>), 139.90 (C<sup>d</sup>), 124.78 (C<sup>e</sup>), 120.97 (C<sup>c</sup>), 102.84 (C<sup>h</sup>), 100.76 (C<sup>g</sup>), -0.20 (C<sup>i</sup>) ppm. IR ν<sub>max</sub> = 3038 (CH), 2960 (CH), 2822 (CH), 2157 (C≡C), 1709 (C=O), 1574 (C=C) cm<sup>-1</sup>. m.p. = 78.6-81.4 °C. LRMS (ESI<sup>+</sup>): m/z = 204.0 ([M+H]<sup>+</sup>). Characterisation is in line with published data.<sup>144</sup>

*3-((3-Azidopropyl)amino)-4-((3,5-bis(trifluoromethyl)phenyl)amino)cyclobut-3-ene-1,2-dione*  
(47)



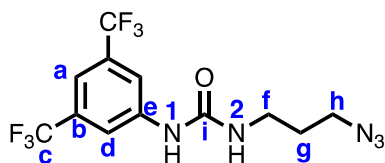
To a stirring solution of 3-((3,5-bis(trifluoromethyl)phenyl)amino)-4-ethoxycyclobut-3-ene-1,2-dione (0.246 g, 0.693 mmol) in EtOH (10.0 mL) and triethylamine (0.386 mL, 2.77 mmol) was added 3-azidopropylamine (0.104 g, 1.05 mmol). The reaction mixture was left to stir overnight at RT behind a blast shield. The reaction mixture was left to cool to RT, after which it was added dropwise to 1% acetic acid (aq., 200 mL) to form a suspension that was filtered and dried to afford the desired product as a yellow solid (0.207 g, 73%).  $^1\text{H}$  NMR  $\delta$  (600 MHz,  $(\text{CD}_3)_2\text{SO}$ ) = 10.21 (s, 1H, N<sup>1</sup>H), 8.01 (s, 2H, C<sup>d</sup>H), 7.74 (s, 1H, N<sup>2</sup>H), 7.66 (s, 1H, C<sup>a</sup>H), 3.68 (q, J = 6.5 Hz, 2H, C<sup>j</sup>H), 3.46 (t, J = 6.7 Hz, 2H, C<sup>l</sup>H), 1.84 (p, J = 6.7 Hz, 2H, C<sup>k</sup>H) ppm.  $^{13}\text{C}$  NMR  $\delta$  (600 MHz,  $(\text{CD}_3)_2\text{SO}$ ) = 184.84 (C<sup>g</sup>), 180.65 (C<sup>h</sup>), 169.84 (C<sup>f</sup>), 162.57 (C<sup>i</sup>), 141.08 (C<sup>e</sup>), 131.38 (q, J = 32.9 Hz, C<sup>b</sup>), 123.23 (q, J = 272.9 Hz, C<sup>c</sup>), 118.10 (C<sup>d</sup>), 114.83 (C<sup>a</sup>), 47.92 (C<sup>l</sup>), 41.41 (C<sup>j</sup>), 29.71 (C<sup>k</sup>) ppm. IR  $\nu_{\text{max}}$  = 3154 (NH), 3080 (NH), 2957 (CH), 2092 (N<sub>3</sub>), 1799 (C=O), 1658 (C=O), 1565 (C=C), 1376 (CF), 1271 (CN), 1117 (CN)  $\text{cm}^{-1}$ . m.p. = 205.1-207.8 °C. LRMS (ESI-): m/z = 406.2 ([M-H]<sup>-</sup>). Characterisation is line with published data.<sup>225</sup>

5-(1-(3-((2-((3,5-Bis(trifluoromethyl)phenyl)amino)-3,4-dioxocyclobut-1-en-1-yl)amino)propyl)-1H-1,2,3-triazol-4-yl)picolinaldehyde (**48**)



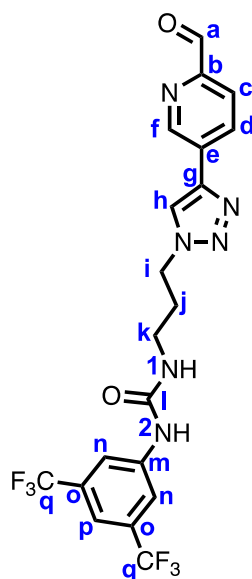
To a degassed solution of 5-ethynylpicolinaldehyde (0.0566 g, 0.432 mmol), 3-((3-azidopropyl)amino)-4-((3,5-bis(trifluoromethyl)phenyl)amino)cyclobut-3-ene-1,2-dione (0.352 g, 0.864 mmol) and DIPEA (0.118 mL, 0.864 mmol) in DMF (10.0 mL) was added CuI (0.0159 g, 0.0864 mmol), and the reaction mixture was stirred at RT for 24 h under an inert atmosphere. The reaction mixture was diluted with DCM (100 mL) and washed with sat. NH<sub>4</sub>Cl (2 x 100 mL). The organic phase was dried (Na<sub>2</sub>SO<sub>4</sub>), and the crude product was purified *via* column chromatography (75% EtOAc in hexanes) to afford the product as a white crystalline solid (0.0371 g, 36%). <sup>1</sup>H NMR  $\delta$  (500 MHz, (CD<sub>3</sub>)<sub>2</sub>CO) = 9.97 (s, 1H, C<sup>a</sup>H), 9.44 (s, 1H, N<sup>2</sup>H), 9.25 (s, 1H, C<sup>f</sup>H), 8.76 (s, 1H, C<sup>h</sup>H), 8.41 (dd, J = 7.8 Hz, 1H, C<sup>d</sup>H), 8.09 (s, 2H, C<sup>q</sup>H), 7.92 (d, J = 8.0 Hz, C<sup>e</sup>H), 7.56 (s, 1H, C<sup>i</sup>H), 7.27 (s, 1H, N<sup>1</sup>H), 4.74 (t, J = 6.6 Hz, C<sup>i</sup>H), 3.88 (q, J = 6.0 Hz, C<sup>k</sup>H), 2.44 (t, J = 6.1 Hz, C<sup>j</sup>H) ppm. IR  $\nu_{\text{max}}$  = 3211 (NH), 3086 (CH), 2993 (CH), 1796 (C=O), 1712 (C=O), 1670 (C=O), 1589 (C=C), 1275 (CN), 1122 (CF) cm<sup>-1</sup>. m.p. = 188.4-191.6 °C. LRMS (ESI<sup>+</sup>): m/z = 539.3 ([M+H]<sup>+</sup>). LRMS (ESI<sup>-</sup>): m/z = 537.3 ([M-H]<sup>-</sup>). Accurate mass (C<sub>23</sub>H<sub>16</sub>F<sub>6</sub>N<sub>6</sub>O<sub>3</sub> [M+H]<sup>+</sup>): m/z = 539.1261 (calculated); 539.1255 (found). Other data could not be obtained due to solubility issues.

*1-(3-Azidopropyl)-3-(3,5-bis(trifluoromethyl)phenyl)urea (49)*



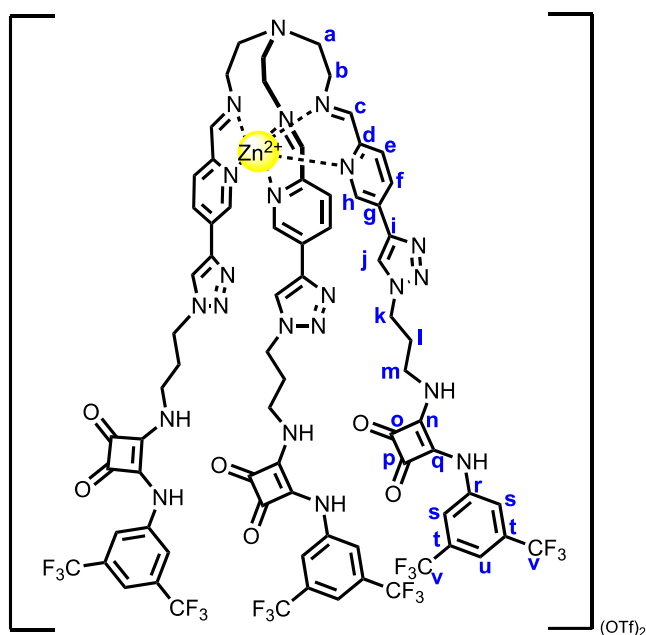
To a solution of 3-azidopropylamine (0.200 g, 2.00 mmol) in DCM (10.0 mL) was added 3,5-bis(trifluoromethyl)phenyl isocyanate (0.347 mL, 2.00 mmol), and the reaction mixture was left to stir at RT for 2 h. The solvent was removed under a compressed air stream until a solid formed. Hexane (20.0 mL) was added to further crash out the solid, which was then filtered and washed with DCM (30.0 mL) to afford the desired product as a white crystalline solid (0.443 g, 62%).  $^1\text{H}$  NMR  $\delta$  (500 MHz,  $(\text{CD}_3)_2\text{SO}$ ) = 9.25 (s, 1H,  $\text{N}^1\text{H}$ ), 8.08 (s, 2H,  $\text{C}^d\text{H}$ ), 7.53 (s, 1H,  $\text{C}^b\text{H}$ ), 6.57 (t,  $J$  = 5.8 Hz, 1H,  $\text{N}^2\text{H}$ ), 3.39 (t,  $J$  = 6.7 Hz, 2H,  $\text{C}^h\text{H}$ ), 3.17 (q,  $J$  = 6.5 Hz, 2H,  $\text{C}^f\text{H}$ ), 1.71 (p,  $J$  = 6.8 Hz, 2H,  $\text{C}^g\text{H}$ ) ppm.  $^{13}\text{C}$  NMR  $\delta$  (500 MHz,  $((\text{CD}_3)_2\text{SO})$ ) = 154.87 ( $\text{C}^i$ ), 142.62 ( $\text{C}^e$ ), 130.59 (q,  $J$  = 32.5 Hz,  $\text{C}^b$ ), 123.39 (q,  $J$  = 272.6 Hz,  $\text{C}^c$ ), 117.29 ( $\text{C}^d$ ), 113.61-113.28 ( $\text{C}^a$ ), 48.50 ( $\text{C}^h$ ), 36.74 ( $\text{C}^f$ ), 28.87 ( $\text{C}^g$ ) ppm. IR  $\nu_{\text{max}}$  = 3334 (NH), 2957 (NH), 2160 ( $\text{N}_3$ ), 1654 ( $\text{C}=\text{O}$ ), 1561 ( $\text{C}=\text{C}$ ), 1268 ( $\text{C}-\text{N}$ ), 1124 ( $\text{C}-\text{N}$ )  $\text{cm}^{-1}$ . m.p. = 92.0-95.8  $^\circ\text{C}$ . m.p. (lit) = 92.0-93.0  $^\circ\text{C}$ . LRMS (ESI+) = 356.3 ( $[\text{M}+\text{H}]^+$ ). Characterisation is in line with published data.<sup>225</sup>

*1-(3,5-Bis(trifluoromethyl)phenyl)-3-(3-(4-(6-formylpyridin-3-yl)-1H-1,2,3-triazol-1-yl)propyl)urea (50)*



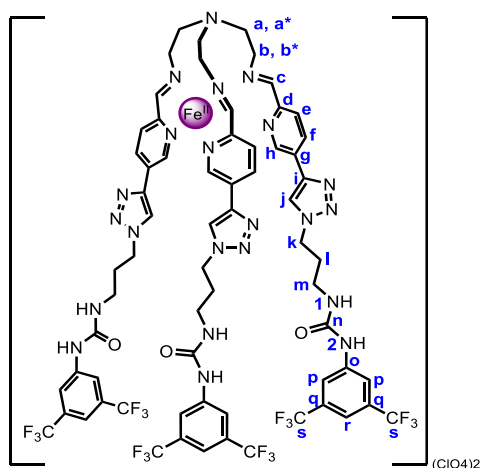
To a degassed solution of 5-ethynylpicolinaldehyde (0.0526 g, 0.401 mmol), 1-(3-azidopropyl)-3-(3,5-bis(trifluoromethyl)phenyl)urea and DIPEA (0.137 mL, 0.801 mmol) in DMF (10.0 mL) was added CuI (0.0153 g, 0.0801 mmol), and the reaction mixture was stirred at RT for 24 h under an inert atmosphere. The reaction mixture was diluted with DCM (100 mL) and washed with sat.  $\text{NH}_4\text{Cl}$  (2 x 100 mL). The organic phase was dried ( $\text{MgSO}_4$ ), and the crude product was purified *via* column chromatography (100% EtOAc) to afford the product as a white crystalline solid (0.0823 g, 43%).  $^1\text{H}$  NMR  $\delta$  (500 MHz,  $(\text{CD}_3)_2\text{CO}$ ) = 10.01 (s, 1H,  $\text{C}^{\text{a}}\text{H}$ ), 9.27 (s, 1H,  $\text{C}^{\text{f}}\text{H}$ ), 8.72 (s, 1H,  $\text{N}^2\text{H}$ ), 8.66 (s, 1H,  $\text{C}^{\text{h}}\text{H}$ ), 8.43 (dd,  $J$  = 8.2, 2.2 Hz, 1H,  $\text{C}^{\text{d}}\text{H}$ ), 8.14 (s, 2H,  $\text{C}^{\text{n}}\text{H}$ ), 7.98 (d,  $J$  = 8.1 Hz, 1H,  $\text{C}^{\text{e}}\text{H}$ ), 7.51 (s, 1H,  $\text{C}^{\text{p}}\text{H}$ ), 6.26 (t,  $J$  = 6.0 Hz, 1H,  $\text{N}^1\text{H}$ ), 4.64 (t,  $J$  = 6.8 Hz, 2H,  $\text{C}^{\text{i}}\text{H}$ ), 3.37 (q,  $J$  = 6.4 Hz, 2H,  $\text{C}^{\text{k}}\text{H}$ ), 2.25 (p,  $J$  = 6.9 Hz, 2H,  $\text{C}^{\text{j}}\text{H}$ ) ppm.  $^{13}\text{C}$  NMR  $\delta$  (500 MHz,  $(\text{CD}_3)_2\text{SO}$ ) = 193.43 ( $\text{C}^{\text{a}}$ ), 155.80 ( $\text{C}^{\text{l}}$ ), 152.90 ( $\text{C}^{\text{b}}$ ), 147.85 ( $\text{C}^{\text{f}}$ ), 144.05 ( $\text{C}^{\text{g}}$ ), 143.57 ( $\text{C}^{\text{m}}$ ), 133.99 ( $\text{C}^{\text{d}}$ ), 132.35 (q,  $J$  = 32.8 Hz,  $\text{C}^{\text{o}}$ ), 132.11 ( $\text{C}^{\text{e}}$ ), 124.50 (q,  $J$  = 271.9 Hz,  $\text{C}^{\text{q}}$ ), 123.74 ( $\text{C}^{\text{h}}$ ), 122.25 ( $\text{C}^{\text{c}}$ ), 118.42 ( $\text{C}^{\text{n}}$ ), 114.80 ( $\text{C}^{\text{p}}$ ), 48.83 ( $\text{C}^{\text{i}}$ ), 37.84 ( $\text{C}^{\text{k}}$ ), 31.40 ( $\text{C}^{\text{j}}$ ) ppm. IR  $\nu_{\text{max}}$  = 3362 (NH), 3302 (NH), 3109 (CH), 3070 (CH), 2912 (CH), 1695 (C=O), 1623 (C=O), 1561 (C=C), 1273 (CN), 1128 (CF)  $\text{cm}^{-1}$ . m.p. = 172.2-175.6  $^{\circ}\text{C}$ . LRMS (ESI $^{+}$ ):  $m/z$  = 487.3 ( $[\text{M}+\text{H}]^{+}$ ). Accurate mass ( $\text{C}_{20}\text{H}_{17}\text{F}_6\text{N}_6\text{O}_2$   $[\text{M}+\text{H}]^{+}$ ):  $m/z$  = 487.1312 (calculated); 487.1310 (found); accurate mass ( $\text{C}_{20}\text{H}_{17}\text{F}_6\text{N}_6\text{O}_2$   $[\text{M}+\text{MeOH}+\text{H}]^{+}$ ):  $m/z$  = 519.1574 (calculated); 519.1571 (found).  $R_f$  = 0.57 (100% EtOAc).

*Zn(II)L complex 51*



A solution of tris(2-aminoethyl)amine (0.123 mL, 0.0820 mmol), 5-(1-(3-((2-((3,5-bis(trifluoromethyl)phenyl)amino)-3,4-dioxocyclobut-1-en-1-yl)amino)propyl)-1H-1,2,3-triazol-4-yl)picolinaldehyde (0.0259 g, 0.242 mmol) and zinc trifluoromethanesulfonate (0.0295 g, 0.0810 mmol) in MeCN (5.00 mL) was stirred at RT overnight. The solvent was subsequently removed, and the residue was dissolved in the minimum amount of MeCN. Et<sub>2</sub>O was added in portions (~20.0 mL) until a yellow solid precipitated. The mixture was centrifuged, and the supernatant was discarded. The pellet was again dissolved in the minimum amount of MeCN, and sonicated – Et<sub>2</sub>O was added until a purple solid precipitated. The mixture was centrifuged, the supernatant was removed, and the pellet was left to dry. The solid was afforded as a fine green solid (0.0223 g, 13%). <sup>1</sup>H NMR: δ (500 MHz, CD<sub>3</sub>CN) = 9.34 (s, 3H, C<sup>c</sup>H), 9.00 (s, 3H, N<sup>2</sup>H), 8.72 (s, 3H, C<sup>f</sup>H), 8.57 (dd, J = 8.1, 2.0 Hz, 3H, C<sup>e</sup>H), 8.47 (s, 3H, C<sup>j</sup>H), 8.08 (s, 6H, C<sup>s</sup>H), 7.94 (d, J = 8.1 Hz, 3H, C<sup>h</sup>H), 7.59 (s, 3H, C<sup>u</sup>H), 6.97 (s, 3H, N<sup>1</sup>H), 4.62 (t, J = 6.4 Hz, 6H, C<sup>k</sup>H), 3.95 (t, J = 6.4 Hz, 6H, C<sup>a</sup>H), 3.74 (q, J = 6.4 Hz, C<sup>b</sup>H and C<sup>m</sup>H), 2.99-2.96 (m, 3H, C<sup>b</sup>H), 2.56-2.52 (m, 3H, C<sup>l</sup>H) ppm. Accurate mass (C<sub>75</sub>H<sub>60</sub>F<sub>18</sub>N<sub>22</sub>O<sub>6</sub>Zn [M]<sup>2+</sup>): m/z = 886.2030 (calculated); 886.2037 (found). Accurate mass (C<sub>75</sub>H<sub>60</sub>F<sub>18</sub>N<sub>22</sub>O<sub>6</sub>Zn [M-H]<sup>+</sup>): m/z = 1770.4059 (calculated); 1771.3980 (found).

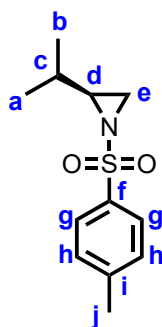
## *Fe(II)L complex 52*



A solution of tris(2-aminoethyl)amine (0.00901 mL, 0.0602 mmol) and 1-(3,5-bis(trifluoromethyl)phenyl)-3-(3-(4-(6-formylpyridin-3-yl)-1H-1,2,3-triazol-1-yl)propyl)urea (0.878 g, 0.181 mmol) in MeCN (7.00 mL) was stirred at 35 °C for 20 mins under an inert atmosphere, after which  $\text{Fe}(\text{ClO}_4)_2$  (0.0218 g, 0.0602 mmol) was added. The reaction mixture was stirred at 50 °C for 24 h under an inert atmosphere. The solvent was subsequently removed, and the residue was dissolved in the minimum amount of MeCN.  $\text{Et}_2\text{O}$  was added in portions (~20.0 mL) until a purple solid precipitated. The mixture was centrifuged, and the supernatant was discarded. The pellet was suspended in DI water, sonicated and centrifuged, and the supernatant was discarded. The pellet was again dissolved in the minimum amount of MeCN, and sonicated –  $\text{Et}_2\text{O}$  was added until a purple solid precipitated. The mixture was centrifuged, the supernatant was removed, and the pellet was left to dry. The solid was afforded as a fine purple solid (0.0779 g, 71%).  $^1\text{H}$  NMR:  $\delta$  (700 MHz,  $\text{CD}_3\text{CN}$ ) = 9.17 (s, 3H,  $\text{C}^{\text{e}}\text{H}$ ), 8.50 (d,  $J$  = 8.1 Hz, 3H,  $\text{C}^{\text{f}}\text{H}$ ), 8.32 (d,  $J$  = 8.1 Hz, 3H,  $\text{C}^{\text{e}}\text{H}$ ), 8.16 (s, 3H,  $\text{C}^{\text{h}}\text{H}$ ), 7.96 (s, 6H,  $\text{C}^{\text{p}}\text{H}$ ), 7.82 (s, 3H,  $\text{C}^{\text{j}}\text{H}$ ), 7.70 (s, 3H,  $\text{N}^2\text{H}$ ), 7.50 (s, 3H,  $\text{C}^{\text{r}}\text{H}$ ), 5.61 (t,  $J$  = 6.0 Hz, 3H,  $\text{N}^1\text{H}$ ), 4.38 (td,  $J$  = 6.0, 2.0 Hz, 3H,  $\text{C}^{\text{k}}\text{H}$ ), 3.65 (d,  $J$  = 10.2 Hz, 3H,  $\text{C}^{\text{a}}\text{H}$  or  $\text{C}^{\text{b}}\text{H}$ ), 3.51 (d,  $J$  = 13.5 Hz, 3H,  $\text{C}^{\text{a}*}\text{H}$  or  $\text{C}^{\text{b}*}\text{H}$ ), 3.20 (td,  $J$  = 13.9, 12.1 Hz, 3H,  $\text{C}^{\text{a}}\text{H}$  or  $\text{C}^{\text{b}}\text{H}$ ), 3.22-3.08 (m, 9H  $\text{C}^{\text{a}*}\text{H}$  or  $\text{C}^{\text{b}*}\text{H}$  AND  $\text{C}^{\text{m}}\text{H}$ ), 2.01 (p,  $J$  = 6.8 Hz, 6H,  $\text{C}^{\text{l}}\text{H}$ ).  $^{13}\text{C}$  NMR:  $\delta$  (700 MHz,  $\text{CD}_3\text{CN}$ ) = 172.10 ( $\text{C}^{\text{c}}$ ), 156.94 ( $\text{C}^{\text{d}}$ ), 155.95 ( $\text{C}^{\text{n}}$ ), 152.19 ( $\text{C}^{\text{h}}$ ), 143.02 ( $\text{C}^{\text{j}}$ ), 142.83 ( $\text{C}^{\text{i}}$ ), 135.18 ( $\text{C}^{\text{f}}$ ), 132.55 ( $\text{C}^{\text{o}}$ ), 132.30 (q,  $J$  = 33.0 Hz,  $\text{C}^{\text{q}}$ ), 124.57 ( $\text{C}^{\text{g}}$ ), 124.54 (q,  $J$  = 271.8 Hz,  $\text{C}^{\text{s}}$ ), 118.77 ( $\text{C}^{\text{p}}$ ), 115.50 ( $\text{C}^{\text{r}}$ ), 60.16 ( $\text{C}^{\text{a}}$ ), 54.80 ( $\text{C}^{\text{b}}$ ), 48.86 ( $\text{C}^{\text{k}}$ ), 37.50 ( $\text{C}^{\text{m}}$ ), 31.23 ( $\text{C}^{\text{l}}$ ) ppm. IR  $\nu_{\text{max}}$  = 3347 (NH), 3110 (NH), 2916 (CH), 2850 (CH), 1686 (C=O), 1604 (C=N), 1561 (C=C), 1275 (CN), 1175 (CF)  $\text{cm}^{-1}$ . Accurate mass ( $\text{C}_{66}\text{H}_{60}\text{F}_{18}\text{N}_{22}\text{O}_3\text{Fe} [\text{M}]^{2+}$ ):  $m/z$  = 803.2135 (calculated); 803.2107 (found).

### 3.1.1 Synthetic procedures for Chapter 3

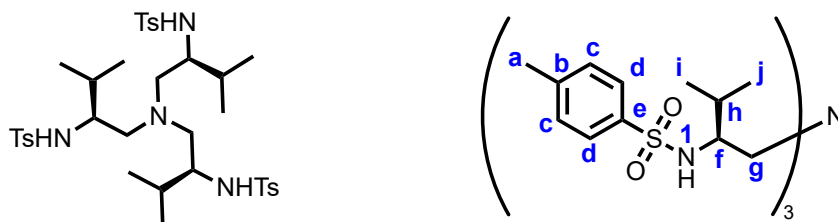
#### *(S)*-2-isopropyl-1-tosylaziridine (**63**)



TsCl (2.12 g, 11.1 mmol) was added to a solution of NEt<sub>3</sub> (5.41 mL, 38.8 mmol) and *(S)*-valinol (1.00 g, 9.69 mmol) in DCM (80.0 mL) at -25 °C, along with 4 Å molecular sieves under anhydrous conditions. The reaction mixture was stirred for 3 h in an ice bath, slowly warming to RT. MsCl (0.789 mL, 10.2 mmol) was then added dropwise over 10 min at -25 °C, and the reaction was left to stir overnight in an ice bath, which slowly warmed to RT again. The mixture was washed with 0.5 M HCl (2 x 50.0 mL); subsequent organic phases were washed with sat Na<sub>2</sub>CO<sub>3</sub> (2 x 50.0 mL) and dried. The crude product was purified *via* flash column chromatography (10% EtOAc in hexanes) to afford the desired aziridine product as a fluffy white solid (1.67 g, 72%). <sup>1</sup>H NMR δ (500 MHz, CDCl<sub>3</sub>) = 7.83 (d, J = 8.0 Hz, 2H, C<sup>g</sup>H), 7.34 (d, J = 7.9 Hz, 2H, C<sup>h</sup>H), 2.62 (d, J = 6.9 Hz, 1H, C<sup>e</sup>H), 2.51 (m, 1H, C<sup>d</sup>H), 2.45 (s, 3H, C<sup>j</sup>H), 2.10 (d, J = 4.6 Hz, 1H, C<sup>e</sup>H), 1.42 (m, 1H, C<sup>c</sup>H), 0.90 (d, J = 6.7 Hz, 3H, C<sup>b</sup>H), 0.80 (d, 6.7 Hz, 3H, C<sup>a</sup>H) ppm. <sup>13</sup>C NMR δ (500 MHz, CDCl<sub>3</sub>) = 144.6 (C<sup>f</sup>), 135.3 (C<sup>i</sup>), 129.7 (C<sup>g</sup>), 128.2 (C<sup>h</sup>), 46.4 (C<sup>e</sup>), 32.9 (C<sup>d</sup>), 30.3 (C<sup>c</sup>), 21.8 (C<sup>j</sup>), 19.7 (C<sup>b</sup>), 19.2 (C<sup>a</sup>) ppm. IR ν<sub>max</sub> (neat) = 3051 (C<sub>6</sub>H<sub>4</sub>), 2965 (CH), 2932 (CH), 2876 (CH), 1317 (SO<sub>2</sub>NH), 1154 (SO<sub>2</sub>NH) cm<sup>-1</sup>. m.p. = 89.3-91.9 °C. [α]<sub>D</sub><sup>30</sup> = +17.7 (c = 1.0, CHCl<sub>3</sub>). LRMS (ESI<sup>+</sup>): m/z = 240.1 ([M+H<sup>+</sup>]). Characterisation is in line with published data.<sup>178</sup>

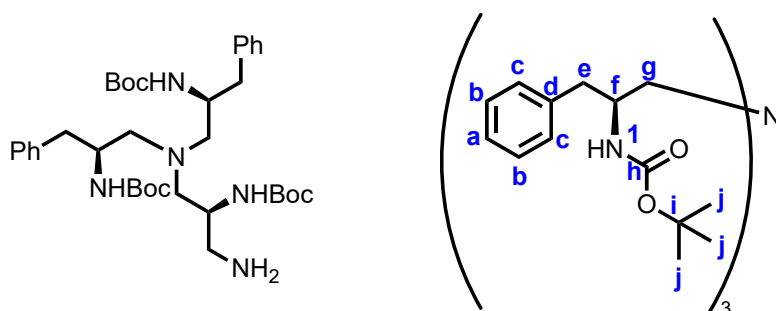


*N,N',N''-((2S, 2'S, 2''S)-nitrilotris(3-methylbutane-1,2-diyl))tris(4-methylbenzenesulfonamide (64)*



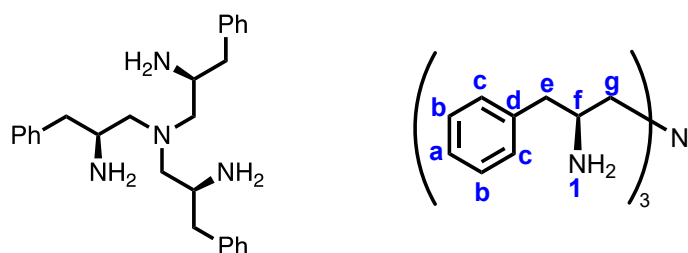
(*S*)-2-isopropyl-1-tosylaziridine (1.00 g, 4.18 mmol) was placed into a microwave tube containing a solution of ammonia (0.54 mL, 2.10 M in methanol, 1.14 mmol) and methanol (0.400 mL). The tube was heated at 50 °C in a sand bath and left to stir for 4 days behind a blast shield, following which the vessel was cooled to RT, and any excess pressure was removed from the vessel. The solvent was removed in vacuo, and the reaction mixture was analysed using NMR. The product was found to be unclear – likely a mixture of the mono-, di- and tri-substituted product. The crude product was refluxed in acetonitrile (15.0 mL) for 10 days at 95 °C. The reaction mixture was then filtered, and the NMR of the solid was taken – once again, the product was found to be unclear. To a G10 microwave vial was added aziridine product (0.314 g, 1.31 mmol) and crude product (0.585 g), and this was then dissolved in methanol (4.00 mL). The vial was heated in an Anton-Paar monowave 400 for 30 mins at 100 °C. Once finished, the vial was left to cool, and a white solid appeared – the reaction mixture was filtered, and the solid was washed with cold methanol (15.0 mL). The subsequent product was left to dry in vacuo overnight to afford the desired product as a crystalline white solid (0.585 g, 63%). <sup>1</sup>H NMR  $\delta$  (500 MHz, CDCl<sub>3</sub>) = 7.83 (d, *J* = 8.3 Hz, 6 H, C<sup>d</sup>H), 7.23 (d, *J* = 7.8 Hz, 6H, C<sup>e</sup>H), 6.19 (d, *J* = 7.0 Hz, 3 H, N<sup>1</sup>H), 3.79-3.86 (m, 3H, C<sup>f</sup>H), 2.93-2.98 (m, 3H, C<sup>g</sup>H), 2.38 (s, 9H, C<sup>a</sup>H), 2.15 (d, *J* = 3.8 Hz, 3H, C<sup>g</sup>H), 1.66-1.72 (m, 3H, C<sup>h</sup>H), 0.80 (d, *J* = 6.9 Hz, 9H, C<sup>i</sup>H), 0.77 (d, *J* = 6.9 Hz, 9H, C<sup>j</sup>H) ppm. <sup>13</sup>C NMR  $\delta$  (500 MHz, CDCl<sub>3</sub>) = 142.6 (C<sup>e</sup>), 140.0 (C<sup>b</sup>), 129.4 (C<sup>d</sup>), 126.7 (C<sup>c</sup>), 55.3 (C<sup>g</sup>), 31.6 (C<sup>f</sup>), 31.1 (C<sup>h</sup>), 21.6 (C<sup>a</sup>), 18.5 (C<sup>i</sup>), 18.3 (C<sup>j</sup>) ppm. IR  $\nu_{\max}$  (neat) = 3229 (-NH), 3063 (C<sub>6</sub>H<sub>4</sub>), 2958 (CH), 2932 (CH), 2874 (CH), 2829 (CH), 1309 (SO<sub>2</sub>NH), 1158 (SO<sub>2</sub>NH) cm<sup>-1</sup>. mp = 191.7 – 193.0 °C.  $[\alpha]^{25}_{\text{D}} = +55.3$  (*c* = 1.0, CHCl<sub>3</sub>). LRMS (ESI<sup>+</sup>): *m/z* = 735.4 ([*M*+H<sup>+</sup>]). Characterisation is in line with published data.<sup>178</sup>

*Tri-tert-butyl ((2S,2'S,2''S)-nitrilotris(3-phenylpropane-1,2-diyl))tricarbamate (65)*



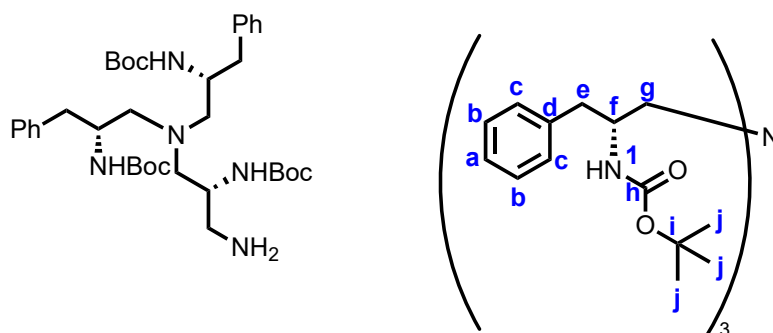
N-Boc-L-phenylalaninal (0.750 g, 3.00 mmol), NaBH(OAc)<sub>3</sub> (1.92 g, 9.00 mmol) and NH<sub>4</sub>OAc (0.0578 g, 0.750 mmol) were dissolved in THF (50.0 mL) and stirred under inert atmosphere for a month. The subsequent reaction mixture was quenched with 10% AcOH in MeOH (25.0 mL), and the solvent was removed *in vacuo*. The residue was dissolved in DCM (50.0 mL) and was washed with 4% KOH (2 x 50.0 mL). The combined organic phases were washed with brine (2 x 50.0 mL), dried with Na<sub>2</sub>SO<sub>4</sub>, and the solvent was removed *in vacuo*. The crude product was purified *via* column chromatography (15 → 30% EtOAc in hexanes + 1% triethylamine), and the solvent was removed *in vacuo* to afford the desired product as a white solid (0.249 g, 46%). <sup>1</sup>H NMR δ (500 MHz, CDCl<sub>3</sub>) = 7.31-7.29 (m, 6H, C<sup>b</sup>H), 7.24-7.20 (m, 9H, C<sup>a</sup>H and C<sup>c</sup>H), 4.76 (d, J = 8.1 Hz, 3H, C<sup>g</sup>H), 3.87 (s, 3H, C<sup>f</sup>H), 3.66 (d, J = 11.0 Hz, C<sup>e</sup>H), 3.56-3.54 (m, 3H, C<sup>e</sup>H), 2.84 (d, J = 7.2 Hz, 3H, C<sup>g</sup>H), 2.42 (s, 3H, N<sup>1</sup>H), 1.41 (s, 27H, C<sup>j</sup>H) ppm. <sup>13</sup>C NMR δ (500 MHz, (CDCl<sub>3</sub>) = 156.31 (C<sup>h</sup>), 137.93 (C<sup>d</sup>), 129.43 (C<sup>c</sup>), 128.70 (C<sup>b</sup>), 126.68 (C<sup>a</sup>), 79.86 (C<sup>i</sup>), 64.55 (C<sup>e</sup>), 53.87 (C<sup>f</sup>), 37.58 (C<sup>g</sup>), 28.48 (C<sup>j</sup>) ppm. IR ν<sub>max</sub> = 3354 (NH), 2982 (CH), 2927 (CH), 2873 (CH), 1684 (C=O), 1602 (C=C), 1314 (CN), 1250 (CO) cm<sup>-1</sup>. m.p. = 99.8-101.9 °C. [α]<sub>D</sub><sup>25</sup> = +29.9 (c = 1.0, CHCl<sub>3</sub>). LRMS (ESI+): m/z = 717.5 ([M+H]<sup>+</sup>). Characterisation is in line with published data.<sup>184</sup>

(S)-N<sup>1</sup>,N<sup>1</sup>-bis((S)-2-amino-3-phenylpropyl)-3-phenylpropane-1,2-diamine (**66**)



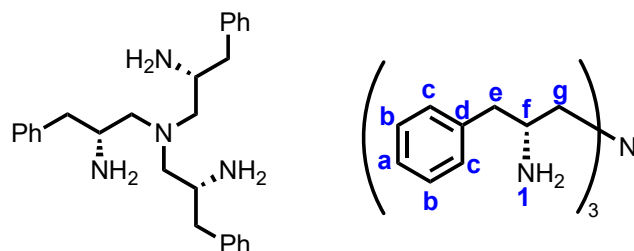
Tri-tert-butyl ((2S,2'S,2''S)-nitrilotris(3-phenylpropane-1,2-diyl))tricarbamate (0.249 g, 0.347 mmol) was dissolved in TFA (3.00 mL) and was stirred at RT for 2 h. TFA was subsequently removed under a gentle stream of compressed air. The residue was dissolved in DCM (15.0 mL) and subsequently evaporated – this was repeated 5 times. The residue was once again dissolved in DCM (50.0 mL), DI water was added, and the biphasic mixture was stirred rapidly. The pH was adjusted to 12 *via* the addition of 20% aq. KOH. The layers were separated, and the aqueous phase was washed with DCM (2 x 50.0 mL). The organic phases were combined and dried (Na<sub>2</sub>SO<sub>4</sub>), and the solvent was removed *in vacuo*. The yellow residue was dissolved in MeOH (5.00 mL) and run through an SCX-II column, which was flushed out with NH<sub>3</sub> in MeOH. The NH<sub>3</sub> in MeOH solution was reduced *in vacuo* to afford the product as a yellow solid (0.0821 g, 56%). <sup>1</sup>H NMR δ (500 MHz, CDCl<sub>3</sub>) = 7.32-7.29 (m, 6H, C<sup>b</sup>H), 7.24-7.18 (m, 9H, C<sup>a</sup>H and C<sup>c</sup>H), 3.63 (dd, J = 10.6, 3.8 Hz, 3H, C<sup>e</sup>H), 3.38 (dd, J = 10.6, 7.1 Hz, 3H, C<sup>e</sup>H), 3.12 (dddd, J = 8.7, 6.9, 5.3, 3.9 Hz, 3H, C<sup>f</sup>H), 2.79 (dd, J = 13.5, 5.2 Hz, 3H, C<sup>g</sup>H), 2.52 (dd, J = 13.5, 8.6 Hz, 3H, C<sup>g</sup>H), 1.91 (s, 6H, N<sup>1</sup>H) ppm. <sup>13</sup>C NMR δ (500 MHz, (CDCl<sub>3</sub>) = 138.81 (C<sup>d</sup>), 129.33 (C<sup>c</sup>), 128.71 (C<sup>b</sup>), 126.55 (C<sup>a</sup>), 66.47 (C<sup>e</sup>), 54.31 (C<sup>f</sup>), 41.06 (C<sup>g</sup>) ppm. IR ν<sub>max</sub> = 3298 (NH), 3024 (CH), 2918 (CH), 2875 (CH), 1620 (C=C), 1603 (C=C), 1277 (CN) cm<sup>-1</sup>. m.p. = 86.5-90.8 °C. [α]<sub>D</sub><sup>25</sup> = +2.80 (c = 1.0, CHCl<sub>3</sub>). LRMS (ESI<sup>+</sup>): m/z = 105.0 ([M+4H]<sup>+</sup>). Characterisation is in line with published data.<sup>184</sup>

Tri-*tert*-butyl ((2*R*,2'*R*,2''*R*)-nitrilotris(3-phenylpropane-1,2-diyl))tricarbamate (**67**)



N-Boc-D-phenylalaninal (2.50 g, 10.0 mmol), NaBH(OAc)<sub>3</sub> (3.18 g, 15.0 mmol) and NH<sub>4</sub>OAc (0.193 g, 2.50 mmol) were dissolved in THF (100 mL) and stirred under inert atmosphere for a month. The subsequent reaction mixture was quenched with 10% AcOH in MeOH (25.0 mL), and the solvent was removed *in vacuo*. The residue was dissolved in DCM (50.0 mL) and was washed with 4% KOH (2 x 50.0 mL). The combined organic phases were washed with brine (2 x 50.0 mL), dried with Na<sub>2</sub>SO<sub>4</sub>, and the solvent was removed *in vacuo*. The crude product was purified *via* column chromatography (15 → 50% EtOAc in hexanes + 1% triethylamine), and the solvent was removed *in vacuo* to afford the desired product as a white solid (45%). <sup>1</sup>H NMR δ (600 MHz, CDCl<sub>3</sub>) = 7.32-7.26 (m, 6H, C<sup>b</sup>H), 7.24-7.20 (m, 9H, C<sup>a</sup>H and C<sup>c</sup>H), 4.92 (s, 3H, C<sup>g</sup>H), 3.87 (s, 3H, C<sup>f</sup>H), 3.63 (dd, J = 10.9, 3.1 Hz, C<sup>e</sup>H), 3.56-3.50 (m, 3H, C<sup>e</sup>H), 2.84 (d, J = 6.2 Hz, 3H, C<sup>g</sup>H), 2.17 (s, 3H, N<sup>1</sup>H), 1.41 (s, 27H, C<sup>j</sup>H) ppm. <sup>13</sup>C NMR δ (600 MHz, CDCl<sub>3</sub>) = 156.24 (C<sup>h</sup>), 137.97 (C<sup>d</sup>), 129.41 (C<sup>c</sup>), 128.57 (C<sup>b</sup>), 126.52 (C<sup>d</sup>), 79.68 (C<sup>i</sup>), 64.08 (C<sup>e</sup>), 53.72 (C<sup>f</sup>), 37.47 (C<sup>g</sup>), 28.42 (C<sup>j</sup>) ppm. IR ν<sub>max</sub> = 3353 (NH), 2975 (CH), 2928 (CH), 2873 (CH), 1684 (C=O), 1603 (C=C), 1315 (CN), 1250 (CO) cm<sup>-1</sup>. m.p. = 97.1-98.8 °C. LRMS (ESI<sup>+</sup>): m/z = 717.8 ([M+H]<sup>+</sup>). [α]<sub>D</sub><sup>25</sup> = +20.9 (c = 0.7, CHCl<sub>3</sub>). Accurate mass (C<sub>42</sub>H<sub>60</sub>N<sub>4</sub>O<sub>6</sub> [M+2DMSO+H]<sup>+</sup>): m/z = 875.5007 (calculated); 875.4178 (found). R<sub>f</sub> = 0.25 (20% EtOAc in hexanes).

*(R)-N<sup>1</sup>,N<sup>1</sup>-bis((R)-2-amino-3-phenylpropyl)-3-phenylpropane-1,2-diamine (68)*



Tri-tert-butyl ((2R,2'R,2''R)-nitrilotris(3-phenylpropane-1,2-diyl))tricarbamate (0.654 g, 0.912 mmol) was dissolved in TFA (10.0 mL) and was stirred at RT for 2 h. TFA was subsequently removed under a gentle stream of compressed air. The residue was dissolved in DCM (20.0 mL) and subsequently evaporated – this was repeated 5 times. The residue was once again dissolved in DCM (50.0 mL), DI water was added, and the biphasic mixture was stirred rapidly. The pH was adjusted to 12 *via* the addition of 20% aq. KOH. The layers were separated, and the aqueous phase was washed with DCM (2 x 50.0 mL). The organic phases were combined and dried (Na<sub>2</sub>SO<sub>4</sub>), and the solvent was removed *in vacuo*. The yellow residue was dissolved in MeOH (5.00 mL) and run through an SCX-II column, which was flushed out with NH<sub>3</sub> in MeOH. The NH<sub>3</sub> in MeOH solution was reduced *in vacuo* to afford the product as a yellow solid (0.109 g, 29%). <sup>1</sup>H NMR  $\delta$  (600 MHz, CDCl<sub>3</sub>) = 7.29-7.27 (m, 6H, C<sup>b</sup>H), 7.22-7.16 (m, 9H, C<sup>a</sup>H and C<sup>c</sup>H), 3.60 (dd, J = 10.9, 3.7 Hz, 3H, C<sup>e</sup>H), 3.38 (dd, J = 10.9, 7.2 Hz, 3H, C<sup>e</sup>H), 3.11-3.06 (m, 3H, C<sup>f</sup>H), 2.98 (s, 6H, N<sup>1</sup>H), 2.76 (dd, J = 13.5, 5.4 Hz, 3H, C<sup>g</sup>H), 2.51 (dd, J = 13.5, 8.6 Hz, 3H, C<sup>g</sup>H) ppm. <sup>13</sup>C NMR  $\delta$  (600 MHz, CDCl<sub>3</sub>) = 138.58 (C<sup>d</sup>), 129.26 (C<sup>c</sup>), 128.62 (C<sup>b</sup>), 126.47 (C<sup>a</sup>), 65.71 (C<sup>e</sup>), 54.23 (C<sup>f</sup>), 40.29 (C<sup>g</sup>) ppm. IR  $\nu_{\text{max}}$  = 3298 (NH), 3023 (CH), 2918 (CH), 2875 (CH), 1663 (C=C), 1602 (C=C), 1263 (CN) cm<sup>-1</sup>. m.p. = 76.2-79 °C.

LRMS (ESI<sup>+</sup>): m/z = 105.0 ([M+4H]<sup>+</sup>). [ $\alpha$ ]<sub>D</sub><sup>25</sup> = +21.7 (c = 1.0, CHCl<sub>3</sub>). Accurate mass (C<sub>27</sub>H<sub>36</sub>N<sub>4</sub> [M+4H]<sup>+</sup>): m/z = 105.0815 (calculated); 105.2737 (calculated). R<sub>f</sub> = 0.36 (25% EtOAc in hexanes + 1% NEt<sub>3</sub>).

## 6.3 Guest binding screens

### For sugars

1.4 mL of a 1 mM host solution was prepared in 1:1 MeCN-d<sub>3</sub>/aqueous solvent (either H<sub>2</sub>O or D<sub>2</sub>O). 10 equivalents of the guest were added to the host solution, and a <sup>1</sup>H NMR spectrum was taken.

### For other guests

0.7 mL of a 2 mM host solution was prepared in MeCN-d<sub>3</sub>. 10 equivalents of the guest were added to the host solution, and a <sup>1</sup>H NMR spectrum was taken.

## 6.4 $^1\text{H}$ NMR titrations

1.5 mL of a 2 mM host solution was prepared, and 0.5 mL was added to an NMR tube and sealed with an airtight subaseal. The remaining 1 mL was used to make a 3 mM guest solution, allowing receptor concentration to stay constant throughout. Aliquots of the host/guest solution were added to the NMR tube, and a  $^1\text{H}$  NMR was taken after each aliquot. Chemical shifts for each peak were calibrated to the solvent peak. The data was plotted on OriginPro to compare changes in chemical shift values between guests.

## 6.5 Vesicle studies

### 6.5.1 General remarks

The vesicles used in transport studies were prepared according to a standard literature protocol. The ionic strengths of both the intravesicular and extravesicular solutions were chosen to be isotonic to avoid the rupturing of vesicle membranes. All solutions were buffered to pH 7.2 with 10 mM sodium phosphate salts. The ionic strengths of the solutions were controlled at 500 mM with the desired internal or external salt as applicable.

### 6.5.2 Vesicle preparation

A lipid film was prepared by evaporating a chloroform solution of POPC *via* rotary evaporation and dried in the desiccator overnight. For the lucigenin assay, 1 mol% of the transporter was added to the dried film as an acetonitrile solution. Using a vortexer, the lipid was suspended in the required internal solution (2 mL) – NaCl or KCl for the chloride-selective electrode experiments and NaNO<sub>3</sub> for the lucigenin assay. Nine freeze-thaw cycles were completed *via* freezing in liquid nitrogen and warming to RT to disrupt the multilamellar vesicles. The vesicle suspension was allowed to stand for 30 minutes, after which the vesicles were extruded 25 times through 200 nm polycarbonate membranes.

### 6.5.3 Chloride/nitrate antiport experiments

Following extrusion, the vesicles were subjected to dialysis in the desired external solution for at least 2 hours to remove unencapsulated internal salts (NaCl). Unilamellar POPC vesicles were then diluted to 2 mM using the external solution (NaNO<sub>3</sub>). A transporter solution in acetonitrile (1 mol% or 10 mol% wrt lipid) was added to start the experiment, and the chloride efflux was monitored using a chloride-selective electrode. At 5 mins, the vesicles were lysed with 100 µL polyethylene glycol *tert*-octylphenyl ether (10% in H<sub>2</sub>O) and a total chloride reading was taken at 7 mins.



#### 6.5.4 Lucigenin assay

Following extrusion, the vesicles were passed through a size-exclusion column pre-eluted with  $\text{NaNO}_3$  to remove unencapsulated lucigenin. The collected liposomes were diluted with  $\text{NaNO}_3$  to give a lipid concentration of 0.4 mM. 3 mL of the liposome suspension was transferred to a quartz cuvette, along with a stirrer bar, and placed into the fluorimeter. After 30 seconds, a pulse of 25 mM NaCl in  $\text{NaNO}_3$  buffer (100  $\mu\text{L}$ ) was added to the liposomes. After 5.5 mins, the vesicles were lysed with 100  $\mu\text{L}$  polyethylene glycol *tert*-octylphenyl ether (10% in  $\text{H}_2\text{O}$ ). The data was processed using the procedures detailed in the literature.<sup>69,226</sup>

#### 6.5.5 Cationophore-coupled assay

Following extrusion, the vesicles were subjected to dialysis in the desired external solution for at least 2 hours to remove unencapsulated internal salts (KCl). Unilamellar POPC vesicles were then diluted to 2 mM using the external solution (KGlu). A transporter solution in acetonitrile (10 mol% wrt lipid) was added to the lipids. After 30 seconds, valinomycin in DMSO (0.1 mol% transporter:lipid) and the chloride efflux was monitored using a chloride-selective electrode. At 5.5 mins, the vesicles were lysed with 100  $\mu\text{L}$  polyethylene glycol *tert*-octylphenyl ether (10% in  $\text{H}_2\text{O}$ ) and a total chloride reading was taken at 7.5 mins.<sup>227</sup>

#### 6.5.6 Sodium/chloride symport experiments

Following extrusion, the vesicles were subjected to dialysis in the desired external solution for at least 2 hours to remove unencapsulated internal salts. Unilamellar POPC vesicles were then diluted to 2 mM using the external solution. A transporter solution in acetonitrile (10 mol% wrt lipid) was added to start the experiment, and the chloride efflux was monitored using a chloride-selective electrode. At 5 mins, the vesicles were lysed with 100  $\mu\text{L}$  polyethylene glycol *tert*-octylphenyl ether (10% in  $\text{H}_2\text{O}$ ) and a total chloride reading was taken at 7 mins.

## 6.6 Fluorescence studies

### 6.6.1 Fluorimeter measurements

3 mL of 20  $\mu$ M fluorophore solution (made up in 1:1 acetonitrile: aqueous solvent) was added to a quartz cuvette and placed in the fluorimeter. The aqueous solvent was either H<sub>2</sub>O or 100 mM trisaminomethane (TRIS) buffer at pH 7.4 or 9. Fluorescence intensity was measured. A 10  $\mu$ L aliquot of 20  $\mu$ M **52** solution (1:1 acetonitrile: aqueous solvent) was added, and fluorescence intensity was measured. Additional aliquots of **47** were added (either a total of 3 or 5 aliquots added). A pulse of 1 M sodium chloride or TBA benzoate (500  $\mu$ L) was added.

### 6.6.2 Plate reader measurements

(IDAs with **52** + HINA and **52** + 7ACC-1)

To each well of a black 96-well plate was added 75  $\mu$ L of 40  $\mu$ M **52** (made up in 1:1 acetonitrile: TRIS buffer at pH 7.4 or 9) and 75  $\mu$ L of 40  $\mu$ M fluorophore (made up in 1:1 acetonitrile: TRIS buffer at pH 7.4 or 9). An 800 mM solution of TBA salt (chloride, bromide, iodide, benzoate) was made up in 1:1 acetonitrile: TRIS buffer at pH 7.4 or 9 and serial dilutions were performed until 12.5 mM. 150  $\mu$ L of each serial dilution was added to the plate (3 columns per salt). Refer to Table 5.1 for further set-up details. The plate reader measurements with 7ACC-1 did not include TBA bromide.

*Table 5.1: Layout of 96-well plate for plate reader measurements. Concentration of TBA salt solution added given in each well (mM). Blue = chloride; orange = bromide; green = iodide; yellow = benzoate.*

	1	2	3	4	5	6	7	8	9	10	11	12
A	0	0	0	0	0	0	0	0	0	0	0	0
B	12.5	12.5	12.5	12.5	12.5	12.5	12.5	12.5	12.5	12.5	12.5	12.5
C	25	25	25	25	25	25	25	25	25	25	25	25
D	50	50	50	50	50	50	50	50	50	50	50	50
E	100	100	100	100	100	100	100	100	100	100	100	100
F	200	200	200	200	200	200	200	200	200	200	200	200
G	400	400	400	400	400	400	400	400	400	400	400	400
H	800	800	800	800	800	800	800	800	800	800	800	800

## 6.7 Computational calculations

All calculations were performed on the UCL NTC cluster. The lowest energy conformations of the SSAs and m-lipids were first optimised at the HF/3-21G level using Gaussian09 with a PCM solvent model for water. Then, using the same computational parameters, a range of SSA-headgroup interaction conformations were optimised. The binding energy for each SSA-headgroup conformation was then calculated using equation 4.1. The energies were obtained from the output file and converted from Hartree to kJ/mol. Cartesian coordinates for the minimised binding conformations are given in the appendix.

## 7 References

- 1 *Supramolecular Chemistry*, John Wiley & Sons, Ltd, 1st edn., 1995.
- 2 J.-M. Lehn, *Angewandte Chemie International Edition in English*, 1988, **27**, 89–112.
- 3 G. M. Cooper, in *The Cell: A Molecular Approach. 2nd edition*, Sinauer Associates, 2000.
- 4 C. J. Pedersen, *Journal of the American Chemical Society*, 1967, **89**, 7017–7036.
- 5 K. Berend, L. H. van Hulsteijn and R. O. B. Gans, *European Journal of Internal Medicine*, 2012, **23**, 203–211.
- 6 J. W. Błaszczuk, *Metabolites*, 2023, **13**, 860.
- 7 M. Bonora, S. Patergnani, A. Rimessi, E. De Marchi, J. M. Suski, A. Bononi, C. Giorgi, S. Marchi, S. Missiroli, F. Poletti, M. R. Wieckowski and P. Pinton, *Purinergic Signalling*, 2012, **8**, 343–357.
- 8 J. Li, Q. Jin, Y. Liang, J. Geng, J. Xia, H. Chen and M. Yun, *International Journal of Environmental Research and Public Health*, 2022, **19**, 1890.
- 9 S. E. Tawfeek, A. M. Shalaby, M. A. Alabiad, A.-A. A. A. Albackoosh, K. M. M. Albakoush and M. M. A. Omira, *Tissue and Cell*, 2021, **73**, 101624.
- 10 J.-B. Kim, *Korean Journal of Pediatrics*, 2014, **57**, 1–18.
- 11 J. K. Badenhoop and F. Weinhold, *The Journal of Chemical Physics*, 1997, **107**, 5422–5432.
- 12 S. C. Patrick, P. D. Beer and J. J. Davis, *Nature Reviews Chemistry*, 2024, **8**, 256–276.
- 13 X.-H. Ding, S. Wang, Y.-H. Li and W. Huang, *Inorganic Chemistry Frontiers*, 2015, **2**, 263–272.
- 14 J. W. Pflugrath and F. A. Quiocho, *Nature*, 1985, **314**, 257–260.
- 15 R. Taylor, O. Kennard and W. Versichel, *Journal of the American Chemical Society*, 1983, **105**, 5761–5766.
- 16 P. A. Wood, F. H. Allen and E. Pidcock, *CrystEngComm*, 2009, **11**, 1563–1571.
- 17 M. C. Etter, Z. Urbanczyk-Lipkowska, M. Zia-Ebrahimi and T. W. Panunto, *Journal of the American Chemical Society*, 1990, **112**, 8415–8426.
- 18 P. J. Smith, M. V. Reddington and C. S. Wilcox, *Tetrahedron Letters*, 1992, **33**, 6085–6088.
- 19 F. M. Pfeffer, A. M. Buschgens, N. W. Barnett, T. Gunnlaugsson and P. E. Kruger, *Tetrahedron Letters*, 2005, **46**, 6579–6584.
- 20 R. Prohens, S. Tomàs, J. Morey, P. M. Deyà, P. Ballester and A. Costa, *Tetrahedron Letters*, 1998, **39**, 1063–1066.
- 21 V. Amendola, G. Bergamaschi, M. Boiocchi, L. Fabbriizzi and M. Milani, *Chemistry – A European Journal*, 2010, **16**, 4368–4380.
- 22 V. Amendola, L. Fabbriizzi, L. Mosca and F.-P. Schmidtchen, *Chemistry – A European Journal*, 2011, **17**, 5972–5981.
- 23 V. Ramalingam, M. E. Domaradzki, S. Jang and R. S. Muthyala, *Organic Letters*, 2008, **10**, 3315–3318.
- 24 V. E. Zwicker, K. K. Y. Yuen, D. G. Smith, J. Ho, L. Qin, P. Turner and K. A. Jolliffe, *Chemistry – A European Journal*, 2018, **24**, 1140–1150.
- 25 D. J. Cram, *Angewandte Chemie International Edition in English*, 1986, **25**, 1039–1057.

- 26K. N. Trueblood, C. B. Knobler, E. Maverick, R. C. Helgeson, S. B. Brown and D. J. Cram, *Journal of the American Chemical Society*, 1981, **103**, 5594–5596.
- 27K. Kavallieratos, C. M. Bertao and R. H. Crabtree, *The Journal of Organic Chemistry*, 1999, **64**, 1675–1683.
- 28M. P. Hughes and B. D. Smith, *The Journal of Organic Chemistry*, 1997, **62**, 4492–4499.
- 29P. V. Santacroce, J. T. Davis, M. E. Light, P. A. Gale, J. C. Iglesias-Sánchez, P. Prados and R. Quesada, *Journal of the American Chemical Society*, 2007, **129**, 1886–1887.
- 30S. J. Coles, J. G. Frey, P. A. Gale, M. B. Hursthouse, M. E. Light, K. Navakhun and G. L. Thomas, *Chemical Communications*, 2003, 568–569.
- 31G. Picci, I. Carreira-Barral, D. Alonso-Carrillo, D. Sanz-González, P. Fernández-López, M. García-Valverde, C. Caltagirone and R. Quesada, *Supramolecular Chemistry*, 2020, **32**, 112–118.
- 32C. R. Yamnitz, S. Negin, I. A. Carasel, R. K. Winter and G. W. Gokel, *Chemical Communications*, 2010, **46**, 2838–2840.
- 33J. O. Wieth, O. S. Andersen, J. Brahm, P. J. Bjerrum, C. L. Borders, R. D. Keynes and J. C. Ellory, *Philosophical Transactions of the Royal Society of London. B, Biological Sciences*, 1997, **299**, 383–399.
- 34S. Valiyaveetil, J. F. J. Engbersen, W. Verboom and D. N. Reinhoudt, *Angewandte Chemie International Edition in English*, 1993, **32**, 900–901.
- 35Md. A. Hossain, J. A. Liljegren, D. Powell and K. Bowman-James, *Inorganic Chemistry*, 2004, **43**, 3751–3755.
- 36S. Saha, B. Akhuli, I. Ravikumar, P. S. Lakshminarayanan and P. Ghosh, *CrystEngComm*, 2014, **16**, 4796.
- 37K. Ghosh, D. Tarafdar, A. Samadder and A. R. Khuda-Bukhsh, *RSC Advances*, 2015, **5**, 35175–35180.
- 38R. Custelcean, B. A. Moyer and B. P. Hay, *Chemical Communications*, 2005, 5971–5973.
- 39R. Custelcean, P. Remy, P. V. Bonnesen, D. Jiang and B. A. Moyer, *Angewandte Chemie International Edition*, 2008, **47**, 1866–1870.
- 40M. Emami Khansari, A. Mirchi, A. Pramanik, C. R. Johnson, J. Leszczynski and Md. A. Hossain, *Scientific Reports*, 2017, **7**, 6032.
- 41K. J. Winstanley, S. J. Allen and D. K. Smith, *Chemical Communications*, 2009, 4299–4301.
- 42N. Busschaert, P. A. Gale, C. J. E. Haynes, M. E. Light, S. J. Moore, C. C. Tong, J. T. Davis and J. William A. Harrell, *Chemical Communications*, 2010, **46**, 6252–6254.
- 43N. Busschaert, M. Wenzel, M. E. Light, P. Iglesias-Hernández, R. Pérez-Tomás and P. A. Gale, *Journal of the American Chemical Society*, 2011, **133**, 14136–14148.
- 44N. J. Yang and M. J. Hinner, *Methods in molecular biology (Clifton, N.J.)*, 2015, **1266**, 29–53.
- 45M. G. Wolfersberger, *Journal of Experimental Biology*, 1994, **196**, 5–6.
- 46T.-C. Hwang and K. L. Kirk, *Cold Spring Harbor Perspectives in Medicine*, 2013, **3**, a009498.
- 47D. T. Clar and C. V. Maani, *Physiology, Ligand Gated Chloride Channel*, StatPearls Publishing, 2024.

- 48 J. A. Payne, in *Current Topics in Membranes*, ed. M. O. Bevensee, Academic Press, 2012, vol. 70, pp. 215–237.
- 49 V. I. Volkov, A. V. Chernyak, N. A. Slesarenko and I. A. Avilova, *International Journal of Molecular Sciences*, 2022, **23**, 5011.
- 50 A. P. Davis, D. N. Sheppard and B. D. Smith, *Chem Soc Rev*, 2007, **36**, 348–357.
- 51 H. Nsairat, D. Khater, U. Sayed, F. Odeh, A. Al Bawab and W. Alshaer, *Heliyon*, 2022, **8**, e09394.
- 52 S. G. M. Ong, L. C. Ming, K. S. Lee and K. H. Yuen, *Pharmaceutics*, 2016, **8**, 25.
- 53 N. Kumar and G. N. Sastry, *Journal of Molecular Graphics and Modelling*, 2021, **108**, 108000.
- 54 E. D. N. S. Abeyrathne, K.-C. Nam, X. Huang and D. U. Ahn, *Food Science and Biotechnology*, 2022, **31**, 1243–1256.
- 55 R. Sousa, A. Oliveira de Moraes Nogueira, V. Marques, R. Clementin and V. Lima, *Bioorganic chemistry*, 2013, **51C**, 8–15.
- 56 D. Drabik, G. Chodaczek, S. Kraszewski and M. Langner, *Langmuir*, 2020, **36**, 3826–3835.
- 57 S. J. Attwood, Y. Choi and Z. Leonenko, *International Journal of Molecular Sciences*, 2013, **14**, 3514–3539.
- 58 C.-P. Chng, K. Jimmy Hsia and C. Huang, *Soft Matter*, 2022, **18**, 7752–7761.
- 59 N. Busschaert, L. E. Karagiannidis, M. Wenzel, C. J. E. Haynes, N. J. Wells, P. G. Young, D. Makuc, J. Plavec, K. A. Jolliffe and P. A. Gale, *Chemical Science*, 2014, **5**, 1118–1127.
- 60 L. Martínez-Crespo and H. Valkenier, *Chempluschem*, 2022, **87**, e202200266.
- 61 J. T. Davis, P. A. Gale, O. A. Okunola, P. Prados, J. C. Iglesias-Sánchez, T. Torroba and R. Quesada, *Nature Chemistry*, 2009, **1**, 138–144.
- 62 A. V. Koulov, T. N. Lambert, R. Shukla, M. Jain, J. M. Boon, B. D. Smith, H. Li, D. N. Sheppard, J.-B. Joos, J. P. Clare and A. P. Davis, *Angewandte Chemie International Edition*, 2003, **42**, 4931–4933.
- 63 S. a. D. N. Dias, S. Divyasarubini, K. T. J. Gamage, R. M. Dalath, M. S. S. Weerasinghe and G. N. Silva, *The Journal of Antibiotics*, 2023, **76**, 425–429.
- 64 M. Vée, E. Jouan and O. Fardel, *Naunyn-Schmiedeberg's Archives of Pharmacology*, 2018, **391**, 361–369.
- 65 S. J. Wezenberg, L.-J. Chen, J. E. Bos, B. L. Feringa, E. N. W. Howe, X. Wu, M. A. Siegler and P. A. Gale, *Journal of the American Chemical Society*, 2022, **144**, 331–338.
- 66 G. A. Woolley, M. K. Kapral and C. M. Deber, *FEBS Letters*, 1987, **224**, 337–342.
- 67 Y. Yang, X. Wu, N. Busschaert, H. Furuta and P. A. Gale, *Chemical Communications*, 2017, **53**, 9230–9233.
- 68 X. Wu and P. A. Gale, *Chemical Communications*, 2021, **57**, 3979–3982.
- 69 M. Chvojka, A. Singh, A. Cataldo, A. Torres-Huerta, M. Konopka, V. Šindelář and H. Valkenier, *Analysis & Sensing*, 2024, **4**, e202300044.
- 70 L. E. Karagiannidis, C. J. E. Haynes, K. J. Holder, I. L. Kirby, S. J. Moore, N. J. Wells and P. A. Gale, *Chemical Communications*, 2014, **50**, 12050–12053.
- 71 H. Valkenier, L. W. Judd, H. Li, S. Hussain, D. N. Sheppard and A. P. Davis, *Journal of the American Chemical Society*, 2014, **136**, 12507–12512.
- 72 K. Bowman-James, *Accounts of Chemical Research*, 2005, **38**, 671–678.

- 73 T. R. Cook, Y.-R. Zheng and P. J. Stang, *Chemical Reviews*, 2013, **113**, 734–777.
- 74 B. S. Pilgrim and N. R. Champness, *ChemPlusChem*, 2020, **85**, 1842–1856.
- 75 S. S. A. Shah, M. Sohail, G. Murtza, A. Waseem, A. Rehman, I. Hussain, M. S. Bashir, S. S. Alarfaji, A. M. Hassan, M. A. Nazir, M. S. Javed and T. Najam, *Chemosphere*, 2024, **349**, 140729.
- 76 Y. Yao, C. Wang, J. Na, M. S. A. Hossain, X. Yan, H. Zhang, M. A. Amin, J. Qi, Y. Yamauchi and J. Li, *Small*, 2022, **18**, 2104387.
- 77 J. M. Gold and A. Raja, *Cisplatin*, StatPearls Publishing, 2024.
- 78 T. R. Cook, V. Vajpayee, M. H. Lee, P. J. Stang and K.-W. Chi, *Accounts of Chemical Research*, 2013, **46**, 2464–2474.
- 79 V. Kumar Singh, V. Kumar Singh, A. Mishra, Varsha, A. Abha Singh, G. Prasad and A. Kumar Singh, *Polyhedron*, 2023, **241**, 116485.
- 80 S. Yadav, S. Prasad Sonkar, K. Singh Tiwari and M. Shukla, *Results in Chemistry*, 2024, **10**, 101743.
- 81 R. J. Ouellette and J. D. Rawn, in *Organic Chemistry (Second Edition)*, Academic Press, 2018, pp. 929–971.
- 82 D. Philp and J. F. Stoddart, *Angewandte Chemie International Edition in English*, 1996, **35**, 1154–1196.
- 83 W. Zhang, J. Zhao and D. Yang, *ChemPlusChem*, 2022, **87**, e202200294.
- 84 B. P. Isaacoff and K. A. Brown, *Nano Letters*, 2017, **17**, 6508–6510.
- 85 T. R. Cook and P. J. Stang, *Chemical Reviews*, 2015, **115**, 7001–7045.
- 86 C. Zhang, T. Jiao, L. Tong, H. Wang, Y. Pan and H. Li, *Chemical Communications*, 2020, **56**, 3903–3906.
- 87 J. C. Bailar, *The Chemistry of the Coordination Compounds*, Reinhold Publishing Corporation, 1956.
- 88 A. Casini, B. Woods and M. Wenzel, *Inorganic Chemistry*, 2017, **56**, 14715–14729.
- 89 N. Dey and C. J. E. Haynes, *ChemPlusChem*, 2021, **86**, 418–433.
- 90 Z. Chen, Z. Tao, Y. Tan, Y. Zhu, A. Wang, S. Lai and Y. Yang, *Energy & Fuels*, 2023, **37**, 5508–5518.
- 91 D. H. Busch, *Accounts of Chemical Research*, 1978, **11**, 392–400.
- 92 J. Hamblin, L. J. Childs, N. W. Alcock and M. J. Hannon, *Journal of the Chemical Society, Dalton Transactions*, 2002, 164–169.
- 93 J. R. Nitschke, *Accounts of Chemical Research*, 2007, **40**, 103–112.
- 94 D. Schultz and J. R. Nitschke, *Proceedings of the National Academy of Sciences*, 2005, **102**, 11191–11195.
- 95 P. Mal, D. Schultz, K. Beyeh, K. Rissanen and J. R. Nitschke, *Angewandte Chemie International Edition*, 2008, **47**, 8297–8301.
- 96 E. G. Percástegui, J. Mosquera, T. K. Ronson, A. J. Plajer, M. Kieffer and J. R. Nitschke, *Chemical Science*, 2019, **10**, 2006–2018.
- 97 D. A. Roberts, B. S. Pilgrim, J. D. Cooper, T. K. Ronson, S. Zarra and J. R. Nitschke, *Journal of the American Chemical Society*, 2015, **137**, 10068–10071.
- 98 E. G. Percástegui, J. Mosquera and J. R. Nitschke, *Angewandte Chemie International Edition*, 2017, **56**, 9136–9140.
- 99 M. E. Belowich and J. F. Stoddart, *Chemical Society Reviews*, 2012, **41**, 2003–2024.

- 100 C. D. Meyer, C. Steven Joiner and J. Fraser Stoddart, *Chemical Society Reviews*, 2007, **36**, 1705–1723.
- 101 L. Hogg, D. A. Leigh, P. J. Lusby, A. Morelli, S. Parsons and J. K. Y. Wong, *Angewandte Chemie International Edition*, 2004, **43**, 1218–1221.
- 102 J.-F. Ayme, J. E. Beves, D. A. Leigh, R. T. McBurney, K. Rissanen and D. Schultz, *Nature Chemistry*, 2012, **4**, 15–20.
- 103 J. Liu, Z. Wang, P. Cheng, M. J. Zaworotko, Y. Chen and Z. Zhang, *Nature Reviews Chemistry*, 2022, **6**, 339–356.
- 104 D. Luo, X.-W. Zhu, X.-P. Zhou and D. Li, *Chemistry – A European Journal*, 2024, **30**, e202400020.
- 105 D. A. Roberts, B. S. Pilgrim and J. R. Nitschke, *Chemical Society Reviews*, 2018, **47**, 626–644.
- 106 E. Krieg, M. M. C. Bastings, P. Besenius and B. Rybtchinski, *Chemical Reviews*, 2016, **116**, 2414–2477.
- 107 A. B. Grommet, J. B. Hoffman, E. G. Percástegui, J. Mosquera, D. J. Howe, J. L. Bolliger and J. R. Nitschke, *Journal of the American Chemical Society*, 2018, **140**, 14770–14776.
- 108 L. H. Uppadine, M. G. B. Drew and P. D. Beer, *Chemical Communications*, 2001, 291–292.
- 109 C. Caltagirone, A. Mulas, F. Isaia, V. Lippolis, P. A. Gale and M. E. Light, *Chemical Communications*, 2009, 6279–6281.
- 110 K. Yang, H. A. Kotak and C. J. E. Haynes, *Coordination Chemistry Reviews*, 2022, **470**, 214705.
- 111 D. Milano, B. Benedetti, M. Boccalon, A. Brugnara, E. Iengo and P. Tecilla, *Chemical Communications*, 2014, **50**, 9157–9160.
- 112 L.-J. Chen, X. Wu, A. M. Gilchrist and P. A. Gale, *Angewandte Chemie International Edition*, 2022, **61**, e202116355.
- 113 P. Wang, M. Fares, R. A. Eladwy, D. J. Bhuyan, X. Wu, W. Lewis, S. J. Loeb, L. K. Macreadie and P. A. Gale, *Chemical Science*, 2024, **15**, 11584–11593.
- 114 A. J. Plajer, J. Zhu, P. Pröhm, F. J. Rizzuto, U. F. Keyser and D. S. Wright, *Journal of the American Chemical Society*, 2020, **142**, 1029–1037.
- 115 M.-H. Chen, Y. Zheng, X.-J. Cai, H. Zhang, F.-X. Wang, C.-P. Tan, W.-H. Chen, L.-N. Ji and Z.-W. Mao, *Chemical Science*, 2019, **10**, 3315–3323.
- 116 M. Fares, X. Wu, D. Ramesh, W. Lewis, P. A. Keller, E. N. W. Howe, R. Pérez-Tomás and P. A. Gale, *Angewandte Chemie International Edition*, 2020, **59**, 17614–17621.
- 117 R. Martínez-Máñez, *ChemistryOpen*, 2014, **3**, 232–232.
- 118 D. Wu, A. C. Sedgwick, T. Gunnlaugsson, E. U. Akkaya, J. Yoon and T. D. James, *Chemical Society Reviews*, 2017, **46**, 7105–7123.
- 119 P. A. Gale and C. Caltagirone, *Coordination Chemistry Reviews*, 2018, **354**, 2–27.
- 120 A. C. Sedgwick, J. T. Brewster, T. Wu, X. Feng, S. D. Bull, X. Qian, J. L. Sessler, T. D. James, E. V. Anslyn and X. Sun, *Chemical Society Reviews*, 2021, **50**, 9–38.
- 121 N. Busschaert, C. Caltagirone, W. V. Rossom and P. A. Gale, *Chemical Reviews*, 2015, **115**, 8038–8155.



- 122 L. D. Adair, K. Yang and E. J. New, in *Molecular Fluorescent Sensors for Cellular Studies*, John Wiley & Sons, Ltd, 2022, pp. 1–35.
- 123 P. K. Samanta and R. Misra, *Journal of Applied Physics*, 2023, **133**, 020901.
- 124 C. Shen, J. L. Kolanowski, C. M.-N. Tran, A. Kaur, M. C. Akerfeldt, M. S. Rahme, T. W. Hambley and E. J. New, *Metallomics*, 2016, **8**, 915–919.
- 125 G. Cox, *Materials Today*, 2002, **5**, 34–41.
- 126 A. Murata, Y. Harada, T. Fukuzumi and K. Nakatani, *Bioorganic & Medicinal Chemistry*, 2013, **21**, 7101–7106.
- 127 L. Fabbrizzi, A. Leone and A. Taglietti, *Angewandte Chemie International Edition*, 2001, **40**, 3066–3069.
- 128 K. Severin, *Current Opinion in Chemical Biology*, 2010, **14**, 737–742.
- 129 R. Dortwegt and E. V. Maughan, in *PACS2001. Proceedings of the 2001 Particle Accelerator Conference (Cat. No.01CH37268)*, IEEE, Chicago, IL, USA, 2001, vol. 2, pp. 1456–1458.
- 130 M. Boiocchi, M. Bonizzoni, L. Fabbrizzi, G. Piovani and A. Taglietti, *Angewandte Chemie International Edition*, 2004, **43**, 3847–3852.
- 131 T. Zhang and E. V. Anslyn, *Tetrahedron*, 2004, **60**, 11117–11124.
- 132 M. S. Han and D. H. Kim, *Angewandte Chemie International Edition*, 2002, **41**, 3809–3811.
- 133 X. Liu, H. Tien Ngo, Z. Ge, S. J. Butler and K. A. Jolliffe, *Chemical Science*, 2013, **4**, 1680–1686.
- 134 K. A. Jolliffe, *Accounts of Chemical Research*, 2017, **50**, 2254–2263.
- 135 X. Liu, D. G. Smith and K. A. Jolliffe, *Chem. Commun.*, 2016, **52**, 8463–8466.
- 136 S. A. Hilderbrand, M. H. Lim and S. J. Lippard, *Journal of the American Chemical Society*, 2004, **126**, 4972–4978.
- 137 A. Buryak and K. Severin, *Angewandte Chemie International Edition*, 2004, **43**, 4771–4774.
- 138 Ü. N. Çolak, E. Yılmaz, S. Durmazel, K. Can, A. Üzer and R. Apak, *Journal of Pharmaceutical and Biomedical Analysis*, 2024, **248**, 116323.
- 139 Y. Takahashi, D. A. P. Tanaka, H. Matsunaga and T. M. Suzuki, *Journal of the Chemical Society, Perkin Transactions 2*, 2002, 759–762.
- 140 M. D. Ludden and M. D. Ward, *Dalton Transactions*, 2021, **50**, 2782–2791.
- 141 S. Turega, W. Cullen, M. Whitehead, C. A. Hunter and M. D. Ward, *Journal of the American Chemical Society*, 2014, **136**, 8475–8483.
- 142 A. Rostami, A. Colin, X. Y. Li, M. G. Chudzinski, A. J. Lough and M. S. Taylor, *The Journal of Organic Chemistry*, 2010, **75**, 3983–3992.
- 143 X. Bao, X. Wu, S. N. Berry, E. N. W. Howe, Y.-T. Chang and P. A. Gale, *Chemical Communications*, 2018, **54**, 1363–1366.
- 144 C. Schouwey, M. Papmeyer, R. Scopelliti and K. Severin, *Dalton Transactions*, 2015, **44**, 2252–2258.
- 145 H. C. Kolb, M. G. Finn and K. B. Sharpless, *Angewandte Chemie International Edition*, 2001, **40**, 2004–2021.
- 146 J. Héron and D. Balcells, *ACS Catalysis*, 2022, **12**, 4744–4753.

- 147 C. Tang, Y. Du, Q. Liang, Z. Cheng and J. Tian, *Molecular Pharmaceutics*, 2018, **15**, 4702–4709.
- 148 3-Azidopropylamine 95.0+%, TCI America, Quantity: 100 mg | Fisher Scientific, <https://www.fishersci.com/shop/products/3-azidopropylamine-tci-america/A2738100MG>, (accessed 30 August 2024).
- 149 Y. Deng, *Water Research*, 1997, **31**, 1347–1354.
- 150 K. H. Kucharzyk, R. L. Crawford, B. Cosens and T. F. Hess, *Journal of Environmental Management*, 2009, **91**, 303–310.
- 151 D. Yang, L. K. S. von Krbek, L. Yu, T. K. Ronson, J. D. Thoburn, J. P. Carpenter, J. L. Greenfield, D. J. Howe, B. Wu and J. R. Nitschke, *Angewandte Chemie International Edition*, 2021, **60**, 4485–4490.
- 152 D. B. Hibbert and P. Thordarson, *Chemical Communications*, 2016, **52**, 12792–12805.
- 153 Fluorescein (FITC) - UK, <https://www.thermofisher.com/uk/en/home/life-science/cell-analysis/fluorophores/fluorescein.html>, (accessed 1 September 2024).
- 154 Spectrum [Calcein Green] | AAT Bioquest, [https://www.aatbio.com/fluorescence-excitation-emission-spectrum-graph-viewer/calcein\\_green?srsId=AfmBOoohigWHVAR8TzUYDr3My8liDUarbKLuYQVvBPGqBxP\\_t7kFvZF](https://www.aatbio.com/fluorescence-excitation-emission-spectrum-graph-viewer/calcein_green?srsId=AfmBOoohigWHVAR8TzUYDr3My8liDUarbKLuYQVvBPGqBxP_t7kFvZF), (accessed 1 September 2024).
- 155 Spectrum [HPTS] | AAT Bioquest, <https://www.aatbio.com/fluorescence-excitation-emission-spectrum-graph-viewer/hpts?srsId=AfmBOoocUDwMugTUo2hy8g645QGqbRrAHHcmsi-v01CVGeIkyJi6RXvq>, (accessed 1 September 2024).
- 156 R. Kang, L. Talamini, E. D’Este, B. M. Estevão, L. D. Cola, W. Kloppe and F. Biedermann, *Chemical Science*, 2021, **12**, 1392–1397.
- 157 7-(Diethylamino)coumarin-3-carboxylic acid BioReagent, fluorescence, = 98.0 HPCE 50995-74-9, <http://www.sigmaaldrich.com/>, (accessed 1 September 2024).
- 158 D. A. Kendall and R. C. MacDonald, *The Journal of Biological Chemistry*, 1982, **257**, 13892–13895.
- 159 J. Tröger, *Ueber einige mittelst nascirenden Formaldehydes entstehende Basen*, Dr. v. Metzger & Wittig, 1887.
- 160 Ö. V. Rúnarsson, J. Artacho and K. Wärnmark, *European Journal of Organic Chemistry*, 2012, **2012**, 7015–7041.
- 161 V. Prelog and P. Wieland, *Helvetica Chimica Acta*, 1944, **27**, 1127–1134.
- 162 S. Goswami and K. Ghosh, *Tetrahedron Letters*, 1997, **38**, 4503–4506.
- 163 M. Harmata and T. Murray, *The Journal of Organic Chemistry*, 1989, **54**, 3761–3763.
- 164 M. Harmata, *Accounts of Chemical Research*, 2004, **37**, 862–873.
- 165 M. Harmata, M. Kahraman, S. Tyagarajan, C. L. Barnes and C. J. Welch, in *Molecular Recognition and Inclusion*, ed. A. W. Coleman, Springer Netherlands, Dordrecht, 1998, pp. 109–116.
- 166 A. V. Lynch, T. J. Blundell and J. W. Steed, *Crystal Growth & Design*, 2024, **24**, 7271–7277.
- 167 A. Jozeliūnaitė, T. Javorskis, V. Vaitkevičius, V. Klimavičius and E. Orentas, *J. Am. Chem. Soc.*, 2022, **144**, 8231–8241.

- 168 Z. Wang, H. Ai, A. Hao and P. Xing, *Chemistry of Materials*, 2022, **34**, 10162–10171.
- 169 C. He, B. Wang, M. Gao and Z. Gu, *Organometallics*, 2017, **36**, 1073–1078.
- 170 B. Mohan, A. Shanmughan, M. K. Noushija, D. Sarkar, P. Patel and S. Shanmugaraju, *Tetrahedron Chem*, 2024, **9**, 100071.
- 171 I. Ahmed, A. Majeed and R. Powell, *Postgraduate Medical Journal*, 2007, **83**, 575–582.
- 172 S. E. Howson, L. E. N. Allan, N. P. Chmel, G. J. Clarkson, R. van Gorkum and P. Scott, *Chem. Commun.*, 2009, 1727–1729.
- 173 A. M. Castilla, M. A. Miller, J. R. Nitschke and M. M. J. Smulders, *Angewandte Chemie International Edition*, 2016, **55**, 10616–10620.
- 174 W. Xue, T. K. Ronson, Z. Lu and J. R. Nitschke, *Journal of the American Chemical Society*, 2022, **144**, 6136–6142.
- 175 W. Xue, L. Pesce, A. Bellamkonda, T. K. Ronson, K. Wu, D. Zhang, N. Vanthuyne, T. Brotin, A. Martinez, G. M. Pavan and J. R. Nitschke, *Journal of the American Chemical Society*, 2023, **145**, 5570–5577.
- 176 G. Li, T. K. Ronson, R. Lavendomme, Z. Huang, C. Fuertes-Espinosa, D. Zhang and J. R. Nitschke, *Chem*, 2023, **9**, 1549–1561.
- 177 F. Lake and C. Moberg, *European Journal of Organic Chemistry*, 2002, **2002**, 3179–3188.
- 178 Y. Pei, K. Brade, E. Brulé, L. Hagberg, F. Lake and C. Moberg, *European Journal of Organic Chemistry*, 2005, **2005**, 2835–2840.
- 179 M. Cernerud, H. Adolfsson and C. Moberg, *Tetrahedron: Asymmetry*, 1997, **8**, 2655–2662.
- 180 S. Hajela, M. Botta, S. Giraudo, J. Xu, K. N. Raymond and S. Aime, *Journal of the American Chemical Society*, 2000, **122**, 11228–11229.
- 181 J. G. Verkade, *Accounts of Chemical Research*, 1993, **26**, 483–489.
- 182 J. G. Verkade and P. B. Kisanga, *Tetrahedron*, 2003, **59**, 7819–7858.
- 183 X. Liu, P. Ilankumaran, I. A. Guzei and J. G. Verkade, *The Journal of Organic Chemistry*, 2000, **65**, 701–706.
- 184 J. You, A. E. Wróblewski and J. G. Verkade, *Tetrahedron*, 2004, **60**, 7877–7883.
- 185 S. P. Hajela, A. R. Johnson, J. Xu, C. J. Sunderland, S. M. Cohen, D. L. Caulder and K. N. Raymond, *Inorganic Chemistry*, 2001, **40**, 3208–3216.
- 186 W. Ye, D. Leow, S. L. M. Goh, C.-T. Tan, C.-H. Chian and C.-H. Tan, *Tetrahedron Letters*, 2006, **47**, 1007–1010.
- 187 T. W. Greene and P. G. M. Wuts, in *Protective Groups in Organic Synthesis*, John Wiley & Sons, Ltd, 1999, pp. 494–653.
- 188 V. Coeffard, C. Thobie-Gautier, I. Beaudet, E. Le Grogneec and J.-P. Quintard, *European Journal of Organic Chemistry*, 2008, **2008**, 383–391.
- 189 T. Paschelke, E. Trumpf, D. Grantz, M. Pankau, N. Grocholski, C. Näther, F. D. Sönnichsen and A. J. McConnell, *Dalton Transactions*, 2023, **52**, 12789–12795.
- 190 J. R. Hiscock, G. P. Bustone, B. Wilson, K. E. Belsey and L. R. Blackholly, *Soft Matter*, 2016, **12**, 4221–4228.

- 191 L. R. Blackholly, H. J. Shepherd and J. R. Hiscock, *CrystEngComm*, 2016, **18**, 7021–7028.
- 192 L. J. White, J. E. Boles, N. Allen, L. S. Alesbrook, J. M. Sutton, C. K. Hind, K. L. F. Hilton, L. R. Blackholly, R. J. Ellaby, G. T. Williams, D. P. Mulvihill and J. R. Hiscock, *Journal of Materials Chemistry B*, 2020, **8**, 4694–4700.
- 193 K. K. L. Ng, R. Devlia, N. L. Foss, L. S. Alesbrook, J. R. Hiscock and A. T. Murray, *Chemical Communications*, 2020, **56**, 11815–11818.
- 194 N. O. Dora, E. Blackburn, J. E. Boles, G. T. Williams, L. J. White, S. E. G. Turner, J. D. Hothersall, T. Askwith, J. A. Doolan, D. P. Mulvihill, M. D. Garrett and J. R. Hiscock, *RSC Advances*, 2021, **11**, 14213–14217.
- 195 K. Yang, J. E. Boles, L. J. White, K. L. F. Hilton, H. Y. Lai, Y. Long, J. R. Hiscock and C. J. E. Haynes, *RSC Advances*, 2022, **12**, 27877–27880.
- 196 S. N. Tyuleva, N. Allen, L. J. White, A. Pépés, H. J. Shepherd, P. J. Saines, R. J. Ellaby, D. P. Mulvihill and J. R. Hiscock, *Chemical Communications*, 2019, **55**, 95–98.
- 197 J. E. Boles, R. J. Ellaby, H. J. Shepherd and J. R. Hiscock, *RSC Advances*, 2021, **11**, 9550–9556.
- 198 N. Allen, L. J. White, J. E. Boles, G. T. Williams, D. F. Chu, R. J. Ellaby, H. J. Shepherd, K. K. L. Ng, L. R. Blackholly, B. Wilson, D. P. Mulvihill and J. R. Hiscock, *ChemMedChem*, 2020, **15**, 2193–2205.
- 199 L. J. White, J. E. Boles, M. Clifford, B. L. Patenall, K. H. L. F. Hilton, K. K. L. Ng, R. J. Ellaby, C. K. Hind, D. P. Mulvihill and J. R. Hiscock, *Chemical Communications*, 2021, **57**, 11839–11842.
- 200 A. Rutkauskaitė, L. J. White, J. E. Boles, K. L. F. Hilton, M. Clifford, B. Patenall, B. R. Streather, D. P. Mulvihill, S. A. Henry, M. Shepherd, J. M. Sutton, C. K. Hind and J. R. Hiscock, *Supramolecular Chemistry*, 2021, **33**, 677–686.
- 201 B. Alberts, A. Johnson, J. Lewis, M. Raff, K. Roberts and P. Walter, in *Molecular Biology of the Cell. 4th edition*, Garland Science, 2002.
- 202 S. Cockcroft, *Essays in Biochemistry*, 2021, **65**, 813–845.
- 203 G. Townshend, G. S. Thompson, L. J. White, J. R. Hiscock and J. L. Ortega-Roldan, *Chemical Communications*, 2020, **56**, 4015–4018.
- 204 E. G. Lewars, in *Computational Chemistry: Introduction to the Theory and Applications of Molecular and Quantum Mechanics*, ed. E. G. Lewars, Springer Netherlands, Dordrecht, 2011, pp. 445–519.
- 205 E. G. Lewars, in *Computational Chemistry: Introduction to the Theory and Applications of Molecular and Quantum Mechanics*, ed. E. G. Lewars, Springer Netherlands, Dordrecht, 2011, pp. 175–390.
- 206 P. R. Rablen, J. W. Lockman and W. L. Jorgensen, *The Journal of Physical Chemistry A*, 1998, **102**, 3782–3797.
- 207 J. Ireta, J. Neugebauer and M. Scheffler, *The Journal of Physical Chemistry A*, 2004, **108**, 5692–5698.
- 208 M. Walker, A. J. A. Harvey, A. Sen and C. E. H. Dessent, *The Journal of Physical Chemistry A*, 2013, **117**, 12590–12600.

- 209 E. G. Lewars, in *Computational Chemistry: Introduction to the Theory and Applications of Molecular and Quantum Mechanics*, ed. E. G. Lewars, Springer Netherlands, Dordrecht, 2011, pp. 1–7.
- 210 Basis Sets, <https://gaussian.com/basissets/>.
- 211 A. V. Marenich, C. J. Cramer and D. G. Truhlar, *The Journal of Physical Chemistry B*, 2009, **113**, 6378–6396.
- 212 T. Steiner, *Angewandte Chemie International Edition*, 2002, **41**, 48–76.
- 213 G. A. Jeffrey, *An Introduction to Hydrogen Bonding*, Oxford University Press, 1997.
- 214 J. E. Boles, C. Bennett, J. Baker, K. L. F. Hilton, H. A. Kotak, E. R. Clark, Y. Long, L. J. White, H. Y. Lai, C. K. Hind, J. M. Sutton, M. D. Garrett, A. Cheasty, J. L. Ortega-Roldan, M. Charles, C. J. E. Haynes and J. R. Hiscock, *Chemical Science*, 2022, **13**, 9761–9773.
- 215 I. Marques, A. R. Colaço, P. J. Costa, N. Busschaert, P. A. Gale and V. Félix, *Soft Matter*, 2014, **10**, 3608–3621.
- 216 X. Niu, J. Zhang, Z. Wang, H. Bu and G. Xie, *Microchemical Journal*, 2025, **212**, 113219.
- 217 J. E. L. Payong, N. G. Léonard, L. M. Anderson-Sanchez, J. W. Ziller and J. Y. Yang, *Dalton Trans.*, 2025, **54**, 934–941.
- 218 H. J. F. Steyn, L. J. White, K. L. F. Hilton, J. R. Hiscock and C. H. Pohl, *ACS Omega*, 2024, **9**, 1770–1785.
- 219 R. Fourie, R. Ells, C. W. Swart, O. M. Sebolai, J. Albertyn and C. H. Pohl, *Front Physiol*, 2016, **7**, 64.
- 220 K. Hilton, H. Steyn, K. Luthuli, M. Rice, B. Streather, E. Sweeney, L. White, F. Morgan, J. Rankin, J. Baker, C. Bennett, H. Wilson, P. Hailey, M. Garrett, J. Ortega-Roldan, J. M. Sutton, C. Hind, C. Pohl and J. Hiscock, *ChemRxiv*, 2025, preprint, DOI: 10.26434/chemrxiv-2025-8b8xn.
- 221 P. Popoola, T. Allam, R. Lilley, C. Manwani, O. Keers, J. Tan, K. Yang, Y. Long, L. White, K. Hilton, J. Rankin, J. Baker, C. Bennett, H. Wilson, E. Morton, A. Keskkula, J. M. Sutton, C. Hind, M. Garrett, C. Haynes and J. Hiscock, *ChemRxiv*, 2025, preprint, DOI: 10.26434/chemrxiv-2025-bjgl9.
- 222 L. E. Brennan, X. Luo, F. Ali Mohammed, K. Kavanagh and R. B. P. Elmes, *Chem. Sci.*, 2025, **16**, 4075–4084.
- 223 W. G. Ryder, A. Levina, M. E. Graziotto, B. A. Hawkins, D. E. Hibbs, E. J. New and P. A. Gale, *Chem*, 2025, **11**, 102247.
- 224 H. Yang, L. Chen, Z. Jiang, L. Li, J. Hu and W.-H. Chen, *Eur. J. Med. Chem.*, 2025, **290**, 117519.
- 225 R. L. Spicer, C. C. Shearman and N. H. Evans, *Chemistry – A European Journal*, 2023, **29**, e202203502.
- 226 H. Li, H. Valkenier, A. G. Thorne, C. M. Dias, J. A. Cooper, M. Kieffer, N. Busschaert, P. A. Gale, D. N. Sheppard and A. P. Davis, *Chemical Science*, 2019, **10**, 9663–9672.
- 227 W. G. Ryder, E. G. Wu, L. Chen, M. Fares, D. A. McNaughton, K. Tran, C. Yu and P. A. Gale, *Organic Chemistry Frontiers*, 2024, **11**, 1290–1298.

## Appendix

### A1 Chapter 2 data

#### A1.1 $^1\text{H}$ NMR

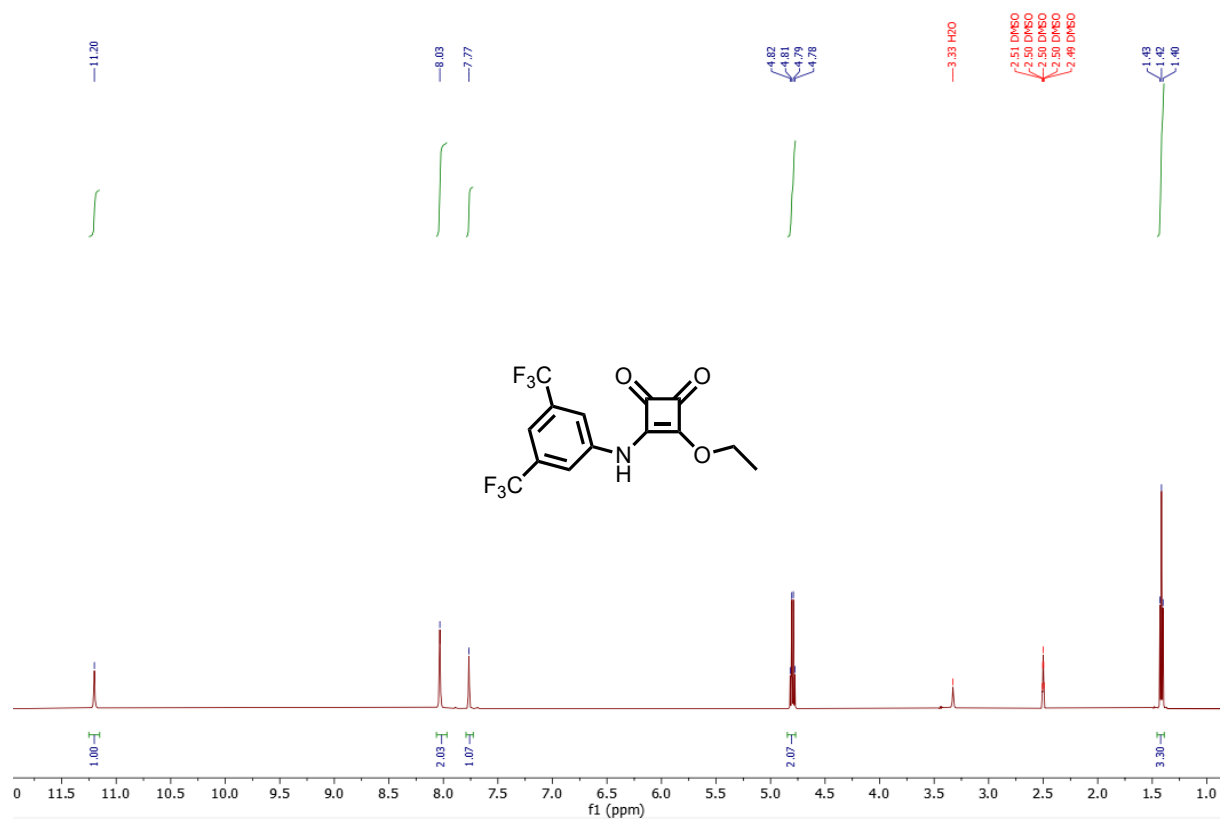


Figure A1.1:  $^1\text{H}$  NMR spectrum of 3-((3,5-bis(trifluoromethyl)phenyl)amino)-4-ethoxycyclobut-3-ene-1,2-dione (**42**) (500 MHz,  $\text{DMSO}-d_6$ ).

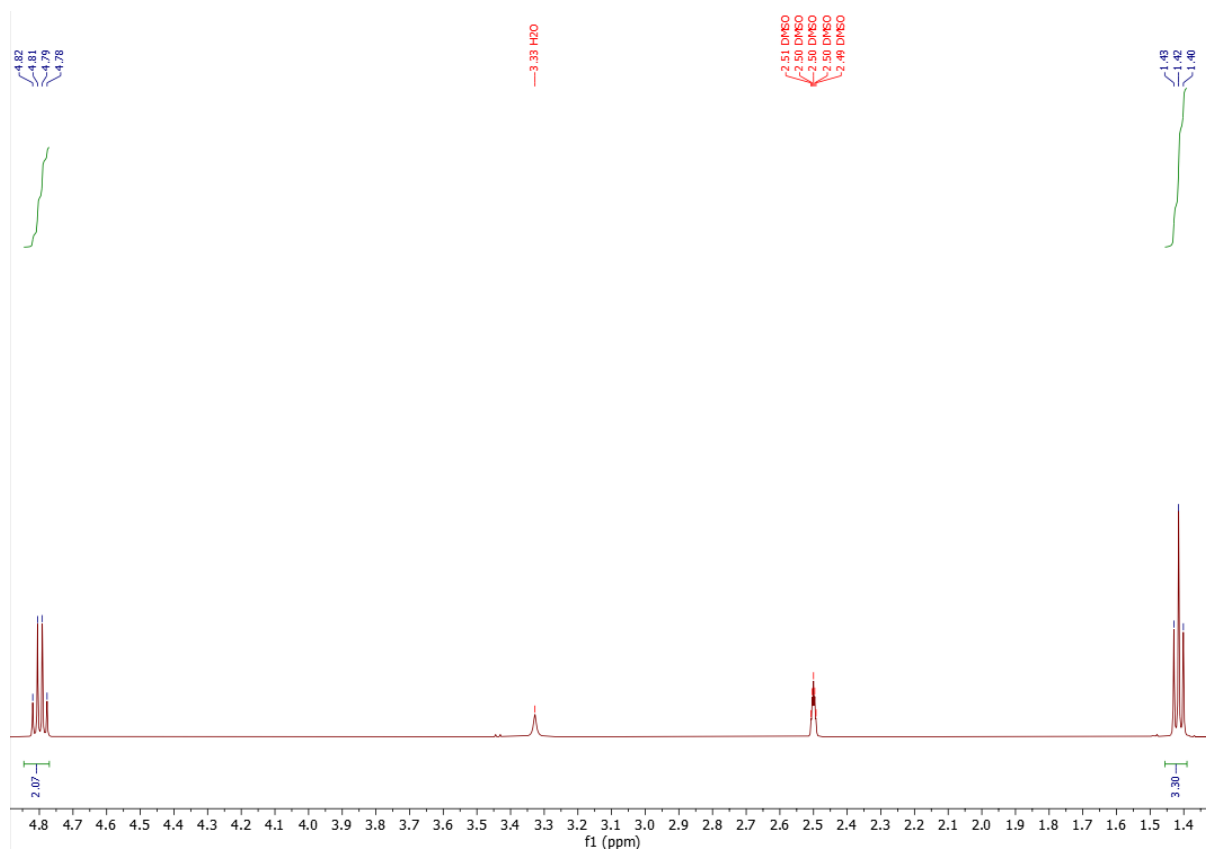


Figure A1.2: Expansion of  $^1\text{H}$  NMR spectrum of 3-((3,5-bis(trifluoromethyl)phenyl)amino)-4-ethoxycyclobut-3-ene-1,2-dione (**42**) (500 MHz,  $\text{DMSO-d}_6$ ).

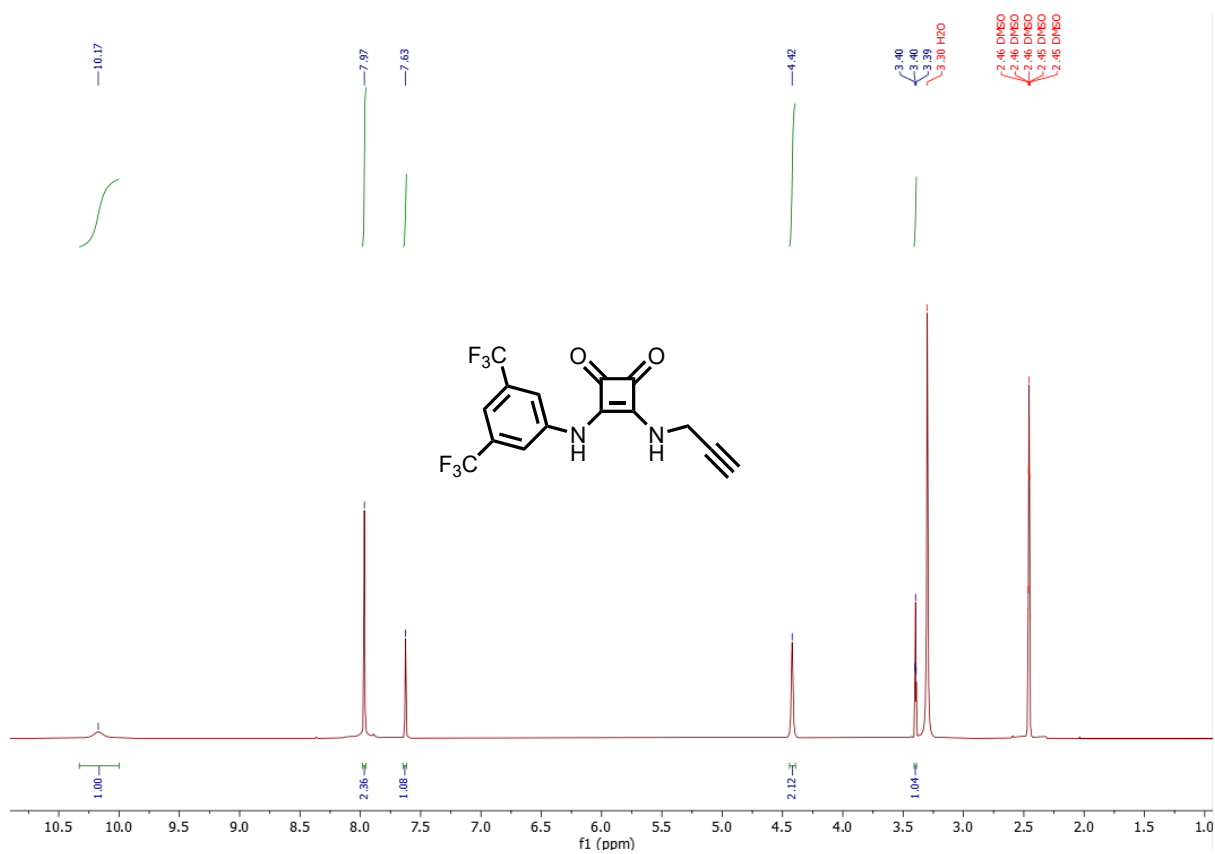


Figure A1.3: <sup>1</sup>H NMR spectrum of 3-((3,5-bis(trifluoromethyl)phenyl)amino)-4-(prop-2-yn-1-ylamino)cyclobut-3-ene-1,2-dione (**43**) (600 MHz, DMSO-d<sub>6</sub>).



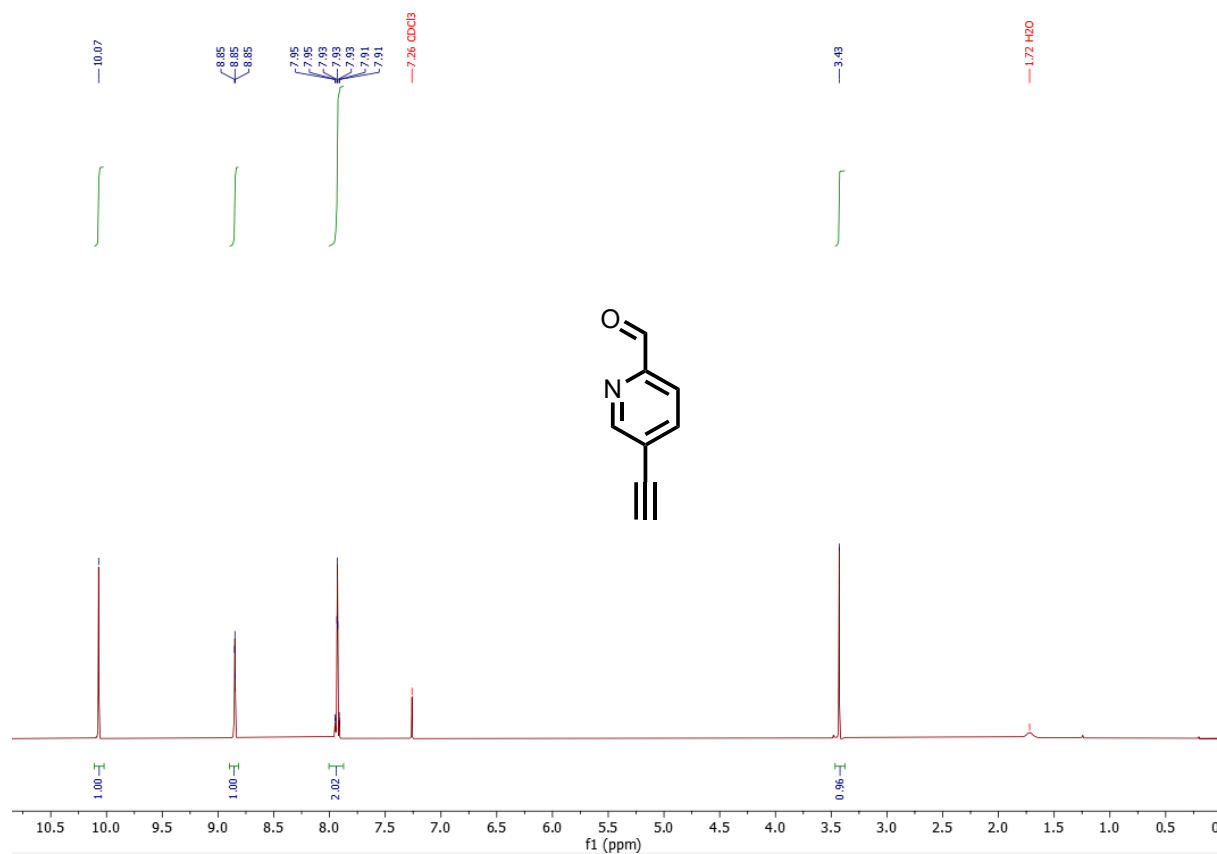


Figure A1.4: <sup>1</sup>H NMR spectrum of 5-ethynylpicolinaldehyde (**44**) (500 MHz, CDCl<sub>3</sub>).

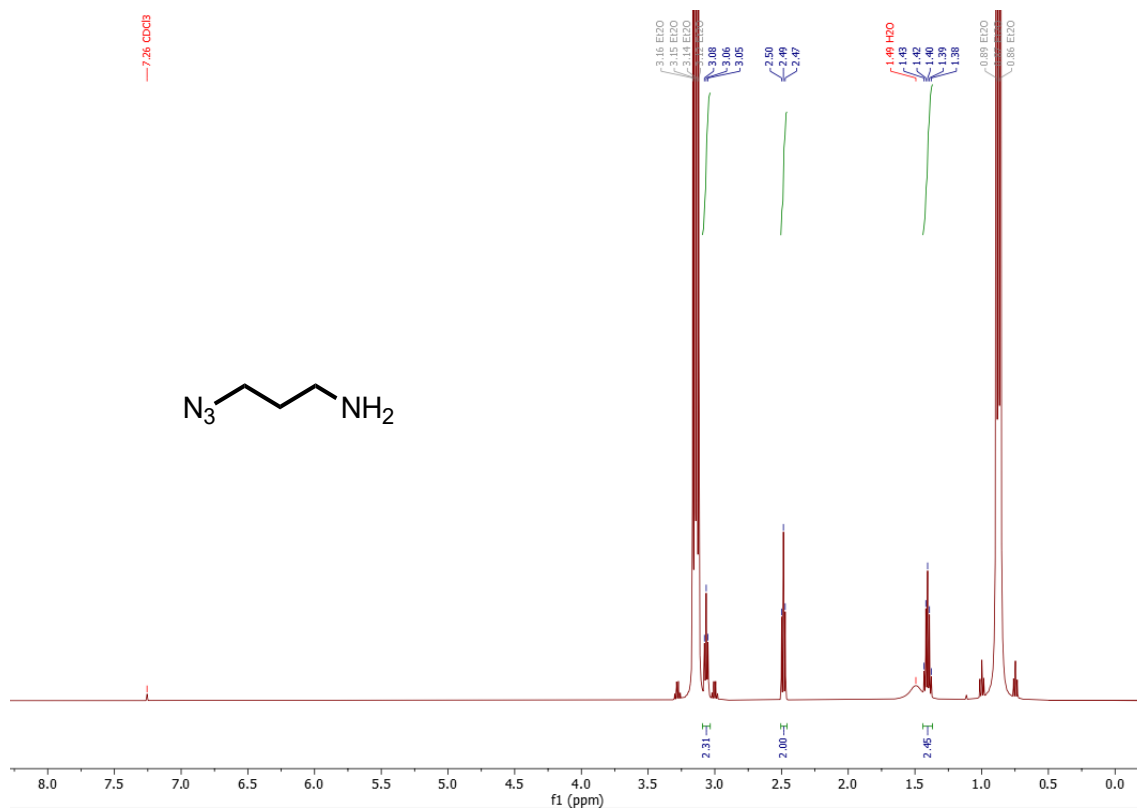


Figure A1.5: <sup>1</sup>H NMR spectrum of 3-azidopropan-1-amine (**45**) (500 MHz, CDCl<sub>3</sub>).

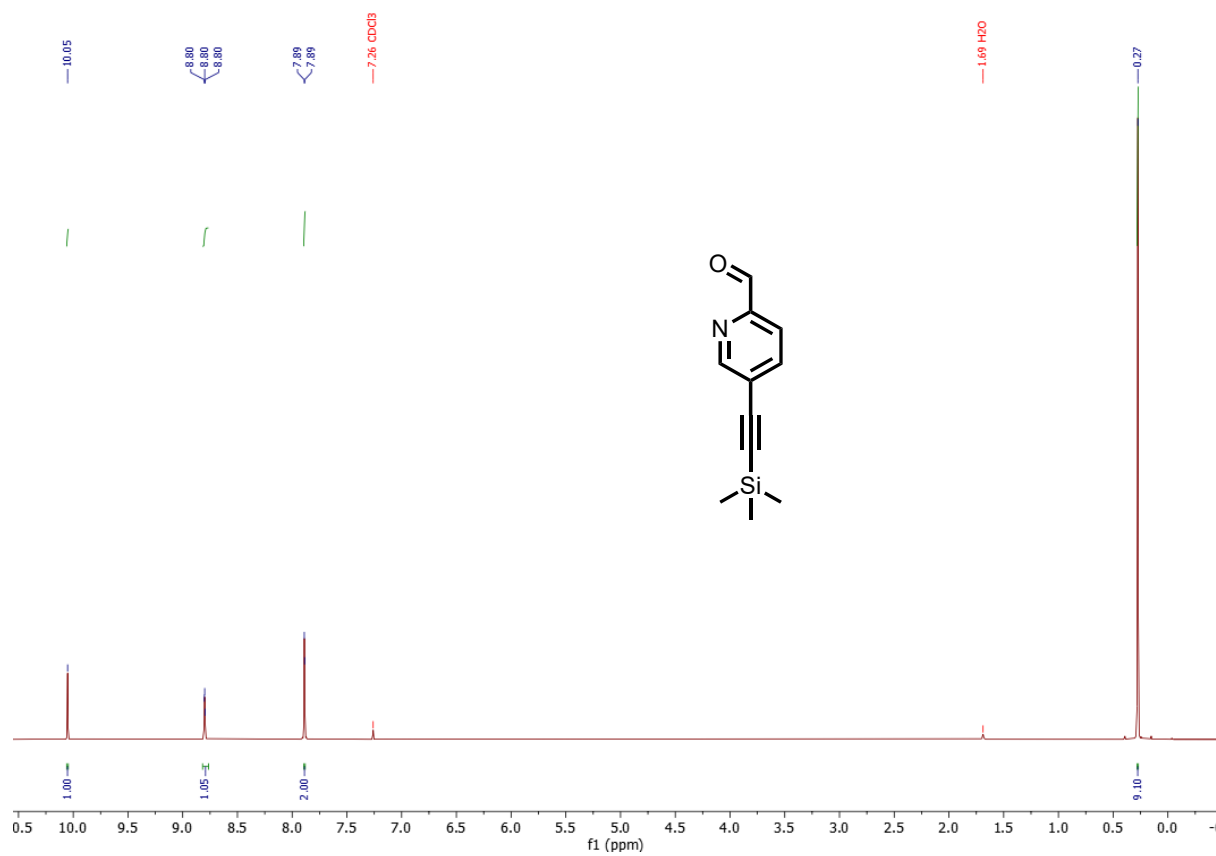


Figure A1.6: <sup>1</sup>H NMR spectrum of 5-((trimethylsilyl)ethynyl)picolinaldehyde (**46**) (500 MHz, CDCl<sub>3</sub>).

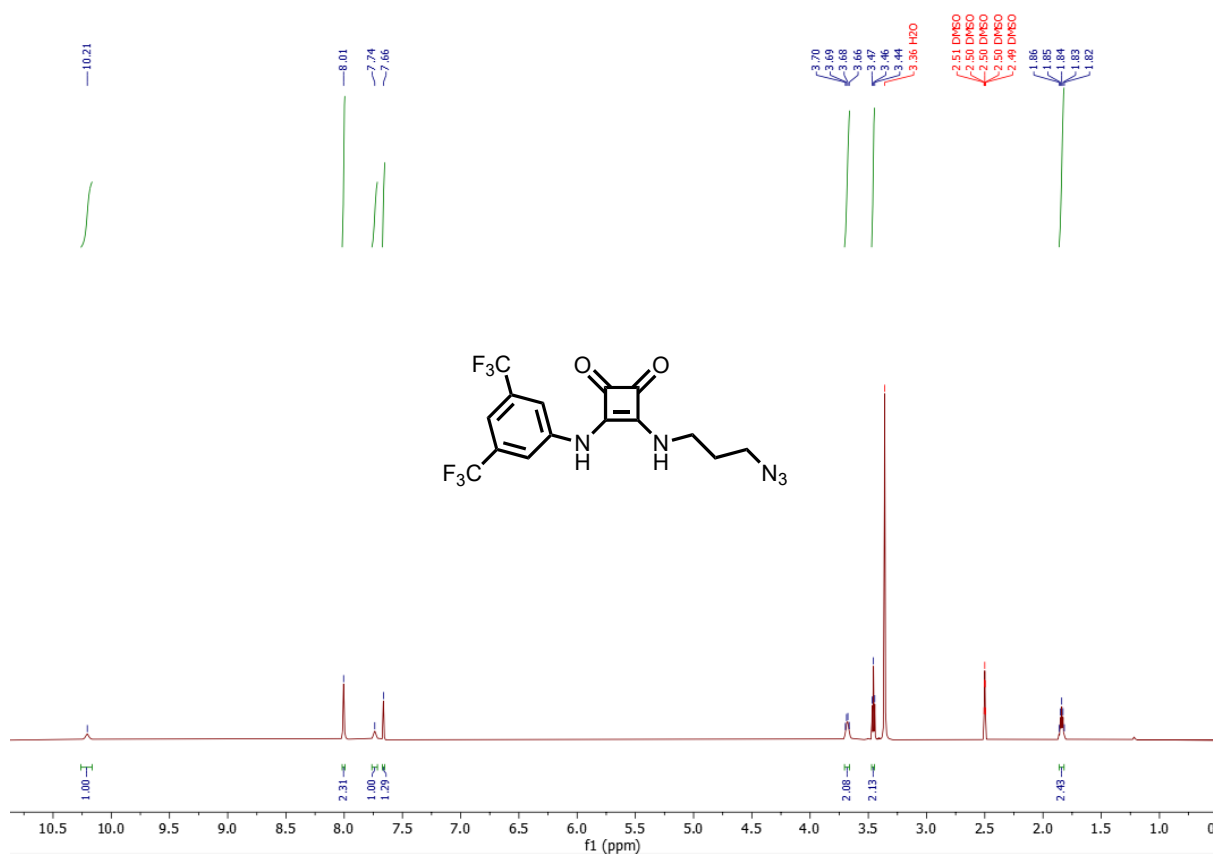


Figure A1.7: <sup>1</sup>H NMR spectrum of 3-((3-azidopropyl)amino)-4-((3,5-bis(trifluoromethyl)phenyl)amino)cyclobut-3-ene-1,2-dione (**47**) (600 MHz, DMSO-d<sub>6</sub>).

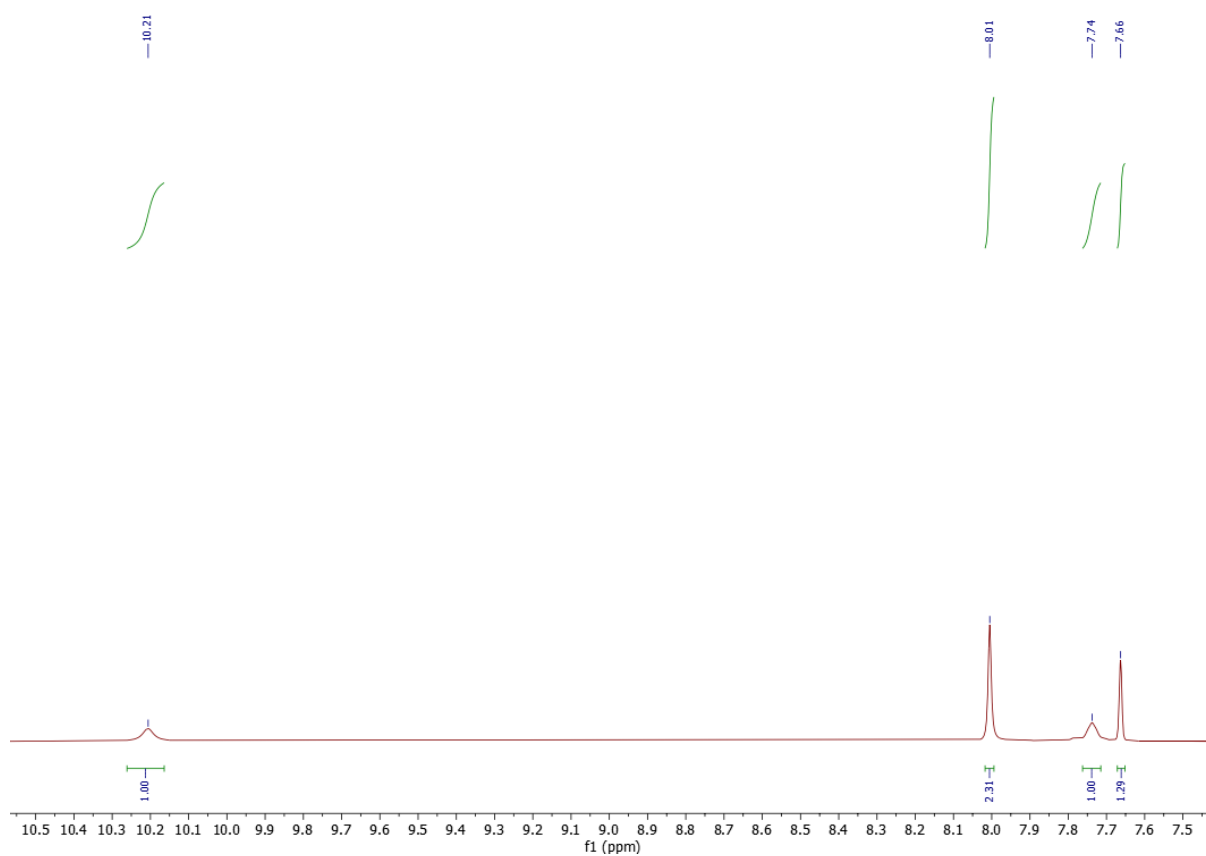


Figure A1.8: Expansion of  $^1\text{H}$  NMR spectrum of 3-((3-azidopropyl)amino)-4-((3,5-bis(trifluoromethyl)phenyl)amino)cyclobut-3-ene-1,2-dione (**47**) (7-11 ppm) (600 MHz,  $\text{DMSO-d}_6$ ).

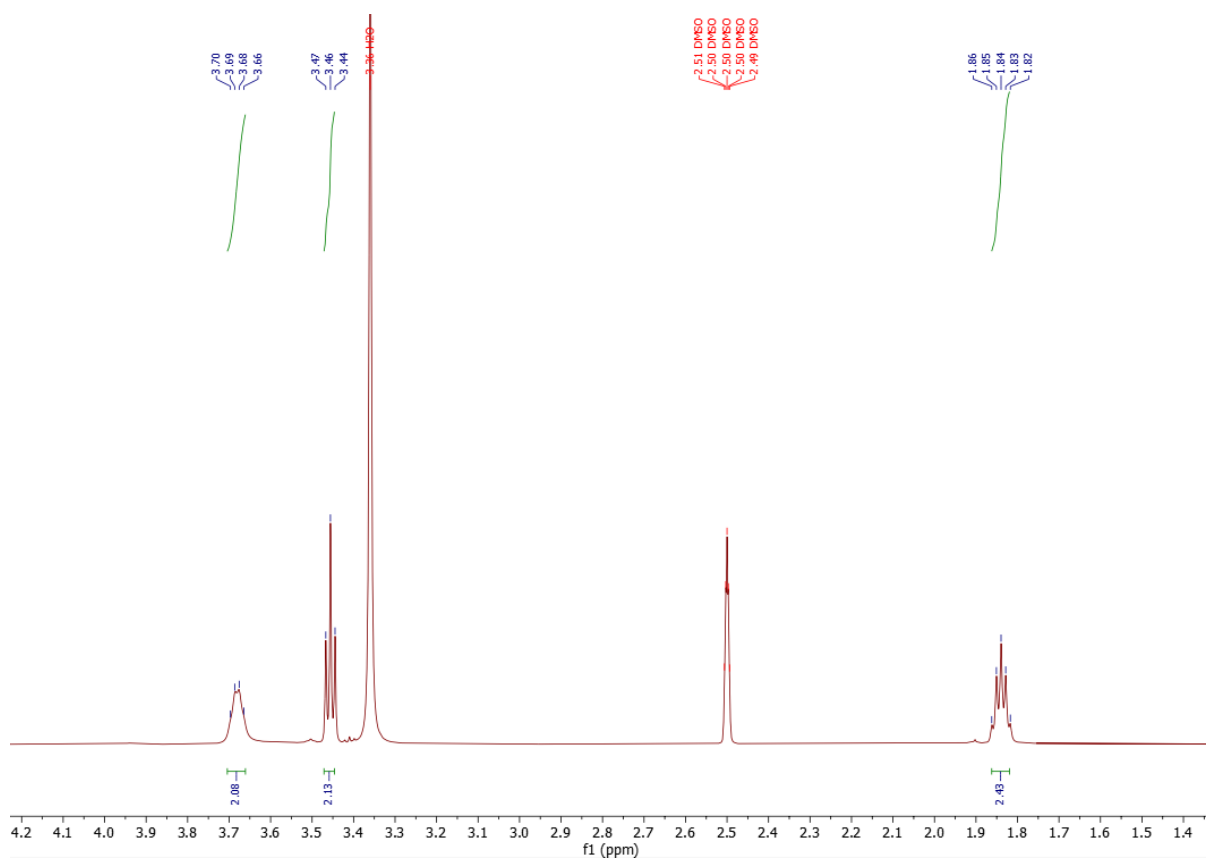


Figure A1.9: Expansion of  $^1\text{H}$  NMR spectrum of 3-((3-azidopropyl)amino)-4-((3,5-bis(trifluoromethyl)phenyl)amino)cyclobut-3-ene-1,2-dione (**47**) (1-5 ppm) (600 MHz,  $\text{DMSO-d}_6$ ).

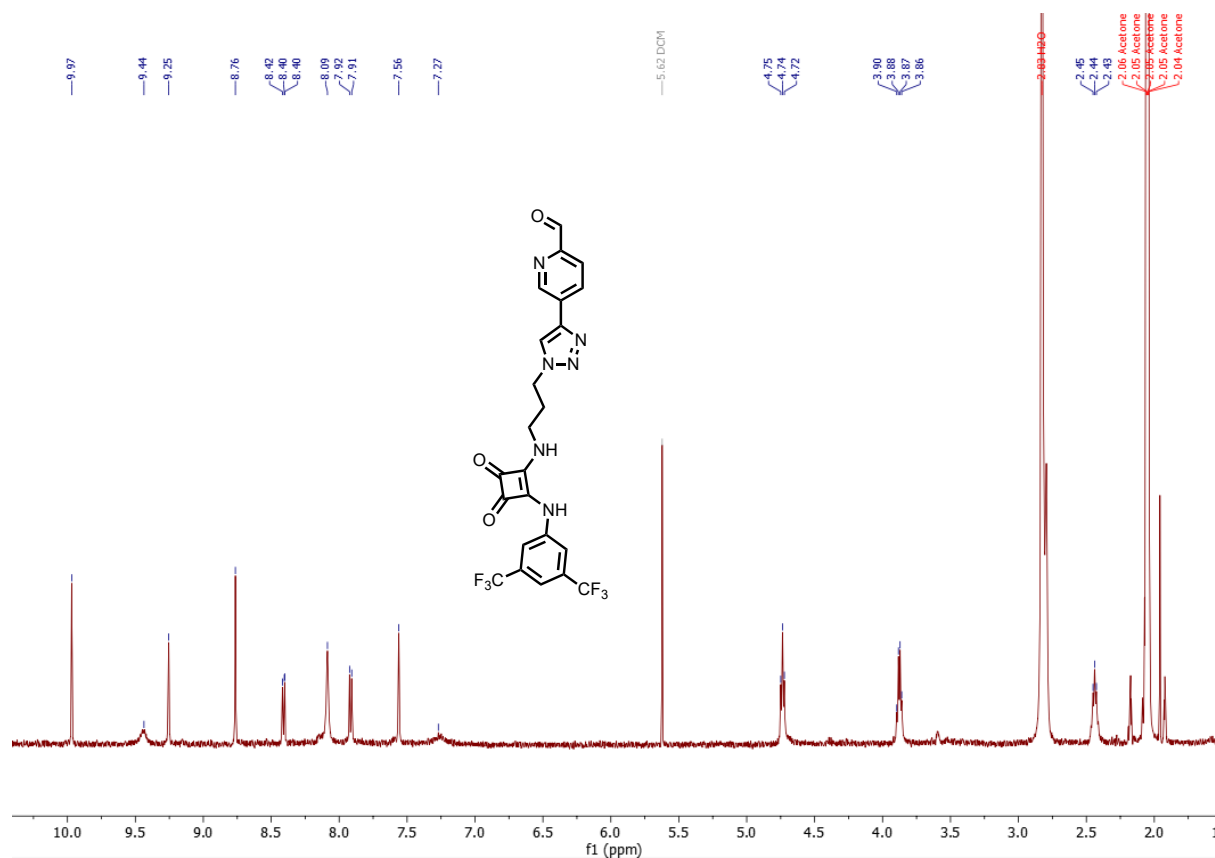


Figure A1.10: <sup>1</sup>H NMR spectrum of 5-(1-(3-((2-((3,5-bis(trifluoromethyl)phenyl)amino)-3,4-dioxocyclobut-1-en-1-yl)amino)propyl)-1H-1,2,3-triazol-4-yl)picolinaldehyde (**48**) (500 MHz, acetone-*d*<sub>6</sub>).

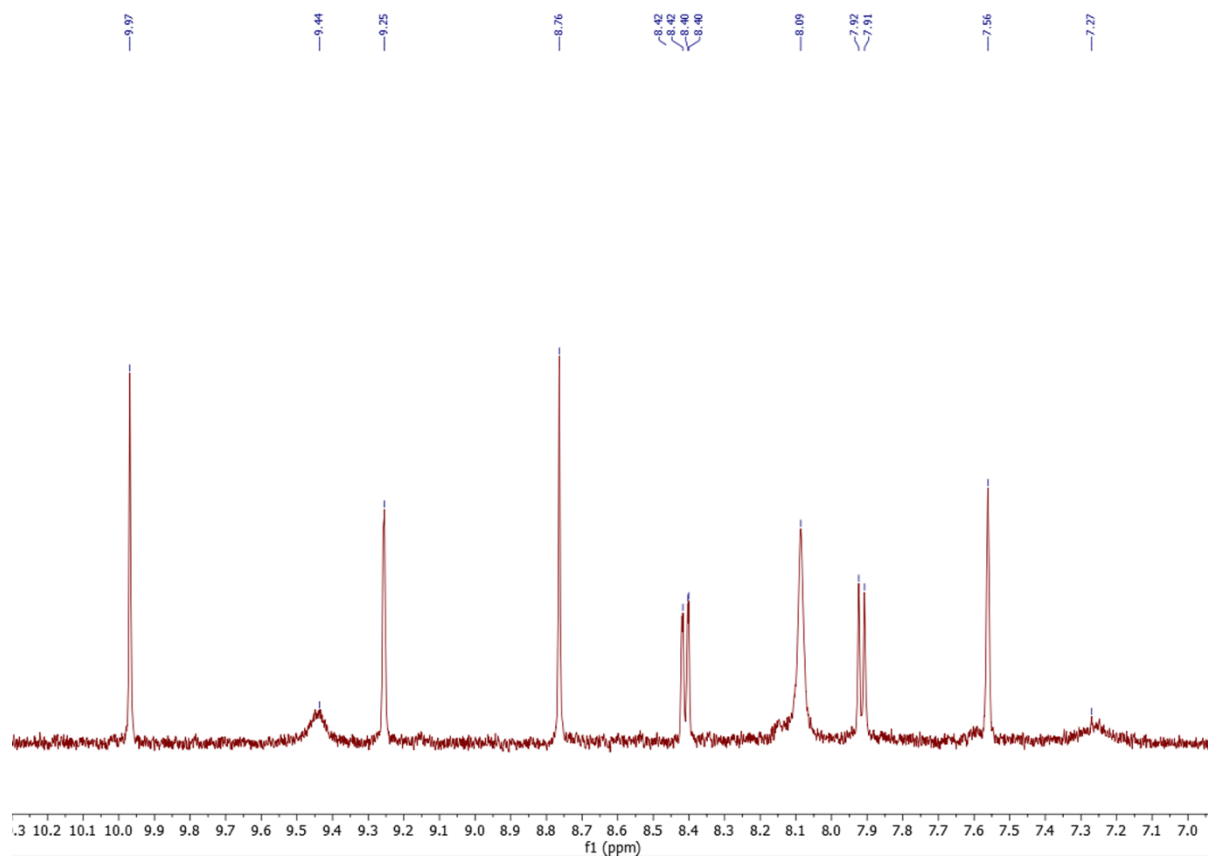


Figure A1.11: Expansion of  $^1\text{H}$  NMR spectrum of 5-(1-(3-((2-((3,5-bis(trifluoromethyl)phenyl)amino)-3,4-dioxocyclobut-1-en-1-yl)amino)propyl)-1H-1,2,3-triazol-4-yl)picolinaldehyde (**48**) (7-11 ppm) (500 MHz, acetone- $d_6$ ).



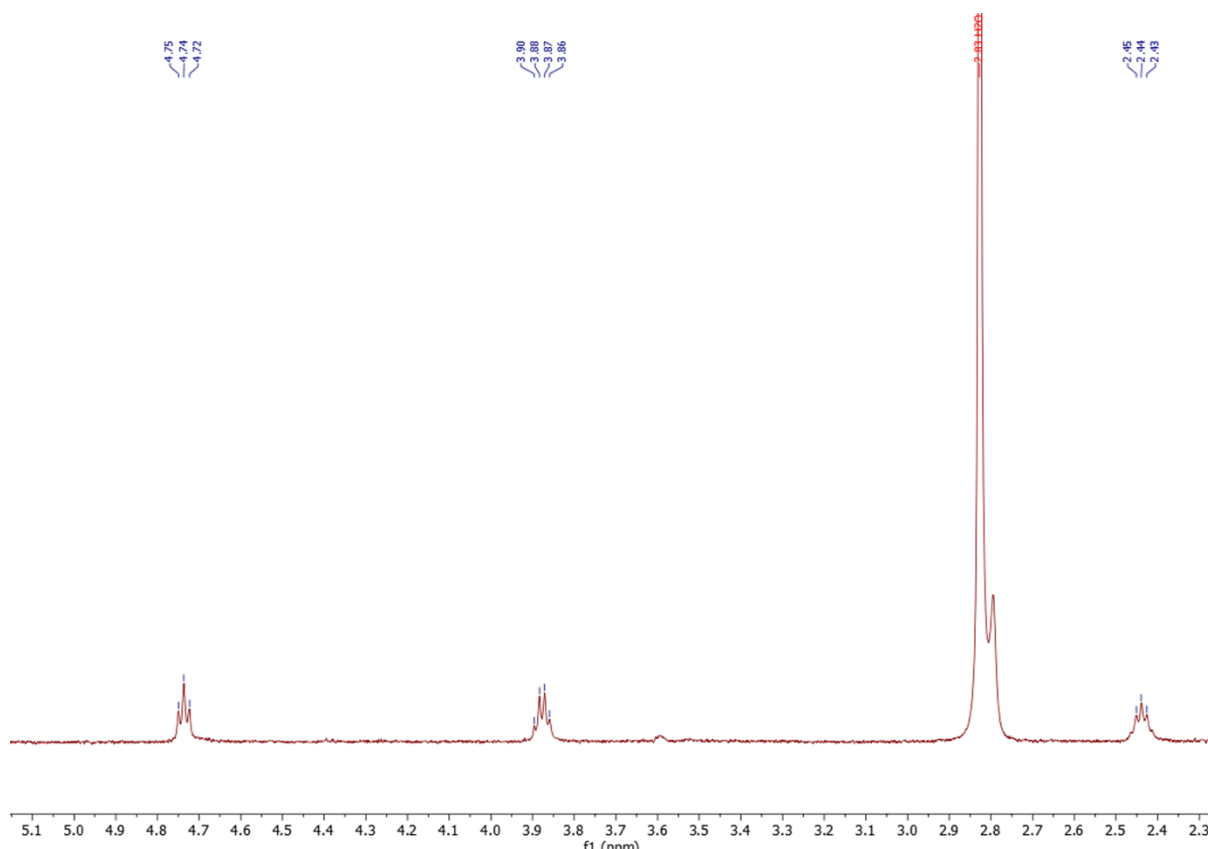


Figure A1.12: Expansion of  $^1\text{H}$  NMR spectrum of 5-(1-(3-((2-((3,5-bis(trifluoromethyl)phenyl)amino)-3,4-dioxocyclobut-1-en-1-yl)amino)propyl)-1H-1,2,3-triazol-4-yl)picolinaldehyde (**48**) (2-6 ppm) (500 MHz,  $\text{acetone-d}_6$ ).

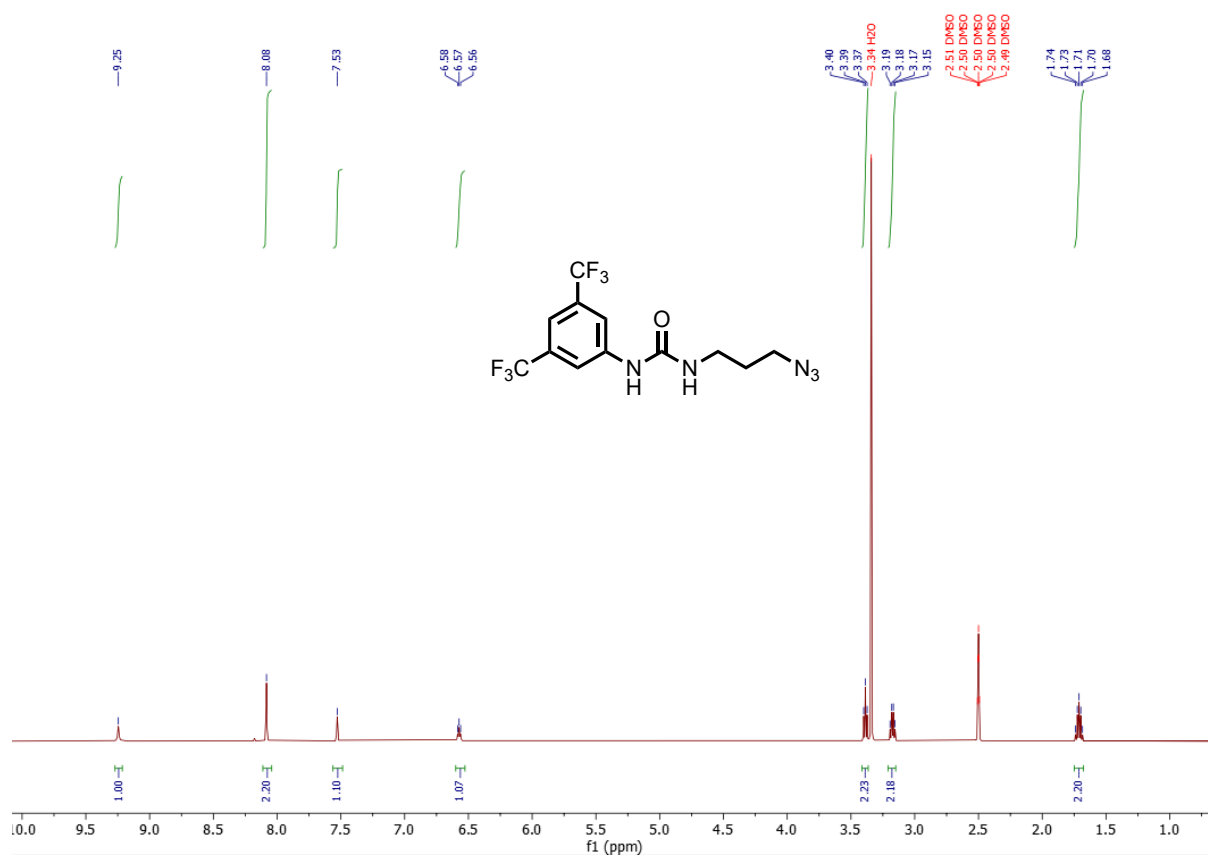


Figure A1.13: <sup>1</sup>H NMR spectrum of 1-(3-azidopropyl)-3-(3,5-bis(trifluoromethyl)phenyl)urea (49) (500 MHz, DMSO-d<sub>6</sub>).

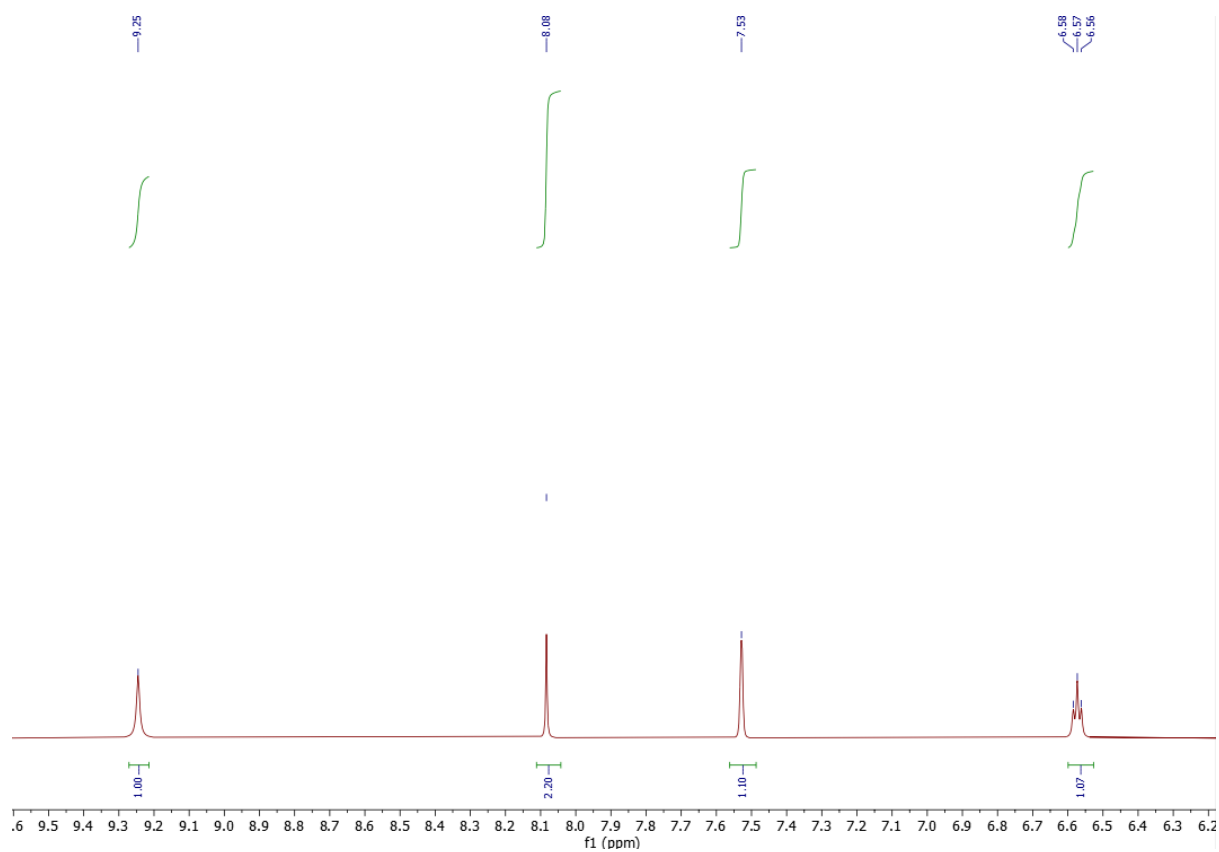


Figure A1.14: Expansion of  $^1\text{H}$  NMR spectrum of 1-(3-azidopropyl)-3-(3,5-bis(trifluoromethyl)phenyl)urea (**49**) (6-10 ppm) (500 MHz,  $\text{DMSO}-d_6$ ).

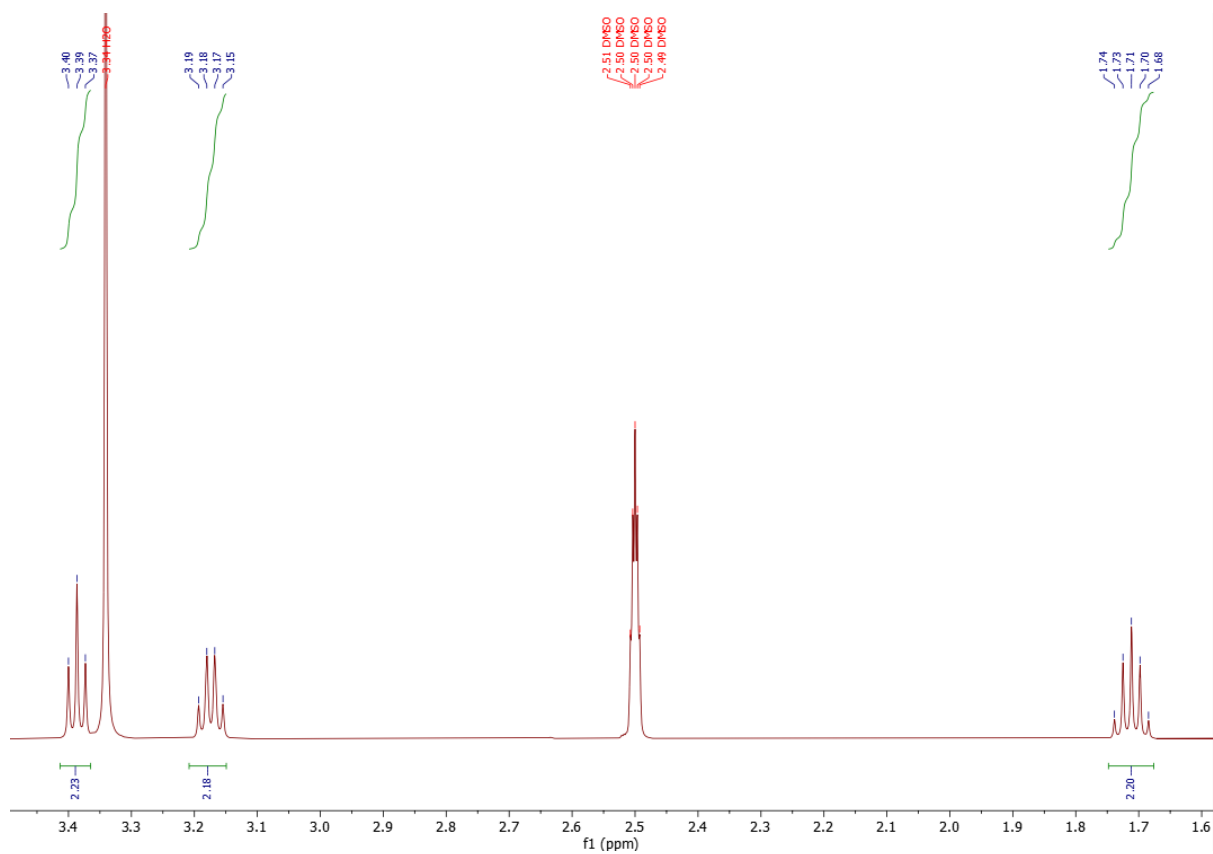


Figure A1.15: Expansion of  $^1\text{H}$  NMR spectrum of 1-(3-azidopropyl)-3-(3,5-bis(trifluoromethyl)phenyl)urea (**49**) (1-4 ppm) (500 MHz,  $\text{DMSO-d}_6$ ).

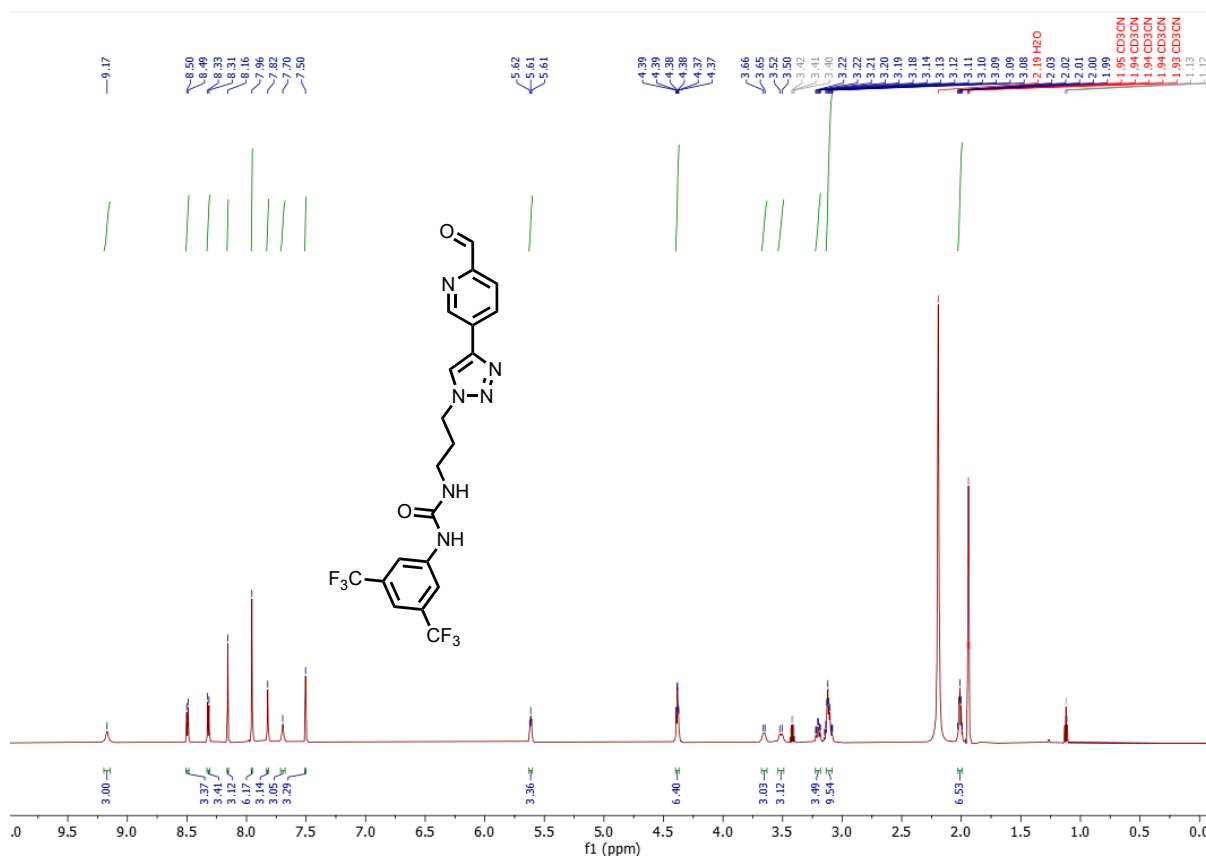


Figure A1.16: <sup>1</sup>H NMR spectrum of 1-(3,5-bis(trifluoromethyl)phenyl)-3-(3-(4-(6-formylpyridin-3-yl)-1H-1,2,3-triazol-1-yl)propyl)urea (**50**) (500 MHz, acetone-d<sub>6</sub>).

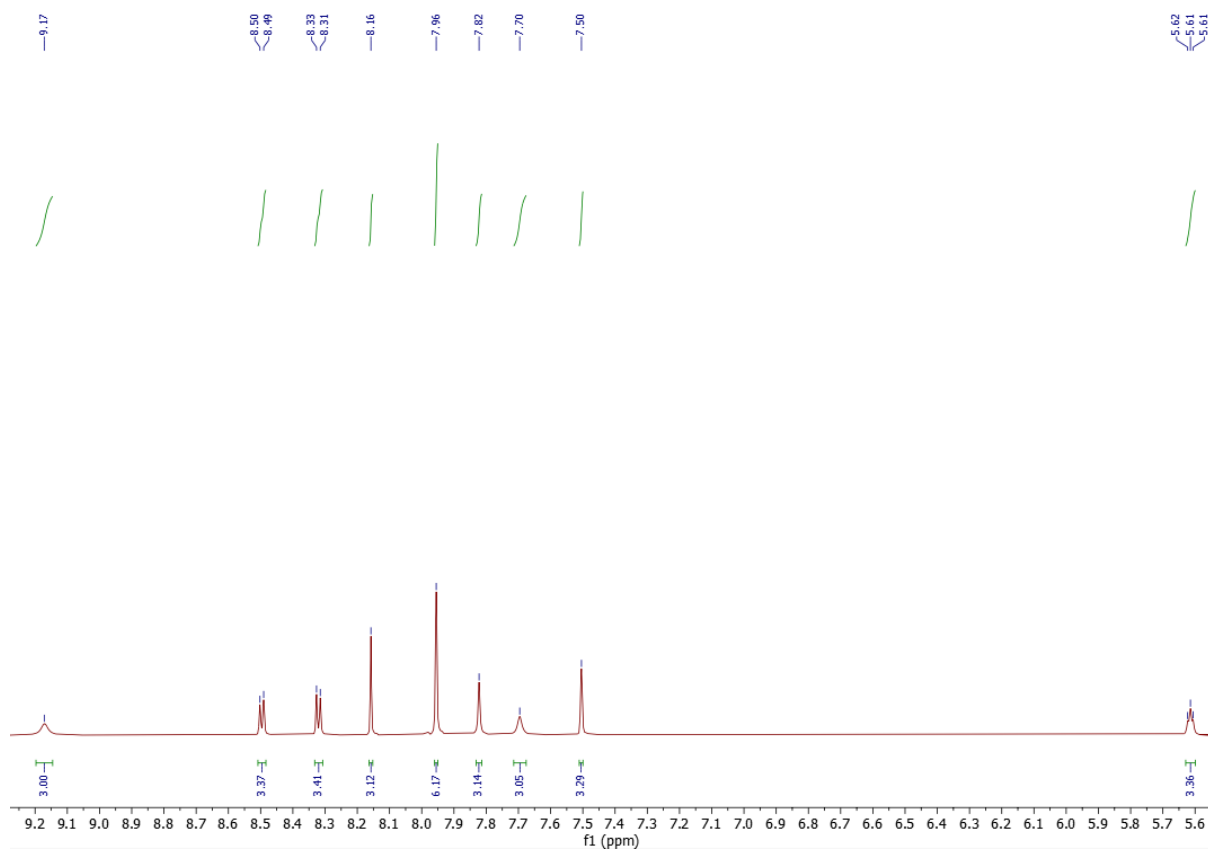


Figure A1.17: Expansion of  $^1\text{H}$  NMR spectrum of 1-(3,5-bis(trifluoromethyl)phenyl)-3-(3-(4-(6-formylpyridin-3-yl)-1H-1,2,3-triazol-1-yl)propyl)urea (**50**) (5-10 ppm) (500 MHz, acetone- $d_6$ ).

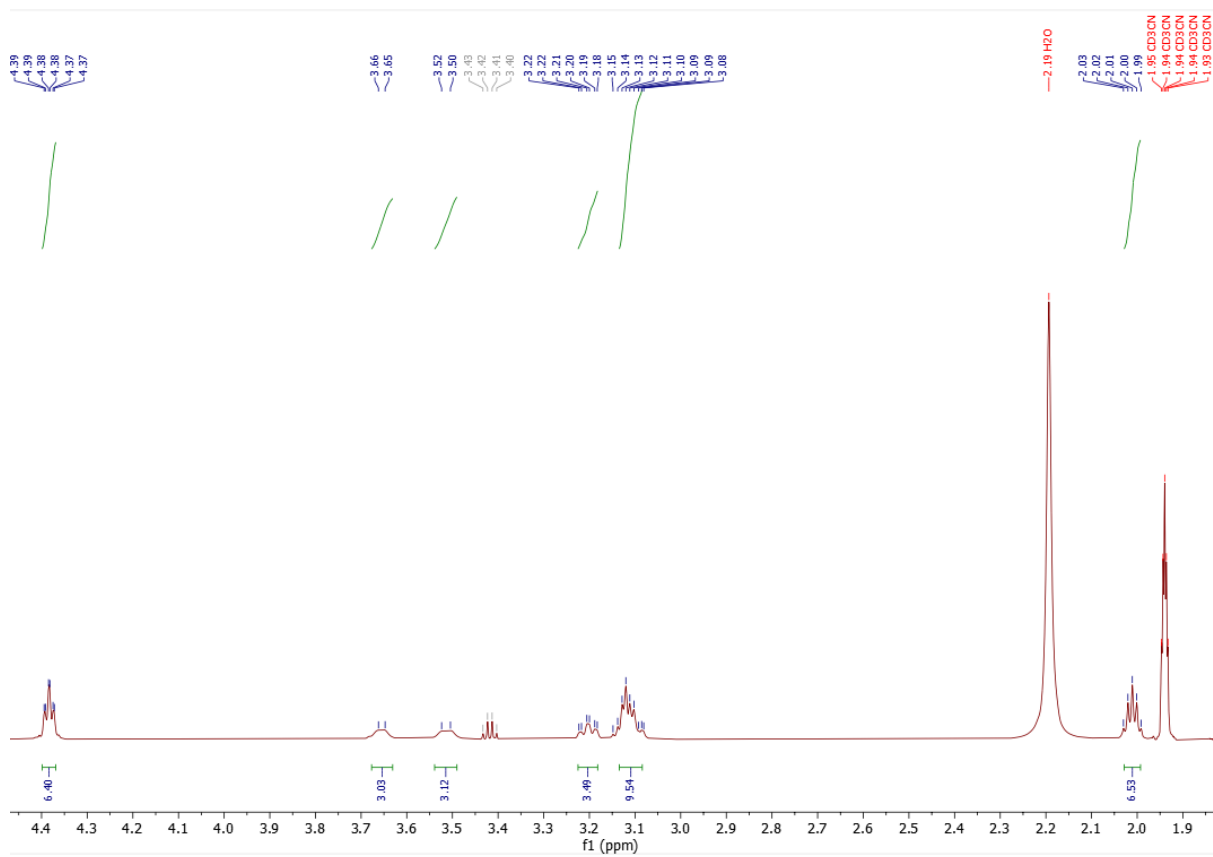


Figure A1.18: Expansion of  $^1\text{H}$  NMR spectrum of 1-(3,5-bis(trifluoromethyl)phenyl)-3-(3-(4-(6-formylpyridin-3-yl)-1H-1,2,3-triazol-1-yl)propyl)urea (**50**) (1-5 ppm) (500 MHz,  $\text{acetone-}d_6$ ).

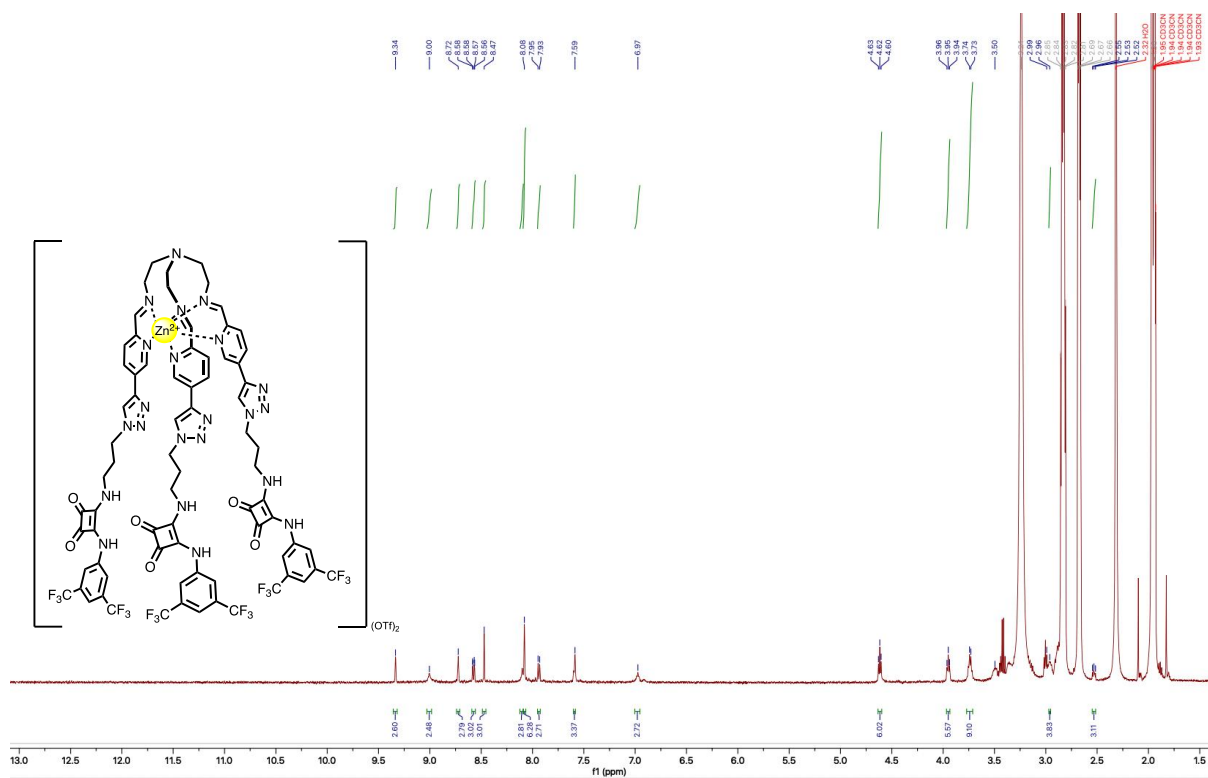


Figure A1.19:  $^1\text{H}$  NMR spectrum of Zn(II)L complex **51** (500 MHz,  $\text{CD}_3\text{CN}$ ).



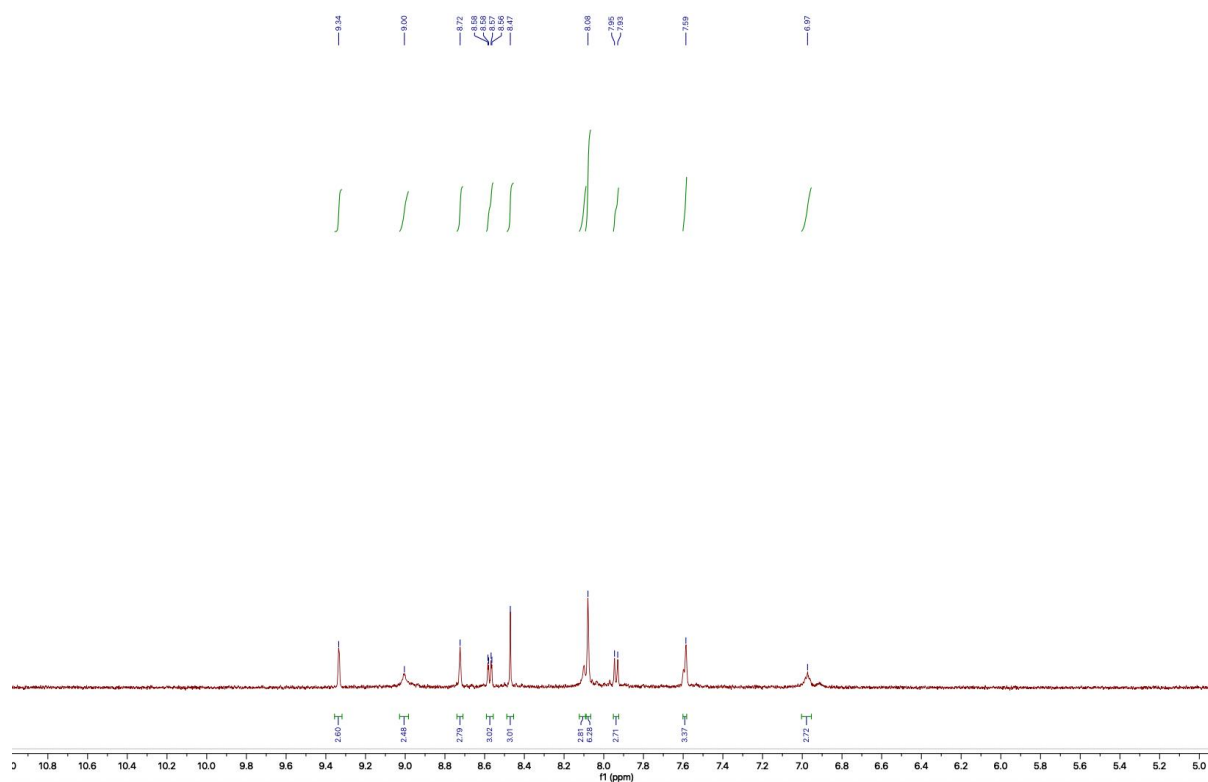


Figure A1.20: Expansion of  $^1\text{H}$  NMR spectrum of Zn(II)L complex **51** (5-11 ppm) (500 MHz,  $\text{CD}_3\text{CN}$ ).

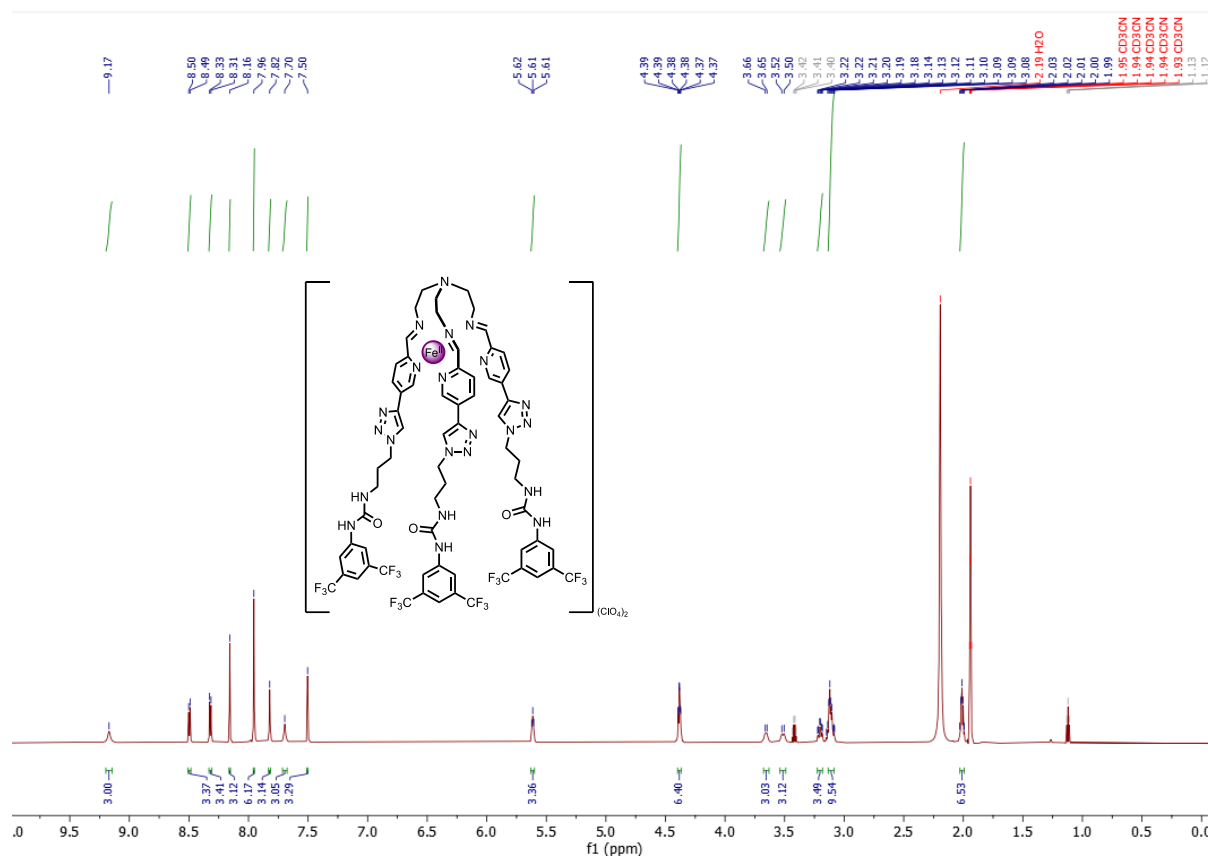


Figure A1.21:  $^1\text{H}$  NMR spectrum of  $\text{Fe(II)L}$  complex **52** (700 MHz,  $\text{CD}_3\text{CN}$ ).

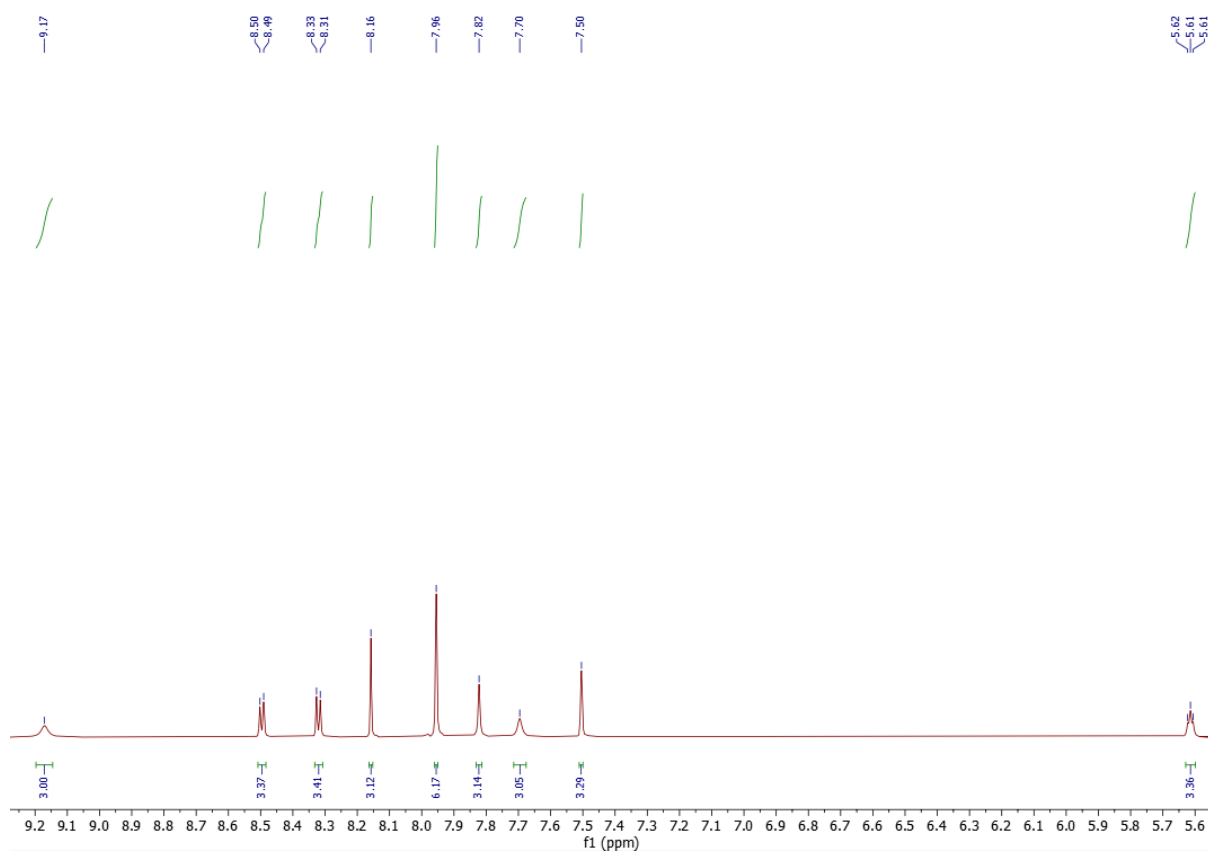


Figure A1.22: Expansion of  $^1\text{H}$  NMR spectrum of Fe(II)L complex **52** (5-10 ppm) (700 MHz,  $\text{CD}_3\text{CN}$ ).

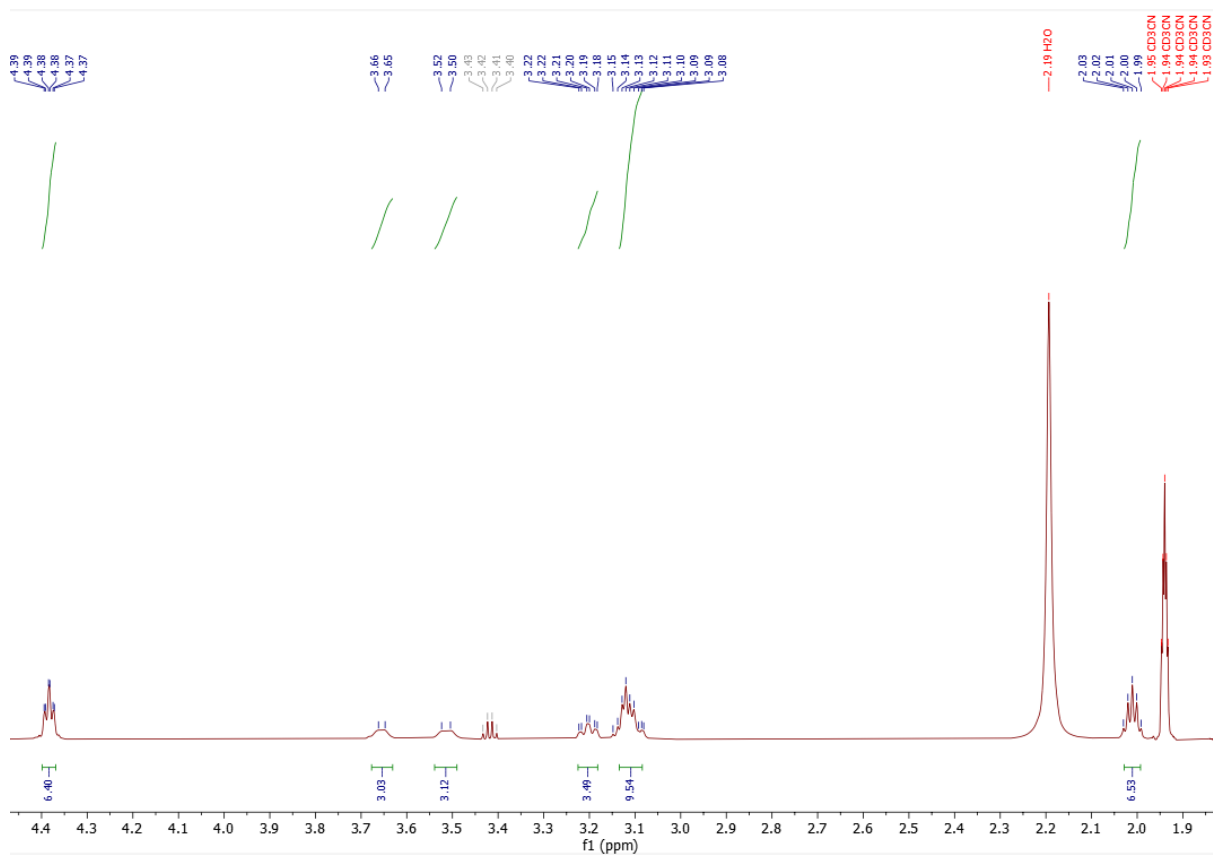


Figure A1.23: Expansion of  $^1\text{H}$  NMR spectrum of Fe(II)L complex **52** (1-5 ppm) (700 MHz,  $\text{CD}_3\text{CN}$ ).

## A1.2 $^{13}\text{C}$ NMR

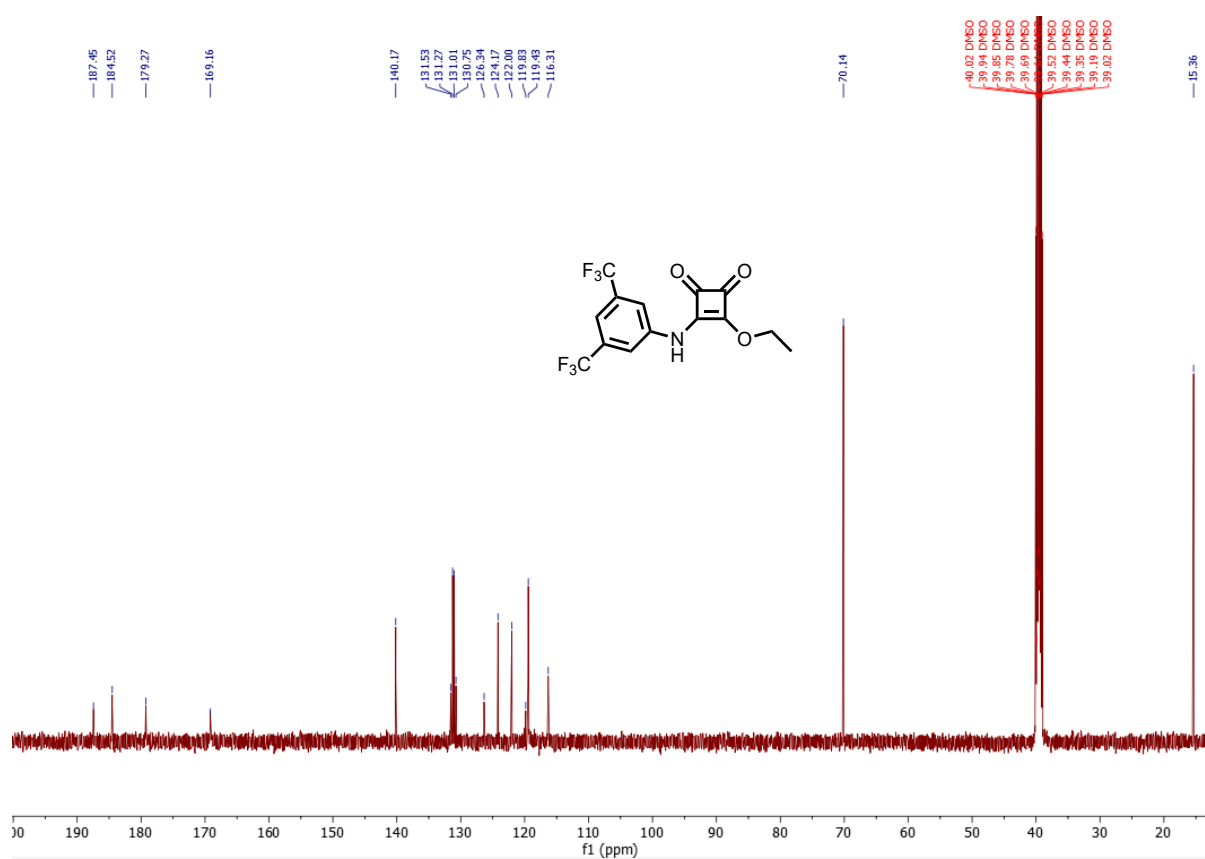


Figure A1.24:  $^{13}\text{C}$  NMR spectrum of 3-((3,5-bis(trifluoromethyl)phenyl)amino)-4-ethoxycyclobut-3-ene-1,2-dione (42) (500 MHz,  $\text{DMSO}-d_6$ ).

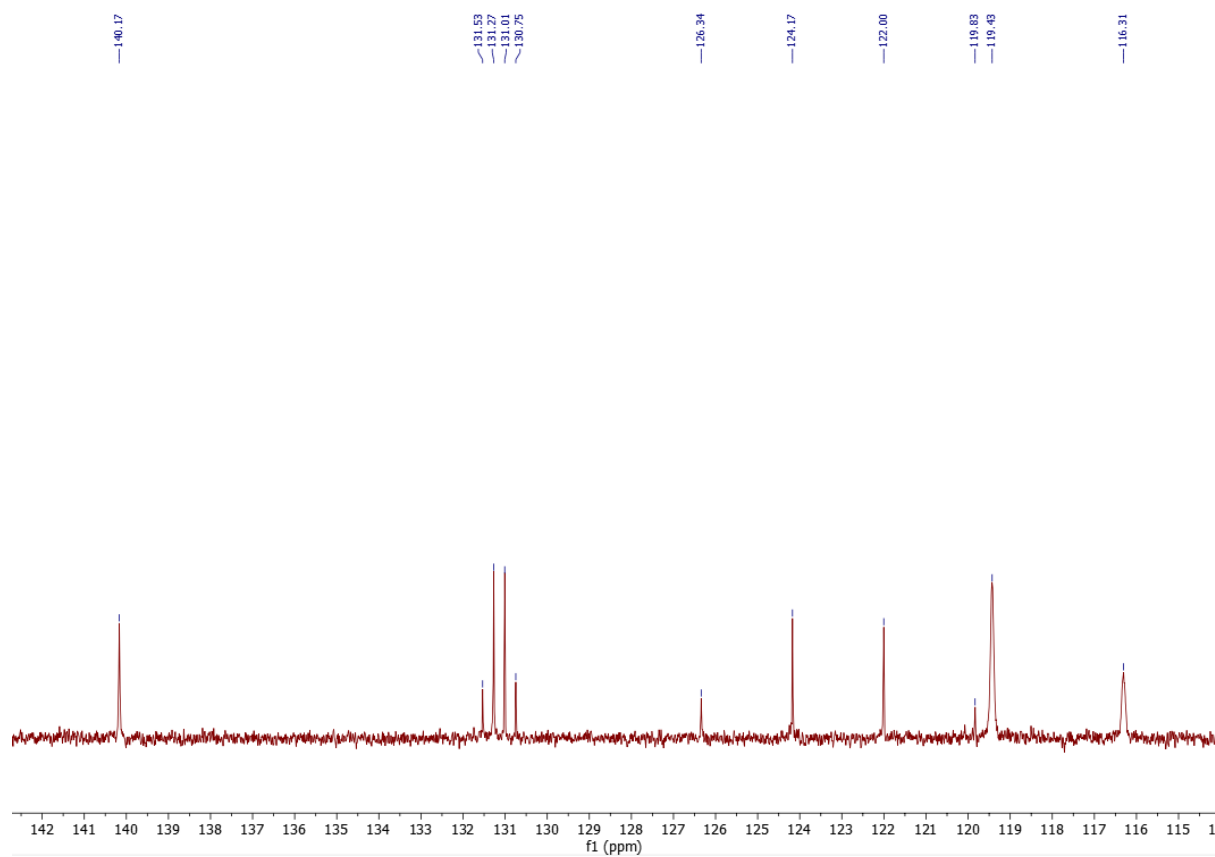


Figure A1.25: Expansion of  $^{13}\text{C}$  NMR spectrum of 3-((3,5-bis(trifluoromethyl)phenyl)amino)-4-ethoxycyclobut-3-ene-1,2-dione (**42**) (500 MHz,  $\text{DMSO}-d_6$ ).

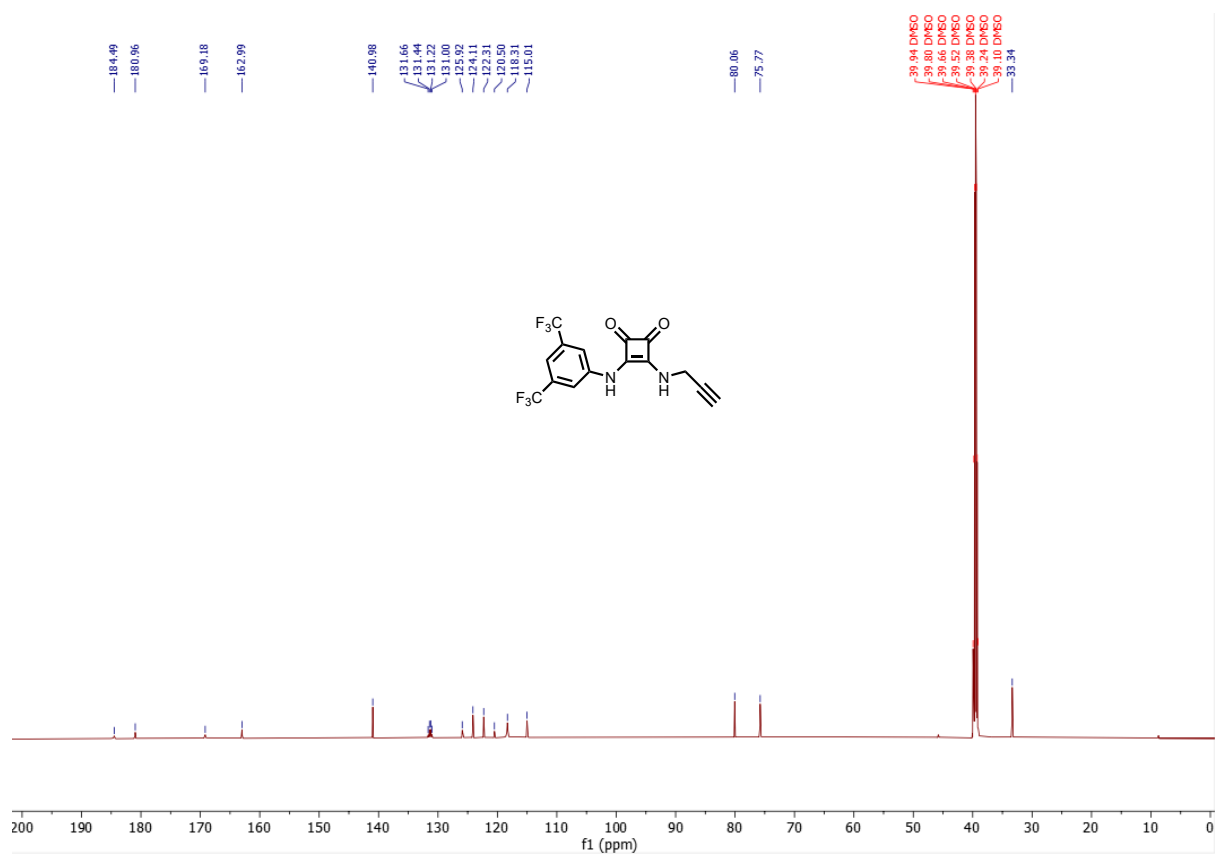


Figure A1.26: <sup>13</sup>C NMR spectrum of 3-((3,5-bis(trifluoromethyl)phenyl)amino)-4-(prop-2-yn-1-ylamino)cyclobut-3-ene-1,2-dione (**43**) (600 MHz, DMSO-d<sub>6</sub>).

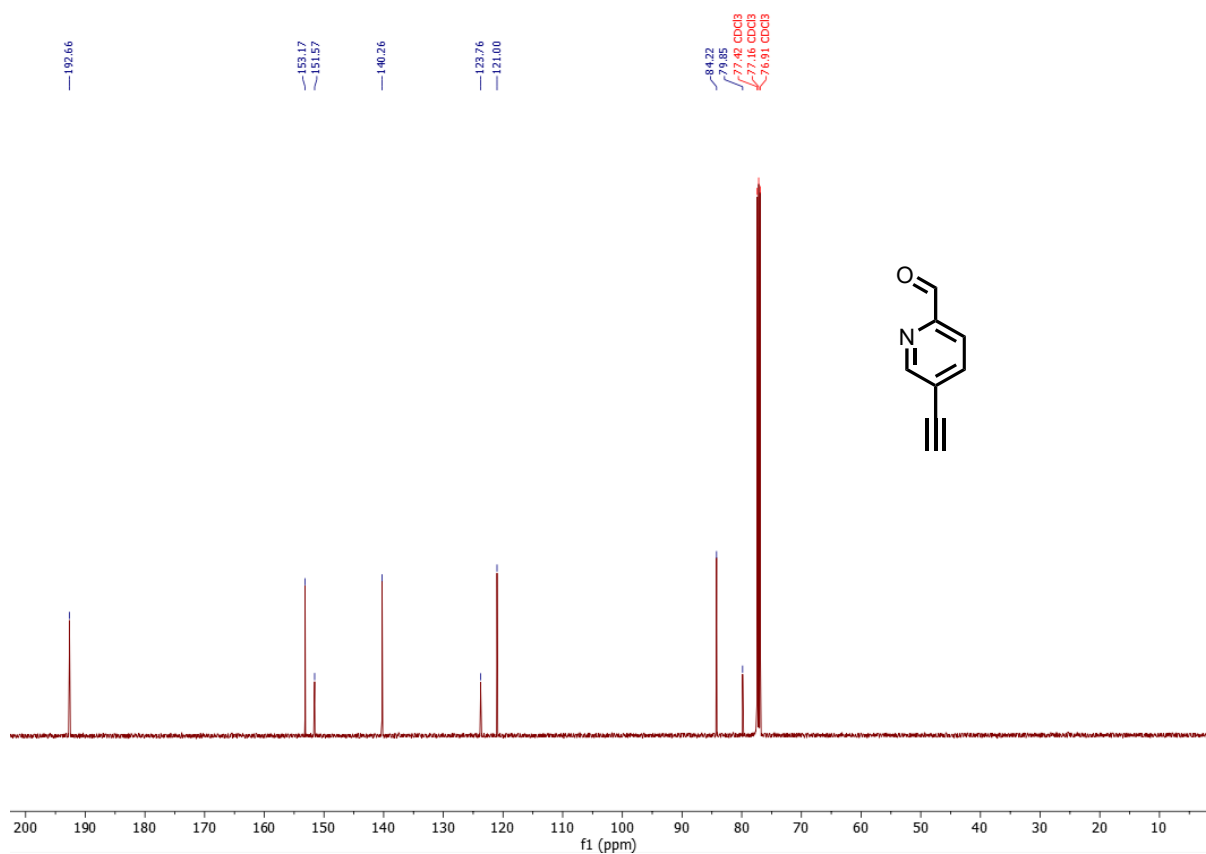


Figure A1.27:  $^{13}\text{C}$  NMR spectrum of 5-ethynylpicolinaldehyde (**44**) (500 MHz,  $\text{CDCl}_3$ ).



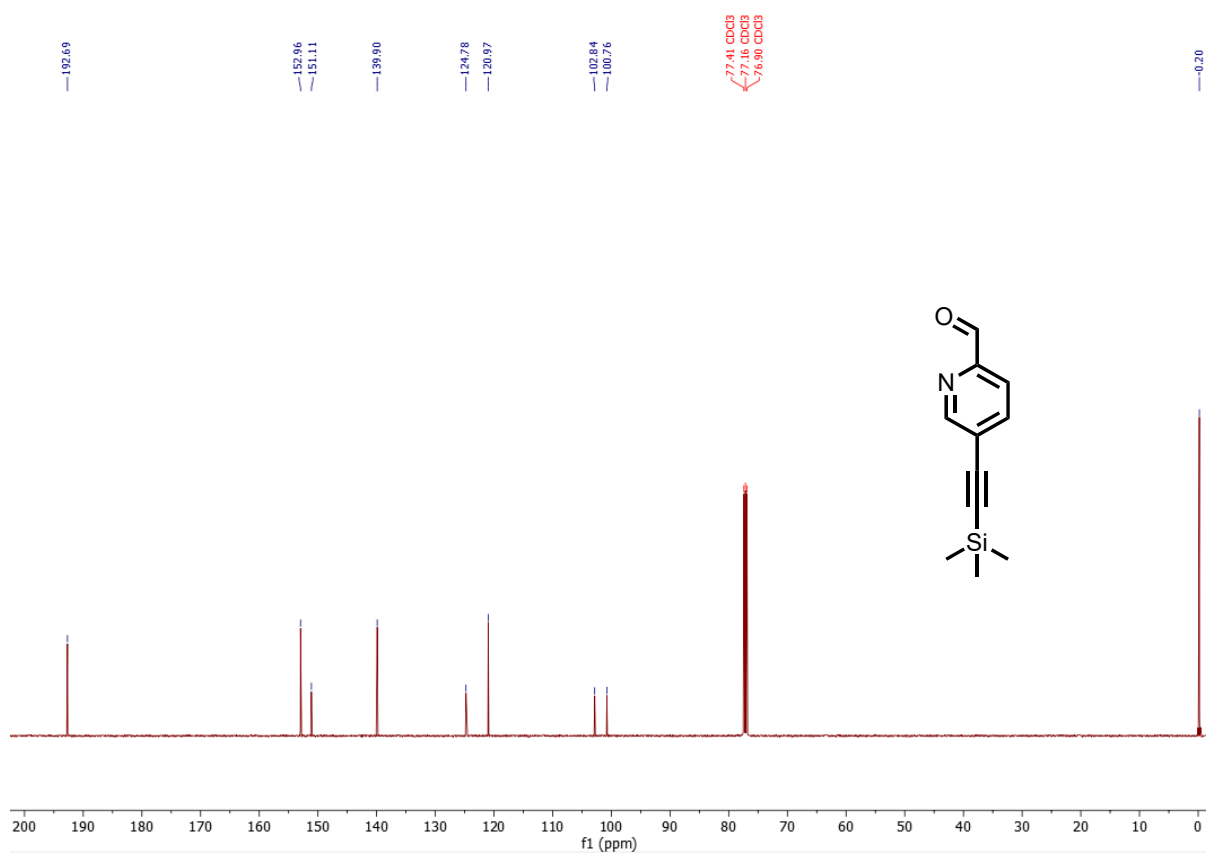


Figure A1.28: <sup>13</sup>C NMR spectrum of 5-((trimethylsilyl)ethynyl)picolinaldehyde (**46**) (500 MHz, CDCl<sub>3</sub>).

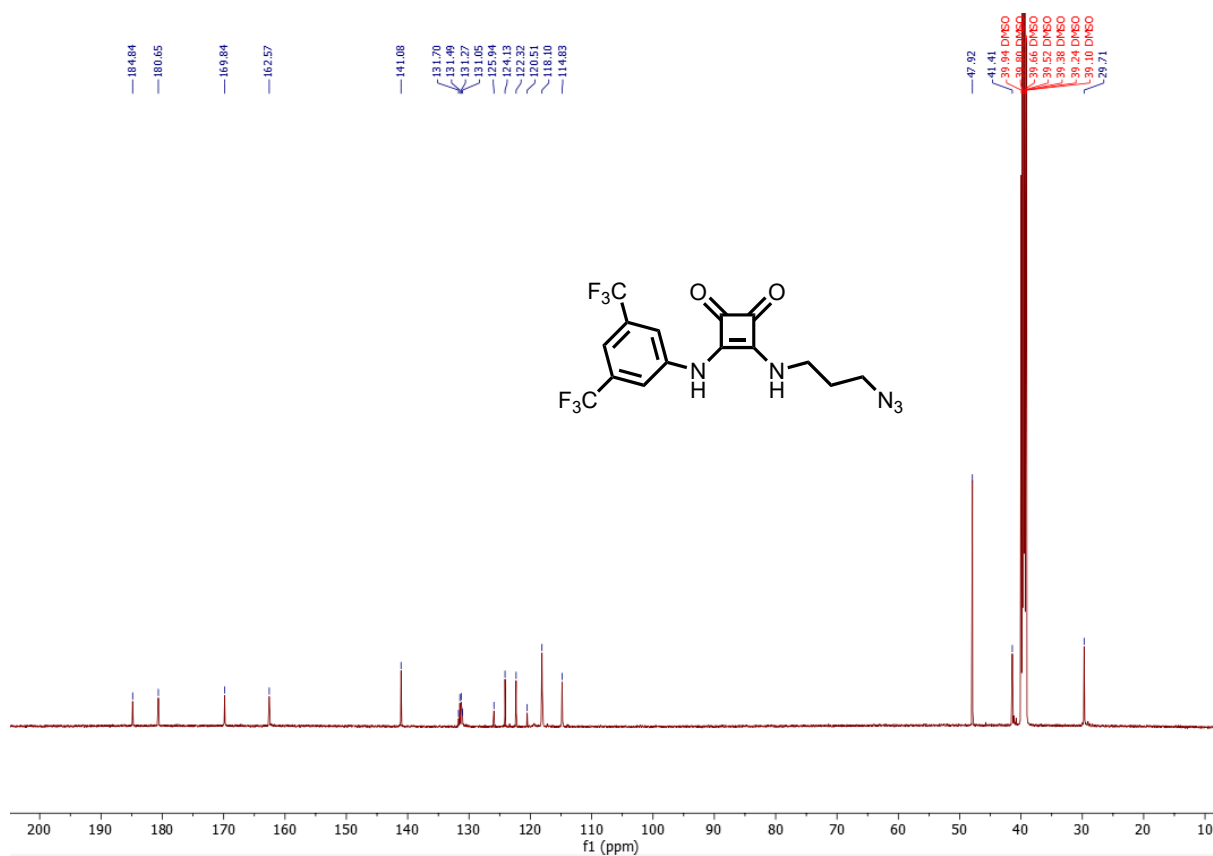


Figure A1.29: <sup>13</sup>C NMR spectrum of 3-((3-azidopropyl)amino)-4-((3,5-bis(trifluoromethyl)phenyl)amino)cyclobut-3-ene-1,2-dione (**47**) (600 MHz, DMSO-*d*<sub>6</sub>).

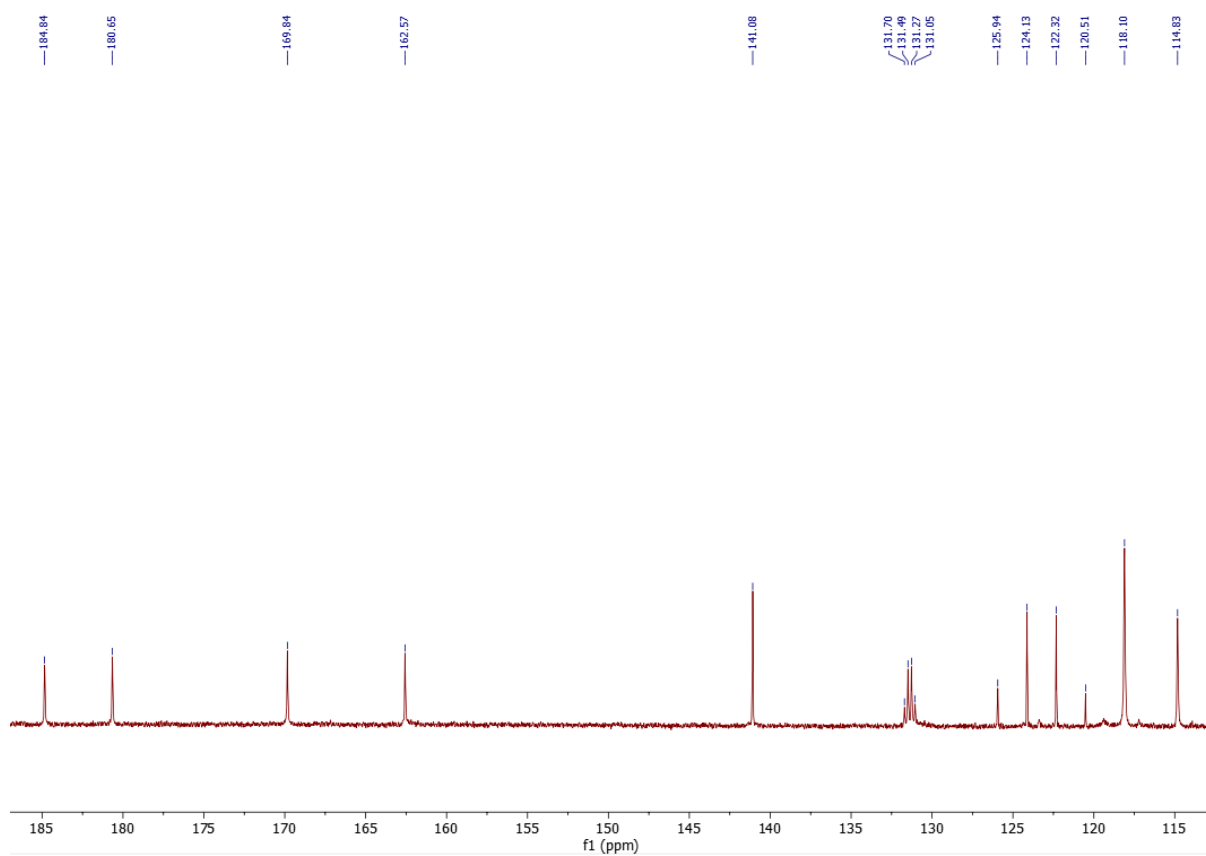


Figure A1.30: Expansion of  $^{13}\text{C}$  NMR spectrum of 3-((3-azidopropyl)amino)-4-((3,5-bis(trifluoromethyl)phenyl)amino)cyclobut-3-ene-1,2-dione (**47**) (600 MHz,  $\text{DMSO-}d_6$ ).

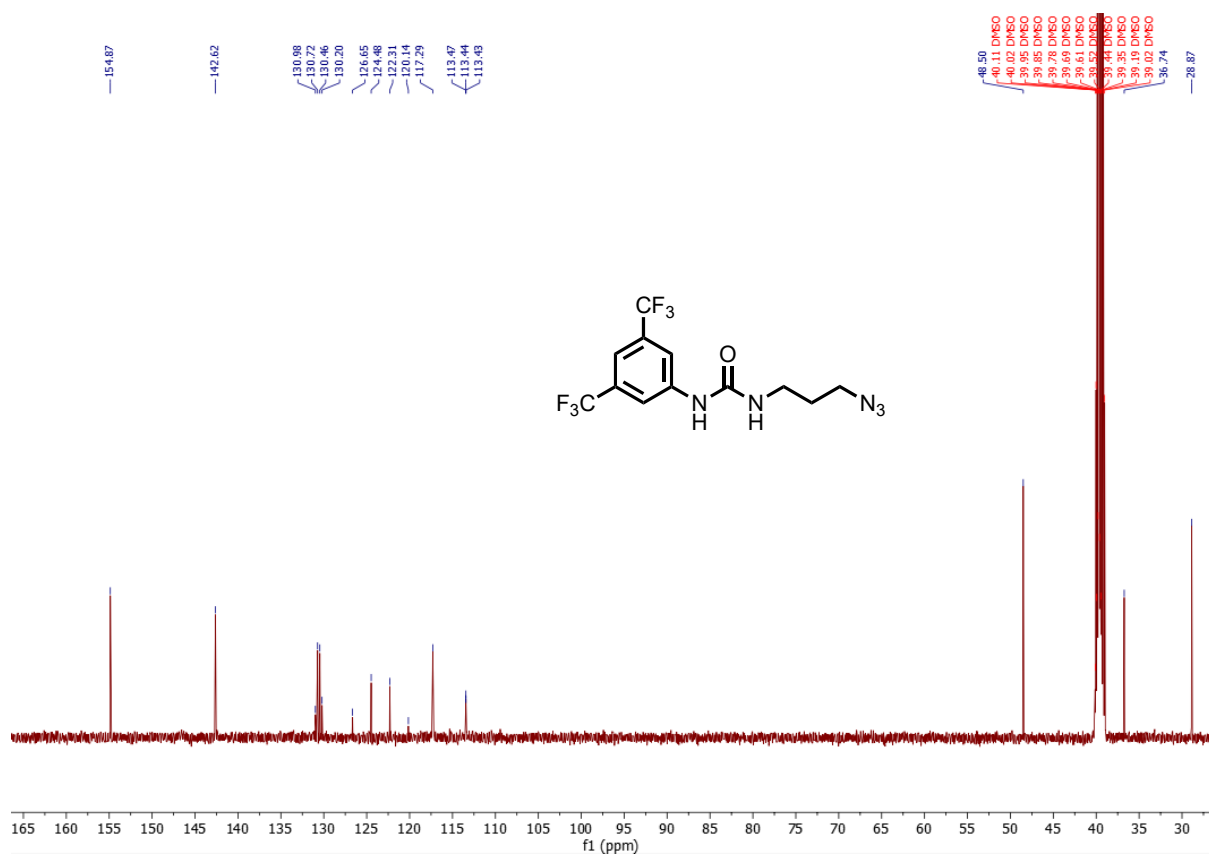


Figure A1.31: <sup>13</sup>C NMR spectrum of 1-(3-azidopropyl)-3-(3,5-bis(trifluoromethyl)phenyl)urea (49) (500 MHz, DMSO-d<sub>6</sub>).

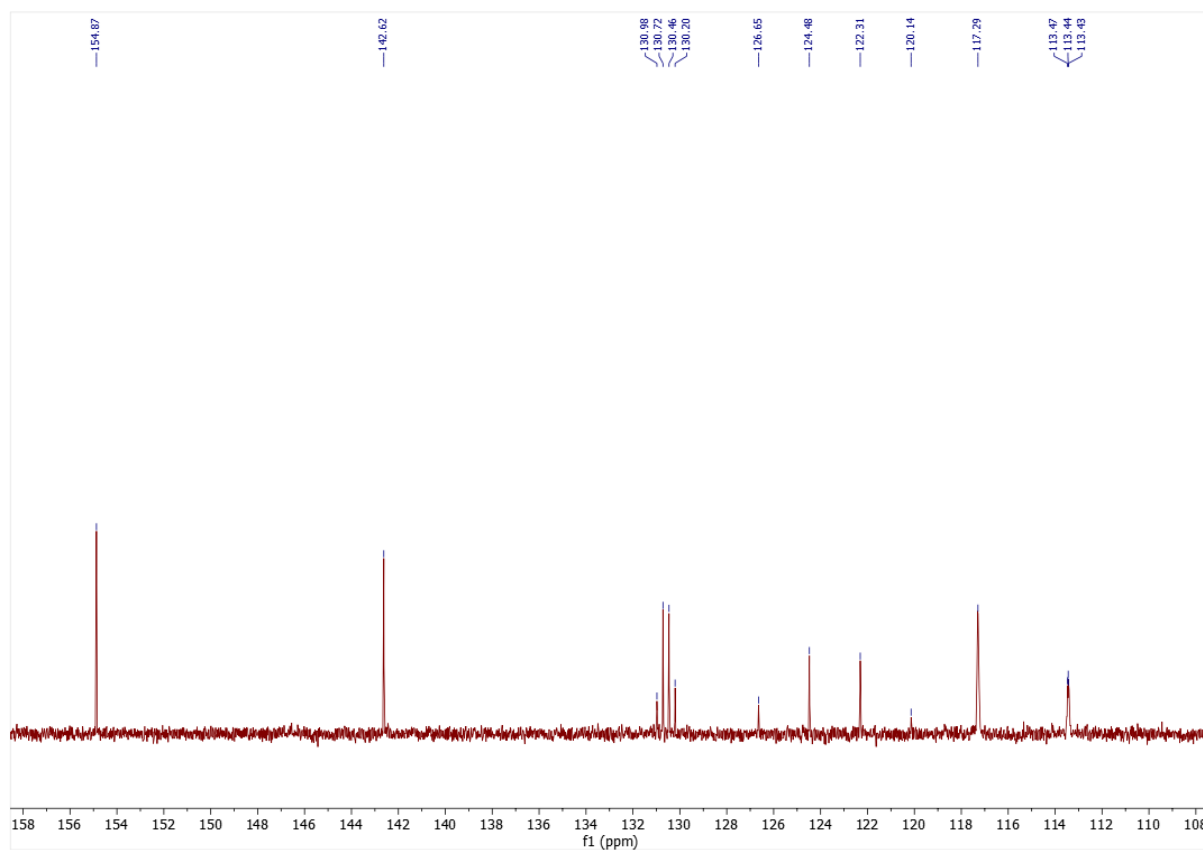


Figure A1.32: Expansion of  $^{13}\text{C}$  NMR spectrum of 1-(3-azidopropyl)-3-(3,5-bis(trifluoromethyl)phenyl)urea (**49**) (500 MHz,  $\text{DMSO-d}_6$ ).

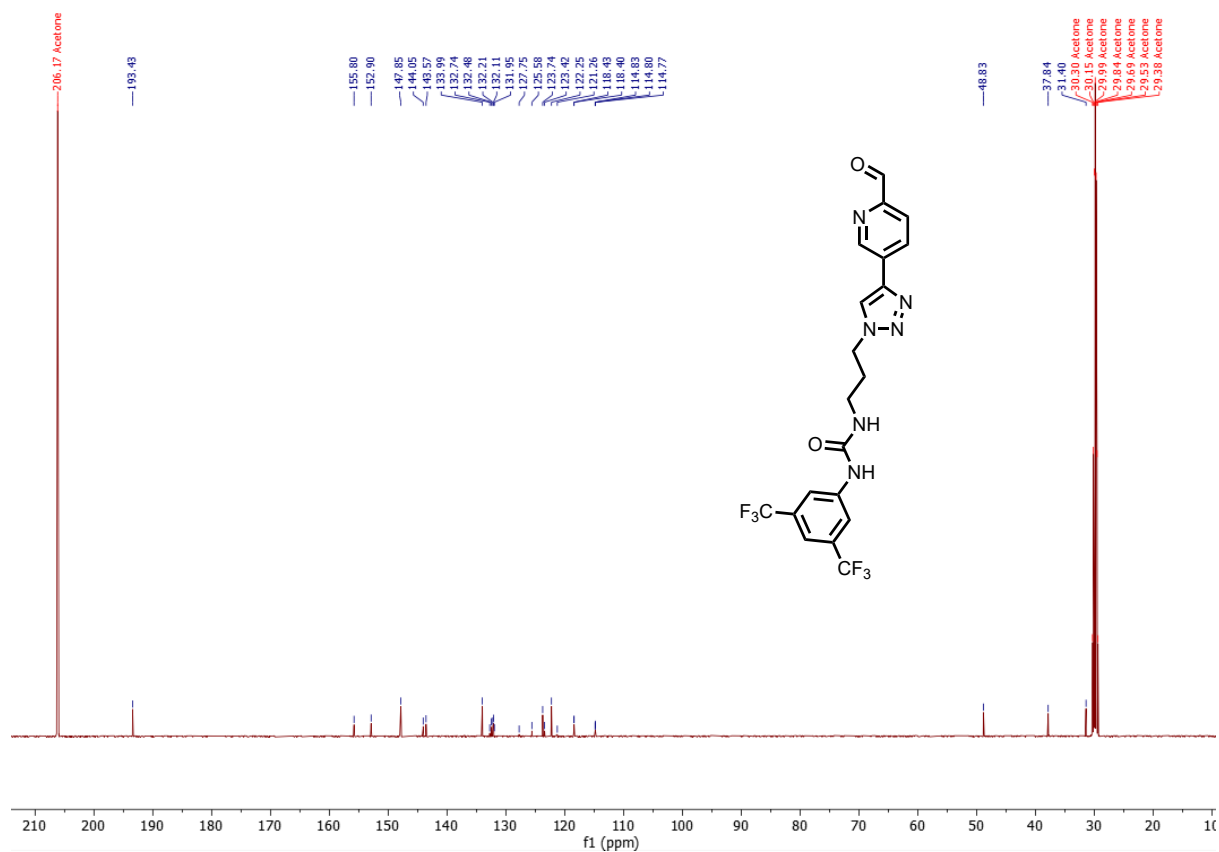


Figure A1.33: <sup>13</sup>C NMR spectrum of 1-(3,5-bis(trifluoromethyl)phenyl)-3-(3-(4-(6-formylpyridin-3-yl)-1H-1,2,3-triazol-1-yl)propyl)urea (**50**) (500 MHz, acetone-d<sub>6</sub>).

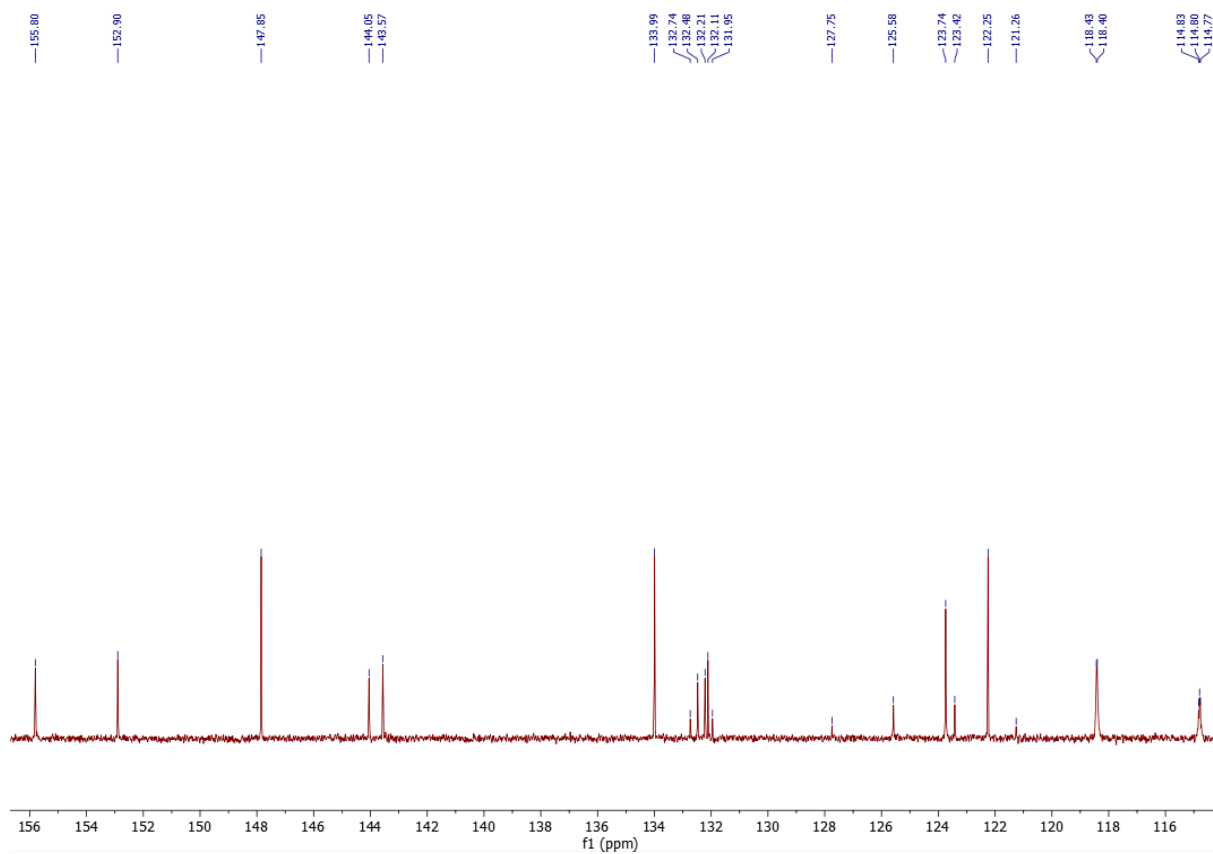


Figure A1.34: Expansion of  $^{13}\text{C}$  NMR spectrum of 1-(3,5-bis(trifluoromethyl)phenyl)-3-(3-(4-(6-formylpyridin-3-yl)-1H-1,2,3-triazol-1-yl)propyl)urea (**50**) (500 MHz, acetone- $d_6$ ).

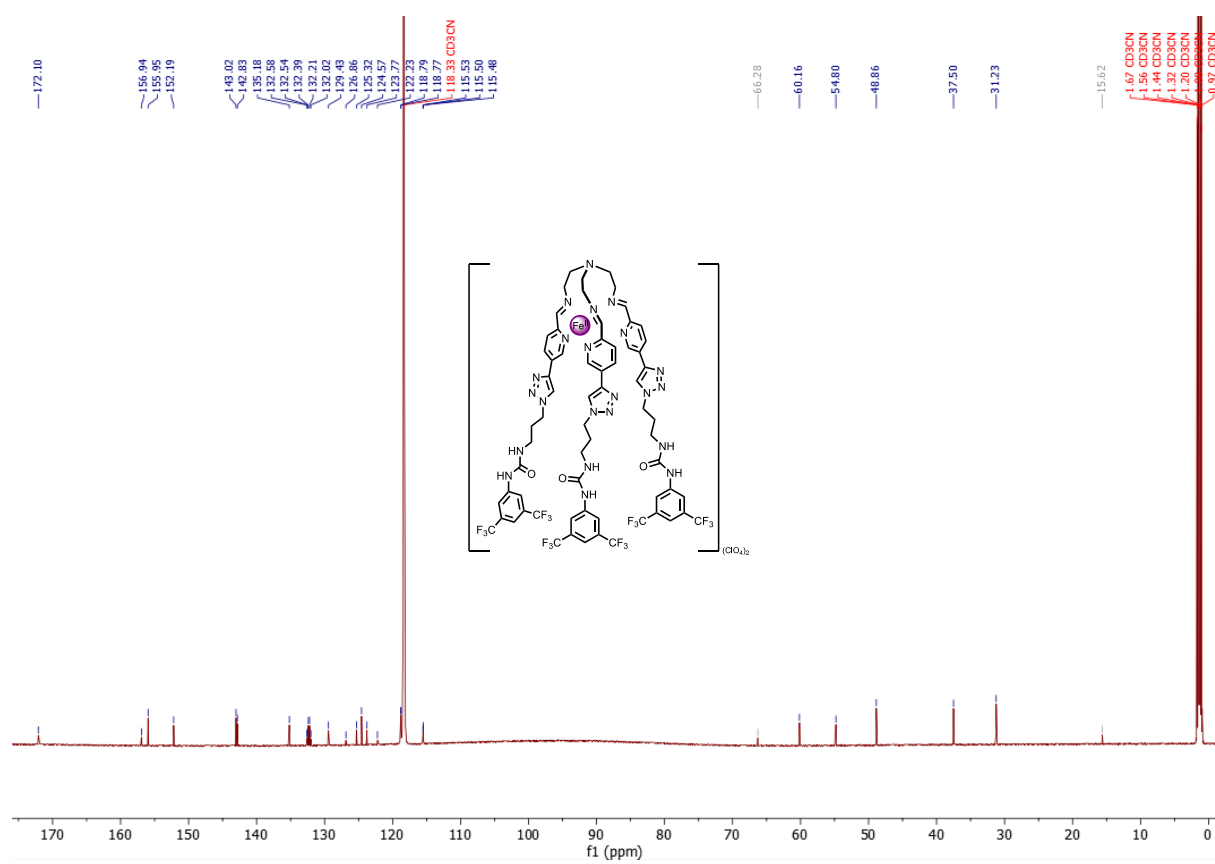


Figure A1.35: <sup>13</sup>C NMR spectrum of Fe(II)L complex **52** (700 MHz, CD<sub>3</sub>CN).



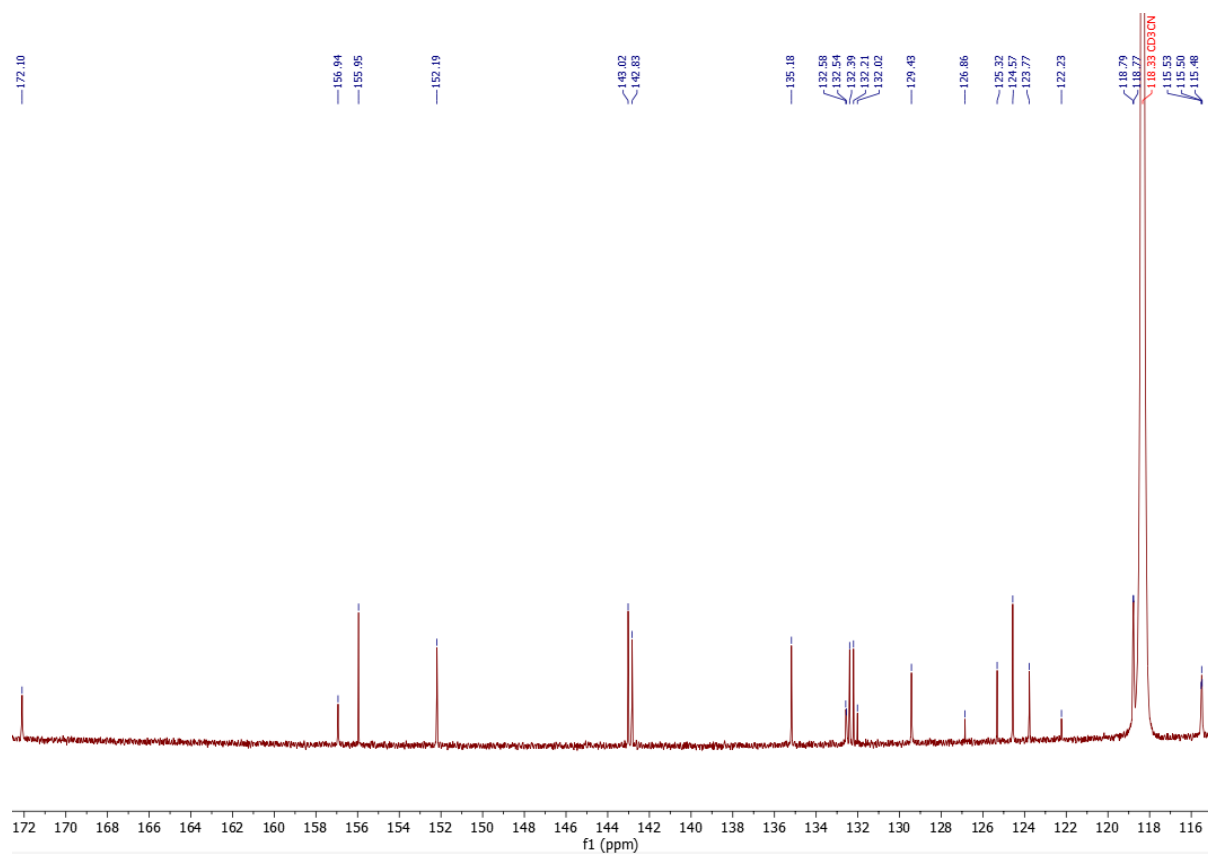


Figure A1.36: Expansion of  $^{13}\text{C}$  NMR spectrum of Fe(II)L complex **52** (110-180 ppm).

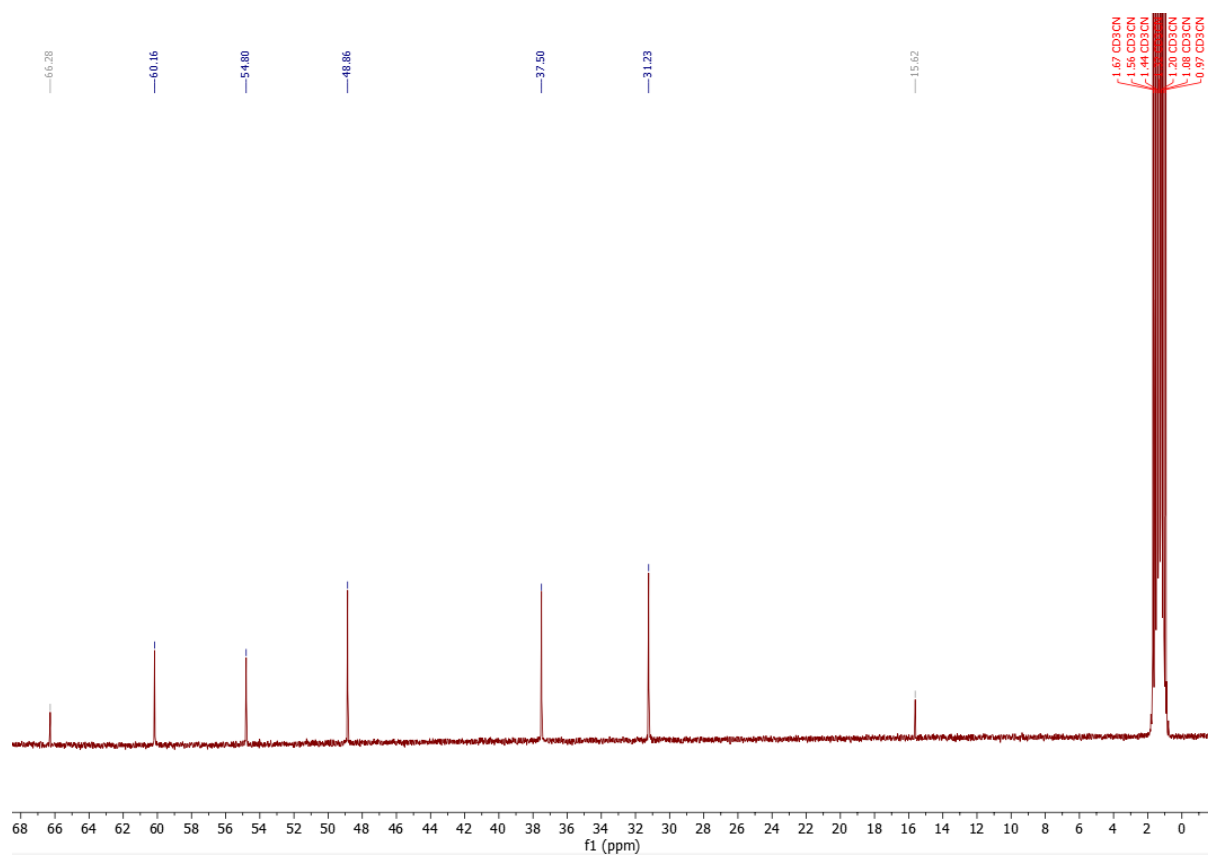


Figure A1.37: Expansion of  $^{13}\text{C}$  NMR spectrum of Fe(II)L complex **52** (0-70 ppm).

### A1.3 IR

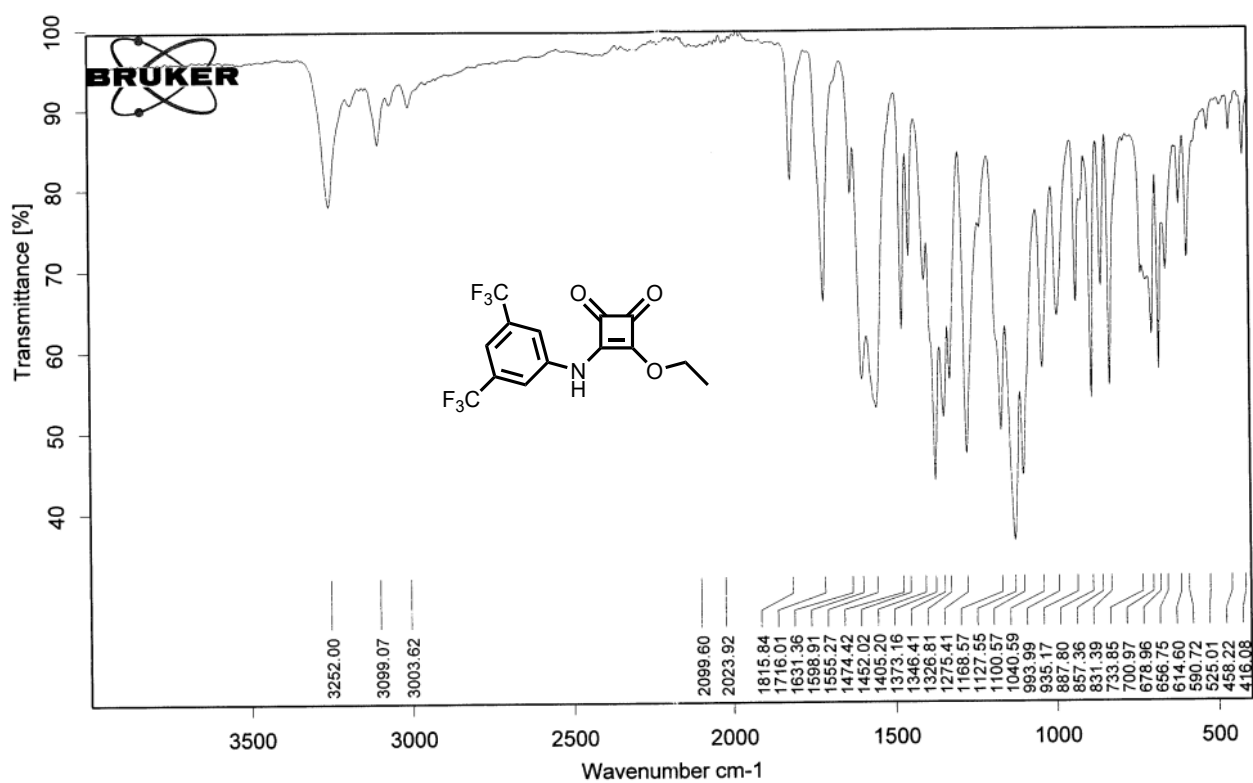


Figure A1.38: IR spectrum of 3-((3,5-bis(trifluoromethyl)phenyl)amino)-4-ethoxycyclobut-3-ene-1,2-dione (**42**).

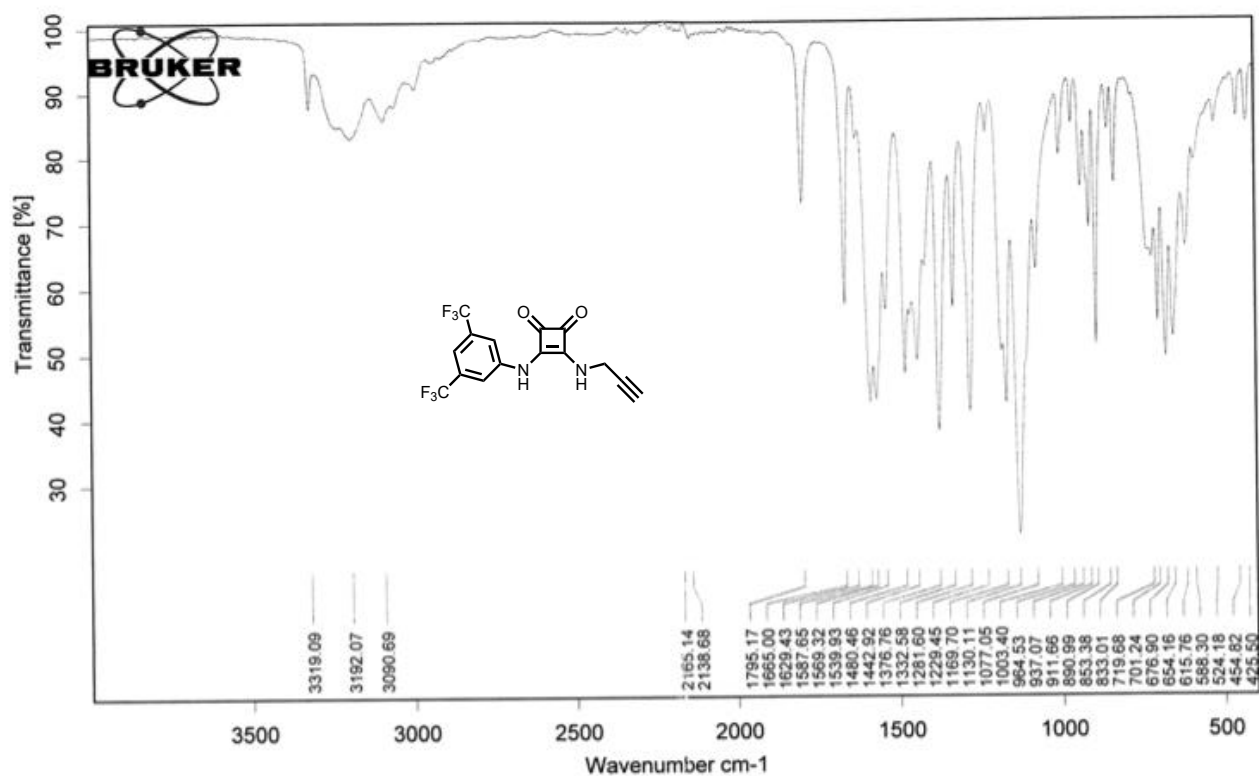


Figure A1.39: IR spectrum of 3-((3,5-bis(trifluoromethyl)phenyl)amino)-4-(prop-2-yn-1-ylamino)cyclobut-3-ene-1,2-dione (**43**).

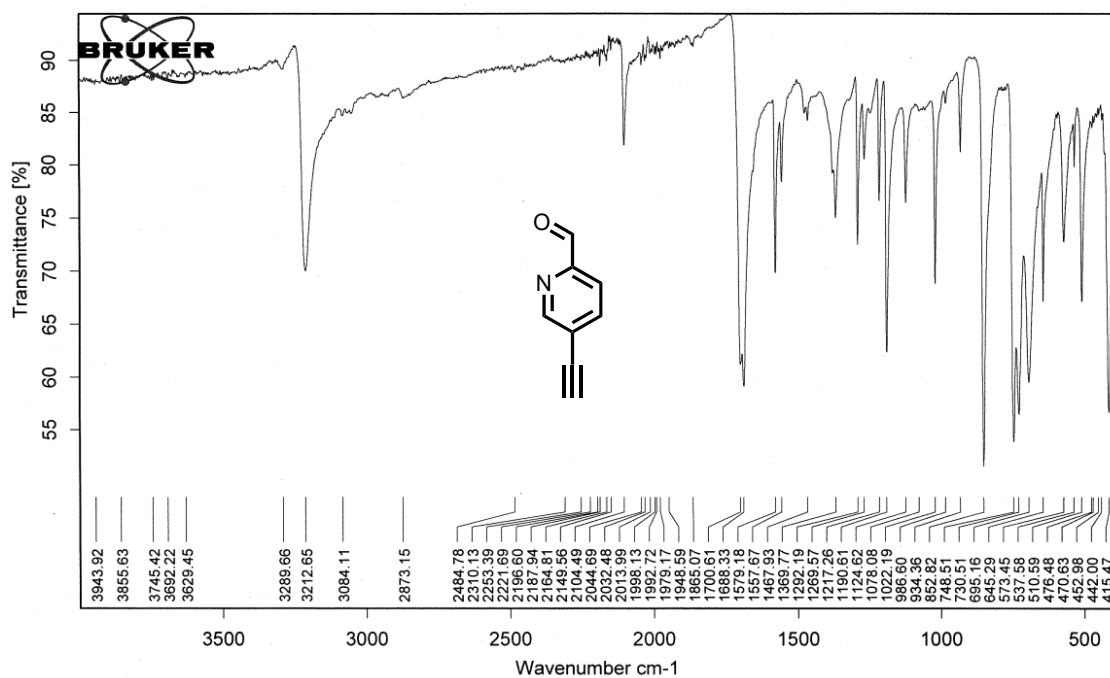


Figure A1.40: IR spectrum of 5-ethynylpicolinaldehyde (44).

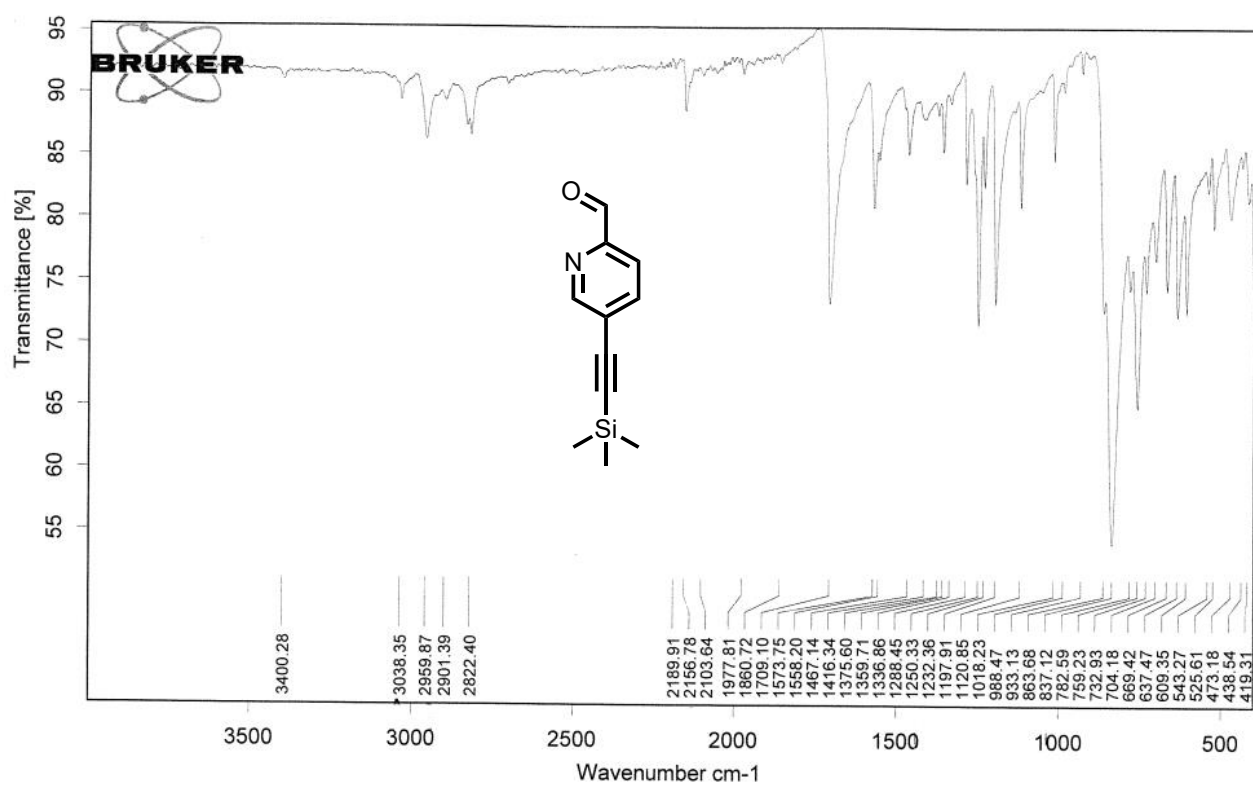


Figure A1.41: IR spectrum of 5-((trimethylsilyl)ethynyl)picolinaldehyde (46).

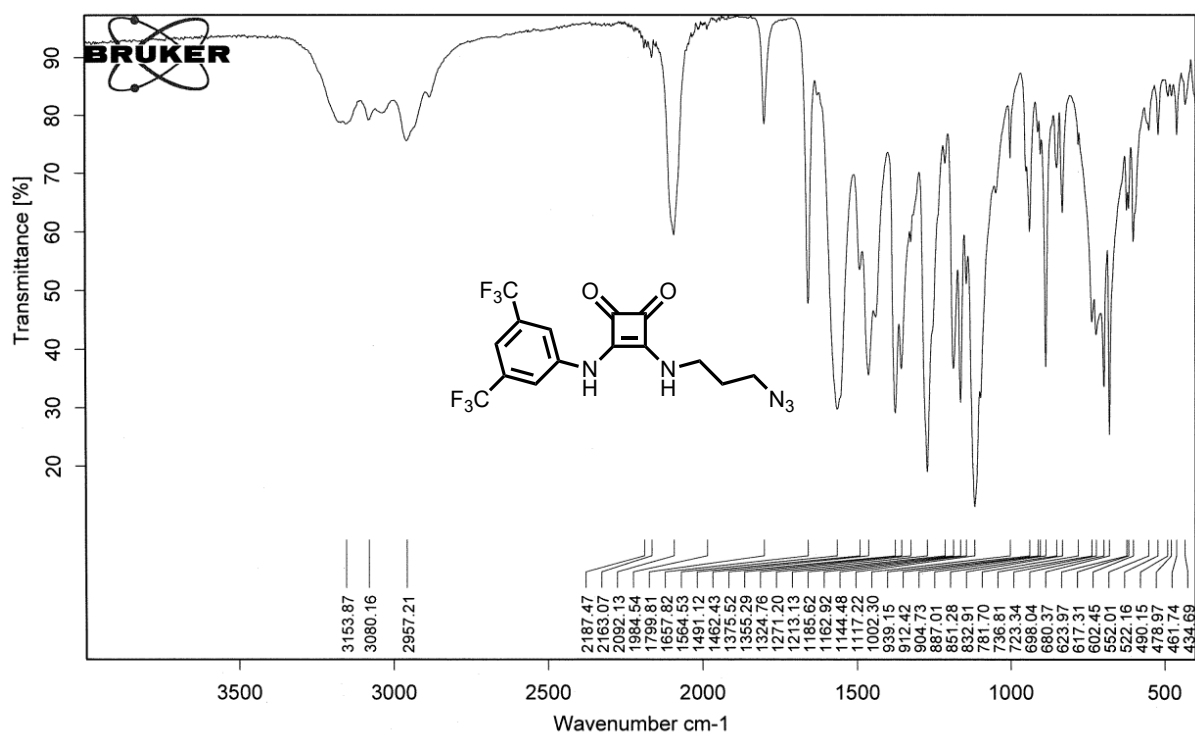


Figure A1.42: IR spectrum of 3-((3-Azidopropyl)amino)-4-((3,5-bis(trifluoromethyl)phenyl)amino)cyclobut-3-ene-1,2-dione (47).

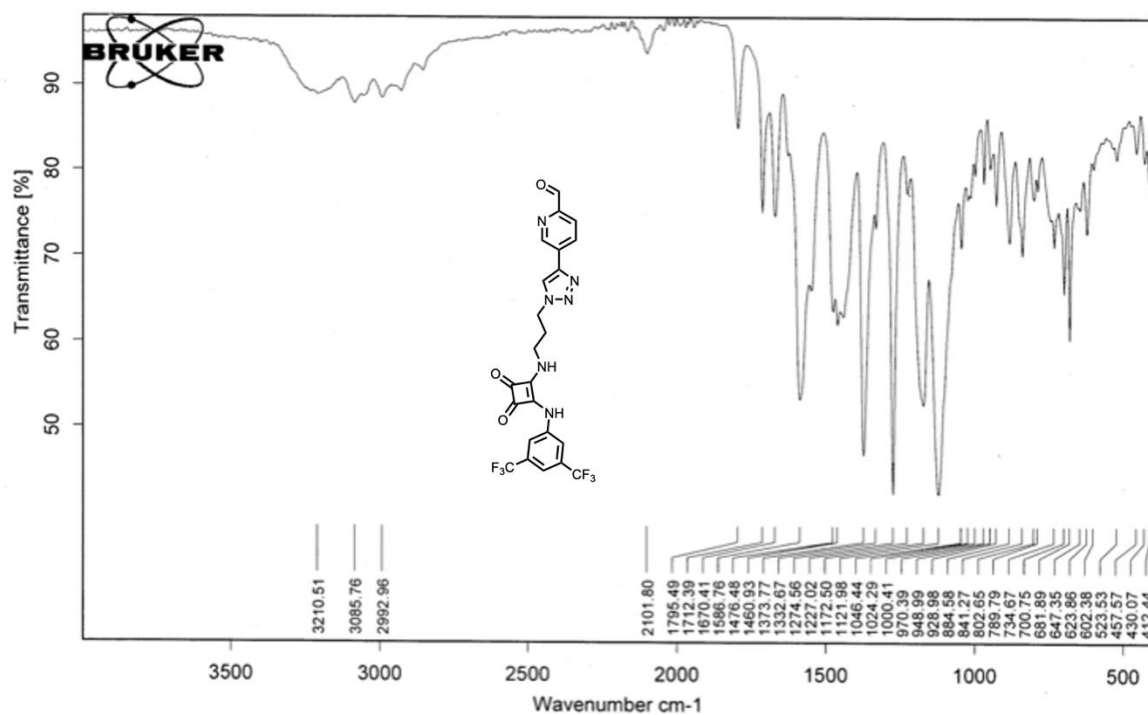


Figure A1.43: IR spectrum of 5-(1-(3-((2-((3,5-bis(trifluoromethyl)phenyl)amino)-3,4-dioxocyclobut-1-en-1-yl)amino)propyl)-1H-1,2,3-triazol-4-yl)picolinaldehyde (**48**).



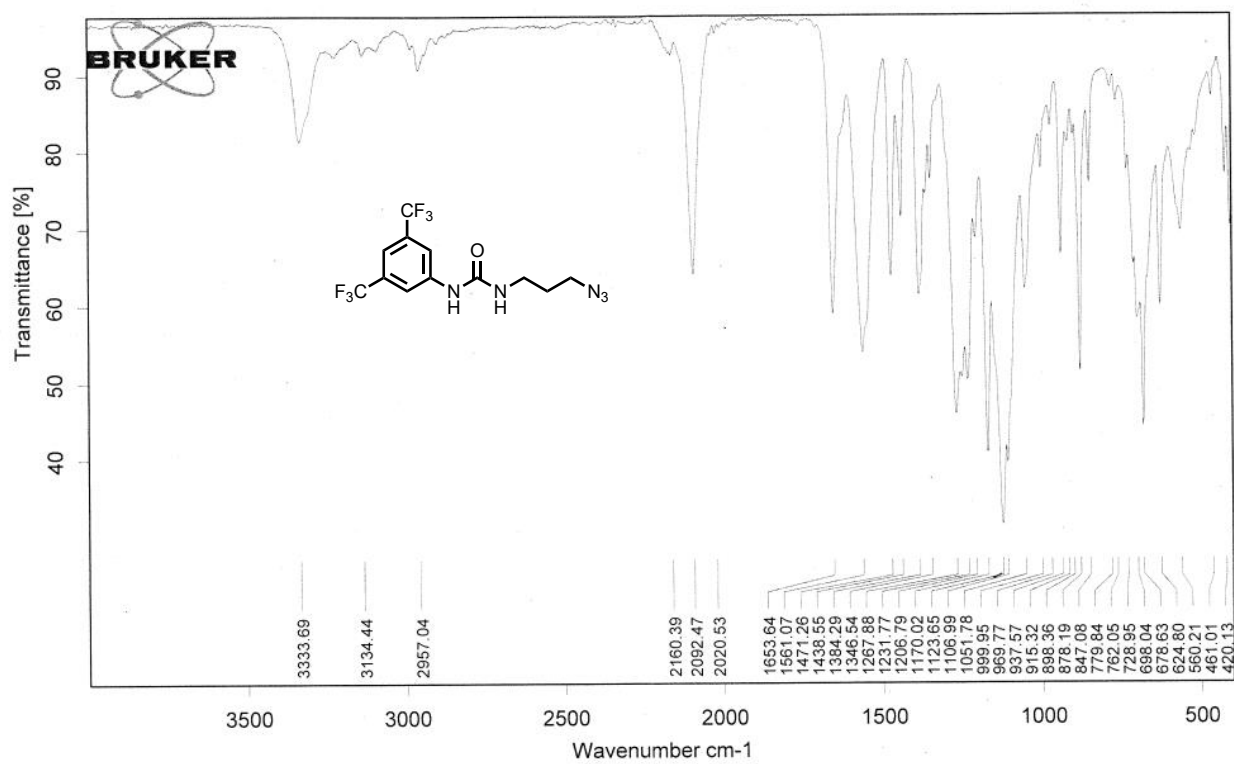


Figure A1.44: IR spectrum of 1-(3-azidopropyl)-3-(3,5-bis(trifluoromethyl)phenyl)urea (**49**).

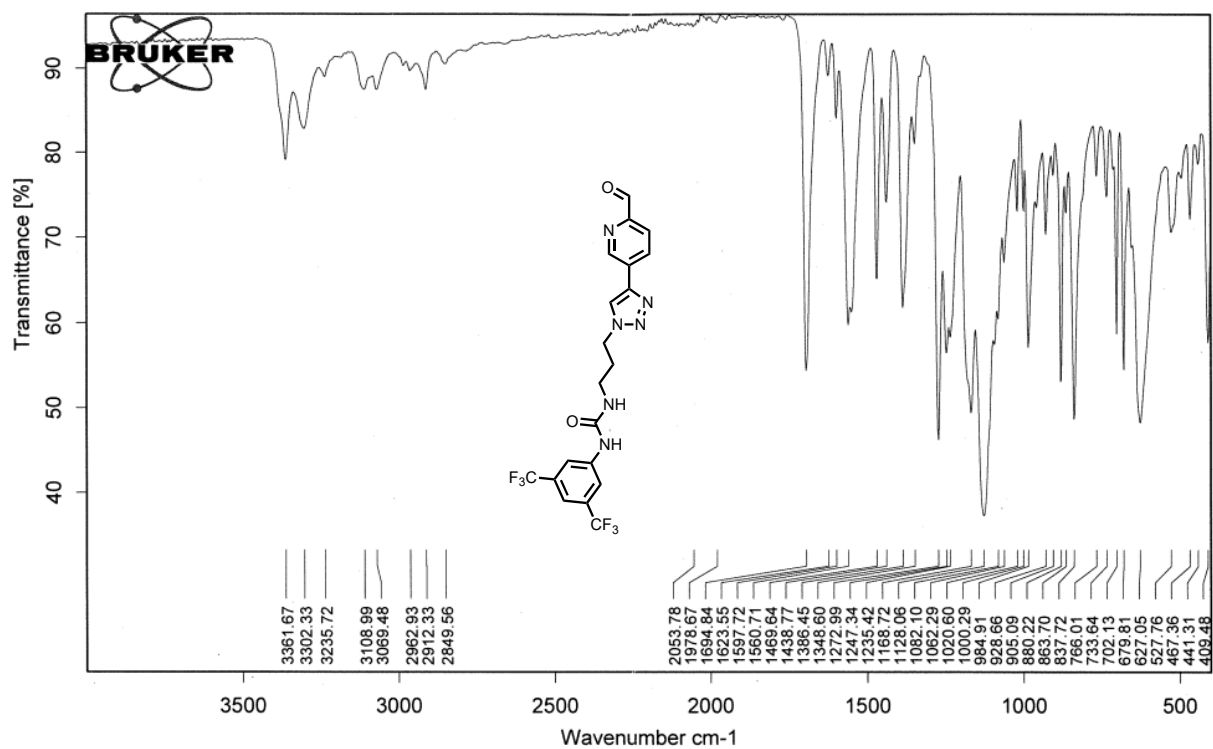


Figure A1.45: IR spectrum of 1-(3,5-bis(trifluoromethyl)phenyl)-3-(3-(4-(6-formylpyridin-3-yl)-1H-1,2,3-triazol-1-yl)propyl)urea (**50**).

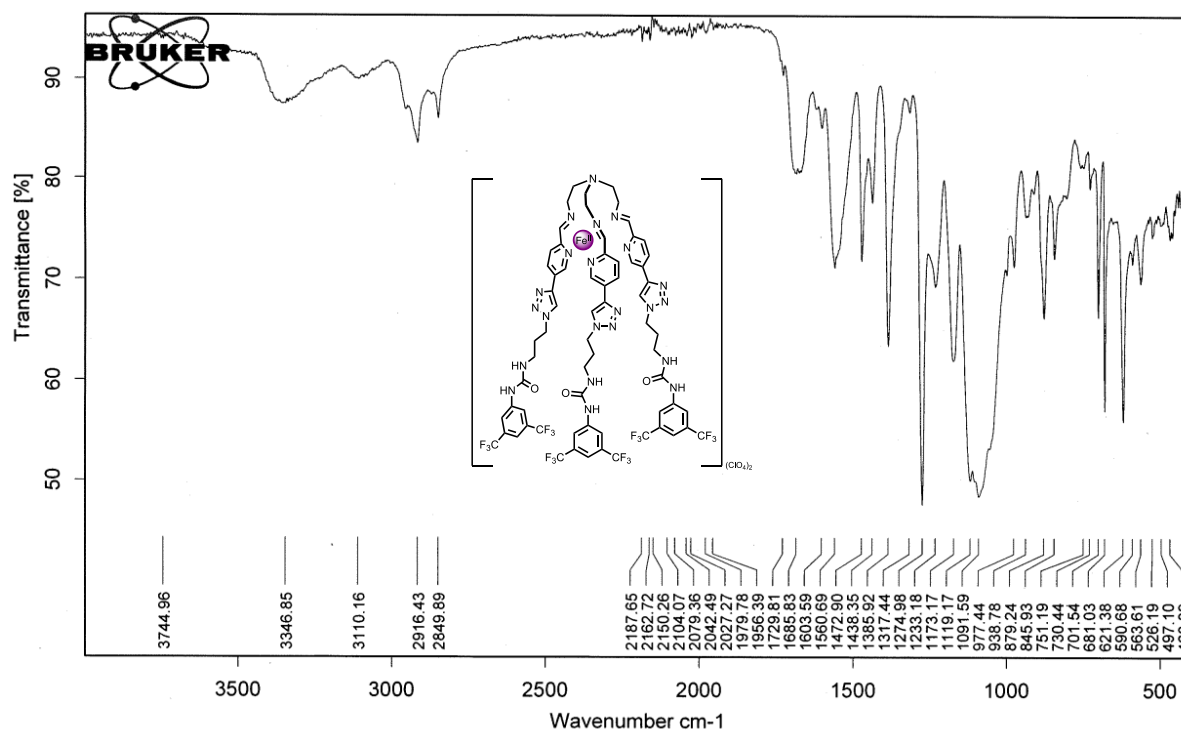


Figure A1.46: IR spectrum of Fe(II)L complex 52.

## A1.4 MS

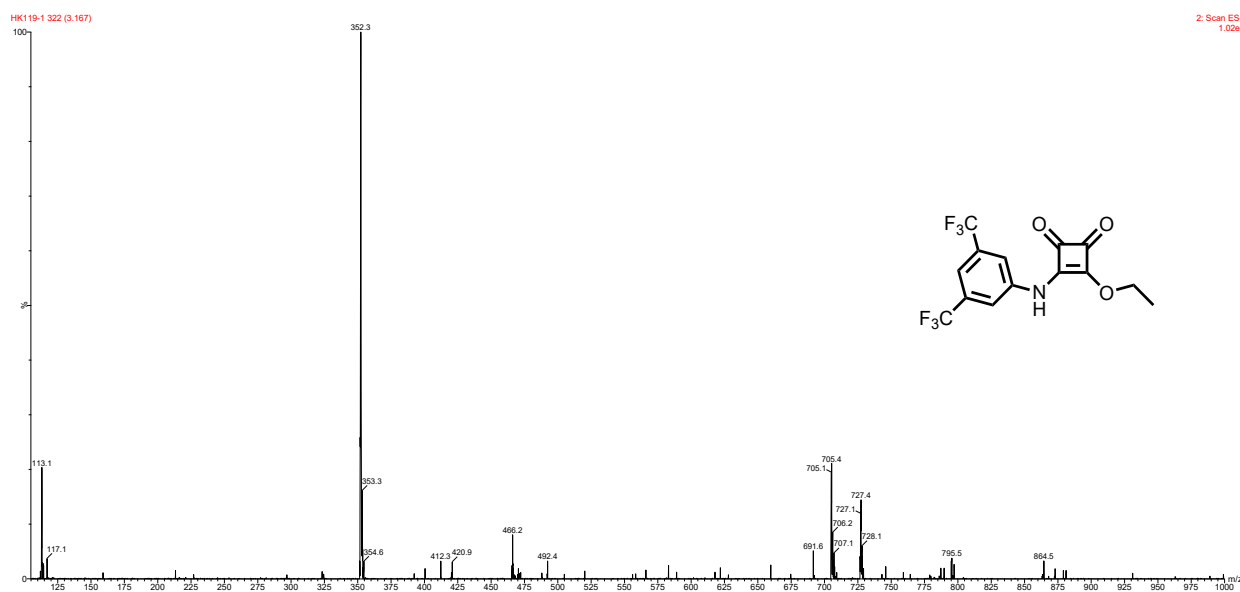


Figure A1.47: Low-resolution mass spectrum of 3-((3,5-bis(trifluoromethyl)phenyl)amino)-4-ethoxycyclobut-3-ene-1,2-dione (**42**) (ESI+).

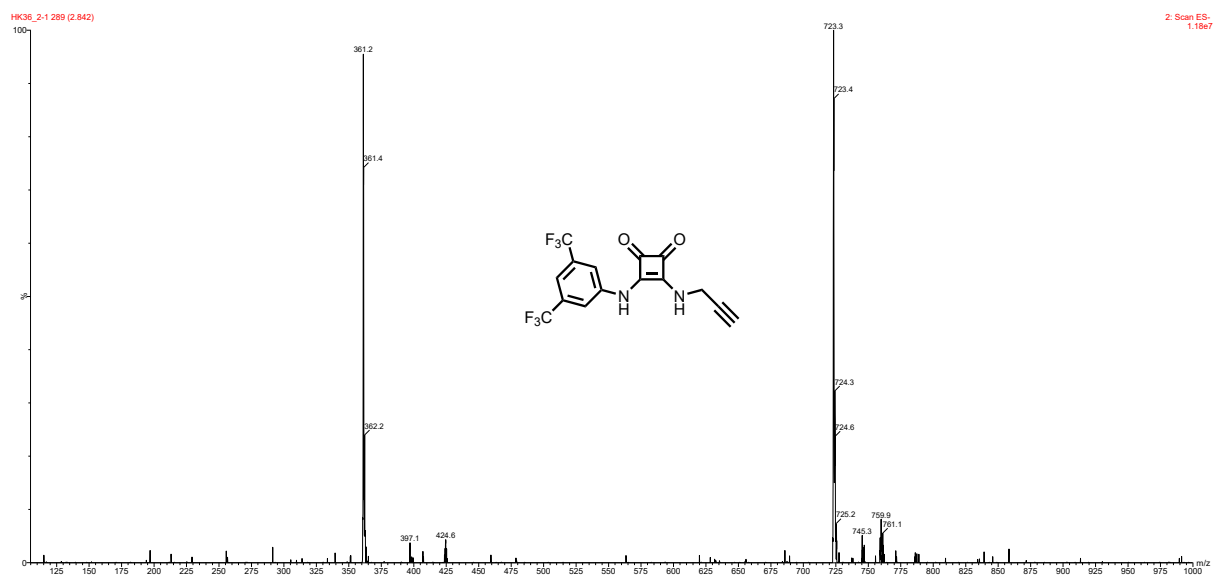


Figure A1.48: Low-resolution mass spectrum of 3-((3,5-bis(trifluoromethyl)phenyl)amino)-4-(prop-2-yn-1-ylamino)cyclobut-3-ene-1,2-dione (**43**) (ESI-).

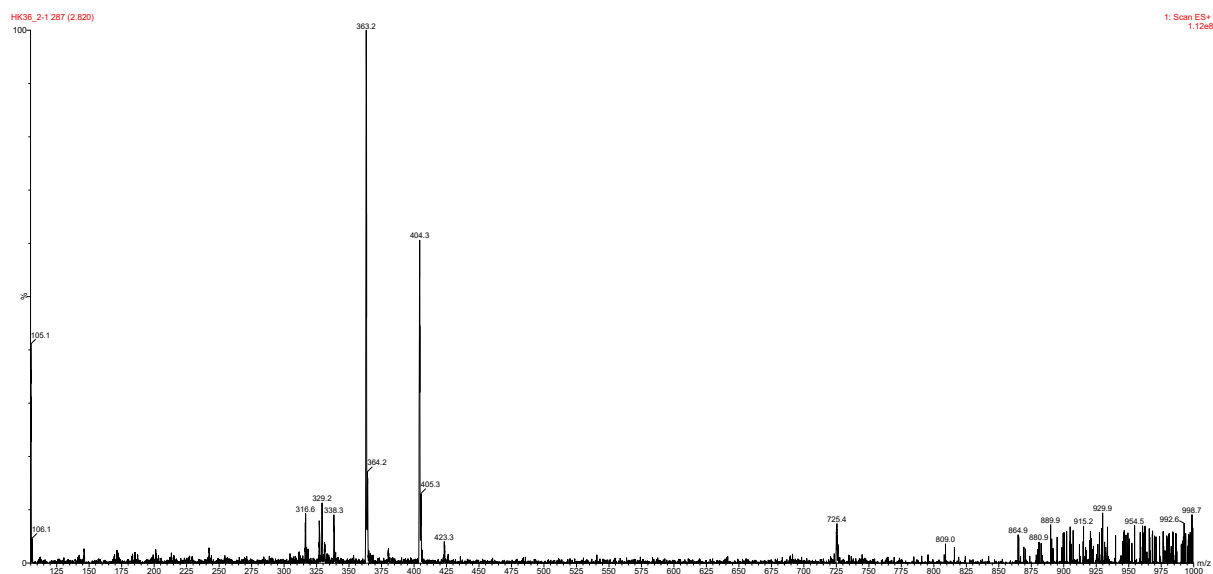


Figure A1.49: Low-resolution mass spectrum of 3-((3,5-bis(trifluoromethyl)phenyl)amino)-4-(prop-2-yn-1-ylamino)cyclobut-3-ene-1,2-dione (**43**) (ESI+).

T: FTMS + p ESI Full ms [120.0000-1800.0000]

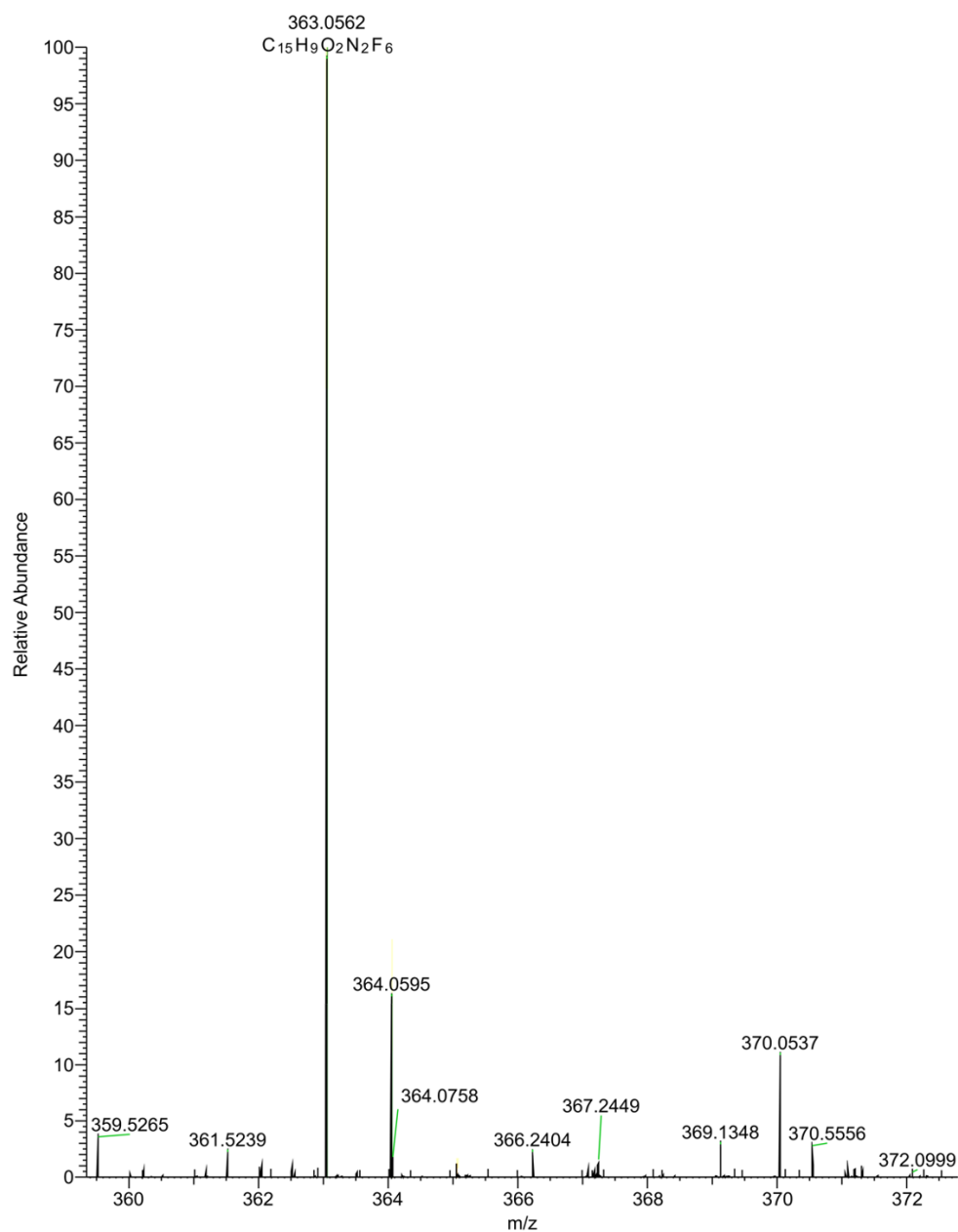


Figure A1.50: High-resolution mass spectrum of 3-((3,5-bis(trifluoromethyl)phenyl)amino)-4-(prop-2-yn-1-ylamino)cyclobut-3-ene-1,2-dione (**43**) (ESI+).

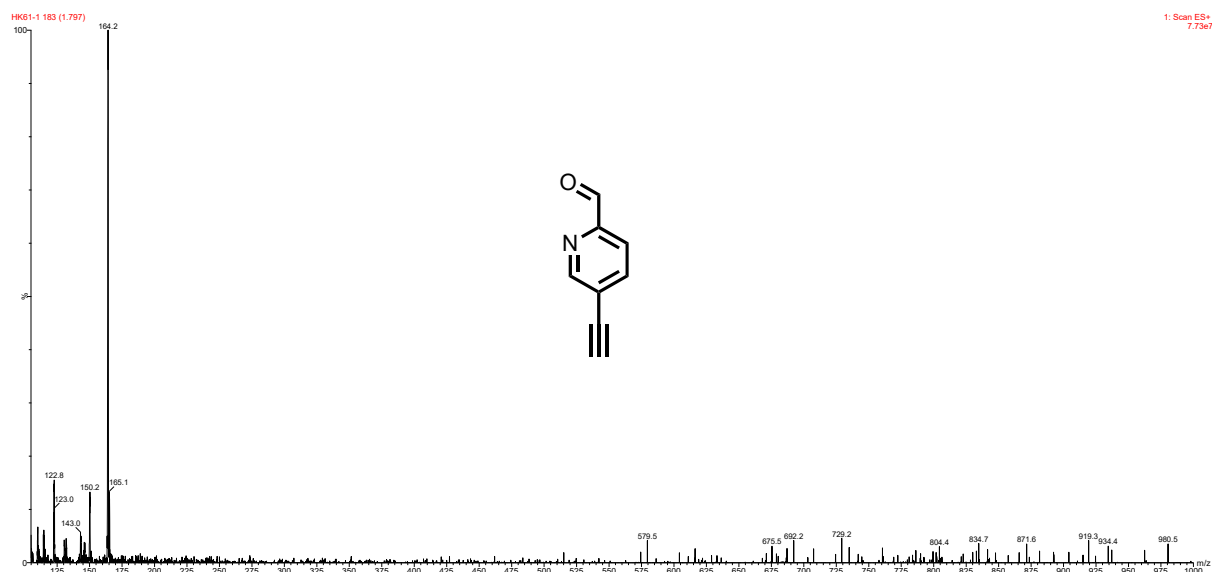


Figure A1.51: Low-res mass spectrum of 5-ethynylpicolinaldehyde (**44**) (ESI+).



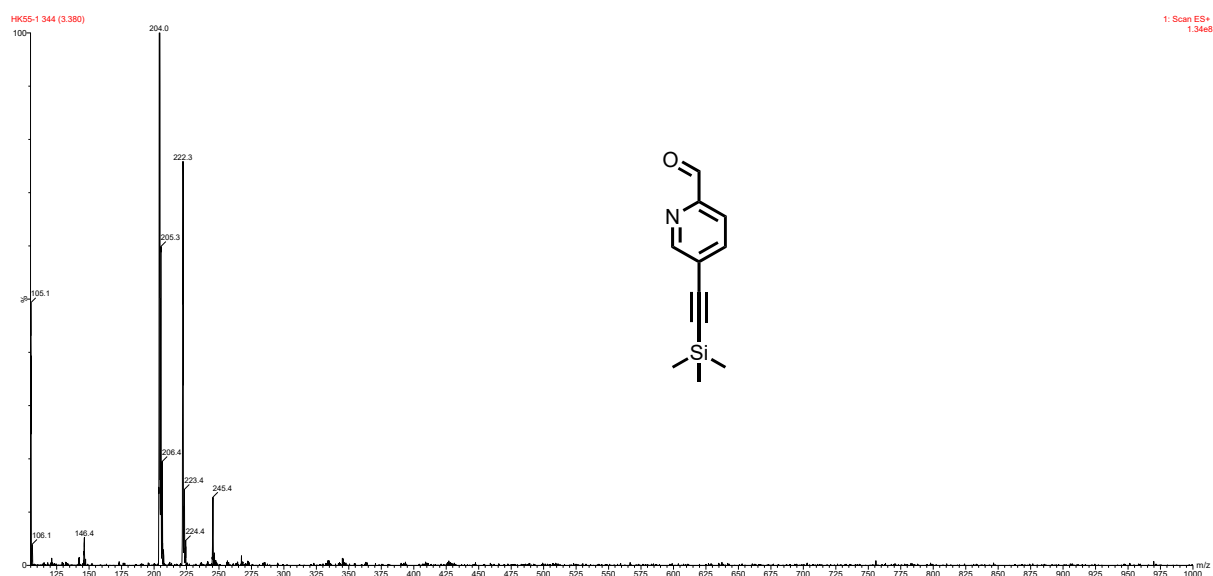


Figure A1.52: Low-resolution mass spectrum of 5-(trimethylsilyl)ethynylpicolinaldehyde (46) (ESI+).

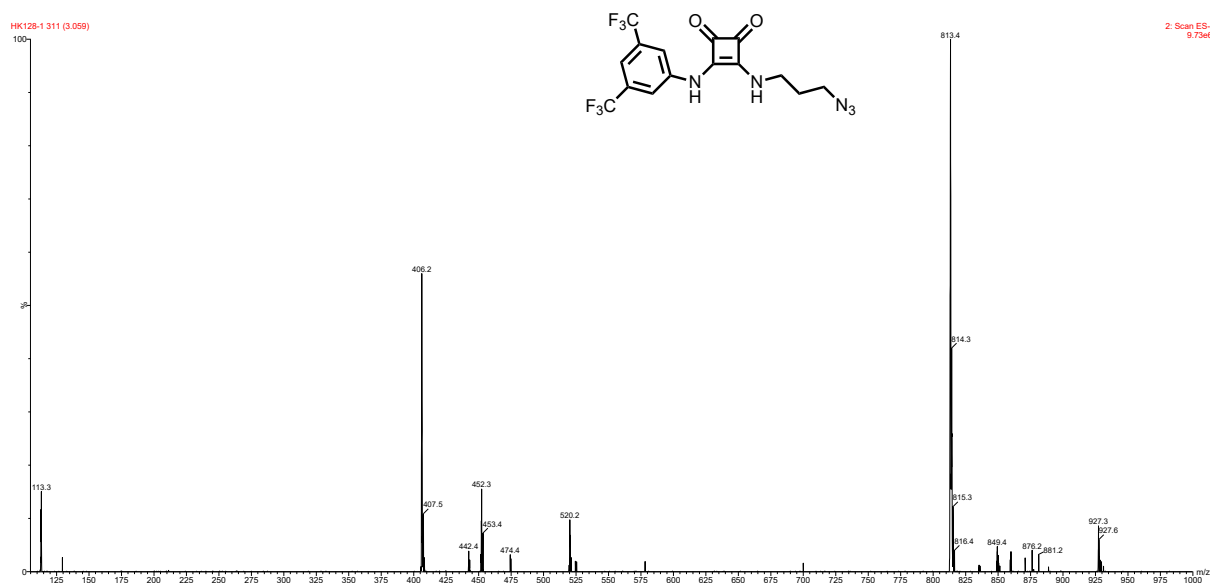
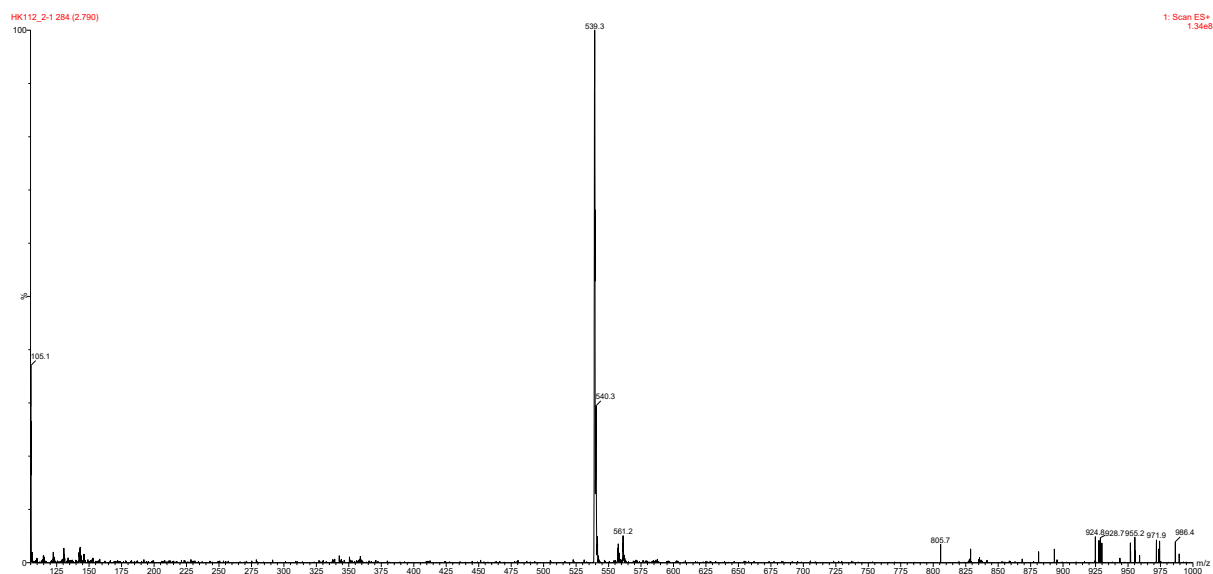
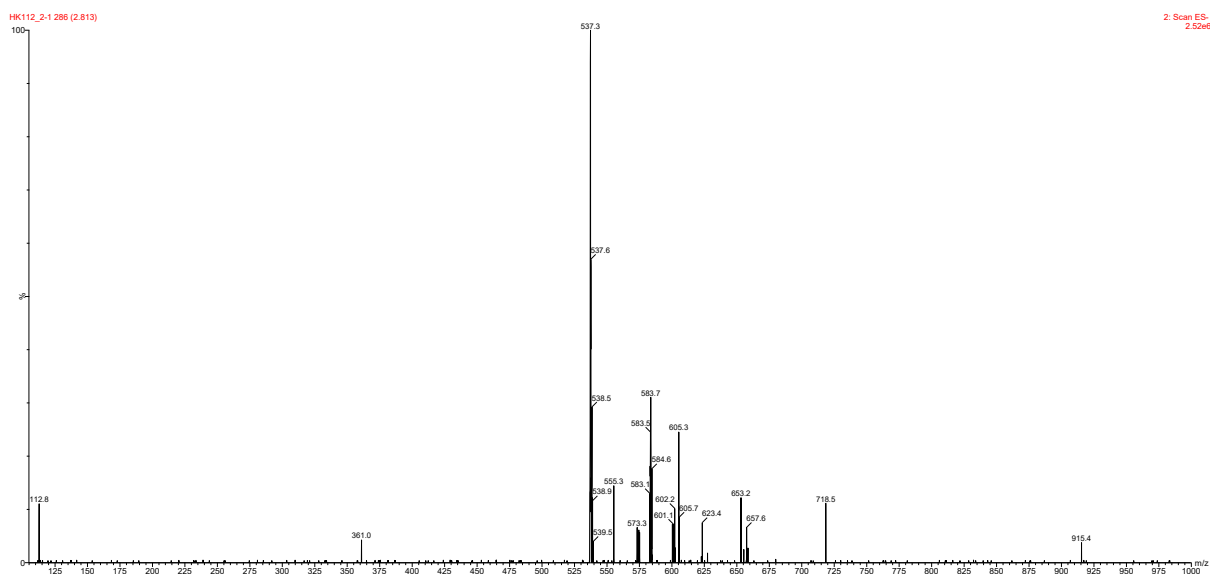


Figure A1.53: Low-resolution mass spectrum of 3-((3-azidopropyl)amino)-4-((3,5-bis(trifluoromethyl)phenyl)amino)cyclobut-3-ene-1,2-dione (**47**) (ESI-).



*Figure A1.54: Low-resolution mass spectrum of 5-(1-(3-((2-((3,5-bis(trifluoromethyl)phenyl)amino)-3,4-dioxocyclobut-1-en-1-yl)amino)propyl)-1H-1,2,3-triazol-4-yl)picolinaldehyde (**48**) (ESI+).*



*Figure A1.55: Low-resolution mass spectrum of 5-(1-(3-((2-((3,5-bis(trifluoromethyl)phenyl)amino)-3,4-dioxocyclobut-1-en-1-yl)amino)propyl)-1H-1,2,3-triazol-4-yl)picolinaldehyde (**48**) (ESI-).*

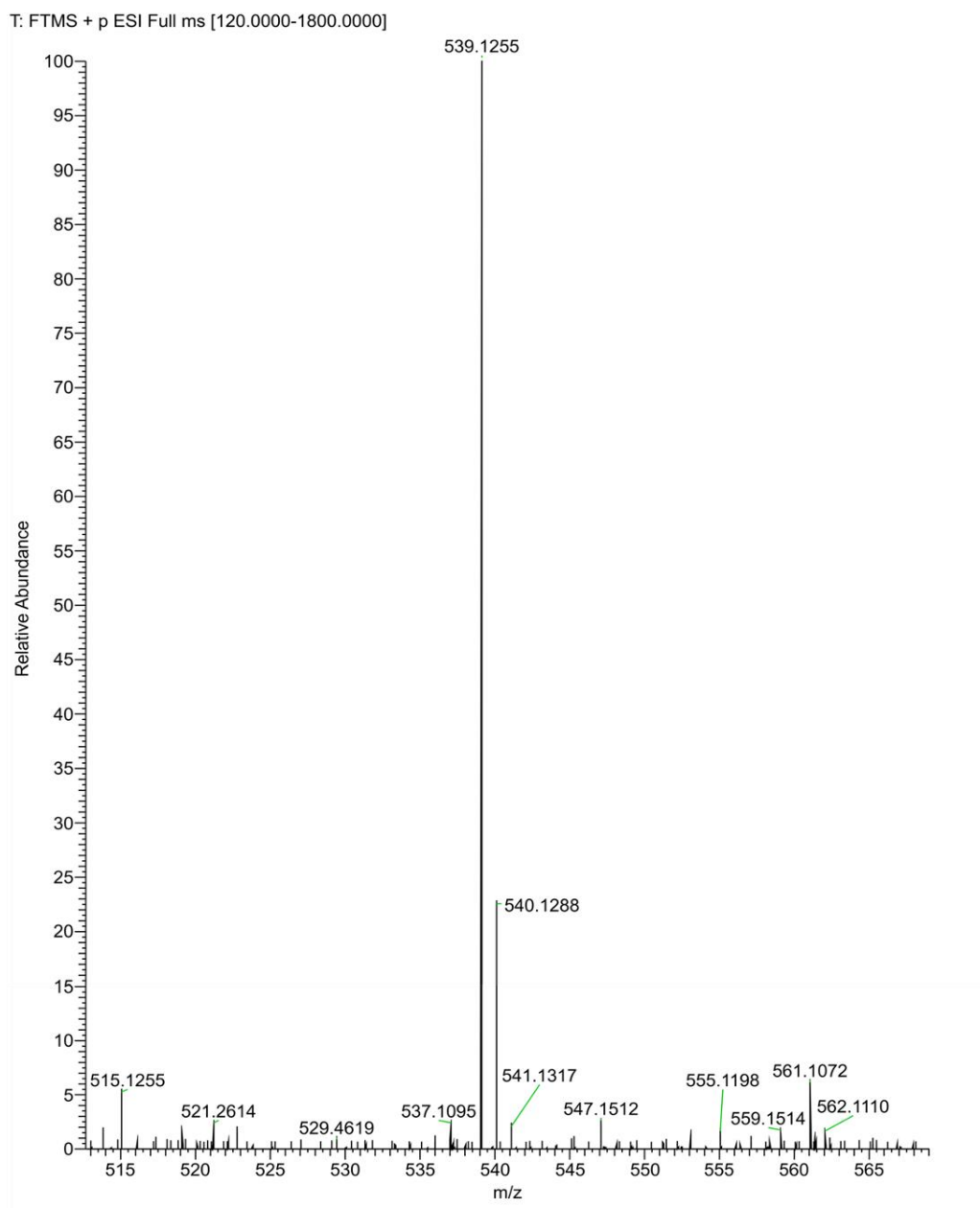


Figure A1.56: High-resolution mass spectrum of 5-(1-(3-((2-((3,5-bis(trifluoromethyl)phenyl)amino)-3,4-dioxocyclobut-1-en-1-yl)amino)propyl)-1H-1,2,3-triazol-4-yl)picolinaldehyde (**48**) (ESI+).

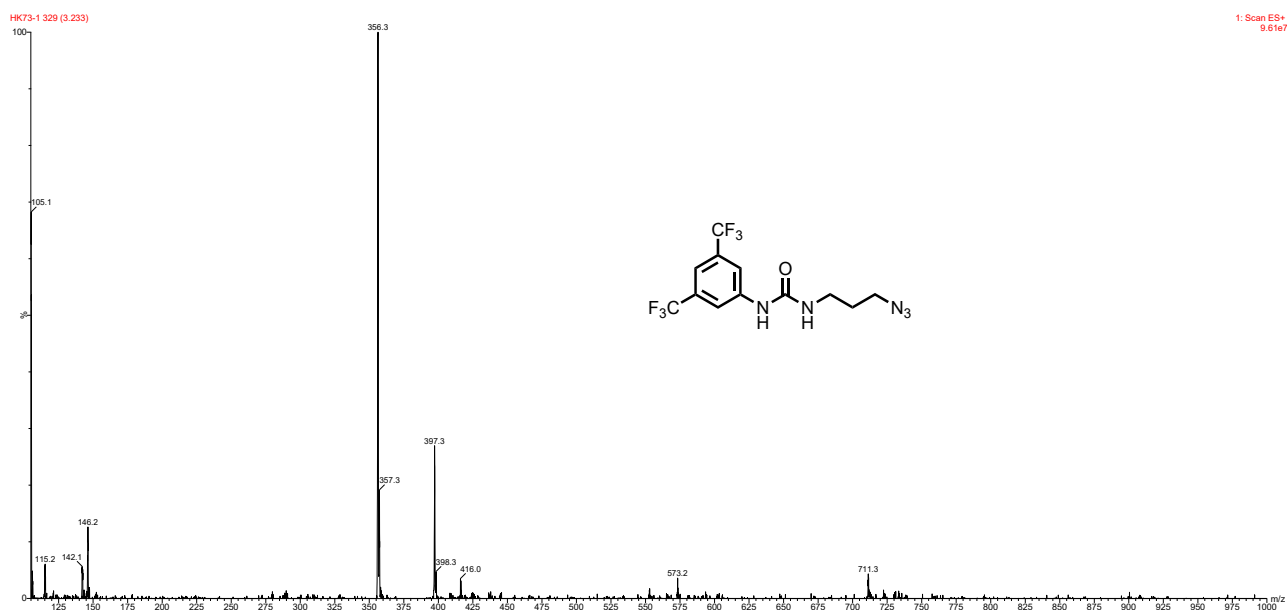


Figure A1.57: Low-resolution mass spectrum of 1-(3-azidopropyl)-3-(3,5-bis(trifluoromethyl)phenyl)urea (**49**) (ESI+).

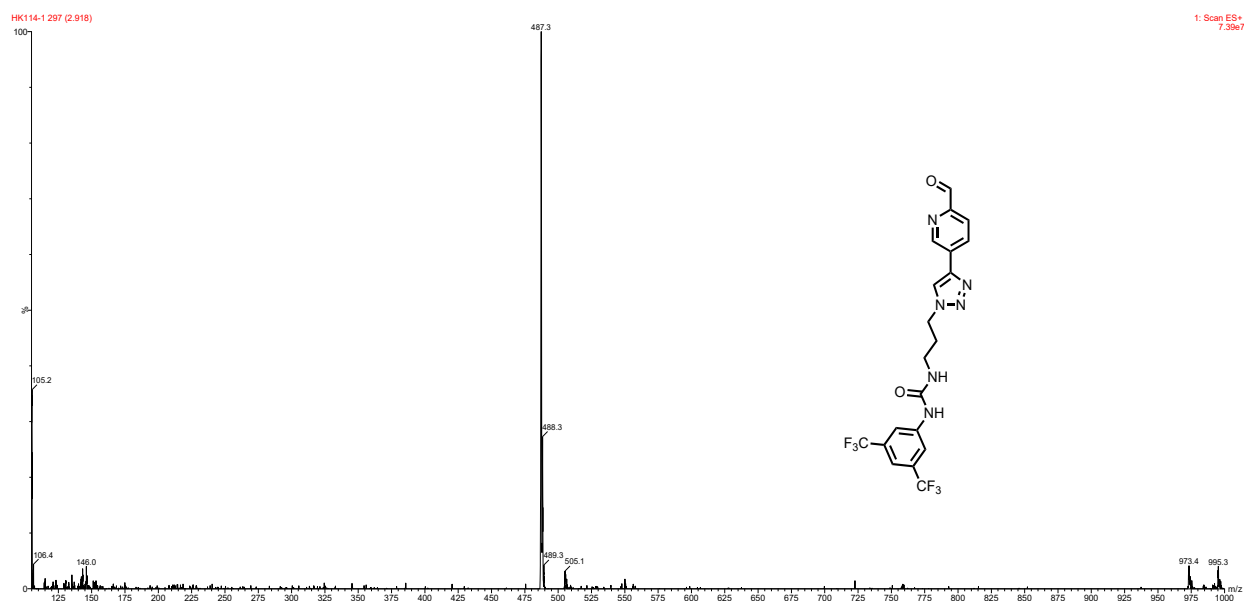


Figure A1.58: Low-resolution mass spectrum of 1-(3,5-bis(trifluoromethyl)phenyl)-3-(3-(4-(6-formylpyridin-3-yl)-1H-1,2,3-triazol-1-yl)propyl)urea (**50**) (ESI+).

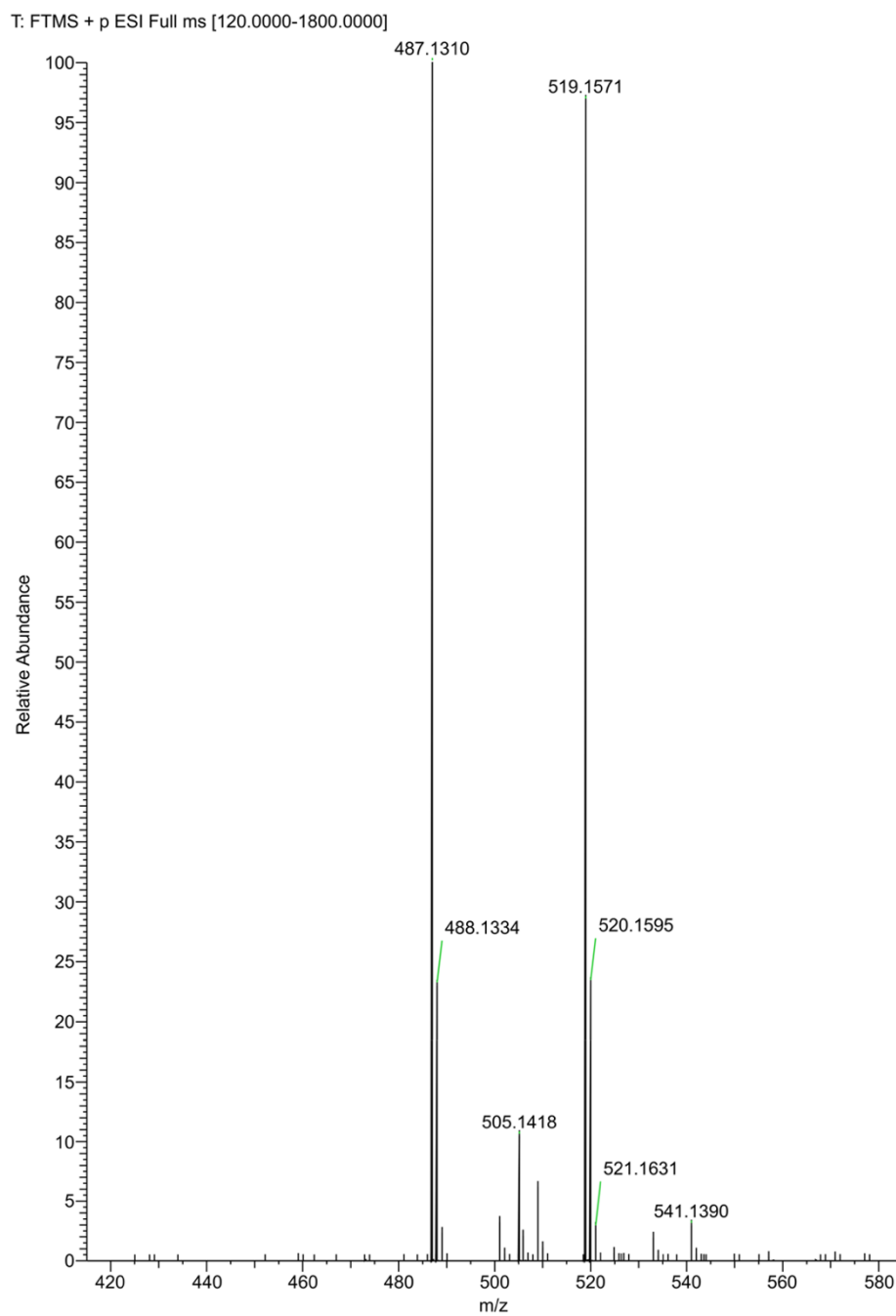


Figure A1.59: High-resolution mass spectrum of 1-(3,5-bis(trifluoromethyl)phenyl)-3-(3-(4-(6-formylpyridin-3-yl)-1H-1,2,3-triazol-1-yl)propyl)urea (**50**) (ESI+).



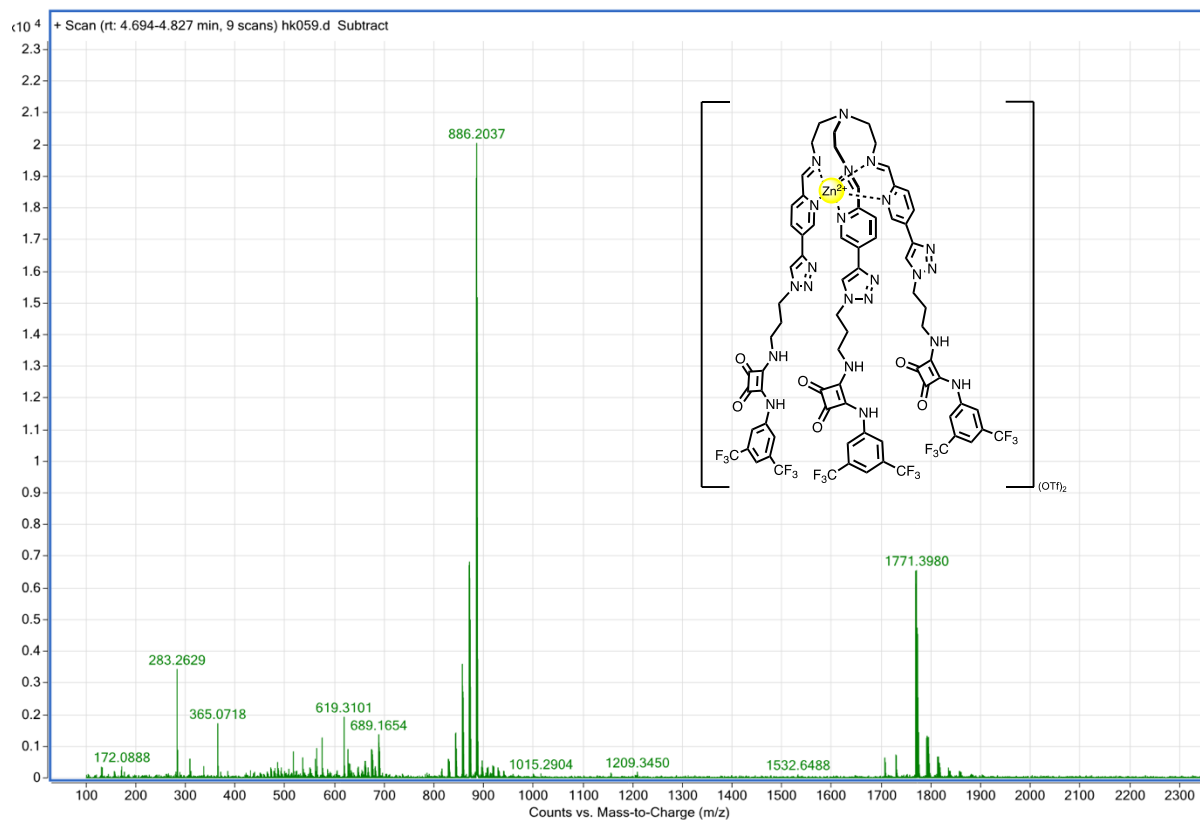


Figure A1.60: High-resolution mass spectrum of Zn(II)L complex **51** (Q-ToF, ESI+).

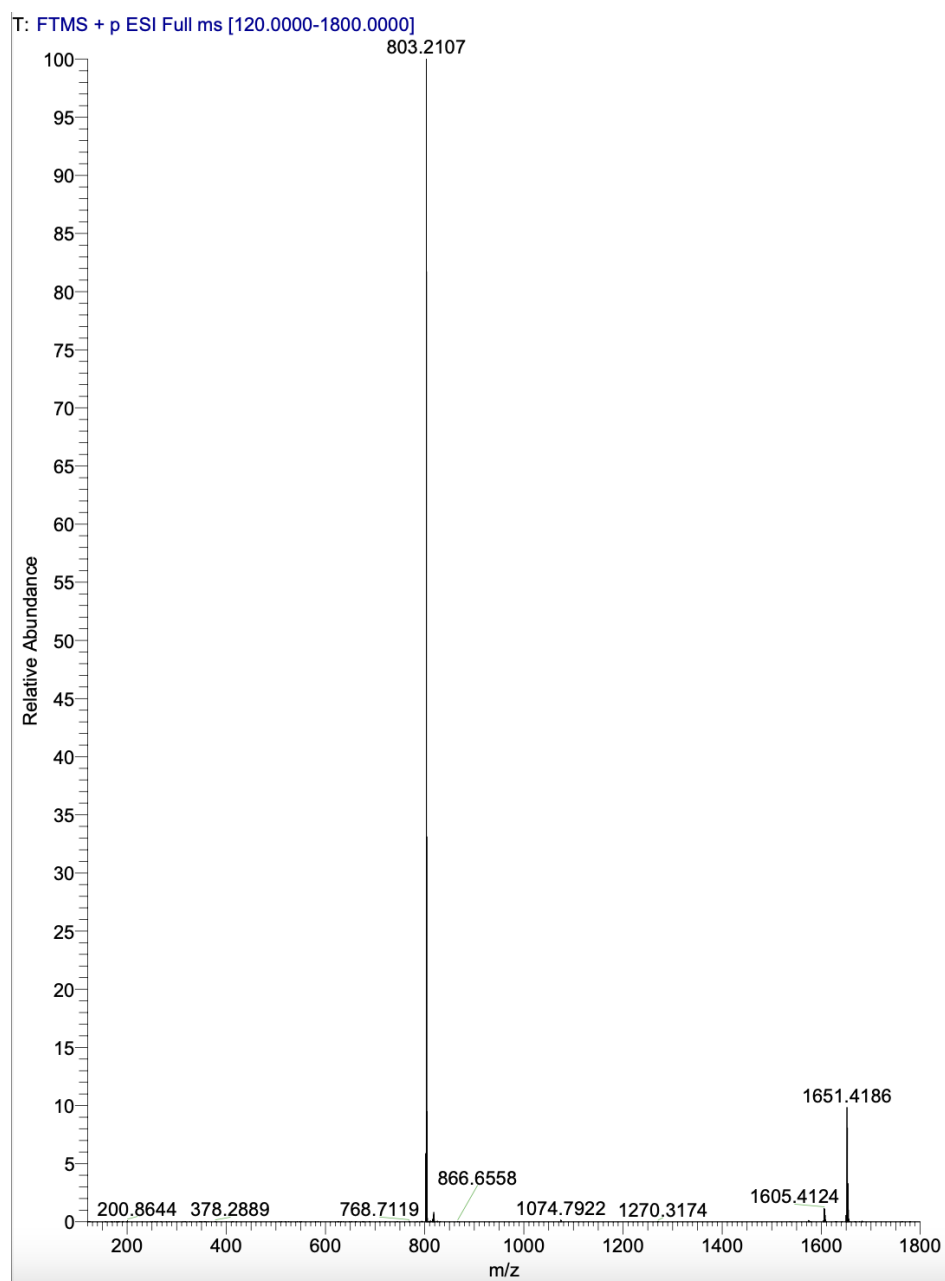


Figure A1.61: High-resolution mass spectrum of Fe(II)L complex **52** (ESI+).

## A1.5 Guest screening data

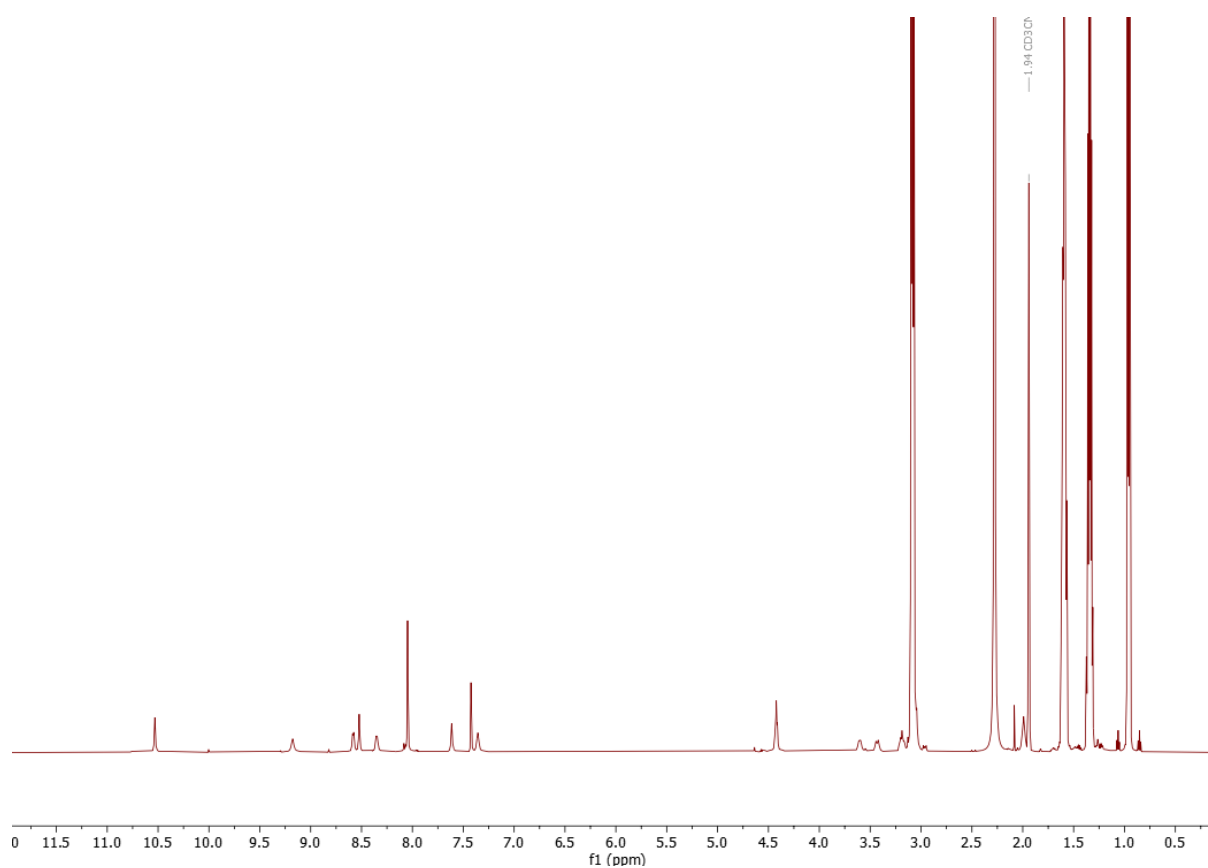
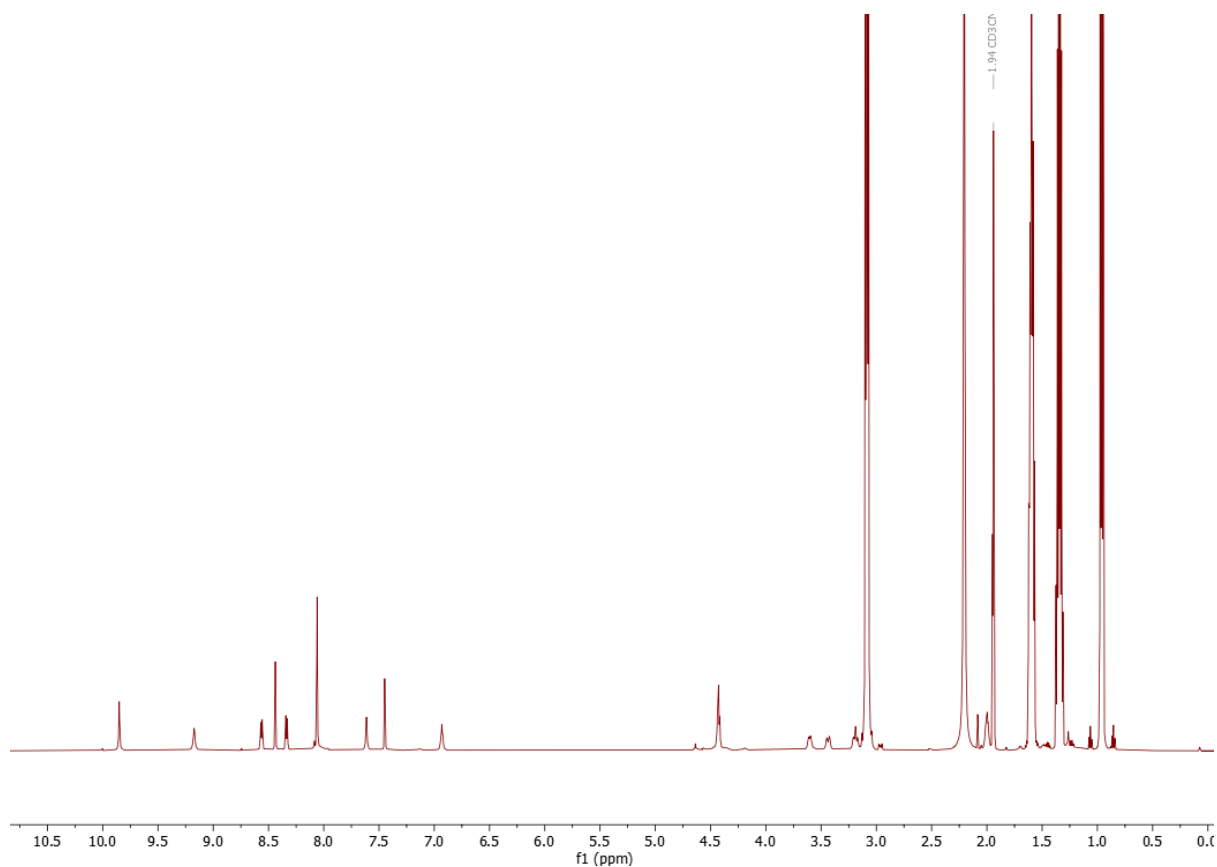


Figure A1.62:  $^1\text{H}$  NMR spectrum of binding of **52** to TBA chloride (10 eq) in  $\text{MeCN-d}_3$  (600 MHz).



*Figure A1.63:  $^1\text{H}$  NMR spectrum of binding of 52 to TBA bromide (10 eq) in MeCN- $\text{d}_3$  (600 MHz).*

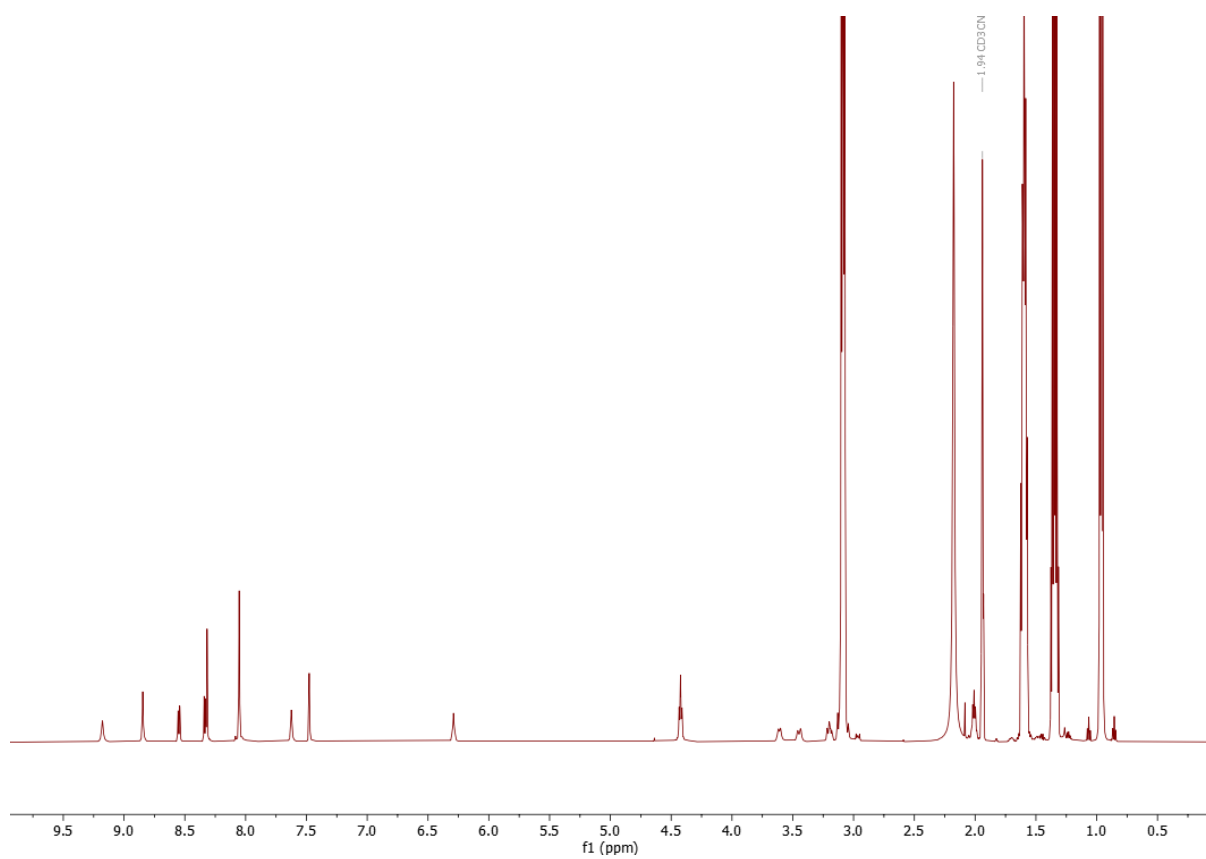


Figure A1.64:  $^1\text{H}$  NMR spectrum of binding of **52** to TBA iodide (10 eq) in  $\text{MeCN-d}_3$  (600 MHz).

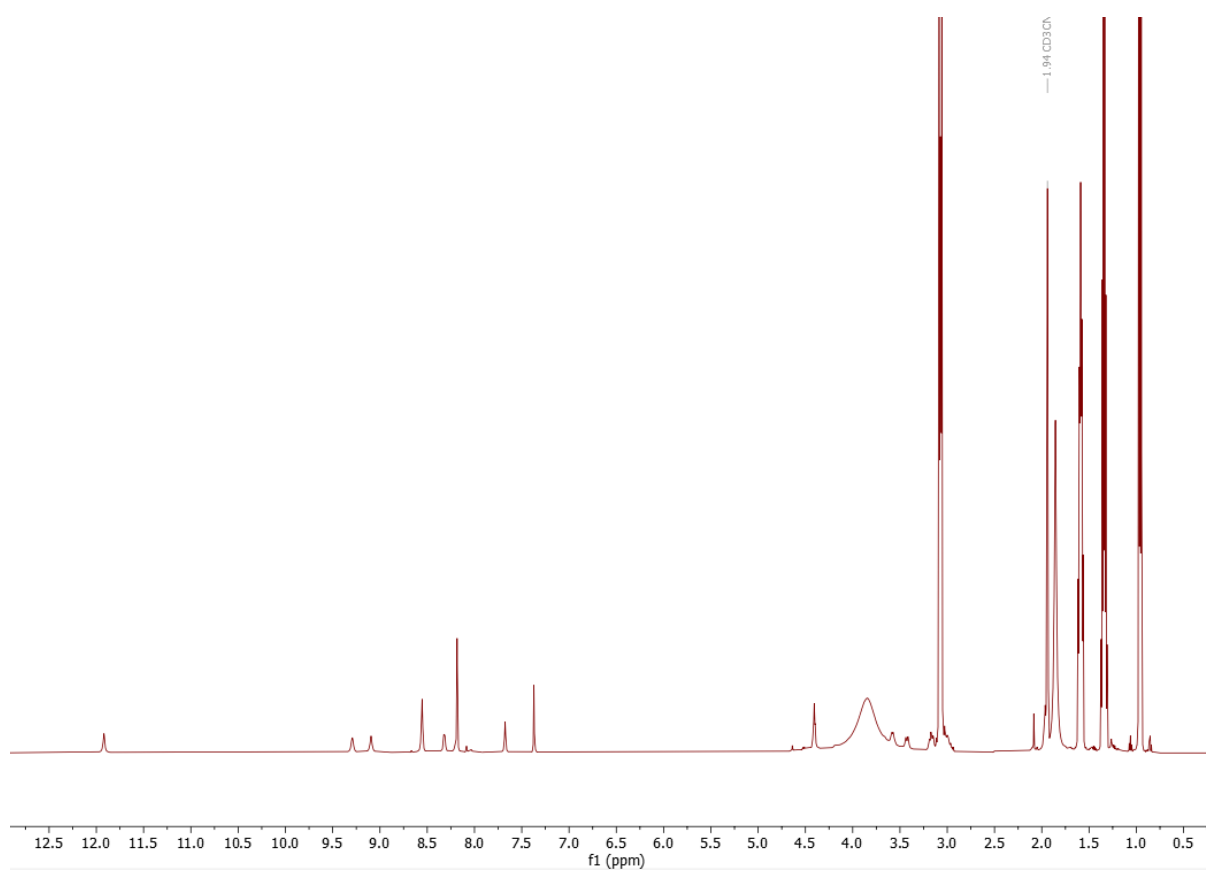


Figure A1.65:  $^1\text{H}$  NMR spectrum of binding of **52** to TBA acetate (10 eq) in  $\text{MeCN-d}_3$  (600 MHz).

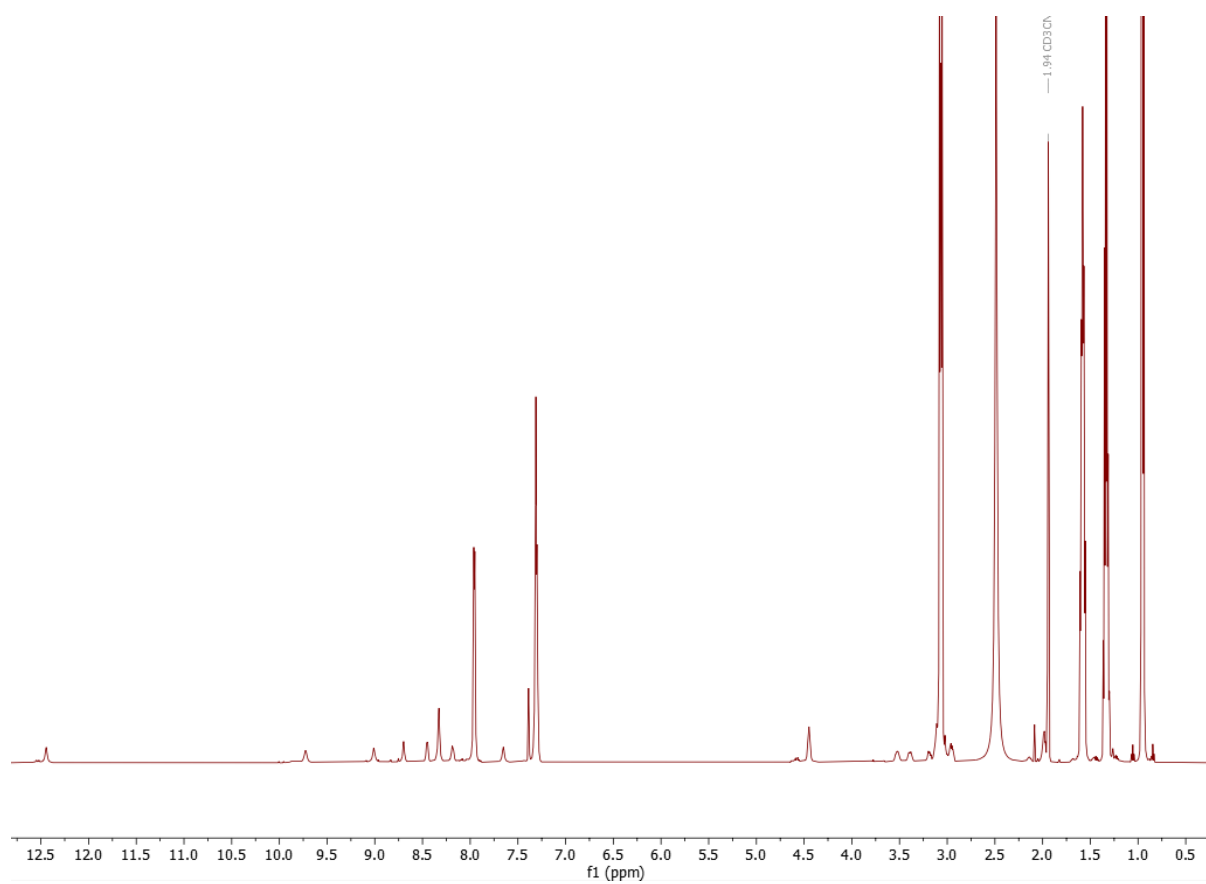


Figure A1.66:  $^1\text{H}$  NMR spectrum of binding of **52** to TBA benzoate in  $\text{MeCN-d}_3$  (600 MHz).

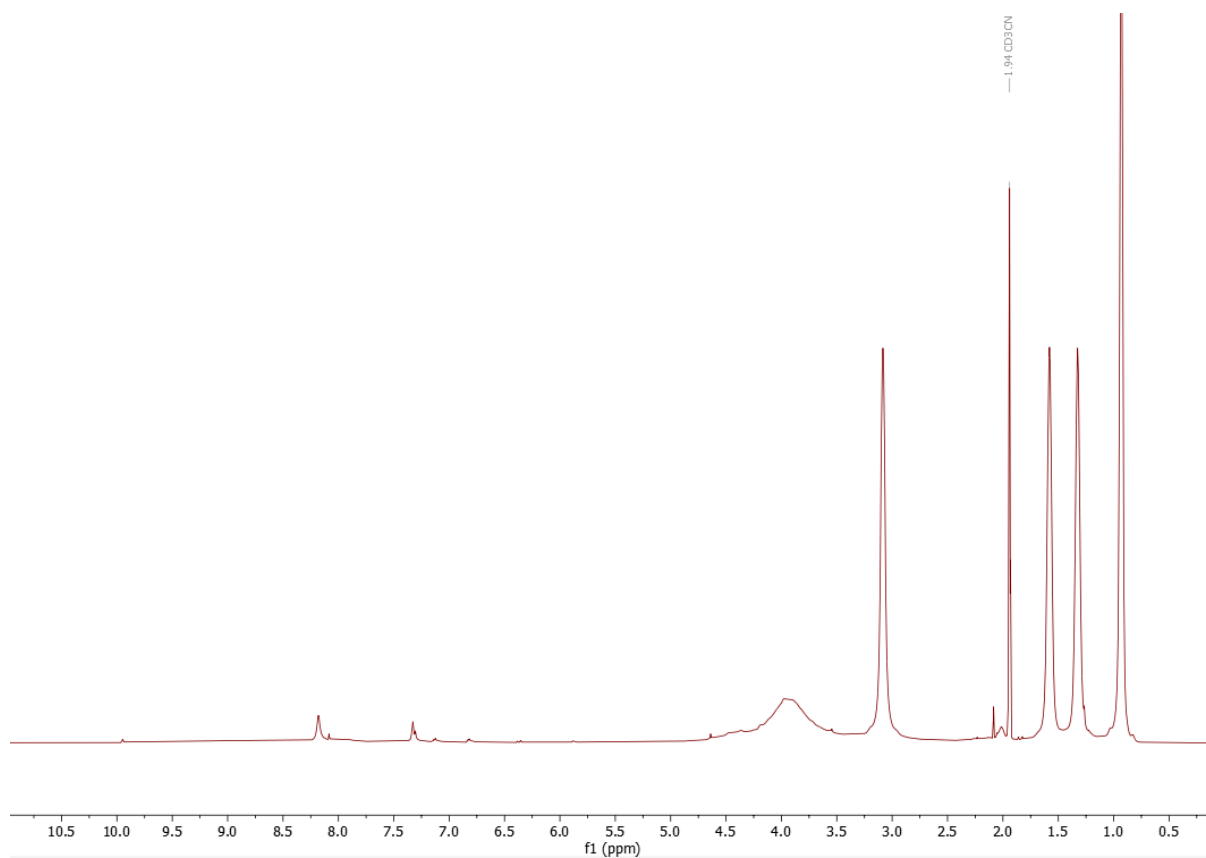


Figure A1.67:  $^1\text{H}$  NMR spectrum of a mixture of **52** and TBA hydrogen phosphate in  $\text{MeCN-d}_3$  (600 MHz).



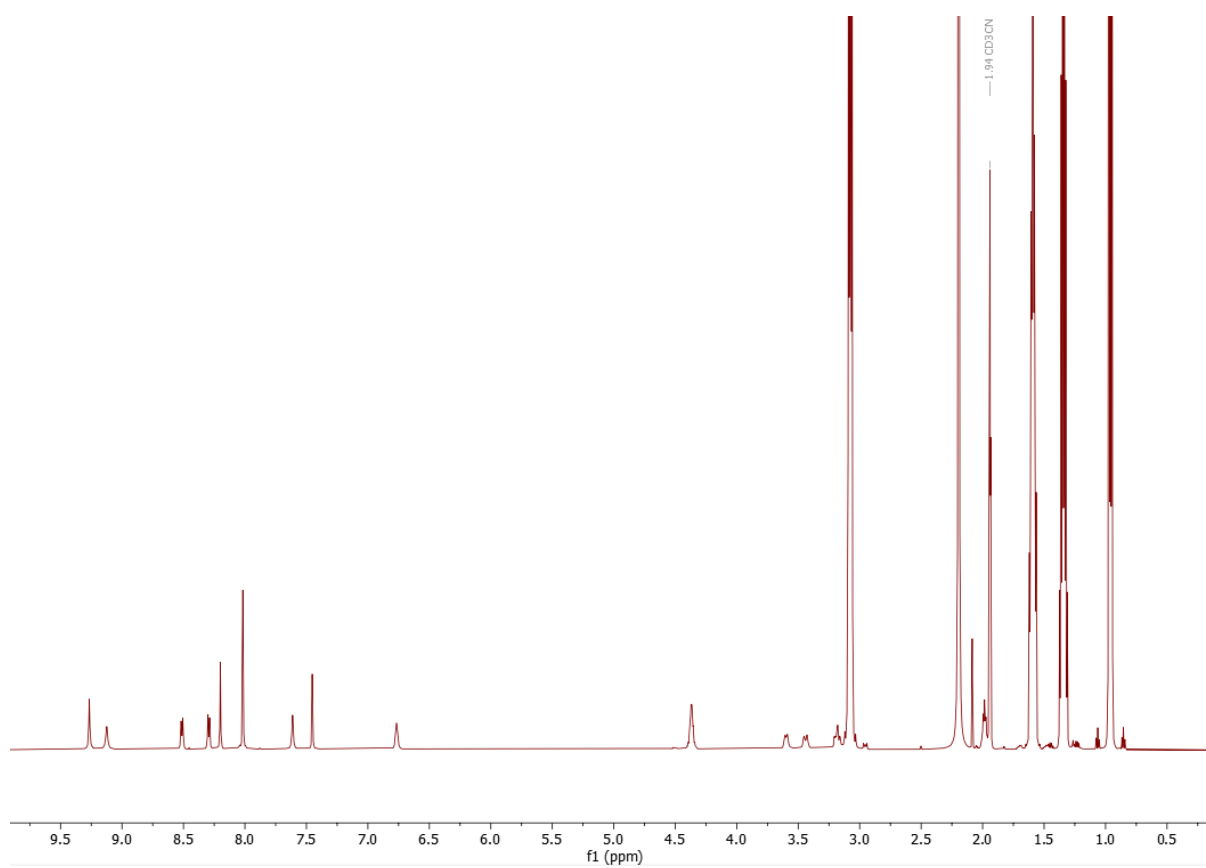


Figure A1.68:  $^1\text{H}$  NMR spectrum of binding of **52** to TBA nitrate in  $\text{MeCN-d}_3$  (600 MHz).

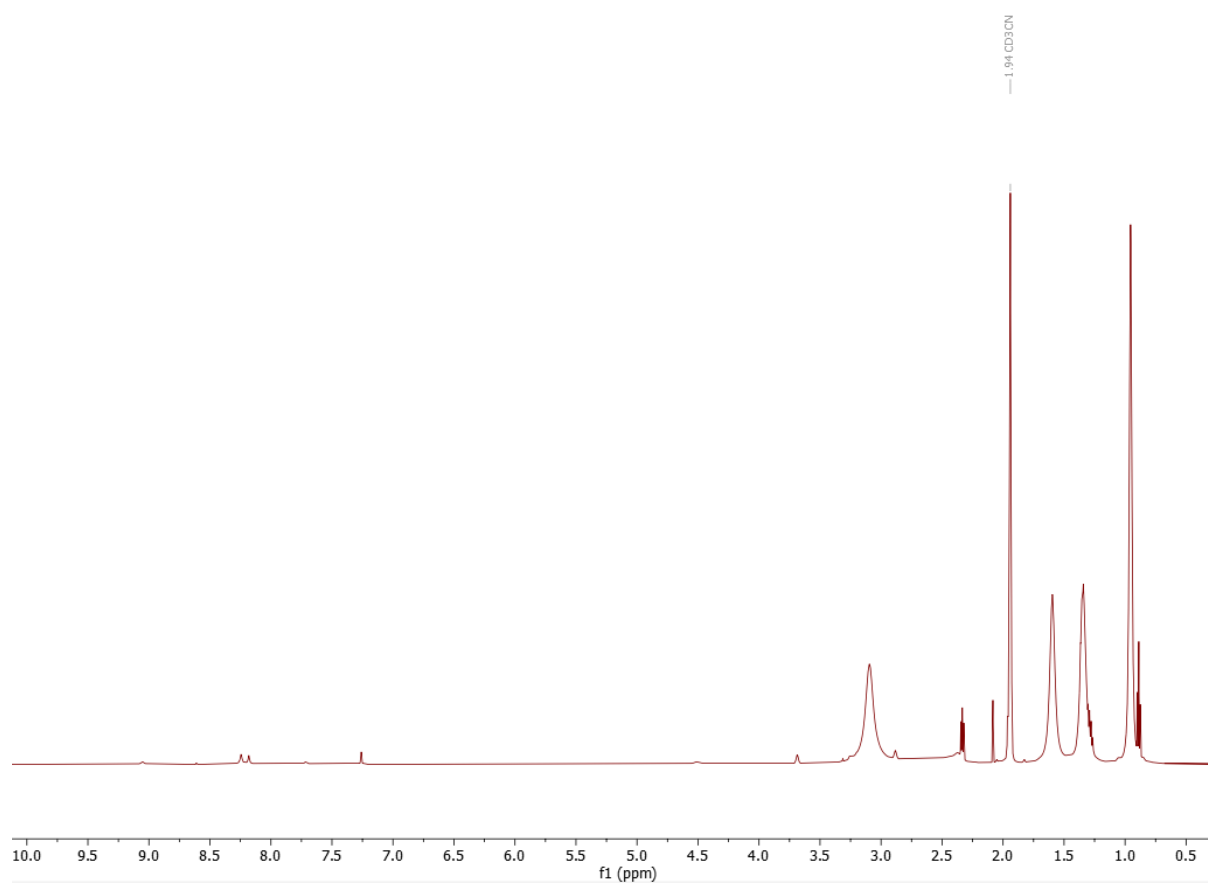


Figure A1.69:  $^1\text{H}$  NMR spectrum of a mixture of **52** and TBA citrate in  $\text{MeCN-d}_3$  (600 MHz).

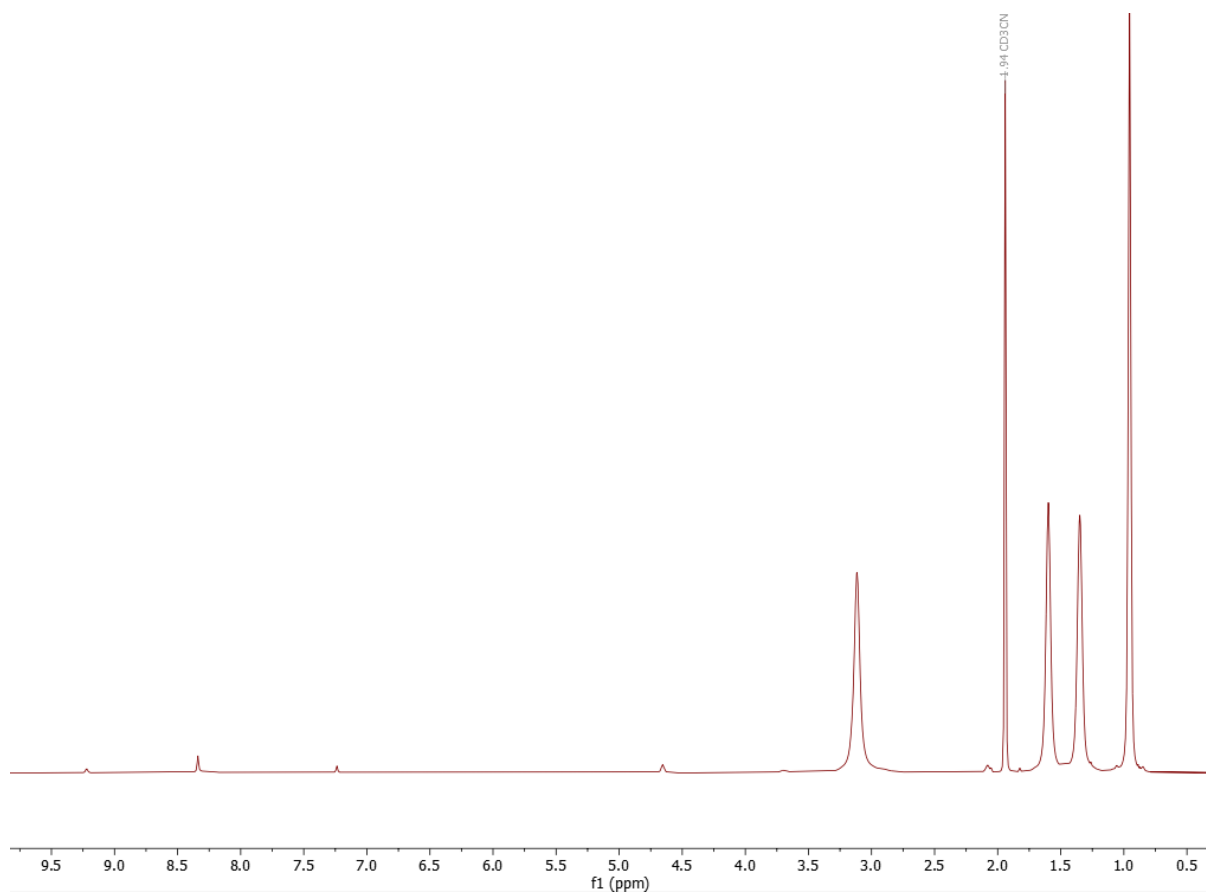
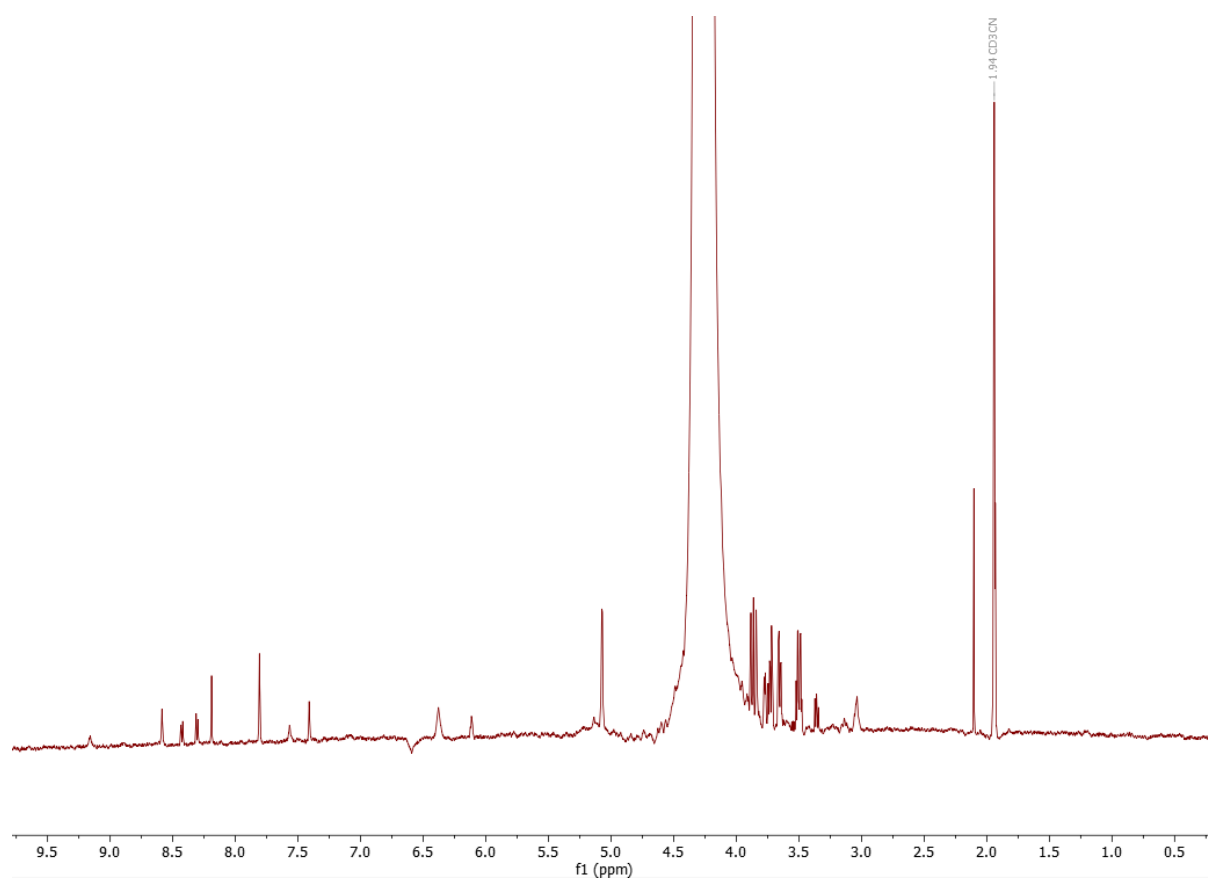
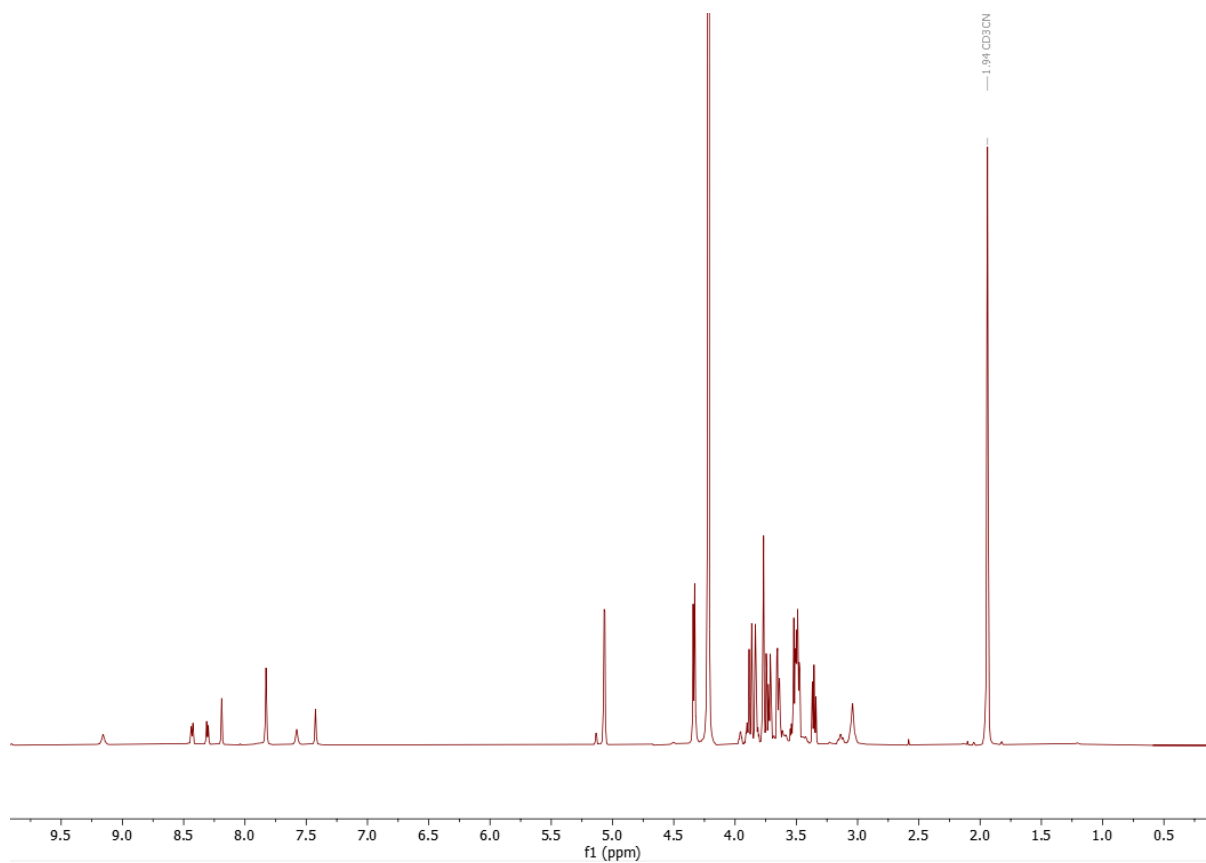


Figure A1.70:  $^1\text{H}$  NMR spectrum of a mixture of **52** and TBA pyrophosphate in  $\text{MeCN-d}_3$  (600 MHz).



*Figure A1.70:  $^1\text{H}$  NMR spectrum of a mixture of **52** and L-arabinose in 1:1 MeCN- $d_3$ /H $_2$ O (600 MHz).*



*Figure A1.71:  $^1\text{H}$  NMR spectrum of a mixture of **52** and L-arabinose in 1:1 MeCN- $d_3$ /D $_2$ O (600 MHz).*

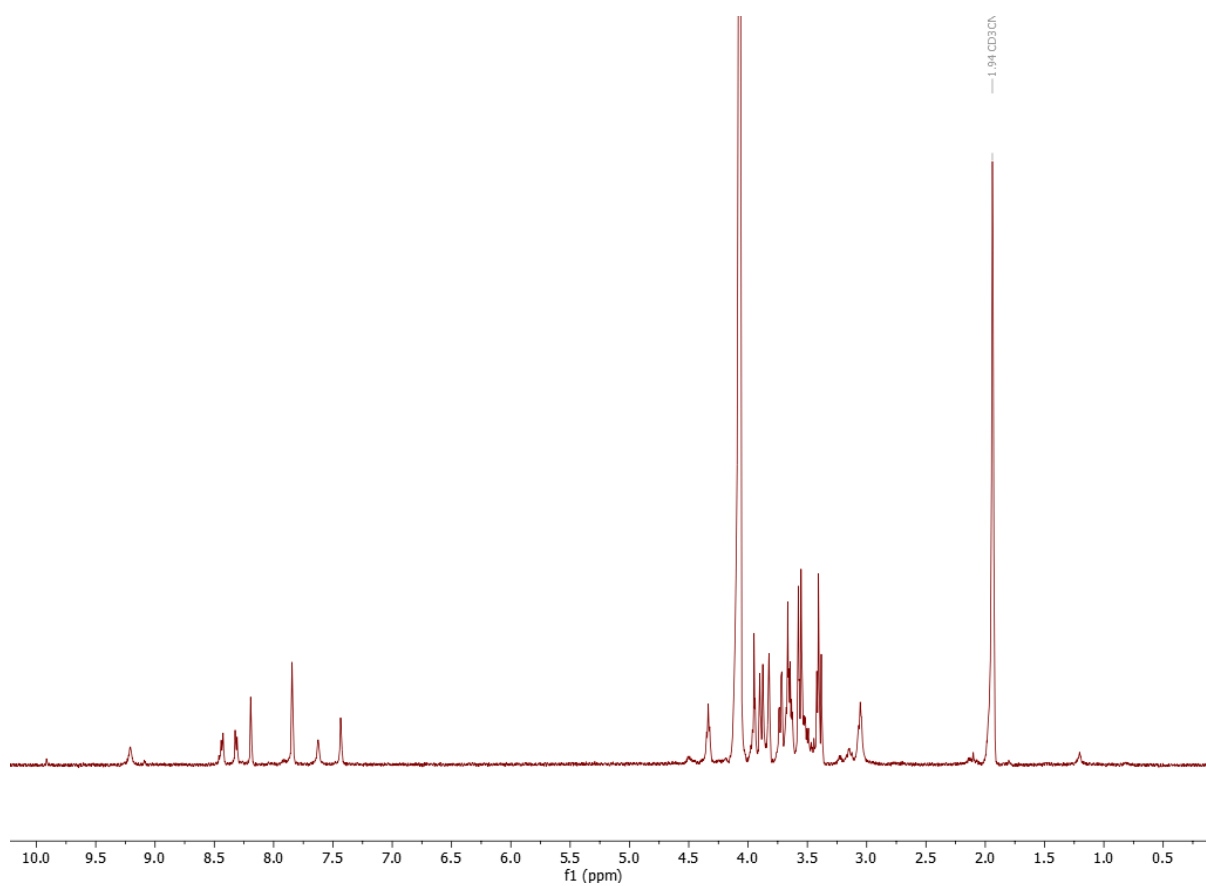
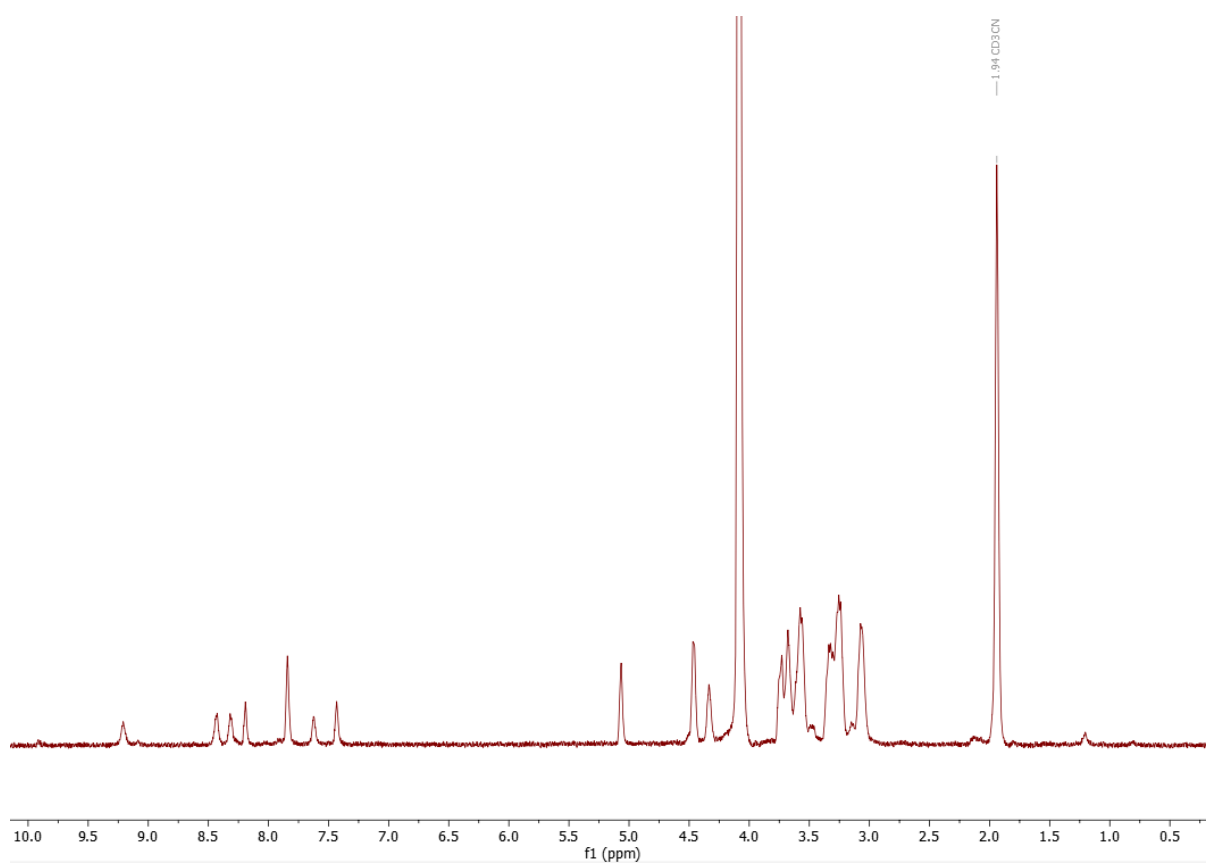
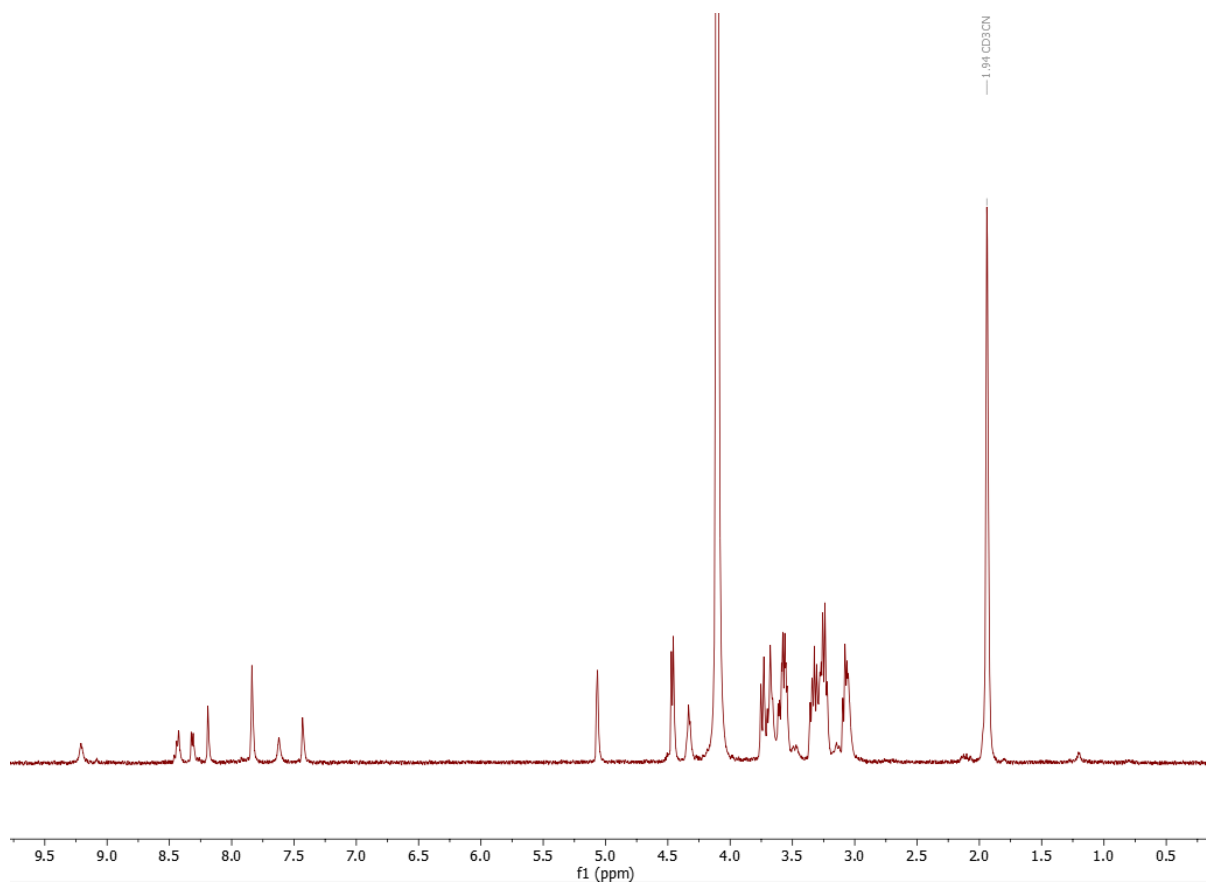


Figure A1.72:  $^1\text{H}$  NMR spectrum of a mixture of **52** and D-fructose in 1:1 MeCN- $d_3$ /D $_2$ O (600 MHz).



*Figure A1.73:  $^1\text{H}$  NMR spectrum of a mixture of **52** and  $\alpha$ -D-glucose in 1:1 MeCN- $d_3$ /D $_2$ O (600 MHz).*



*Figure A1.74:  $^1\text{H}$  NMR spectrum of a mixture of **52** and L-glucose in 1:1 MeCN- $d_3$ /D $_2$ O (600 MHz).*



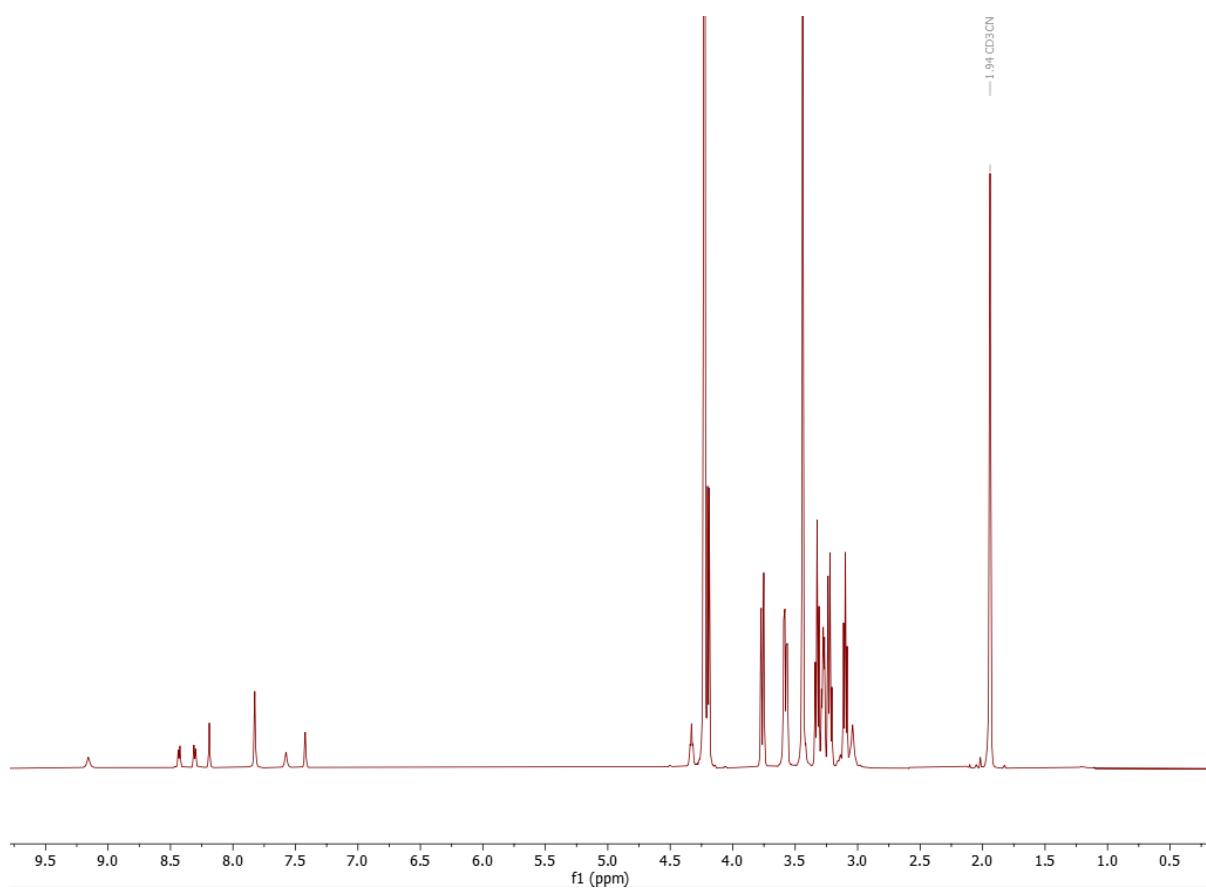


*Figure A1.75:  $^1\text{H}$  NMR spectrum of a mixture of **52** and methyl- $\beta$ -D-glucopyranoside in 1:1 MeCN- $d_3$ /D $_2$ O (600 MHz).*

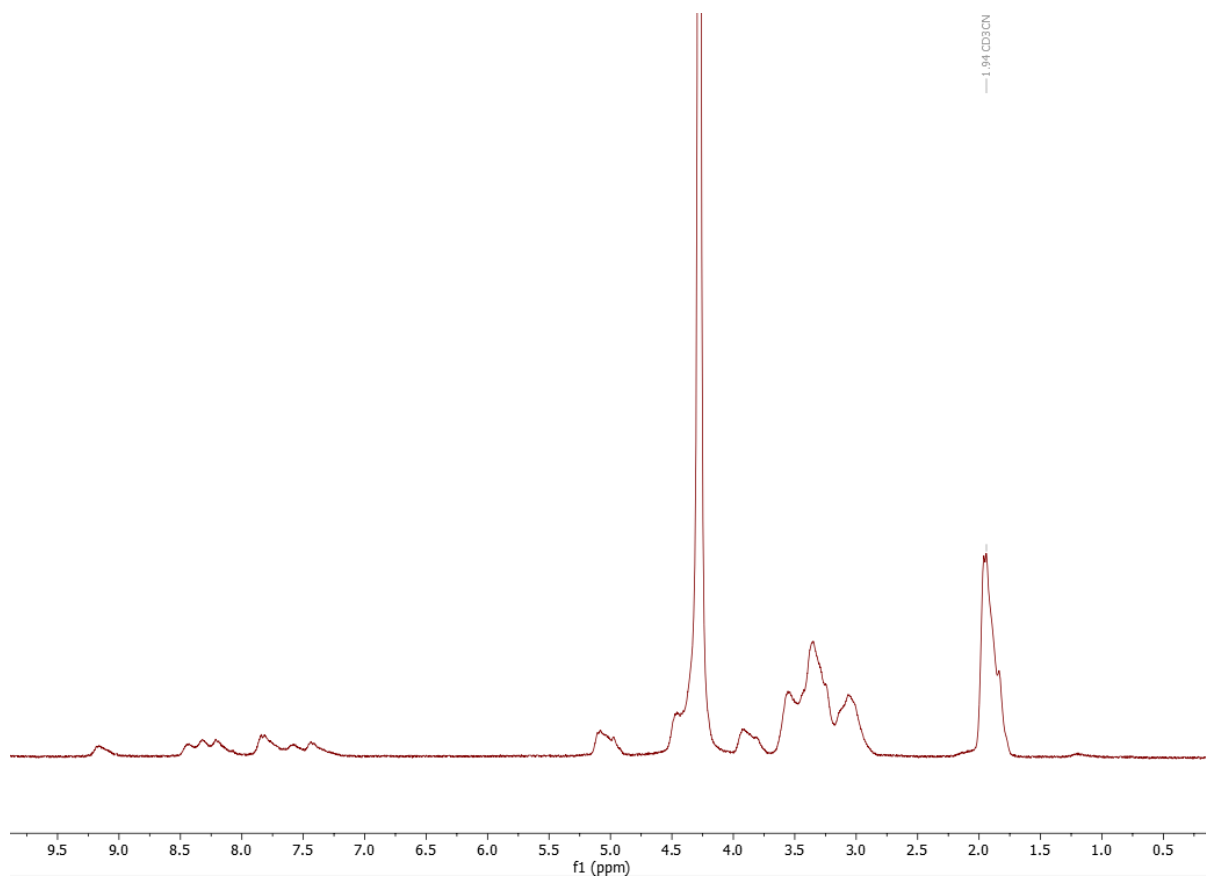


*Figure A1.75:  $^1\text{H}$  NMR spectrum of a mixture of **52** and sodium glucuronate in 1:1 MeCN- $d_3/\text{D}_2\text{O}$  (600 MHz).*

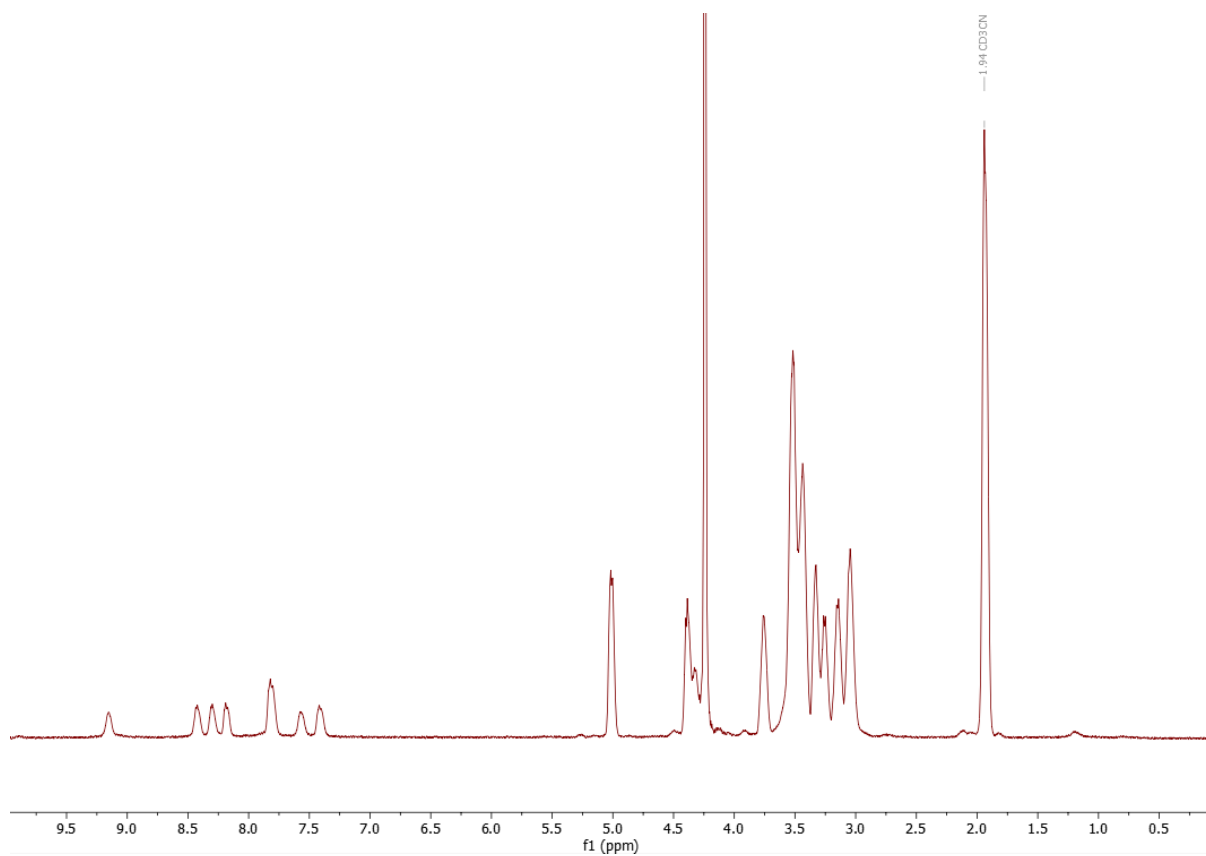


*Figure A1.76:  $^1\text{H}$  NMR spectrum of a mixture of **52** and D-xylose in 1:1 MeCN- $d_3$ /D $_2$ O (600 MHz).*

## A1.6 Titration data

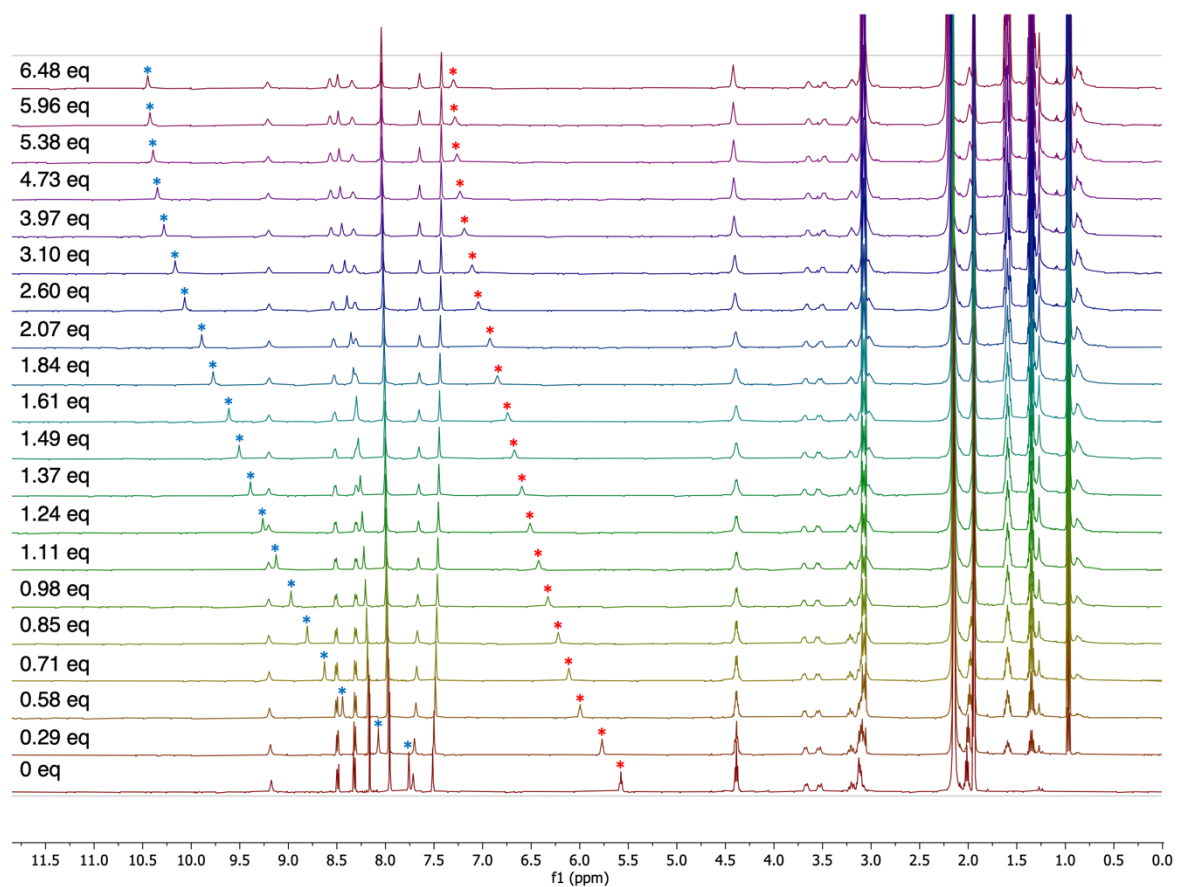


Figure A1.77:  $^1\text{H}$  NMR spectrum of titration of **52** with TBA chloride (0-6.48 eq) in  $\text{MeCN-d}_3$  (500 MHz). \* = aliphatic proton on **52**; \* = aromatic proton on **52**.

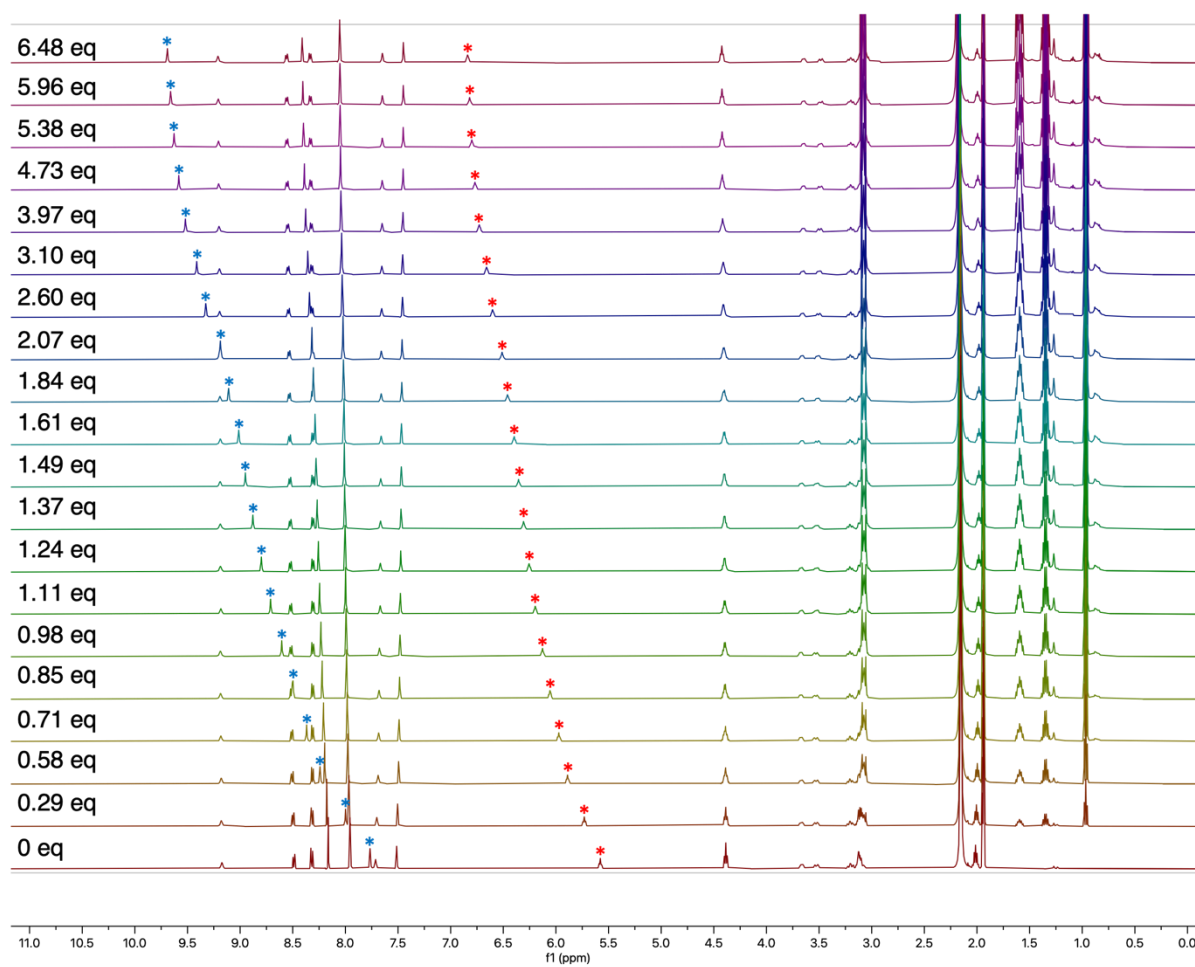


Figure A1.78:  $^1\text{H}$  NMR spectrum of titration of **52** with TBA bromide (0-6.48 eq) in  $\text{MeCN-d}_3$  (500 MHz). \* = aliphatic proton on **52**; \* = aromatic proton on **52**.

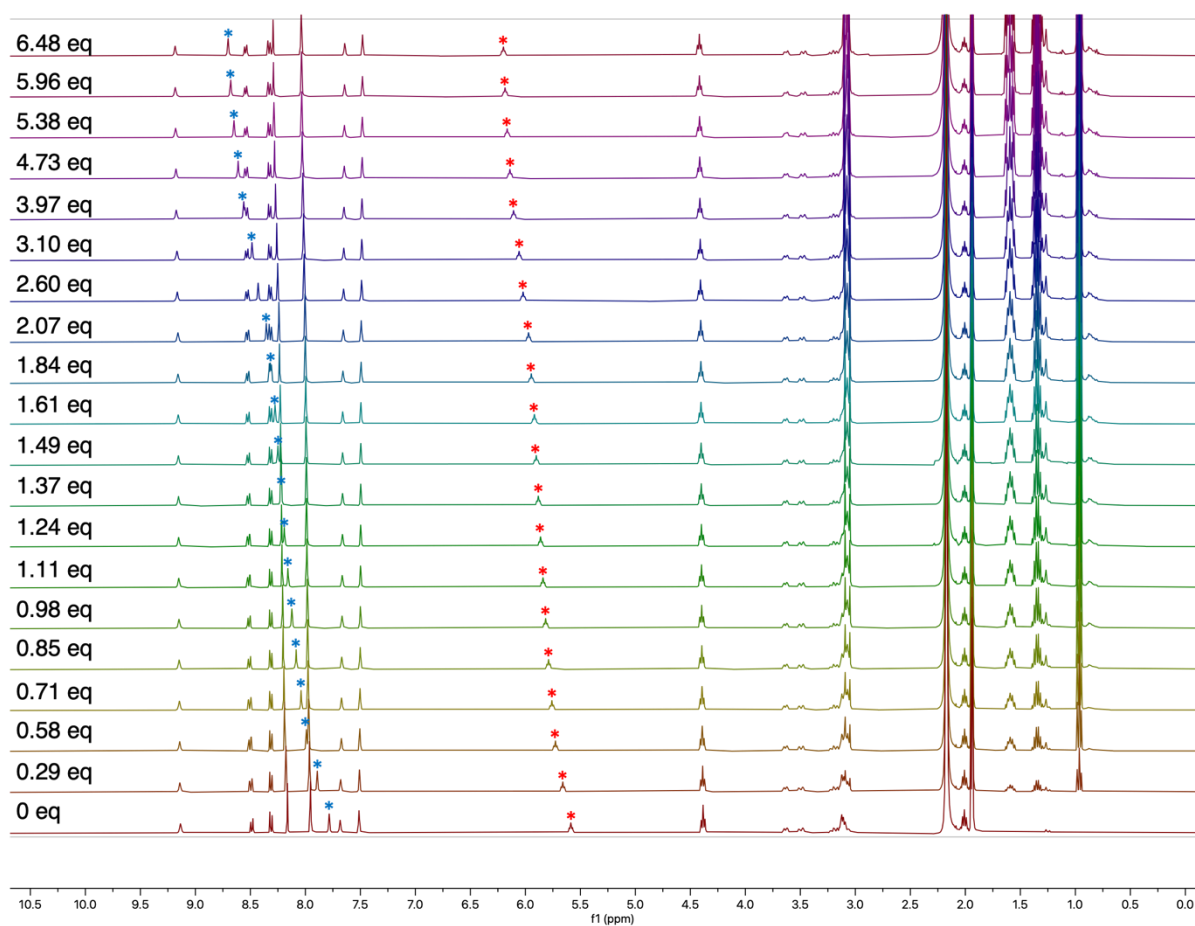


Figure A1.79:  $^1\text{H}$  NMR spectrum of titration of **52** with TBA iodide (0-6.48 eq) in  $\text{MeCN-d}_3$  (400 MHz). \* = aliphatic proton on **52**; \* = aromatic proton on **52**.

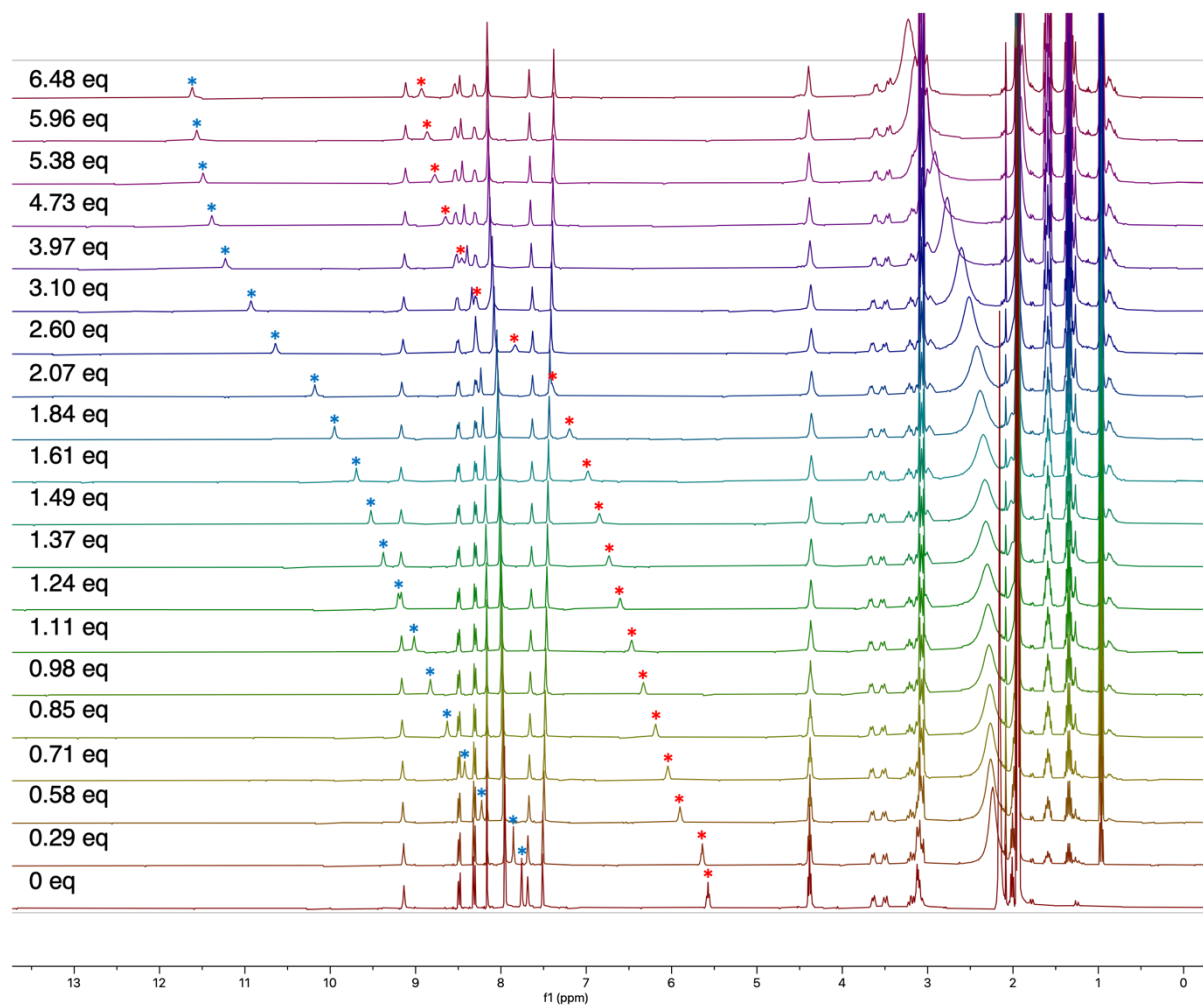


Figure A1.80:  $^1\text{H}$  NMR spectrum of titration of **52** with TBA acetate (0-6.48 eq) in  $\text{MeCN-d}_3$  (400 MHz). \* = aliphatic proton on **52**; \* = aromatic proton on **52**.

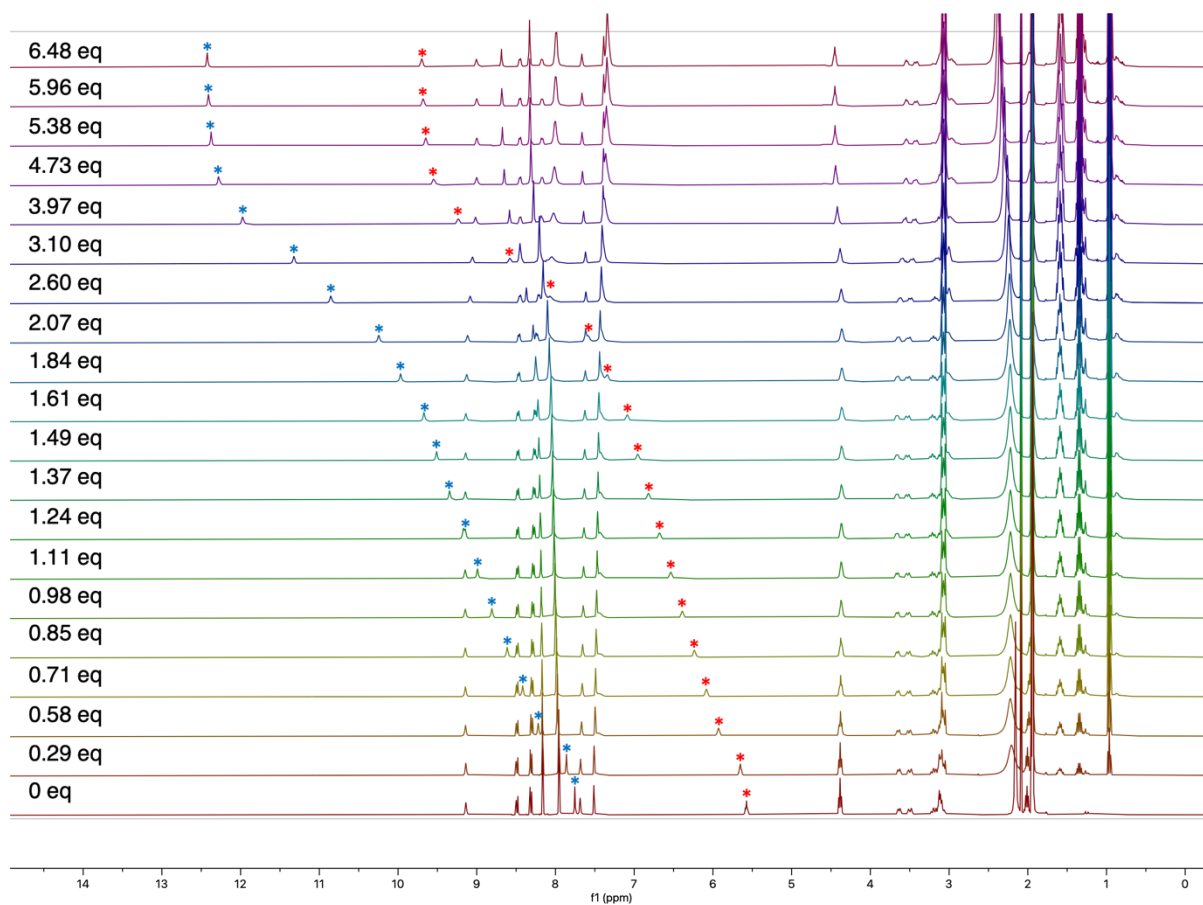


Figure A1.80:  $^1\text{H}$  NMR spectrum of titration of **52** with TBA benzoate (0-6.48 eq) in  $\text{MeCN-d}_3$  (400 MHz). \* = aliphatic proton on **52**; \* = aromatic proton on **52**.



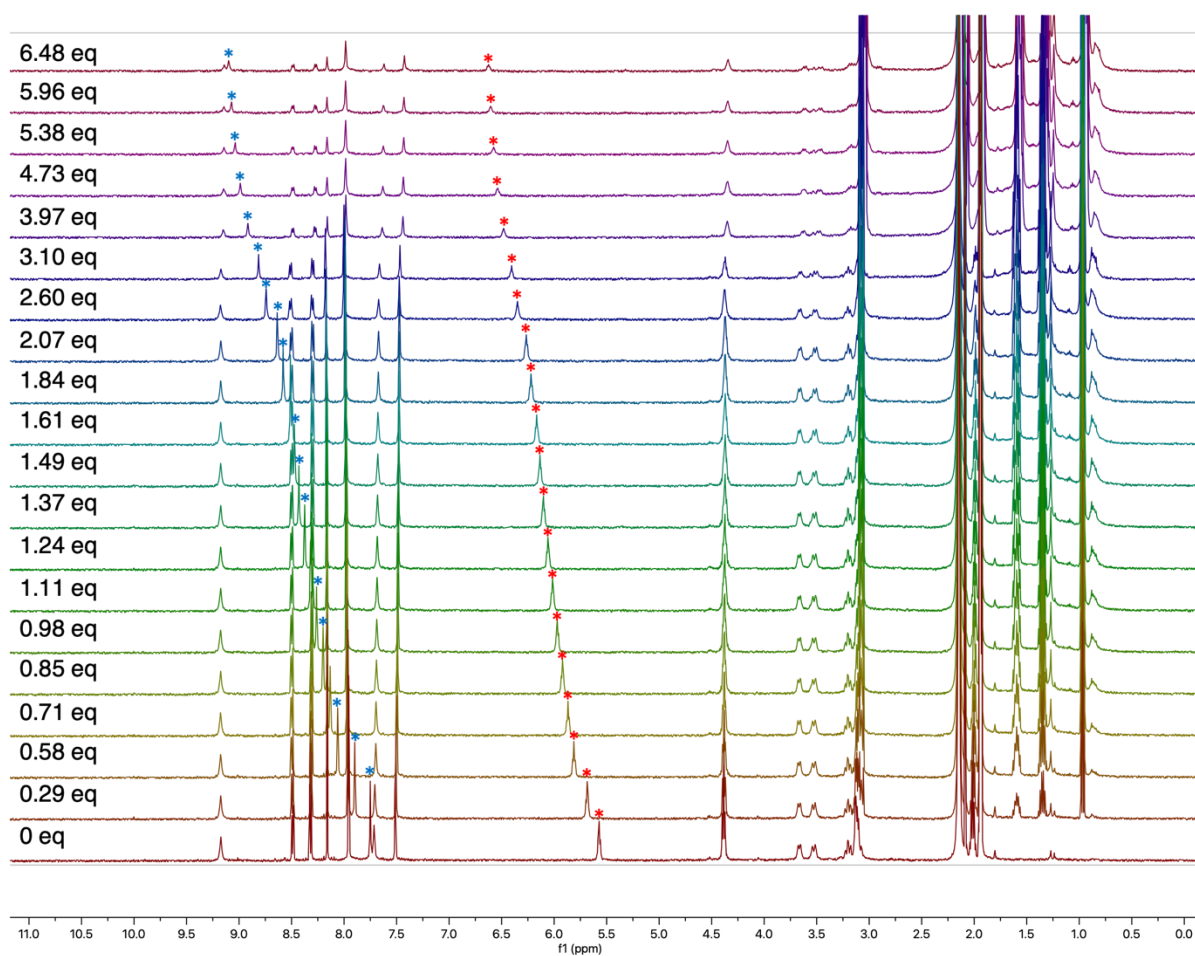


Figure A1.81:  $^1\text{H}$  NMR spectrum of titration of **52** with TBA nitrate (0-6.48 eq) in  $\text{MeCN-d}_3$  (400 MHz). \* = aliphatic proton on **52**; \* = aromatic proton on **52**.

## A1.7 Fluorescence data

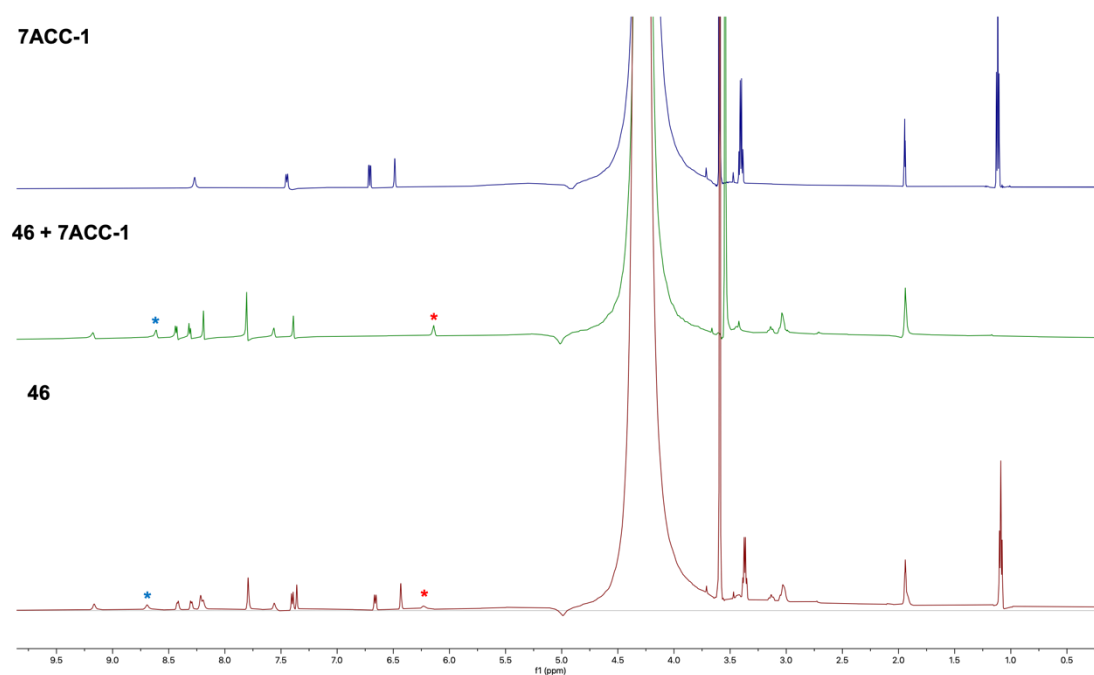


Figure A1.82:  $^1\text{H}$  NMR spectrum of binding of 7ACC-1 in 1:1 MeCN- $d_3$ /TRIS pH 7.4 (top)  $^1\text{H}$  NMR spectrum of binding of 7ACC-1 (10 eq) with **52** in 1:1 MeCN- $d_3$ /TRIS pH 7.4; **52** in 1:1 MeCN- $d_3$ /TRIS pH 7.4 (bottom). \* = aliphatic proton on **52**; \* = aromatic proton on **52**.

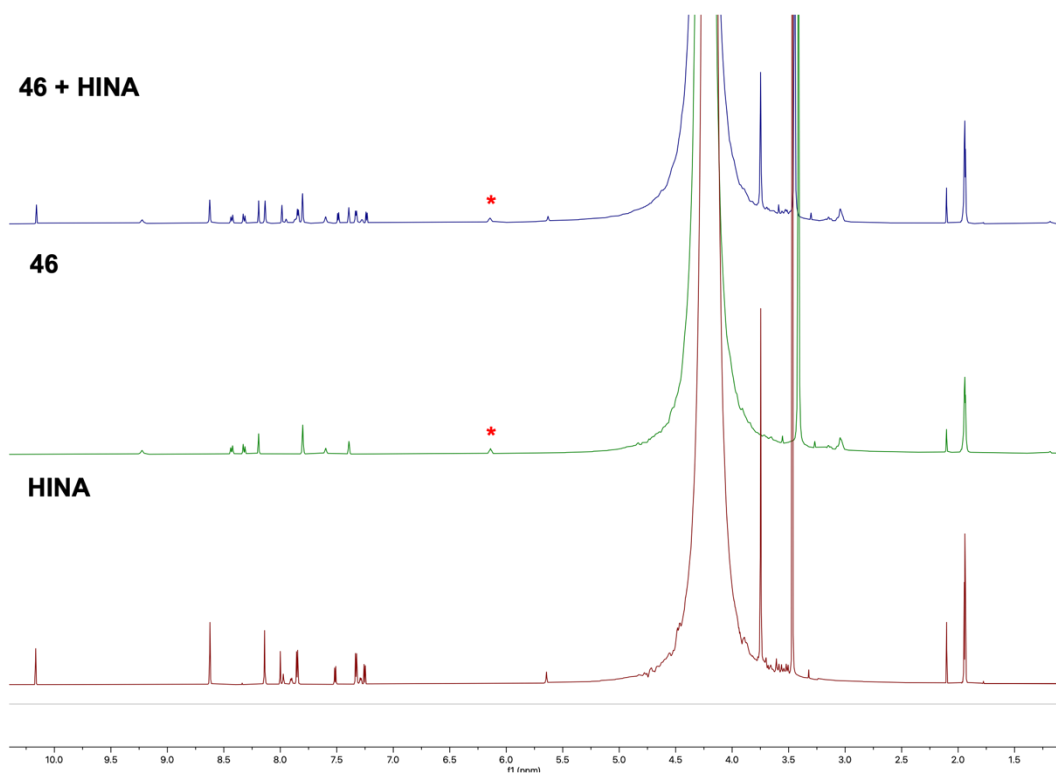


Figure A1.83:  $^1\text{H}$  NMR spectrum of binding of HINA (6.48 eq) with **52** in 1:1 MeCN- $d_3$ /TRIS pH 9 (top); **52** in 1:1 MeCN- $d_3$ /TRIS pH 9 (middle); HINA in 1:1 MeCN- $d_3$ /TRIS pH 9 (bottom). \* = aliphatic proton on **52**.

## A1.8 Vesicles studies data

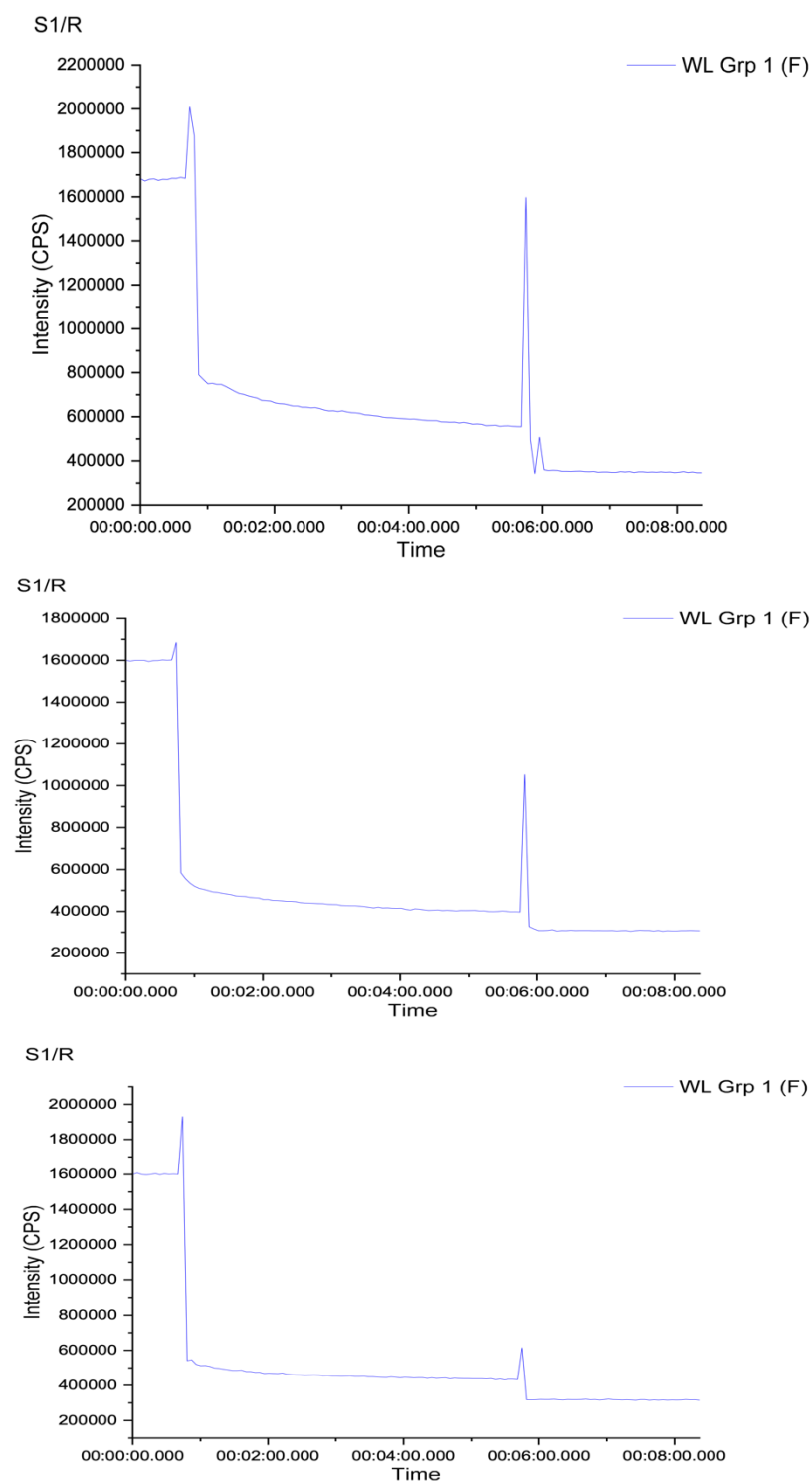


Figure A1.84: Fluorescence intensity of 52-containing vesicles (1:5000 transporter:lipid ratio) during lucigenin assay. Each graph corresponds to a triplicate.

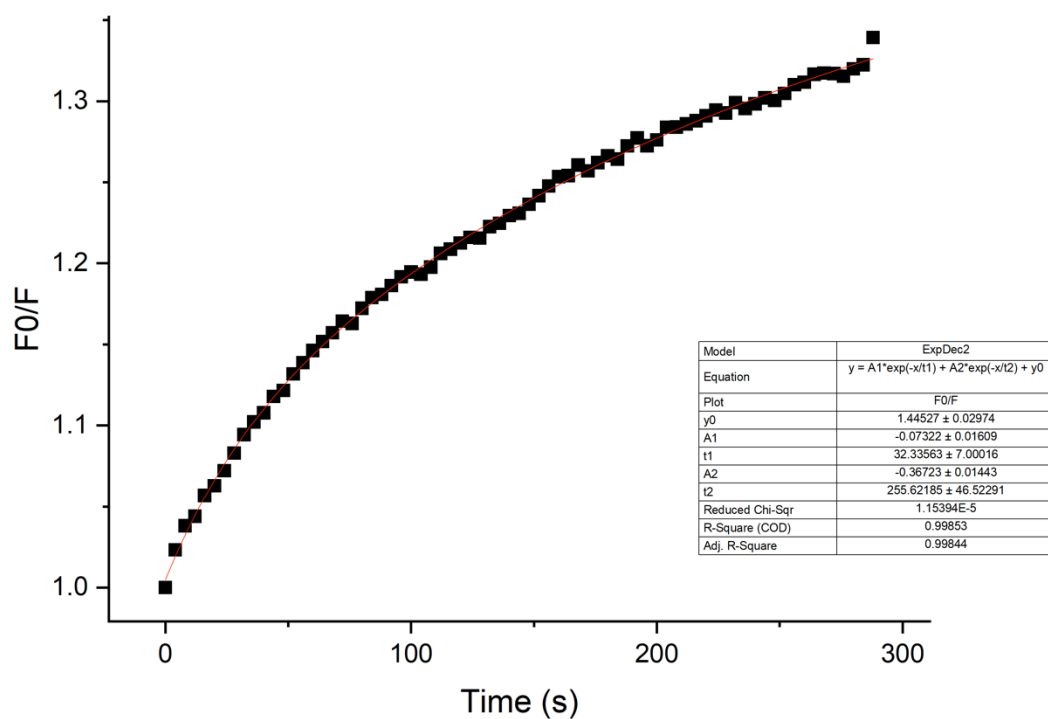
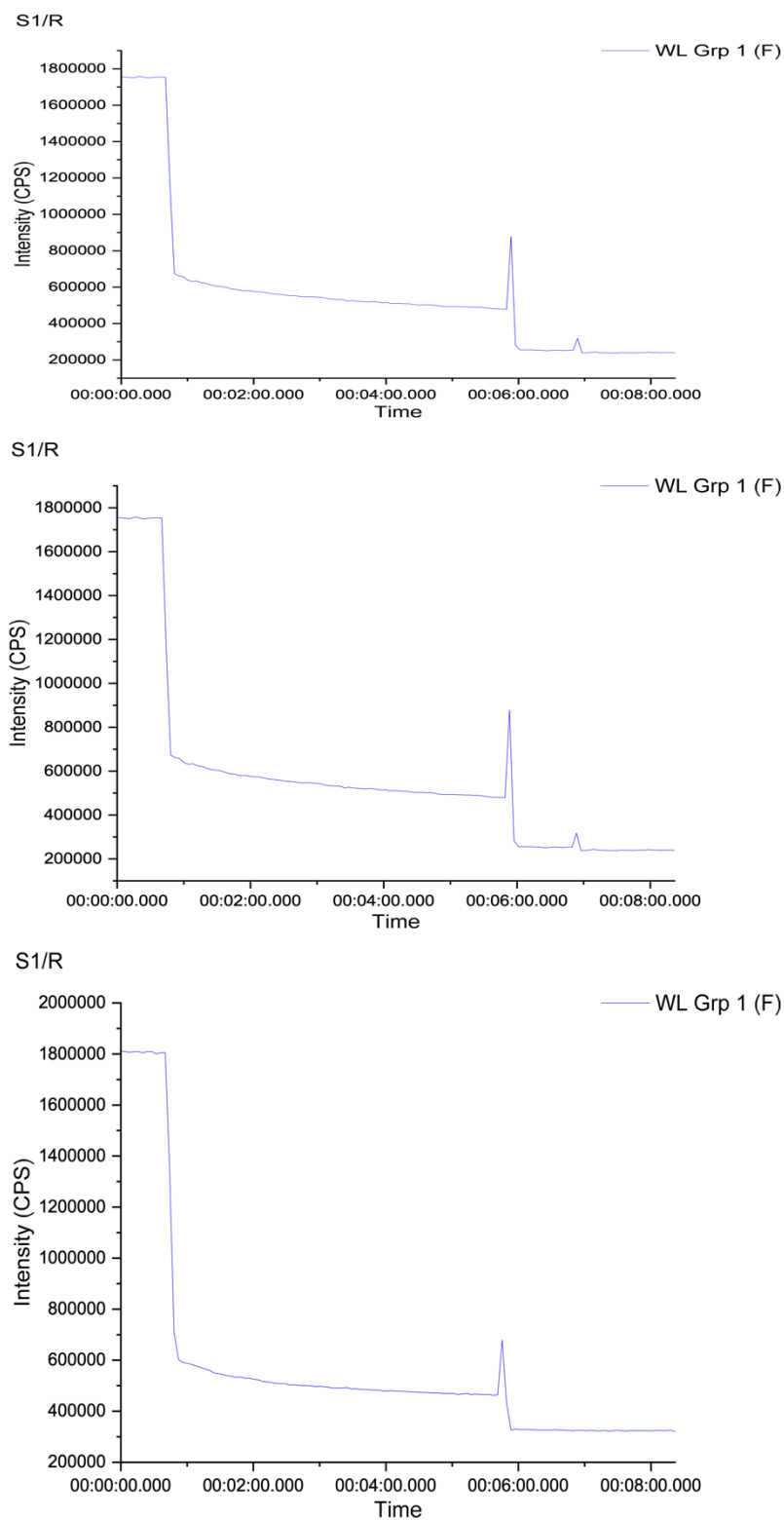
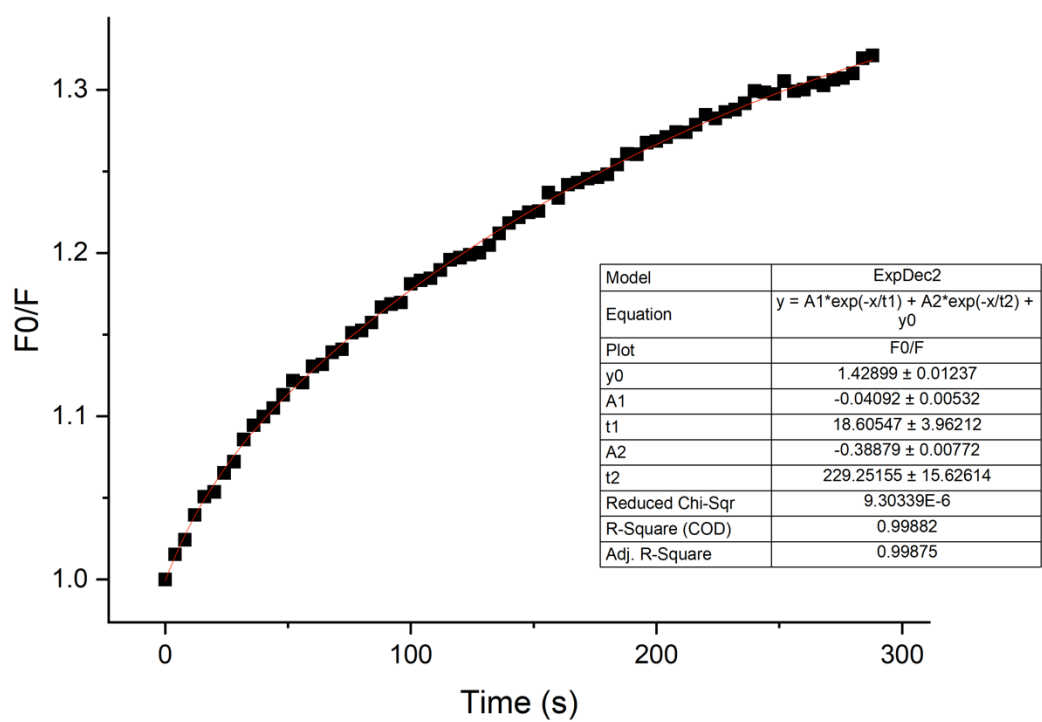


Figure A1.85: Inverse of the averaged and normalised data from 0-300 seconds from lucigenin assay fitted with a double exponential function for vesicles pre-incorporated with

52.



*Figure A1.86: Fluorescence intensity of control vesicles (no transporter) during lucigenin assay. Each graph corresponds to a triplicate.*



*Figure A1.87: Inverse of the averaged and normalised data from 0-300 seconds from lucigenin assay fitted with a double exponential function for control vesicles (no transporter).*

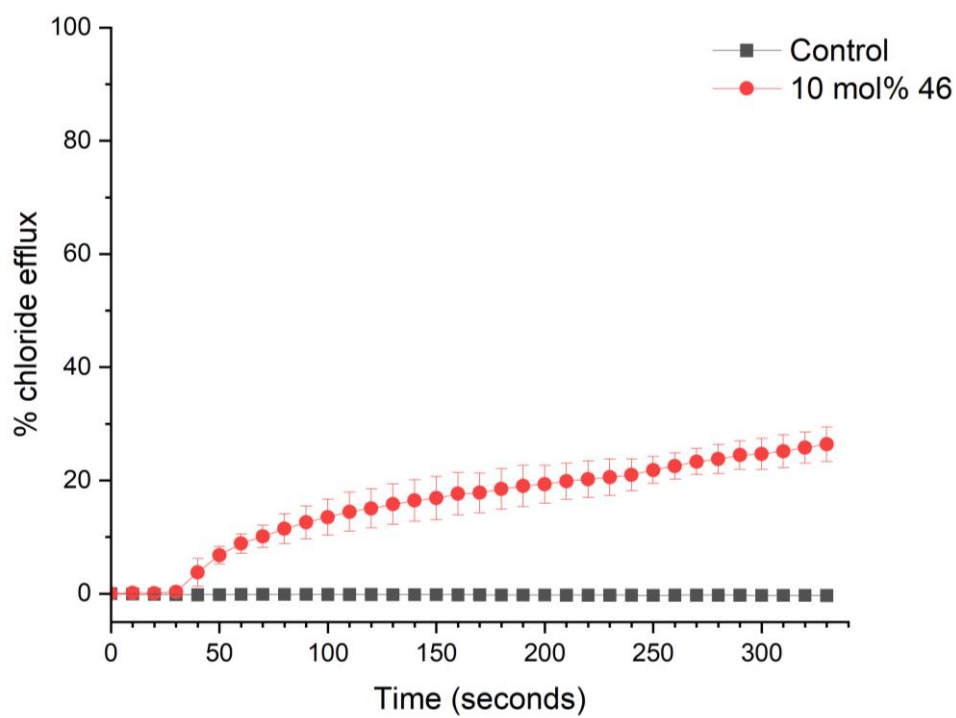


Figure A1.88: Chloride efflux promoted by control (black) and **52** at 10 mol% (red). Control = acetonitrile only. Internal buffer = NaCl; external buffer = NaGlu.



## A2 Chapter 3 data

### A2.1 $^1\text{H}$ NMR

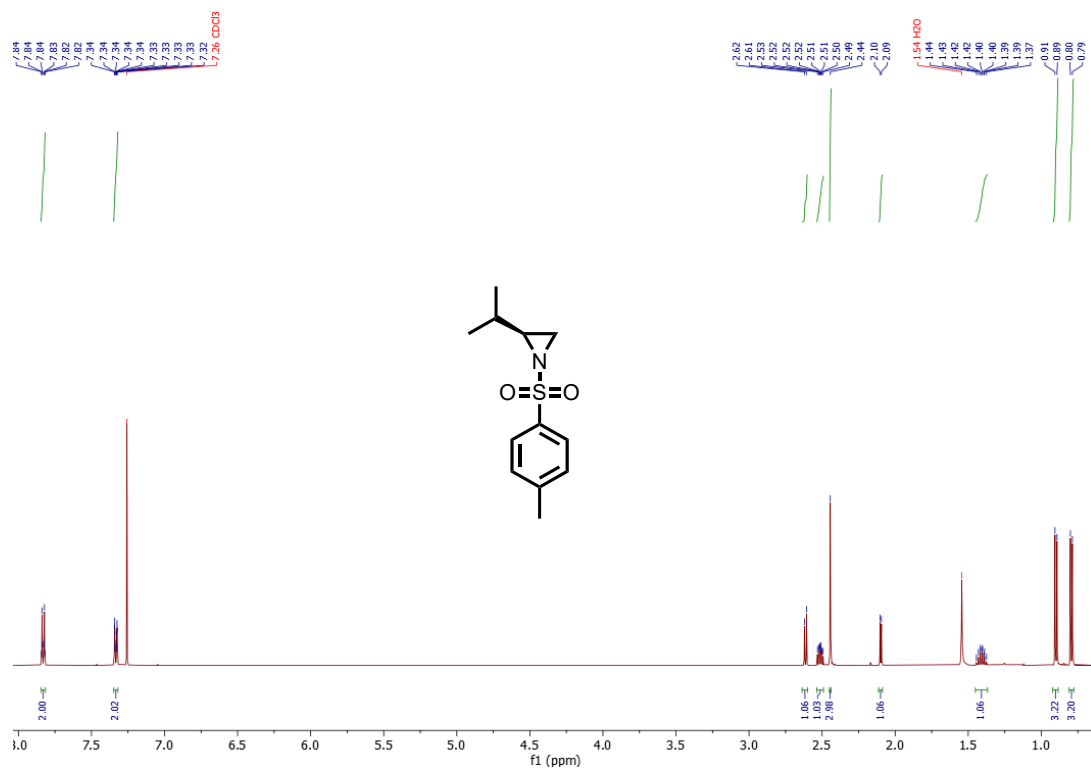


Figure A2.1:  $^1\text{H}$  NMR spectrum of (S)-2-isopropyl-1-tosylaziridine (**63**) (500 MHz,  $\text{CDCl}_3$ ).

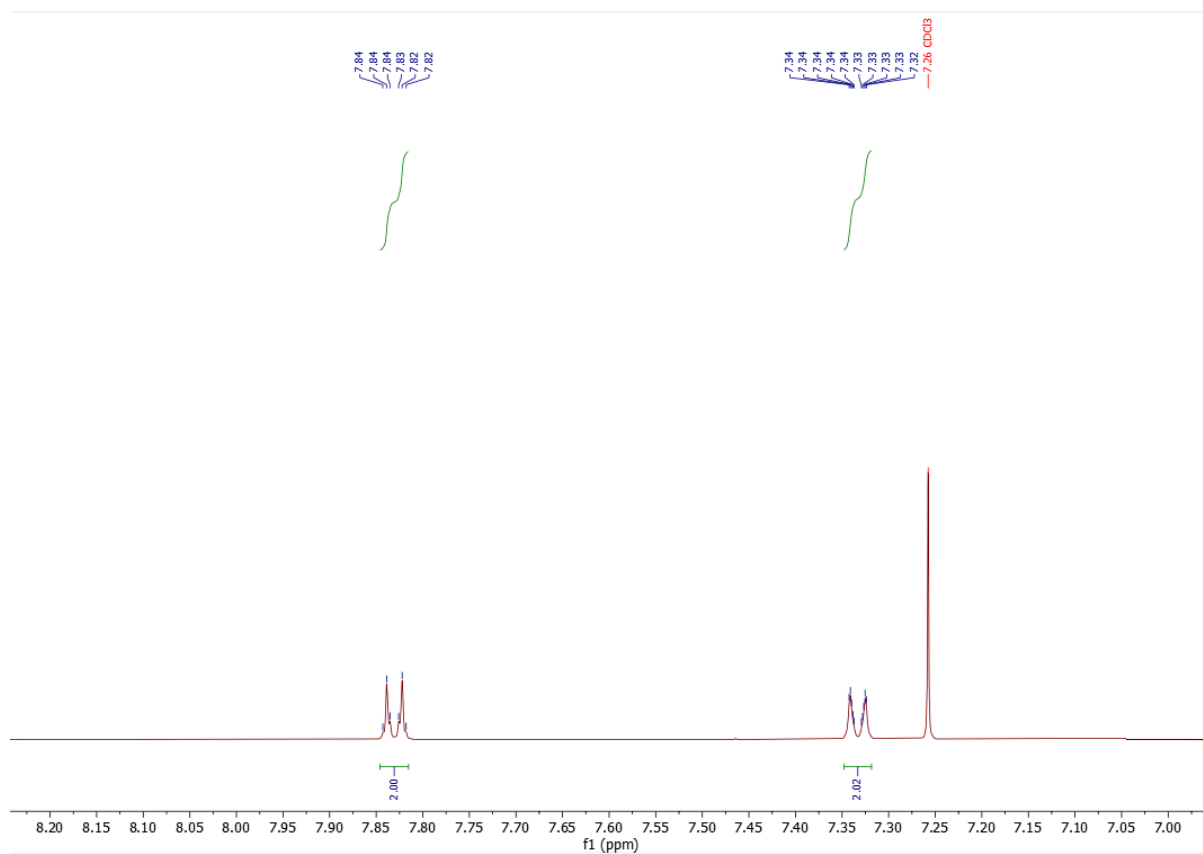


Figure A2.2: Expansion of  $^1\text{H}$  NMR spectrum of (S)-2-isopropyl-1-tosylaziridine (**63**) (7-9 ppm) (500 MHz,  $\text{CDCl}_3$ ).

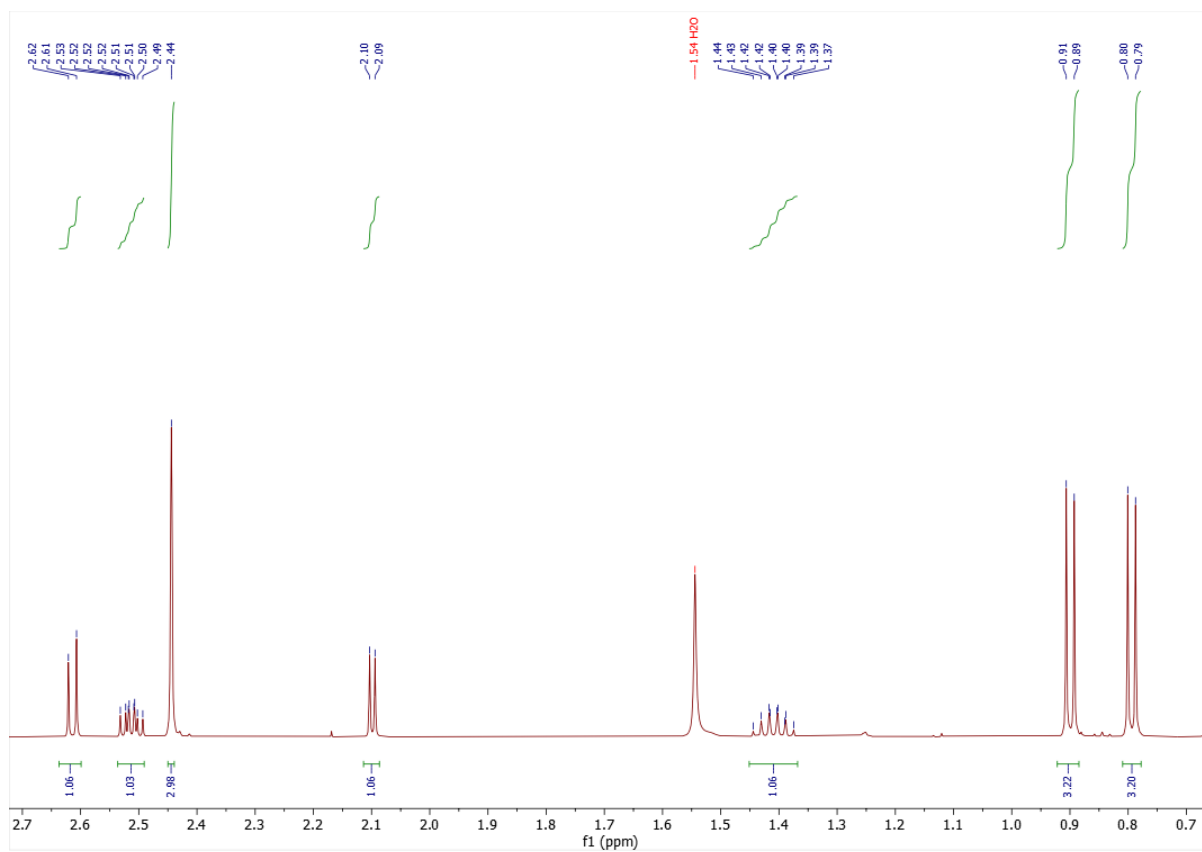


Figure A2.3: Expansion of  $^1\text{H}$  NMR spectrum of (S)-2-isopropyl-1-tosylaziridine (**63**) (0-3 ppm) (500 MHz,  $\text{CDCl}_3$ ).

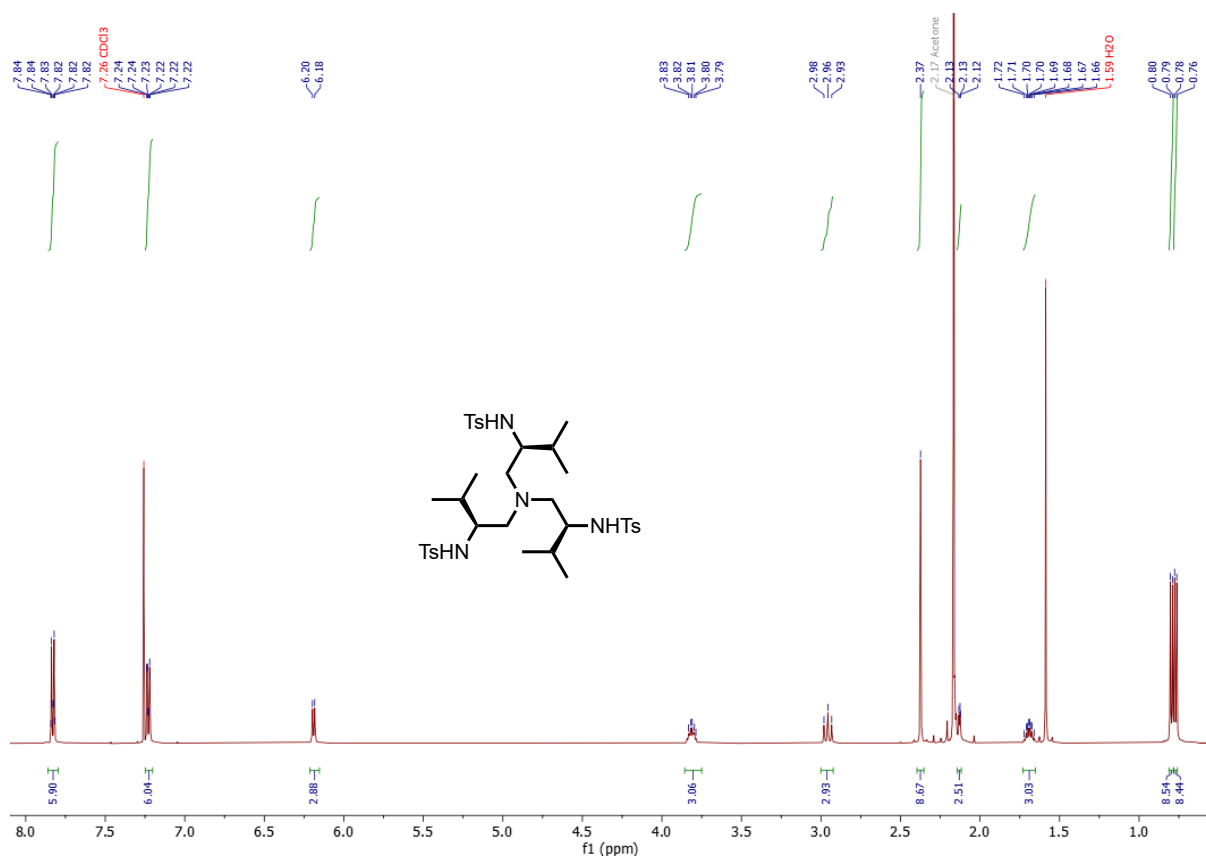


Figure A2.4: <sup>1</sup>H NMR spectrum of *N,N',N''*-((2*S*, 2'*S*, 2''*S*)-nitrilotris(3-methylbutane-1,2-diyl))tris(4-methylbenzenesulfonamide (**64**)) (500 MHz, CDCl<sub>3</sub>).

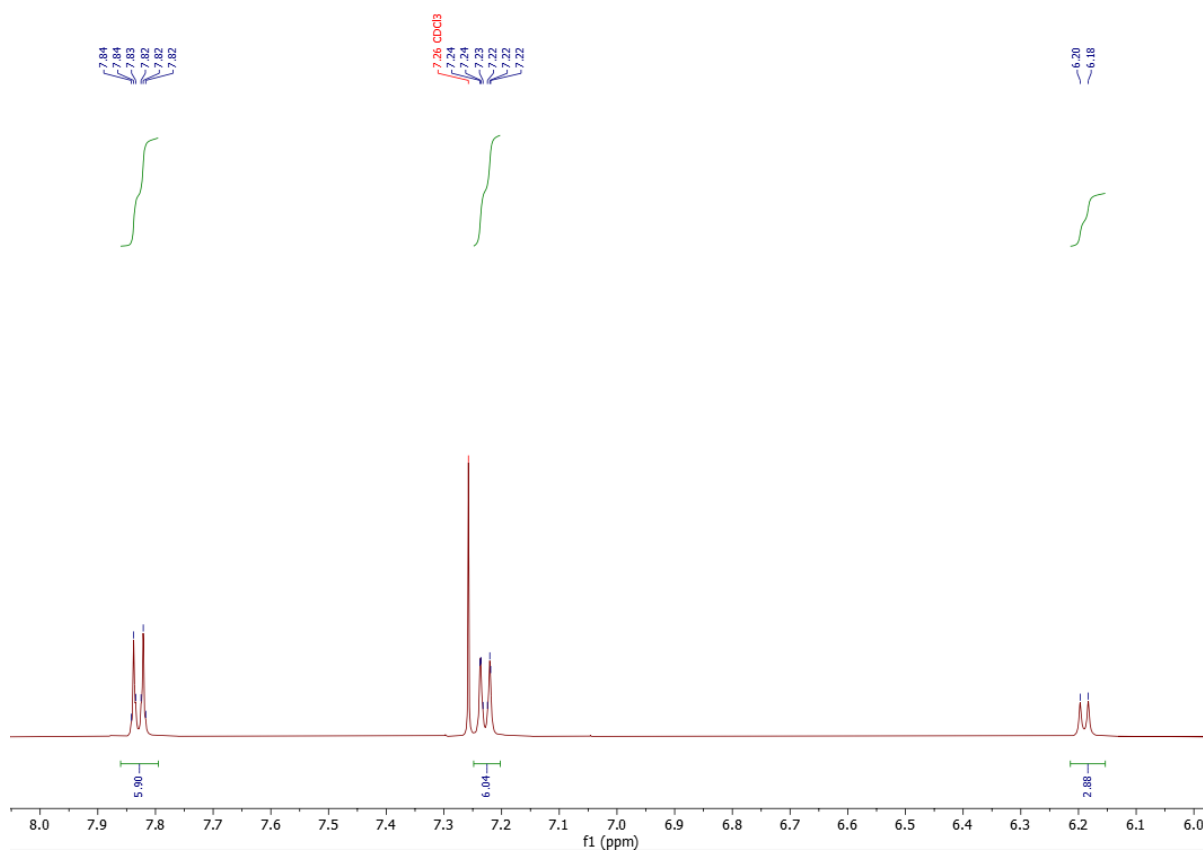


Figure A2.5: Expansion of  $^1\text{H}$  NMR spectrum of  $N,N',N''$ -((2*S*, 2'*S*, 2''*S*)-nitrilotris(3-methylbutane-1,2-diyl))tris(4-methylbenzenesulfonamide (**64**)) (6-8 ppm) (500 MHz,  $\text{CDCl}_3$ ).

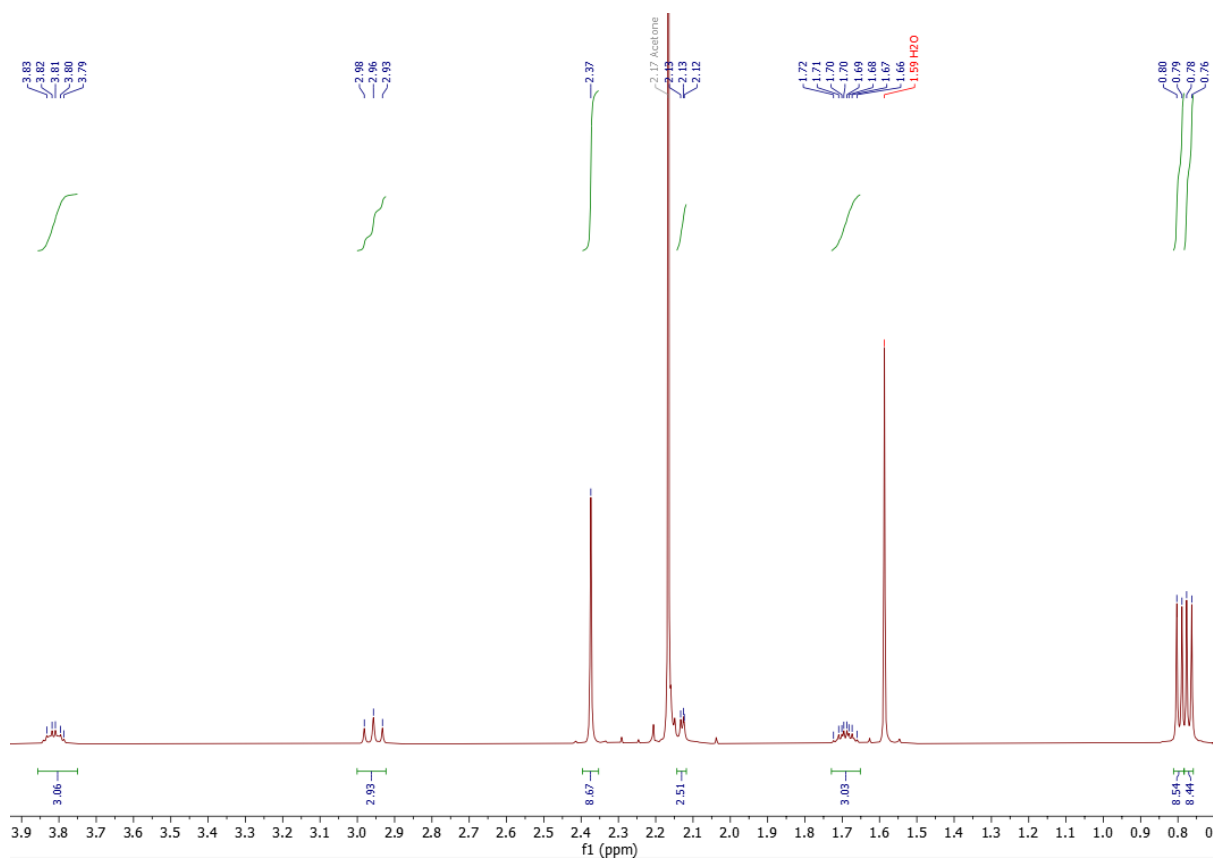


Figure A2.6: Expansion of  $^1\text{H}$  NMR spectrum of  $N,N',N''$ -((2*S*, 2'*S*, 2''*S*)-nitrilotris(3-methylbutane-1,2-diyl))tris(4-methylbenzenesulfonamide (**64**)) (0-4 ppm) (500 MHz,  $\text{CDCl}_3$ ).



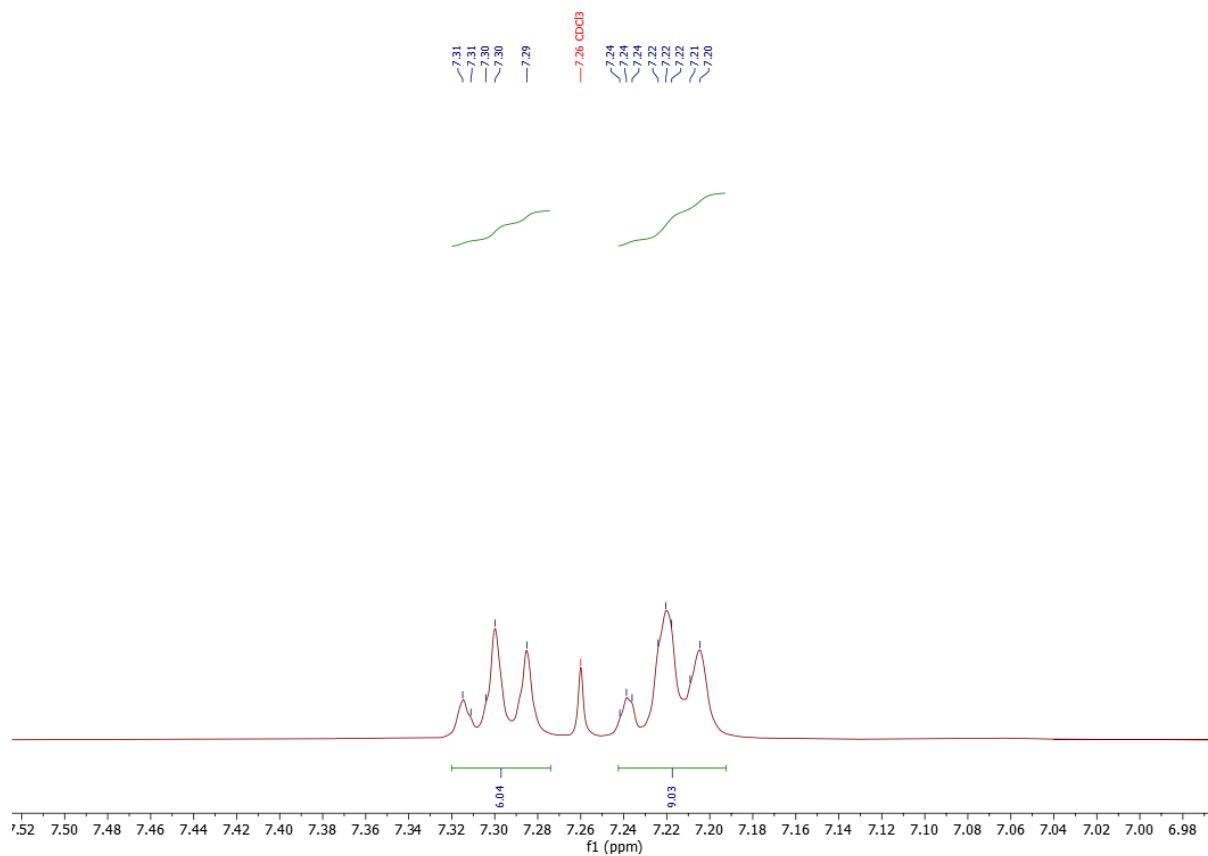


Figure A2.8: Expansion of  $^1\text{H}$  NMR spectrum of tri-*tert*-butyl ((2*S*,2'*S*,2''*S*)-nitrilotris(3-phenylpropane-1,2-diyl))tricarbamate (**65**) (6-8 ppm) (500 MHz,  $\text{CDCl}_3$ ).



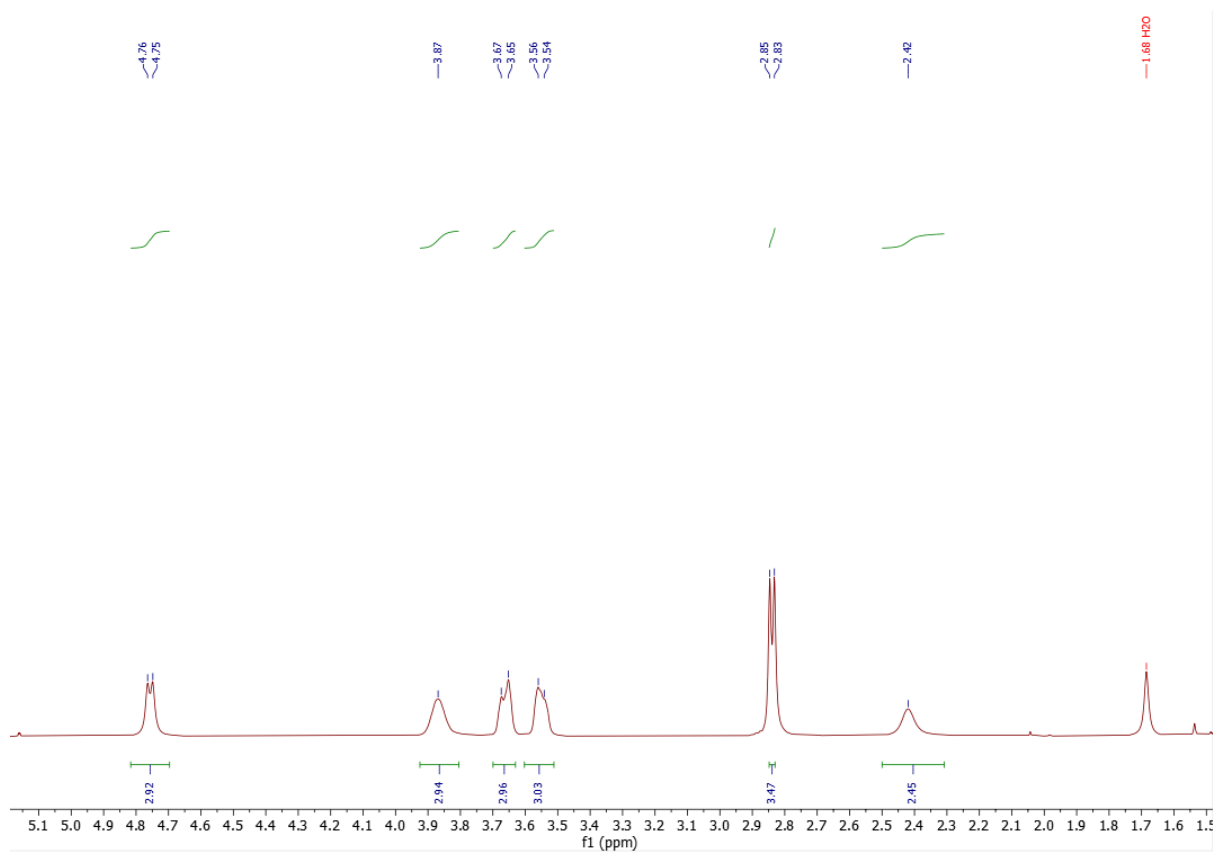


Figure A2.9: Expansion of  $^1\text{H}$  NMR spectrum of tri-*tert*-butyl ((2*S*,2'*S*,2''*S*)-nitrilotris(3-phenylpropane-1,2-diyl))tricarbamate (**65**) (1-6 ppm) (500 MHz,  $\text{CDCl}_3$ ).

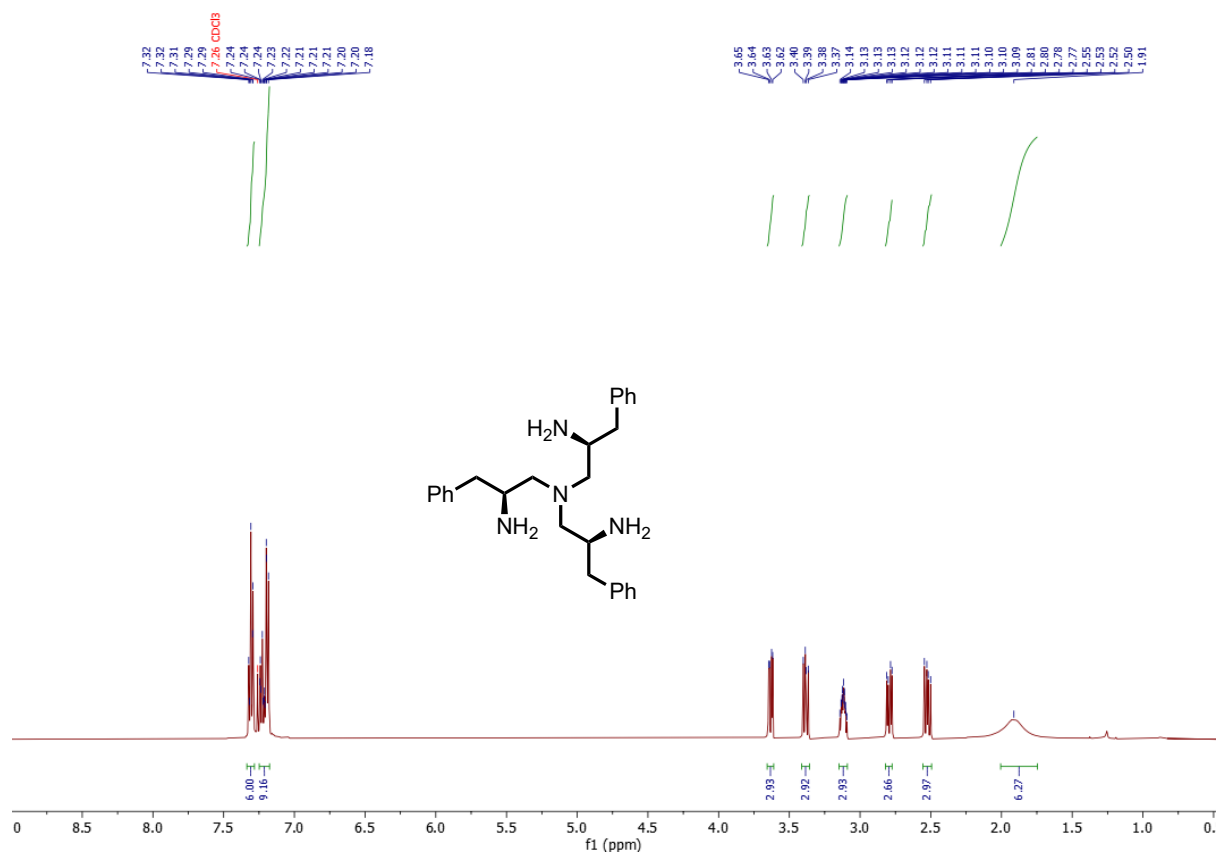


Figure A2.10: <sup>1</sup>H NMR spectrum of (S)-N<sup>1</sup>,N<sup>1</sup>-bis((S)-2-amino-3-phenylpropyl)-3-phenylpropane-1,2-diamine (**66**) (500 MHz, CDCl<sub>3</sub>).

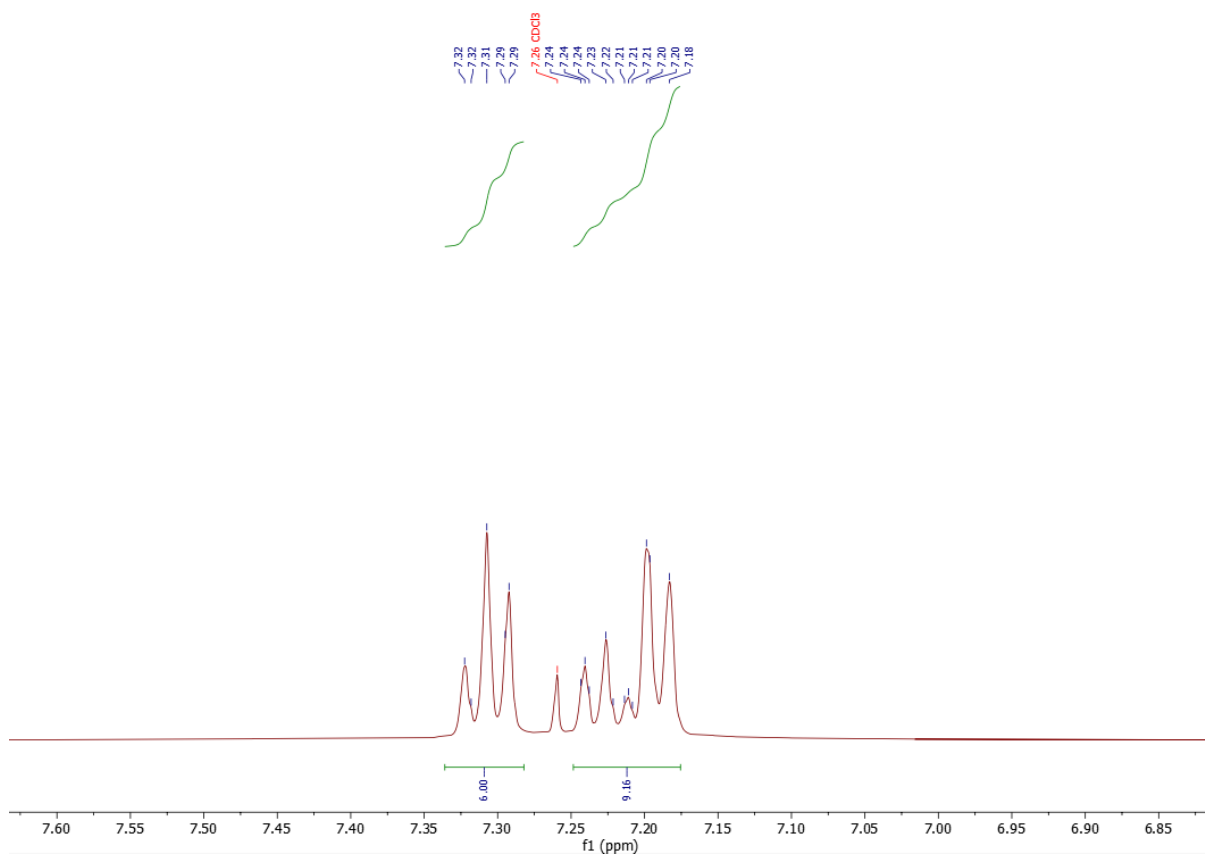


Figure A2.11: Expansion of  $^1\text{H}$  NMR spectrum of  $(S)\text{-}N^1,N^1\text{-bis}((S)\text{-}2\text{-amino-3-phenylpropyl})\text{-3-phenylpropane-1,2-diamine}$  (**66**) (6–8 ppm) (500 MHz,  $\text{CDCl}_3$ ).

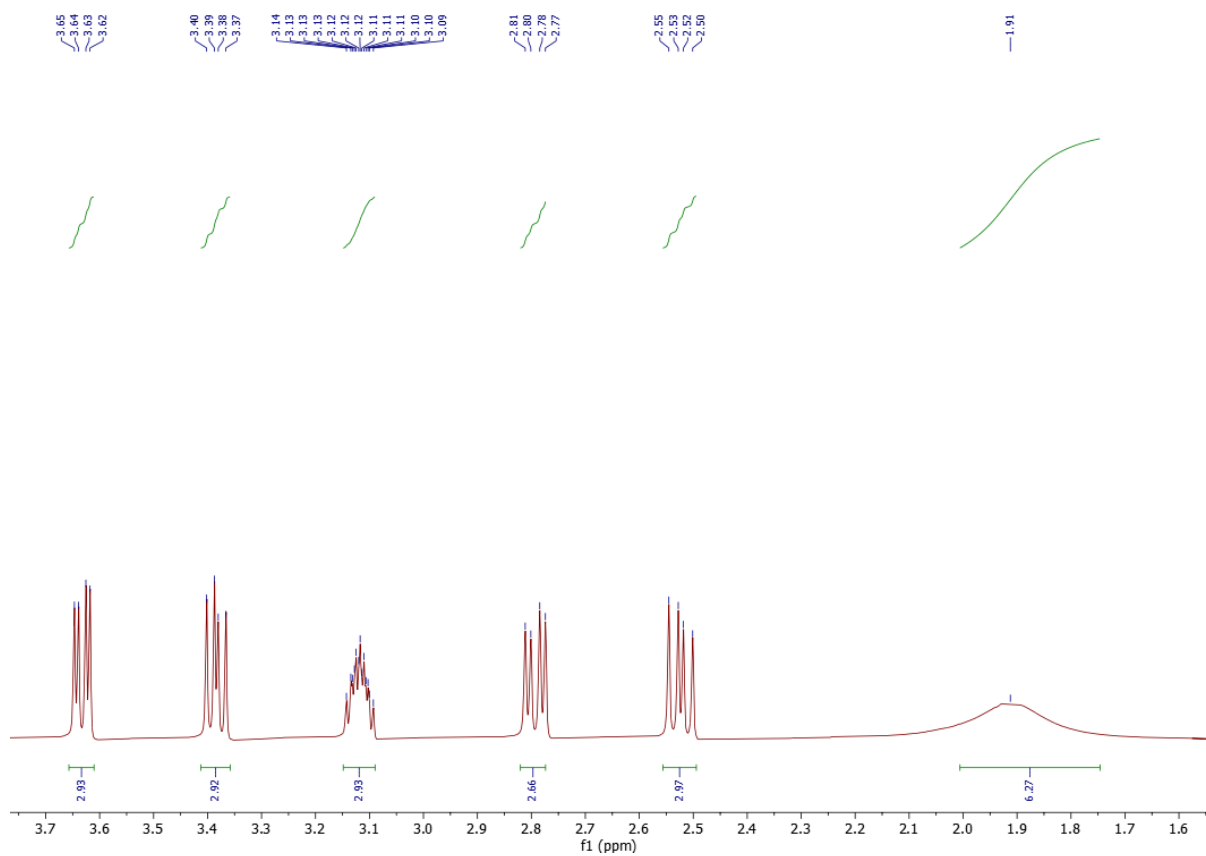


Figure A2.12: Expansion of  $^1\text{H}$  NMR spectrum of  $(S)\text{-}N^1,N^1\text{-bis}((S)\text{-}2\text{-amino-3-phenylpropyl})\text{-3-phenylpropane-1,2-diamine}$  (**66**) (1-4 ppm) (500 MHz,  $\text{CDCl}_3$ ).

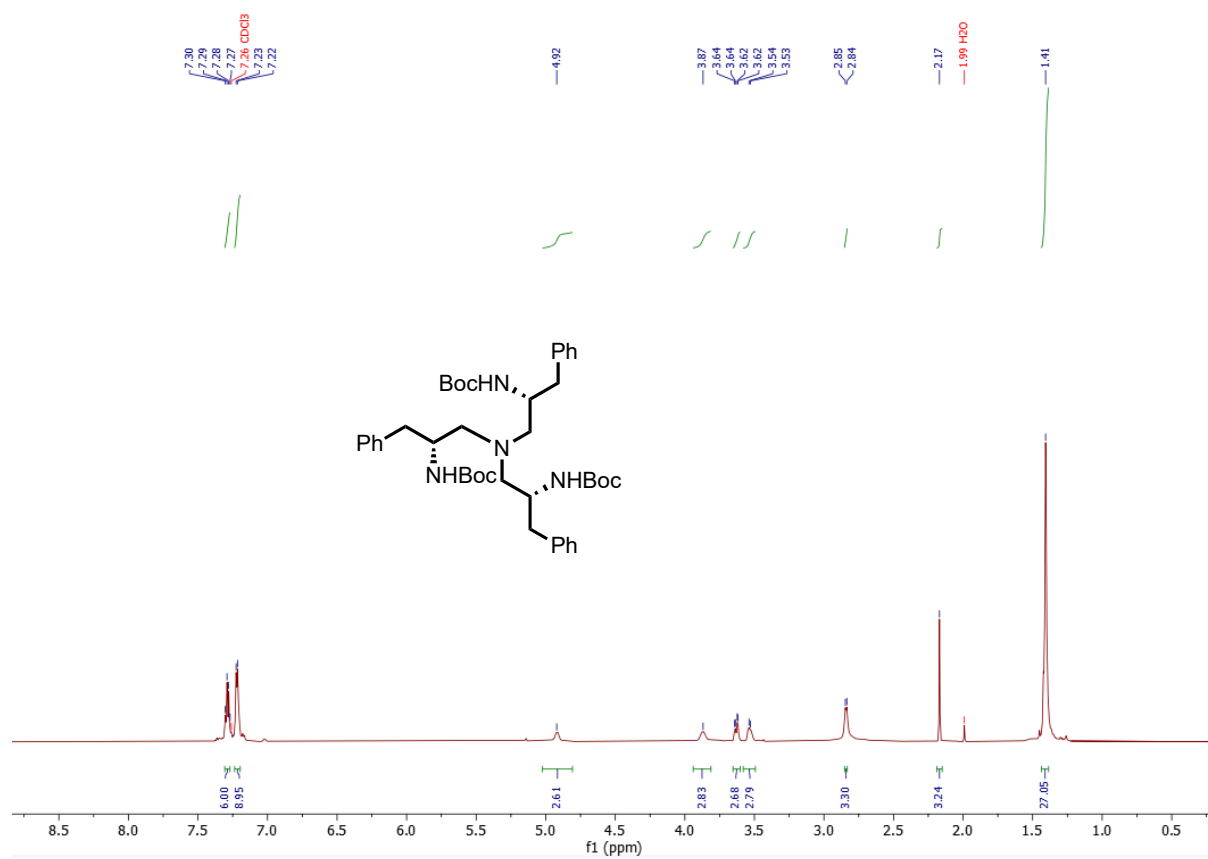


Figure A2.13: <sup>1</sup>H NMR spectrum of tri-*tert*-butyl ((2*R*,2'*R*,2''*R*)-nitrilotris(3-phenylpropane-1,2-diyl))tricarbamate (**67**) (600 MHz, CDCl<sub>3</sub>).

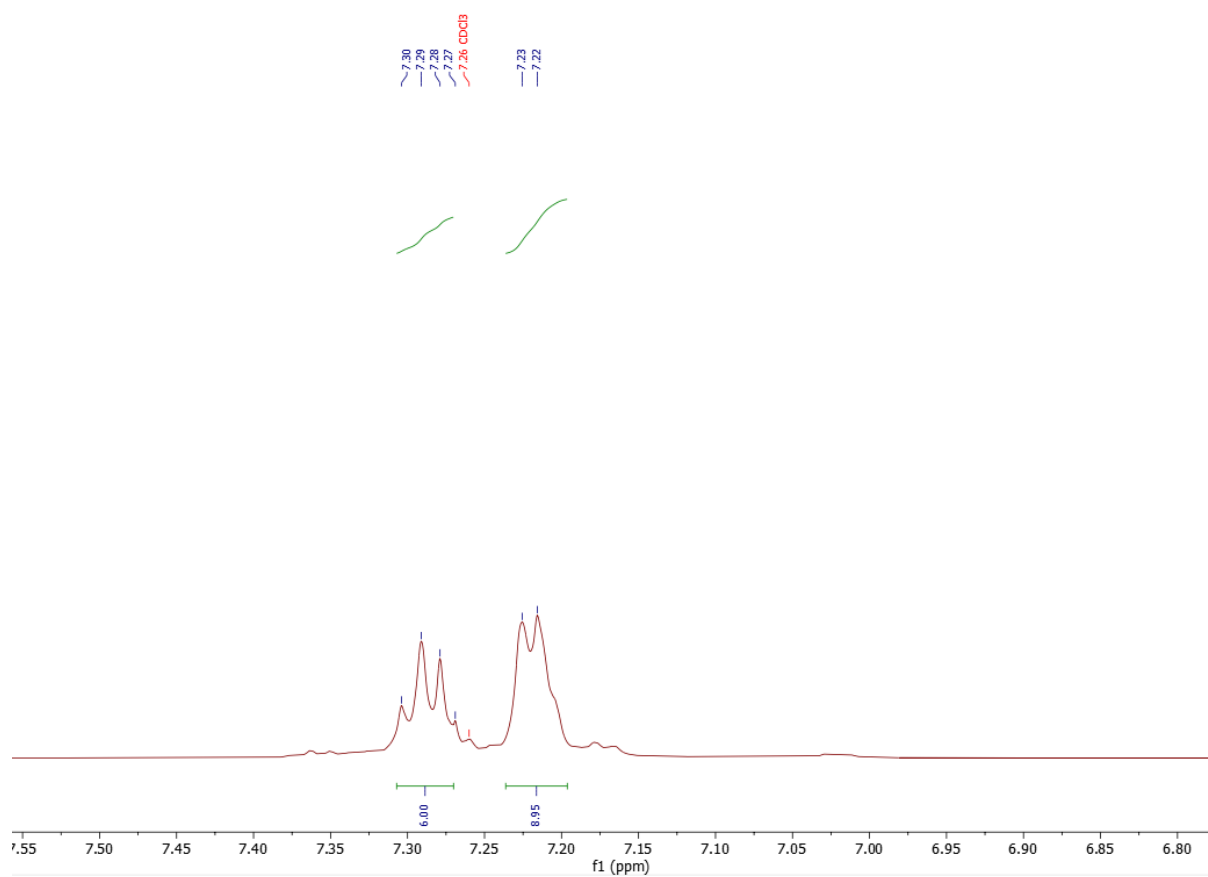


Figure A2.14: Expansion of  $^1\text{H}$  NMR spectrum of tri-*tert*-butyl ((2*R*,2'*R*,2''*R*)-nitrilotris(3-phenylpropane-1,2-diyl))tricarbamate (**67**) (6-8 ppm) (600 MHz,  $\text{CDCl}_3$ ).

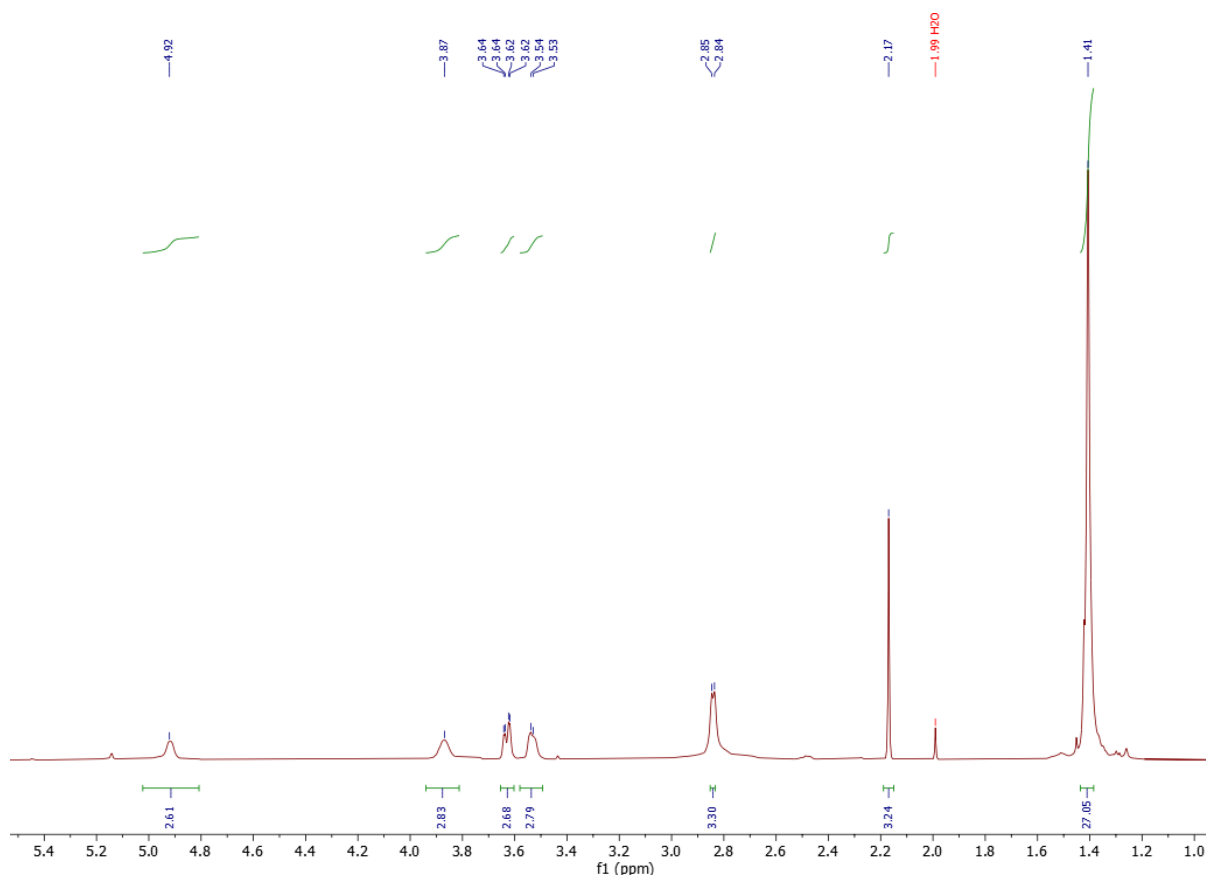


Figure A2.15: Expansion of  $^1\text{H}$  NMR spectrum of tri-*tert*-butyl ((2*R*,2'*R*,2''*R*)-nitrilotris(3-phenylpropane-1,2-diyl))tricarbamate (**67**) (1-6 ppm) (600 MHz,  $\text{CDCl}_3$ ).

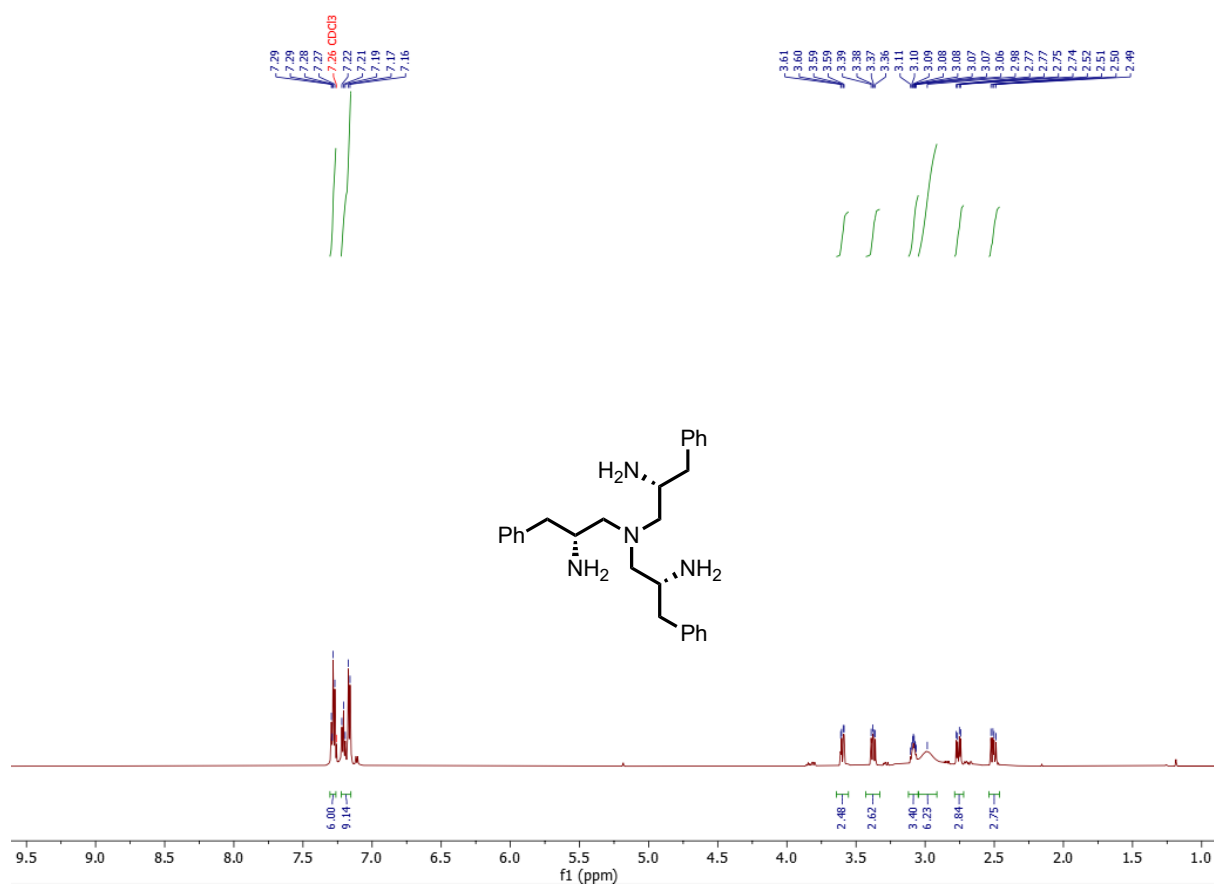


Figure A2.16: <sup>1</sup>H NMR spectrum of (R)-N<sup>1</sup>,N<sup>1</sup>-bis((R)-2-amino-3-phenylpropyl)-3-phenylpropane-1,2-diamine (**68**) (600 MHz, CDCl<sub>3</sub>).



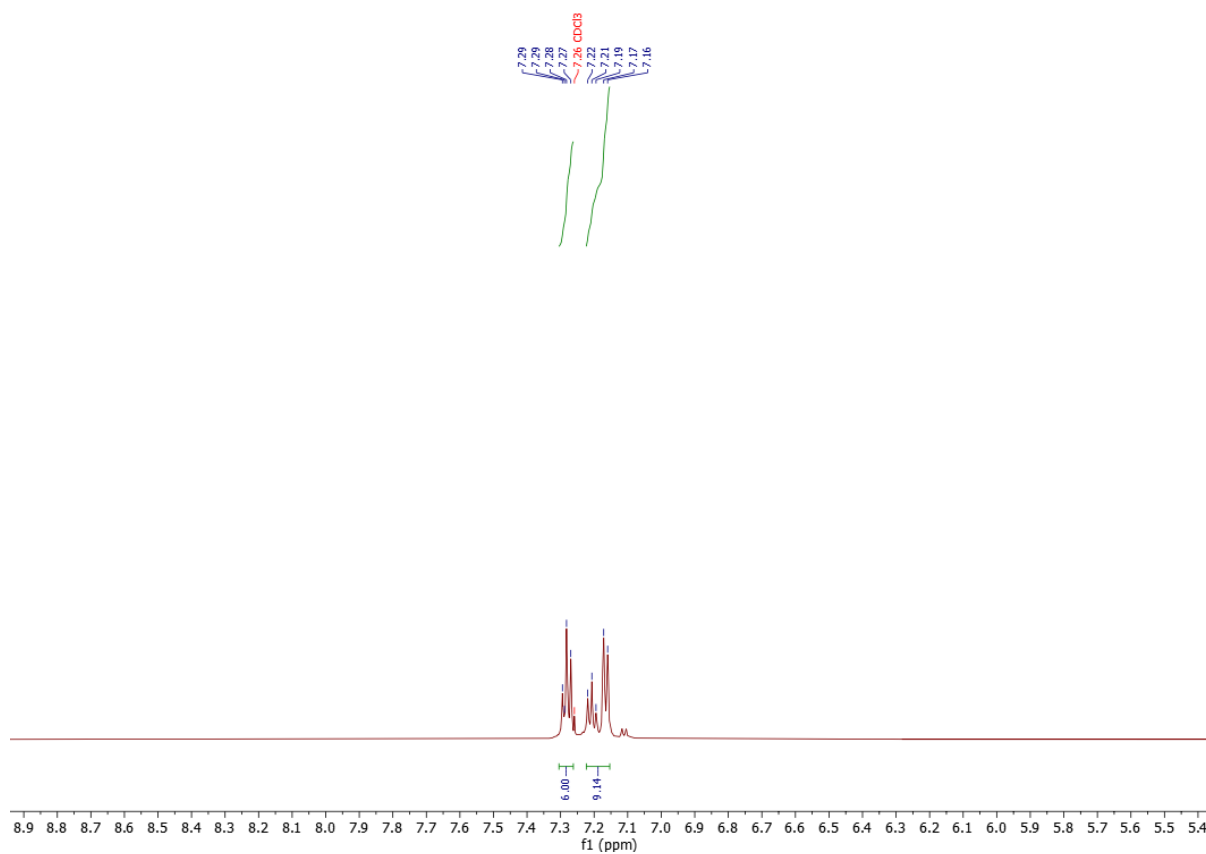


Figure A2.17: Expansion of  $^1\text{H}$  NMR spectrum of  $(R)\text{-}N^1,N^1\text{-bis}((R)\text{-}2\text{-amino-3-phenylpropyl})\text{-3-phenylpropane-1,2-diamine}$  (**68**) (5-9 ppm) (600 MHz,  $\text{CDCl}_3$ ).

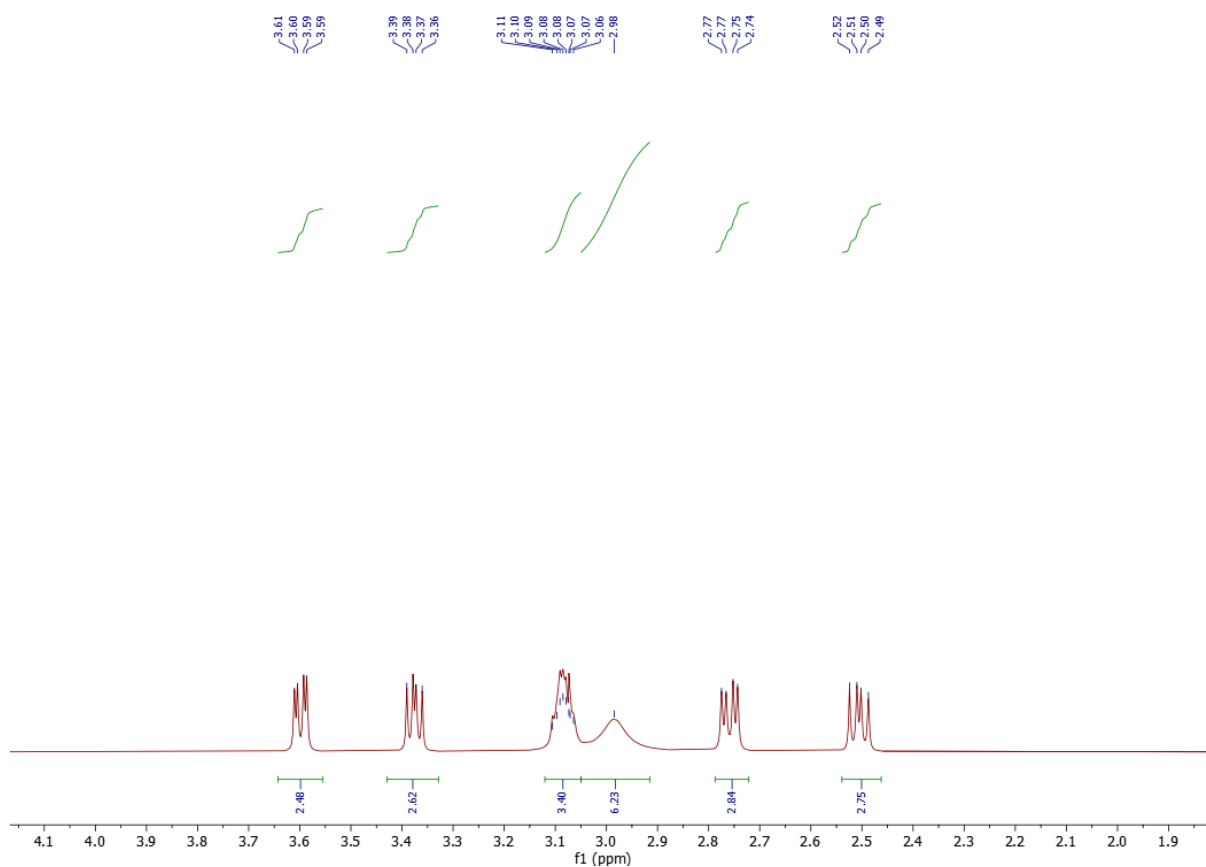


Figure A2.18: Expansion of  $^1\text{H}$  NMR spectrum of (R)- $N^1,N^1$ -bis((R)-2-amino-3-phenylpropyl)-3-phenylpropane-1,2-diamine (**68**) (1-5 ppm) (600 MHz,  $\text{CDCl}_3$ ).





## A2.2 $^{13}\text{C}$ NMR

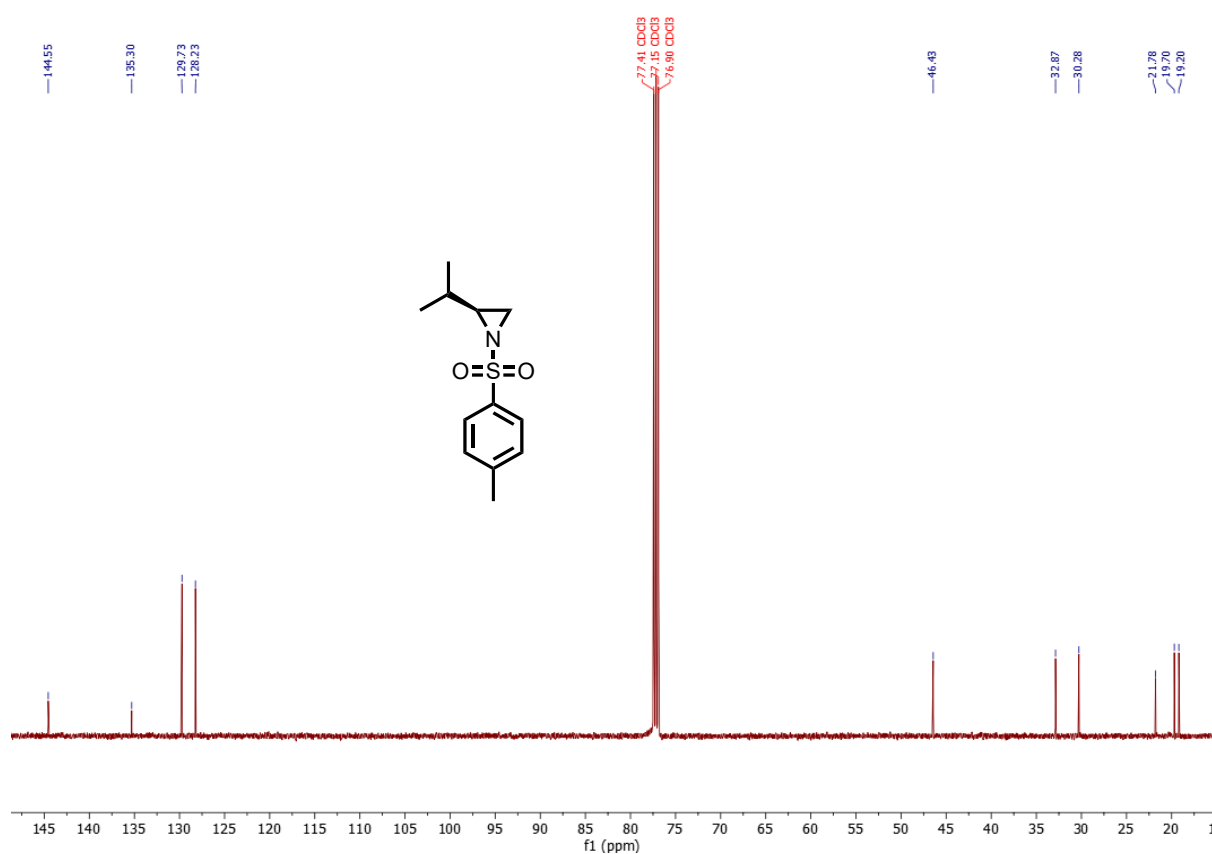


Figure A2.21:  $^{13}\text{C}$  NMR spectrum of (S)-2-isopropyl-1-tosylaziridine (**63**) (500 MHz,  $\text{CDCl}_3$ ).

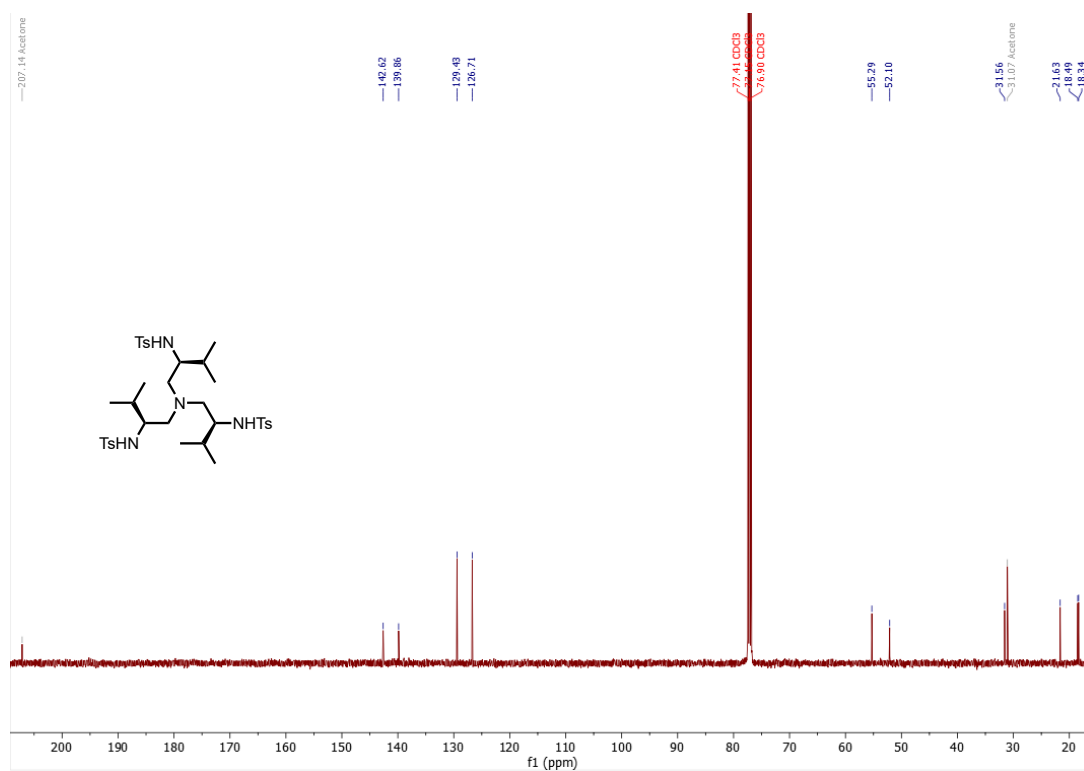


Figure A2.22: <sup>13</sup>C NMR spectrum of *N,N',N''*-((2*S*, 2'*S*, 2''*S*)-nitrilotris(3-methylbutane-1,2-diyl))tris(4-methylbenzenesulfonamide (**64**) (500 MHz, CDCl<sub>3</sub>).

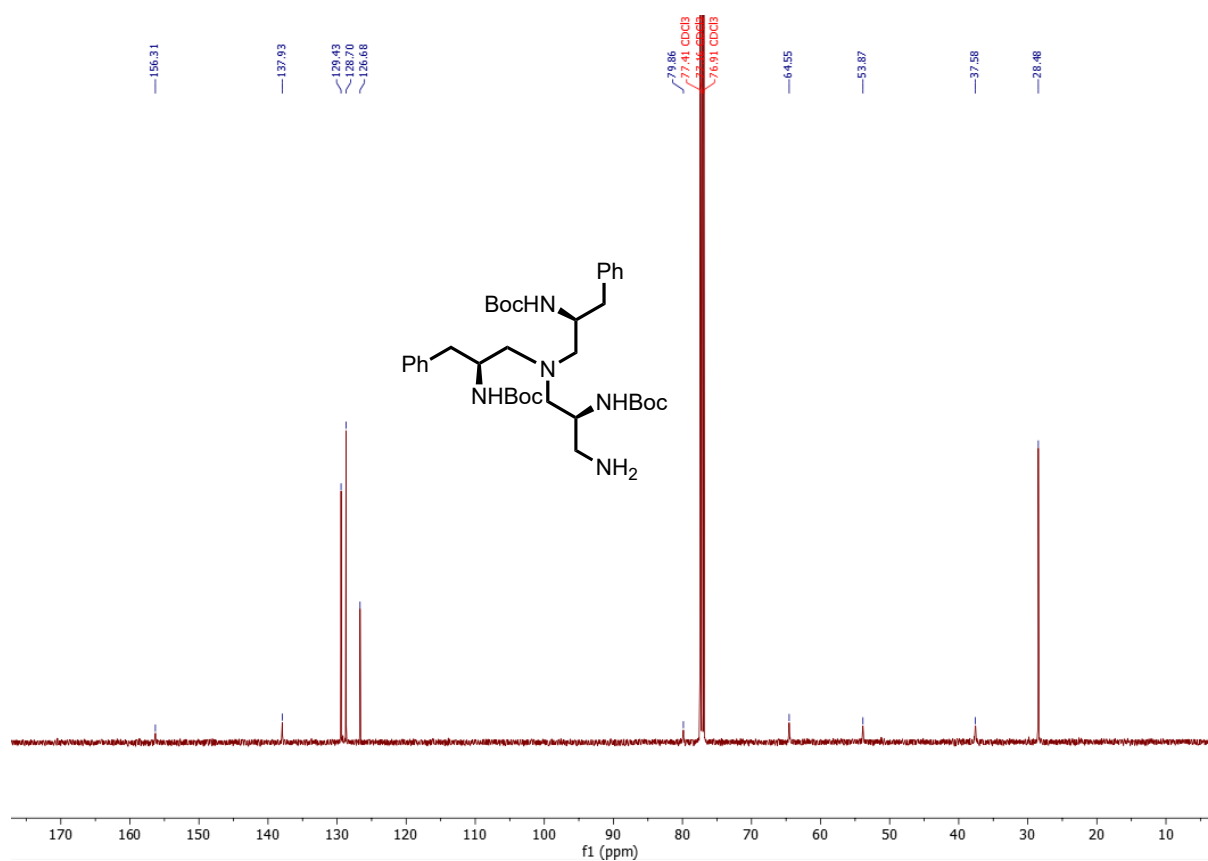


Figure A2.23: <sup>13</sup>C NMR spectrum of tri-tert-butyl ((2*S*,2'*S*,2''*S*)-nitrilotris(3-phenylpropane-1,2-diyl))tricarbamate (**65**) (500 MHz, CDCl<sub>3</sub>).

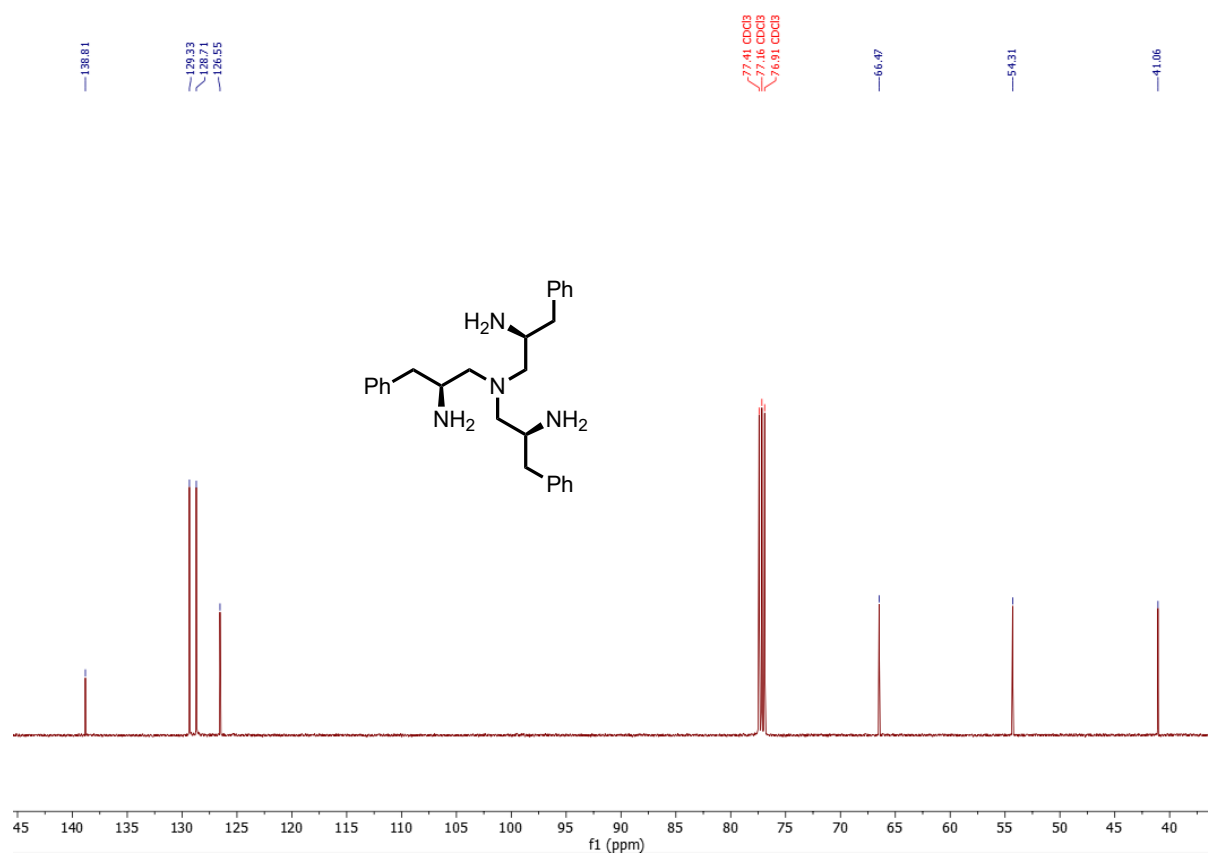


Figure A2.24: <sup>13</sup>C NMR spectrum of *(S)*-*N*<sup>1</sup>,*N*<sup>1</sup>-bis(*(S)*-2-amino-3-phenylpropyl)-3-phenylpropane-1,2-diamine (**66**) (500 MHz, CDCl<sub>3</sub>).



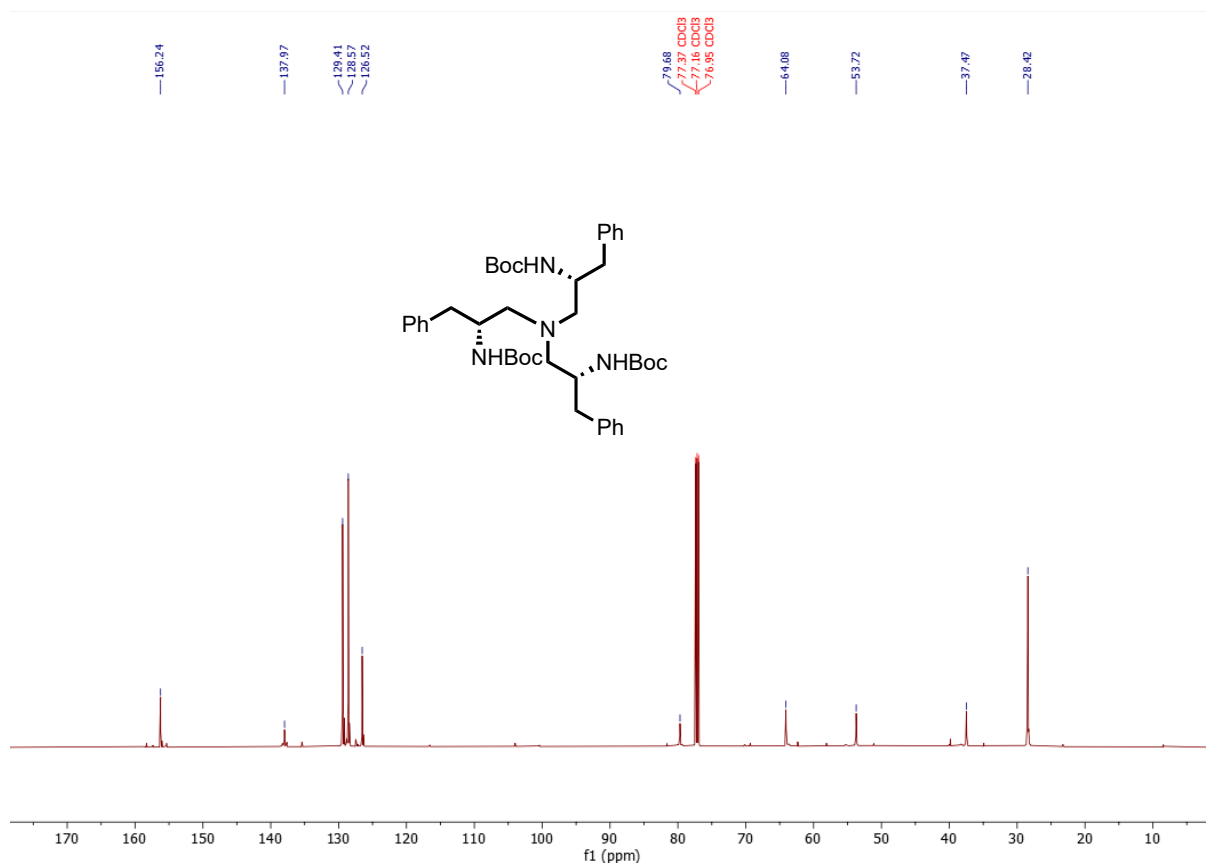


Figure A2.25: <sup>13</sup>C NMR spectrum of tri-tert-butyl ((2R,2'R,2''R)-nitrilotris(3-phenylpropane-1,2-diyl))tricarbamate (**67**) (600 MHz, CDCl<sub>3</sub>).

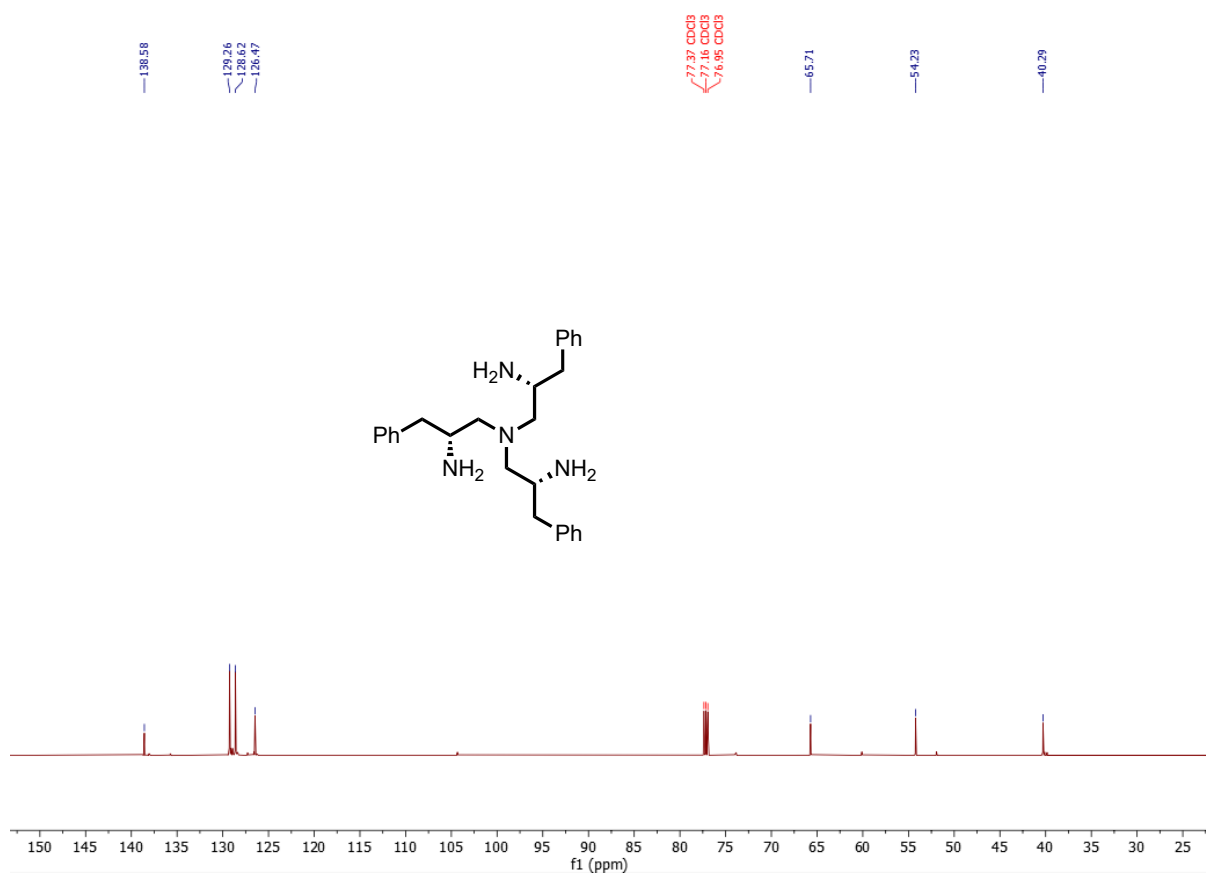


Figure A2.26: <sup>13</sup>C NMR spectrum of (R)-N<sup>1</sup>,N<sup>1</sup>-bis((R)-2-amino-3-phenylpropyl)-3-phenylpropane-1,2-diamine (**68**) (600 MHz, CDCl<sub>3</sub>).

## A2.3 IR

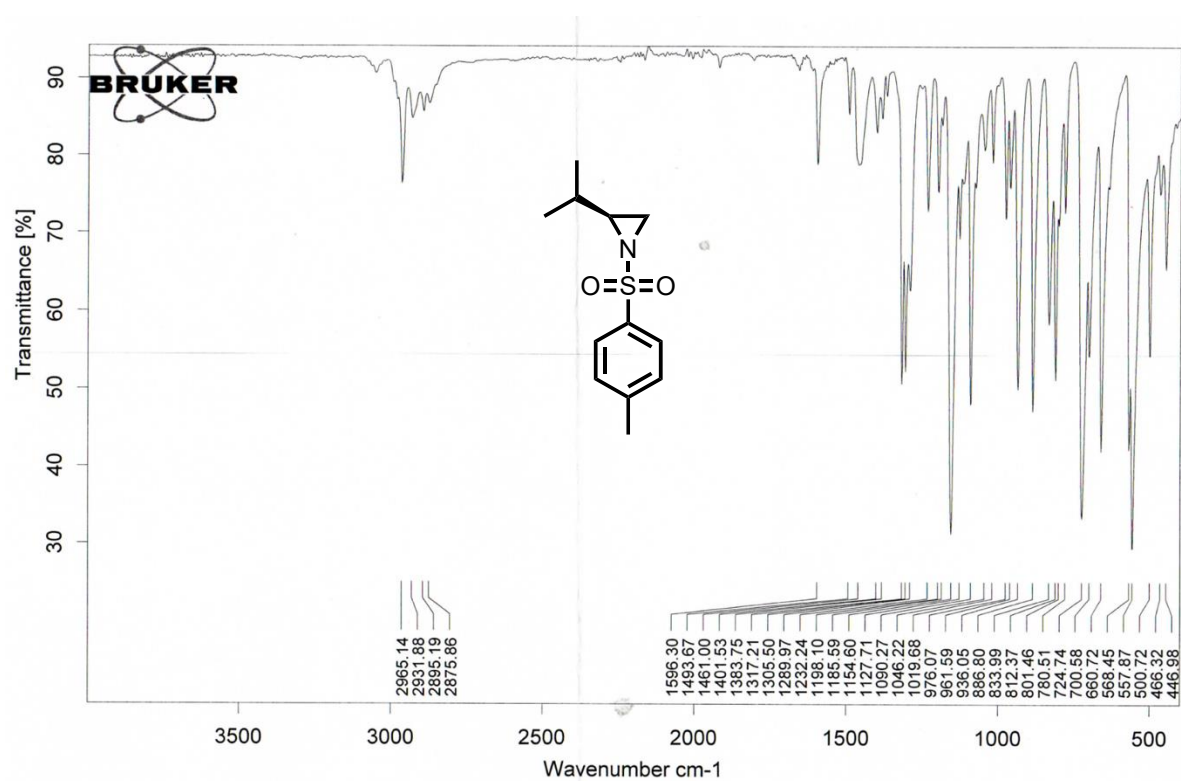


Figure A2.27: IR spectrum of (S)-2-isopropyl-1-tosylaziridine (63).

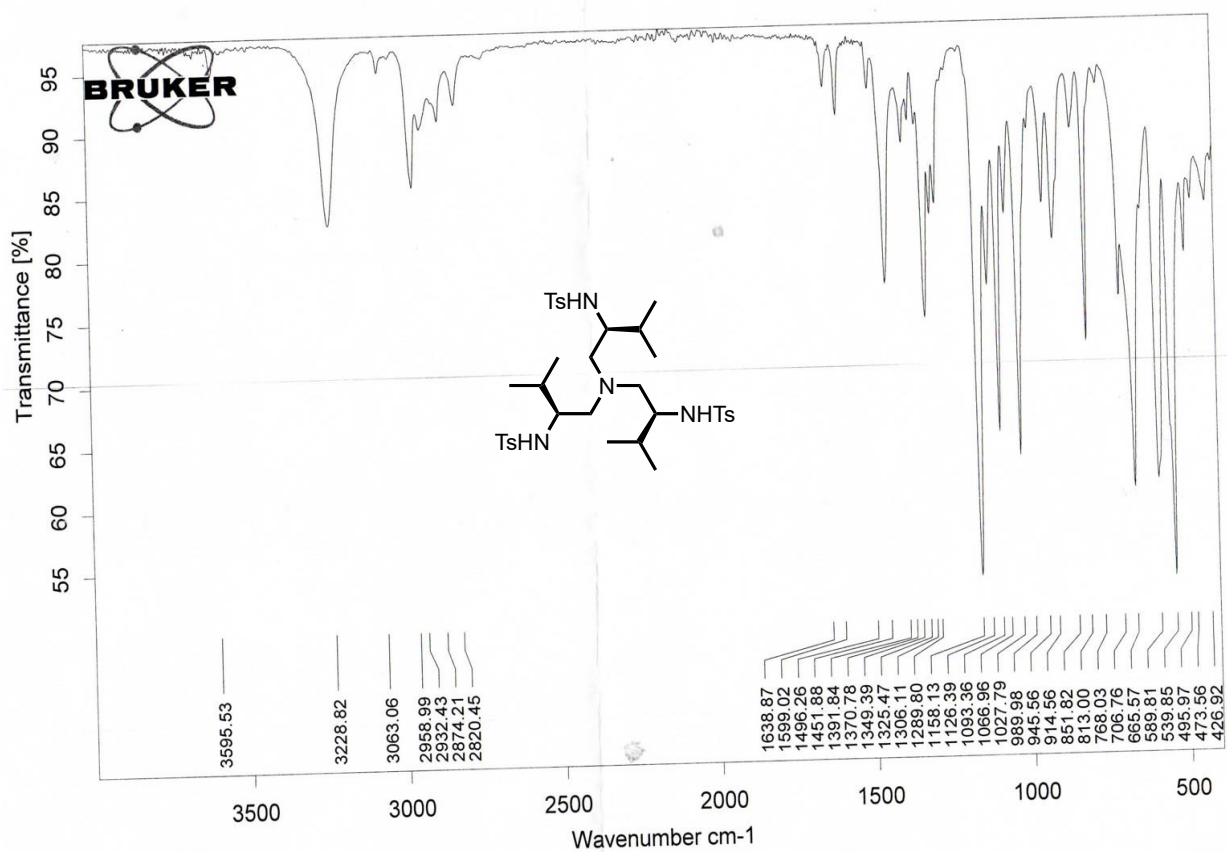


Figure A2.28: IR spectrum of *N,N,N'*-((2*S*, 2'*S*, 2''*S*)-nitrilotris(3-methylbutane-1,2-diyl))tris(4-methylbenzenesulfonamide) (**64**).

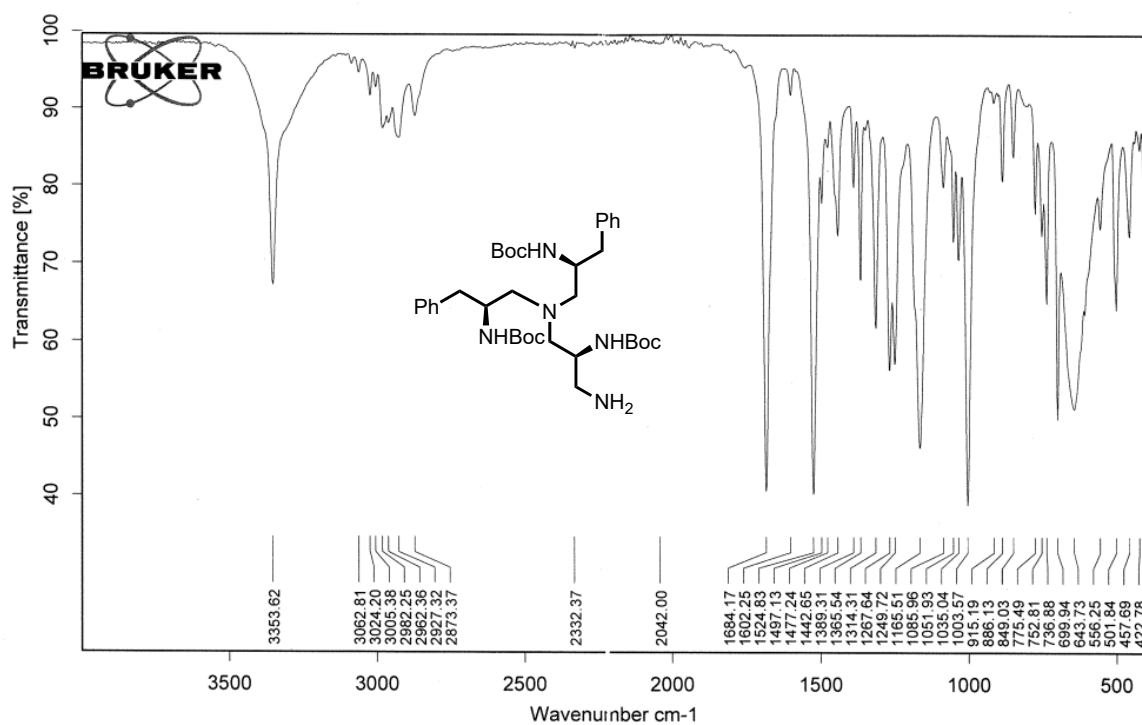


Figure A2.29: IR spectrum of tri-tert-butyl ((2S,2'S,2''S)-nitrilotris(3-phenylpropane-1,2-diyl))tricarbamate (**65**).

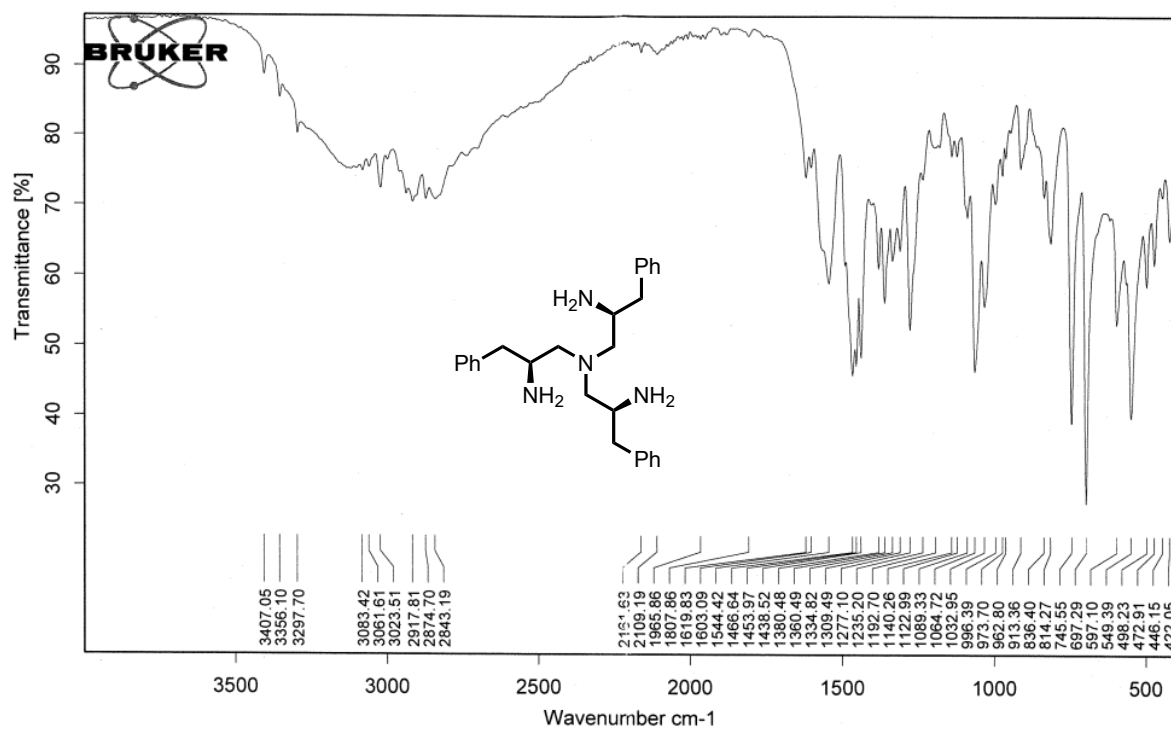


Figure A2.30: IR spectrum of (S)-N¹,N¹-bis((S)-2-amino-3-phenylpropyl)-3-phenylpropane-1,2-diamine (66).

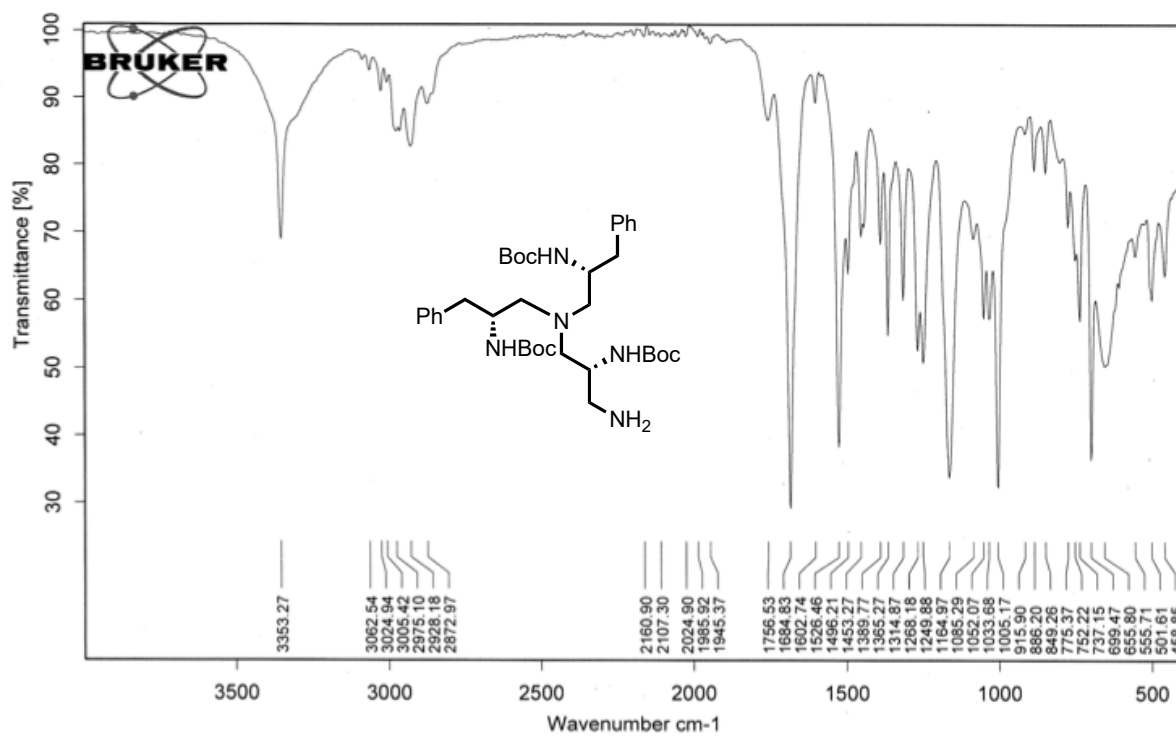


Figure A2.31: IR spectrum of tri-tert-butyl ((2R,2'R,2''R)-nitrilotris(3-phenylpropane-1,2-diyl))tricarbamate (**67**).

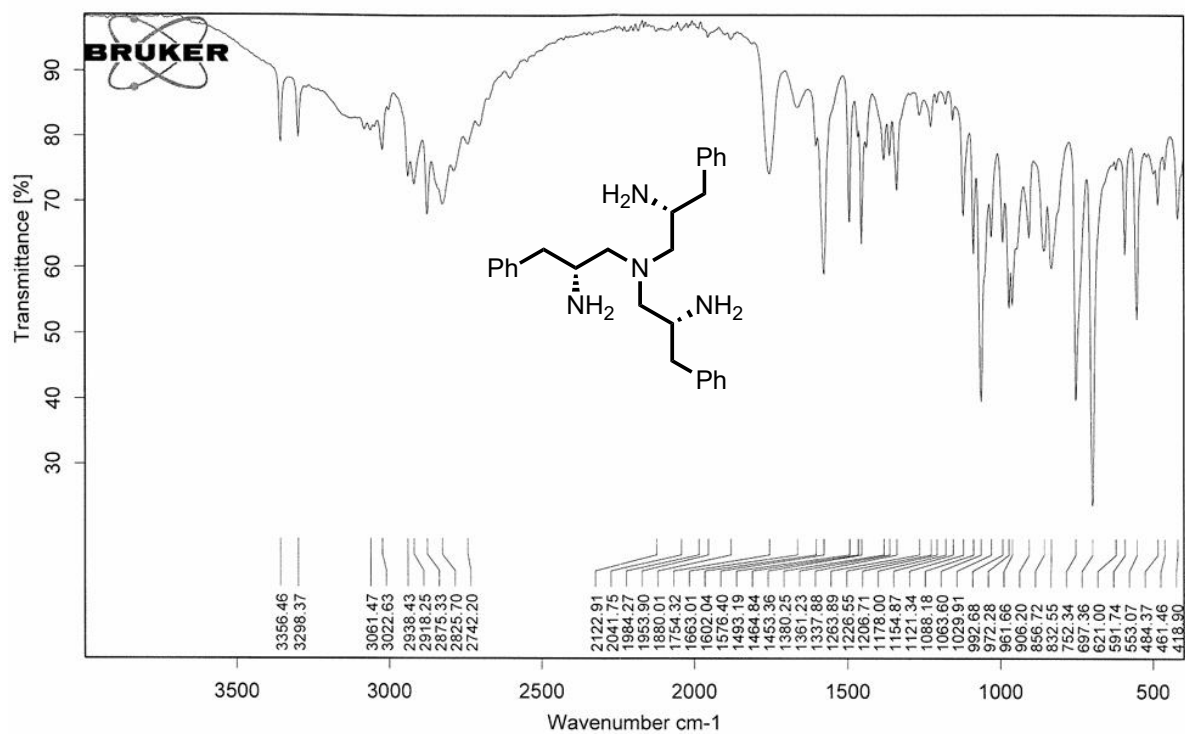


Figure A2.32: IR spectrum of (R)-N¹,N¹-bis((R)-2-amino-3-phenylpropyl)-3-phenylpropane-1,2-diamine (**68**).



## A2.4 MS

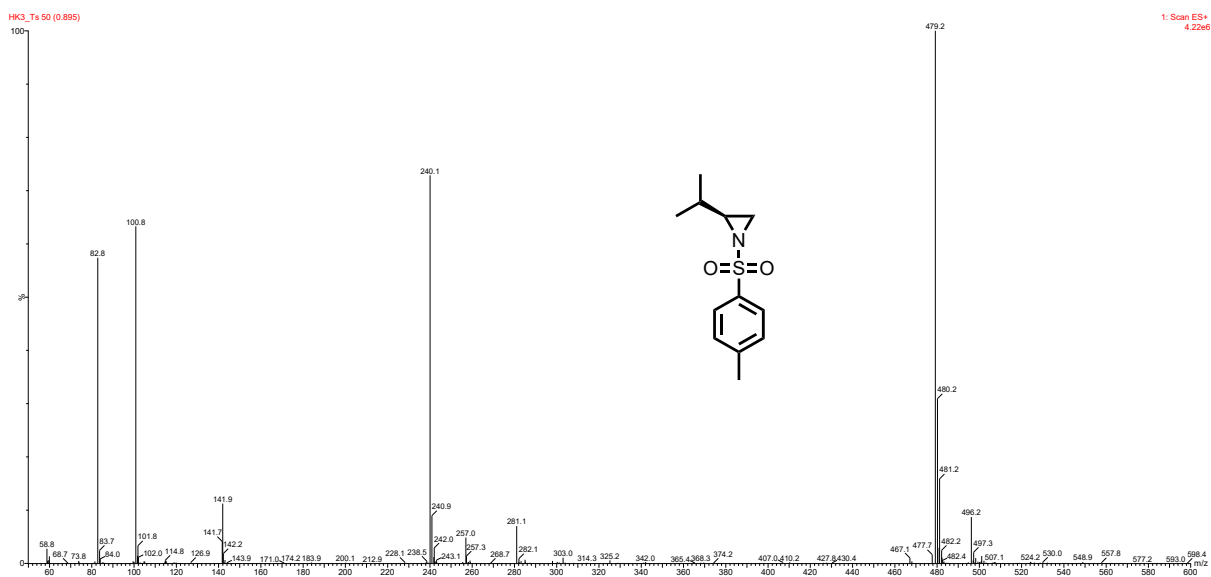


Figure A2.33: Low-resolution mass spectrum of (S)-2-isopropyl-1-tosylaziridine (**63**) (ESI+).

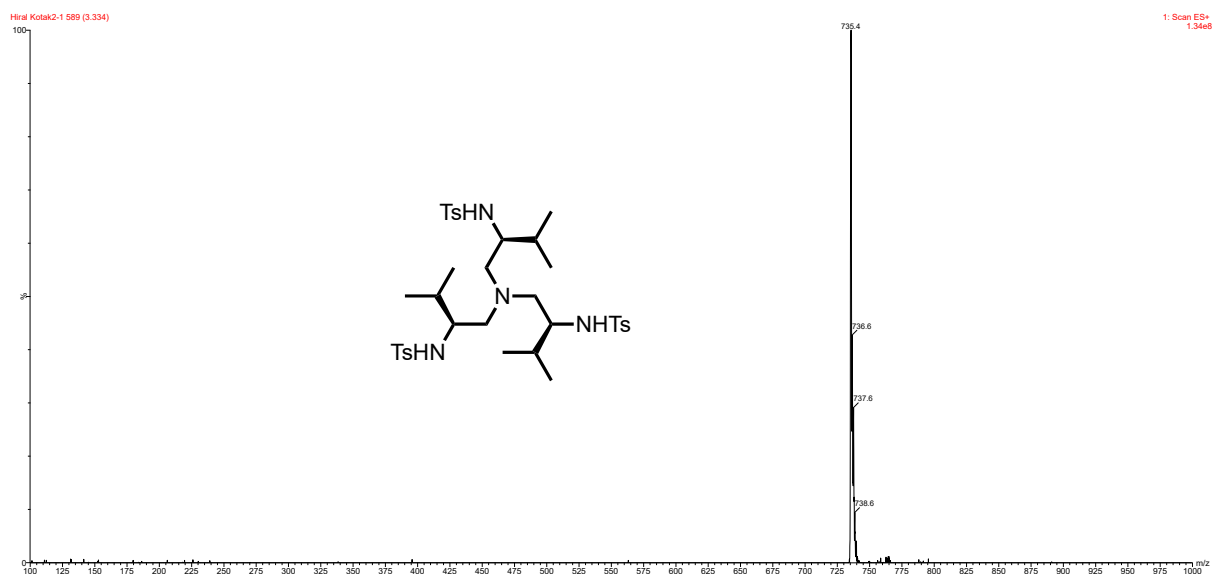


Figure A2.34: Low-resolution mass spectrum of *N,N,N'*-((2*S*, 2'*S*, 2''*S*)-nitrilotris(3-methylbutane-1,2-diyl))tris(4-methylbenzenesulfonamide (**64**)) (ESI+).

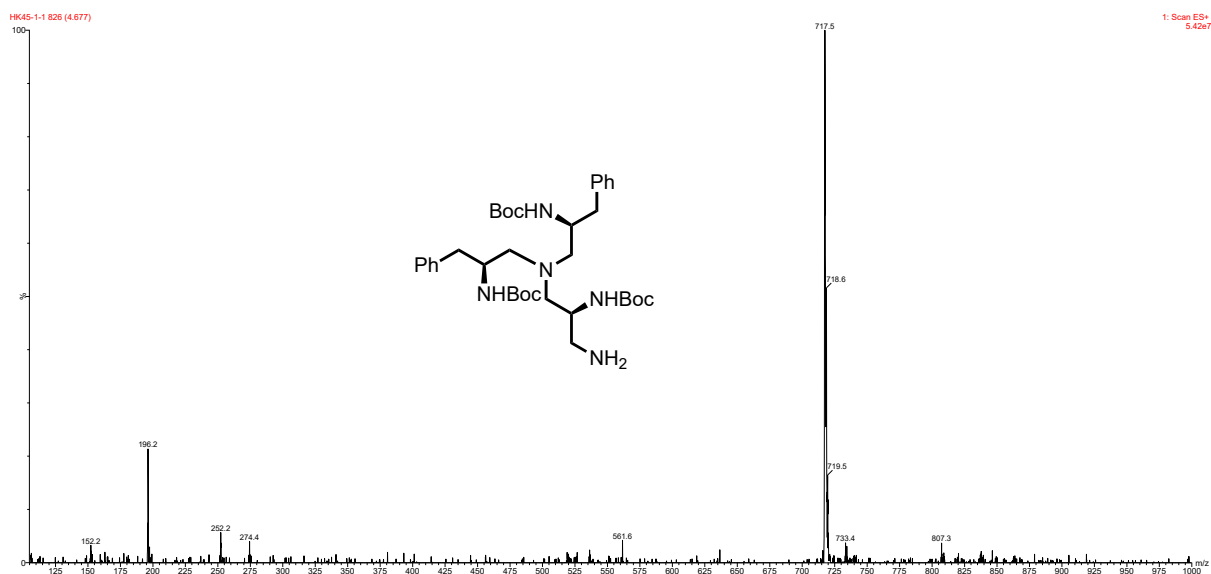


Figure A2.35: Low-resolution mass spectrum of tri-tert-butyl ((2S,2'S,2''S)-nitrilotris(3-phenylpropane-1,2-diyl))tricarbamate (**65**) (ESI+).

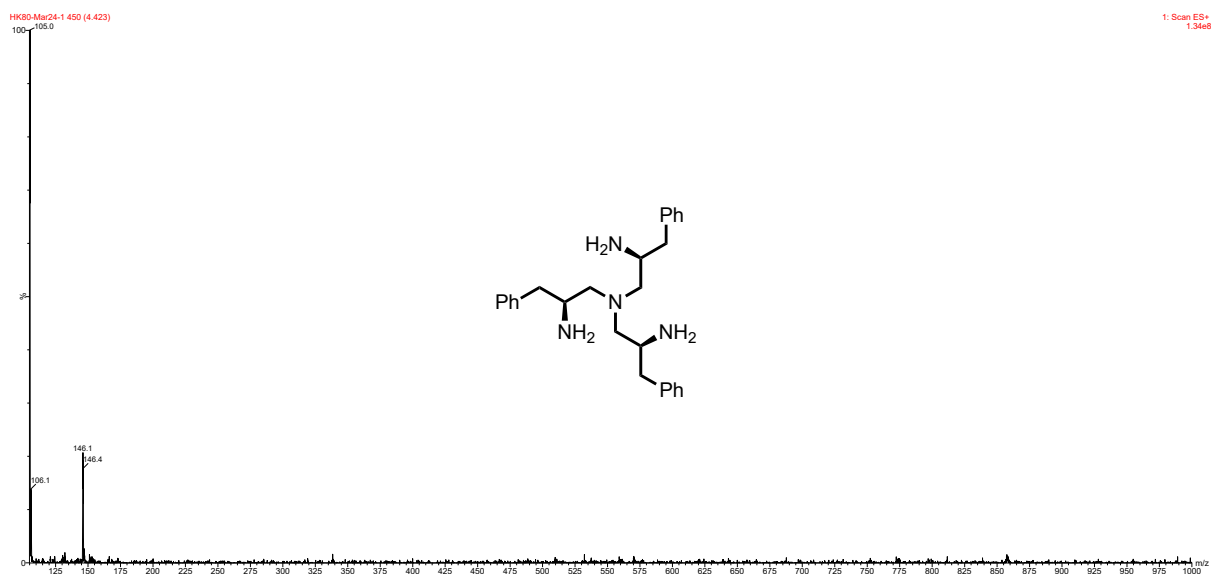


Figure A2.36: Low-resolution mass spectrum of (S)-N<sup>1</sup>,N<sup>1</sup>-bis((S)-2-amino-3-phenylpropyl)-3-phenylpropane-1,2-diamine (**66**) (ESI+).

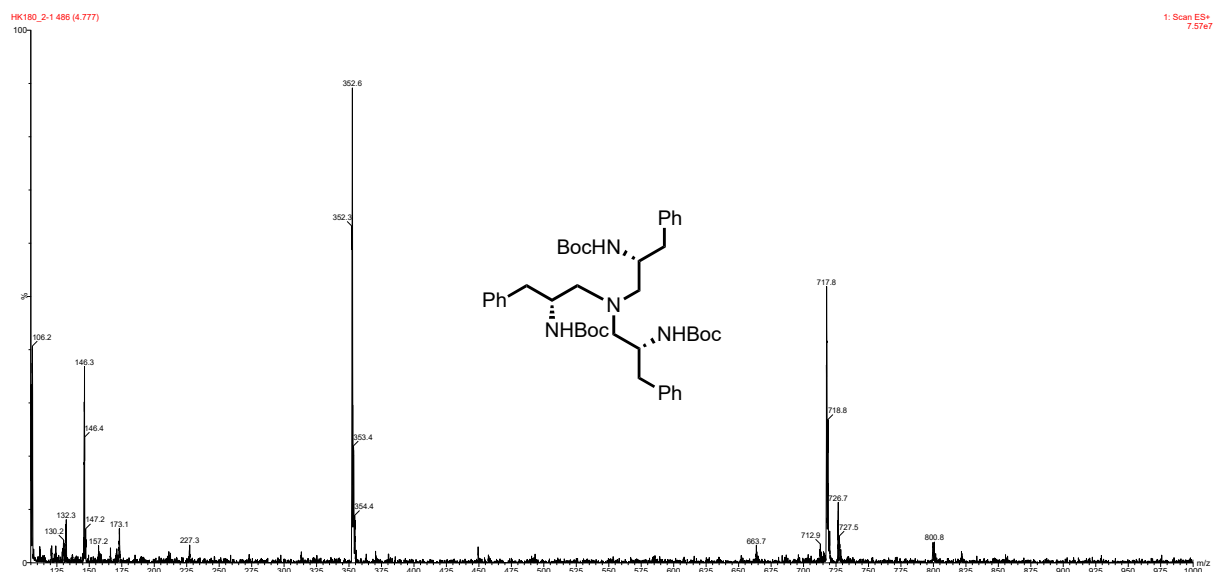


Figure A2.37: Low-resolution mass spectrum of tri-tert-butyl ((2R,2'R,2''R)-nitrilotris(3-phenylpropane-1,2-diyl))tricarbamate (**67**) (ESI+).

T: FTMS + p ESI Full ms [120.0000-1800.0000]

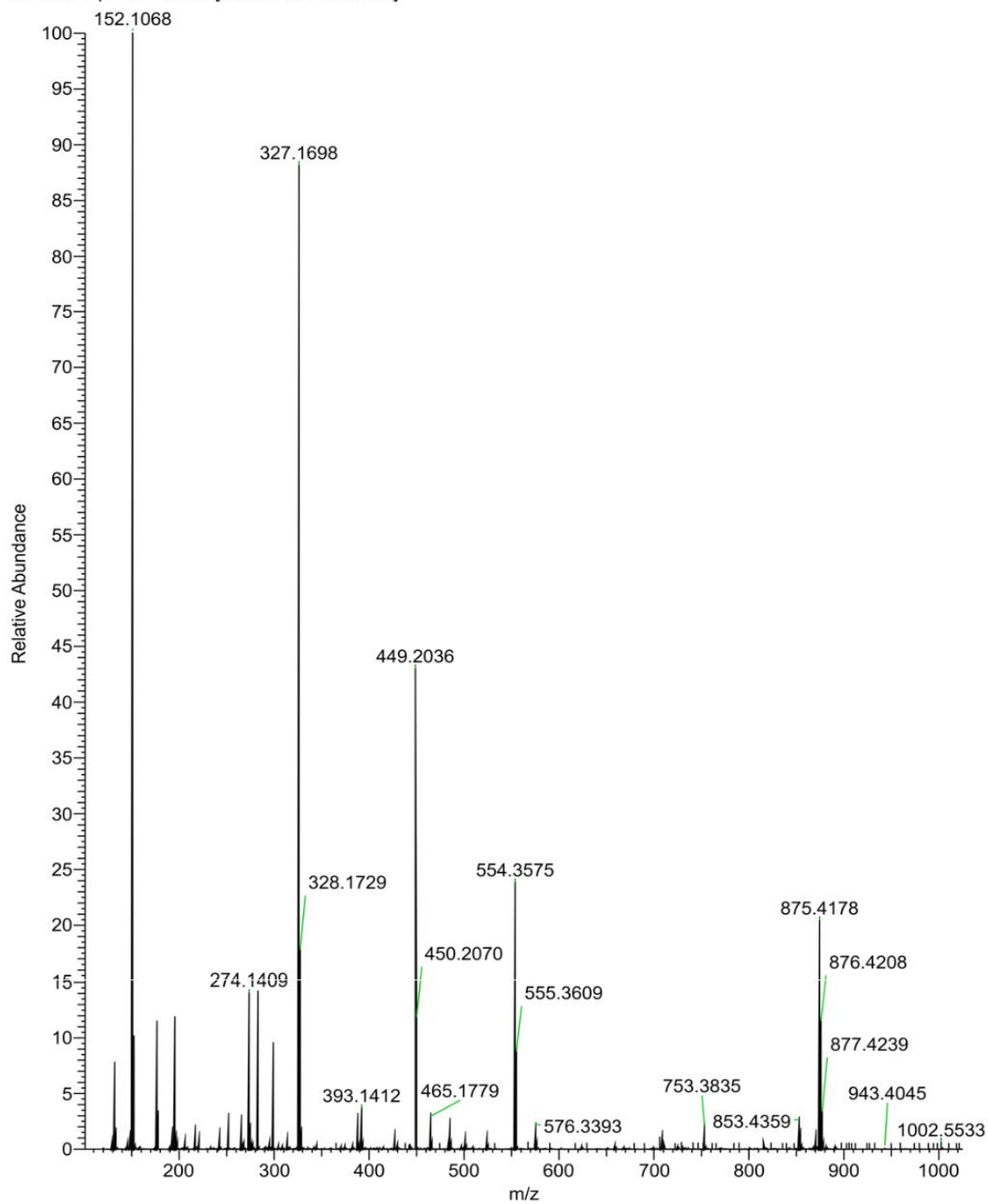


Figure A2.38: High-resolution mass spectrum of tri-tert-butyl ((2R,2'R,2''R)-nitrilotris(3-phenylpropane-1,2-diyl))tricarbamate (**67**) (ESI+).

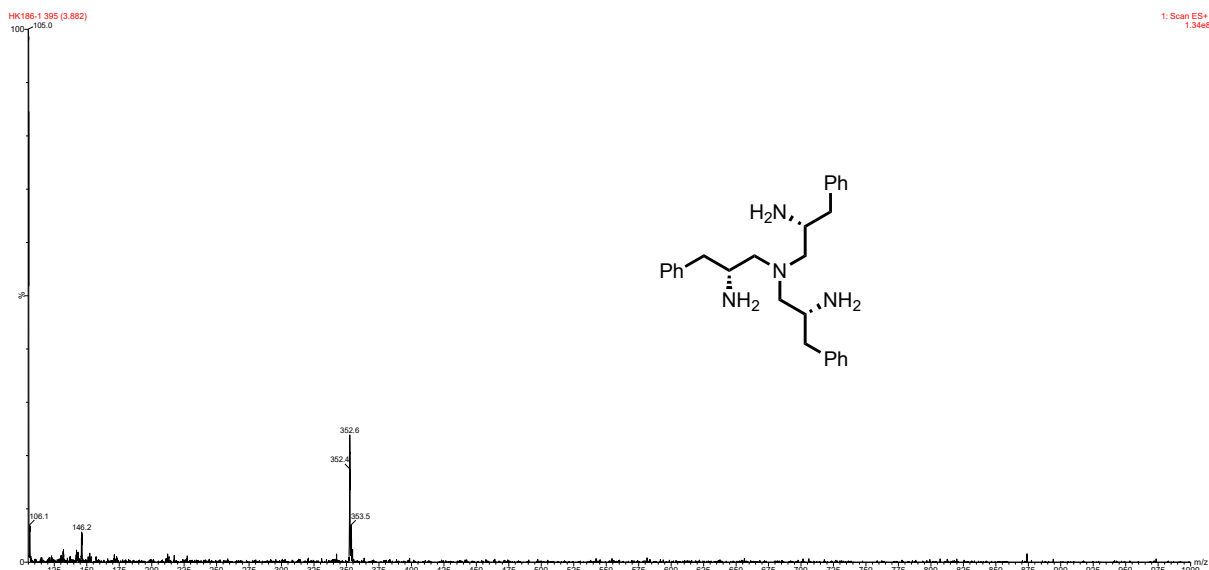


Figure A2.39: Low-resolution mass spectrum of (R)-N<sup>1</sup>,N<sup>1</sup>-bis((R)-2-amino-3-phenylpropyl)-3-phenylpropane-1,2-diamine (**68**) (ESI+).

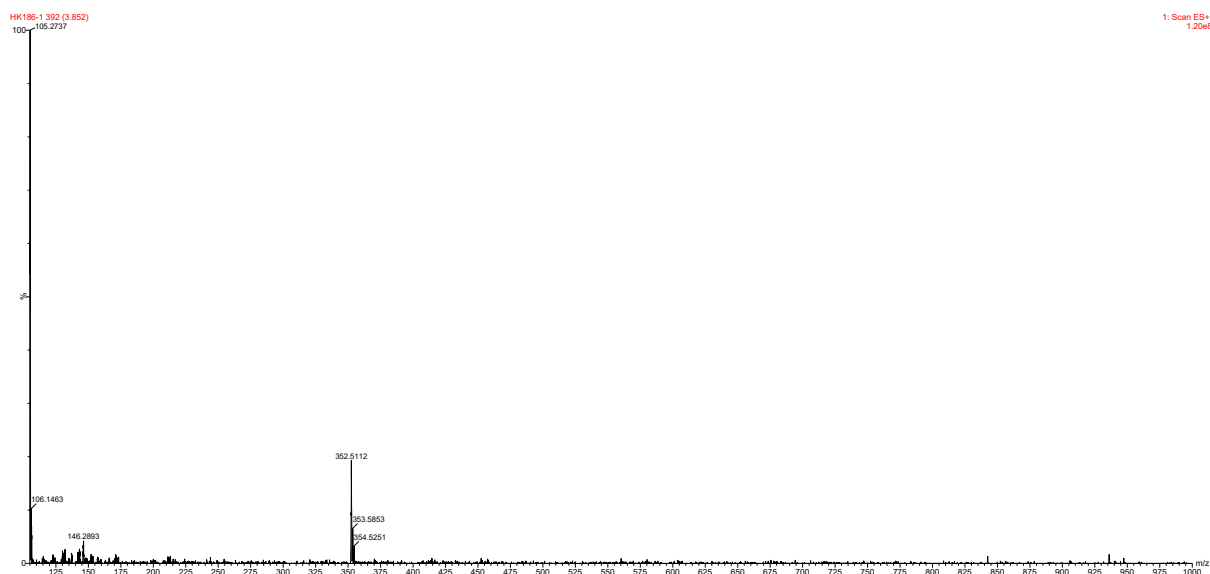


Figure A2.40: High-resolution mass spectrum of (R)- $N^1,N^1$ -bis((R)-2-amino-3-phenylpropyl)-3-phenylpropane-1,2-diamine (**68**) (ESI+).



### **A3 Chapter 4 data**

### A3.1 Cartesian coordinates calculated using ab initio methods

*Table 3.1: Cartesian coordinates (given in angstroms) generated for structure A, calculated using HF methods after energy minimisation calculations.*

Atom		X	Y	Z
1	O	-3.3602690	1.7078880	0.1401930
2	S	-2.6684830	3.1330930	0.0515130
3	C	-1.5639000	2.9919140	-1.4006180
4	N	-0.6789990	1.9008690	-1.2147100
5	C	0.6257400	2.0926540	-0.8802630
6	N	1.2537320	0.9061900	-0.6274680
7	C	2.5828170	0.6958480	-0.3055050
8	C	3.5276190	1.7120310	-0.1589370
9	C	4.8312040	1.3996750	0.1651800
10	C	5.2173380	0.0871450	0.3478650
11	C	6.6016120	-0.2315860	0.7470240
12	F	7.4876160	0.6897310	0.2977730
13	F	6.7807620	-0.2834540	2.0945650
14	F	7.0003540	-1.4408310	0.2825830
15	C	4.2881550	-0.9284590	0.1986540
16	C	2.9860080	-0.6333860	-0.1247510
17	O	1.1549870	3.2044230	-0.8345150
18	O	-3.6801820	4.2836740	-0.3084310
19	O	-1.7728990	3.4406970	1.3096830
20	H	-1.0218290	3.9160410	-1.4854660
21	H	-2.2222540	2.8504110	-2.2412300
22	H	-1.0351490	0.9518140	-1.2090240
23	H	0.6415440	0.0878650	-0.6821810
24	H	3.2256590	2.7221630	-0.3035800
25	H	5.5511760	2.1861880	0.2673520
26	H	4.5870370	-1.9492450	0.3251600
27	H	2.2677360	-1.4199010	-0.2498290
28	C	-5.0251540	0.1085820	2.1663120
29	N	-5.0014030	-1.0173940	1.1427700
30	C	-5.8585450	-2.1542050	1.6423660
31	C	-5.5570650	-0.4708390	-0.1596810
32	C	-3.5505550	-1.4383530	0.9621750
33	C	-3.3502510	-2.6948120	0.1063540
34	O	-1.9221230	-2.9152720	0.0849990
35	P	-0.9581040	-2.3148610	-1.1131910
36	O	-0.7960840	-0.7836530	-0.8864180
37	O	0.4503390	-3.0039600	-0.6459410
38	C	0.5632380	-4.3935440	-0.2335380
39	O	-1.4535180	-2.8139870	-2.4834070
40	H	-3.1557930	-1.6354640	1.9466440
41	H	-3.0340480	-0.5982750	0.5257700
42	H	-3.7217880	-2.5800210	-0.9010200
43	H	-3.7873260	-3.5688410	0.5551480
44	H	0.2417620	-5.0495960	-1.0304430
45	H	-0.0368610	-4.5672890	0.6446140
46	H	1.6043200	-4.5638090	-0.0196780
47	H	-5.4090810	-2.5612720	2.5345800
48	H	-5.9364310	-2.9099960	0.8787900
49	H	-6.8388830	-1.7650610	1.8661530
50	H	-4.4193440	0.9059140	1.7681870
51	H	-4.6325730	-0.2711340	3.0966400
52	H	-6.0497450	0.4220610	2.2936230
53	H	-4.9434450	0.3703310	-0.4386710
54	H	-6.5764990	-0.1633310	0.0150320
55	H	-5.5343710	-1.2472760	-0.9064710

Table A3.2: Cartesian coordinates (given in angstroms) generated for structure **B**, calculated using HF methods after energy minimisation calculations.

Atom		X	Y	Z
1	O	-3.7595850	-1.5487370	0.2603580
2	S	-2.7926390	-2.7834510	0.5068000
3	C	-1.8530430	-2.4171690	2.0461490
4	N	-0.9610130	-1.3430340	1.8029950
5	C	0.3062380	-1.6056560	1.3801220
6	N	0.9561500	-0.5017620	0.9037540
7	C	2.2956140	-0.4112780	0.5435700
8	C	3.2146220	-1.4575500	0.6253290
9	C	4.5273580	-1.2525220	0.2528810
10	C	4.9473810	-0.0208750	-0.2058470
11	C	6.3406540	0.1695720	-0.6526070
12	F	7.2031700	-0.6446320	0.0023700
13	F	6.5275840	-0.0895730	-1.9749910
14	F	6.7649870	1.4436810	-0.4700100
15	C	4.0427340	1.0241070	-0.2904170
16	C	2.7338030	0.8359430	0.0794660
17	O	0.8074150	-2.7294560	1.4481760
18	O	-3.5756980	-4.1211960	0.7894930
19	O	-1.7113810	-2.9060670	-0.6405470
20	H	-1.3297730	-3.3238280	2.2899760
21	H	-2.5862320	-2.1724850	2.7947650
22	H	-1.2904500	-0.3893170	1.9783830
23	H	0.4217620	0.3525830	0.7337410
24	H	2.8872800	-2.4080890	0.9722610
25	H	5.2271580	-2.0600600	0.3287360
26	H	4.3661530	1.9853860	-0.6349060
27	H	2.0224700	1.6337870	0.0245060
28	C	-2.7581130	1.0747060	-4.3112910
29	N	-2.8551440	0.4762570	-2.9236310
30	C	-4.2121060	-0.1827160	-2.7593450
31	C	-1.7848300	-0.5920410	-2.7897600
32	C	-2.6295520	1.5943030	-1.9061940
33	C	-3.3421820	1.4095030	-0.5609580
34	O	-2.8198870	2.4846150	0.2678870
35	P	-1.5067510	2.2406200	1.2283120
36	O	-0.2692300	1.9233630	0.3353700
37	O	-1.3581560	3.7335280	1.8585020
38	C	-2.4708120	4.4993460	2.3984130
39	O	-1.8569590	1.1800130	2.3074540
40	H	-2.9729780	2.5122240	-2.3542130
41	H	-1.5710450	1.6556860	-1.7181900
42	H	-3.1713970	0.4459500	-0.1089340
43	H	-4.4012760	1.5810190	-0.6417560
44	H	-2.9157230	3.9764550	3.2332240
45	H	-3.2127350	4.6625320	1.6333550
46	H	-2.0591520	5.4368460	2.7311060
47	H	-4.9758740	0.5769880	-2.8121340
48	H	-4.2291580	-0.7026690	-1.8137660
49	H	-4.3373260	-0.8836070	-3.5700580
50	H	-1.7974010	1.5548270	-4.4117110
51	H	-3.5526520	1.7930780	-4.4341480
52	H	-2.8561970	0.2809600	-5.0339970
53	H	-0.8212650	-0.1133020	-2.8664960
54	H	-1.9140450	-1.2880350	-3.6049940
55	H	-1.8870340	-1.1210370	-1.8569730

Table A3.3: Cartesian coordinates (given in angstroms) generated for structure **C**, calculated using HF methods after energy minimisation calculations.

Atom		X	Y	Z
1	O	2.0500320	-3.5509280	1.1871810
2	S	3.0075620	-2.8846540	0.1311920
3	C	2.0287270	-2.4682110	-1.3617700
4	N	1.1043410	-1.4375750	-1.0676140
5	C	-0.2174200	-1.6907020	-0.8783140
6	N	-0.9040980	-0.5509290	-0.5589110
7	C	-2.2649740	-0.4194240	-0.3355440
8	C	-3.1787990	-1.4723360	-0.3995110
9	C	-4.5174150	-1.2383430	-0.1661320
10	C	-4.9714970	0.0308110	0.1321140
11	C	-6.3991650	0.2579980	0.4292610
12	F	-7.2015770	-0.6126780	-0.2290210
13	F	-6.7088940	0.1163060	1.7458540
14	F	-6.7949620	1.5101980	0.0956430
15	C	-4.0747750	1.0824910	0.1947350
16	C	-2.7383200	0.8621770	-0.0357720
17	O	-0.7150470	-2.8096880	-1.0007420
18	O	3.5423870	-1.4860190	0.6432960
19	O	4.1572750	-3.8272490	-0.3806910
20	H	1.5253500	-3.3669170	-1.6694750
21	H	2.7592970	-2.1638050	-2.0921450
22	H	1.4191110	-0.4833970	-0.9490600
23	H	-0.3345390	0.2904570	-0.4932810
24	H	-2.8266130	-2.4485710	-0.6333910
25	H	-5.2115260	-2.0518410	-0.2274760
26	H	-4.4224230	2.0715710	0.4127460
27	H	-2.0455220	1.6780520	0.0080050
28	H	5.0290430	0.5509450	2.6292560
29	H	5.9897650	0.6526220	0.4107830
30	C	4.6094050	1.2185030	1.8938940
31	H	5.0303070	2.2042350	2.0040660
32	N	4.9853400	0.6864180	0.5249770
33	H	4.5765640	-0.2716150	0.4296910
34	C	3.0906700	1.2629550	2.0533040
35	H	4.5511600	1.3050140	-0.2183960
36	H	2.8489450	1.4423740	3.0870050
37	H	2.6660380	0.3262750	1.7289370
38	O	2.5139770	2.3763000	1.3147500
39	O	3.5376320	2.2007920	-1.0552640
40	P	2.1863560	2.3383260	-0.2898770
41	O	1.1017950	1.2658010	-0.5828980
42	O	1.5951260	3.8436270	-0.4616830
43	H	2.8927760	4.5055620	-1.9584040
44	C	1.8807030	4.6732340	-1.6259070
45	H	1.7487800	5.6950420	-1.3141700
46	H	1.1887010	4.4377300	-2.4207970

Table A3.4: Cartesian coordinates (given in angstroms) generated for structure **D**, calculated using HF methods after energy minimisation calculations.

Atom		X	Y	Z
1	O	2.5760190	-2.2585860	1.3095420
2	S	3.6775460	-2.2505030	0.1665310
3	C	2.7822360	-2.2724660	-1.4484460
4	N	1.7222230	-1.3429300	-1.3933680
5	C	0.4732100	-1.7444660	-1.0257610
6	N	-0.3505520	-0.6772100	-0.8017100
7	C	-1.7060410	-0.7005810	-0.5047280
8	C	-2.4643570	-1.8670240	-0.4019780
9	C	-3.8109400	-1.7899300	-0.1136920
10	C	-4.4221530	-0.5674030	0.0772840
11	C	-5.8517540	-0.5007050	0.4375700
12	F	-6.5555240	-1.5404350	-0.0715730
13	F	-6.0752180	-0.5308310	1.7789190
14	F	-6.4351480	0.6406120	-0.0019280
15	C	-3.6775390	0.5947530	-0.0238110
16	C	-2.3350390	0.5338560	-0.3111070
17	O	0.1466740	-2.9270570	-0.9371510
18	O	4.4618060	-0.8592770	0.1904960
19	O	4.6401420	-3.4950890	0.1891930
20	H	2.4190940	-3.2753800	-1.5786980
21	H	3.5218910	-2.0186490	-2.1875290
22	H	1.8975220	-0.3437360	-1.4432570
23	H	0.1106000	0.2269860	-0.8567680
24	H	-1.9899780	-2.8079960	-0.5483130
25	H	-4.3869650	-2.6905200	-0.0466210
26	H	-4.1495310	1.5464290	0.1127960
27	H	-1.7546820	1.4312150	-0.3894720
28	H	2.9777860	-0.8298280	2.5113380
29	N	3.4482370	0.0631260	2.3477810
30	H	3.9713260	0.3568030	3.1620440
31	H	4.0748580	-0.1732160	1.5430570
32	C	2.4363550	1.0928120	1.8846350
33	C	3.1556050	2.2021210	1.1199420
34	O	2.1622790	3.1246060	0.6194840
35	P	1.4070400	2.8173070	-0.8171790
36	O	1.5846590	1.2853500	-1.0282780
37	O	-0.1549850	3.0612400	-0.3789970
38	C	-0.5873610	4.1986990	0.4194250
39	O	1.8539210	3.7989930	-1.9151070
40	H	1.9048330	1.4738850	2.7396870
41	H	1.7741720	0.5814840	1.2103130
42	H	3.7144560	1.7578860	0.3106130
43	H	3.8128470	2.7651720	1.7603480
44	H	-0.0643110	4.2059600	1.3620350
45	H	-1.6451150	4.0763340	0.5757840
46	H	-0.3989450	5.1211670	-0.1113260

Table A3.5: Cartesian coordinates (given in angstroms) generated for structure *E*, calculated using HF methods after energy minimisation calculations.

Atom		X	Y	Z
1	O	1.9687590	-3.2273150	1.2730920
2	S	3.1020920	-2.7980880	0.2695200
3	C	2.2961560	-2.2448760	-1.2841820
4	N	1.3677420	-1.2060880	-1.0200800
5	C	0.0490850	-1.5082200	-0.8456980
6	N	-0.7021030	-0.4472790	-0.4359970
7	C	-2.0825050	-0.4181620	-0.2662630
8	C	-2.9378930	-1.4914970	-0.5144400
9	C	-4.2965310	-1.3493130	-0.3192470
10	C	-4.8252680	-0.1539230	0.1222200
11	C	-6.2732780	-0.0324890	0.3802910
13	F	-6.6260710	-0.3508520	1.6548060
14	F	-6.7212230	1.2315840	0.1853840
15	C	-3.9845990	0.9182390	0.3688460
16	C	-2.6305350	0.7918460	0.1777240
17	O	-0.3954090	-2.6370170	-1.0610370
18	O	3.9003020	-1.5395580	0.8169180
19	O	4.0606530	-3.9653800	-0.1696780
20	H	1.8079010	-3.1137300	-1.6860040
21	H	3.0958800	-1.9197970	-1.9273450
22	H	1.7116760	-0.2509640	-1.0220910
23	H	-0.2307410	0.4240220	-0.1789890
24	H	-2.5284720	-2.4136280	-0.8505380
25	H	-4.9456060	-2.1773460	-0.5206870
26	H	-4.3911240	1.8519900	0.7006980
27	H	-1.9684700	1.6121380	0.3621870
28	H	5.6778580	0.9947930	1.7081000
29	H	5.6949580	0.6971690	-0.7477260
30	C	4.9673160	1.4903490	1.0661080
31	H	5.3212990	2.4758680	0.8129210
32	N	4.8462230	0.6703260	-0.2000860
33	H	4.6012760	-0.3134330	0.0766370
34	C	3.6120750	1.5789100	1.7630270
35	H	4.0172090	1.0124330	-0.7496450
36	H	3.7546250	1.8894670	2.7835630
37	H	3.1316570	0.6123800	1.7404850
38	O	2.7794660	2.6093650	1.1599510
39	O	2.4910660	1.3804930	-1.0771140
40	P	1.7741780	2.3832260	-0.1081980
41	O	0.3443500	1.9651870	0.3278800
42	O	1.7732770	3.8948420	-0.7037450
43	H	0.6236580	4.2106440	-2.4158950
44	C	0.6266710	4.4957490	-1.3745240
45	H	0.7442620	5.5617090	-1.2831220
46	H	-0.2879290	4.1739090	-0.9022260

Table A3.6: Cartesian coordinates (given in angstroms) generated for structure **F**, calculated using HF methods after energy minimisation calculations.

Atom		X	Y	Z
1	O	-3.4772110	-4.0376160	-0.5359890
2	S	-3.1546650	-2.5254670	-0.2332080
3	C	-2.3690820	-1.8145880	-1.7773380
4	N	-1.4351410	-0.8075460	-1.4542530
5	C	-0.1552070	-1.1865990	-1.1622740
6	N	0.6468930	-0.1723700	-0.7306000
7	C	2.0077890	-0.2547490	-0.4365430
8	C	2.7899410	-1.3963050	-0.6048270
9	C	4.1347380	-1.3608680	-0.2961090
10	C	4.7187410	-0.2062260	0.1817780
11	C	6.1682220	-0.1674040	0.4577520
12	F	6.6492520	-1.3775370	0.8316360
13	F	6.9148680	0.2062080	-0.6159530
14	F	6.4766700	0.7145990	1.4390610
15	C	3.9474980	0.9293670	0.3612560
16	C	2.6080340	0.9095720	0.0578910
17	O	0.2143860	-2.3534670	-1.3018010
18	O	-4.4719090	-1.6610570	0.0479640
19	O	-2.1348840	-2.3147750	0.9738840
20	H	-3.1978890	-1.4353890	-2.3490190
21	H	-1.9077910	-2.6688570	-2.2377350
22	H	-1.7393440	0.1717220	-1.4619850
23	H	0.2507660	0.7467890	-0.5439060
24	H	2.3364100	-2.2891120	-0.9621630
25	H	4.7257950	-2.2453830	-0.4214600
26	H	4.3930850	1.8233490	0.7476990
27	H	1.9942560	1.7746320	0.2010880
28	H	-3.0881660	-1.5743710	2.4021690
29	N	-3.9242540	-0.9979190	2.5836020
30	H	-4.4941930	-1.2207110	1.7413080
31	H	-4.3869870	-1.2789600	3.4374100
32	C	-3.5536130	0.4755410	2.5841340
33	C	-2.9696340	0.7655600	1.2137580
34	O	-2.5030160	2.1384970	1.2114750
35	P	-1.6916730	2.5908610	-0.1527870
36	O	-2.3061230	1.7967200	-1.3432110
37	O	-2.1234080	4.1605090	-0.2234150
38	C	-2.3740340	4.8343920	-1.4912960
39	O	-0.1599280	2.4106790	0.0472170
40	H	-2.8272530	0.6428750	3.3610580
41	H	-4.4453270	1.0497700	2.7704210
42	H	-3.7048690	0.6203140	0.4455520
43	H	-2.1498460	0.0901330	1.0352650
44	H	-3.0206870	5.6677210	-1.2761580
45	H	-2.8486070	4.1542430	-2.1806530
46	H	-1.4428440	5.1891500	-1.9077720

Table A3.7: Cartesian coordinates (given in angstroms) generated for structure **G**, calculated using HF methods after energy minimisation calculations.

Atom		X	Y	Z
1	O	4.2061910	-1.2960630	-0.2561230
2	S	3.1520740	-2.4766460	-0.1829840
3	C	2.1839990	-2.3767500	-1.7552530
4	N	1.2021860	-1.3704740	-1.6337350
5	C	-0.0636050	-1.7051590	-1.2410950
6	N	-0.8138330	-0.5984070	-0.9832200
7	C	-2.1471160	-0.5347730	-0.6129680
8	C	-2.9801830	-1.6475860	-0.4971600
9	C	-4.2998810	-1.4854670	-0.1306030
10	C	-4.8097270	-0.2289000	0.1254570
11	C	-6.2082270	-0.0716650	0.5691050
12	F	-7.0095760	-1.0536230	0.0899590
13	F	-6.3567890	-0.1067490	1.9208980
14	F	-6.7374740	1.1130250	0.1777210
15	C	-3.9893270	0.8808460	0.0127220
16	C	-2.6720060	0.7374590	-0.3515480
17	O	-0.4514910	-2.8708150	-1.1652320
18	O	3.8362200	-3.8929250	-0.1322820
19	O	2.1024500	-2.2307770	0.9780260
20	H	1.7306680	-3.3420010	-1.8850960
21	H	2.9119450	-2.1675680	-2.5197570
22	H	1.4487780	-0.3855780	-1.6283850
23	H	-0.2924270	0.2783160	-1.0606370
24	H	-2.5812460	-2.6146050	-0.6936690
25	H	-4.9346810	-2.3447660	-0.0531020
26	H	-4.3845710	1.8581580	0.2029610
27	H	-2.0365710	1.5995300	-0.4305620
28	C	3.8433790	0.1568750	2.7380380
29	C	3.4339240	1.3178300	1.7922250
30	C	1.9231180	1.3502290	1.6269990
31	O	1.5593580	2.5836720	0.9484160
32	P	0.9230680	2.6994840	-0.5537070
33	O	-0.4855340	3.3383880	-0.4953430
34	O	1.9494870	3.7366540	-1.2914510
35	C	3.2025650	3.2820350	-1.8820960
36	O	1.0426080	1.3089460	-1.2528480
37	O	4.0916190	1.2376070	0.5142640
38	H	3.7410670	2.2603740	2.2196900
39	H	1.4372230	1.3594320	2.5861900
40	H	1.5914060	0.4981900	1.0570520
41	H	3.0014780	2.7113660	-2.7769660
42	H	3.7422470	2.6757210	-1.1727260
43	H	3.7589860	4.1711170	-2.1300370
44	H	4.1962930	0.5648050	3.6737710
45	H	4.6585670	-0.3773120	2.2671820
46	O	2.7549760	-0.7208360	3.0713330
47	H	2.5365870	-1.3174280	2.3165700
48	H	4.0625810	0.3139600	0.1693260



Table A3.8: Cartesian coordinates (given in angstroms) generated for structure **H**, calculated using HF methods after energy minimisation calculations.

Atom		X	Y	Z
1	O	-3.7282970	4.0108590	-0.1439650
2	S	-3.0604940	2.5846440	-0.1843250
3	C	-2.1103290	2.4881430	-1.7663270
4	N	-1.1361490	1.4677550	-1.6719970
5	C	0.1217360	1.7749740	-1.2378080
6	N	0.8648670	0.6545420	-1.0138780
7	C	2.1808900	0.5761370	-0.5846860
8	C	3.0215760	1.6797370	-0.4385580
9	C	4.3240180	1.5039350	-0.0203140
10	C	4.8094280	0.2425300	0.2584510
11	C	6.1882280	0.0710370	0.7556080
12	F	7.0195560	1.0388760	0.2994230
13	F	6.2863940	0.1152400	2.1116530
14	F	6.7160330	-1.1233960	0.3931960
15	C	3.9805060	-0.8575880	0.1203010
16	C	2.6796130	-0.6999220	-0.2942890
17	O	0.5133060	2.9333870	-1.0992860
18	O	-2.0299530	2.3188980	0.9855440
19	O	-4.1305800	1.4155140	-0.3033580
20	H	-1.6471750	3.4497090	-1.8889170
21	H	-2.8446410	2.2959490	-2.5288020
22	H	-1.3862120	0.4888250	-1.7405670
23	H	0.3597790	-0.2186200	-1.1747070
24	H	2.6414200	2.6509960	-0.6501350
25	H	4.9651260	2.3562970	0.0789810
26	H	4.3551530	-1.8383300	0.3331190
27	H	2.0345240	-1.5535110	-0.3797730
28	C	-3.8414540	0.0575490	2.7246070
29	C	-2.9199330	-1.1088530	2.3894650
30	C	-2.4383790	-1.0329410	0.9546820
31	O	-1.7518040	-2.3005150	0.7162360
32	P	-0.9423240	-2.5994770	-0.6777960
33	O	0.4265050	-3.2510940	-0.3702320
34	O	-1.9681870	-3.6565300	-1.3968180
35	C	-2.1431220	-3.6996400	-2.8392000
36	O	-0.9410760	-1.2831620	-1.5185970
37	O	-3.6360460	-2.3452490	2.5809970
38	H	-2.0588290	-1.0713980	3.0480310
39	H	-1.7785020	-0.1966800	0.8109250
40	H	-3.2770490	-0.9464490	0.2876000
41	H	-1.3148900	-4.2187220	-3.3009450
42	H	-2.2082800	-2.6981290	-3.2337540
43	H	-3.0572370	-4.2377670	-3.0253760
44	H	-3.2560010	0.9659890	2.6759270
45	H	-4.2106610	-0.0767120	3.7319900
46	O	-4.9738560	0.1291900	1.8453000
47	H	-4.7263610	0.6400310	1.0370570
48	H	-3.1430500	-3.0271520	2.0999970

Table A3.9: Cartesian coordinates (given in angstroms) generated for structure **I**, calculated using HF methods after energy minimisation calculations.

Atom		X	Y	Z
1	O	-3.9974000	4.0997540	-0.0346190
2	S	-2.9183660	3.0197780	0.3467010
3	C	-2.0569580	2.6627080	-1.2321140
4	N	-1.0987480	1.6344090	-1.0653940
5	C	0.2218650	1.9156830	-0.8777440
6	N	0.9442000	0.7779420	-0.6601080
7	C	2.2987430	0.6616410	-0.4049390
8	C	3.2013070	1.7247860	-0.4372050
9	C	4.5377360	1.5013840	-0.1803000
10	C	4.9974300	0.2325800	0.1104110
11	C	6.4208140	0.0143760	0.4323630
12	F	7.2280720	0.9042160	-0.1939450
13	F	6.7034150	0.1352080	1.7574430
14	F	6.8367500	-1.2278510	0.0852190
15	C	4.1085070	-0.8281560	0.1482530
16	C	2.7741020	-0.6207510	-0.1033990
17	O	0.6819610	3.0565900	-0.9209920
18	O	-1.8488510	3.5203540	1.3875640
19	O	-3.5583140	1.6434130	0.7989410
20	H	-1.5910430	3.5831750	-1.5348390
21	H	-2.8372520	2.3820580	-1.9189290
22	H	-1.3780380	0.6623170	-1.0541050
23	H	0.3970540	-0.0862200	-0.7018020
24	H	2.8413880	2.7008270	-0.6621020
25	H	5.2255360	2.3217180	-0.2180440
26	H	4.4620860	-1.8147850	0.3686770
27	H	2.0808850	-1.4375830	-0.0585930
28	C	-5.6119090	-1.1416830	0.8624040
29	C	-4.3889550	-2.0391860	0.6536060
30	C	-3.1323910	-1.4145770	1.2577830
31	O	-1.9898780	-2.3139400	1.0971360
32	P	-1.2116460	-2.5083710	-0.3276700
33	O	-0.9121530	-1.1101130	-0.9421310
34	O	0.1926540	-3.1596440	0.2049970
35	C	0.7301360	-4.4202950	-0.2880810
36	O	-1.9737130	-3.5473810	-1.1993410
37	O	-4.2520240	-2.2421160	-0.7613310
38	H	-4.5723170	-2.9771110	1.1685980
39	H	-3.2521200	-1.2894090	2.3219290
40	H	-2.9168450	-0.4644860	0.8025440
41	H	1.1393630	-4.9470530	0.5581370
42	H	1.5102360	-4.2147100	-1.0050540
43	H	-0.0524700	-4.9984830	-0.7517190
44	H	-5.7250670	-0.9481950	1.9260750
45	H	-6.4808810	-1.6931000	0.5329810
46	O	-5.5899170	0.0656710	0.0961520
47	H	-4.8599410	0.6709270	0.3558110
48	H	-3.5758240	-2.9231710	-0.9789200

Table A3.10: Cartesian coordinates (given in angstroms) generated for structure **J**,  
calculated using HF methods after energy minimisation calculations.

Atom		X	Y	Z
1	O	-3.5694980	-1.3640170	-0.3507670
2	S	-2.9909280	-2.8100650	-0.0363630
3	C	-1.9803090	-2.5369860	1.4709400
4	N	-1.0280540	-1.5241590	1.2193230
5	C	0.2809120	-1.8180220	0.9759700
6	N	0.9813040	-0.6919760	0.6561240
7	C	2.3290610	-0.5680900	0.3728040
8	C	3.2315980	-1.6316560	0.3690650
9	C	4.5600660	-1.4067860	0.0744940
10	C	5.0107730	-0.1354460	-0.2178570
11	C	6.4229370	0.0857400	-0.5832900
12	F	7.2485660	-0.8185310	-0.0029640
13	F	6.6604850	-0.0085670	-1.9195370
14	F	6.8551900	1.3195800	-0.2256770
15	C	4.1218880	0.9266490	-0.2125850
16	C	2.7951410	0.7205830	0.0785530
17	O	0.7456290	-2.9557170	1.0580560
18	O	-4.1179140	-3.8278400	0.3699270
19	O	-2.0472920	-3.3114550	-1.1909340
20	H	-1.5035610	-3.4712400	1.7060800
21	H	-2.6903330	-2.2591290	2.2314100
22	H	-1.3189650	-0.5557320	1.1178050
23	H	0.4064720	0.1565690	0.6280530
24	H	2.8782630	-2.6094370	0.5978460
25	H	5.2479480	-2.2278900	0.0820650
26	H	4.4717310	1.9160490	-0.4274100
27	H	2.1071230	1.5452070	0.0847660
28	C	-4.9657530	0.9746110	-2.0408760
29	C	-4.1293170	1.7729000	-1.0373140
30	C	-2.7015590	1.9061970	-1.5453950
31	O	-2.0030070	2.9264960	-0.7848850
32	P	-0.9442220	2.6317280	0.4288730
33	O	0.4313830	3.2635740	0.1071420
34	O	-1.6214470	3.4211660	1.6914140
35	C	-2.5060620	2.7464930	2.6329880
36	O	-0.9663400	1.1049960	0.7392370
37	O	-4.1555990	1.1824940	0.2791200
38	H	-4.5535220	2.7595640	-0.9298700
39	H	-2.6934300	2.2306010	-2.5731790
40	H	-2.1960560	0.9610200	-1.4526980
41	H	-1.9427640	2.0505910	3.2372070
42	H	-3.2800480	2.2233790	2.0969560
43	H	-2.9245420	3.5187180	3.2572900
44	H	-5.2160680	1.6108850	-2.8777870
45	H	-5.8856620	0.6714060	-1.5520950
46	O	-4.2477920	-0.1487170	-2.5793290
47	H	-3.9958670	-0.7532360	-1.8426910
48	H	-3.8446990	0.2534470	0.2336010

Table A3.11: Cartesian coordinates (given in angstroms) generated for structure **K**,  
calculated using HF methods after energy minimisation calculations.

Atom		X	Y	Z
1	O	3.2117420	-1.2702600	0.4151150
2	S	2.6557860	-2.6846220	-0.0308770
3	C	1.7191220	-2.3695730	-1.5800920
4	N	0.7866930	-1.3276610	-1.3513070
5	C	-0.4951620	-1.6162200	-1.0008640
6	N	-1.1517460	-0.5454080	-0.4597800
7	C	-2.5097580	-0.4478510	-0.1944180
8	C	-3.4622110	-1.4199290	-0.5048700
9	C	-4.7930430	-1.1970190	-0.2167580
10	C	-5.1999790	-0.0216880	0.3826270
11	C	-6.6184950	0.1796100	0.7345050
12	F	-7.4520030	-0.4761540	-0.1089670
13	F	-6.9389310	-0.2631860	1.9802830
14	F	-6.9677590	1.4891100	0.7147980
15	C	-4.2628170	0.9478210	0.6973930
16	C	-2.9358800	0.7408170	0.4131370
17	O	-0.9950620	-2.7308710	-1.1686230
18	O	3.7957630	-3.6960970	-0.4206760
19	O	1.6316080	-3.2457670	1.0257370
20	H	1.2360240	-3.2943350	-1.8382910
21	H	2.4567860	-2.0944940	-2.3139900
22	H	1.1172820	-0.3644740	-1.4665000
23	H	-0.5916220	0.2473200	-0.1046200
24	H	-3.1453260	-2.3307070	-0.9531910
25	H	-5.5176340	-1.9449980	-0.4684460
26	H	-4.5747110	1.8652330	1.1538700
27	H	-2.1988280	1.4820110	0.6455550
28	C	5.3948280	0.6602960	2.1581540
29	C	4.7010300	1.4420340	1.0415000
30	C	3.2536790	1.7367090	1.3862190
31	O	2.6880230	2.5623120	0.3288400
32	P	1.3649560	2.1112910	-0.5186050
33	O	0.3098830	1.5231930	0.4670010
34	O	0.9097960	3.5874260	-1.0548690
35	C	0.4314470	3.8169730	-2.4068290
36	O	1.7132560	1.2160140	-1.7409270
37	O	4.8328450	0.6681460	-0.1659750
38	H	5.2250790	2.3710880	0.8750950
39	H	3.1933020	2.3000450	2.3051120
40	H	2.6994040	0.8161450	1.4804240
41	H	-0.5995840	3.5043950	-2.4961860
42	H	1.0333180	3.2727870	-3.1168230
43	H	0.5076350	4.8765520	-2.5844490
44	H	4.8109100	-0.2245240	2.3835530
45	H	5.5126960	1.2558470	3.0501220
46	O	6.7109180	0.2916750	1.6899420
47	H	6.5976810	0.0799630	0.7489200
48	H	4.2475260	-0.1277800	-0.0872220

Table A3.12: Cartesian coordinates (given in angstroms) generated for structure **L**,  
calculated using HF methods after energy minimisation calculations.

Atom		X	Y	Z
1	O	4.0724620	-1.1581120	-0.5791910
2	S	2.9564960	-2.2779720	-0.6847100
3	C	1.9503840	-1.8523820	-2.1851950
4	N	1.0116800	-0.8506820	-1.8494480
5	C	-0.2331080	-1.2351880	-1.4419770
6	N	-0.9656130	-0.2326270	-0.8812360
7	C	-2.3072140	-0.2848230	-0.5191300
8	C	-3.1490670	-1.3766720	-0.7304930
9	C	-4.4738720	-1.3096120	-0.3500300
10	C	-4.9812570	-0.1723850	0.2438670
11	C	-6.3855740	-0.1335670	0.6950420
12	F	-7.1850650	-0.9309600	-0.0538850
13	F	-6.5558110	-0.5490500	1.9792030
14	F	-6.9015010	1.1188820	0.6488630
15	C	-4.1529970	0.9163120	0.4598330
16	C	-2.8331960	0.8649850	0.0845740
17	O	-0.6380730	-2.3896420	-1.5967360
18	O	3.5485570	-3.7204830	-0.9059790
19	O	1.9446630	-2.1892740	0.5412970
20	H	1.4681800	-2.7676940	-2.4733500
21	H	2.6667930	-1.5225350	-2.9171920
22	H	1.3220870	0.1260080	-1.8580260
23	H	-0.4981720	0.6389000	-0.6075840
24	H	-2.7544340	-2.2561990	-1.1795690
25	H	-5.1144550	-2.1499610	-0.5260420
26	H	-4.5443030	1.8049280	0.9122020
27	H	-2.1779480	1.6957480	0.2454930
28	C	3.5507660	-0.5269340	3.3184970
29	C	3.6844780	0.6669010	2.3620650
30	C	2.3690640	0.9394790	1.6433200
31	O	2.5724860	2.0977530	0.7828890
32	P	1.5327310	2.4261000	-0.4358070
33	O	0.0867890	2.1042380	0.0449780
34	O	1.7938710	4.0329730	-0.5558470
35	C	1.6892640	4.7511760	-1.8158240
36	O	1.9587370	1.7267420	-1.7595790
37	O	4.7651120	0.4528270	1.4522860
38	H	3.9286670	1.5444050	2.9447670
39	H	1.5922540	1.1646150	2.3585210
40	H	2.0740080	0.0827790	1.0600280
41	H	0.6599990	5.0238310	-2.0002750
42	H	2.0532760	4.1353740	-2.6232700
43	H	2.2909350	5.6392680	-1.7191800
44	H	2.6648340	-0.4040970	3.9355000
45	H	4.4101610	-0.5294020	3.9736350
46	O	3.5678820	-1.7940720	2.6470910
47	H	2.8596350	-1.8998980	1.9751560
48	H	4.5165950	-0.2240380	0.7818540

Table A3.13: Cartesian coordinates (given in angstroms) generated for structure **M**,  
calculated using HF methods after energy minimisation calculations.

Atom		X	Y	Z
1	O	3.0556030	-4.2096070	-0.5394800
2	S	2.7543530	-2.6694740	-0.3889500
3	C	1.8222240	-2.1739460	-1.9185450
4	N	0.9423700	-1.1010850	-1.6410640
5	C	-0.3200950	-1.3953580	-1.2235170
6	N	-1.0516590	-0.3127190	-0.8305820
7	C	-2.3916310	-0.3089820	-0.4517200
8	C	-3.2324210	-1.4214070	-0.4845050
9	C	-4.5538030	-1.2983230	-0.1061720
10	C	-5.0591320	-0.0840180	0.3098300
11	C	-6.4602330	0.0222260	0.7604670
12	F	-7.2634310	-0.8809370	0.1480350
13	F	-6.6200140	-0.1926040	2.0941660
14	F	-6.9789070	1.2523950	0.5273030
15	C	-4.2318690	1.0256540	0.3480480
16	C	-2.9149410	0.9190910	-0.0266010
17	O	-0.7491780	-2.5523180	-1.2304140
18	O	1.8519920	-2.3130960	0.8602620
19	O	4.0825000	-1.7959370	-0.4197120
20	H	1.2888780	-3.0602510	-2.2080210
21	H	2.5840550	-1.9049810	-2.6291790
22	H	1.3052350	-0.1450420	-1.7097780
23	H	-0.6034520	0.6006260	-0.7458450
24	H	-2.8405510	-2.3580580	-0.7999050
25	H	-5.1934030	-2.1567020	-0.1457870
26	H	-4.6212750	1.9729090	0.6618380
27	H	-2.2613210	1.7661120	-0.0012730
28	C	4.1575150	-0.4679800	2.6850790
29	C	3.4214410	0.8323780	2.3781960
30	C	2.8714810	0.8099510	0.9721760
31	O	2.2996400	2.1399140	0.7390030
32	P	1.4472210	2.3753050	-0.6434940
33	O	-0.0795700	2.2475460	-0.3695970
34	O	1.8686860	3.9197970	-0.9664270
35	C	2.0204720	4.4023310	-2.3313620
36	O	2.0103930	1.4236220	-1.7385230
37	O	4.3321610	1.9424290	2.5159070
38	H	2.5979600	0.9364970	3.0760570
39	H	2.1231760	0.0429020	0.8743570
40	H	3.6568690	0.6353040	0.2626440
41	H	1.0544270	4.6555120	-2.7438510
42	H	2.4894200	3.6449380	-2.9393700
43	H	2.6382350	5.2828190	-2.2818670
44	H	3.4233880	-1.2643870	2.6996170
45	H	4.6098920	-0.3847530	3.6633830
46	O	5.2002610	-0.7492180	1.7412160
47	H	4.8199870	-1.1887980	0.9420130
48	H	3.9227520	2.6995630	2.0704380

Table A3.14: Cartesian coordinates (given in angstroms) generated for structure N, calculated using HF methods after energy minimisation calculations.

Atom		X	Y	Z
1	O	3.7140740	-3.9132620	-0.7065010
2	S	2.7752820	-2.7479970	-0.2232300
3	C	1.8431180	-2.2017660	-1.7097870
4	N	0.9357240	-1.1771970	-1.3528450
5	C	-0.3540850	-1.4917160	-1.0511380
6	N	-1.0511860	-0.4459600	-0.5177710
7	C	-2.4143460	-0.4003280	-0.2529500
8	C	-3.3080620	-1.4446330	-0.4915760
9	C	-4.6482600	-1.2840210	-0.2052300
10	C	-5.1212450	-0.0992240	0.3205800
11	C	-6.5474380	0.0402450	0.6723420
12	F	-7.3444810	-0.7241930	-0.1128730
13	F	-6.8315970	-0.3301700	1.9501270
14	F	-6.9765280	1.3212250	0.5630480
15	C	-4.2419620	0.9434260	0.5610470
16	C	-2.9060370	0.7992480	0.2787250
17	O	-0.8286780	-2.6102590	-1.2628000
18	O	1.7357570	-3.1637490	0.8818910
19	O	3.6005070	-1.4664390	0.2250390
20	H	1.3391980	-3.0762670	-2.0796780
21	H	2.5903420	-1.8570840	-2.4034760
22	H	1.2692300	-0.2052100	-1.3938450
23	H	-0.5400110	0.3955100	-0.2298650
24	H	-2.9405120	-2.3590130	-0.8914930
25	H	-5.3275620	-2.0887900	-0.4014580
26	H	-4.6058860	1.8692410	0.9582780
27	H	-2.2125040	1.5952710	0.4542650
28	C	5.2822100	0.5055270	2.1998960
29	C	4.6139130	1.4199110	1.1679170
30	C	3.1534930	1.6288200	1.5377410
31	O	2.5853650	2.6402430	0.6590310
32	P	1.3864640	2.3301360	-0.4053860
33	O	0.1037340	1.8834430	0.3596100
34	O	1.2314390	3.8393440	-1.0121490
35	C	0.9198690	4.0821750	-2.4107490
36	O	1.8308870	1.3640790	-1.5400790
37	O	4.7419120	0.9066660	-0.1678400
38	H	5.1147740	2.3767410	1.1724480
39	H	3.0611280	1.9921360	2.5487380
40	H	2.6236770	0.6943700	1.4442940
41	H	-0.1481700	4.0259050	-2.5669940
42	H	1.4158620	3.3539140	-3.0323500
43	H	1.2689930	5.0749930	-2.6401780
44	H	5.4721910	1.0654880	3.1045950
45	H	6.2328460	0.1794790	1.7910810
46	O	4.4511220	-0.6072950	2.5742030
47	H	4.1525360	-1.0863340	1.7667480
48	H	4.2581190	0.0577550	-0.2412050

Table 3.15: Cartesian coordinates (given in angstroms) generated for structure **O**, calculated using HF methods after energy minimisation calculations.

Atom		X	Y	Z
1	C	-7.2618430	-0.8990310	-0.4926540
2	N	-5.9626240	-1.5230690	-0.9700010
3	C	-6.2311440	-2.9680170	-1.3391780
4	C	-5.4836580	-0.7649570	-2.1909800
5	C	-4.9554100	-1.4238500	0.1655680
6	C	-3.5577690	-1.9561150	-0.1544130
7	O	-2.8644110	-1.8275300	1.1049090
8	P	-1.4322590	-1.0248000	1.2577730
9	O	-1.2540280	-0.1601030	-0.0289890
10	O	-1.8428140	-0.0754590	2.5221450
11	C	-0.9328130	0.9278460	3.0716170
12	O	-0.2880800	-1.9996600	1.6231260
13	H	-5.3598050	-1.9780280	0.9969190
14	H	-4.8836380	-0.3812050	0.4315880
15	H	-3.0559410	-1.3675130	-0.9020150
16	H	-3.5682540	-2.9961700	-0.4326770
17	H	-1.3968170	1.2869240	3.9757420
18	H	-0.7895610	1.7399680	2.3745160
19	H	0.0182560	0.4702630	3.3114300
20	H	-6.5482800	-3.4955640	-0.4538490
21	H	-5.3335240	-3.4071280	-1.7393010
22	H	-7.0098200	-2.9864790	-2.0845100
23	H	-7.0759070	0.1338200	-0.2464410
24	H	-7.6023660	-1.4380600	0.3764890
25	H	-7.9863410	-0.9711260	-1.2875630
26	H	-5.2693130	0.2515600	-1.9016990
27	H	-6.2674910	-0.7861110	-2.9308160
28	H	-4.6004280	-1.2413820	-2.5810880
29	C	4.8115930	0.2771620	-0.9666630
30	C	3.5986540	0.9221290	-1.0816690
31	C	2.4369400	0.3229760	-0.5900280
32	C	2.5360550	-0.9300830	0.0313090
33	C	3.7526410	-1.5602260	0.1357390
34	C	4.8969970	-0.9624220	-0.3649190
35	C	6.2065550	-1.6204780	-0.2001770
36	N	1.1762320	0.8815050	-0.6876110
37	C	0.8472150	2.1677410	-1.0477590
38	O	1.6727270	3.0336470	-1.3510850
39	N	-0.4899050	2.3647520	-1.0661230
40	C	-1.0085380	3.7147650	-0.9698130
41	C	-0.8497980	4.3133050	0.4499610
42	O	-0.2199310	3.6357650	1.2989740
43	O	-1.3613500	5.4464110	0.5984320
44	F	7.0858320	-1.2591840	-1.1659890
45	F	6.1059520	-2.9721960	-0.2270300
46	F	6.8197560	-1.3274970	0.9788540
47	H	5.6940660	0.7412950	-1.3583600
48	H	3.5289450	1.8823700	-1.5346930
49	H	1.6571820	-1.3810530	0.4510700
50	H	3.8143650	-2.5208420	0.6062520
51	H	0.3804150	0.3051450	-0.4189830
52	H	-1.0543950	1.6124370	-0.7051100
53	H	-2.0583450	3.7174650	-1.2305770
54	H	-0.4898890	4.3599510	-1.6650350



Table A3.16: Cartesian coordinates (given in angstroms) generated for structure *P*,  
calculated using HF methods after energy minimisation calculations.

Atom		X	Y	Z
1	O	-2.5784940	2.3919150	0.2104090
2	C	-2.9200990	2.9764690	-0.8597980
3	C	-2.2936210	2.4876240	-2.1833500
4	N	-1.3958030	1.3639420	-2.0219090
5	C	-0.1429370	1.5710500	-1.5817940
6	N	0.5002190	0.4288870	-1.1576170
7	C	1.8412300	0.2980680	-0.8321220
8	C	2.7952130	1.3106370	-0.9533810
9	C	4.1114510	1.0623810	-0.6247890
10	C	4.5053680	-0.1798920	-0.1696120
11	C	5.9050800	-0.4153840	0.2306480
12	F	6.7728300	0.3632370	-0.4602110
13	F	6.1479050	-0.1534250	1.5438360
14	F	6.2791330	-1.7050000	0.0450610
15	C	3.5674630	-1.1909510	-0.0432740
16	C	2.2538990	-0.9601160	-0.3693310
17	O	0.3895580	2.6880080	-1.5727010
18	O	-3.7238370	3.9207550	-0.9728450
19	H	-1.7757140	3.3225250	-2.6324570
20	H	-3.1013850	2.2016030	-2.8441320
21	H	-1.8020880	0.4370460	-2.0742390
22	H	-0.0532060	-0.4075840	-0.9710820
23	H	2.4862870	2.2699200	-1.2927810
24	H	4.8359510	1.8443620	-0.7318810
25	H	3.8686260	-2.1599870	0.3000120
26	H	1.5171790	-1.7313140	-0.2780940
27	C	-1.1580930	0.0047470	4.3197670
28	N	-1.7267750	0.4531910	2.9930520
29	C	-2.8595800	1.4355970	3.2295230
30	C	-0.6384320	1.1628070	2.2037260
31	C	-2.2021410	-0.7824340	2.2390250
32	C	-3.1997910	-0.4981840	1.1083260
33	O	-3.2842910	-1.7414220	0.3582460
34	P	-2.2733560	-2.0396400	-0.9074810
35	O	-0.8018800	-1.9096720	-0.4100040
36	O	-2.6228100	-3.6113750	-1.1563800
37	C	-3.9705840	-4.1554860	-1.1439250
38	O	-2.6729460	-1.1521630	-2.1163270
39	H	-2.6537710	-1.4455940	2.9596180
40	H	-1.3334130	-1.2444350	1.8022100
41	H	-2.8961460	0.3283000	0.4857710
42	H	-4.1895180	-0.3117250	1.4876550
43	H	-4.5720500	-3.6915730	-1.9132290
44	H	-4.4262800	-3.9944010	-0.1804310
45	H	-3.8737630	-5.2091220	-1.3436130
46	H	-3.6908690	0.9066990	3.6690510
47	H	-3.1109100	1.8843890	2.2808520
48	H	-2.5029960	2.1919070	3.9117860
49	H	-0.3714940	-0.7096500	4.1335060
50	H	-1.9463910	-0.4471330	4.9005150
51	H	-0.7644170	0.8677420	4.8321600
52	H	0.1461880	0.4533820	1.9955150
53	H	-0.2597250	1.9660210	2.8179580
54	H	-1.0810190	1.5577990	1.3036790

Table A3.17: Cartesian coordinates (given in angstroms) generated for structure **Q**,  
calculated using HF methods after energy minimisation calculations.

Atom		X	Y	Z
1	C	-2.8232400	3.3147680	0.0036420
2	C	-2.5841810	2.6571970	-1.3677540
3	N	-1.7277090	1.4874810	-1.2918650
4	C	-0.4224900	1.6721250	-1.0023780
5	N	0.2949440	0.5174280	-0.8249660
6	C	1.6472850	0.4128380	-0.5252380
7	C	2.5319880	1.4891500	-0.4444090
8	C	3.8621760	1.2688060	-0.1519550
9	C	4.3365420	-0.0087840	0.0643030
10	C	5.7500250	-0.2257730	0.4268280
11	F	6.5616550	0.7308360	-0.0851430
12	F	5.9755560	-0.2155780	1.7685060
13	F	6.2096280	-1.4246990	-0.0074810
14	C	3.4672490	-1.0839620	-0.0133240
15	C	2.1406000	-0.8801720	-0.3025490
16	O	0.0690040	2.8037040	-0.9178390
17	O	-2.7999330	2.5411190	1.0243820
18	O	-3.0710270	4.5257980	0.0119870
19	H	-2.1680270	3.4012240	-2.0267150
20	H	-3.5417680	2.3411990	-1.7652750
21	H	-2.1716170	0.5857920	-1.2433940
22	H	-0.1871920	-0.3807180	-0.8854050
23	H	2.1631110	2.4724000	-0.6103050
24	H	4.5339350	2.1018110	-0.1024100
25	H	3.8310660	-2.0789320	0.1454290
26	H	1.4562310	-1.7008980	-0.3601170
27	H	-3.8134670	0.4086420	3.2340200
28	H	-5.2805870	0.6517210	1.2481040
29	C	-3.8025980	-0.2864590	2.4093420
30	H	-4.4584730	-1.1158650	2.6172290
31	N	-4.2929060	0.4462680	1.1851830
32	H	-3.7246110	1.3611120	1.0931200
33	C	-2.3837640	-0.7939130	2.1781800
34	H	-4.0834380	-0.1209920	0.3298520
35	H	-1.9392820	-1.0672110	3.1196280
36	H	-1.7886390	-0.0199450	1.7129750
37	O	-2.3969940	-2.0115450	1.3822800
38	O	-3.2683290	-0.9652720	-0.8023190
39	P	-2.3046450	-2.0699040	-0.2517180
40	O	-0.8376150	-1.9827700	-0.7550720
41	O	-2.8969390	-3.5654960	-0.4829940
42	H	-2.9713290	-4.2413570	-2.4551030
43	C	-2.4347680	-4.4538430	-1.5424960
44	H	-2.6464490	-5.4570050	-1.2145890
45	H	-1.3759200	-4.3218440	-1.6992460

Table A3.18: Cartesian coordinates (given in angstroms) generated for structure **R**,  
calculated using HF methods after energy minimisation calculations.

Atom		X	Y	Z
1	C	-3.5656650	2.8786250	-0.2767130
2	C	-2.0971440	3.3372950	-0.2472700
3	N	-1.2337840	2.1797180	-0.2237060
4	C	0.1034910	2.2679440	-0.1604980
5	N	0.7051450	1.0327220	-0.1341090
6	C	2.0536020	0.7481890	-0.0736760
7	C	3.0686600	1.7068250	-0.0296940
8	C	4.3880660	1.3115400	0.0286930
9	C	4.7266390	-0.0273730	0.0445370
10	C	6.1393890	-0.4347000	0.1610220
11	F	6.9794630	0.4666560	-0.4032030
12	F	6.5633990	-0.5711040	1.4467340
13	F	6.3742240	-1.6335250	-0.4262200
14	C	3.7289950	-0.9864080	-0.0028130
15	C	2.4110040	-0.6064840	-0.0611700
16	O	0.7120560	3.3441370	-0.1289950
17	O	-3.7453490	1.6160560	-0.2395240
18	O	-4.4326170	3.7558330	-0.3326100
19	H	-1.9546560	3.9630250	0.6266960
20	H	-1.9211990	3.9572460	-1.1190560
21	H	-1.6935030	1.2884750	-0.2482210
22	H	0.0677100	0.2349460	-0.1581110
23	H	2.8024120	2.7368030	-0.0452580
24	H	5.1589010	2.0552460	0.0531340
25	H	3.9851870	-2.0263540	-0.0032910
26	H	1.6338380	-1.3425250	-0.1016920
27	H	-5.8960050	-0.1343400	1.8011190
28	H	-6.2419350	-0.4292840	-0.5680730
29	C	-5.2760810	-0.8294600	1.2567630
30	H	-5.6740760	-1.8269960	1.3474170
31	N	-5.3004460	-0.4274520	-0.2010520
32	H	-4.8486420	0.5306610	-0.2901760
33	C	-3.8489590	-0.7735630	1.7990070
34	H	-4.6800050	-1.0767010	-0.7562060
35	H	-3.8715620	-0.8860020	2.8697430
36	H	-3.3961620	0.1668350	1.5308540
37	O	-3.0569510	-1.8847350	1.2986670
38	O	-3.3905840	-1.8971290	-1.2695990
39	P	-2.2998010	-1.9130100	-0.1560700
40	O	-1.1974890	-0.8263550	-0.2046450
41	O	-1.6476500	-3.4039950	-0.0521170
42	H	-2.4874190	-4.2097080	-1.7848450
43	C	-1.5992790	-4.3191370	-1.1830800
44	H	-1.5398990	-5.3135350	-0.7742830
45	H	-0.7237700	-4.1160560	-1.7825120

Table A3.19: Cartesian coordinates (given in angstroms) generated for structure *S*,  
calculated using HF methods after energy minimisation calculations.

Atom		X	Y	Z
1	C	-3.4902090	-1.6466640	-0.1270090
2	C	-2.1620980	-1.8456610	-0.4818740
3	C	-1.3274880	-0.7372150	-0.6973130
4	C	-1.8542280	0.5589150	-0.5488550
5	C	-3.1807460	0.7429510	-0.1961750
6	C	-4.0064010	-0.3610970	0.0152150
7	C	-5.4228600	-0.1705780	0.4499120
8	N	0.0088340	-0.8253990	-1.0697670
9	C	0.7922070	-1.9580600	-1.1428770
10	O	0.4148510	-3.0901770	-0.8593880
11	N	2.0570910	-1.6808560	-1.6074870
12	C	3.1297130	-2.6128070	-1.3303560
13	C	3.7411410	-2.3384220	0.0408710
14	O	2.8405650	-2.3933200	1.0073070
15	O	4.9092280	-2.0461230	0.2075520
16	F	-6.2266480	-1.1471180	-0.0062720
17	F	-5.9315600	0.9980400	0.0233920
18	F	-5.5536910	-0.1731720	1.7918860
19	H	-4.1336710	-2.5067970	0.0318220
20	H	-1.7651110	-2.8437540	-0.5959320
21	H	-1.2060940	1.4177720	-0.7130550
22	H	-3.5777720	1.7474310	-0.0891170
23	H	0.4926720	0.0606370	-1.2727370
24	H	2.2975620	-0.6927380	-1.7028060
25	H	3.9113190	-2.5233420	-2.0857330
26	H	2.7141130	-3.6228230	-1.3515580
27	H	3.1839300	-1.8844220	1.8403540
28	N	3.3357930	-0.7384480	2.9746840
29	H	3.1053020	-1.0948380	3.9001810
30	H	4.2676310	-0.3317230	3.0480410
31	C	2.3587310	0.2863440	2.5728810
32	C	2.7491730	0.8602150	1.2223240
33	O	1.7292730	1.7607060	0.8137360
34	P	1.9146150	2.3727240	-0.7005020
35	O	1.7876750	1.2377560	-1.6916120
36	O	0.5114000	3.1887880	-0.7795180
37	C	0.3623510	4.3208280	0.0738040
38	O	3.0953670	3.2843430	-0.7459000
39	H	2.2698830	1.0978080	3.3047060
40	H	1.3807360	-0.1955390	2.4781300
41	H	2.8395020	0.0518420	0.4874430
42	H	3.7134660	1.3825580	1.2852800
43	H	-0.5803450	4.8016040	-0.1905600
44	H	1.1884170	5.0221600	-0.0727760
45	H	0.3317090	4.0082110	1.1220730

Table A3.20: Cartesian coordinates (given in angstroms) generated for structure **T**,  
calculated using HF methods after energy minimisation calculations.

Atom		X	Y	Z
1	O	3.503412	1.54027	0.220174
2	C	3.356874	2.782669	0.435073
3	C	1.903637	3.270422	0.599069
4	N	1.008092	2.137568	0.626084
5	C	-0.318027	2.252941	0.447499
6	N	-0.943884	1.029228	0.431547
7	C	-2.278951	0.758525	0.215046
8	C	-3.272567	1.734656	0.102329
9	C	-4.584900	1.366361	-0.102334
10	C	-4.937433	0.034913	-0.199647
11	C	-6.335661	-0.344866	-0.472605
12	F	-7.217646	0.553363	0.030172
13	F	-6.628051	-0.436188	-1.798841
14	F	-6.647654	-1.556497	0.049243
15	C	-3.960012	-0.940625	-0.093194
16	C	-2.646840	-0.591832	0.109489
17	O	-0.894805	3.339071	0.304996
18	O	4.243640	3.643184	0.519133
19	H	1.669258	3.932701	-0.226599
20	H	1.852534	3.860871	1.507514
21	H	1.432875	1.227671	0.696683
22	H	-0.315180	0.232725	0.594887
23	H	-2.993404	2.758914	0.175448
24	H	-5.338927	2.124000	-0.176597
25	H	-4.229670	-1.975016	-0.165010
26	H	-1.892612	-1.353075	0.172386
27	C	4.972525	-0.154549	-2.242594
28	C	4.318205	-1.119812	-1.254032
29	C	2.808464	-1.139120	-1.411225
30	O	2.271272	-2.281358	-0.695029
31	P	1.153847	-2.203111	0.505285
32	O	-0.124244	-2.985101	0.122247
33	O	1.927265	-3.000347	1.707913
34	C	3.047918	-2.399548	2.418915
35	O	0.996086	-0.709797	0.917609
36	O	4.730532	-0.710298	0.069530
37	H	4.706132	-2.114667	-1.409024
38	H	2.544275	-1.258247	-2.452186
39	H	2.396751	-0.225767	-1.019303
40	H	2.684061	-1.662029	3.119686
41	H	3.729993	-1.935736	1.722884
42	H	3.536182	-3.200416	2.950131
43	H	4.515371	0.820520	-2.131328
44	H	4.866103	-0.495579	-3.260674
45	O	6.384534	-0.088435	-1.940829
46	H	6.445850	-0.130058	-0.972938
47	H	4.332482	0.187867	0.249493

Table A3.21: Cartesian coordinates (given in angstroms) generated for structure U, calculated using HF methods after energy minimisation calculations.

Atom		X	Y	Z
1	O	4.1690690	-2.2013370	-0.3672220
2	C	2.9446980	-2.4784420	-0.3111400
3	C	2.1952380	-2.7737820	-1.6177380
4	N	1.1639910	-1.7508770	-1.7551740
5	C	-0.0919940	-1.9686140	-1.2906830
6	N	-0.7292280	-0.7835470	-1.0153790
7	C	-2.0365630	-0.5813140	-0.6215190
8	C	-2.9978620	-1.5909280	-0.5451840
9	C	-4.2870080	-1.2896490	-0.1609320
10	C	-4.6438140	0.0061290	0.1551930
11	C	-6.0120940	0.3077560	0.6156610
12	F	-6.9279570	-0.5399400	0.0869250
13	F	-6.1670770	0.2147210	1.9643760
14	F	-6.3923680	1.5686650	0.2948340
15	C	-3.6960360	1.0137170	0.0877370
16	C	-2.4068760	0.7312880	-0.2939420
17	O	-0.5971650	-3.0854120	-1.1553340
18	O	2.2285700	-2.4548320	0.7279720
19	H	1.7153160	-3.7380900	-1.5675000
20	H	2.8822990	-2.7357540	-2.4470410
21	H	1.4747290	-0.7880870	-1.7441050
22	H	-0.1162100	0.0337780	-1.0631700
23	H	-2.7140380	-2.5890880	-0.7819640
24	H	-5.0196110	-2.0700700	-0.1162030
25	H	-3.9706460	2.0209600	0.3278280
26	H	-1.6723690	1.5135410	-0.3327950
27	C	4.2607010	-0.5552520	2.7181040
28	C	4.0039260	0.5837990	1.7020370
29	C	2.5077500	0.8329130	1.5709290
30	O	2.3056690	2.0931450	0.8763480
31	P	1.4672980	2.3124230	-0.5116840
32	O	0.1761980	3.1273850	-0.2650860
33	O	2.5316110	3.2216590	-1.3597250
34	C	3.7742900	2.6472950	-1.8608710
35	O	1.3149050	0.9357420	-1.2262840
36	O	4.6157560	0.3337610	0.4221350
37	H	4.4598190	1.4918510	2.0673070
38	H	2.0587210	0.9235830	2.5456670
39	H	2.0418360	0.0283200	1.0288950
40	H	3.5867660	2.1349520	-2.7935940
41	H	4.1897340	1.9571750	-1.1417340
42	H	4.4483370	3.4721390	-2.0271300
43	H	4.5065760	-0.1185900	3.6758030
44	H	5.1237520	-1.1152780	2.3733960
45	O	3.1237050	-1.3964400	2.9491890
46	H	2.8312890	-1.8582430	2.1183230
47	H	4.4748290	-0.5983300	0.1300750

Table A3.22: Cartesian coordinates (given in angstroms) generated for structure V, calculated using HF methods after energy minimisation calculations.

Atom		X	Y	Z
1	C	2.8151010	-2.7488900	-0.2942630
2	C	2.1740970	-2.7635610	-1.6976220
3	N	1.1620100	-1.7250210	-1.7905260
4	C	-0.0890630	-1.9500190	-1.3239310
5	N	-0.7382450	-0.7748090	-1.0296570
6	C	-2.0355460	-0.6065230	-0.5833490
7	C	-2.9926200	-1.6229390	-0.5568830
8	C	-4.2732730	-1.3554790	-0.1223160
9	C	-4.6260410	-0.0871130	0.2936520
10	C	-5.9843940	0.1757570	0.8045690
11	F	-6.9100810	-0.6355510	0.2373240
12	F	-6.1087750	-0.0134680	2.1463840
13	F	-6.3745320	1.4548700	0.5828880
14	C	-3.6812690	0.9251130	0.2810430
15	C	-2.3998570	0.6752980	-0.1476010
16	O	-0.5913910	-3.0706700	-1.2090310
17	O	2.0685970	-2.4745920	0.6694890
18	O	4.0562960	-2.9942710	-0.2421680
19	H	1.7069980	-3.7228840	-1.8721960
20	H	2.9452800	-2.6036660	-2.4342140
21	H	1.4746130	-0.7656060	-1.7792450
22	H	-0.1569430	0.0592150	-1.1192960
23	H	-2.7120260	-2.6008340	-0.8689980
24	H	-5.0027880	-2.1401070	-0.1178230
25	H	-3.9507610	1.9102140	0.6046070
26	H	-1.6625820	1.4553160	-0.1278800
27	C	4.3249510	-0.9038010	2.3968570
28	C	3.6310330	0.4387630	2.1966740
29	C	3.0267240	0.5336510	0.8149310
30	O	2.4970120	1.8918150	0.7052340
31	P	1.4251810	2.3050840	-0.4657560
32	O	0.1587780	2.9419200	0.1557850
33	O	2.3143540	3.4155540	-1.2834960
34	C	2.1665030	3.6045650	-2.7165660
35	O	1.2244750	1.0688560	-1.3966160
36	O	4.5940330	1.5028980	2.3601590
37	H	2.8431830	0.5365460	2.9357610
38	H	2.2585000	-0.2016130	0.6734990
39	H	3.8079740	0.3960400	0.0862490
40	H	1.2848560	4.1937820	-2.9275420
41	H	2.0887220	2.6481880	-3.2091240
42	H	3.0432050	4.1314320	-3.0542790
43	H	3.5577660	-1.6608210	2.4648500
44	H	4.8769970	-0.8637910	3.3275150
45	O	5.2296410	-1.2034320	1.3214360
46	H	4.8458180	-1.9160260	0.7474020
47	H	4.1951850	2.3009540	1.9814590

Table A3.23: Cartesian coordinates (given in angstroms) generated for structure *W*,  
calculated using HF methods after energy minimisation calculations.

Atom		X	Y	Z
1	O	-4.1605700	3.9622320	-0.1373850
2	C	-3.3481750	3.0292620	-0.1902810
3	C	-1.8799370	3.4112740	-0.4390000
4	N	-1.0426520	2.2335600	-0.4616700
5	C	0.2954480	2.3105390	-0.3572120
6	N	0.8914240	1.0747270	-0.3102570
7	C	2.2344040	0.7907550	-0.1483140
8	C	3.2516610	1.7476480	-0.1927650
9	C	4.5679130	1.3672190	-0.0407320
10	C	4.9007290	0.0423390	0.1583680
11	C	6.3067020	-0.3465680	0.3732040
12	F	7.1704780	0.4876150	-0.2553830
13	F	6.6813270	-0.3383720	1.6816820
14	F	6.5625260	-1.6031630	-0.0664960
15	C	3.8998290	-0.9132410	0.2111400
16	C	2.5824540	-0.5516600	0.0634000
17	O	0.9050200	3.3865230	-0.2988530
18	O	-3.5969480	1.7876620	-0.0692970
19	H	-1.5709030	4.0912770	0.3450730
20	H	-1.8367970	3.9626730	-1.3730050
21	H	-1.5041810	1.3414700	-0.4830170
22	H	0.2424680	0.2830630	-0.4040340
23	H	2.9891590	2.7680080	-0.3406790
24	H	5.3393600	2.1091870	-0.0884650
25	H	4.1535900	-1.9427290	0.3655470
26	H	1.8109350	-1.2947130	0.1322710
27	C	-5.6258950	-0.2946090	1.5382790
28	C	-4.7314660	-1.5083620	1.2033480
29	C	-3.2670000	-1.1188840	1.2933670
30	O	-2.4450000	-2.2591490	0.9225590
31	P	-1.1887470	-2.1553720	-0.1217730
32	O	0.0781980	-2.7835970	0.5098610
33	O	-1.7322310	-3.0808440	-1.3652270
34	C	-1.4985690	-2.7166230	-2.7507980
35	O	-1.0832420	-0.6864370	-0.6357320
36	O	-5.0693380	-1.9241470	-0.1337570
37	H	-4.9297720	-2.3291340	1.8759460
38	H	-3.0255230	-0.8546650	2.3142290
39	H	-3.0588310	-0.2841100	0.6491230
40	H	-0.4987840	-3.0016170	-3.0487290
41	H	-1.6233760	-1.6539860	-2.8819550
42	H	-2.2184750	-3.2570000	-3.3428190
43	H	-5.2150050	0.2750550	2.3635780
44	H	-6.6115980	-0.6383000	1.8164100
45	O	-5.7746010	0.5013340	0.3489680
46	H	-4.9647360	1.0763680	0.1864560
47	H	-5.4155980	-1.1161510	-0.5551840



Table A3.24: Cartesian coordinates (given in angstroms) generated for structure X, calculated using HF methods after energy minimisation calculations.

Atom		X	Y	Z
1	O	-4.2888410	3.9190560	0.0165920
2	C	-3.4495810	3.0204800	-0.1367220
3	C	-1.9815420	3.4705040	-0.2472910
4	N	-1.1132470	2.3227680	-0.3819390
5	C	0.2197370	2.4124450	-0.2345190
6	N	0.8399400	1.1904870	-0.3097980
7	C	2.1839560	0.9122540	-0.1686800
8	C	3.1878640	1.8779000	-0.0633450
9	C	4.5065290	1.4935610	0.0546190
10	C	4.8548080	0.1574490	0.0718970
11	C	6.2632890	-0.2412780	0.2504630
12	F	7.1229650	0.6827060	-0.2432910
13	F	6.6213390	-0.4120820	1.5522430
14	F	6.5407900	-1.4208790	-0.3572190
15	C	3.8671560	-0.8085750	-0.0251300
16	C	2.5490850	-0.4415060	-0.1413890
17	O	0.8065670	3.4848420	-0.0417420
18	O	-3.6659140	1.7709320	-0.2224230
19	H	-1.7368760	4.0429140	0.6389170
20	H	-1.9031860	4.1440960	-1.0946010
21	H	-1.5599570	1.4347220	-0.5214850
22	H	0.2159670	0.3941110	-0.4853650
23	H	2.9130540	2.9057850	-0.0736730
24	H	5.2690040	2.2430630	0.1233240
25	H	4.1316410	-1.8466030	-0.0137550
26	H	1.7818260	-1.1878010	-0.1931310
27	C	-5.8868130	-0.7016900	0.9818140
28	C	-4.6688710	-1.5854300	0.6881430
29	C	-3.3917120	-0.9695060	1.2606600
30	O	-2.2602660	-1.8846680	1.0902140
31	P	-1.4568840	-2.0332540	-0.3274900
32	O	-1.0130300	-0.6301580	-0.8259940
33	O	-0.1450920	-2.8676380	0.1881130
34	C	0.3012020	-4.1095210	-0.4261250
35	O	-2.2899100	-2.9241050	-1.2953590
36	O	-4.6027240	-1.7490060	-0.7351170
37	H	-4.8229860	-2.5372210	1.1884260
38	H	-3.4914350	-0.8340330	2.3257610
39	H	-3.1791310	-0.0312440	0.7783490
40	H	0.6674200	-4.7432970	0.3646010
41	H	1.0976090	-3.8963580	-1.1231730
42	H	-0.5193880	-4.5822440	-0.9407630
43	H	-5.9126650	-0.5058880	2.0518590
44	H	-6.7707860	-1.2758150	0.7377170
45	O	-5.9605860	0.5053560	0.2223880
46	H	-5.0903760	0.9543720	0.0754930
47	H	-3.8614190	-2.3396380	-1.0093110

Table A3.25: Cartesian coordinates (given in angstroms) generated for structure *Y*,  
calculated using HF methods after energy minimisation calculations.

Atom		X	Y	Z
1	O	3.6311130	1.6467910	-0.2269950
2	C	3.4248370	2.8820230	0.0411730
3	C	1.9903530	3.2726490	0.4294160
4	N	1.1122100	2.1313720	0.3347880
5	C	-0.2265690	2.2523780	0.3170040
6	N	-0.8481520	1.0367020	0.1650930
7	C	-2.1963250	0.7705530	0.0633060
8	C	-3.2002760	1.7374700	0.1606360
9	C	-4.5251170	1.3733690	0.0506070
10	C	-4.8798910	0.0551780	-0.1560820
11	C	-6.2965190	-0.3159290	-0.3257440
12	F	-7.1288850	0.5250230	0.3353880
13	F	-6.7150220	-0.2970450	-1.6208450
14	F	-6.5526350	-1.5718550	0.1162010
15	C	-3.8925620	-0.9117160	-0.2534870
16	C	-2.5672070	-0.5672940	-0.1475500
17	O	-0.8149810	3.3367730	0.4191330
18	O	4.2611970	3.7889570	0.0159930
19	H	1.6711530	4.0673510	-0.2333080
20	H	2.0191720	3.6880330	1.4324390
21	H	1.5361080	1.2245010	0.2168230
22	H	-0.1971820	0.2415670	0.1243530
23	H	-2.9191660	2.7512130	0.3216000
24	H	-5.2860860	2.1226590	0.1363930
25	H	-4.1643270	-1.9369310	-0.4054180
26	H	-1.8077650	-1.3219270	-0.2304140
27	C	5.7678370	-0.7060090	-1.0095490
28	C	4.6524350	-1.4724940	-0.2950220
29	C	3.5155760	-1.7619060	-1.2638950
30	O	2.5683050	-2.6842870	-0.6636850
31	P	1.2071170	-2.2126900	0.1194980
32	O	-0.0229510	-2.9446910	-0.4719450
33	O	1.4607900	-2.7478940	1.6465510
34	C	1.8217580	-1.8484900	2.7327680
35	O	1.1634180	-0.6567710	0.1334030
36	O	4.1742640	-0.7505960	0.8571680
37	H	5.0462620	-2.4078200	0.0743740
38	H	3.8898430	-2.2452410	-2.1522310
39	H	3.0234380	-0.8415080	-1.5218070
40	H	1.0487010	-1.1091340	2.8834390
41	H	2.7534130	-1.3645550	2.4997500
42	H	1.9150980	-2.4638860	3.6126980
43	H	6.3017690	-1.3801930	-1.6649130
44	H	6.4595690	-0.3421050	-0.2563680
45	O	5.2609150	0.3585050	-1.8303140
46	H	4.7090500	0.9677800	-1.2784710
47	H	3.8281160	0.1259520	0.5767810

Table A3.26: Cartesian coordinates (given in angstroms) generated for structure **Z**,  
calculated using HF methods after energy minimisation calculations.

Atom		X	Y	Z
1	O	-3.1010370	1.8009090	-0.1431400
2	C	-3.1799140	2.4432990	-1.2346200
3	C	-1.9857070	2.3449870	-2.2031360
4	N	-1.0542220	1.2930220	-1.8551080
5	C	0.1813650	1.5763870	-1.4068730
6	N	0.8419870	0.4955110	-0.8716980
7	C	2.1702960	0.4401290	-0.4808660
8	C	3.0923210	1.4786910	-0.6275520
9	C	4.4006750	1.3028410	-0.2277230
10	C	4.8179900	0.1085860	0.3241320
11	C	6.2064040	-0.0479650	0.7956520
12	F	7.0736670	0.7263960	0.0992470
13	F	6.3813620	0.2937550	2.1012930
14	F	6.6374110	-1.3296680	0.6981810
15	C	3.9112100	-0.9272090	0.4781460
16	C	2.6063510	-0.7682750	0.0828720
17	O	0.6799920	2.7093150	-1.4717730
18	O	-4.1165790	3.1684200	-1.6087610
19	H	-1.4588130	3.2879200	-2.1984590
20	H	-2.3891950	2.1961720	-3.1969360
21	H	-1.4267480	0.3510480	-1.8537060
22	H	0.3107610	-0.3540280	-0.6593290
23	H	2.7659280	2.4012500	-1.0436850
24	H	5.1010810	2.1033950	-0.3556610
25	H	4.2307830	-1.8596670	0.8978570
26	H	1.8928350	-1.5581320	0.1954850
27	C	-3.6415000	0.6676570	3.3947240
28	C	-3.8854020	-0.2688510	2.2055410
29	C	-2.5751500	-0.7049710	1.5809150
30	O	-2.8763150	-1.7523090	0.6133750
31	P	-1.8392520	-2.0673140	-0.6147930
32	O	-0.3891630	-1.8269770	-0.1005070
33	O	-2.1581500	-3.6613720	-0.7938050
34	C	-2.0738220	-4.3353160	-2.0781680
35	O	-2.2298990	-1.3084560	-1.9133580
36	O	-4.7348490	0.4363060	1.2838560
37	H	-4.4277620	-1.1405380	2.5415660
38	H	-1.9075680	-1.1025790	2.3308440
39	H	-2.1218840	0.1371300	1.0850800
40	H	-1.0546430	-4.6398240	-2.2700090
41	H	-2.4101030	-3.6771520	-2.8641990
42	H	-2.7085530	-5.2037280	-2.0185790
43	H	-2.9377750	1.4427930	3.1070560
44	H	-3.2487840	0.1327170	4.2459470
45	O	-4.9086650	1.2491740	3.7647710
46	H	-5.3833010	1.3501150	2.9212580
47	H	-4.1771770	1.0287150	0.6929880

Table A3.27: Cartesian coordinates (given in angstroms) generated for structure AA, calculated using HF methods, after energy minimisation calculations.

Atom		X	Y	Z
1	O	4.1515740	-2.0095050	-1.0632230
2	C	2.9056620	-2.1223210	-1.0039540
3	C	2.0842940	-1.9240010	-2.2858920
4	N	1.0570640	-0.9274450	-2.0190480
5	C	-0.1610710	-1.3099050	-1.5830530
6	N	-0.8323580	-0.3175810	-0.9084190
7	C	-2.1656160	-0.3151530	-0.5352670
8	C	-3.0883010	-1.3101760	-0.8637500
9	C	-4.4037540	-1.1900130	-0.4669310
10	C	-4.8261820	-0.0956330	0.2607420
11	C	-6.2229820	-0.0059150	0.7252060
12	F	-7.0798810	-0.6514560	-0.1028290
13	F	-6.4252150	-0.5516200	1.9553520
14	F	-6.6457040	1.2781510	0.8270280
15	C	-3.9180790	0.8950710	0.5965440
16	C	-2.6063850	0.7908500	0.2056380
17	O	-0.6323950	-2.4338200	-1.7877240
18	O	2.2332900	-2.3375940	0.0506210
19	H	1.6060030	-2.8507170	-2.5636900
20	H	2.7365910	-1.5910230	-3.0765940
21	H	1.3918100	0.0263950	-1.9156430
22	H	-0.2902740	0.4690880	-0.5377850
23	H	-2.7568010	-2.1593890	-1.4119430
24	H	-5.1053470	-1.9542410	-0.7342920
25	H	-4.2418070	1.7504180	1.1544820
26	H	-1.8911900	1.5465410	0.4573590
27	C	4.1647460	-1.4136280	2.8519310
28	C	4.2521160	-0.1390340	1.9971770
29	C	2.8602720	0.3498720	1.6071590
30	O	3.0077410	1.6161140	0.9015160
31	P	1.9104960	2.1074450	-0.2081230
32	O	0.4805450	1.7644630	0.3053800
33	O	2.2056670	3.7140710	-0.1361960
34	C	2.1008550	4.5781120	-1.2995470
35	O	2.2558310	1.5801820	-1.6299490
36	O	5.1135820	-0.3352160	0.8717830
37	H	4.7067400	0.6360760	2.5985300
38	H	2.2728050	0.5195310	2.4976520
39	H	2.3652540	-0.3794290	0.9885710
40	H	1.0786640	4.9062000	-1.4251060
41	H	2.4235610	4.0497590	-2.1829880
42	H	2.7363200	5.4286310	-1.1167960
43	H	3.4340650	-1.2589970	3.6419830
44	H	5.1261880	-1.5638270	3.3246480
45	O	3.8948000	-2.6021230	2.1008960
46	H	3.2143010	-2.4889460	1.3891610
47	H	4.7814130	-1.0395530	0.2697670

Table A3.28: Cartesian coordinates (given in angstroms) generated for structure **AB**,  
calculated using HF methods, after energy minimisation calculations.

Atom		X	Y	Z
1	O	-3.4990670	3.8379020	-1.0559680
2	C	-2.6861090	2.9107330	-0.9045180
3	C	-2.1116540	2.3038230	-2.2002590
4	N	-1.2144700	1.1922590	-1.9692750
5	C	0.0356430	1.4427770	-1.5366950
6	N	0.7036160	0.3414900	-1.0555010
7	C	2.0265710	0.2840260	-0.6430170
8	C	2.9401470	1.3362290	-0.7349820
9	C	4.2413850	1.1606590	-0.3121680
10	C	4.6601400	-0.0472020	0.2078220
11	C	6.0392800	-0.2045930	0.7057410
12	F	6.9141650	0.5979690	0.0521190
13	F	6.1814020	0.1004560	2.0243720
14	F	6.4850220	-1.4787920	0.5807250
15	C	3.7620850	-1.0970800	0.3061010
16	C	2.4640630	-0.9382690	-0.1114920
17	O	0.5452800	2.5690760	-1.5941820
18	O	-2.2834410	2.4184320	0.1960180
19	H	-1.6076110	3.0912870	-2.7411080
20	H	-2.9448250	1.9649190	-2.8016200
21	H	-1.6457600	0.2791540	-1.8889950
22	H	0.1926300	-0.5315800	-0.9155700
23	H	2.6128430	2.2680120	-1.1286670
24	H	4.9352380	1.9725210	-0.3977160
25	H	4.0826450	-2.0397260	0.7015630
26	H	1.7568800	-1.7382320	-0.0380250
27	C	-3.3002600	1.1546230	3.2430200
28	C	-3.3127850	-0.2692180	2.6847140
29	C	-2.3527470	-0.4287800	1.5161430
30	O	-2.6820630	-1.7203580	0.9073450
31	P	-2.0233990	-2.1185610	-0.5446780
32	O	-0.4724310	-2.0778710	-0.4278010
33	O	-2.5815670	-3.6504720	-0.6370950
34	C	-2.9661730	-4.2600230	-1.9002130
35	O	-2.6399740	-1.2555960	-1.6803150
36	O	-4.6474280	-0.5789710	2.2448530
37	H	-3.0114560	-0.9481660	3.4751060
38	H	-1.3275190	-0.4417490	1.8550350
39	H	-2.4870690	0.3563440	0.7917860
40	H	-2.0991960	-4.6913480	-2.3798280
41	H	-3.4096190	-3.5197560	-2.5474910
42	H	-3.6786620	-5.0342640	-1.6698810
43	H	-2.2935320	1.3669670	3.5966020
44	H	-3.9574220	1.1758920	4.1019220
45	O	-3.7770260	2.1450070	2.3349030
46	H	-3.1807280	2.2852570	1.5511550
47	H	-4.5709640	-1.3334890	1.6411410

Table A3.29: Cartesian coordinates (given in angstroms) generated for structure AC, calculated using HF methods after energy minimisation calculations.

Atom		X	Y	Z
1	O	-3.6148440	3.9172690	-0.6162300
2	C	-3.0482650	2.8188920	-0.6046460
3	C	-1.9966940	2.5684880	-1.6959690
4	N	-1.0976450	1.4746910	-1.3872290
5	C	0.1753480	1.7155240	-1.0249310
6	N	0.8422350	0.6061920	-0.5603930
7	C	2.1960600	0.5051270	-0.2813120
8	C	3.1294570	1.5285550	-0.4608330
9	C	4.4603530	1.3088180	-0.1732560
10	C	4.8903460	0.0845150	0.2969880
11	C	6.3071930	-0.1197530	0.6506010
12	F	7.1367470	0.6525390	-0.0927350
13	F	6.5955980	0.1807250	1.9462710
14	F	6.6943570	-1.4083110	0.4846510
15	C	3.9734250	-0.9373530	0.4808000
16	C	2.6458220	-0.7348290	0.1966620
17	O	0.7009550	2.8354920	-1.1052780
18	O	-3.2866270	1.8517170	0.2010890
19	H	-1.4283970	3.4719620	-1.8350720
20	H	-2.5286060	2.3605340	-2.6194130
21	H	-1.4870960	0.5363080	-1.4010520
22	H	0.3040420	-0.2329780	-0.3237540
23	H	2.7940600	2.4733060	-0.8150770
24	H	5.1676890	2.0992000	-0.3247750
25	H	4.3024300	-1.8931030	0.8357570
26	H	1.9242930	-1.5137580	0.3310400
27	C	-5.1234130	0.2967170	2.4311550
28	C	-4.6813870	-0.7497790	1.4031200
29	C	-3.2324940	-1.1403030	1.6524700
30	O	-2.8745290	-2.2213270	0.7460290
31	P	-1.7363320	-2.0650880	-0.4170220
32	O	-0.3705460	-1.7124930	0.2459740
33	O	-1.7596680	-3.6137470	-0.9463210
34	C	-1.5391210	-3.9532510	-2.3409370
35	O	-2.1707240	-1.1221300	-1.5725740
36	O	-4.8575680	-0.2745610	0.0601700
37	H	-5.3045120	-1.6266660	1.5060080
38	H	-3.0989960	-1.5046310	2.6590780
39	H	-2.6011940	-0.2810710	1.4942270
40	H	-0.4793970	-4.0265770	-2.5419090
41	H	-1.9767990	-3.2014050	-2.9783050
42	H	-2.0071150	-4.9089220	-2.5096110
43	H	-5.2597180	-0.1790080	3.3928620
44	H	-6.0812770	0.6919970	2.1074730
45	O	-4.1515710	1.3393240	2.6166120
46	H	-3.8605610	1.6928840	1.7382950
47	H	-4.2451070	0.4829120	-0.0860110

### A3.2 Cartesian coordinates calculated using DFT methods

Table A3.30: Cartesian coordinates (given in angstroms) generated for structure **O**, calculated using DFT methods after energy minimisation calculations.

Atom		X	Y	Z
1	C	-5.7261150	-0.5694850	1.8820220
2	N	-4.9287770	-0.5565200	0.6151430
3	C	-5.8063700	-0.0728990	-0.4956800
4	C	-3.7661550	0.3791840	0.7949410
5	C	-4.4502080	-1.9644300	0.3483250
6	C	-3.7622670	-2.1541360	-1.0144850
7	O	-2.5707050	-2.9108530	-0.8708790
8	P	-1.1782350	-2.1018190	-0.5842420
9	O	-1.1998000	-0.7994630	-1.3547100
10	O	-1.4251840	-1.7590320	0.9945370
11	C	-0.5969810	-0.7258450	1.5388820
12	O	-0.0482890	-3.0586520	-0.7623850
13	H	-5.3299120	-2.6043750	0.4417050
14	H	-3.7414520	-2.2033220	1.1432820
15	H	-3.5247100	-1.2011770	-1.4963550
16	H	-4.4135090	-2.7179230	-1.6849260
17	H	-0.7911030	-0.6989720	2.6129970
18	H	-0.8422160	0.2472020	1.0990090
19	H	0.4634330	-0.9592040	1.3792410
20	H	-6.5982940	-0.8045460	-0.6593370
21	H	-5.2111470	0.0530450	-1.3989510
22	H	-6.2318870	0.8869450	-0.2027580
23	H	-5.1088220	-0.9909860	2.6752860
24	H	-6.6179970	-1.1778060	1.7306690
25	H	-6.0033650	0.4560640	2.1252780
26	H	-3.2398400	0.1053100	1.7083070
27	H	-4.1445450	1.4003170	0.8656180
28	H	-3.0811480	0.2816830	-0.0495760
29	C	4.5807310	1.2167850	-0.0264980
30	C	3.3014780	1.6237670	-0.3820590
31	C	2.3078140	0.6609220	-0.6283950
32	C	2.6363590	-0.7041070	-0.5207270
33	C	3.9168620	-1.0954790	-0.1658790
34	C	4.8970290	-0.1352660	0.0842400
35	C	6.2611750	-0.5472550	0.5302090
36	N	1.0051420	0.9633830	-0.9968250
37	C	0.3694800	2.1968420	-0.9497570
38	O	0.9277590	3.2447100	-0.6346450
39	N	-0.9313130	2.1195870	-1.3624640
40	C	-1.8504850	3.1661860	-0.9699470
41	C	-2.3336710	3.0777240	0.5037160
42	O	-1.6929220	2.3251470	1.2744530
43	O	-3.3413360	3.7739980	0.7708040
44	F	7.2145920	0.2913510	0.0869960
45	F	6.5851670	-1.7798900	0.1036390
46	F	6.3770280	-0.5686920	1.8736450
47	H	5.3448290	1.9661560	0.1576300
48	H	3.0595130	2.6727200	-0.4698410
49	H	1.8711230	-1.4552920	-0.7131910
50	H	4.1551390	-2.1514860	-0.0866330
51	H	0.3852570	0.1657360	-1.1714450
52	H	-1.3148480	1.1755570	-1.3755690
53	H	-2.7242440	3.1370350	-1.6271660
54	H	-1.3613830	4.1326380	-1.1199980

Table A3.31: Cartesian coordinates (given in angstroms) generated for structure *P*, calculated using DFT methods after energy minimisation calculations.

Atom		X	Y	Z
1	O	2.7495590	-2.3803560	0.4335420
2	C	3.1436980	-2.9699330	-0.6070680
3	C	2.7605660	-2.3505110	-1.9790730
4	N	1.8636030	-1.2173270	-1.9459580
5	C	0.5594810	-1.4201770	-1.6347680
6	N	-0.1556950	-0.2474140	-1.4145190
7	C	-1.5113620	-0.1481540	-1.1153750
8	C	-2.4407490	-1.1852010	-1.3012820
9	C	-3.7768260	-0.9836510	-0.9730090
10	C	-4.2109750	0.2373430	-0.4669200
11	C	-5.6361630	0.4403920	-0.0691190
12	F	-6.4580150	-0.4573460	-0.6363560
13	F	-5.8165030	0.3376030	1.2632410
14	F	-6.0832510	1.6628830	-0.4106350
15	C	-3.2945440	1.2744760	-0.2865540
16	C	-1.9606030	1.0873440	-0.6053550
17	O	0.0492860	-2.5402480	-1.5695410
18	O	3.8370650	-4.0040040	-0.6813500
19	H	2.3219400	-3.1431150	-2.5909650
20	H	3.6838890	-2.0332750	-2.4736570
21	H	2.2834220	-0.2916800	-1.8167890
22	H	0.3649340	0.6326960	-1.3117480
23	H	-2.1101870	-2.1339590	-1.6963640
24	H	-4.4890860	-1.7884760	-1.1242890
25	H	-3.6278430	2.2328750	0.1005810
26	H	-1.2379020	1.8871630	-0.4729490
27	C	-0.4980730	-0.4535540	3.6844040
28	N	0.5847520	-0.7663770	2.7019910
29	C	1.6683350	-1.5516130	3.3773480
30	C	0.0132850	-1.6033400	1.5960600
31	C	1.1128680	0.5436450	2.1663980
32	C	2.4454170	0.4520120	1.4257240
33	O	2.7843120	1.7794820	1.0383720
34	P	2.4526090	2.1770200	-0.5211350
35	O	0.9626990	2.2809300	-0.7029760
36	O	3.0523640	3.6769070	-0.5113790
37	C	4.4678450	3.8235280	-0.4047990
38	O	3.2323450	1.2720230	-1.4341200
39	H	1.2244640	1.2123290	3.0238380
40	H	0.3483380	0.9497250	1.4962640
41	H	2.3987270	-0.2352480	0.5744550
42	H	3.2404940	0.0981920	2.0865330
43	H	4.9702180	3.3004590	-1.2224980
44	H	4.8225920	3.4300920	0.5525160
45	H	4.6831980	4.8909340	-0.4622810
46	H	2.1809580	-0.9042120	4.0904090
47	H	2.3461060	-1.9282600	2.6078900
48	H	1.1975220	-2.3840380	3.9015010
49	H	-1.2458140	0.1661570	3.1874210
50	H	-0.0635910	0.0808530	4.5294170
51	H	-0.9451250	-1.3899150	4.0179150
52	H	-0.8056960	-1.0502790	1.1354170
53	H	-0.3652690	-2.5251950	2.0414000
54	H	0.8116410	-1.8330590	0.8861000



Table A3.32: Cartesian coordinates (given in angstroms) generated for structure **Q**,  
calculated using DFT methods after energy minimisation calculations.

Atom		X	Y	Z
1	C	-2.6689970	3.5241850	-0.1659850
2	C	-2.6913550	2.4872960	-1.2915410
3	N	-1.8388910	1.3530450	-1.0347330
4	C	-0.5026500	1.5684150	-0.8875000
5	N	0.2366050	0.4139930	-0.7310420
6	C	1.6055790	0.3128480	-0.4957900
7	C	2.4903160	1.4026480	-0.4532570
8	C	3.8412010	1.1815670	-0.2134410
9	C	4.3314960	-0.1066480	-0.0185780
10	C	5.7757400	-0.3183920	0.2989980
11	F	6.5639070	0.5984440	-0.2886810
12	F	6.0267120	-0.2386160	1.6216010
13	F	6.2085600	-1.5288820	-0.0944840
14	C	3.4567110	-1.1924600	-0.0622520
15	C	2.1083090	-0.9868410	-0.2985060
16	O	-0.0285910	2.7051750	-0.8873890
17	O	-2.7283120	3.0538180	1.0654940
18	O	-2.6281720	4.7148020	-0.4004030
19	H	-2.4151090	3.0113660	-2.2110490
20	H	-3.7143520	2.1111090	-1.3971690
21	H	-2.2533150	0.4157480	-1.0592570
22	H	-0.2645280	-0.4871650	-0.7526910
23	H	2.1154710	2.4032480	-0.6090610
24	H	4.5214690	2.0273520	-0.1865970
25	H	3.8331350	-2.2000110	0.0838090
26	H	1.4160460	-1.8232490	-0.3337300
27	H	-2.7254020	0.7608780	3.2557870
28	H	-4.7372760	0.9935280	1.7315880
29	C	-3.1472920	0.0080760	2.5809100
30	H	-3.8487880	-0.6059450	3.1582380
31	N	-3.8043380	0.6915280	1.4553620
32	H	-3.0343950	2.0635700	1.1075000
33	C	-2.0306500	-0.8883770	2.0832210
34	H	-3.9166390	0.0405080	0.6700440
35	H	-1.4374620	-1.2526700	2.9256730
36	H	-1.3630930	-0.3315910	1.4113920
37	O	-2.5856970	-2.0321310	1.4247720
38	O	-3.2991870	-1.0942560	-0.8623130
39	P	-2.4220430	-2.1271310	-0.1902630
40	O	-0.9623830	-2.1287780	-0.5692190
41	O	-3.0713000	-3.6026820	-0.3264790
42	H	-4.0362190	-3.3757110	-2.1554310
43	C	-3.3293400	-4.0461230	-1.6583920
44	H	-3.7592860	-5.0449510	-1.5842540
45	H	-2.4011200	-4.0922560	-2.2369130

Table A3.33: Cartesian coordinates (given in angstroms) generated for structure **R**, calculated using DFT methods after energy minimisation calculations.

Atom		X	Y	Z
1	C	-3.7849500	2.3981670	-0.2974220
2	C	-2.4184860	3.0638070	-0.5342490
3	N	-1.4387600	2.0373520	-0.8282090
4	C	-0.1400360	2.1662350	-0.4526910
5	N	0.5475650	0.9638460	-0.5181310
6	C	1.8984890	0.7420930	-0.3014830
7	C	2.8555060	1.7577860	-0.1368530
8	C	4.1911690	1.4211310	0.0420920
9	C	4.5986140	0.0894080	0.0604710
10	C	6.0324290	-0.2509100	0.3033020
11	F	6.8640610	0.6839050	-0.1895920
12	F	6.3231380	-0.3574730	1.6156820
13	F	6.3746940	-1.4248450	-0.2545200
14	C	3.6528380	-0.9237850	-0.0987010
15	C	2.3191310	-0.6008110	-0.2776510
16	O	0.3602870	3.2325490	-0.0962850
17	O	-3.9880810	1.3477110	-0.9938750
18	O	-4.5579950	2.8940710	0.5320950
19	H	-2.1223010	3.6216440	0.3566170
20	H	-2.5111240	3.7823420	-1.3608010
21	H	-1.8118470	1.1153800	-1.0568140
22	H	-0.0356790	0.1319620	-0.6616090
23	H	2.5444770	2.7922330	-0.1541090
24	H	4.9273210	2.2105980	0.1596450
25	H	3.9606620	-1.9645210	-0.0894390
26	H	1.5788820	-1.3862430	-0.4067710
27	H	-4.7427800	0.8021550	2.1273170
28	H	-6.1426880	-0.4709950	0.5938190
29	C	-4.4598770	-0.2005880	1.8002820
30	H	-4.8199580	-0.9410100	2.5168420
31	N	-5.1274020	-0.4401690	0.4910230
32	H	-4.8376640	0.3583170	-0.1930960
33	C	-2.9460740	-0.2861050	1.6763550
34	H	-4.7938050	-1.3254100	0.0491330
35	H	-2.5135900	-0.0423160	2.6498360
36	H	-2.5630580	0.4279570	0.9402960
37	O	-2.5212920	-1.6049710	1.3485700
38	O	-3.6198930	-2.3607540	-0.8423320
39	P	-2.2959020	-1.9964450	-0.2214720
40	O	-1.4456210	-0.9582270	-0.9097360
41	O	-1.4238820	-3.3290860	0.0868790
42	H	-1.8883950	-4.3955590	-1.6391390
43	C	-1.0171920	-4.0713680	-1.0614140
44	H	-0.4717610	-4.9447660	-0.7036270
45	H	-0.3625480	-3.4672870	-1.6976960

Table A3.34: Cartesian coordinates (given in angstroms) generated for structure *S*,  
calculated using DFT methods after energy minimisation calculations.

Atom		X	Y	Z
1	C	-3.4902090	-1.6466640	-0.1270090
2	C	-2.1620980	-1.8456610	-0.4818740
3	C	-1.3274880	-0.7372150	-0.6973130
4	C	-1.8542280	0.5589150	-0.5488550
5	C	-3.1807460	0.7429510	-0.1961750
6	C	-4.0064010	-0.3610970	0.0152150
7	C	-5.4228600	-0.1705780	0.4499120
8	N	0.0088340	-0.8253990	-1.0697670
9	C	0.7922070	-1.9580600	-1.1428770
10	O	0.4148510	-3.0901770	-0.8593880
11	N	2.0570910	-1.6808560	-1.6074870
12	C	3.1297130	-2.6128070	-1.3303560
13	C	3.7411410	-2.3384220	0.0408710
14	O	2.8405650	-2.3933200	1.0073070
15	O	4.9092280	-2.0461230	0.2075520
16	F	-6.2266480	-1.1471180	-0.0062720
17	F	-5.9315600	0.9980400	0.0233920
18	F	-5.5536910	-0.1731720	1.7918860
19	H	-4.1336710	-2.5067970	0.0318220
20	H	-1.7651110	-2.8437540	-0.5959320
21	H	-1.2060940	1.4177720	-0.7130550
22	H	-3.5777720	1.7474310	-0.0891170
23	H	0.4926720	0.0606370	-1.2727370
24	H	2.2975620	-0.6927380	-1.7028060
25	H	3.9113190	-2.5233420	-2.0857330
26	H	2.7141130	-3.6228230	-1.3515580
27	H	3.1839300	-1.8844220	1.8403540
28	N	3.3357930	-0.7384480	2.9746840
29	H	3.1053020	-1.0948380	3.9001810
30	H	4.2676310	-0.3317230	3.0480410
31	C	2.3587310	0.2863440	2.5728810
32	C	2.7491730	0.8602150	1.2223240
33	O	1.7292730	1.7607060	0.8137360
34	P	1.9146150	2.3727240	-0.7005020
35	O	1.7876750	1.2377560	-1.6916120
36	O	0.5114000	3.1887880	-0.7795180
37	C	0.3623510	4.3208280	0.0738040
38	O	3.0953670	3.2843430	-0.7459000
39	H	2.2698830	1.0978080	3.3047060
40	H	1.3807360	-0.1955390	2.4781300
41	H	2.8395020	0.0518420	0.4874430
42	H	3.7134660	1.3825580	1.2852800
43	H	-0.5803450	4.8016040	-0.1905600
44	H	1.1884170	5.0221600	-0.0727760
45	H	0.3317090	4.0082110	1.1220730

Table A3.35: Cartesian coordinates (given in angstroms) generated for structure *T*,  
calculated using DFT methods after energy minimisation calculations.

Atom		X	Y	Z
1	O	-3.7766150	0.8500320	-1.1784820
2	C	-3.6663020	2.0513820	-0.8124970
3	C	-2.3465680	2.7483860	-1.1909890
4	N	-1.3132690	1.7537800	-1.3980040
5	C	-0.0366810	1.9758190	-0.9783650
6	N	0.7075220	0.8111250	-0.9085860
7	C	2.0431750	0.6794150	-0.5569670
8	C	2.9457620	1.7521800	-0.4640710
9	C	4.2720970	1.5092910	-0.1300360
10	C	4.7220990	0.2134870	0.1093610
11	C	6.1374240	-0.0252430	0.5204510
12	F	6.9758640	0.8941730	0.0105580
13	F	6.3010160	0.0187140	1.8587310
14	F	6.5817060	-1.2324940	0.1282030
15	C	3.8293270	-0.8553620	0.0188030
16	C	2.5036390	-0.6285730	-0.3098900
17	O	0.3969570	3.0942450	-0.7004060
18	O	-4.5018040	2.7269810	-0.1709160
19	H	-2.0529470	3.4302200	-0.3890530
20	H	-2.5123330	3.3564470	-2.0912150
21	H	-1.6540850	0.7940910	-1.4770460
22	H	0.1753530	-0.0644720	-1.0333050
23	H	2.6000040	2.7579940	-0.6543610
24	H	4.9670560	2.3411070	-0.0662250
25	H	4.1743500	-1.8680750	0.2038170
26	H	1.8019730	-1.4598120	-0.3676730
27	C	-3.5649660	1.0878160	2.3239740
28	C	-3.5268250	-0.3858390	1.8555310
29	C	-2.1145950	-0.6741290	1.3623470
30	O	-1.9711070	-2.0413700	1.0014290
31	P	-1.1254070	-2.4681780	-0.3334660
32	O	0.1273670	-3.1866550	0.0517580
33	O	-2.1431880	-3.5777270	-0.9497890
34	C	-3.3977160	-3.0951870	-1.4275190
35	O	-1.0564910	-1.2835540	-1.2726700
36	O	-4.5027240	-0.6746920	0.8839510
37	H	-3.7541980	-1.0406460	2.7065640
38	H	-1.3887380	-0.4286970	2.1508280
39	H	-1.9118530	-0.0376420	0.4950180
40	H	-3.2536690	-2.4793630	-2.3207460
41	H	-3.8992960	-2.5009080	-0.6561940
42	H	-4.0034380	-3.9674810	-1.6795090
43	H	-2.9013840	1.6909870	1.6816480
44	H	-3.1640240	1.1495400	3.3426510
45	O	-4.8596850	1.6357080	2.3250360
46	H	-5.0115820	1.9243790	1.3993370
47	H	-4.3180480	-0.1172650	0.0860760

Table A3.36: Cartesian coordinates (given in angstroms) generated for structure *U*, calculated using DFT methods after energy minimisation calculations.

Atom		X	Y	Z
1	O	4.0828140	-2.5197110	-0.1362980
2	C	2.8291720	-2.5378530	-0.2187050
3	C	2.1941930	-2.7863590	-1.6019360
4	N	1.1757500	-1.7872140	-1.8731000
5	C	-0.0854150	-1.9817290	-1.3613710
6	N	-0.7215840	-0.7840530	-1.0876100
7	C	-2.0305020	-0.5896990	-0.6669130
8	C	-3.0136380	-1.5918780	-0.6565890
9	C	-4.3037660	-1.2869510	-0.2382690
10	C	-4.6351810	0.0024920	0.1663500
11	C	-6.0070400	0.3186500	0.6635960
12	F	-6.9275920	-0.5528530	0.2187170
13	F	-6.0831610	0.2983100	2.0099630
14	F	-6.4072790	1.5474660	0.2876670
15	C	-3.6604140	1.0021710	0.1566960
16	C	-2.3710260	0.7131000	-0.2539940
17	O	-0.6009760	-3.0866650	-1.2180370
18	O	2.0195730	-2.3314400	0.7216480
19	H	1.7190840	-3.7706040	-1.6206100
20	H	2.9646040	-2.7499880	-2.3752400
21	H	1.5100220	-0.8274880	-1.7771830
22	H	-0.1130030	0.0446950	-1.0972690
23	H	-2.7592070	-2.5929710	-0.9731430
24	H	-5.0609500	-2.0649540	-0.2375890
25	H	-3.9149380	2.0112130	0.4674430
26	H	-1.6058100	1.4894160	-0.2567410
27	C	4.2629650	-0.5394670	2.7289120
28	C	4.0738790	0.5224720	1.6309200
29	C	2.6091660	0.9235160	1.5045760
30	O	2.5296360	2.1399640	0.7627550
31	P	1.4981730	2.3038630	-0.4884250
32	O	0.2273160	2.9686090	-0.0632460
33	O	2.3537830	3.3879690	-1.3487110
34	C	3.5558690	2.9099680	-1.9482450
35	O	1.4283660	1.0034650	-1.2574530
36	O	4.6145660	0.1370030	0.3814250
37	H	4.6338910	1.4201190	1.9251920
38	H	2.1739080	1.0889600	2.4971250
39	H	2.0538530	0.1233600	1.0029740
40	H	3.3265780	2.3121310	-2.8352770
41	H	4.1269700	2.2977910	-1.2421100
42	H	4.1429590	3.7830730	-2.2385070
43	H	4.4409900	-0.0294170	3.6828180
44	H	5.1775490	-1.1042350	2.4843790
45	O	3.1583600	-1.3860420	2.9399450
46	H	2.8642300	-1.7881140	2.0808990
47	H	4.4127170	-0.8141880	0.2306910

Table A3.37: Cartesian coordinates (given in angstroms) generated for structure V, calculated using DFT methods after energy minimisation calculations.

Atom		X	Y	Z
1	C	3.2038190	-2.5900630	-0.1836890
2	C	2.3404100	-2.9957220	-1.3974560
3	N	1.3295560	-1.9716600	-1.6166400
4	C	0.0711180	-2.1186490	-1.1073950
5	N	-0.6399620	-0.9291660	-1.1300350
6	C	-1.9340130	-0.7017820	-0.6791830
7	C	-2.8418320	-1.7195450	-0.3444870
8	C	-4.1221510	-1.3882440	0.0821600
9	C	-4.5218240	-0.0583330	0.1749530
10	C	-5.8835150	0.2899100	0.6795420
11	F	-6.7695070	-0.7004420	0.4770510
12	F	-5.8933280	0.5416890	2.0045370
13	F	-6.3755380	1.3922850	0.0865460
14	C	-3.6240810	0.9566860	-0.1588810
15	C	-2.3438430	0.6415680	-0.5803030
16	O	-0.3911430	-3.1861500	-0.7104150
17	O	2.8230480	-2.9464540	0.9482310
18	O	4.1891630	-1.8428130	-0.4572610
19	H	1.8224850	-3.9371870	-1.2147200
20	H	2.9617640	-3.0799860	-2.2934110
21	H	1.6579280	-1.0149140	-1.7584920
22	H	-0.1031920	-0.1089710	-1.4295520
23	H	-2.5372910	-2.7528170	-0.4216370
24	H	-4.8202310	-2.1804930	0.3341480
25	H	-3.9288370	1.9966280	-0.0912880
26	H	-1.6407440	1.4355400	-0.8271860
27	C	3.9081740	-0.3771660	2.6643200
28	C	2.8979220	0.6828070	2.2316910
29	C	2.1896240	0.3024030	0.9443620
30	O	1.2402240	1.3388010	0.6455660
31	P	1.2789500	2.0337160	-0.8199050
32	O	0.1929870	3.0585780	-0.8769860
33	O	2.7500150	2.7435590	-0.6699680
34	C	3.2941720	3.3360270	-1.8455250
35	O	1.3607310	0.9670840	-1.8911140
36	O	3.5699440	1.9214120	2.0805270
37	H	2.1330920	0.7639430	3.0238550
38	H	1.6586420	-0.6486210	1.0563970
39	H	2.9217810	0.1951750	0.1370900
40	H	2.6385990	4.1323450	-2.2136800
41	H	3.4252400	2.5821040	-2.6271630
42	H	4.2622930	3.7607940	-1.5783470
43	H	3.3672380	-1.3183590	2.8360330
44	H	4.3410840	-0.0507180	3.6185780
45	O	4.9667150	-0.5495270	1.7574420
46	H	4.6472350	-1.0928510	0.9872510
47	H	3.1094870	2.4213180	1.3853920

Table A3.38: Cartesian coordinates (given in angstroms) generated for structure *W*, calculated using DFT methods after energy minimisation calculations.

Atom		X	Y	Z
1	O	4.3861970	3.4550360	0.0306870
2	C	3.5725260	2.6730280	0.5478210
3	C	2.1227480	3.1763890	0.6860880
4	N	1.2003530	2.0812300	0.8890630
5	C	-0.1114620	2.2095000	0.5601730
6	N	-0.7991460	1.0102580	0.6079680
7	C	-2.1408400	0.7909170	0.3346660
8	C	-3.1009210	1.8086840	0.1961840
9	C	-4.4258700	1.4754550	-0.0528280
10	C	-4.8203150	0.1441130	-0.1639890
11	C	-6.2398360	-0.1828300	-0.4906700
12	F	-7.1030570	0.6692020	0.0920960
13	F	-6.4908520	-0.1200860	-1.8148060
14	F	-6.5804080	-1.4227220	-0.0994740
15	C	-3.8714700	-0.8697640	-0.0285620
16	C	-2.5461510	-0.5529400	0.2178840
17	O	-0.6199950	3.2890950	0.2515720
18	O	3.8007930	1.5061040	0.9899490
19	H	1.8545260	3.7316200	-0.2169780
20	H	2.0855860	3.8917450	1.5199710
21	H	1.6111780	1.1639070	1.0578960
22	H	-0.2296570	0.1725610	0.8130690
23	H	-2.7992610	2.8420610	0.2862070
24	H	-5.1643860	2.2655950	-0.1530840
25	H	-4.1703320	-1.9096930	-0.1154090
26	H	-1.8012780	-1.3424160	0.3074680
27	C	4.8195980	0.4755390	-1.8161420
28	C	3.8948330	-0.7425100	-1.9072960
29	C	2.7905940	-0.6461660	-0.8707160
30	O	1.8888580	-1.7458420	-1.0062560
31	P	1.1182320	-2.2092830	0.3471050
32	O	-0.0665940	-3.0325580	-0.0470070
33	O	2.2985170	-3.1487330	0.9842020
34	C	2.1114570	-3.5466290	2.3369270
35	O	0.9343630	-1.0196140	1.2666330
36	O	4.6737240	-1.9108270	-1.7069380
37	H	3.4542800	-0.8135140	-2.9091250
38	H	2.2352410	0.2935510	-0.9872350
39	H	3.2396980	-0.6360730	0.1260270
40	H	1.1825330	-4.1170160	2.4521380
41	H	2.0811940	-2.6737900	2.9957530
42	H	2.9550390	-4.1825240	2.6097500
43	H	4.2479370	1.4123220	-1.8636210
44	H	5.5134460	0.4512570	-2.6639870
45	O	5.5846800	0.4016570	-0.6291420
46	H	5.0329090	0.8358960	0.0797840
47	H	5.2845820	-1.6554680	-0.9916010

Table A3.39: Cartesian coordinates (given in angstroms) generated for structure **X**, calculated using DFT methods after energy minimisation calculations.

Atom		X	Y	Z
1	O	-4.7621460	2.9608390	0.5096580
2	C	-3.8395770	2.5505330	-0.2137550
3	C	-2.4174550	3.0417960	0.1317170
4	N	-1.4262420	2.1266460	-0.3865160
5	C	-0.1182770	2.2235470	-0.0449890
6	N	0.6405850	1.1682220	-0.5244100
7	C	1.9959640	0.9446520	-0.3340660
8	C	2.8884000	1.8658690	0.2402710
9	C	4.2306750	1.5317020	0.3693420
10	C	4.7080450	0.2971260	-0.0650040
11	C	6.1439330	-0.0554970	0.1419160
12	F	6.9571430	0.9996070	-0.0465200
13	F	6.3904820	-0.4948730	1.3928290
14	F	6.5541490	-1.0284140	-0.6894650
15	C	3.8280240	-0.6186820	-0.6429500
16	C	2.4896530	-0.2956150	-0.7803810
17	O	0.3305650	3.1589830	0.6190480
18	O	-3.9271150	1.7720940	-1.2096310
19	H	-2.3297990	3.1307020	1.2190430
20	H	-2.2813620	4.0493110	-0.2851930
21	H	-1.7751780	1.3527730	-0.9442230
22	H	0.1106890	0.3705870	-0.9090520
23	H	2.5221410	2.8231530	0.5808990
24	H	4.9171430	2.2490650	0.8096880
25	H	4.1912700	-1.5803150	-0.9915910
26	H	1.7923000	-0.9962490	-1.2301610
27	C	-5.6212510	-0.5127740	0.6539050
28	C	-4.3667360	-1.3319400	0.9632900
29	C	-3.1254220	-0.5161000	0.6465410
30	O	-1.9290430	-1.2212010	0.9928340
31	P	-1.1391120	-1.9729270	-0.2175320
32	O	-0.9150200	-1.0052530	-1.3584710
33	O	0.2433000	-2.1939830	0.6110950
34	C	1.0665180	-3.2813180	0.2017060
35	O	-1.7902050	-3.2967660	-0.5141980
36	O	-4.4188110	-2.5261200	0.2103820
37	H	-4.3661840	-1.5540250	2.0452250
38	H	-3.1315030	0.4149310	1.2248940
39	H	-3.1237230	-0.2591500	-0.4153420
40	H	2.0011450	-3.2008880	0.7588780
41	H	1.2901510	-3.2350340	-0.8706950
42	H	0.5811040	-4.2360350	0.4211330
43	H	-5.6268950	0.3781810	1.3003080
44	H	-6.4932220	-1.1233570	0.9166870
45	O	-5.7461690	-0.1620580	-0.7038410
46	H	-5.1490260	0.6065230	-0.8866610
47	H	-3.5165260	-2.8992990	0.1237700



Table A3.40: Cartesian coordinates (given in angstroms) generated for structure *Y*, calculated using DFT methods after energy minimisation calculations.

Atom		X	Y	Z
1	O	3.8951440	1.4290000	-0.6196770
2	C	3.7093130	2.6648050	-0.3654780
3	C	2.2494080	3.0900080	-0.1253740
4	N	1.3370310	1.9854830	-0.2975240
5	C	0.0024840	2.1515250	-0.1333220
6	N	-0.7205570	1.0050800	-0.4304040
7	C	-2.0771030	0.7820940	-0.2558220
8	C	-2.9889600	1.7453980	0.2088080
9	C	-4.3312050	1.4142150	0.3512920
10	C	-4.7901820	0.1379520	0.0393560
11	C	-6.2412700	-0.1965660	0.1456400
12	F	-6.8789670	0.5756400	1.0418670
13	F	-6.8949790	-0.0382720	-1.0237070
14	F	-6.4366910	-1.4761420	0.5114950
15	C	-3.8902680	-0.8230050	-0.4249900
16	C	-2.5516030	-0.5067650	-0.5703570
17	O	-0.5028180	3.2125100	0.2382960
18	O	4.5675500	3.5504480	-0.2899120
19	H	2.0139290	3.9123940	-0.8126790
20	H	2.1769130	3.5034070	0.8879030
21	H	1.7170900	1.0922350	-0.6166110
22	H	-0.1530160	0.2064730	-0.7417410
23	H	-2.6359350	2.7355000	0.4564490
24	H	-5.0266080	2.1630110	0.7178490
25	H	-4.2374850	-1.8234780	-0.6643780
26	H	-1.8492760	-1.2601380	-0.9158080
27	C	5.7409150	-0.9515600	0.8091060
28	C	4.2895860	-1.3763540	1.0494770
29	C	3.7208140	-2.0726020	-0.1788250
30	O	2.4602350	-2.6608410	0.1337390
31	P	1.0912330	-2.1639530	-0.6034110
32	O	0.5372230	-3.2483550	-1.4699530
33	O	0.0954600	-2.0554020	0.6816370
34	C	0.4593770	-1.1885690	1.7512580
35	O	1.3122960	-0.7821250	-1.1810820
36	O	3.4695230	-0.2965220	1.4464210
37	H	4.2805540	-2.0870070	1.8870360
38	H	4.3963340	-2.8711340	-0.5085080
39	H	3.6120080	-1.3434650	-0.9861280
40	H	0.8587800	-0.2430060	1.3749160
41	H	1.2235320	-1.6580290	2.3771240
42	H	-0.4457120	-1.0039980	2.3349330
43	H	6.3794710	-1.8430290	0.8048640
44	H	6.0507370	-0.3248980	1.6601430
45	O	5.9507210	-0.2983090	-0.4249450
46	H	5.3242710	0.4621090	-0.4859870
47	H	3.4358360	0.3306820	0.6895870

Table A3.41: Cartesian coordinates (given in angstroms) generated for structure **Z**,  
calculated using DFT methods after energy minimisation calculations.

Atom		X	Y	Z
1	O	2.3712590	-2.1842030	-0.1821660
2	C	3.1222560	-2.3572620	-1.1885200
3	C	2.6774090	-1.6721360	-2.5045270
4	N	1.7165710	-0.6051810	-2.3284520
5	C	0.4146400	-0.9444480	-2.0898360
6	N	-0.3143150	0.0763470	-1.4987190
7	C	-1.6412110	0.0344660	-1.0885890
8	C	-2.5468870	-0.9899230	-1.4111430
9	C	-3.8579050	-0.9200750	-0.9541050
10	C	-4.2917170	0.1557660	-0.1853590
11	C	-5.6859500	0.1978780	0.3465670
12	F	-6.5380370	-0.5314100	-0.3934050
13	F	-5.7722300	-0.2800440	1.6051960
14	F	-6.1711030	1.4522230	0.3914390
15	C	-3.3973080	1.1785780	0.1356270
16	C	-2.0885010	1.1203320	-0.3088950
17	O	-0.0734100	-2.0245720	-2.4185660
18	O	4.1663420	-3.0291730	-1.2458470
19	H	2.2467650	-2.4314690	-3.1629900
20	H	3.5666390	-1.2724220	-2.9989600
21	H	2.1037740	0.1951590	-1.8192170
22	H	0.2008490	0.9106510	-1.1822420
23	H	-2.2182560	-1.8247890	-2.0117710
24	H	-4.5522290	-1.7142370	-1.2106720
25	H	-3.7280400	2.0239200	0.7315660
26	H	-1.3811470	1.9087740	-0.0652890
27	C	0.8399370	-1.8704930	2.8395470
28	C	1.8875670	-0.7801590	2.6061180
29	C	1.3976860	0.2179110	1.5747960
30	O	2.2960330	1.3304240	1.5264520
31	P	2.3420120	2.0973300	0.0925160
32	O	0.9327430	2.3757100	-0.3784310
33	O	3.0343620	3.4542080	0.6632350
34	C	3.3822430	4.4197220	-0.3240240
35	O	3.2628110	1.4008070	-0.8732320
36	O	3.1040470	-1.3965880	2.2279350
37	H	2.0823000	-0.2617290	3.5540430
38	H	0.3909120	0.5753770	1.8295860
39	H	1.3575130	-0.2931410	0.6052720
40	H	2.4939800	4.7445580	-0.8763780
41	H	4.1139190	4.0084970	-1.0261060
42	H	3.8156880	5.2743550	0.1966450
43	H	0.5327210	-2.2791380	1.8630640
44	H	-0.0466240	-1.4685310	3.3405400
45	O	1.3893070	-2.8822820	3.6607530
46	H	2.3151490	-2.9401000	3.3629370
47	H	2.9509390	-1.7763620	1.3163420

Table A3.42: Cartesian coordinates (given in angstroms) generated for structure AA, calculated using DFT methods after energy minimisation calculations.

Atom		X	Y	Z
1	O	4.0671950	-2.0890920	-0.8892910
2	C	2.8176260	-2.1272730	-0.9549990
3	C	2.1593620	-1.8880110	-2.3301380
4	N	1.1228540	-0.8786340	-2.2296360
5	C	-0.1283710	-1.2457940	-1.8215670
6	N	-0.8051180	-0.2151530	-1.1882840
7	C	-2.1185880	-0.2276490	-0.7374950
8	C	-3.0676080	-1.2075360	-1.0726440
9	C	-4.3634890	-1.1089770	-0.5799930
10	C	-4.7386000	-0.0470740	0.2382250
11	C	-6.1166310	0.0206970	0.8086740
12	F	-7.0143820	-0.6325520	0.0516940
13	F	-6.1919460	-0.5234140	2.0407860
14	F	-6.5483780	1.2886660	0.9349540
15	C	-3.8011940	0.9322460	0.5708090
16	C	-2.5070590	0.8448140	0.0894400
17	O	-0.6185280	-2.3526230	-2.0379410
18	O	2.0169850	-2.3177000	0.0039780
19	H	1.7037450	-2.8152750	-2.6873570
20	H	2.9168800	-1.5637160	-3.0469980
21	H	1.4882480	0.0273260	-1.9161580
22	H	-0.2405520	0.5775280	-0.8464290
23	H	-2.7815340	-2.0333010	-1.7071160
24	H	-5.0924420	-1.8685900	-0.8454550
25	H	-4.0875780	1.7667690	1.2036210
26	H	-1.7660600	1.5984310	0.3418930
27	C	3.6835400	-1.5168190	2.9970910
28	C	3.9255330	-0.2276900	2.1985980
29	C	2.6281920	0.3666340	1.6600070
30	O	2.9030210	1.6675060	1.1302740
31	P	2.0924110	2.0631040	-0.2181200
32	O	0.6034910	1.9267620	0.0026130
33	O	2.5254880	3.6322370	-0.1927030
34	C	2.0232660	4.4170770	-1.2689190
35	O	2.6730410	1.3766240	-1.4264410
36	O	4.8783010	-0.4280490	1.1817390
37	H	4.3516510	0.5167600	2.8852800
38	H	1.8961850	0.4687490	2.4709190
39	H	2.2039640	-0.2933950	0.8939070
40	H	0.9282550	4.4201470	-1.2663670
41	H	2.3815530	4.0316780	-2.2288220
42	H	2.3890730	5.4346940	-1.1268910
43	H	2.8244930	-1.3677150	3.6735130
44	H	4.5618170	-1.6968390	3.6277210
45	O	3.5318980	-2.6589850	2.1911090
46	H	2.9142950	-2.4840660	1.4314370
47	H	4.5670450	-1.1648240	0.6044060

Table A3.43: Cartesian coordinates (given in angstroms) generated for structure **AB**,  
calculated using DFT methods after energy minimisation calculations.

Atom		X	Y	Z
1	O	3.9647360	-3.4090940	-0.9706170
2	C	2.9031200	-2.7667860	-0.8663970
3	C	2.3024380	-2.2275820	-2.1873430
4	N	1.3421460	-1.1599320	-2.0290190
5	C	0.0811730	-1.4602670	-1.6151160
6	N	-0.6190250	-0.3577950	-1.1447310
7	C	-1.9434240	-0.3132030	-0.7276330
8	C	-2.8428380	-1.3913880	-0.7995830
9	C	-4.1501450	-1.2286020	-0.3583620
10	C	-4.5876630	-0.0097770	0.1536380
11	C	-5.9791710	0.1255240	0.6768000
12	F	-6.8540670	-0.6348230	-0.0053520
13	F	-6.0849190	-0.2509150	1.9677020
14	F	-6.4229570	1.3934490	0.6173530
15	C	-3.7007060	1.0648930	0.2249460
16	C	-2.3954740	0.9173630	-0.2109090
17	O	-0.4062490	-2.5873920	-1.6972930
18	O	2.2577400	-2.5218110	0.1938910
19	H	1.8230390	-3.0609370	-2.7093160
20	H	3.1225940	-1.8726940	-2.8168710
21	H	1.7445870	-0.2463590	-1.8006780
22	H	-0.1128200	0.5339250	-1.0510530
23	H	-2.5096160	-2.3378730	-1.1979190
24	H	-4.8400630	-2.0648580	-0.4225030
25	H	-4.0351190	2.0204300	0.6167390
26	H	-1.6955950	1.7467630	-0.1618930
27	C	2.8096310	-1.3799880	3.0443370
28	C	2.7403730	0.0960390	2.6692360
29	C	2.5339730	0.2964670	1.1814940
30	O	2.5448970	1.7131570	0.9488510
31	P	2.0809390	2.1460820	-0.5534640
32	O	0.5741980	2.1823620	-0.6428610
33	O	2.6750960	3.6560670	-0.4721480
34	C	2.4411010	4.4650830	-1.6215130
35	O	2.8154020	1.3199830	-1.5743210
36	O	3.9474640	0.7246850	3.0709890
37	H	1.8862030	0.5453510	3.2032730
38	H	1.5889520	-0.1512290	0.8496100
39	H	3.3476590	-0.1734000	0.6224340
40	H	1.3679850	4.6120340	-1.7790690
41	H	2.8788820	4.0042130	-2.5130560
42	H	2.9176370	5.4291740	-1.4414310
43	H	1.8035440	-1.8090160	2.9221480
44	H	3.0683890	-1.4387550	4.1091530
45	O	3.7652780	-2.1058540	2.3134730
46	H	3.3026960	-2.3792090	1.4736440
47	H	3.9397810	1.6024270	2.6563700

Table S44: Cartesian coordinates (given in angstroms) generated for structure AC, calculated using DFT methods after energy minimisation calculations.

Atom		X	Y	Z
1	O	4.2523900	-3.6949370	-0.0126030
2	C	3.4702420	-2.7526330	-0.2129030
3	C	1.9796270	-3.1084840	-0.3576820
4	N	1.1402110	-1.9422790	-0.2105110
5	C	-0.2060880	-2.0789530	-0.1758840
6	N	-0.8745950	-0.8719540	-0.0053340
7	C	-2.2482830	-0.6807000	0.0379450
8	C	-3.1953650	-1.6264520	-0.3919780
9	C	-4.5495540	-1.3222880	-0.3363970
10	C	-4.9868770	-0.0865080	0.1341860
11	C	-6.4469950	0.2023440	0.2455110
12	F	-7.1688670	-0.4624180	-0.6735260
13	F	-6.9523840	-0.1493890	1.4458400
14	F	-6.7180860	1.5112540	0.0954960
15	C	-4.0519760	0.8592000	0.5571210
16	C	-2.6995180	0.5682160	0.5099020
17	O	-0.7783980	-3.1686770	-0.2562480
18	O	3.7638910	-1.5243400	-0.3343260
19	H	1.7230620	-3.8573490	0.3973960
20	H	1.8368540	-3.5923350	-1.3357480
21	H	1.5661200	-1.0280720	-0.4060250
22	H	-0.3155000	-0.0635410	0.2979950
23	H	-2.8620210	-2.5852180	-0.7606090
24	H	-5.2736100	-2.0568090	-0.6759390
25	H	-4.3842900	1.8262830	0.9218940
26	H	-1.9606420	1.2937190	0.8399650
27	C	6.1099250	0.6474710	0.7848210
28	C	4.9737600	1.4803030	0.1904420
29	C	3.7569520	1.4759400	1.1040600
30	O	2.7856290	2.4190420	0.6405360
31	P	1.4479850	1.8233970	-0.0620390
32	O	0.3967680	1.4988200	0.9734920
33	O	1.0564680	3.1982040	-0.8430200
34	C	-0.1011730	3.1013210	-1.6673360
35	O	1.7855910	0.7354570	-1.0462950
36	O	4.6357910	1.0489250	-1.1137860
37	H	5.3314350	2.5159670	0.0980410
38	H	4.0427850	1.7677640	2.1195270
39	H	3.3413480	0.4617230	1.1367300
40	H	-0.9747890	2.7997390	-1.0783420
41	H	0.0588190	2.3743590	-2.4699590
42	H	-0.2774220	4.0877630	-2.0976780
43	H	6.5326320	1.1789970	1.6475360
44	H	6.9006820	0.5815010	0.0197290
45	O	5.7080590	-0.6251600	1.2338180
46	H	5.1069440	-1.0254870	0.5509160
47	H	3.9049830	0.4033180	-1.0376200